Controlling Ice Growth – From Nucleation to Recrystallization

Marcus Diamante

B.Sc. Honours Biopharmaceutical Sciences – University of Ottawa, 2018

A thesis submitted to the University of Ottawa in partial fulfillment of the requirements for the Doctorate in Philosophy degree in Chemistry

Department of Chemistry and Biomolecular Sciences
Faculty of Science
University of Ottawa

Candidate	Supervisor
Marcus Diamante	Robert N. Ben

Abstract

The growing demand for advanced cellular therapies has facilitated a substantial need for efficient cryopreservation methods for a wide range of biological materials. As a result, a wide range of novel cryoprotective agents (CPAs) have been investigated to supplement traditional cryopreservation protocols, with the aim to improve not just post-thaw recovery, but post-thaw viability and functional capacity (e.g. proliferation and differentiation). Controlling ice recrystallization is a strategy to improve the outcome of cryopreservation, and small molecule ice recrystallization inhibitors (IRIs) have proven effective for many complex and clinically relevant cell types. The Ben lab has spent over two decades characterizing a diverse library of IRI active CPAs, however the structural requirements for IRI activity are still not fully understood.

The temperature of ice crystal nucleation is also a vital factor impacting cryopreservation outcomes. As an essential step of the cryopreservation process, ice nucleation is the phenomena of an ordered, solid ice embryo forming in supercooled water. Ice nucleation can be considered either homogeneous in pure water, or heterogeneous when a foreign body lowers the energy barrier required for ice nucleation. It has been established in cellular models that it is beneficial to induce controlled, heterogeneous ice nucleation prior to a sample spontaneously nucleating. Through induced nucleation, the degree of supercooling of the sample is limited. This in turn limits thermal shock generated by latent heat release through ice nucleation and can limit the degree of intracellular ice formation observed. The use of induced heterogeneous ice nucleation can also generate a more consistent cryopreservation protocol, as the temperature of spontaneous ice nucleation can be widely variable, even in identically prepared samples.

The research described in this thesis leverages the decades of research from the Ben lab to further the understanding of IRI and ice nucleation activity (INA) of small molecules. This work implements an in-house assay for the characterization of ice nucleation activity. With an understanding of small molecule INA activity, the degree of interaction between small molecule INA and IRI activity is examined herein. In parallel, this work reports synthetically accessible scaffolds containing the structural components required for IRI activity in *N*-functionalized gluconamides. The structure activity relationship investigations elucidate not only a novel set of highly IRI active small molecules, but also an improved understanding of the functional tolerance for further derivatization. Collectively, the work described herein sets the groundwork for the targeted generation of not only specialized small molecule IRIs, but the first attempts to generate dual-action IRI / INA active small molecule CPAs.

Acknowledgements

I would first like to acknowledge my supervisor Dr. Robert Ben; I am continually grateful for affording me the opportunity to learn in a diverse interdisciplinary setting and having the patience to allow me to find my niche within the group research. Providing enough slack to chase a hunch and the guiding perspective to help me discern what I had / hadn't found once I got there; you have allowed me to preform research I am personally invested in and can be proud of.

I would like to acknowledge the members of my thesis advisory committee during my graduate studies: Dr. Fabien Gagosz, Dr. Bill Ogilvie, and Dr. Christopher Boddy have all provided me invaluable feedback throughout the years. Be it keeping me on my toes (I still could not confidently answer "what is hot?") or providing direction to my projects (heptonamides will be on the docket one day!), you have all shaped how I think about / tackle scientific problems and have been supportive of my progress along the way. I would also like to thank Dr. Corrie daCosta for agreeing to join my committee and evaluate my thesis submission; your genuine enthusiasm for research is contagious, and I am appreciative of your time in this process.

Having no practical research experience prior to my graduate studies, I could not have generated a fraction of the work presented in this thesis without the exceptional mentors I have had the opportunity to absorb knowledge from early in my graduate studies. From my first day, Julia Meyer was never shy to call me over and talk me through something she knew I had not seen / done before; even if it was "so I don't have to bother formally teaching you this later", this shotgun exposure to the day in the life of a senior graduate researcher was fundamental to my scientific development. Julia always knew the line between letting me fail on my own (troubleshooting at Maison after) and stepping to tell me I am an idiot before I wasted valuable time or compound. Almost in direct contrast, Dr. David Fabian León Rayo was never spotted without a smile and was always excited about an intermediate I brought over, regardless of the reaction outcomes. David was always generous with his time, be it explaining to me his decision-making process or showing off the new lab gadget he had devised.

Throughout my studies I have grown an appreciation for the idea (championed by Professor Ben) of "learning through osmosis"; having such a wide range of current / previous Ben lab members to talk shop with over the years has not only broadened my scientific understanding, but made the process enjoyable. I would like to specifically acknowledge Victoria Siltamäki, who graciously donated her time and brainpower to help me work through the editing process of this thesis. I would also like to thank the undergraduate students I have had the opportunity to work with throughout my degree; you have each provided unique perspectives and provided me the opportunity to develop as a scientific communicator / teacher.

Outside of the lab I need to acknowledge my family and friends (many of whom I have made throughout my graduate studies) who have supported me through this process. Especially I would like to thank my partner, Leah; for your support and patience, I am forever grateful.

Table of Contents

List of figures

Chapter 1

bars represent the propagated standard deviation of the pooled sample set. **(B)** Scatter plot of the average nucleation temperature calculated for each compound assessed in each solvent. Error bars represent the standard deviation of nucleation temperature for each observed nucleation event. **(C)** Table of nucleation statistics generated for the assessment of the preliminary compound screen in each of the three solvents. For each condition, 30 droplets were loaded onto the assay, and N represents the number of nucleation events observed in the analyzed cooling cycle.

Figure 3.7 Violin plot of the nucleation temperature (T_{nuc} °C) of tested compound set (**Figure 3.5**) solvated in AgI / PBS and PBS. Significance (Two-Way ANOVA, Tukey's PHT, $p < 0.0001$, $n \geq 23$) is indicated as a significant increase in T_{nuc}Avr in green and a significant decrease in T_{nuc}Avr in purple as compared to the respective solvent alone. ǂOnly 3 nucleation events were measured for compound **3.05** at 100 mM in PBS of the 30 droplets assessed.

Figure 3.8 (A) Scatter plot of pooled positive controls (Snomax® ($n = 300$), and AgI / PBS suspension ($n = 89$)) as well as sample preparations of compounds **3.02** and **3.04** at 30 mM in both AgI / PBS and PBS solutions ($n = 30$). **(B)** The same data presented in **(A)** but presented as a violin plot, highlighting the narrow nucleation window observed with compounds **3.02** and **3.04**.

Figure 3.9 (A) Scatter plot of *O*-aryl glycosides bearing a bromine atom (*para*- position) at varying concentrations plotted against the range of measured nucleation ($n = 30$). Linear regression ($R^2 = 0.71$) is generated from the pooled set of *O*-aryl glycosides across all tested conditions. **(B)** Violin plot of 30 mM **3.02** in PBS prepared at different droplet volumes ($n = 30$).

Figure 3.10 Example droplets of **3.02** dissolved in PBS loaded into the Freeze-Float assay at various droplet volumes.

Figure 3.11 (A) *p*-Chlorophenyl pyranoside generated by Waren Mendizza for assessment of INA activity. **(B)** *p*-Chlorobenzyl functionalized Wittig salt generated by Sarah Musca for assessment of INA activity.

Figure 3.12 (A) Scatter plot of average nucleation temperature for *O*-(*p*-halo)-pyranosides solvated in PBS with respect to concentration ($n = 30$). **(B)** Violin plot of the same data presented in **(A)**, note that due to the grouped nature of data input, the x-axis depicts the concentration tested directly, and is not linearly scaled.

Figure 3.13 (A) Violin plot of average nucleation temperatures for compound **3.07** assessed at varying concentrations in either AgI / PBS or PBS solvent ($n \geq 29$). ǂ100mM **3.07** solvated in AgI / PBS only observed 14 nucleation events. **(B)** IRI activity of compound **3.07** in PBS when assessed on the modified SCA. Four-parameter dose response curve is generated for the compound, and the resulting IC_{50} value is 21 mM.

Figure 3.14 (A) Ice recrystallization inhibition activity measured for each compound. Reference values taken in the absence of AgI, IC_{50} values normalizing the rate of ice crystal growth to PBS, and IC_{50} values normalized to the AgI / PBS. **(B)** Example four-parameter dose response curve generated for model IRI compound **4.01**, treated with each of the three conditions outlined in **(A)**.

Chapter 4

Figure 4.1 General structure of *N*-aryl gluconamides.

Figure 4.2 A visual representation of the data obtained through the modified SCA for the known IRI **4.01**. Ice crystal images are obtained following a 5-minute annealing period at -6.4 °C. In the absence of **4.01** (PBS control) ice crystals (examples outlined in red) grow larger than those in the presence of an 8 mM solution of **4.01**. A dose response relationship can be generated from obtained ice crystal images for a given compound (fit to a nonlinear four-parameter dose response curve) and the IC_{50} can be extracted. Ice crystal images are scaled to equivalent magnification (scale bar = 0.1 mm).

Figure 4.3 *N*-aryl gluconamide IRIs tested on the original 30-minute SCA, %MGS is measured at 22 mM unless otherwise specified. %MGS values were extracted with the use of a plot digitizer from previously reported bar-graphs. **(A)** *N*-aryl gluconamides used as the training set for 3D-QSAR model calibration. **(B)** *N*-aryl gluconamides which were predicted by the 3D-QSAR model as potentially possessing IRI activity (%MGS < 70 % at 22 mM). Subsequent IRI activity measured (%MGS) is indicated beside each derivative. **(C)** *N*-aryl gluconamides which were predicted by the 3D-QSAR model to likely not be IRI active (%MGS > 70 %). Subsequent IRI activity measured (%MGS) is indicated beside each derivative.

Figure 4.4 Previously synthesized *N*-functionalized small molecule carbohydrates, assessed with the original 30-minute SCA, %MGS is measured at 22 mM. Listed %MGS values were extracted with the use of a plot digitizer from previously reported bar-graphs. **(A)** Selected **3.02** derivatives generated, including C_3 and C_6 *N*-glycosidated glucosamine compounds. **(B)** *N*-cycloalkyl gluconamide and *N*-cycloalkyl arabinose derivatives bearing various cycloalkyl ring sizes.

Figure 4.5 Aryl pyranose IRIs bearing various ring functionalization. IC_{50} values were obtained on the modified SCA in PBS, compounds indicated with an IC_{50} value of N/A failed to achieve a relative rate of ice crystal growth below 50% before becoming solubility limited. Author of first publication is indicated for each derivative. Listed IC_{50} values were extracted with a plot digitizer from previously reported bar-graphs. **(A)** Reference small molecule carbohydrates. **(B)** Phosphonate and ammonium containing small molecule carbohydrate derivatives. **(C)** Small molecule *O*-aryl pyranoside derived (**3.02**, **3.03**) compounds bearing an azide functional group.

Figure 4.6. C_6-modified *N*-aryl gluconamide derivatives. IRI activity was assessed on the original 30-minute SCA. Only one representative concentration was selected for representation in this figure as compound solubility and assessed concentrations varied between compounds. Listed %MGS values were extracted with the use of a plot digitizer from previously reported bar-graphs.

Figure 4.7 Truncated derivatives of IRI **4.01** and the four-parameter dose response curve for each compound. IC_{50} values were obtained on the modified SCA, compounds indicated with an IC_{50} value of N/A failed to achieve a relative rate of ice crystal growth below 50% before becoming solubility limited. All compounds were assessed up to the measured aqueous solubility limit in PBS at room temperature.

Figure 4.8 Truncated derivatives of IRI **4.02** and the four-parameter dose response curve for each compound. IC_{50} values were obtained on the modified SCA, compounds indicated with an IC_{50} value of N/A failed to achieve a relative rate of ice crystal growth below 50% before becoming solubility limited. All compounds were assessed up to the measured aqueous solubility limit in PBS at room temperature.

Figure 4.9 Truncated derivatives of IRI **4.03** and the four-parameter dose response curve for each compound. IC_{50} values were obtained on the modified SCA, compounds indicated with an IC_{50} value of N/A failed to achieve a relative rate of ice crystal growth below 50% before becoming solubility limited. All compounds were assessed up to the measured aqueous solubility limit in PBS at room temperature.

Figure 4.10 Truncated derivatives of IRI **4.04** and the four-parameter dose response curve for each compound. IC_{50} values were obtained on the modified SCA, compounds indicated with an IC_{50} value of N/A failed to achieve a relative rate of ice crystal growth below 50% before becoming solubility limited. All compounds were assessed up to the measured aqueous solubility limit in PBS at room temperature.

Figure 4.11 The four-parameter dose response curve for C_4-deoxy-*N*-aryl gluconamide derivatives of IRIs **4.01** and **4.04**. IC_{50} values were obtained on the modified SCA, compounds indicated with an IC_{50} value of N/A failed to achieve a relative rate of ice crystal growth below 50% before becoming solubility limited. All compounds were tested up to the measured aqueous solubility limit in PBS at room temperature.

Figure 4.12 The four-parameter dose response curve for hydroxyhexylamide derivatives of **4.01**. IC_{50} values were obtained on the modified SCA. All compounds were tested up to the measured aqueous solubility limit in PBS at room temperature.

Chapter 5

Figure 5.1 Surfactant derived IRIs tested on the original 30-minute splat cooling assay. The percent mean grain size (%MGS) is measured at 22 mM unless otherwise specified. **(A)** *N*-alkyl-2-(α-D-galactosyl)-ethylamides, assessed at either 22 mM (n = 0 – 7) or 5.5 μM (n = 6 – 16).[3] **(B)** *O*-(octyl)-β-D-pyranosides assessed for IRI activity at 22 mM.

Figure 5.2 Correlation of *N*-alkyl aldonamide IRI activity (%MGS at 22 mM) and the amphiphilicity of the substrate. Data points were extracted with the use of a plot digitizer from previously reported scatter plot for use of trendline generation and statistics. [*] *N*-hexyl-D-gluconamide was excluded from the linear regression. **(A)** Linear correlation (R^2 = 0.84) between IRI activity (%MGS) and the ratio of polar surface area to total molecular surface area (calculated by MarvinSketch™). 95 % confidence bands are indicated with dashed lines. **(B)** Linear correlation (R^2 = 0.84) between IRI activity (%MGS) and the proportion of methylene units present on the alkyl extension with respect to hydroxyls present on the carbohydrate chain. 95 % confidence bands are indicated with dashed lines.

Figure 5.3 Correlation of *N*-alkyl aldonamide IRI activity (%MGS at 22 mM) against the amphiphilicity of the substrate. Data points were extracted with the use of a plot digitizer from previously reported scatter plot for use of trendline generation and statistics. Linear regressions are calculated for the data set as a whole (Black trendline, R^2 = 0.01), just for *N*-cycloalkyl-D-arabinosides (Blue trendline, R^2 = 0.003), and just for *N*-cycloalkyl-D-gluconamide substrates (Red trendline, R^2 = 0.98).

Figure 5.4 *N*-alkyl-D-gluconamide substrates assessed on the modified SCA. Compound identification number, alkyl size, and IRI activity (IC_{50} value) are indicated for each substrate. **(A)** Linear *N*-alkyl-D-gluconamides assessed for IRI activity. **(B)** *N*-cycloalkyl-D-gluconamides assessed for IRI activity. **(C)** *N,N*-dialkyl-D-gluconamides assessed for IRI activity. *The IC_{50} value of compound **5.04** is extrapolated for use as a frame of reference due to solubility limitations not allowing for a complete dose-response curve to be obtained.

Figure 5.5 Correlation between alkyl size (n = total number of methylene units present in *N*-functionalization minus 2, as directly shown in structural representation) and apparent aqueous solubility in PBS at room temperature.

Figure 5.6 IRI activity and cytotoxicity of *N*- and *N,N*-hexyl gluconamide compounds. Technical replicates (n) are represented as the smallest number of wells utilized for a tested concentration within the sample set. **(A)** IRI activity of *N*- and *N,N*-hexyl gluconamides in PBS when assessed on the modified SCA. Dose response relationship is generated for each compound, and the resulting IC_{50} value is indicated in **Figure 5.4**. **(B)** Cellular viability of *N*- and *N,N*-hexyl gluconamides when assessed in HepG2 cells following 24-hour incubation utilizing a metabolic indicator of cellular death (the resazurin cellular viability assay). **(C)** Assessment of membrane cytotoxicity of linear *N*- and *N,N*-hexyl gluconamides, assessing cellular viability both metabolically (resazurin stain) as well as with a membrane indicator of cellular death (lactate dehydrogenase (LDH)) in HepG2 cells following 24-hour incubation.

Figure 5.7 Truncated derivatives of **5.04** and the dose response curve for each compound. IC_{50} values were obtained on the modified SCA, compounds indicated with an IC_{50} value of N/A failed to achieve a relative rate of ice crystal growth below 50%. All compounds were tested up to the measured aqueous solubility limit in PBS at room temperature.

Figure 5.8 Comparison of IRI activity for *N*-functionalized gluconamide (square icon) and *N*-functionalized 6-hydroxyhexylamide derivative (triangle icon). Four-parameter dose response relationship is generated for each compound using the modified SCA.

Figure 5.9 Four-parameter dose response relationships to compare *N*-alkyl gluconamides (square icons) to the respective *N*-alkyl-6-hydroxyhexanamides (triangle icons). IC_{50} values were obtained on the modified SCA, compounds indicated with an IC_{50} value of N/A failed to achieve a relative rate of ice crystal growth below 50%. All compounds were tested up to the measured aqueous solubility limit in PBS at room temperature.

Figure 5.10 IRI activity and cytotoxicity of *N*-hexyl and *N*-octyl 6-hydroxyhexanamide derivates and the corresponding *N*-alkyl gluconamide. **(A)** Cellular viability of HepG2 cells measured metabolically with resazurin cellular viability assay following 24-hour incubation. n ≥ 5, N = 1 for *N*-hexyl compounds (**5.02**, **5.13**), n ≥ 11, N = 1 for *N*-octyl compounds (**5.04**, **5.14**). **(B)** Data summary of IRI activity (presented in **Figure 5.9**) and cellular viability. Compounds indicated with an LD_{50} value of N/A failed to achieve a relative viability below 50% prior to the maximum aqueous solubility.

Figure 5.11 IRI activity and cytotoxicity of *N*-(2-(2-methoxyethoxy)ethyl)-gluconamide (**5.18**) and *N*-alkyl gluconamides of similar chain length. **(A)** The four-parameter dose response curve for each compound. **(B)** Cellular viability of HepG2 cells measured metabolically with resazurin cellular viability assay and by membrane integrity (LDH assay) following 24-hour incubation.

Figure 5.12 Computational assessment of **4.01** derived model compounds. Optimized geometry is visualized as ball and stick diagrams with Chemcraft software. Hydrogen bonding interactions are represented with a dashed white line (hydrogen bonding length ≤ 2.0 Å). IRI activity for each compound is represented with the four-parameter dose response curve obtained from the modified splat cooling assay.

Figure 5.13 Computational assessment of compound set relating to known IRI **4.01** targeting the ability for C_4 to hydrogen bond with the amide. Each compound indicator number, legend symbol and line structure are represented above or below the respective ORCA optimized 3-dimensional structure. Optimized geometry is visualized as ball and stick diagrams with Chemcraft software. Hydrogen bonding interactions are represented with a dashed white line (hydrogen bonding length ≤ 2.0 Å). IRI activity for each compound is represented with the four-parameter dose response curve obtained from the modified SCA.

Figure 5.14 Computational assessment of compound set relating to **5.14**, targeting the tolerance for hydrogen bond acceptor at the C_4 position. Compound **5.14** is represented in both the lowest energy CREST optimized geometry (Left), as well as the lowest energy conformation found by CREST to contain an intramolecular 9-membered ring (Right). Optimized geometry is visualized as ball and stick diagrams with Chemcraft software. Hydrogen bonding interactions are represented with a dashed white line (hydrogen bonding length ≤ 2.0 Å). The distance between N-**H** and C_6-**O**H is indicated (in white text, Å) for compounds **5.20** and **5.23** to highlight the similarities between conformations. IRI activity for each compound is represented with the four-parameter dose response curve obtained from the modified SCA.

Appendix III

Figure A1 Example shell script input for the CREST conformation search of compound **4.01** .xyz input file.

Figure A2 (A) Example structural input file for the ORCA optimization of compound **4.01** which was extracted following CREST optimization (**Figure A1**). **(B)** Example shell script used in conjunction with the structural input file to direct the ORCA optimization suite.

Figure A3 Example workflow for analysis of ice nucleation events. **(A)** Automatically generated spreadsheet obtained from temperature logger. Time, sample number, and channel temperatures are copied from this sheet into the analysis sheet. **(B)** Identification of a nucleation event (outlined with a light blue box), whereby the image creation date is extracted, and used to denote a nucleation event on the analysis sheet (highlighted in red). **(C)** Example analysis sheet, containing temperature data (purple box), whereby the input of a given time (red box) will automatically report the temperature logged at that time. Average nucleation temperature can be extracted from each measured nucleation event.

List of schemes

Chapter 4

Chapter 5

List of tables

Chapter 3

List of abbreviations

%MGS	Percent Mean Grain Size
.inp	ASCII input file
.mol	MDL Molfile
.sh	Bourne shell script
µL	Microlitre
Ac_2O	Acetic anhydride
AcOH	Acetic acid
AFGP	Antifreeze glycoprotein
AFP	Antifreeze protein
ALPB	Analytical Linearized Poisson–Boltzmann
ANOVA	Analysis of variance
$BF_3•OEt_2$	Borontrifluoride diethyletherate
BnBr	Benzyl bromide
br	Broad
CAS	Chemical Abstracts Service
$CDCl_3$	Deuterochloroform
cm	Centimeter
CNT	Central Nucleation Theory
CPA	Cryopreservation agent
CPCM	Conductor-like Polarizable Continuum solvent Model
CREST	Conformer-Rotamer Ensemble Sampling Tool
d	Doublet
D_2O	Deuterium oxide
DCC	Dicyclohexylcarbodiimide
DCM	Dichloromethane
DIPEA	Diisopropylethylamine

DIS	Dynamic Ice Shaping
DMAP	Dimethylaminopyridine
DMF	*N,N*-Dimethylformamide
DMP	2,2-Dimethoxypropane
DMSO	Dimethyl sulfoxide
DPBS	Dulbecco's Phosphate-Buffered Saline
EI	Efficacy Index
Et_2O	Diethyl ether
Et_3N	Triethylamine
EtOAc	Ethyl acetate
EtOH	Ethanol
FBS	Fetal Bovine Serum
GCC	GNU Compiler Collection
GFN2-xTB	General Fragment Neural network 2 - extended Tight-Binding
GMP	Good Manufacturing Practice
H_2SO_4	Sulfuric acid
HBTU	N,N,N',N'-Tetramethyl-*O*-(1H-benzotriazol-1-yl)uranium hexafluorophosphate
HCl	Hydrochloric acid
HepG2	Human hepatocellular carcinoma
I_2	Iodide
IC_{50}	Concentration required for 50% inhibition
ICP-MS	Inductively Coupled Plasma Mass Spectroscopy
IIF	Intracellular Ice Formation
iMTD-GC	Iterative Meta-Dynamics - Genetic structure Crossing algorithms
INA	Ice nucleating agent
INDe	Isochoric nucleation detection device
INT	Iodonitrotetrazolium chloride

IRI	Ice recrystallization inhibitor
K_2CO_3	Potassium carbonate
kcal	Kilocalorie
KH_2PO_4	Monopotassium phosphate
LD_{50}	Concentration required for 50% cellular death
LDH	Lactate dehydrogenase
LED	Light emitting diode
LRMS	Low-resolution mass spectroscopy
m	Multiplet
MeCN	Acetonitrile
MeI	Iodomethane
MEM	Minimum Essential Medium
MeOD	Tetradeuteromethanol
MeOH	Methanol
MHz	Megahertz
mL	Milliliter
mm	Millimeter
MSA	Molecular surface area
Na_2CO_3	Sodium carbonate
Na_2SO_3	Sodium sulfite
Na_2SO_4	Sodium sulfate
$NaCNBH_3$	Sodium cyanoborohydride
NAD(P)H	Nicotinamide Adenine Dinucleotide (Phosphate)
NaH	Sodium hydride
NaOMe	Sodium methoxide
NEAA	Non-Essential Amino Acid
NH_4Cl	Ammonium chloride

NMR	Nuclear Magnetic Resonance
PBS	Phosphate-Buffered saline
Pd/C	Palladium on activated carbon support
PEG	Polyethylene glycol
Pen-Strep	Penicillin-Streptomycin
PHT	Post Hoc Test
P_L	Lower plateau
PPh_3	Triphenylphosphine
ps	Picosecond
PSA	Polar surface area
P_T	Upper plateau
PTSA	*p*-Toluenesulfonic acid
px	Pixel
q	Quartet
QLL	Quasi-Liquid Layer
quin	Quintet
RCF	Rate Controlled Freezer
ROI	Region of interest
s	Singlet
SCA	Splat Cooling Assay
StdEnv	Standard software environment
t	Tripplet
T_{avr}	Average temperature
TBDMSCl	*tert*-Butyldimethylsilyl chloride
^tBuOH	*tert*-Butyl alcohol
Tf_2O	Trifluoromethanesulfonic anhydride
TFA	Trifluoroacetic acid

T_g	Glass transition temperature
T_h	Homogenous ice nucleation temperature
THF	Tetrahydrofuran
TINA	Twin-plate Ice Nucleation Assay
TLC	Thin-Layer Chromatography
T_m	Melting point
TMA	Trimethylaluminum
T_{nuc}	Nucleation temperature
T_{nuc}Avr	Average nucleation temperature
TWE	Transient Warming Event
UW	University of Wisconsin hypothermic storage media
v_{norm}	Normalized rate of ice crystal growth
wt.%	Weight percent (mass per volume)

1. Introduction

1.1 Biopreservation

The generation and application of biological materials and biological therapies has become a highly valuable component of modern healthcare.[1,2] The stability, transportation and storage of biological commodity items are of particular interest with the rapid development of modern biotherapeutics. There are arguably four major methods for storing and preserving biological materials, each presenting a unique set of considerations to be made when prior to application. Three of the major biopreservation methods rely on storage at low temperatures, whereby chemical reactions (and by extension cellular metabolism and stress) are slower as a function of lower temperature.[3] Interestingly, specialized methods have been developed which do not rely on reduced temperature to delay the onset of biological decomposition. Normothermic storage utilizes specialized perfusion machines designed to keep a target organ functional outside of the human body.[4] This method focuses on the preservation of whole organs, primarily for short term transport (several hours) prior to transplantation. First demonstrated with the preservation of kidneys[5,6] and then liver,[7–9] whole organs can be stored at physiological temperature. The organ is administered oxygenated blood and medications as needed while attached to a perfusion machine. This approach has been found to reduce organ waste, and increase storage time for liver transplantation when compared to traditional cold storage.[9] However, this highly engineered solution is only currently applied to two major organ systems, and is reliant on cost prohibitive patented products. In addition, the use of normothermic storage relies on perfusion and can not be applied without existing vasculature; this prohibits the application of normothermic storage to smaller tissue or cellular systems and is not a broadly applicable method. The growing field of biopreservation allows for the rational design of hyper-specific solutions to address a single fragment sector such as short-term whole liver preservation; the ingenuity of normothermic devices (and their success) help to rationalize the targeted design of novel cryopreservation agents described in this thesis.

1.1.1 Hypothermic storage

The simplest method of biopreservation, utilized specifically for short term storage (hours to days) of highly complex biological materials (such as whole organs) is hypothermic storage; holding the material of interest slightly above the freezing point, this method of biopreservation is widely applicable for complex material on large scale and does not strictly require the utilization of any specialized devices or chemical additives. The major considerations when designing

hypothermic storage protocol for organs, is the mitigation of oxidative stress and inflammatory response;[10] this damage is a direct result of cooling the hypoxic organ, generating radical oxygen species and cytokines within the preserved tissues. During hypothermic storage temperatures are not low enough to completely halt metabolic processes; as a result, metabolically active cells will rapidly deplete adenosine triphosphate reserves generating excess adenosine diphosphate, and depolarizing cellular membranes.[10] To combat cellular damage and reperfusion injury, several preservation solutions have been developed[11–13] and assessed[14–18] in the hypothermic preservation of biological materials. The optimized use of modern hypothermic storage formulations are capable of storing fragile cell lines for several days.[19]

Modern adaptations to basic hypothermic storage have been developed in recent years; primarily, the use of alginate hydrogels have been utilized to greatly improve the hypothermic storage of fragile cell material.[20–24] Related freeze-avoidance techniques have also been developed,[25,26] pushing storage below 0 °C without the formation of ice through the generation of supercooled solutions. The use of chemical additives such as polyethylene glycol,[27] 3-*O*-methylglucose,[25] or concentrated hypothermic storage media (such as UW[13] or HypoThermosol)[28] have been shown to successfully depress the freezing temperature of hypothermic storage media; this depression allows for storage at lower temperatures, increasing the effective storage time. The use of a physical barrier (such as oil) has also been utilized, allowing for the storage of biological materials in a supercooled state without the formation of ice.[26,29]

1.1.2 Vitrification

In stark contrast to the mild, short-term (hours to days) storage accessible with hypothermic storage techniques, vitrification is the most extreme of the biopreservation strategies. Utilizing the fastest cooling / warming rates, lowest storage temperature, and highest concentration of chemical additives required. When applied successfully, vitrification can effectively store biological material for 10+ years.[30] Overall, vitrification can be defined as the process by which a liquid solution transitions to the solid state through an extreme increase in viscosity, avoiding ice nucleation and subsequent crystallization (**Figure 1.1**);[31] if done under ideal conditions, there is no cellular damage as a result of ice during the cooling process.[30,31] There are several methodologies to achieve traditional vitrification of a sample, with the key components being high solute concentrations and high rate of cooling.[32] The replacement of a large proportion of water with a polar organic solvent (most commonly dimethyl sulfoxide (DMSO) or glycerol) depresses not only the melting point of a solution, but also the ice nucleation temperature.[31] Simultaneously, the use of direct liquid nitrogen submersion allows for a rapid rate of cooling where molecules in

solution do not have enough time or energy to orient into an ordered crystal lattice, preventing ice nucleation.[32] With the nucleation temperature of the solution greatly lowered (~ -80 °C) by the addition of organic additives (20 – 60 wt%), the rapid cooling of the sample can achieve the glass transition temperature (whereby the sample viscosity becomes high enough to prohibit molecular movement, and in turn the generation of a crystal lattice, typically ~ -120 °C) prior to an ice nucleation event.[31] During storage it is imperative that the amorphous solid remains stable to allow for long term storage (10+ years) of the sample.[33]

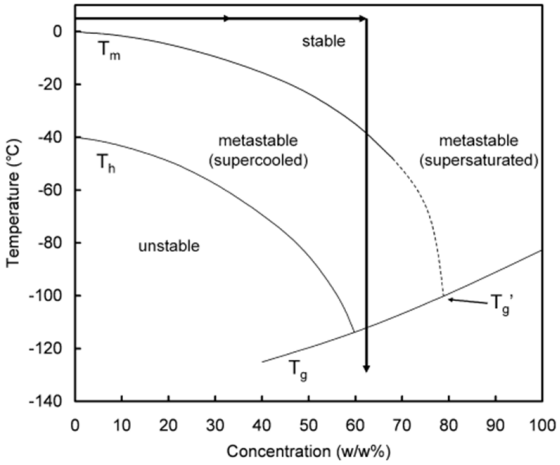

Figure 1.1 Phase diagram of non-equilibrium vitrification, whereby the melting point (T_m), homogenous ice nucleation temperature (T_h), and glass transition temperature (T_g) are plotted as a function of CPA (glycerol) concentration. T_g' is the intersection of T_m and T_g, representing when vitrification will successfully occur. T_m is represented as a whole line when stable, and as a dashed line once below the eutectic temperature. This diagram is reproduced from Wowk[34] with licence (6062010812934) from Elsevier without modification.

Despite the allure of long-term storage without cellular decomposition or the formation of ice, several key challenges exist to the successful application of vitrification for biological material. The most immediate challenge with traditional vitrification is the requirement for high concentrations of cytotoxic additives (such as DMSO or glycerol), which require specialized techniques for both the addition and removal.[35,36] Significant physical challenges also exist, as the extremely rapid cooling rates afforded by a direct liquid nitrogen plunge (> 10,000 °C / min)[37] are not accessible (or easily implemented) for sample warming. If sample warming is too slow, intercellular ice formation will occur rapidly which is extremely detrimental to the sample.[35] Alternatively, if sample heating is too fast or non-uniform, sample shearing or torsion will occur during the warming process.[38] Consequently, the warming of vitrified samples remains the largest challenge for successful implementation. Modern adaptations have attempted to mitigate the

mechanical considerations which must be made during the vitrification process,[39–41] however thin, robust, uniform samples of small volume (such as plant shoots[42–44] and gametes[45–49]) will be the most conducive to traditional vitrification protocol. Despite being the primary focus for vitrification research for almost a century, the vitrification of whole organs remains elusive without major caveats.[50–54] Currently the broad application of vitrification as a general method of biopreservation remains theoretical.

1.1.3 Cryopreservation

The most flexible and widely applied method of biopreservation for cells and tissues is cryopreservation. Similar to vitrification, storage of cryopreserved material occurs at very low temperatures (typically below -120 °C), however the cooling and warming processes are both controlled (and extremely slow with respect to vitrification). The process of cryopreservation includes several vital events, each of which will be described in the subsequent sub-sections; these include: the suspension of biological material into aqueous media (including any supplemental additives), controlled cooling of the sample, initiation of the first ice nucleation event, long term storage at the hold temperature, controlled warming following storage, as well as final washouts and resuspensions as required. The overarching goal of all work presented in this thesis is the improved control of ice during cryopreservation and the mitigation of cellular damage caused by ice during the cryopreservation process. Subsequent sections will outline in detail the cryopreservation process, and the considerations that need to be made when designing effective cryopreservation protocol. These considerations will shape the rational design of the work described in this thesis and serve to provide a broader prospective as to the application of this work.

1.2 Cryomedia and cryoprotective agents

For cryopreservation to occur, the target biological material first needs to be suspended in the chosen cryopreservation solution; the basis of any cryopreservation solution addresses similar concerns as traditional normothermic culture media for the given biological component. The chosen media will be pH buffered (typically with the addition of phosphates or bicarbonates), and supplemented with energy containing compounds (such as adenosine or glucose) as well as additional ions (generally Na^+ and K^+ salts).[14] These components will support the survival of the cells over time under standard culture conditions, but to prepare the biological material for cryopreservation, several other additives need to be included into the cryopreservation solution.

For almost a century, it has been known that the addition of high viscosity, polar organic molecules, which do not ionize in solution is beneficial to the outcomes of cryopreservation;[55–57] these compounds which are typically cytotoxic at physiological temperatures, have been identified as playing several key roles to protect the cell during the cooling and warming processes. The most common additive beyond traditional cellular media is a cellularly penetrating polar organic molecule; these compounds (most commonly DMSO, glycerol or ethylene glycol) are capable of replacing water within a cell, protecting the cell from a number of damage vectors during the cooling and warming processes.[14,58,59] The mechanisms by which these cell permeable additives aid cryopreservation will be explained in detail when discussing the cooling process (**Section 1.3**). With respect to the composition of cryopreservation solutions, the use of 10 wt.% DMSO has become a standard starting point for general cryopreservation protocol.[60]

Additional additives may be included to address a specific vector of cellular damage that the biological material of interest is susceptible to. One prominent example is the addition of an ice recrystallization inhibition (IRI) agent, which is designed specifically to mitigate the growth of ice crystals during periods of cooling and warming; the proposed mechanism of these additives will be explained in detail (**Section 1.3.2**), but in general, these compounds serve to supplement the protection afforded by a permeating agent such as DMSO. Hydroxyethyl starch is another common cryopreservation additive,[61] it is unable to penetrate into the cell but is able to regulate the transfer of water across the cellular membrane;[62] this is of particular interest for highly hydrated cellular systems such as red blood cells.[63] Similarly, the addition of trehalose has been found to efficiently stabilize cellular proteins,[64,65] which can be particularly useful when utilizing high cooling rates, or when freeze-drying samples.

The choice of media, osmotic regulator, and additional cryoprotective agents (CPAs) form the basis of cryopreservation protocol fundamentals and will dictate the subsequent choices made when designing a cryopreservation protocol. Ideally one cryopreservation method would fit all substrates, however when considering different cell sizes, permeability, complexity, fragility, metabolism etc., the use of specialized cryopreservation solutions and methodology for each given application are often required. Proprietary cryopreservation solutions are commercially available (such as CryoStor® or BloodStor®) to begin cryopreservation investigations, however adjustments or additives are typically required to optimize individual cell outcomes.

1.3 Cooling the biological material

Once the cryopreservation solution is chosen, and the material of interest is prepared for storage, the sample can begin cooling. Unlike vitrification, where cooling is achieved by a direct plunge in liquid nitrogen, cryopreservation requires a controlled cooling rate,[66,67] whereby the ideal cooling rate will vary depending on the chosen cell type.[68–70] The two key components to consider for this cooling process is the permeability of the cellular membrane, and the formation of ice.[70] As previously described, the use of a permeating CPA (such as glycerol or DMSO) is required for successful cryopreservation (**Figure 1.2**); without intracellular replacement of water, once the system cools and ice forms, intra-cellular ice formation (IIF) will occur, which can be extremely detrimental to the biological material.[71] Beyond IIF, once extracellular ice is formed, many solutes are excluded from the ice lattice and concentrated at the boundary between ice crystals. This local increase in concentration of solutes is detrimental as it will actively dehydrate the surrounding cells, and can shift the local pH (commonly termed solute effects).[72]

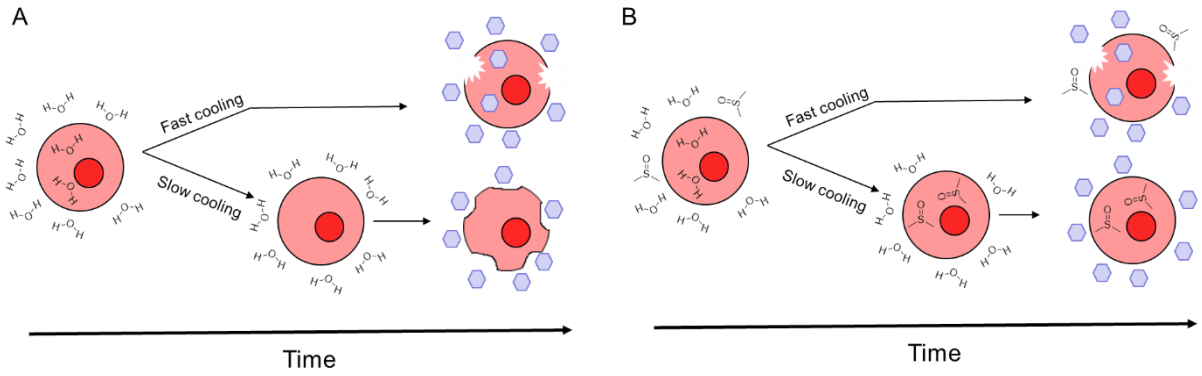

Figure 1.2 Generic visual representation of the consequences of altered cooling rates as described by Mazur.[73] **(A)** Generic cellular response to cooling in the absence of an adequate osmotic regulator (such as DMSO). **(B)** Generic cellular response to cooling in the presence of an osmotic regulator (DMSO).

The use of additives such as DMSO or glycerol, increase membrane permeability, promoting the replacement of intracellular water with CPAs, protecting against IIF and solute effects.[68] The rate of cooling will have a direct effect of the ability of CPAs to protect cells from mechanical and osmotic damage (**Figure 1.2**). If the rate of cooling is too slow, solute effects are accentuated causing an increase in osmotic damage and dehydration; if the cooling rate is too fast, intracellular water will not be completely displaced causing increased IIF.[73,74] In theory, each cellular system possesses an optimal cooling rate to minimize both IIF and damage from solute effects, however,

it is understood that the composition of cryopreservation solution will also have an effect on the optimal cooling rate for a system.[75]

1.3.1 Ice nucleation

Ice nucleation is a requisite part of the cryopreservation freezing process, it occurs when an ordered ice nucleus is formed, which then promotes the orientation of surrounding water molecules into an ice crystal lattice.[76] Ice nucleation by nature is a stochastic event,[77] whereby random fluctuations in fluid density can give rise to the formation of an ice nucleus. The probability of homogenous (without external influence in pure water) ice nucleation is loosely correlated to the activity (solutes present / solute concentration, pressure, volume, shape) of water,[78,79] typically occurring between – 20 °C and – 38 °C.[80] As homogeneous nucleation occurs well below the melting point of a solution, it will remain in a metastable, supercooled state until ice nucleation occurs. As discussed previously (**Section 1.1.1**), the supercooling of solutions forms the basis of natural[81,82] and modern freeze-avoidance preservation strategies;[25,26] however, when cooling at a controlled rate well below the nucleation temperature of a solution (during the cryopreservation process) ice nucleation is unavoidable.

During cryopreservation, induced heterogeneous ice nucleation has been found to be beneficial to cryopreservation outcomes.[83–87] Should the formation of an ice nucleus be promoted by an external factor (localized temperature shift,[88] electrical shock,[89] magnetic field,[90] pressure shift,[91] chemical additive,[84] or a physical particle[92]) it is deemed to be heterogeneous ice nucleation and will occur prior to the homogeneous nucleation temperature. The benefit of inducing ice nucleation prior to homogeneous nucleation is to limit the degree of supercooling in a sample.[93] Thermodynamically, the degree of supercooling will directly control the magnitude of thermal shock imparted on the system as a result of exothermic ice formation.[93] Beyond latent heat release, the degree of supercooling has also been found to influence the damage caused by IIF and osmotic effects;[94–96] whereby a given cell type may possess not only an optimal cooling rate, but also an optimal heterogeneous nucleation temperature.[96]

The mechanism of ice nucleation has been well established, with a central nucleation theory[97–99] defining the variables involved in influencing the probability of ice nucleation.[100] Extensions from the central nucleation theory have established thermodynamic models to accurately calculate the free energy required to form a solid nucleus within a bulk liquid.[101,102] In practice, an efficient cryopreservation protocol will induce (or delay) ice nucleation to a specific temperature opposed

to relying on stochastic events; subsequent sub-sections will describe common methods and applications of ice nucleation control.

1.3.1.1 Inducing ice nucleation

The classical nucleation theory defines four key variables to influence the probability of ice nucleation: the melting point of the solution (degree of supercooling), the interfacial tension between ice nucleus and water, the presence (and shape / size) of foreign bodies, and the kinetic ability for water to interact with the ice nucleus.[100] The simplest variable to manipulate with respect to inducing ice nucleation is the addition of foreign bodies; whereby a particle in suspension will lower the free energy of the system at the particle – solvent boundary, increasing the probability of nucleation to occur around the particle.[103,104] For a given particle, three major factors can dictate the magnitude of impact when considering ice nucleation: the size / shape of the particle,[105–108] hydrophobicity,[109–111] and surface similarity to crystalline ice[92] (lowering interfacial tension). The use of heterogeneous particles (such as silver iodide (AgI))[92,110,112,113] has been widely studied in the field of atmospheric science,[114–116] but has not translated to the field of cryopreservation; additives such as AgI, bacterial extracts, and natural proteins have found applications in the food sciences,[117,118] but are not viable good manufacturing practice (GMP) options for cellular applications.

Without the addition of heterogeneous foreign particles, ice nucleation can be induced through modulation of the interfacial tension between solid ice nuclei and water; this approach is what facilitates the anti-freeze function of natural anti-freeze proteins[119–121] as well as novel techniques such as electrical shock,[89] or the application of magnetic fields.[90] As ice nuclei form, the more similar in orientation the surrounding water molecules are, the lower in energy the interface becomes, and the more stable (more likely to persist) the ice nucleus becomes.[100] The orientation of bulk water molecules (be it chemically, electrostatically or magnetically) into an ice-like lattice will lower the interfacial tension should an ice nucleus form, increasing the probability of a successful nucleation event to occur.

The most common method of induced ice nucleation utilized in cryopreservation protocols is through dramatic temperature cycling, either through a drastic shift in cooling rates (shock cooling) or physically touching the exterior of the sample with a pre-cooled metal instrument (seeding).[122–124] By dramatically lowering the temperature below the melting point and increasing the degree of supercooling, ice nucleation is induced. One major consideration when inducing nucleation through seeding is the directional growth of ice.[93,125] The directional growth of ice may be

detrimental to the cryopreservation of sensitive cell types when compared to uniformly (more homogeneous) induced ice nucleation.

1.3.1.2 Suppressing ice nucleation

The simplest approach to the suppression of ice nucleation is the physical removal of any ice nucleator, forcing ice nucleation to occur homogeneously; this strategy is employed by the surface-sealing supercooling methods described previously (**Section 1.1.1**).[26,29] Another direct method is the suppression of the melting point of a solution; this approach is heavily utilized in the vitrification process with the addition of high concentrations of polar organic molecules (such as DMSO or glycerol) that are capable of generating stronger hydrogen bonds with water than water – water interactions.[126] Through the disruption of water hydrogen bonding networks, the melting point of the solution is lowered, which in turn limits the degree of supercooling. The addition of large quantities of additives such as DMSO will also increase the viscosity of the solution, which will lower the relative molecular motion,[127] decreasing the kinetic probability of ice nucleation. Natural antifreeze proteins function along a similar vector, either sequestering water molecules or foreign particles, limiting the kinetic movement of water while also disrupting the interface between an ice nucleus and the surrounding environment.[128,129] More complex methods such as increased pressure,[130] or alternating magnetic fields can be utilized to suppress ice nucleation events; however the direct application of these methods to the preservation of biological materials remains impractical at this time.

1.3.1.3 Measuring ice nucleation

The base components required to assess the nucleation temperature of an aqueous solution include: an isolated hydrophobic environment for sample loading, temperature control of the loading environment, and the ability to visualize the loaded sample; the earliest implementation of these components is the drop-freezing assay.[131] This implementation utilized a Styrofoam box containing a chilled metal plate coated with a solid silicone film on which sample droplets were loaded. The cryostage is cooled, and nucleation events are visualized through an optical microscope (**Figure 1.3 (A)**). Many improvements to the drop-freezing assay have been established over the years, improving sample loading[132] cooling methodology[133] and monitoring.[134] One notable iteration on the drop-freezing assay approach was the development of the emulsion-freezing assay;[135] whereby an emulsion of n-heptane (containing emulsifier) and aqueous sample is prepared (through sonication) and placed in a sealed, cooled chamber under an optical microscope (**Figure 1.3 (B)**).[135,136] This allows for the generation of several isolated droplets within a sealed hydrophobic environment. As the temperature is lowered in the sealed

chamber, nucleation events are visualized throughout the plate. The introduction of ice nucleating agents such as AgI within the prepared emulsion allows for the direct monitoring of a compound's ability to inhibit ice nucleation.[137–139]

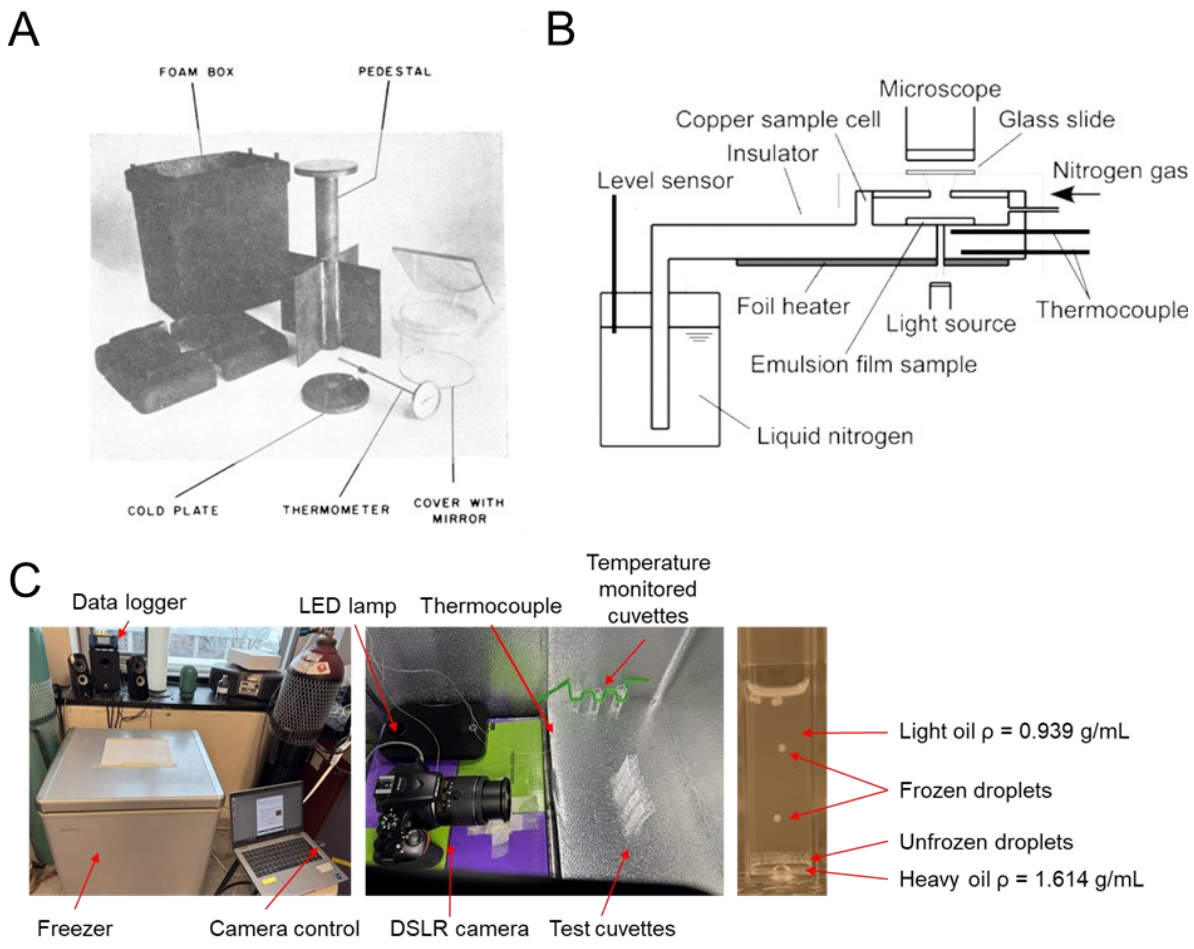

Figure 1.3 General schemes for instrumentation utilized in different INA assays. Schematic of the drop-freezing assay is reproduced from Vali[131] with licence (6062011108195) from AIP Publishing without modification. Schematic of the emulsion freezing assay reprinted with permission from Inada,[135] Copyright 2011 American Chemical Society. **(A)** Disassembled components of the initial drop-freezing assay. **(B)** Schematic for the cryostage utilized in the emulsion-freezing assay. **(C)** Inner and outer components utilized in the Ben lab Freeze-Float assay.

Designed with similar principles to the emulsion-freezing assay, the Freeze-Float assay is a modern iteration which implements the same key components, but without the use of any specialized equipment.[140] Utilizing a commodity freezer opposed to a cryostage makes the implementation of a Freeze-Float assay more accessible. Disposable cuvettes are loaded with a heavy (ρ = 1.67 g / mL) oil buffer layer and a light (ρ = 0.9167 g / mL) oil layer supplemented with

emulsifier to act as a vertical adaptation of the isolated system generated between coverslips in the emulsion-freezing assay. Several cuvettes can be employed in parallel to increase the throughput of the assay, with more advanced implementations utilizing robotic loading of up to 1920 droplets placed within a controlled rate freezer.[141] The cuvettes are cooled with the freezer and imaged with a remote camera (frozen droplets are less dense than the light oil and will float), and nucleation events can be visually identified. The implementation of a Freeze-Float assay workflow is described in **Chapter 3** of this work, and a detailed operating procedure for the Ben lab Freeze-Float assay can be found in **Appendix III**.

An alternate approach to measuring ice nucleation activity was devised by Consiglio et al. to fully automate the measurement of nucleation events;[142] instead of visually tracking nucleation events, the expansion of frozen samples[143] is utilized to track nucleation as a function of pressure change on a sealed system.[142] A specialized sealed chamber is loaded with an aqueous sample and programed to progress through cooling cycles, tracking a sharp increase in chamber pressure as a nucleation event. However, this method is designed to analyze samples larger than 1 mL opposed to the previous implementations which analyze microdroplets.

1.3.2 Ice recrystallization

Once the supercooled solution has undergone ice nucleation, the formation of ice is propagated throughout the sample, drastically reducing the unfrozen fraction. While the sample continues to cool following ice nucleation, the size of generated ice crystals is not static; through the thermodynamically driven process of ice recrystallization, larger ice crystals will form at the expense of smaller ice crystals.[144] The phenomena of recrystallization has been studied extensively in the earth sciences with respect to the generation of mineral deposits,[145,146] and has been adapted to the food sciences.[147–149] In the metallurgic sciences, crystal growth is defined as the phenomena of grain boundary migration.[150,151] In general, deformation in the crystalline structure at the interface of crystal boundaries causes novel nucleation events, with the newly generated crystal being disordered with respect to the surrounding crystals, they are quickly incorporated into the growing (larger) crystal lattice (**Figure 1.4 (A)**). This process facilitates the transfer of molecules from one crystal to another until the smaller crystal is completely consumed;[150] in theory, given a constant driving force (be it pressure or temperature) recrystallization will occur until only one large crystal remains. When considering grain boundary migration between two ice crystals, it is common for each crystal to have a given curvature. Smaller ice crystals will have a larger (sharper) angle of curvature than a larger crystal, making it relatively less ordered, and in turn less thermodynamically favorable (**Figure 1.4 (B)**). The driving

force for ice recrystallization when considering only grain boundary migration is the minimization of interfacial curvature in the system, reducing the total system energy.[144]

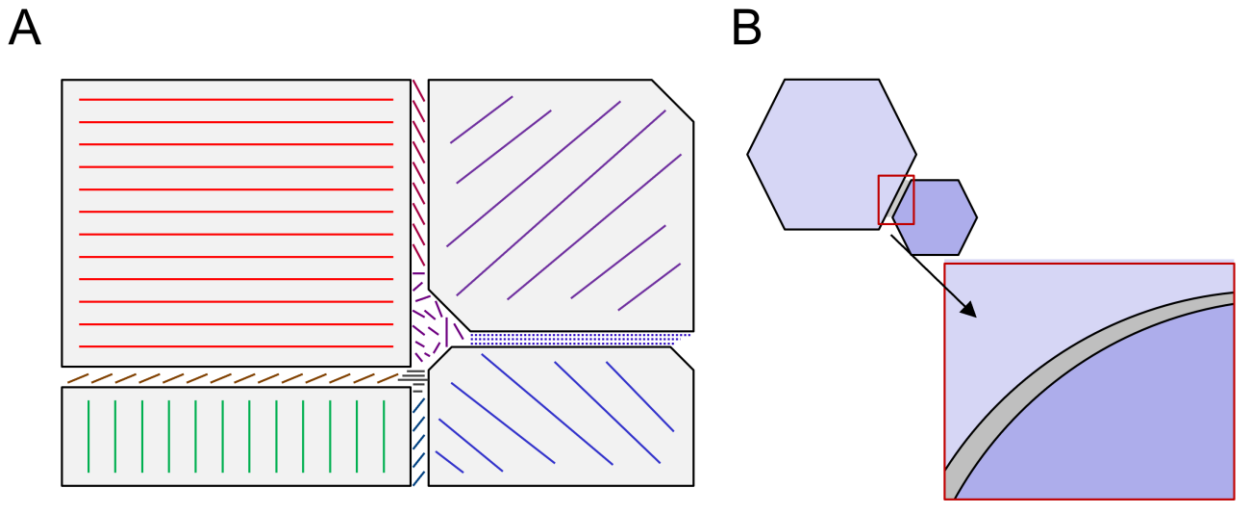

Figure 1.4 Adapted visual representations of the driving forces behind ice recrystallization.[144] **(A)** Generic scheme of four metal crystals interfacing, with the mixed grain boundaries indicated with the corresponding blended colour and net vectors. **(B)** Visualization of the interfacial curvature between two ice crystals, with the bulk water indicated in the interface in grey.

When examining crystalline ice (opposed to mineral crystallization) it is important to note the presence of a thin semi-ordered liquid layer surrounding the solid ice lattice, this layer is called the quasi-liquid layer (QLL),[152,153] and needs to be considered when discussing the recrystallization of ice. A mechanistic explanation (Lifshitz-Slyozov-Wagner theory or Ostwald ripening) of ice recrystallization posits the driving force of ice recrystallization being the minimization of interfacial surface area between solid ice and bulk water.[154,155] Through the generation of larger ice crystals, the total number of crystals decreases (assuming a fixed volume), which in turn decreases the surface area to volume ratio, minimizing the free energy of the system.[156–158]

The generation of large ice crystals as a result of uncontrolled ice crystal growth during controlled temperature change (cooling and warming) is detrimental to the outcomes of cryopreservation; larger ice crystals can not only cause increased mechanical damage, osmotic damage (and dehydration) is exaggerated as the unfrozen fraction of the system decreases.[159–161] The inhibition of ice recrystallization has proven to benefit the cryopreservation outcomes for a number of clinically relevant cell types.[162–167]

1.3.2.1 Measuring ice recrystallization

In order to develop CPAs capable of inhibiting ice recrystallization, a robust assay is required to determine IRI activity. Initially published by Knight in 1988, the splat cooling assay (SCA) serves as the fundamental starting point of most modern IRI assessments.[168] The SCA utilizes an aluminum block cooled with dry ice onto which a 10 µL aqueous droplet is flash frozen, allowed to anneal at a constant temperature, and subsequently imaged. The basic process had been utilized previously in the field of metallurgy,[169] which when applied to the study of ice, facilitated the need for aqueous compound preparation. The initial IRI assessment of previously assessed antifreeze proteins (AFPs)[170–172] on the SCA revealed a propensity for false positive assessments of inactive AFPs; the addition of ions (initially NaCl) to the aqueous solution was found to mitigate this issue.[173] Thus, subsequent iterations of the SCA do not assess compounds with pure water, but instead commonly use phosphate buffered saline (PBS) as the aqueous solvent.[174] Alternative approaches to IRI assay design have been developed,[175,176] most notably the sucrose sandwich assay, which was designed to accommodate aqueous solutions with high solute concentrations.[177]

In this work a modified version of the traditional SCA is employed,[174] aiming to be as representative of practical cryopreservation conditions as possible. This approach uses a 5-minute annealing time, gathering the rate of ice crystal growth at varying concentrations. An in-depth explanation of the modern SCA procedures can be found in **Appendix III**, but it is worth noting the method by which ice growth is assessed; the area of each ice crystal is measured and "placed" into a respective bin, with "Bin 1" defined to include any crystal which could be formed instantaneously upon freezing (≤ 0.001 mm^2).[174] Each subsequent bin includes any crystals measured to be < 0.001 mm^2 larger than the previous bin (i.e. "Bin 3" would include crystals measuring an area of (0.002 – 0.003 mm^2]). The normalized rate of ice crystal growth (v_{norm}) is calculated as the proportional area of crystals remaining in "Bin 1" divided by the annealing time (5 minutes),[174] defining the proportion of ice crystals which were allowed to recrystallize during the annealing period. The rate of a given concentration is then normalized to the rate of the sample's solvent (PBS), controlling for minor run to run variation. A rate of "zero" would indicate that following annealing, no ice crystal area was measured to be larger than what is accessible upon immediate freezing.

Once assessed at several concentrations (up to the maximum aqueous solubility), a dose response curve can be generated, graphing the rate of ice crystal growth as a function of log compound concentration (fit to a standard four-parameter dose response curve) (**Figure 1.5 (A)**).

From the generated four-parameter dose response curve, the concentration required for 50% inhibition (IC_{50}) can be extracted, which is utilized as a baseline measurement of IRI activity for novel compounds. Due to a combination of poor aqueous solubility and poor IRI activity, it is not possible to generate a full dose response relationship for all novel compounds; for all compound presented in this work, the maximum aqueous solubility will be represented as the highest concentration assessed, any compound which fails to generate a rate of ice crystal growth ≤ 50% will have the activity denoted as “N/A”. The extrapolation of incomplete dose response curves (compounds which are unable to reach a rate of zero) is not accurate for defining absolute activity, but is extremely valuable in the structure function assessment of partially IRI active model compounds.

From the established workflow it is possible to plot the proportional area for each distinct bin (**Figure 1.5 (B)**), however this is typically utilized only when attempting to decouple several IRI inactive compounds; this form of analysis has been utilized by previous graduate students examining the modified SCA at longer time points,[178] and the assessment of IRI inactive resins,[179] but is not utilized in the work presented in this thesis.

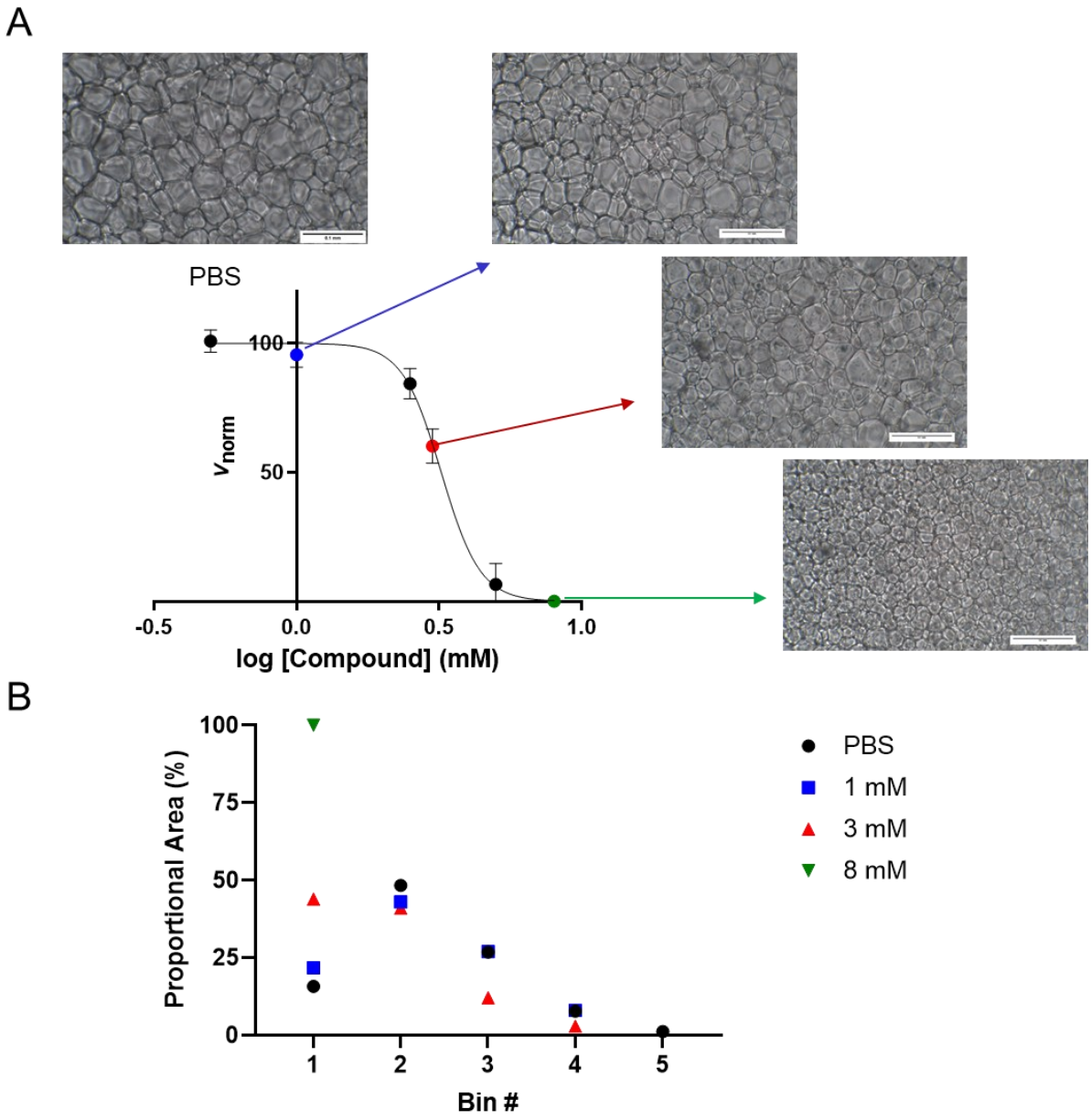

Figure 1.5 Example data analysis / output from the modified SCA (using compound **4.01**). **(A)** Four-parameter dose response curve for compound **4.01**. Representative images (from the triplicate analyzed) are indicated for the negative control (PBS, black), upper plateau (1 mM, blue), hill slope (3 mM, red), and lower plateau (8 mM, green). All images are set to the same scale (scale bar = 0.1 mm). **(B)** Proportional distribution of binned ice crystal areas generated through the SCA analysis of compound **4.01**. Data points displayed represent the proportional crystal areas for the entire triplicate collected (opposed to only the representative image displayed in **(A)**). Standard bin increments are utilized, with bin 1 representing crystal areas (0 - 0.001 mm^2) and each subsequent bin encompassing 0.001 mm^2 in area.

1.3.2.2 Ice recrystallization inhibitors

The first reported compounds to possess the ability to inhibit the phenomena of ice recrystallization are natural (AFPs) and antifreeze glycoproteins (AFGP);[180,181] these proteins were found to be the source of freeze tolerance observed in arctic fish species,[182–184] insects,[185–187] bacteria,[188,189] and plants.[190,191] These proteins typically function by binding to the surface of hexagonal ice,[192,193] increasing the energy required for crystal growth. This has been described as the Gibbs-Thomson model,[194–196] whereby at low protein concentrations hydrogen bonding interaction between the protein and ice lattice occur, but at higher concentrations proteins begin to aggregate together at the ice interface.[128] Iterations on the Gibbs-Thomson model have subsequently been proposed (such as the Flory-Huggins model),[197,198] furthering the mechanistic understanding of this inhibition process. As a result of the ice binding mechanism utilized by natural AF(G)Ps, if applied beyond natural conditions (like what is commonly used for cryopreservation), the ice crystal growth that does occur is most favorable along the c-axis (basal plane) opposed to the a-axis (prism plane) (**Figure 1.6 (A)**). This irregular growth along the basal plane, referred to as dynamic ice shaping (DIS), results in irregular shaped ice crystals, which are detrimental to biological samples.[199]

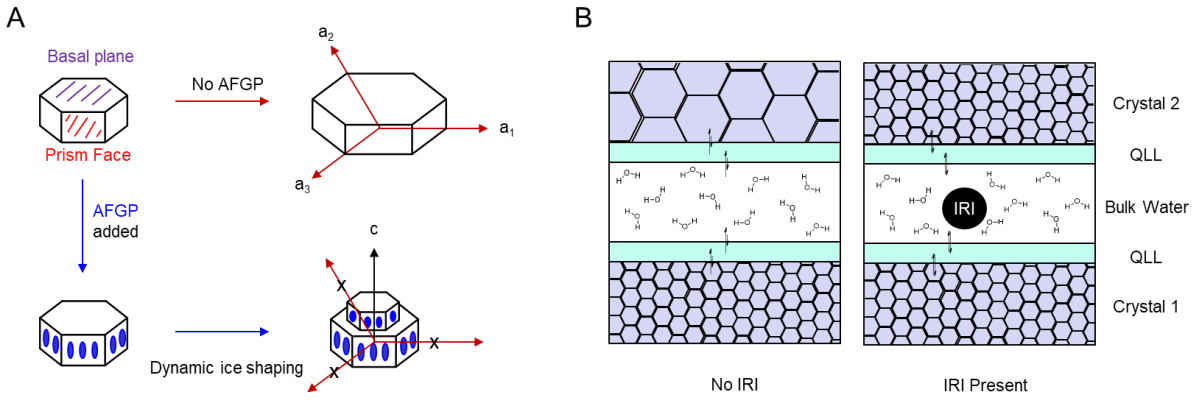

Figure 1.6 Adapted illustration of the proposed mechanisms of ice recrystallization inhibition. **(A)** Ice recrystallization inhibition activity through the use of an ice binding IRI (such as natural AFGPs). The top pathway represents uncontrolled ice growth along the a axis, where the inhibition pathway forces growth along the c-axis, resulting in DIS.[144] **(B)** Graphical representation of the interface between ice surfaces (shown as ice sheets opposed to an individual crystal for clarity); the presence of a non-ice binding IRI in the bulk water will influence the transfer of water from one ice crystal to the QLL then into the bulk water.[200,201]

The development of AF(G)P analogues which possess IRI activity, without exhibiting DIS was successful,[199,202–204] but ultimately too arduous a process to allow for expeditious derivatization.

Consequently, the subsequent development of IRI active molecules that do not cause DIS can be separated into two distinct categories, synthetic macromolecules,[205–211] and small molecules. The following introductory sections, and all work described in this thesis will focus solely on the development and evaluation of small molecule IRIs.

It has been observed that alteration of the carbohydrate component of AFGP analogues had a direct impact on the measured IRI activity,[200] leading to the identification of small molecule carbohydrates which independently exhibit IRI activity. As these small molecule IRIs do not demonstrate DIS, the mechanism of action is not well understood. The degree of hydration (number of non-exchangeable bound water molecules) has been correlated to measured IRI activity of reducing sugars,[200,212,213] however, the accurate assessment of hydration index is difficult to obtain for many synthetically modified carbohydrates. The importance of hydration is hypothesized to be due to bulk water – IRI interactions, increasing the energy barrier of a given water transfer from one ice crystal to another (**Figure 1.6 (B)**).[201,214] From this understanding, the first small molecule carbohydrate IRIs were derived from known hydrogelators and surfactants.[214,215] These compounds are known to effectively disrupt bulk water,[216] and were utilized as a starting point for small molecule IRI development. However, the surfactant-based IRIs required use well below the critical micelle concentration as to not disrupt the cellular membranes of preserved biological material. From initial *O*-alkyl-pyranosides and *N*-alkyl-gluconamides, it was established that a balance between hydrophobic (ability to disrupt water) and hydrophilic (solubility in aqueous media) components was required for a small molecule carbohydrate to be an effective IRI.[202,214,215] The initial surfactant based carbohydrate IRIs were found to be mechanically difficult to work with and feared to be cytotoxic to cellular membranes even below the critical micelle concentration; these concerns limited cryopreservation application of surfactant derived small molecule IRIs, driving the assessment of alternative hydrophobic moieties.[217,218] The transition to *O*- and *N*-aryl carbohydrate derived IRIs has resulted in a number of model compounds, the application of which has been found to improve the cryopreservation of a number of clinically relevant cell types.[162,165–167,217]

1.4 Storage of cooled sample and transient warming events

Following the controlled cooling process, the expectation is that cryopreserved biological material is held at a consistent storage temperature (e.g. - 80 or - 196 °C) until required for use, at which time it can undergo the warming process; however, in practice, transient warming events (TWE) occurring during the cold storage period is common.[219] These warming events subject the material to the same dangers (mechanical and osmotic) experienced during the standard cooling

and warming process. The impact of TWEs differ depending on cell type and cryopreservation protocol,[220–223] but the use of designed CPAs can help mitigate damage caused by TWEs.[224] It has been noted that the IRI activity measured with the SCA does not directly translate to protection during TWEs; for example, red blood cells supplemented with two separate compounds demonstrating comparable IRI activity have varying viability following the onset of TWEs.[224] No current project within the Ben lab is aimed to address protection against TWEs specifically, however screening for TWE protection is actively being incorporated into our cryopreservation assessment workflow.

1.5 Warming of cryopreserved sample and warming rates

The process of cryopreservation to this point has been framed with respect to the cooling and storage process, in which the formation of ice (and the subsequent damage mitigation) is intuitive; however, the warming phase of cryopreservation is arguably the most important with respect to obtaining a positive post-thaw outcome. Like with cooling rates, it has been long established that the warming rate of a sample is not only vital, but cell type specific.[66] Should a sample be warmed too slowly, locally melted water may diffuse into the cell and nucleate, causing IIF.[70,163] Similarly, as more energy is introduced into the system, the thermodynamically driven process of ice recrystallization is amplified. When assessing IRI activity, the SCA mimics the warming process (flash freezing at – 80 °C, and annealing at a warmer – 6.4 °C)[174] opposed to the freezing process. Generally, it is thought that the faster a sample can be practically warmed, the better the cryopreservation outcome;[66] whereby either the sample is warmed fast enough to escape re-nucleation (and recrystallization) of the melting ice, or it is not, resulting in mechanical and osmotic damage.[225] For larger samples such as organs or tissues, non-uniform warming can result in sample fracture due to mechanical stress, and should washouts be required,[226] the use of a rapid warming rate may worsen CPA cytotoxicity. The warming process is a major concern when considering vitrification protocol design, with several novel technologies developed for uniform rewarming;[227–229] however for cryopreserved samples, if ice growth is controlled, the use of a standard 37 °C water bath for thawing is typically sufficient for small volume samples.

1.6 Washout and reconstitution

Once warmed above the solution melting point, cryopreserved samples typically require the immediate removal of cryoprotective agents. Depending on the chosen CPAs and desired use case, this process can pose serious complications; one prominent example is the deglycerolization of cryopreserved red blood cells.[230–233] The standard cryopreservation protocol for the long-term storage of red blood cells in North America utilizes a high (40 wt.%)[234,235]

concentration of glycerol as the chosen CPA; as the preserved sample is intended for intravenous injection, the glycerol needs to be removed prior to the use of any cryopreserved blood products. Commercial devices have been developed to automate the washing cycles required to remove glycerol from the cryopreserved blood, however, this process typically takes about one hour to complete.[236] The delay caused by deglycerolization facilitates the need for preemptive preparation of red blood cell units in high pressure environments (such as active combat areas), which can lead to either wastage under low demand or lag under high demand.[237] Investigations into CPA additives (such as IRIs) have been shown to decrease the required concentration of glycerol (therefore decreasing the deglycerolization time),[162,224,238] although any additive utilized with this purpose would either need to be completely biocompatible or easily removed.

1.6.1 CPA cytotoxicity

It has been well established that all common penetrating osmotic regulators (DMSO, glycerol, ethylene glycol)[239–241] are cytotoxic at the commonly utilized concentrations. However, the protection provided from these penetrating CPAs during the cryopreservation process justifies the design of removal processes. Specific "DMSO-free" cryopreservation protocol have been proposed for a number of cell types,[242–245] however many of these alternative protocol still require the use of glycerol or ethylene glycol.[246–249] When designing novel CPA additives, it is vital to not only consider the efficacy, but also the cytotoxicity, as the ultimate goal is the preservation of biological material. Several commercially available methods have been developed to assess cellular death following treatment with a given compound.[250,251] For the work described in this thesis, two methods to detect cellular death are utilized; a metabolic indicator of cellular death (resazurin cell viability assay) is used for a general assessment of novel CPAs, and a membrane integrity assessment (lactate dehydrogenase assay) is utilized specifically for suspected surfactants. A detailed explanation of the methodology of the cytotoxicity assays performed can be found in **Appendix III**, with the standard protocol remaining consistent with other assessments made in the Ben laboratory.[178,218,252–254] The general assessment of compound cytotoxicity is performed through the visualization of blue resazurin metabolized into pink resorufin through the use of NAD(P)H dehydrogenase by viable cells (**Figure 1.7 (A)**);[255] human hepatocellular carcinoma (HepG2) cells are incubated in the presence of a target CPA, with metabolic function assessed after 24 hours. As the addition of cryoadditives is typically directly prior to cooling (on the order of minutes), assessing cytotoxicity following a 24-hour incubation represents a cytotoxic extreme, which cellular damage will not exceed under any cryopreservation protocol. As metabolic cell death is a general indicator, and can arise from a myriad of potential pathways,[256]

the use of a membrane-damage specific indicator of cell death can also be beneficial. Lactate dehydrogenase (LDH) is an enzyme found in all cells that is rapidly released upon cellular membrane damage. With the addition of yellow iodonitrotetrazolium chloride (INT),[257] LDH with NADH will convert INT into a red formazan dye, with the conversion being directly correlated to the concentration of LDH present in the cell culture supernatant (**Figure 1.7 (B)**).[257]

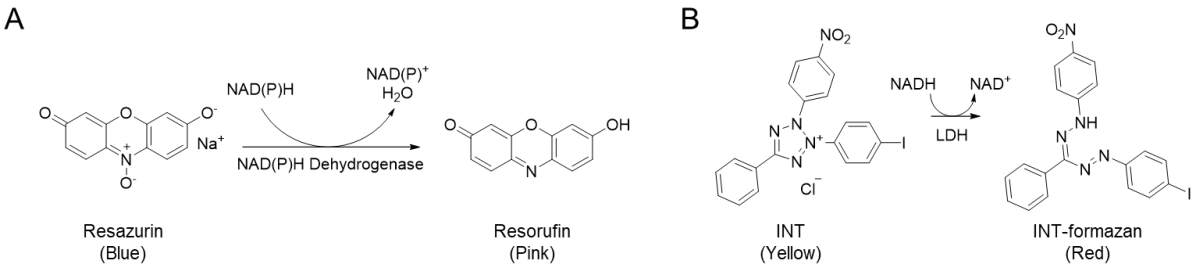

Figure 1.7 Enzymatic conversion of dyes utilized by cytotoxicity assays. **(A)** Conversion of resazurin to resorufin utilized in the resazurin cellular viability assay. **(B)** Conversion of INT to INT-formazan utilized by the lactate dehydrogenase assay.

More robust assessments of cytotoxicity (be it of a given compound or storage condition) are commonly performed in the Ben laboratory through the use an Annexin V / Propidium Iodide staining assessed by flow cytometry.[252] This method allows for differentiation beyond binary live / dead analysis (e.g. identifying early / late-apoptotic populations). In this thesis, only simple Resazurin / LDH cytotoxicity assessments are performed, but does not preclude the assessment of any generated novel compound identified in this work being explored in more detail in future.

1.7 References

(1) Elliott, C. Medicine as a Commodity. In *The Routledge Companion to Philosophy of Medicine*; Routledge, 2016; p 10.

(2) Parry, B. New Spaces of Biological Commodification: The Dynamics of Trade in Genetic Resources and "Bioinformation." *Interdisciplinary Science Reviews* **2006**, *31* (1), 19–31. https://doi.org/10.1179/030801806X84228.

(3) *Advances in Biopreservation*, 1st ed.; Baust, J. G., Baust, J. M., Eds.; CRC Press: Boca Raton, 2006. https://doi.org/10.1201/9781420004229.

(4) Viana, P.; Castillo-Flores, S.; Mora, M. M. R.; Cabral, T. D. D.; Martins, P. N.; Kueht II, M.; Faria, I. Normothermic Machine Perfusion vs. Static Cold Storage in Liver Transplantation: A Systematic Review and Meta-Analysis. *Artificial Organs* **2025**, *49* (6), 945–954. https://doi.org/10.1111/aor.14960.

(5) Polyak, M. M. R.; Arrington, B. O.; Stubenbord, W. T.; Boykin, J.; Brown, T.; Jean-Jacques, M. A.; Estevez, J.; Kapur, S.; Kinkhabwala, M. THE INFLUENCE OF PULSATILE PRESERVATION ON RENAL TRANSPLANTATION IN THE 1990s 1. *Transplantation* **2000**, *69* (2), 249.

(6) Schold, J. D.; Kaplan, B.; Howard, R. J.; Reed, A. I.; Foley, D. P.; Meier-Kriesche, H.-U. Are We Frozen in Time? Analysis of the Utilization and Efficacy of Pulsatile Perfusion in Renal

Transplantation. *American Journal of Transplantation* **2005**, *5* (7), 1681–1688. https://doi.org/10.1111/j.1600-6143.2005.00910.x.

(7) Guarrera, J. V.; Henry, S. D.; Samstein, B.; Odeh-Ramadan, R.; Kinkhabwala, M.; Goldstein, M. J.; Ratner, L. E.; Renz, J. F.; Lee, H. T.; Brown, R. S.; Emond, J. C. Hypothermic Machine Preservation in Human Liver Transplantation: The First Clinical Series. *American Journal of Transplantation* **2010**, *10* (2), 372–381. https://doi.org/10.1111/j.1600-6143.2009.02932.x.

(8) Ravikumar, R.; Leuvenink, H.; Friend, P. J. Normothermic Liver Preservation: A New Paradigm? *Transplant International* **2015**, *28* (6), 690–699. https://doi.org/10.1111/tri.12576.

(9) Nasralla, D.; Coussios, C. C.; Mergental, H.; Akhtar, M. Z.; Butler, A. J.; Ceresa, C. D. L.; Chiocchia, V.; Dutton, S. J.; García-Valdecasas, J. C.; Heaton, N.; Imber, C.; Jassem, W.; Jochmans, I.; Karani, J.; Knight, S. R.; Kocabayoglu, P.; Malagò, M.; Mirza, D.; Morris, P. J.; Pallan, A.; Paul, A.; Pavel, M.; Perera, M. T. P. R.; Pirenne, J.; Ravikumar, R.; Russell, L.; Upponi, S.; Watson, C. J. E.; Weissenbacher, A.; Ploeg, R. J.; Friend, P. J. A Randomized Trial of Normothermic Preservation in Liver Transplantation. *Nature* **2018**, *557* (7703), 50–56. https://doi.org/10.1038/s41586-018-0047-9.

(10) Guibert, E. E.; Petrenko, A. Y.; Balaban, C. L.; Somov, A. Y.; Rodriguez, J. V.; Fuller, B. J. Organ Preservation: Current Concepts and New Strategies for the Next Decade. *Transfus Med Hemother* **2011**, *38* (2), 125–142. https://doi.org/10.1159/000327033.

(11) Collins, G. M.; Bravo-Shugarman, M.; Terasaki, P. I. KIDNEY PRESERVATION FOR TRANSPORTATION: Initial Perfusion and 30 Hours' Ice Storage. *The Lancet* **1969**, *294* (7632), 1219–1222. https://doi.org/10.1016/S0140-6736(69)90753-3.

(12) Wahlberg, J. A.; Love, R.; Landegaard, L.; Southard, J. H.; Belzer, F. O. 72-Hour Preservation of the Canine Pancreas. *Transplantation* **1987**, *43* (1), 5–8. https://doi.org/10.1097/00007890-198701000-00002.

(13) Southard, J. H.; Belzer, F. O. The University of Wisconsin Organ Preservation Solution: Components, Comparisons, and Modifications. *Transplantation Reviews* **1993**, *7* (4), 176–190. https://doi.org/10.1016/S0955-470X(05)80025-4.

(14) Baust, J. M. Advances in Media for Cryopreservation and Hypothermic Storage. *BioProcess International* **2005**.

(15) Michel, P.; Vial, R.; Rodriguez, C.; Ferrera, R. A Comparative Study of the Most Widely Used Solutions for Cardiac Graft Preservation during Hypothermia. *The Journal of Heart and Lung Transplantation* **2002**, *21* (9), 1030–1039. https://doi.org/10.1016/S1053-2498(02)00414-X.

(16) Pahernik, S. A.; Thasler, W. E.; Mueller-Hoecker, J.; Schildberg, F. W.; Koebe, H. G. Hypothermic Storage of Pig Hepatocytes: Influence of Different Storage Solutions and Cell Density. *Cryobiology* **1996**, *33* (5), 552–566. https://doi.org/10.1006/cryo.1996.0059.

(17) Ostrowska, A.; Gu, K.; Bode, D. C.; Van Buskirk, R. G. Hypothermic Storage of Isolated Human Hepatocytes: A Comparison between University of Wisconsin Solution and a Hypothermosol Platform. *Arch Toxicol* **2009**, *83* (5), 493–502. https://doi.org/10.1007/s00204-009-0419-x.

(18) Ścieżyńska, A.; Soszyńska, M.; Szpak, P.; Krześniak, N.; Malejczyk, J.; Kalaszczyńska, I. Influence of Hypothermic Storage Fluids on Mesenchymal Stem Cell Stability: A Comprehensive Review and Personal Experience. *Cells* **2021**, *10* (5), 1043. https://doi.org/10.3390/cells10051043.

(19) Petrenko, Y.; Chudickova, M.; Vackova, I.; Groh, T.; Kosnarova, E.; Cejkova, J.; Turnovcova, K.; Petrenko, A.; Sykova, E.; Kubinova, S. Clinically Relevant Solution for the Hypothermic Storage and Transportation of Human Multipotent Mesenchymal Stromal Cells. *Stem Cells International* **2019**, *2019* (1), 5909524. https://doi.org/10.1155/2019/5909524.

(20) Mahler, S.; Desille, M.; Frémond, B.; Chesné, C.; Guillouzo, A.; Campion, J.-P.; Clément, B. Hypothermic Storage and Cryopreservation of Hepatocytes: The Protective Effect of Alginate Gel against Cell Damages. *Cell Transplant* **2003**, *12* (6), 579–592. https://doi.org/10.3727/000000003108747181.

(21) Mayer, F. Q.; Baldo, G.; De Carvalho, T. G.; Lagranha, V. L.; Giugliani, R.; Matte, U. Effects of Cryopreservation and Hypothermic Storage on Cell Viability and Enzyme Activity in Recombinant Encapsulated Cells Overexpressing Alpha-L-Iduronidase. *Artificial Organs* **2010**, *34* (5), 434–439. https://doi.org/10.1111/j.1525-1594.2009.00880.x.

(22) Wright, B.; Cave, R. A.; Cook, J. P.; Khutoryanskiy, V. V.; Mi, S.; Chen, B.; Leyland, M.; Connon, C. J. Enhanced Viability of Corneal Epithelial Cells for Efficient Transport/Storage Using a Structurally Modified Calcium Alginate Hydrogel. *Regenerative Medicine* **2012**, *7* (3), 295–307. https://doi.org/10.2217/rme.12.7.

(23) Swioklo, S.; Constantinescu, A.; Connon, C. J. Alginate-Encapsulation for the Improved Hypothermic Preservation of Human Adipose-Derived Stem Cells. *Stem Cells Transl Med* **2016**, *5* (3), 339–349. https://doi.org/10.5966/sctm.2015-0131.

(24) Zhang, C.; Zhou, Y.; Zhang, L.; Wu, L.; Chen, Y.; Xie, D.; Chen, W. Hydrogel Cryopreservation System: An Effective Method for Cell Storage. *Int J Mol Sci* **2018**, *19* (11), 3330. https://doi.org/10.3390/ijms19113330.

(25) Berendsen, T. A.; Bruinsma, B. G.; Puts, C. F.; Saeidi, N.; Usta, O. B.; Uygun, B. E.; Izamis, M.-L.; Toner, M.; Yarmush, M. L.; Uygun, K. Supercooling Enables Long-Term Transplantation Survival Following 4 Days of Liver Preservation. *Nat Med* **2014**, *20* (7), 790–793. https://doi.org/10.1038/nm.3588.

(26) Huang, H.; Yarmush, M. L.; Usta, O. B. Long-Term Deep-Supercooling of Large-Volume Water and Red Cell Suspensions via Surface Sealing with Immiscible Liquids. *Nat Commun* **2018**, *9* (1), 3201. https://doi.org/10.1038/s41467-018-05636-0.

(27) Puts, C. F.; Berendsen, T. A.; Bruinsma, B. G.; Ozer, S.; Luitje, M.; Usta, O. B.; Yarmush, M. L.; Uygun, K. Polyethylene Glycol Protects Primary Hepatocytes during Supercooling Preservation. *Cryobiology* **2015**, *71* (1), 125–129. https://doi.org/10.1016/j.cryobiol.2015.04.010.

(28) Usta, O. B.; Kim, Y.; Ozer, S.; Bruinsma, B. G.; Lee, J.; Demir, E.; Berendsen, T. A.; Puts, C. F.; Izamis, M.-L.; Uygun, K.; Uygun, B. E.; Yarmush, M. L. Supercooling as a Viable Non-Freezing Cell Preservation Method of Rat Hepatocytes. *PLOS ONE* **2013**, *8* (7), e69334. https://doi.org/10.1371/journal.pone.0069334.

(29) Huang, H.; Rey-Bedón, C.; Yarmush, M. L.; Usta, O. B. Deep-Supercooling for Extended Preservation of Adipose-Derived Stem Cells. *Cryobiology* **2020**, *92*, 67–75. https://doi.org/10.1016/j.cryobiol.2019.11.004.

(30) Taylor, M. J.; Weegman, B. P.; Baicu, S. C.; Giwa, S. E. New Approaches to Cryopreservation of Cells, Tissues, and Organs. *Transfusion Medicine and Hemotherapy* **2019**, *46* (3), 197–215. https://doi.org/10.1159/000499453.

(31) Fahy, G. M.; MacFarlane, D. R.; Angell, C. A.; Meryman, H. T. Vitrification as an Approach to Cryopreservation. *Cryobiology* **1984**, *21* (4), 407–426. https://doi.org/10.1016/0011-2240(84)90079-8.

(32) Taylor, M. J.; Song, Y. C.; Brockbank, K. G. M. Vitrification in Tissue Preservation: New Developments. In *Life in the Frozen State*; CRC Press, 2004.

(33) Boutron, P.; Mehl, P.; Kaufmann, A.; Angibaud, P. Glass-Forming Tendency and Stability of the Amorphous State in the Aqueous Solutions of Linear Polyalcohols with Four Carbons: I. Binary

Systems Water-Polyalcohol. *Cryobiology* **1986**, *23* (5), 453–469. https://doi.org/10.1016/0011-2240(86)90031-3.
(34) Wowk, B. Thermodynamic Aspects of Vitrification. *Cryobiology* **2010**, *60* (1), 11–22. https://doi.org/10.1016/j.cryobiol.2009.05.007.
(35) Fahy, G. M.; Wowk, B. Principles of Cryopreservation by Vitrification. In *Cryopreservation and Freeze-Drying Protocols*; Wolkers, W. F., Oldenhof, H., Eds.; Springer: New York, NY, 2015; pp 21–82. https://doi.org/10.1007/978-1-4939-2193-5_2.
(36) Tucker, M., J.; Liebermann, J. *Vitrification in Assisted Reproduction*, Second.; reproductive Medicine and Assissted Reporductive Techniques Series; CRC Press: Boca Raton, 2016.
(37) Balaban, B.; Urman, B.; Ata, B.; Isiklar, A.; Larman, M. G.; Hamilton, R.; Gardner, D. K. A Randomized Controlled Study of Human Day 3 Embryo Cryopreservation by Slow Freezing or Vitrification: Vitrification Is Associated with Higher Survival, Metabolism and Blastocyst Formation. *Human Reproduction* **2008**, *23* (9), 1976–1982. https://doi.org/10.1093/humrep/den222.
(38) Steif, P. S.; Palastro, M. C.; Rabin, Y. The Effect of Temperature Gradients on Stress Development during Cryopreservation via Vitrification. *Cell Preservation Technology* **2007**, *5* (2), 104–115. https://doi.org/10.1089/cpt.2007.9994.
(39) Sharma, A.; Rao, J. S.; Han, Z.; Gangwar, L.; Namsrai, B.; Gao, Z.; Ring, H. L.; Magnuson, E.; Etheridge, M.; Wowk, B.; Fahy, G. M.; Garwood, M.; Finger, E. B.; Bischof, J. C. Vitrification and Nanowarming of Kidneys. *Advanced Science* **2021**, *8* (19), 2101691. https://doi.org/10.1002/advs.202101691.
(40) Preciado, J. A.; Rubinsky, B. Isochoric Preservation: A Novel Characterization Method. *Cryobiology* **2010**, *60* (1), 23–29. https://doi.org/10.1016/j.cryobiol.2009.06.010.
(41) Kilbride, P.; Rull, M. V.; Townsend, A.; Wilson, H.; Morris, J. Shear-Thickening Fluids in Biologically Relevant Agents. *Biorheology* **2019**, *56* (1), 39–50. https://doi.org/10.3233/BIR-180196.
(42) Benito, M. E. G.; Clavero-Ramirez, I.; López-Aranda, J. M. Review. The Use of Cryopreservation for Germplasm Conservation of Vegetatively Propagated Crops. *Spanish Journal of Agricultural Research* **2004**, *2* (3), 341–351. https://doi.org/10.5424/sjar/2004023-88.
(43) Gonzalez-Arnao, M. T.; Panta, A.; Roca, W. M.; Escobar, R. H.; Engelmann, F. Development and Large Scale Application of Cryopreservation Techniques for Shoot and Somatic Embryo Cultures of Tropical Crops. *Plant Cell Tiss Organ Cult* **2008**, *92* (1), 1–13. https://doi.org/10.1007/s11240-007-9303-7.
(44) Tsvetkov, I.; Benelli, C.; Capuana, M.; Carlo, A. D.; Lambardi, M. Application of Vitrification-Derived Cryotechniques for Long-Term Storage of Poplar and Aspen (Populus Spp.) Germplasm. *Agricultural and Food Science* **2009**, *18* (2), 160–166. https://doi.org/10.2137/145960609789267515.
(45) Kuwayama, M.; Vajta, G.; Kato, O.; Leibo, S. P. Highly Efficient Vitrification Method for Cryopreservation of Human Oocytes. *Reproductive BioMedicine Online (Reproductive Healthcare Limited)* **2005**, *11* (3), 300–308. https://doi.org/10.1016/S1472-6483(10)60837-1.
(46) Papatheodorou, A.; Vanderzwalmen, P.; Panagiotidis, Y.; Prapas, N.; Zikopoulos, K.; Georgiou, I.; Prapas, Y. Open versus Closed Oocyte Vitrification System: A Prospective Randomized Sibling-Oocyte Study. *Reproductive BioMedicine Online* **2013**, *26* (6), 595–602. https://doi.org/10.1016/j.rbmo.2013.02.014.
(47) Du, S.; Shen, C.; Zhang, J. A Comparative Analysis of the Clinical Pregnancy and Perinatal Outcomes between Oocyte Vitrification and Embryo Vitrification Based on the Propensity

Score Matching Method. *J Assist Reprod Genet* **2024**, *41* (4), 875–883. https://doi.org/10.1007/s10815-024-03055-3.
(48) Hezavehei, M.; Sharafi, M.; Kouchesfahani, H. M.; Henkel, R.; Agarwal, A.; Esmaeili, V.; Shahverdi, A. Sperm Cryopreservation: A Review on Current Molecular Cryobiology and Advanced Approaches. *Reproductive BioMedicine Online* **2018**, *37* (3), 327–339. https://doi.org/10.1016/j.rbmo.2018.05.012.
(49) Shah, D.; Rasappan; Shila; Gunasekaran, K. A Simple Method of Human Sperm Vitrification. *MethodsX* **2019**, *6*, 2198–2204. https://doi.org/10.1016/j.mex.2019.09.022.
(50) Fahy, G. M.; Ali, S. E. Cryopreservation of the Mammalian Kidney. *Cryobiology* **1997**, *35* (2), 114–131. https://doi.org/10.1006/cryo.1997.2026.
(51) Fahy, G. M.; Wowk, B.; Wu, J.; Phan, J.; Rasch, C.; Chang, A.; Zendejas, E. Cryopreservation of Organs by Vitrification: Perspectives and Recent Advances. *Cryobiology* **2004**, *48* (2), 157–178. https://doi.org/10.1016/j.cryobiol.2004.02.002.
(52) Marco-Jiménez, F.; Garcia-Dominguez, X.; Jimenez-Trigos, E.; Vera-Donoso, C. D.; Vicente, J. S. Vitrification of Kidney Precursors as a New Source for Organ Transplantation. *Cryobiology* **2015**, *70* (3), 278–282. https://doi.org/10.1016/j.cryobiol.2015.04.007.
(53) Arav, A. Cryopreservation by Directional Freezing and Vitrification Focusing on Large Tissues and Organs. *Cells* **2022**, *11* (7), 1072. https://doi.org/10.3390/cells11071072.
(54) Sharma, A.; Lee, C. Y.; Namsrai, B.-E.; Han, Z.; Tobolt, D.; Rao, J. S.; Gao, Z.; Etheridge, M. L.; Garwood, M.; Clemens, M. G.; Bischof, J. C.; Finger, E. B. Cryopreservation of Whole Rat Livers by Vitrification and Nanowarming. *Ann Biomed Eng* **2023**, *51* (3), 566–577. https://doi.org/10.1007/s10439-022-03064-2.
(55) Polge, C.; Smith, A. U.; Parkes, A. S. Revival of Spermatozoa after Vitrification and Dehydration at Low Temperatures. *Nature* **1949**, *164* (4172), 666–666. https://doi.org/10.1038/164666a0.
(56) Lovelock, J. E. The Protective Action of Neutral Solutes against Haemolysis by Freezing and Thawing. *Biochemical Journal* **1954**, *56* (2), 265–270. https://doi.org/10.1042/bj0560265.
(57) Lovelock, J. E.; Bishop, M. W. H. Prevention of Freezing Damage to Living Cells by Dimethyl Sulphoxide. *Nature* **1959**, *183* (4672), 1394–1395. https://doi.org/10.1038/1831394a0.
(58) Whaley, D.; Damyar, K.; Witek, R. P.; Mendoza, A.; Alexander, M.; Lakey, J. R. Cryopreservation: An Overview of Principles and Cell-Specific Considerations. *Cell Transplant* **2021**, *30*, 0963689721999617. https://doi.org/10.1177/0963689721999617.
(59) Meneghel, J.; Kilbride, P.; Morris, G. J. Cryopreservation as a Key Element in the Successful Delivery of Cell-Based Therapies—A Review. *Front. Med.* **2020**, *7*. https://doi.org/10.3389/fmed.2020.592242.
(60) Erol, O. D.; Pervin, B.; Seker, M. E.; Aerts-Kaya, F. Effects of Storage Media, Supplements and Cryopreservation Methods on Quality of Stem Cells. *World J Stem Cells* **2021**, *13* (9), 1197–1214. https://doi.org/10.4252/wjsc.v13.i9.1197.
(61) McGann, L. E. Differing Actions of Penetrating and Nonpenetrating Cryoprotective Agents. *Cryobiology* **1978**, *15* (4), 382–390. https://doi.org/10.1016/0011-2240(78)90056-1.
(62) Bakaltcheva, I.; Ganong, J. P.; Holtz, B. L.; Peat, R. A.; Reid, T. Effects of High-Molecular-Weight Cryoprotectants on Platelets and the Coagulation System. *Cryobiology* **2000**, *40* (4), 283–293. https://doi.org/10.1006/cryo.2000.2247.
(63) Scott, K. L.; Lecak, J.; Acker, J. P. Biopreservation of Red Blood Cells: Past, Present, and Future. *Transfusion Medicine Reviews* **2005**, *19* (2), 127–142. https://doi.org/10.1016/j.tmrv.2004.11.004.
(64) Elbein, A. D.; Pan, Y. T.; Pastuszak, I.; Carroll, D. New Insights on Trehalose: A Multifunctional Molecule. *Glycobiology* **2003**, *13* (4), 17R-27R. https://doi.org/10.1093/glycob/cwg047.

(65) Jain, N. K.; Roy, I. Trehalose and Protein Stability. *Current Protocols in Protein Science* **2010**, *59* (1), 4.9.1-4.9.12. https://doi.org/10.1002/0471140864.ps0409s59.
(66) Mazur, P. Physical Factors Implicated in the Death of Microorganisms at Subzero Temperatures. *Annals of the New York Academy of Sciences* **1960**, *85* (2), 610–629. https://doi.org/10.1111/j.1749-6632.1960.tb49986.x.
(67) Mazur, P. Physical and Temporal Factors Involved in the Death of Yeast at Subzero Temperatures. *Biophysical Journal* **1961**, *1* (3), 247–264. https://doi.org/10.1016/S0006-3495(61)86887-2.
(68) Mazur, P. Cryobiology: The Freezing of Biological Systems. *Science* **1970**, *168* (3934), 939–949.
(69) Leibo, S. P.; Farrant, J.; Mazur, P.; Hanna, M. G.; Smith, L. H. Effects of Preezing on Marrow Stem Cell Suspensions: Interactions of Cooling and Warming Rates in the Presence of Pvp, Sucrose, or Glycerol. *Cryobiology* **1970**, *6* (4), 315–332. https://doi.org/10.1016/S0011-2240(70)80086-4.
(70) Mazur, P.; Leibo, S. P.; Chu, E. H. Y. A Two-Factor Hypothesis of Freezing Injury: Evidence from Chinese Hamster Tissue-Culture Cells. *Experimental Cell Research* **1972**, *71* (2), 345–355. https://doi.org/10.1016/0014-4827(72)90303-5.
(71) Muldrew, K.; McGann, L. E. Mechanisms of Intracellular Ice Formation. *Biophysical Journal* **1990**, *57* (3), 525–532. https://doi.org/10.1016/S0006-3495(90)82568-6.
(72) Lovelock, J. E. The Haemolysis of Human Red Blood-Cells by Freezing and Thawing. *Biochimica et Biophysica Acta* **1953**, *10*, 414–426. https://doi.org/10.1016/0006-3002(53)90273-X.
(73) Mazur, P. Kinetics of Water Loss from Cells at Subzero Temperatures and the Likelihood of Intracellular Freezing. *J Gen Physiol* **1963**, *47* (2), 347–369. https://doi.org/10.1085/jgp.47.2.347.
(74) Pegg, D. E. - Principles of Cryopreservation. In *Preservation of Human Oocytes*; CRC Press, 2009.
(75) Devismita, D.; Kumar, A. Effect of Cryoprotectant on Optimal Cooling Rate during Cryopreservation. *Cryobiology* **2015**, *70* (1), 53–59. https://doi.org/10.1016/j.cryobiol.2014.12.002.
(76) Zachariassen, K. E.; Kristiansen, E. Ice Nucleation and Antinucleation in Nature. *Cryobiology* **2000**, *41* (4), 257–279. https://doi.org/10.1006/cryo.2000.2289.
(77) Debenedetti, P. G. *Metastable Liquids: Concepts and Principles*; Princeton University Press, 1996; Vol. 1. https://doi.org/10.2307/j.ctv10crfs5.
(78) Koop, T.; Luo, B.; Tsias, A.; Peter, T. Water Activity as the Determinant for Homogeneous Ice Nucleation in Aqueous Solutions. *Nature* **2000**, *406* (6796), 611–614. https://doi.org/10.1038/35020537.
(79) Leberman, R.; Soper, A. K. Effect of High Salt Concentrations on Water Structure. *Nature* **1995**, *378* (6555), 364–366. https://doi.org/10.1038/378364a0.
(80) Langham, E. J.; Mason, B. J.-N. The Heterogeneous and Homogeneous Nucleation of Supercooled Water. *Proceedings of the Royal Society of London. Series A. Mathematical and Physical Sciences* **1997**, *247* (1251), 493–504. https://doi.org/10.1098/rspa.1958.0207.
(81) Storey, K. B.; Storey, J. M. Freeze Tolerance in Animals. *Physiological Reviews* **1988**, *68* (1), 27–84. https://doi.org/10.1152/physrev.1988.68.1.27.
(82) Wisniewski, M.; Gusta, L.; Neuner, G. Adaptive Mechanisms of Freeze Avoidance in Plants: A Brief Update. *Environmental and Experimental Botany* **2014**, *99*, 133–140. https://doi.org/10.1016/j.envexpbot.2013.11.011.

(83) Zavos, P. M.; Graham, E. F. Effects of Various Degrees of Supercooling and Nucleation Temperatures on Fertility of Frozen Turkey Spermatozoa. *Cryobiology* **1983**, *20* (5), 553–559. https://doi.org/10.1016/0011-2240(83)90043-3.

(84) Missous, G.; Thammavongs, B.; Dieuleveux, V.; Guéguen, M.; Panoff, J. M. Improvement of the Cryopreservation of the Fungal Starter *Geotrichum Candidum* by Artificial Nucleation and Temperature Downshift Control. *Cryobiology* **2007**, *55* (1), 66–71. https://doi.org/10.1016/j.cryobiol.2007.05.004.

(85) Lauterboeck, L.; Hofmann, N.; Mueller, T.; Glasmacher, B. Active Control of the Nucleation Temperature Enhances Freezing Survival of Multipotent Mesenchymal Stromal Cells. *Cryobiology* **2015**, *71* (3), 384–390. https://doi.org/10.1016/j.cryobiol.2015.10.145.

(86) Daily, M. I.; Whale, T. F.; Partanen, R.; Harrison, A. D.; Kilbride, P.; Lamb, S.; Morris, G. J.; Picton, H. M.; Murray, B. J. Cryopreservation of Primary Cultures of Mammalian Somatic Cells in 96-Well Plates Benefits from Control of Ice Nucleation. *Cryobiology* **2020**, *93*, 62–69. https://doi.org/10.1016/j.cryobiol.2020.02.008.

(87) Dan, N.; Shelake, S.; Luo, W.-C.; Rahman, M.; Lu, J.; Bogner, R. H.; Lu, X. Impact of Controlled Ice Nucleation on Intracellular Dehydration, Ice Formation and Their Implications on T Cell Freeze–Thaw Viability. *International Journal of Pharmaceutics* **2024**, *665* (Complete). https://doi.org/10.1016/j.ijpharm.2024.124694.

(88) Fuller, B.; Paynter, S. Fundamentals of Cryobiology in Reproductive Medicine. *Reprod Biomed Online* **2004**, *9* (6), 680–691. https://doi.org/10.1016/s1472-6483(10)61780-4.

(89) Ma, Y. H.; Qin, G. F.; Li, J.; Ding, G. R.; Xu, S. L.; Zhou, Y.; Guo, G. Z. AC Electric Field Enhances Cryopreservation Efficiency of Sprague-Dawley Rat Liver During a Slow Freezing Procedure. *Biopreservation and Biobanking* **2016**, *14* (1), 23–28. https://doi.org/10.1089/bio.2015.0042.

(90) Kojima, S.; Kaku, M.; Kawata, T.; Sumi, H.; Shikata, H.; Abonti, T. R.; Kojima, S.; Fujita, T.; Motokawa, M.; Tanne, K. Cryopreservation of Rat MSCs by Use of a Programmed Freezer with Magnetic Field. *Cryobiology* **2013**, *67* (3), 258–263. https://doi.org/10.1016/j.cryobiol.2013.08.003.

(91) Greer, N. Freezing under Pressure: A New Method for Cryopreservation. *Cryobiology* **2015**, *70* (1), 66–70. https://doi.org/10.1016/j.cryobiol.2014.12.005.

(92) Vonnegut, B. The Nucleation of Ice Formation by Silver Iodide. *Journal of Applied Physics* **1947**, *18* (7), 593–595. https://doi.org/10.1063/1.1697813.

(93) Morris, G. J.; Acton, E. Controlled Ice Nucleation in Cryopreservation--a Review. *Cryobiology* **2013**, *66* (2), 85–92. https://doi.org/10.1016/j.cryobiol.2012.11.007.

(94) Pitt, R. E.; Chandrasekaran, M.; Parks, J. E. Performance of a Kinetic Model for Intracellular Ice Formation Based on the Extent of Supercooling. *Cryobiology* **1992**, *29* (3), 359–373. https://doi.org/10.1016/0011-2240(92)90037-3.

(95) Karlsson, J. O.; Cravalho, E. G.; Borel Rinkes, I. H.; Tompkins, R. G.; Yarmush, M. L.; Toner, M. Nucleation and Growth of Ice Crystals inside Cultured Hepatocytes during Freezing in the Presence of Dimethyl Sulfoxide. *Biophys J* **1993**, *65* (6), 2524–2536. https://doi.org/10.1016/S0006-3495(93)81319-5.

(96) Wolkers, W. F.; Balasubramanian, S. K.; Ongstad, E. L.; Zec, H. C.; Bischof, J. C. Effects of Freezing on Membranes and Proteins in LNCaP Prostate Tumor Cells. *Biochimica et Biophysica Acta (BBA) - Biomembranes* **2007**, *1768* (3), 728–736. https://doi.org/10.1016/j.bbamem.2006.12.007.

(97) Gibbs, W. J. *Gibbs G.W. - Collected Works. Thermodynamics. Volume 1-Longmans (1928).Pdf*; Longmans, Green and Co.: New York, 1928; Vol. 1.

(98) Volmer, M.; Weber, A. Keimbildung in übersättigten Gebilden. *Zeitschrift für Physikalische Chemie* **1926**, *119U* (1), 277–301. https://doi.org/10.1515/zpch-1926-11927.
(99) Becker, R.; Döring, W. Kinetische Behandlung Der Keimbildung in Übersättigten Dämpfen. *Annalen der Physik* **1935**, *416* (8), 719–752. https://doi.org/10.1002/andp.19354160806.
(100) Lin, M.; Cao, H.; Li, J. Control Strategies of Ice Nucleation, Growth, and Recrystallization for Cryopreservation. *Acta Biomaterialia* **2023**, *155*, 35–56. https://doi.org/10.1016/j.actbio.2022.10.056.
(101) Kalikmanov, V. I. Classical Nucleation Theory. In *Nucleation Theory*; Kalikmanov, V. I., Ed.; Springer Netherlands: Dordrecht, 2013; pp 17–41. https://doi.org/10.1007/978-90-481-3643-8_3.
(102) Prestipino, S.; Laio, A.; Tosatti, E. Systematic Improvement of Classical Nucleation Theory. *Phys. Rev. Lett.* **2012**, *108* (22), 225701. https://doi.org/10.1103/PhysRevLett.108.225701.
(103) Liu, X. Y. Interfacial Effect of Molecules on Nucleation Kinetics. *J. Phys. Chem. B* **2001**, *105* (47), 11550–11558. https://doi.org/10.1021/jp010671z.
(104) Liu, X. Y.; Maiwa, K.; Tsukamoto, K. Heterogeneous Two-Dimensional Nucleation and Growth Kinetics. *The Journal of Chemical Physics* **1997**, *106* (5), 1870–1879. https://doi.org/10.1063/1.473325.
(105) Liu, X. Y. A New Kinetic Model for Three-Dimensional Heterogeneous Nucleation. *The Journal of Chemical Physics* **1999**, *111* (4), 1628–1635. https://doi.org/10.1063/1.479391.
(106) Cooper, S. J.; Nicholson, C. E.; Liu, J. A Simple Classical Model for Predicting Onset Crystallization Temperatures on Curved Substrates and Its Implications for Phase Transitions in Confined Volumes. *The Journal of Chemical Physics* **2008**, *129* (12), 124715. https://doi.org/10.1063/1.2977993.
(107) Liu, X. Y.; Du, N. Zero-Sized Effect of Nano-Particles and Inverse Homogeneous Nucleation: PRINCIPLES OF FREEZING AND ANTIFREEZE*. *Journal of Biological Chemistry* **2004**, *279* (7), 6124–6131. https://doi.org/10.1074/jbc.M310487200.
(108) Bai, G.; Gao, D.; Liu, Z.; Zhou, X.; Wang, J. Probing the Critical Nucleus Size for Ice Formation with Graphene Oxide Nanosheets. *Nature* **2019**, *576* (7787), 437–441. https://doi.org/10.1038/s41586-019-1827-6.
(109) Zettlemoyer, A. C.; Tcheurekdjian, N.; Chessick, J. J. Surface Properties of Silver Iodide. *Nature* **1961**, *192* (4803), 653–653. https://doi.org/10.1038/192653a0.
(110) Rowland, S. C.; Layton, R. G.; Smith, D. R. Photolytic Activation of Silver Iodide in the Nucleation of Ice. **1964**.
(111) Fitzner, M.; Sosso, G. C.; Cox, S. J.; Michaelides, A. The Many Faces of Heterogeneous Ice Nucleation: Interplay Between Surface Morphology and Hydrophobicity. *J. Am. Chem. Soc.* **2015**, *137* (42), 13658–13669. https://doi.org/10.1021/jacs.5b08748.
(112) Layton, R. G.; Stefer, J. Nucleation of Ice on Silver Iodide. *J. Atmos. Sci.* **1964**, *26*, 518–521.
(113) Soni, A.; Patey, G. N. Ice Nucleation by the Primary Prism Face of Silver Iodide. *J. Phys. Chem. C* **2022**, *126* (15), 6716–6723. https://doi.org/10.1021/acs.jpcc.1c10227.
(114) DeMott, P. J. Quantitative Descriptions of Ice Formation Mechanisms of Silver Iodide-Type Aerosols. *Atmospheric Research* **1995**, *38* (1), 63–99. https://doi.org/10.1016/0169-8095(94)00088-U.
(115) Hoose, C.; Möhler, O. Heterogeneous Ice Nucleation on Atmospheric Aerosols: A Review of Results from Laboratory Experiments. *Atmospheric Chemistry and Physics* **2012**, *12* (20), 9817–9854. https://doi.org/10.5194/acp-12-9817-2012.

(116) Roudsari, G.; Lbadaoui-Darvas, M.; Welti, A.; Nenes, A.; Laaksonen, A. The Molecular Scale Mechanism of Deposition Ice Nucleation on Silver Iodide. *Environmental Science: Atmospheres* **2024**, *4* (2), 243–251. https://doi.org/10.1039/D3EA00140G.
(117) Li, J.; Lee, T.-C. Bacterial Ice Nucleation and Its Potential Application in the Food Industry. *Trends in Food Science & Technology* **1995**, *6* (8), 259–265. https://doi.org/10.1016/S0924-2244(00)89110-4.
(118) Petzold, G.; Aguilera, J. M. Ice Morphology: Fundamentals and Technological Applications in Foods. *Food Biophysics* **2009**, *4* (4), 378–396. https://doi.org/10.1007/s11483-009-9136-5.
(119) Wilson, P. W.; Osterday, K. E.; Heneghan, A. F.; Haymet, A. D. J. Type I Antifreeze Proteins Enhance Ice Nucleation above Certain Concentrations. *J Biol Chem* **2010**, *285* (45), 34741–34745. https://doi.org/10.1074/jbc.M110.171983.
(120) Liu, K.; Wang, C.; Ma, J.; Shi, G.; Yao, X.; Fang, H.; Song, Y.; Wang, J. Janus Effect of Antifreeze Proteins on Ice Nucleation. *Proceedings of the National Academy of Sciences* **2016**, *113* (51), 14739–14744. https://doi.org/10.1073/pnas.1614379114.
(121) Eickhoff, L.; Dreischmeier, K.; Zipori, A.; Sirotinskaya, V.; Adar, C.; Reicher, N.; Braslavsky, I.; Rudich, Y.; Koop, T. Contrasting Behavior of Antifreeze Proteins: Ice Growth Inhibitors and Ice Nucleation Promoters. *J. Phys. Chem. Lett.* **2019**, *10* (5), 966–972. https://doi.org/10.1021/acs.jpclett.8b03719.
(122) Diener, B.; Utesch, D.; Beer, N.; Dürk, H.; Oesch, F. A Method for the Cryopreservation of Liver Parenchymal Cells for Studies of Xenobiotics. *Cryobiology* **1993**, *30* (2), 116–127. https://doi.org/10.1006/cryo.1993.1011.
(123) Perez-Oteyza, J.; Bornstein, R.; Corral, M.; Hermosa, V.; Alegre, A.; Torrabadella, M.; Ramos, P.; Garcia, J.; Odriozola, J.; Navarro, J. L. Controlled-Rate versus Uncontrolled-Rate Cryopreservation of Peripheral Blood Progenitor Cells: A Prospective Multicenter Study. Group for Cryobiology and Biology of Bone Marrow Transplantation (CBTMO), Spain. *Haematologica* **1998**, *83* (11), 1001–1005. https://doi.org/10.3324/%2525x.
(124) von Mach, M.-A.; Schlosser, J.; Weiland, M.; Feilen, P. J.; Ringel, F.; Hengstler, J. G.; Weilemann, L. S.; Beyer, J.; Kann, P.; Weber, M. M.; Schneider, S. Cryopreservation of Islets of Langerhans: Optimization of Protocols Using Rat Pancreatic Tissue. *EXCLI Journal* **2003**, No. 2, 6–21.
(125) Nagashima, K.; Furukawa, Y. Nonequilibrium Effect of Anisotropic Interface Kinetics on the Directional Growth of Ice Crystals. *Journal of Crystal Growth* **1997**, *171* (3), 577–585. https://doi.org/10.1016/S0022-0248(96)00664-1.
(126) Vishnyakov, A.; Lyubartsev, A. P.; Laaksonen, A. Molecular Dynamics Simulations of Dimethyl Sulfoxide and Dimethyl Sulfoxide−Water Mixture. *J. Phys. Chem. A* **2001**, *105* (10), 1702–1710. https://doi.org/10.1021/jp0007336.
(127) Davies, D. B.; Matheson, A. J. Influence of Molecular Rotation on the Viscosity of Liquids. *The Journal of Chemical Physics* **1966**, *45* (3), 1000–1006. https://doi.org/10.1063/1.1727649.
(128) Yeh, Y.; Feeney, R. E. Antifreeze Proteins: Structures and Mechanisms of Function. *Chem. Rev.* **1996**, *96* (2), 601–618. https://doi.org/10.1021/cr950260c.
(129) Du, N.; Liu, X. Y.; Hew, C. L. Ice Nucleation Inhibition: MECHANISM OF ANTIFREEZE BY ANTIFREEZE PROTEIN *. *Journal of Biological Chemistry* **2003**, *278* (38), 36000–36004. https://doi.org/10.1074/jbc.M305222200.
(130) Angell, C. A. Supercooled Water. *Annual Review of Physical Chemistry* **1983**, *34* (Volume 34, 1983), 593–630. https://doi.org/10.1146/annurev.pc.34.100183.003113.
(131) Vali, G. Supercooling of Water and Nucleation of Ice (Drop Freezer). *American Journal of Physics* **1971**, *39* (10), 1125–1128. https://doi.org/10.1119/1.1976585.

(132) Peckhaus, A.; Kiselev, A.; Hiron, T.; Ebert, M.; Leisner, T. A Comparative Study of K-Rich and Na/Ca-Rich Feldspar Ice-Nucleating Particles in a Nanoliter Droplet Freezing Assay. *Atmospheric Chemistry and Physics* **2016**, *16* (18), 11477–11496. https://doi.org/10.5194/acp-16-11477-2016.
(133) Miller, A. J.; Brennan, K. P.; Mignani, C.; Wieder, J.; David, R. O.; Borduas-Dedekind, N. Development of the Drop Freezing Ice Nuclei Counter (FINC), Intercomparison of Droplet Freezing Techniques, and Use of Soluble Lignin as an Atmospheric Ice Nucleation Standard. *Atmospheric Measurement Techniques* **2021**, *14* (4), 3131–3151. https://doi.org/10.5194/amt-14-3131-2021.
(134) Kunert, A. T.; Lamneck, M.; Helleis, F.; Pöschl, U.; Pöhlker, M. L.; Fröhlich-Nowoisky, J. Twin-Plate Ice Nucleation Assay (TINA) with Infrared Detection for High-Throughput Droplet Freezing Experiments with Biological Ice Nuclei in Laboratory and Field Samples. *Atmospheric Measurement Techniques* **2018**, *11* (11), 6327–6337. https://doi.org/10.5194/amt-11-6327-2018.
(135) Inada, T.; Koyama, T.; Goto, F.; Seto, T. Ice Nucleation in Emulsified Aqueous Solutions of Antifreeze Protein Type III and Poly(Vinyl Alcohol). *J. Phys. Chem. B* **2011**, *115* (24), 7914–7922. https://doi.org/10.1021/jp111745v.
(136) Wood, G. R.; Walton, A. G. Homogeneous Nucleation Kinetics of Ice from Water. *Journal of Applied Physics* **1970**, *41* (7), 3027–3036. https://doi.org/10.1063/1.1659359.
(137) Inada, T.; Koyama, T.; Goto, F.; Seto, T. Inactivation of Ice Nucleating Activity of Silver Iodide by Antifreeze Proteins and Synthetic Polymers. *J. Phys. Chem. B* **2012**, *116* (18), 5364–5371. https://doi.org/10.1021/jp300535z.
(138) Koyama, T.; Inada, T.; Kuwabara, C.; Arakawa, K.; Fujikawa, S. Anti-Ice Nucleating Activity of Polyphenol Compounds against Silver Iodide. *Cryobiology* **2014**, *69* (2), 223–228. https://doi.org/10.1016/j.cryobiol.2014.07.009.
(139) Inada, T.; Koyama, T.; Tomita, H.; Fuse, T.; Kuwabara, C.; Arakawa, K.; Fujikawa, S. Anti-Ice Nucleating Activity of Surfactants against Silver Iodide in Water-in-Oil Emulsions. *J. Phys. Chem. B* **2017**, *121* (27), 6580–6587. https://doi.org/10.1021/acs.jpcb.7b02644.
(140) Kamijo, Y.; Derda, R. Freeze–Float Selection of Ice Nucleators. *Langmuir* **2019**, *35* (2), 359–364. https://doi.org/10.1021/acs.langmuir.8b02902.
(141) Kamijo, Y.; Derda, R. Freeze-Float System for High-Throughput Measurement of Ice Nucleation. ChemRxiv November 2, 2021. https://doi.org/10.26434/chemrxiv-2021-19l62.
(142) Consiglio, A. N.; Lilley, D.; Prasher, R.; Rubinsky, B.; Powell-Palm, M. J. Methods to Stabilize Aqueous Supercooling Identified by Use of an Isochoric Nucleation Detection (INDe) Device. *Cryobiology* **2022**, *106*, 91–101. https://doi.org/10.1016/j.cryobiol.2022.03.003.
(143) Powell, R. W. Thermal Conductivities and Expansion Coefficients of Water and Ice. *Advances in Physics* **1958**, *7* (26), 276–297. https://doi.org/10.1080/00018735800101277.
(144) Capicciotti, C. J.; Doshi, M.; Ben, R. N. Ice Recrystallization Inhibitors: From Biological Antifreezes to Small Molecules. In *Recent Developments in the Study of Recrystallization*; Wilson, P., Ed.; InTech, 2013. https://doi.org/10.5772/54992.
(145) Doherty, R. D.; Hughes, D. A.; Humphreys, F. J.; Jonas, J. J.; Jensen, D. J.; Kassner, M. E.; King, W. E.; McNelley, T. R.; McQueen, H. J.; Rollett, A. D. Current Issues in Recrystallization: A Review. *Materials Science and Engineering: A* **1997**, *238* (2), 219–274. https://doi.org/10.1016/S0921-5093(97)00424-3.
(146) Rios, P. R.; Siciliano Jr, F.; Sandim, H. R. Z.; Plaut, R. L.; Padilha, A. F. Nucleation and Growth during Recrystallization. *Mat. Res.* **2005**, *8*, 225–238. https://doi.org/10.1590/S1516-14392005000300002.

(147) Hartel, R. W. Mechanisms and Kinetics of Recrystallization in Ice Cream. In *The Properties of Water in Foods ISOPOW 6*; Reid, D. S., Ed.; Springer US: Boston, MA, 1998; pp 287–319. https://doi.org/10.1007/978-1-4613-0311-4_14.
(148) ADAPA, S.; SCHMIDT ,K. A.; JEON ,I. J.; HERALD ,T. J.; and FLORES, R. A. Mechanisms of Ice Crystallization and Recrystallization in Ice Cream: A Review. *Food Reviews International* **2000**, *16* (3), 259–271. https://doi.org/10.1081/FRI-100100289.
(149) Regand, A.; Goff, H. D. Structure and Ice Recrystallization in Frozen Stabilized Ice Cream Model Systems. *Food Hydrocolloids* **2003**, *17* (1), 95–102. https://doi.org/10.1016/S0268-005X(02)00042-5.
(150) Drury, M. R.; Urai, J. L. Deformation-Related Recrystallization Processes. *Tectonophysics* **1990**, *172* (3), 235–253. https://doi.org/10.1016/0040-1951(90)90033-5.
(151) Vandermeer, R. A.; Juul Jensen, D. The Migration of High Angle Grain Boundaries during Recrystallization. *Interface Science* **1998**, *6* (1), 95–104. https://doi.org/10.1023/A:1008668604733.
(152) Fletcher, N. H. Surface Structure of Water and Ice. *The Philosophical Magazine: A Journal of Theoretical Experimental and Applied Physics* **1962**, *7* (74), 255–269. https://doi.org/10.1080/14786436208211860.
(153) Fletcher, N. H. Surface Structure of Water and Ice: II. A Revised Model. *The Philosophical Magazine: A Journal of Theoretical Experimental and Applied Physics* **1968**, *18* (156), 1287–1300. https://doi.org/10.1080/14786436808227758.
(154) Lifshitz, I. M.; Slyozov, V. V. The Kinetics of Precipitation from Supersaturated Solid Solutions. *Journal of Physics and Chemistry of Solids* **1961**, *19* (1), 35–50. https://doi.org/10.1016/0022-3697(61)90054-3.
(155) Voorhees, P. W. The Theory of Ostwald Ripening. *J Stat Phys* **1985**, *38* (1), 231–252. https://doi.org/10.1007/BF01017860.
(156) Sutton, R. L.; Lips, A.; Piccirillo, G.; Sztehlo, A. Kinetics of Ice Recrystallization in Aqueous Fructose Solutions. *Journal of Food Science* **1996**, *61* (4), 741–745. https://doi.org/10.1111/j.1365-2621.1996.tb12194.x.
(157) Pronk, P.; Infante Ferreira, C. A.; Witkamp, G. J. A Dynamic Model of Ostwald Ripening in Ice Suspensions. *Journal of Crystal Growth* **2005**, *275* (1), e1355–e1361. https://doi.org/10.1016/j.jcrysgro.2004.11.173.
(158) Hagiwara, T.; Hartel, R. W.; Matsukawa, S. Relationship between Recrystallization Rate of Ice Crystals in Sugar Solutions and Water Mobility in Freeze-Concentrated Matrix. *Food Biophysics* **2006**, *1* (2), 74–82. https://doi.org/10.1007/s11483-006-9009-0.
(159) Mazur, P. Freezing of Living Cells: Mechanisms and Implications. *Am J Physiol* **1984**, *247* (3 Pt 1), C125-142. https://doi.org/10.1152/ajpcell.1984.247.3.C125.
(160) Shimada, K.; Asahina, E. Visualization of Intracellular Ice Crystals Formed in Very Rapidly Frozen Cells at −27 °C. *Cryobiology* **1975**, *12* (3), 209–218. https://doi.org/10.1016/0011-2240(75)90019-X.
(161) Farrant, J.; Walter, C. A.; Lee, H.; McGann, L. E. Use of Two-Step Cooling Procedures to Examine Factors Influencing Cell Survival Following Freezing and Thawing. *Cryobiology* **1977**, *14* (3), 273–286. https://doi.org/10.1016/0011-2240(77)90176-6.
(162) Capicciotti, C. J.; Kurach, J. D. R.; Turner, T. R.; Mancini, R. S.; Acker, J. P.; Ben, R. N. Small Molecule Ice Recrystallization Inhibitors Enable Freezing of Human Red Blood Cells with Reduced Glycerol Concentrations. *Sci Rep* **2015**, *5* (1), 9692. https://doi.org/10.1038/srep09692.

(163) Poisson, J. S.; Acker, J. P.; Briard, J. G.; Meyer, J. E.; Ben, R. N. Modulating Intracellular Ice Growth with Cell-Permeating Small-Molecule Ice Recrystallization Inhibitors. *Langmuir* **2019**, *35* (23), 7452–7458. https://doi.org/10.1021/acs.langmuir.8b02126.
(164) Jahan, S.; Adam, M. K.; Manesia, J. K.; Doxtator, E.; Ben, R. N.; Pineault, N. Inhibition of Ice Recrystallization during Cryopreservation of Cord Blood Grafts Improves Platelet Engraftment. *Transfusion* **2020**, *60* (4), 769–778. https://doi.org/10.1111/trf.15759.
(165) Khan, S.; Poisson, J.; Davila, L.; Ben, R. N.; Courtman, D. W. Small-Molecule Ice Recrystallization Inhibitors Improve Post-Thaw Recovery of Mesenchymal Stromal Cells. *Cytotherapy* **2019**, *21* (5, Supplement), S76. https://doi.org/10.1016/j.jcyt.2019.03.477.
(166) Waters, L.; Ben, R.; Acker, J. P.; Padula, M. P.; Marks, D. C.; Johnson, L. Characterizing the Ability of an Ice Recrystallization Inhibitor to Improve Platelet Cryopreservation. *Cryobiology* **2020**, *96*, 152–158. https://doi.org/10.1016/j.cryobiol.2020.07.003.
(167) Alasmar, S.; Huang, J.; Chopra, K.; Baumann, E.; Aylsworth, A.; Hewitt, M.; Sandhu, J. K.; Tauskela, J. S.; Ben, R. N.; Jezierski, A. Improved Cryopreservation of Human Induced Pluripotent Stem Cell (iPSC) and iPSC-Derived Neurons Using Ice-Recrystallization Inhibitors. *Stem Cells* **2023**, *41* (11), 1006–1021. https://doi.org/10.1093/stmcls/sxad059.
(168) Knight, C. A.; Hallett, J.; DeVries, A. L. Solute Effects on Ice Recrystallization: An Assessment Technique. *Cryobiology* **1988**, *25* (1), 55–60. https://doi.org/10.1016/0011-2240(88)90020-X.
(169) Jones, H. Splat Cooling and Metastable Phases. *Rep. Prog. Phys.* **1973**, *36* (11), 1425. https://doi.org/10.1088/0034-4885/36/11/002.
(170) Knight, C. A.; De Vries, A. L.; Oolman, L. D. Fish Antifreeze Protein and the Freezing and Recrystallization of Ice. *Nature* **1984**, *308* (5956), 295–296. https://doi.org/10.1038/308295a0.
(171) Wen, D.; Laursen, R. A. Structure-Function Relationships in an Antifreeze Polypeptide. The Role of Neutral, Polar Amino Acids. *Journal of Biological Chemistry* **1992**, *267* (20), 14102–14108. https://doi.org/10.1016/S0021-9258(19)49684-1.
(172) Wen, D.; Laursen, R. A. A Model for Binding of an Antifreeze Polypeptide to Ice. *Biophysical Journal* **1992**, *63* (6), 1659–1662. https://doi.org/10.1016/S0006-3495(92)81750-2.
(173) Knight, C. A.; Wen, D.; Laursen, R. A. Nonequilibrium Antifreeze Peptides and the Recrystallization of Ice. *Cryobiology* **1995**, *32* (1), 23–34. https://doi.org/10.1006/cryo.1995.1002.
(174) Abraham, S.; Keillor, K.; Capicciotti, C. J.; Perley-Robertson, G. E.; Keillor, J. W.; Ben, R. N. Quantitative Analysis of the Efficacy and Potency of Novel Small Molecule Ice Recrystallization Inhibitors. *Crystal Growth & Design* **2015**, *15* (10), 5034–5039. https://doi.org/10.1021/acs.cgd.5b00995.
(175) Mitchell, D. E.; Congdon, T.; Rodger, A.; Gibson, M. I. Gold Nanoparticle Aggregation as a Probe of Antifreeze (Glyco) Protein-Inspired Ice Recrystallization Inhibition and Identification of New IRI Active Macromolecules. *Sci Rep* **2015**, *5* (1), 15716. https://doi.org/10.1038/srep15716.
(176) Graham, L. A.; Agrawal, P.; Oleschuk, R. D.; Davies, P. L. High-Capacity Ice-Recrystallization Endpoint Assay Employing Superhydrophobic Coatings That Is Equivalent to the 'Splat' Assay. *Cryobiology* **2018**, *81*, 138–144. https://doi.org/10.1016/j.cryobiol.2018.01.011.
(177) SMALLWOOD, M.; WORRALL, D.; BYASS, L.; ELIAS, L.; ASHFORD, D.; DOUCET, C. J.; HOLT, C.; TELFORD, J.; LILLFORD, P.; BOWLES, D. J. Isolation and Characterization of a Novel Antifreeze Protein from Carrot (Daucus Carota). *Biochemical Journal* **1999**, *340* (2), 385–391. https://doi.org/10.1042/bj3400385.
(178) McMunn, L. E. Investigating the Cryopreservation and Ice Recrystallization Inhibition of O-Aryl-Glucopyranosides. PhD Thesis, University of Ottawa, 2025.

(179) Mohammed Saleem, A. The Effect of Organic Resins on Ice Recrystallization. MSc Thesis, Univerity of Ottawa, 2025.
(180) DeVries, A. L.; Wohlschlag, D. E. Freezing Resistance in Some Antarctic Fishes. *Science* **1969**, *163* (3871), 1073–1075. https://doi.org/10.1126/science.163.3871.1073.
(181) DeVries, A. L.; Komatsu, S. K.; Feeney, R. E. Chemical and Physical Properties of Freezing Point-Depressing Glycoproteins from Antarctic Fishes. *Journal of Biological Chemistry* **1970**, *245* (11), 2901–2908. https://doi.org/10.1016/S0021-9258(18)63073-X.
(182) Scholander, P. F.; Flagg, W.; Walters, V.; Irving, L. Climatic Adaptation in Arctic and Tropical Poikilotherms. *Physiological Zoology* **1953**, *26* (1), 67–92.
(183) Scholander, P. F.; van Dam, L.; Kanwisher, J. W.; Hammel, H. T.; Gordon, M. S. Supercooling and Osmoregulation in Arctic Fish. *Journal of Cellular and Comparative Physiology* **1957**, *49* (1), 5–24. https://doi.org/10.1002/jcp.1030490103.
(184) Meryman, H. T. Cryoprotective Agents. *Cryobiology* **1971**, *8* (2), 173–183. https://doi.org/10.1016/0011-2240(71)90024-1.
(185) Schneppenheim, R.; Theede, H. Isolation and Characterization of Freezing-Point Depressing Peptides from Larvae of *Tenebrio Molitor*. *Comparative Biochemistry and Physiology Part B: Comparative Biochemistry* **1980**, *67* (4), 561–568. https://doi.org/10.1016/0305-0491(80)90415-0.
(186) Hew, C. L.; Kao, M. H.; So, Y.-P.; Lim, K.-P. Presence of Cystine-Containing Antifreeze Proteins in the Spruce Bud Worm, Choristoneura Fumiferana. *Can. J. Zool.* **1983**, *61* (10), 2324–2328. https://doi.org/10.1139/z83-307.
(187) Duman, J. G.; Bennett, V.; Sformo, T.; Hochstrasser, R.; Barnes, B. M. Antifreeze Proteins in Alaskan Insects and Spiders. *Journal of Insect Physiology* **2004**, *50* (4), 259–266. https://doi.org/10.1016/j.jinsphys.2003.12.003.
(188) Gilbert, J. A.; Hill, P. J.; Dodd, C. E. R.; Laybourn-Parry, J. Demonstration of Antifreeze Protein Activity in Antarctic Lake Bacteria. *Microbiology* **2004**, *150* (1), 171–180. https://doi.org/10.1099/mic.0.26610-0.
(189) Muryoi, N.; Sato, M.; Kaneko, S.; Kawahara, H.; Obata, H.; Yaish, M. W. F.; Griffith, M.; Glick, B. R. Cloning and Expression of afpA, a Gene Encoding an Antifreeze Protein from the Arctic Plant Growth-Promoting Rhizobacterium Pseudomonas Putida GR12-2. *Journal of Bacteriology* **2004**, *186* (17), 5661–5671. https://doi.org/10.1128/jb.186.17.5661-5671.2004.
(190) Atıcı, Ö.; Nalbantoğlu, B. Antifreeze Proteins in Higher Plants. *Phytochemistry* **2003**, *64* (7), 1187–1196. https://doi.org/10.1016/S0031-9422(03)00420-5.
(191) Griffith, M.; Yaish, M. W. F. Antifreeze Proteins in Overwintering Plants: A Tale of Two Activities. *Trends in Plant Science* **2004**, *9* (8), 399–405. https://doi.org/10.1016/j.tplants.2004.06.007.
(192) Raymond, J. A.; DeVries, A. L. Adsorption Inhibition as a Mechanism of Freezing Resistance in Polar Fishes. *Proceedings of the National Academy of Sciences* **1977**, *74* (6), 2589–2593. https://doi.org/10.1073/pnas.74.6.2589.
(193) Meister, K.; DeVries, A. L.; Bakker, H. J.; Drori, R. Antifreeze Glycoproteins Bind Irreversibly to Ice. *J. Am. Chem. Soc.* **2018**, *140* (30), 9365–9368. https://doi.org/10.1021/jacs.8b04966.
(194) Raymond, J. A.; DeVries, A. L. Freezing Behavior of Fish Blood Glycoproteins with Antifreeze Properties. *Cryobiology* **1972**, *9* (6), 541–547. https://doi.org/10.1016/0011-2240(72)90176-9.
(195) Kerr, W. L.; Osuga, D. T.; Feeney, R. E.; Yeh, Y. Effects of Antifreeze Glycoproteins on Linear Crystallization Velocities of Ice. *Journal of Crystal Growth* **1987**, *85* (3), 449–452. https://doi.org/10.1016/0022-0248(87)90475-1.
(196) Hew, C. L.; Yang, D. S. C. Protein Interaction with Ice. *European Journal of Biochemistry* **1992**, *203* (1–2), 33–42. https://doi.org/10.1111/j.1432-1033.1992.tb19824.x.

(197) Li, Q.; Luo, L. The Kinetic Theory of Thermal Hysteresis of a Macromolecule Solution. *Chemical Physics Letters* **1993**, *216* (3), 453–457. https://doi.org/10.1016/0009-2614(93)90126-L.
(198) Li, Q.; Luo, L. Further Discussion on the Thermal Hysteresis of the Ice Growth Inhibitor. *Chemical Physics Letters* **1994**, *223* (3), 181–184. https://doi.org/10.1016/0009-2614(94)00430-7.
(199) Tam, R. Y.; Rowley, C. N.; Petrov, I.; Zhang, T.; Afagh, N. A.; Woo, T. K.; Ben, R. N. Solution Conformation of C-Linked Antifreeze Glycoprotein Analogues and Modulation of Ice Recrystallization. *J. Am. Chem. Soc.* **2009**, *131* (43), 15745–15753. https://doi.org/10.1021/ja904169a.
(200) Tam, R. Y.; Ferreira, S. S.; Czechura, P.; Chaytor, J. L.; Ben, R. N. Hydration Index—A Better Parameter for Explaining Small Molecule Hydration in Inhibition of Ice Recrystallization. *J. Am. Chem. Soc.* **2008**, *130* (51), 17494–17501. https://doi.org/10.1021/ja806284x.
(201) McMunn, L. E.; D'Costa, A. S.; Bordenave, N.; Ben, R. N. Probing the Mechanism of Action of Small-Molecule Ice Recrystallization Inhibitors Using Proton Nuclear Magnetic Resonance Relaxation. *J. Phys. Chem. Lett.* **2023**, *14* (26), 6043–6050. https://doi.org/10.1021/acs.jpclett.3c00845.
(202) Liu, S.; Ben, R. N. C-Linked Galactosyl Serine AFGP Analogues as Potent Recrystallization Inhibitors. *Org. Lett.* **2005**, *7* (12), 2385–2388. https://doi.org/10.1021/ol050677x.
(203) Czechura, P.; Tam, R. Y.; Dimitrijevic, E.; Murphy, A. V.; Ben, R. N. The Importance of Hydration for Inhibiting Ice Recrystallization with C-Linked Antifreeze Glycoproteins. *J. Am. Chem. Soc.* **2008**, *130* (10), 2928–2929. https://doi.org/10.1021/ja7103262.
(204) Balcerzak, A. K.; Capicciotti, C. J.; Briard, J. G.; Ben, R. N. Designing Ice Recrystallization Inhibitors: From Antifreeze (Glyco)Proteins to Small Molecules. *RSC Adv.* **2014**, *4* (80), 42682–42696. https://doi.org/10.1039/C4RA06893A.
(205) Inada, T.; Lu, S.-S. Inhibition of Recrystallization of Ice Grains by Adsorption of Poly(Vinyl Alcohol) onto Ice Surfaces. *Crystal Growth & Design* **2003**, *3* (5), 747–752. https://doi.org/10.1021/cg0340300.
(206) Gibson, M. I.; Barker, C. A.; Spain, S. G.; Albertin, L.; Cameron, N. R. Inhibition of Ice Crystal Growth by Synthetic Glycopolymers: Implications for the Rational Design of Antifreeze Glycoprotein Mimics. *Biomacromolecules* **2009**, *10* (2), 328–333. https://doi.org/10.1021/bm801069x.
(207) Gibson, M. I. Slowing the Growth of Ice with Synthetic Macromolecules: Beyond Antifreeze(Glyco) Proteins. *Polym. Chem.* **2010**, *1* (8), 1141–1152. https://doi.org/10.1039/C0PY00089B.
(208) Biggs, C. I.; Bailey, T. L.; Ben Graham; Stubbs, C.; Fayter, A.; Gibson, M. I. Polymer Mimics of Biomacromolecular Antifreezes. *Nat Commun* **2017**, *8* (1), 1546. https://doi.org/10.1038/s41467-017-01421-7.
(209) Biggs, C. I.; Stubbs, C.; Graham, B.; Fayter, A. E. R.; Hasan, M.; Gibson, M. I. Mimicking the Ice Recrystallization Activity of Biological Antifreezes. When Is a New Polymer "Active"? *Macromolecular Bioscience* **2019**, *19* (7), 1900082. https://doi.org/10.1002/mabi.201900082.
(210) Stubbs, C.; Bailey, T. L.; Murray, K.; Gibson, M. I. Polyampholytes as Emerging Macromolecular Cryoprotectants. *Biomacromolecules* **2020**, *21* (1), 7–17. https://doi.org/10.1021/acs.biomac.9b01053.
(211) Bachtiger, F.; Congdon, T. R.; Stubbs, C.; Gibson, M. I.; Sosso, G. C. The Atomistic Details of the Ice Recrystallisation Inhibition Activity of PVA. *Nat Commun* **2021**, *12* (1), 1323. https://doi.org/10.1038/s41467-021-21717-z.

(212) Tam, R. Y. Studies Into the Structural Features of C-Linked Antifreeze Glycoprotein Analogues Responsible for Ice-Recrystallization Inhibition Activity. PhD Thesis, University of Ottawa, 2011.
(213) Capicciotti, C. J. The Rational Design of Potent Ice Recrystallization Inhibitors for Use as Novel Cryoprotectants. PhD Thesis, University of Ottawa, 2014.
(214) Trant, J. F.; Biggs, R. A.; Capicciotti, C. J.; Ben, R. N. Developing Highly Active Small Molecule Ice Recrystallization Inhibitors Based upon C-Linked Antifreeze Glycoprotein Analogues. *RSC Adv.* **2013**, *3* (48), 26005–26009. https://doi.org/10.1039/C3RA43835J.
(215) Capicciotti, C. J.; Leclère, M.; Perras, F. A.; Bryce, D. L.; Paulin, H.; Harden, J.; Liu, Y.; Ben, R. N. Potent Inhibition of Ice Recrystallization by Low Molecular Weight Carbohydrate-Based Surfactants and Hydrogelators. *Chem. Sci.* **2012**, *3* (5), 1408–1416. https://doi.org/10.1039/C2SC00885H.
(216) De, S.; Malik, S.; Ghosh, A.; Saha, R.; Saha, B. A Review on Natural Surfactants. *RSC Advances* **2015**, *5* (81), 65757–65767. https://doi.org/10.1039/C5RA11101C.
(217) Briard, J. G.; Jahan, S.; Chandran, P.; Allan, D.; Pineault, N.; Ben, R. N. Small-Molecule Ice Recrystallization Inhibitors Improve the Post-Thaw Function of Hematopoietic Stem and Progenitor Cells. *ACS Omega* **2016**, *1* (5), 1010–1018. https://doi.org/10.1021/acsomega.6b00178.
(218) Adam, M. K. Improving the Engraftment Activities of Cryopreserved Human Umbilical Cord Blood Through the Development of Novel Glyco(Peptide)-Based Aryl Ice Recrystallization Inhibitors, Univerity of Ottawa, 2020. http://dx.doi.org/10.20381/ruor-25034.
(219) Jahan, S.; Kaushal, R.; Pasha, R.; Pineault, N. Current and Future Perspectives for the Cryopreservation of Cord Blood Stem Cells. *Transfusion Medicine Reviews* **2021**, *35* (2), 95–102. https://doi.org/10.1016/j.tmrv.2021.01.003.
(220) Carrell, D. T.; Wilcox, A. L.; Urry, R. L. Effect of Fluctuations in Temperature Encountered during Handling and Shipment of Human Cryopreserved Semen. *Andrologia* **1996**, *28* (6), 315–319. https://doi.org/10.1111/j.1439-0272.1996.tb02808.x.
(221) Smith, J. G.; Joseph, H. R.; Green, T.; Field, J. A.; Wooters, M.; Kaufhold, R. M.; Antonello, J.; Caulfield, M. J. Establishing Acceptance Criteria for Cell-Mediated-Immunity Assays Using Frozen Peripheral Blood Mononuclear Cells Stored under Optimal and Suboptimal Conditions. *Clinical and Vaccine Immunology* **2007**, *14* (5), 527–537. https://doi.org/10.1128/CVI.00435-06.
(222) Quintana, A. B.; Coda Zabetta, C. D.; Baumgartner, N. O.; Biancardi, M. E.; Bessone, V.; Rodriguez, J. V.; Mamprin, M. E.; Furno, G.; Guibert, E. E.; Sujatovich, V. Morphological and Biochemical Analysis of Human Cardiac Valve Allografts after an Increment of the Cryostorage Temperature. *Cryobiology* **2009**, *59* (1), 96–101. https://doi.org/10.1016/j.cryobiol.2009.05.003.
(223) Germann, A.; Oh, Y.-J.; Schmidt, T.; Schön, U.; Zimmermann, H.; von Briesen, H. Temperature Fluctuations during Deep Temperature Cryopreservation Reduce PBMC Recovery, Viability and T-Cell Function. *Cryobiology* **2013**, *67* (2), 193–200. https://doi.org/10.1016/j.cryobiol.2013.06.012.
(224) Briard, J. G.; Poisson, J. S.; Turner, T. R.; Capicciotti, C. J.; Acker, J. P.; Ben, R. N. Small Molecule Ice Recrystallization Inhibitors Mitigate Red Blood Cell Lysis during Freezing, Transient Warming and Thawing. *Sci Rep* **2016**, *6* (1), 23619. https://doi.org/10.1038/srep23619.
(225) Pegg, D. E. Principles of Cryopreservation. In *Cryopreservation and Freeze-Drying Protocols*; Wolkers, W. F., Oldenhof, H., Eds.; Springer: New York, NY, 2015; pp 3–19. https://doi.org/10.1007/978-1-4939-2193-5_1.

(226) Baust, J. G.; Gao ,Dayong; and Baust, J. M. Cryopreservation: An Emerging Paradigm Change. *Organogenesis* **2009**, *5* (3), 90–96. https://doi.org/10.4161/org.5.3.10021.
(227) Etheridge, M. L.; Xu, Y.; Rott, L.; Choi, J.; Glasmacher, B.; Bischof, J. C. RF Heating of Magnetic Nanoparticles Improves the Thawing of Cryopreserved Biomaterials. *Technology* **2014**, *02* (03), 229–242. https://doi.org/10.1142/S2339547814500204.
(228) Jin, B.; Mazur, P. High Survival of Mouse Oocytes/Embryos after Vitrification without Permeating Cryoprotectants Followed by Ultra-Rapid Warming with an IR Laser Pulse. *Sci Rep* **2015**, *5* (1), 9271. https://doi.org/10.1038/srep09271.
(229) Zhang, Y.; Ukpai, G.; Grigoropoulos, A.; Powell-Palm, M. J.; Weegman, B. P.; Taylor, M. J.; Rubinsky, B. Isochoric Vitrification: An Experimental Study to Establish Proof of Concept. *Cryobiology* **2018**, *83*, 48–55. https://doi.org/10.1016/j.cryobiol.2018.06.005.
(230) Smith, A. U. PREVENTION OF HÆMOLYSIS DURING FREEZING AND THAWING OF RED BLOOD-CELLS. *The Lancet* **1950**, *256* (6644), 910–911. https://doi.org/10.1016/S0140-6736(50)91861-7.
(231) Meryman, H. T.; Hornblower, M. A Simplified Procedure for Deglycerolizing Red Blood Cells Frozen in a High Glycerol Concentration. *Transfusion* **1977**, *17* (5), 438–442. https://doi.org/10.1046/j.1537-2995.1977.17578014580.x.
(232) Meryman, H. T. Frozen Red Cells. *Transfusion Medicine Reviews* **1989**, *3* (2), 121–127. https://doi.org/10.1016/S0887-7963(89)70073-0.
(233) Valeri, C. R.; Ragno, G.; Pivacek, L. E.; Cassidy, G. P.; Srey, R.; Hansson-Wicher, M.; Leavy, M. E. An Experiment with Glycerol-Frozen Red Blood Cells Stored at –80°C for up to 37 Years. *Vox Sanguinis* **2000**, *79* (3), 168–174. https://doi.org/10.1159/000031236.
(234) Tullis, J. L.; Ketchel, M. M.; Pyle, H. M.; Pennell, R. B.; Gibson, J. G., II; Tinch, R. J.; Driscoll, S. G. STUDIES ON THE IN VIVO SURVIVAL OF GLYCEROLIZED AND FROZEN HUMAN RED BLOOD CELLS. *Journal of the American Medical Association* **1958**, *168* (4), 399–404. https://doi.org/10.1001/jama.1958.03000040035008.
(235) Meryman, H. T.; Hornblower, M. A Method for Freezing and Washing Red Blood Cells Using a High Glycerol Concentration. *Transfusion* **1972**, *12* (3), 145–156. https://doi.org/10.1111/j.1537-2995.1972.tb00001.x.
(236) Turner, T.; Hansen, A.; Kurach, J.; Acker, J. P. From Development to Implementation: Adjusting the Hematocrit of Deglycerolized Red Cell Concentrates to Meet Regulatory Standards. *Transfus Med Hemother* **2017**, *44* (1), 30–38. https://doi.org/10.1159/000449039.
(237) Ramsey, G. Frozen Red Blood Cells: Cold Comfort in a Disaster? *Transfusion* **2008**, *48* (10), 2053–2055. https://doi.org/10.1111/j.1537-2995.2008.01915.x.
(238) Poisson, J. S.; Briard, J. G.; Turner, T. R.; Acker, J. P.; Ben, R. N. Hydroxyethyl Starch Supplemented with Ice Recrystallization Inhibitors Greatly Improves Cryopreservation of Human Red Blood Cells. *BioProcessing Journal* **2016**, *15* (4), 16–21. https://doi.org/10.12665/J154.Ben.
(239) Nguyen, S. T.; Nguyen, H. T.-L.; Truong, K. D. Comparative Cytotoxic Effects of Methanol, Ethanol and DMSO on Human Cancer Cell Lines. *Biomedical Research and Therapy* **2020**, *7* (7), 3855–3859. https://doi.org/10.15419/bmrat.v7i7.614.
(240) Armitage, W. J.; Mazur, P. Toxic and Osmotic Effects of Glycerol on Human Granulocytes. *American Journal of Physiology-Cell Physiology* **1984**, *247* (5), C382–C389. https://doi.org/10.1152/ajpcell.1984.247.5.C382.
(241) Bove, K. E. Ethylene Glycol Toxicity. *Am J Clin Pathol* **1966**, *45* (1), 46–50. https://doi.org/10.1093/ajcp/45.1.46.

(242) Matsumura, K.; Hayashi ,Fumiaki; Nagashima ,Toshio; and Hyon, S. H. Long-Term Cryopreservation of Human Mesenchymal Stem Cells Using Carboxylated Poly-l-Lysine without the Addition of Proteins or Dimethyl Sulfoxide. *Journal of Biomaterials Science, Polymer Edition* **2013**, *24* (12), 1484–1497. https://doi.org/10.1080/09205063.2013.771318.
(243) Deller, R. C.; Vatish, M.; Mitchell, D. A.; Gibson, M. I. Synthetic Polymers Enable Non-Vitreous Cellular Cryopreservation by Reducing Ice Crystal Growth during Thawing. *Nat Commun* **2014**, *5* (1), 3244. https://doi.org/10.1038/ncomms4244.
(244) El Assal, R.; Abou-Elkacem, L.; Tocchio, A.; Pasley, S.; Matosevic, S.; Kaplan, D. L.; Zylberberg, C.; Demirci, U. Bioinspired Preservation of Natural Killer Cells for Cancer Immunotherapy. *Advanced Science* **2019**, *6* (6), 1802045. https://doi.org/10.1002/advs.201802045.
(245) Liu, M.; Zhang, X.; Guo, H.; Zhu, Y.; Wen, C.; Sui, X.; Yang, J.; Zhang, L. Dimethyl Sulfoxide-Free Cryopreservation of Chondrocytes Based on Zwitterionic Molecule and Polymers. *Biomacromolecules* **2019**, *20* (10), 3980–3988. https://doi.org/10.1021/acs.biomac.9b01024.
(246) Ntai, A.; La Spada, A.; De Blasio, P.; Biunno, I. Trehalose to Cryopreserve Human Pluripotent Stem Cells. *Stem Cell Research* **2018**, *31*, 102–112. https://doi.org/10.1016/j.scr.2018.07.021.
(247) Pollock, K.; Samsonraj, R. M.; Dudakovic, A.; Thaler, R.; Stumbras, A.; McKenna, D. H.; Dosa, P. I.; van Wijnen, A. J.; Hubel, A. Improved Post-Thaw Function and Epigenetic Changes in Mesenchymal Stromal Cells Cryopreserved Using Multicomponent Osmolyte Solutions. *Stem Cells and Development* **2017**, *26* (11), 828–842. https://doi.org/10.1089/scd.2016.0347.
(248) Li, R.; Hornberger, K.; Dutton, J. R.; Hubel, A. Cryopreservation of Human iPS Cell Aggregates in a DMSO-Free Solution—An Optimization and Comparative Study. *Front. Bioeng. Biotechnol.* **2020**, *8*. https://doi.org/10.3389/fbioe.2020.00001.
(249) Kaushal, R.; Jahan, S.; McGregor, C.; Pineault, N. Dimethyl Sulfoxide-Free Cryopreservation Solutions for Hematopoietic Stem Cell Grafts. *Cytotherapy* **2022**, *24* (3), 272–281. https://doi.org/10.1016/j.jcyt.2021.09.002.
(250) Loo, D. T.; Rillema, J. R. Chapter 14 Measurement of Cell Death. In *Methods in Cell Biology*; Mather, J. P., Barnes, D., Eds.; Animal Cell Culture Methods; Academic Press, 1998; Vol. 57, pp 251–264. https://doi.org/10.1016/S0091-679X(08)61583-6.
(251) Banfalvi, G. Methods to Detect Apoptotic Cell Death. *Apoptosis* **2017**, *22* (2), 306–323. https://doi.org/10.1007/s10495-016-1333-3.
(252) Poisson, J. S. Synthesis and In Vitro Applications of Ice Recrystallization Inhibitors, University of Ottawa, 2019.
(253) Ampaw, A. Addressing Solubility Limitations in Small-Molecule Ice Recrystallization Inhibitors and Evaluating Their Use in Hematopoietic Stem Cell and Red Blood Cell Cryopreservation. PhD Thesis, University of Ottawa, 2022.
(254) Alasmar, S. Cryopreservation of Induced Pluripotent Stem Cell Derived Neurons and Primary T-Cells and Natural Killer Cells Using Ice Recrystallization Inhibitor Technology. PhD Thesis, Université d'Ottawa / University of Ottawa, 2022.
(255) O'Brien, J.; Wilson, I.; Orton, T.; Pognan, F. Investigation of the Alamar Blue (Resazurin) Fluorescent Dye for the Assessment of Mammalian Cell Cytotoxicity. *European Journal of Biochemistry* **2000**, *267* (17), 5421–5426. https://doi.org/10.1046/j.1432-1327.2000.01606.x.
(256) Yuan, J.; Ofengeim, D. A Guide to Cell Death Pathways. *Nat Rev Mol Cell Biol* **2024**, *25* (5), 379–395. https://doi.org/10.1038/s41580-023-00689-6.
(257) Kumar, P.; Nagarajan, A.; Uchil, P. D. Analysis of Cell Viability by the Lactate Dehydrogenase Assay. *Cold Spring Harb Protoc* **2018**, *2018* (6), pdb.prot095497. https://doi.org/10.1101/pdb.prot095497.

2 Goals and objectives

2.1 Thesis goals

The development of novel cryoprotective agents (CPAs) in the Ben laboratory has spanned over two decades,[1,2] and produced numerous functional ice recrystallization inhibitors (IRIs) with various cell based applications.[3–7] The work presented in this thesis aims to leverage the library of small molecules of known IRI activity and cryoprotective efficacy. A major focus of this work is to expand the library of small molecule CPAs and to provide rationale as to why a given molecule is IRI active and / or an effective CPA. A better understanding of why a given compound possesses (or lacks) CPA efficacy, which will aid in the development of novel strategies and scaffolds for the rational design of next-generation CPA compounds.

2.2 Objective 1 – Develop and implement an ice nucleation activity (INA) assay and assess the relationship between INA and IRI activity

Deliberately influencing the ice nucleation temperature of a solution has been shown to be a beneficial strategy in both the fields of cryopreservation[8–12] and supercooled storage.[13,14] Induced ice nucleation during the cryopreservation process can limit cellular damage caused by intracellular ice formation, solute effects and the latent heat release of nucleation.[15–18] Recent work has demonstrated that inducing ice nucleation at a warmer temperature provides a synergistic benefit with IRI active polymers,[19] however the relationship between IRI activity and ice nucleation temperature has not been explored with small molecules. In contrast, supressing ice nucleation can be harnessed in the supercooled storage of cells, whereby storage at colder temperatures (above the nucleation temperature) can greatly prolong the storage of biological materials, without the formation of ice. **Chapter 3** of this work aims to examine the relationship between the capacity for a compound to influence ice nucleation and ice recrystallization utilizing previously established small molecule IRIs.[7,20]

Prior to assessing the ice nucleation activity for a given compound, the implementation of an INA assay will be required. With an in-house INA assay, examination of both the capacity to induce (or suppress) ice nucleation as well as the consistency of induced nucleation (at a range of nucleation temperatures) will be possible. Several distinct INA assays have been characterized in literature,[21–25] and an adaptation of the Freeze-Float assay[26] was chosen for our implementation. This assay will be developed, then assessed for consistency (including: cooling rates, temperature homogeneity and operator error), then used to generate baseline assessments

of positive (AgI, Snomax®) and negative controls (phosphate buffered saline (PBS), water) for ice nucleation activity.

With ability to assess INA activity, the first half of **Objective 1** of this thesis is to assess the capacity for a set of small molecule carbohydrates of known IRI activity to influence ice nucleation. Once characterized, subsequent INA assessments will be determined. Any measurable result (inducing, suppressing, or not affecting ice nucleation) will provide insight as to the ability for small molecule IRIs to act as INA active compounds; by extension, the ice nucleation temperature measured will be compared to the known IRI activity of a given compound (or compound family) to discern the relationship between the two phenomena. Should any specific compound (or set of compounds) exhibit the capacity to induce or suppress ice nucleation, it will provide information as to structural components that may be required to generate small molecules capable of modulating ice nucleation temperature.

In complement, the second half of **Objective 1** of this thesis is to determine the influence of ice nucleation temperature on ice crystal grain size; this is of particular interest due to the synergistic relationship recently reported with IRI active polymers.[19] Utilizing the modified splat cooling assay (SCA), IRI activity will be assessed in the presence or absence of INA active silver iodide (AgI) particles. Utilizing the same compound set (of known IRI activity solvated in PBS) as the first half of this objective, compounds will be solvated in AgI / PBS suspensions and assessed for IRI activity. The resulting IRI activity in the presence of INA active AgI particles will further elucidate the relationship between INA and IRI activity; should no change in IRI activity be observed, this will indicate that the ice nucleation temperature does not influence the IRI activity of small molecule IRIs. However, should the IRI activity differ, this will indicate a synergistic or antagonistic relationship between INA and IRI activity, which has yet to be characterized in small molecules.

Ultimately, the establishment of a library of biocompatible small molecule CPAs of known ice nucleating activity will aid in not only in the development of novel cryopreservation protocols, but guide ongoing attempts to develop dual-action biocompatible IRI / INA active small molecules. **Objective 1** of this thesis represents the foundation to developing an understanding of small molecule INAs, as well as the relationship between INA and IRI activity.

2.3 Objective 2 - Identify structural components required for IRI activity in *N*-aryl gluconamides

Through the development of small molecule carbohydrate IRIs, three major families of compounds have been established: the *N*-alkyl aldonamides, based upon characterized surfactants, these compounds represent extremely IRI active, but poorly soluble and highly toxic derivatives.[27,28] The *O*-aryl pyranosides present a less active, but more biocompatible set of small molecule carbohydrate IRIs,[20] which have been very effective for the cryopreservation of red blood cells.[29–31] More recently, the *N*-aryl gluconamide IRIs have excelled in the cryopreservation of HSPCs,[7] MSCs,[4] platelets,[3,5] and iPSCs.[6]

Previous studies by the Ben laboratory with *N*-aryl gluconamides have focused on the impact of modifying *N*-aryl substitution on IRI activity,[32,33] resulting in a number of small molecule IRI CPAs. However, limited investigations have examined positional importance for *N*-aryl gluconamide IRIs beyond aryl substitution. **Objective 2** of this thesis (**Chapter 4**) will begin with the most successful small molecule IRI generated to date, *N*-(2-fluorophenyl)-D-gluconamide (compound **4.01**) and examine which structural features are required for its measured IRI activity. A systematic approach will be utilized to reduce the length of the carbohydrate polyol chain and assess IRI activity after each modification (**Figure 2.1**); should a dramatic loss in IRI activity occur, this will indicate the removed position was highly important for IRI activity. Should a modification not result in a change to the IRI activity, this position could be a potential site for modification. It is expected that with each subsequent modification, the resulting IRI activity will decrease until IRI activity is no longer measurable.

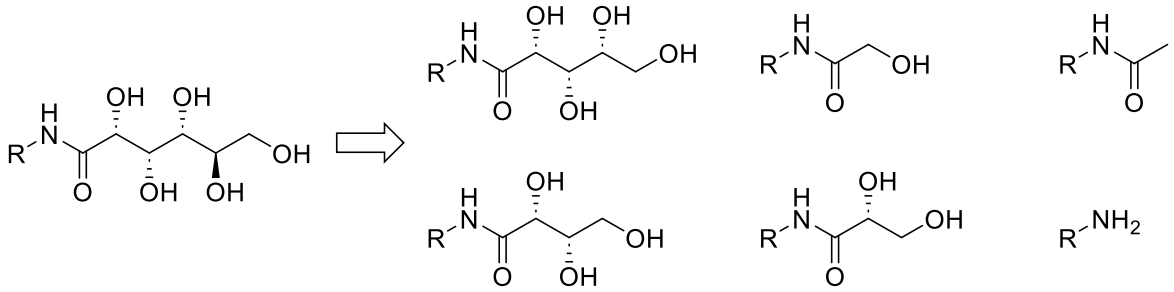

Figure 2.1 Generic compound set of *N*-functionalized derivatives of incrementally reduced polyol chain length.

Subsequent assessment of *N*-(3-fluorophenyl)-D- gluconamide (**4.02**) and *N*-(4-fluorophenyl)-D-gluconamide (**4.03**) will analyze the regioselective effects of *N*-aryl fluorination on IRI activity. As well, *N*-(4-methoxyphenyl)-D-gluconamide (**4.04**) will be examined as an IRI active[33] *N*-aryl

gluconamide bearing an electron rich aryl ring, opposed to the electron poor aryl ring present in **4.01**. Once the IRI assessment of modified *N*-aryl gluconamides with reduced polyol chains is complete, compounds of will be compared based upon common *N*-functionalization (to determine hydroxyl importance) and common polyol chain length (to determine the effect of *N*-functionalization).

The second phase of **Objective 2** will be to selectively dehydroxylate positions identified as low importance for IRI activity. The selective removal of a targeted position will verify how much IRI activity is retained with the remaining functionality. Through targeted dehydroxylation, the minimum structural components required for IRI activity will be able to be identified. The resulting compound possessing only the minimum structural components required for IRI activity will be used as a starting scaffold for future development of *N*-aryl gluconaimde derived IRIs.

2.4 Objective 3 - Identify structural components required for IRI activity in *N*-alkyl gluconamides

Being the first set of small molecule carbohydrate IRIs identified by the Ben lab,[27,28] and possessing some of the most active small molecule IRIs to date, *N*-alkyl gluconamide IRIs have yet to be successfully applied to cellular cryopreservation. *N*-alkyl gluconamides of sufficient alkyl chain length are more IRI active (IC_{50} < 3 mM) than *N*-aryl gluconamides such as **4.01**. However, these small molecule carbohydrates also have poor aqueous solubility and surfactant-like cytotoxicity. As there have been many assessments of *N*-alkyl gluconamides,[32,34–36] utilizing different iterations of the SCA, the first phase of **Objective 3** will be to generate a consistent assessment of *N*-alkyl gluconamide IRI activity on the current modified SCA (**Figure 2.2**). The second phase of **Objective 3** will be to select a model IRI active *N*-alkyl gluconamide and incrementally reduce the length of its polyol chain. A prime candidate is predicted to be *N*-(octyl)-D-gluconamide (**5.04**), as it has been successfully utilized in the cryopreservation of viral particles.[37] With a better understanding of structural requirements for IRI activity, targeted dehydroxylation will be utilized to highlight the minimum structural requirement for IRI activity in *N*-alkyl gluconamides.

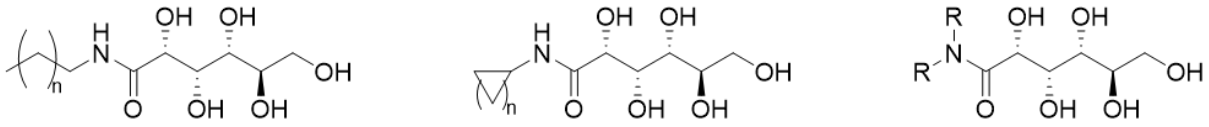

5.01 n = 1
5.02 n = 4
5.03 n = 5
5.04 n = 6

5.05 n = 1
5.06 n = 3
5.07 n = 4
5.08 n = 5
5.09 n = 6

5.10 R = C_6H_{13}
5.11 R = C_6H_{11}

Figure 2.2 Initial *N*-alkyl gluconamide compound set for IRI analysis on the modern SCA.

For *N*-alkyl gluconamides, cytotoxicity (in particularly caused by membrane instability) is a primary concern. Cytotoxicity of model *N*-alkyl gluconamide derivatives will be determined metabolically with the resazurin cellular viability assay.[38] As metabolic death can arise from several distinct mechanisms,[39] confirmation of membrane integrity will be assessed with the lactate dehydrogenase (LDH) assay.[40] The proportion of cellular death measured by the LDH assay with respect to the cellular death measured by the resazurin assay will be used to determine the degree of membrane damage caused by the target compound. Should a novel modification provide improved IRI activity but also increase cytotoxicity, it may provide mechanistic understanding but not be directly applicable as a CPA.

2.5 References

(1) Capicciotti, C. J.; Doshi, M.; Ben, R. N. Ice Recrystallization Inhibitors: From Biological Antifreezes to Small Molecules. In *Recent Developments in the Study of Recrystallization*; Wilson, P., Ed.; InTech, 2013. https://doi.org/10.5772/54992.

(2) McMunn, L. E.; Walsh, E. M.; Ben, R. N. PERSPECTIVE: Targeted Development and Optimization of Small-Molecule Ice Recrystallization Inhibitors (IRIs) for the Cryopreservation of Biological Systems. *Cryoletters* **2024**, *45* (2), 69–87. https://doi.org/10.54680/fr24210110112.

(3) Jahan, S.; Adam, M. K.; Manesia, J. K.; Doxtator, E.; Ben, R. N.; Pineault, N. Inhibition of Ice Recrystallization during Cryopreservation of Cord Blood Grafts Improves Platelet Engraftment. *Transfusion* **2020**, *60* (4), 769–778. https://doi.org/10.1111/trf.15759.

(4) Khan, S.; Poisson, J.; Davila, L.; Ben, R. N.; Courtman, D. W. Small-Molecule Ice Recrystallization Inhibitors Improve Post-Thaw Recovery of Mesenchymal Stromal Cells. *Cytotherapy* **2019**, *21* (5, Supplement), S76. https://doi.org/10.1016/j.jcyt.2019.03.477.

(5) Waters, L.; Ben, R.; Acker, J. P.; Padula, M. P.; Marks, D. C.; Johnson, L. Characterizing the Ability of an Ice Recrystallization Inhibitor to Improve Platelet Cryopreservation. *Cryobiology* **2020**, *96*, 152–158. https://doi.org/10.1016/j.cryobiol.2020.07.003.

(6) Alasmar, S.; Huang, J.; Chopra, K.; Baumann, E.; Aylsworth, A.; Hewitt, M.; Sandhu, J. K.; Tauskela, J. S.; Ben, R. N.; Jezierski, A. Improved Cryopreservation of Human Induced Pluripotent Stem Cell (iPSC) and iPSC-Derived Neurons Using Ice-Recrystallization Inhibitors. *Stem Cells* **2023**, *41* (11), 1006–1021. https://doi.org/10.1093/stmcls/sxad059.

(7) Briard, J. G.; Jahan, S.; Chandran, P.; Allan, D.; Pineault, N.; Ben, R. N. Small-Molecule Ice Recrystallization Inhibitors Improve the Post-Thaw Function of Hematopoietic Stem and

Progenitor Cells. *ACS Omega* **2016**, *1* (5), 1010–1018. https://doi.org/10.1021/acsomega.6b00178.
(8) Zavos, P. M.; Graham, E. F. Effects of Various Degrees of Supercooling and Nucleation Temperatures on Fertility of Frozen Turkey Spermatozoa. *Cryobiology* **1983**, *20* (5), 553–559. https://doi.org/10.1016/0011-2240(83)90043-3.
(9) Missous, G.; Thammavongs, B.; Dieuleveux, V.; Guéguen, M.; Panoff, J. M. Improvement of the Cryopreservation of the Fungal Starter *Geotrichum Candidum* by Artificial Nucleation and Temperature Downshift Control. *Cryobiology* **2007**, *55* (1), 66–71. https://doi.org/10.1016/j.cryobiol.2007.05.004.
(10) Lauterboeck, L.; Hofmann, N.; Mueller, T.; Glasmacher, B. Active Control of the Nucleation Temperature Enhances Freezing Survival of Multipotent Mesenchymal Stromal Cells. *Cryobiology* **2015**, *71* (3), 384–390. https://doi.org/10.1016/j.cryobiol.2015.10.145.
(11) Daily, M. I.; Whale, T. F.; Partanen, R.; Harrison, A. D.; Kilbride, P.; Lamb, S.; Morris, G. J.; Picton, H. M.; Murray, B. J. Cryopreservation of Primary Cultures of Mammalian Somatic Cells in 96-Well Plates Benefits from Control of Ice Nucleation. *Cryobiology* **2020**, *93*, 62–69. https://doi.org/10.1016/j.cryobiol.2020.02.008.
(12) Dan, N.; Shelake, S.; Luo, W.-C.; Rahman, M.; Lu, J.; Bogner, R. H.; Lu, X. Impact of Controlled Ice Nucleation on Intracellular Dehydration, Ice Formation and Their Implications on T Cell Freeze–Thaw Viability. *International Journal of Pharmaceutics* **2024**, *665* (Complete). https://doi.org/10.1016/j.ijpharm.2024.124694.
(13) Huang, H.; Yarmush, M. L.; Usta, O. B. Long-Term Deep-Supercooling of Large-Volume Water and Red Cell Suspensions via Surface Sealing with Immiscible Liquids. *Nat Commun* **2018**, *9* (1), 3201. https://doi.org/10.1038/s41467-018-05636-0.
(14) Huang, H.; Rey-Bedón, C.; Yarmush, M. L.; Usta, O. B. Deep-Supercooling for Extended Preservation of Adipose-Derived Stem Cells. *Cryobiology* **2020**, *92*, 67–75. https://doi.org/10.1016/j.cryobiol.2019.11.004.
(15) Morris, G. J.; Acton, E. Controlled Ice Nucleation in Cryopreservation--a Review. *Cryobiology* **2013**, *66* (2), 85–92. https://doi.org/10.1016/j.cryobiol.2012.11.007.
(16) Pitt, R. E.; Chandrasekaran, M.; Parks, J. E. Performance of a Kinetic Model for Intracellular Ice Formation Based on the Extent of Supercooling. *Cryobiology* **1992**, *29* (3), 359–373. https://doi.org/10.1016/0011-2240(92)90037-3.
(17) Karlsson, J. O.; Cravalho, E. G.; Borel Rinkes, I. H.; Tompkins, R. G.; Yarmush, M. L.; Toner, M. Nucleation and Growth of Ice Crystals inside Cultured Hepatocytes during Freezing in the Presence of Dimethyl Sulfoxide. *Biophys J* **1993**, *65* (6), 2524–2536. https://doi.org/10.1016/S0006-3495(93)81319-5.
(18) Wolkers, W. F.; Balasubramanian, S. K.; Ongstad, E. L.; Zec, H. C.; Bischof, J. C. Effects of Freezing on Membranes and Proteins in LNCaP Prostate Tumor Cells. *Biochimica et Biophysica Acta (BBA) - Biomembranes* **2007**, *1768* (3), 728–736. https://doi.org/10.1016/j.bbamem.2006.12.007.
(19) Mousazadehkasin, M.; Mitchell, N.; Asenath-Smith, E.; Tsavalas, J. G. Ice Nucleation Promotion Impact on the Ice Recrystallization Inhibition Activity of Polyols. *Biomacromolecules* **2023**, *24* (2), 678–689. https://doi.org/10.1021/acs.biomac.2c01120.
(20) Capicciotti, C. J.; Mancini, R. S.; Turner, T. R.; Koyama, T.; Alteen, M. G.; Doshi, M.; Inada, T.; Acker, J. P.; Ben, R. N. O-Aryl-Glycoside Ice Recrystallization Inhibitors as Novel Cryoprotectants: A Structure–Function Study. *ACS Omega* **2016**, *1* (4), 656–662. https://doi.org/10.1021/acsomega.6b00163.
(21) Vali, G. Supercooling of Water and Nucleation of Ice (Drop Freezer). *American Journal of Physics* **1971**, *39* (10), 1125–1128. https://doi.org/10.1119/1.1976585.

(22) Inada, T.; Koyama, T.; Goto, F.; Seto, T. Ice Nucleation in Emulsified Aqueous Solutions of Antifreeze Protein Type III and Poly(Vinyl Alcohol). *J. Phys. Chem. B* **2011**, *115* (24), 7914–7922. https://doi.org/10.1021/jp111745v.
(23) Consiglio, A. N.; Lilley, D.; Prasher, R.; Rubinsky, B.; Powell-Palm, M. J. Methods to Stabilize Aqueous Supercooling Identified by Use of an Isochoric Nucleation Detection (INDe) Device. *Cryobiology* **2022**, *106*, 91–101. https://doi.org/10.1016/j.cryobiol.2022.03.003.
(24) Kunert, A. T.; Lamneck, M.; Helleis, F.; Pöschl, U.; Pöhlker, M. L.; Fröhlich-Nowoisky, J. Twin-Plate Ice Nucleation Assay (TINA) with Infrared Detection for High-Throughput Droplet Freezing Experiments with Biological Ice Nuclei in Laboratory and Field Samples. *Atmospheric Measurement Techniques* **2018**, *11* (11), 6327–6337. https://doi.org/10.5194/amt-11-6327-2018.
(25) Kamijo, Y.; Derda, R. Freeze-Float System for High-Throughput Measurement of Ice Nucleation. ChemRxiv November 2, 2021. https://doi.org/10.26434/chemrxiv-2021-19l62.
(26) Kamijo, Y.; Derda, R. Freeze–Float Selection of Ice Nucleators. *Langmuir* **2019**, *35* (2), 359–364. https://doi.org/10.1021/acs.langmuir.8b02902.
(27) Capicciotti, C. J.; Leclère, M.; Perras, F. A.; Bryce, D. L.; Paulin, H.; Harden, J.; Liu, Y.; Ben, R. N. Potent Inhibition of Ice Recrystallization by Low Molecular Weight Carbohydrate-Based Surfactants and Hydrogelators. *Chem. Sci.* **2012**, *3* (5), 1408–1416. https://doi.org/10.1039/C2SC00885H.
(28) Trant, J. F.; Biggs, R. A.; Capicciotti, C. J.; Ben, R. N. Developing Highly Active Small Molecule Ice Recrystallization Inhibitors Based upon C-Linked Antifreeze Glycoprotein Analogues. *RSC Adv.* **2013**, *3* (48), 26005–26009. https://doi.org/10.1039/C3RA43835J.
(29) Briard, J. G.; Poisson, J. S.; Turner, T. R.; Capicciotti, C. J.; Acker, J. P.; Ben, R. N. Small Molecule Ice Recrystallization Inhibitors Mitigate Red Blood Cell Lysis during Freezing, Transient Warming and Thawing. *Sci Rep* **2016**, *6* (1), 23619. https://doi.org/10.1038/srep23619.
(30) Capicciotti, C. J.; Kurach, J. D. R.; Turner, T. R.; Mancini, R. S.; Acker, J. P.; Ben, R. N. Small Molecule Ice Recrystallization Inhibitors Enable Freezing of Human Red Blood Cells with Reduced Glycerol Concentrations. *Sci Rep* **2015**, *5* (1), 9692. https://doi.org/10.1038/srep09692.
(31) Poisson, J. S.; Briard, J. G.; Turner, T. R.; Acker, J. P.; Ben, R. N. Hydroxyethyl Starch Supplemented with Ice Recrystallization Inhibitors Greatly Improves Cryopreservation of Human Red Blood Cells. *BioProcessing Journal* **2016**, *15* (4), 16–21. https://doi.org/10.12665/J154.Ben.
(32) Briard, J. G. The Rational Design and Use of Novel Small-Molecule Ice Recrystallization Inhibitors for the Cryopreservation of Hematopoietic Stem Cells and Red Blood Cells. PhD Thesis, University of Ottawa, 2016.
(33) Briard, J. G.; Fernandez, M.; De Luna, P.; Woo, Tom. K.; Ben, R. N. QSAR Accelerated Discovery of Potent Ice Recrystallization Inhibitors. *Sci Rep* **2016**, *6* (1), 26403. https://doi.org/10.1038/srep26403.
(34) Tam, R. Y.; Ferreira, S. S.; Czechura, P.; Chaytor, J. L.; Ben, R. N. Hydration Index—A Better Parameter for Explaining Small Molecule Hydration in Inhibition of Ice Recrystallization. *J. Am. Chem. Soc.* **2008**, *130* (51), 17494–17501. https://doi.org/10.1021/ja806284x.
(35) Capicciotti, C. J. The Rational Design of Potent Ice Recrystallization Inhibitors for Use as Novel Cryoprotectants. PhD Thesis, University of Ottawa, 2014.
(36) Newell, K. Enabling the Effective Transport of RNA Oligonucleotide Constructs and RNA Viruses: Preservation and Stabilization of Viruses Using Ice Recrystallization Inhibitors. Unpublished Honours Thesis, University of Ottawa, 2021.

(37) Balcerzak, A. K. Elucidating the Key Structural Features of Carbohydrates and Surfactants Necessary for Inhibiting Ice Recrystallization. PhD Thesis, University of Ottawa, 2014.
(38) O'Brien, J.; Wilson, I.; Orton, T.; Pognan, F. Investigation of the Alamar Blue (Resazurin) Fluorescent Dye for the Assessment of Mammalian Cell Cytotoxicity. *European Journal of Biochemistry* **2000**, *267* (17), 5421–5426. https://doi.org/10.1046/j.1432-1327.2000.01606.x.
(39) Yuan, J.; Ofengeim, D. A Guide to Cell Death Pathways. *Nat Rev Mol Cell Biol* **2024**, *25* (5), 379–395. https://doi.org/10.1038/s41580-023-00689-6.
(40) Kumar, P.; Nagarajan, A.; Uchil, P. D. Analysis of Cell Viability by the Lactate Dehydrogenase Assay. *Cold Spring Harb Protoc* **2018**, *2018* (6), pdb.prot095497. https://doi.org/10.1101/pdb.prot095497.

3. Investigation of the Relationship Between Ice Nucleation Activity (INA) and Ice Recrystallization Inhibition (IRI) Activity

3.1 Introduction

With the aim of developing novel cryopreservation agents (CPAs) to improve cryopreservation, twenty years of work have been committed to the design of IRIs in the Ben lab.[1–5] The phenomena of ice recrystallization is a major cause of cellular damage during cryopreservation,[6,7] and is often neglected by traditional cryopreservation protocol. The addition of bio-compatible IRIs to supplement traditional CPA regiments, aims to improve post-thaw recovery, viability and functionality.[1,2,8] Ice nucleation, like ice recrystallization, is important to control during the cryopreservation process. Ice nucleation is the phenomena of an ordered ice embryo forming in supercooled water, inducing subsequent phase change throughout the sample. The controlled mechanical nucleation of cryopreserved material has been found to be beneficial when compared to uncontrolled nucleation.[9,10] However, many cryopreservation protocols neglect to control when a cryopreserved sample undergoes nucleation.[11]

The goal of this work is to preform the first investigations towards the rational design of a bio-compatible small molecule CPA capable of modulating not only IRI activity, but also ice nucleation. The phenomena of ice recrystallization and ice nucleation have recently been investigated in designer macromolecule CPAs.[12] Through the investigation of IRI active glycerol-grafted poly(vinyl alcohol) polymers, a synergistic relationship was identified between INA and IRI activity.[12] This study concluded that if ice nucleation occurs at a warmer temperature the resulting crystal dimensions will be smaller, ultimately making an IRI more active. Designer macromolecules have been recently proposed to promote ice nucleation,[13,14] however the simultaneous application of both IRI and INA active CPAs to cryopreserved material has yet to be examined.

IRI active macromolecules function by binding to the ice crystal surface,[15,16] but in contrast, it has been established that small molecule carbohydrate IRIs described by the Ben lab do not bind ice.[17,18] The exact mechanism of small molecule IRI activity is not fully understood, however it has been established that small molecule IRIs interact with bulk water as opposed to ice.[18] Due to the fact that these molecules are relatively easy to synthesize, the generation and subsequent study of synthetic small molecule CPAs is preferable to the design of macromolecules. As small molecule carbohydrates function by a different mechanism than macromolecule IRIs, it is not known what relationship exists between small molecule INA and IRI activity. When considering

the application to small molecule carbohydrates, the synergy between an elevated ice nucleation temperature (T_{nuc}) and improved IRI activity can be reasonably extended to small molecule IRIs; should sample nucleation yield smaller initial ice crystals, IRI activity should be improved regardless of mechanism. However, the generation of a homogenous small molecule ice nucleator poses substantial challenges.

Ice nucleation is a stochastic event that is either homogeneous (in pure water), or heterogeneous (when a foreign body induces ice nucleation). The foremost mechanism of heterogenous ice nucleation, the central nucleation theory (CNT), has been generally accepted for almost a century[19–21] and describes a number of thermodynamic and kinetic variables which influence the probability of an ordered ice embryo forming in solution. These variables include: the melting point of the solution (T_m), the interfacial tension between ice embryo and water, the presence or shape of foreign bodies, and the kinetic ability for water molecules to interface with the ice embryo.[22] Each of these traditional variables can be targeted to influence the temperature of heterogeneous ice nucleation in a sample.[23–26] A small molecule carbohydrate can reasonably depress the melting point of a solution at very high concentrations (supressing ice nucleation),[27,28] however it is difficult to rationalize the capacity to raise the solution T_m. The hydration of simple monosaccharides is an active field of study,[29–32] and it has been demonstrated that monosaccharide isomerism has a direct impact on how compatible the solvated complex is with ordered ice.[33] Solvation shells are not known for our IRIs, but resulting solvation shells could reasonably coordinate towards or against an ice – like lattice, influencing the interfacial tension of a generated ice embryo. As small molecule IRIs are solvated at room temperature, it is possible that as temperature is lowered during the cooling process, small precipitates form; the formation of small particles could act as a foreign body inducing ice nucleation. From the examination of ^{1}H NMR relaxation times, it has been determined that the introduction of small molecule IRI **4.01** decreased the molecular motion of bulk water,[18] which would contribute to supressing ice nucleation. However since these measurements were performed above the solution T_m and were found to be temperature dependent,[18] this relationship may not apply to supercooled solutions. The potential magnitude of each of these CNT factors is not known for small molecule CPAs, however the mechanism of any INA active small molecule will differ from established macromolecules.

The generation of bio-compatible small molecules capable of promoting ice nucleation would be beneficial to the development of novel cryopreservation protocols. Alternatively, novel methods for the supercooled storage of red blood cells have increased the shelf life of red blood cell units

from the traditional 6 weeks to 23 weeks by lowering the storage temperature from 4 °C, to -8 °C.[34,35] Should a small molecule CPA be identified with the capacity to lower T_m, and by extension the T_{nuc} at bio-compatible concentrations, it could be effectively applied to the storage of supercooled solutions.

Given that the Ben lab has access to a library of bio-compatible small molecule IRIs, the aim of this preliminary investigation was to leverage known IRI small molecules and assess their capacity to influence ice nucleation. To allow for assessment of ice nucleation activity, the implementation of an ice nucleation assay was required. The basic components required for an ice nucleation activity assay consist of an isolated aqueous sample, placed into a cooled environment where nucleation events can be detected. The simplest ice nucleation activity assay is the drop freezing method, whereby an aqueous sample is placed onto an oiled aluminum plate which is slowly cooled under a microscope.[36,37] One notable adaptation of the drop freezing assay is the emulsion freezing assay, whereby the aqueous samples are sealed into a hydrophobic suspension between two thin pieces of glass. The generated emulsion is placed into a cooling chamber under a microscope, where nucleation events within aqueous droplets can be imaged.[38] A modern adaptation of these INA assays has recently been published by Kamijo and Derda;[39] the Freeze-Float assay implements components of the drop freezing method and emulsion freezing assay.[39] The Freeze-Float assay was developed utilizing commodity components, without the need of any specially designed machines.[39] Rather than utilizing a cryo-stage, samples are prepared in disposable cuvettes and cooled within a commodity grade freezer. The use of a larger commercial freezer also allows for imaging to be accomplished with a commercially available DSLR camera opposed to specialized microscope fitted optics. Due to the ease of implementation and capacity for relatively high-throughput screening, the Freeze-Float assay was chosen as the INA assay to complement our modified splat cooling assay (SCA) for IRI assessment (**Figure 3.1**).

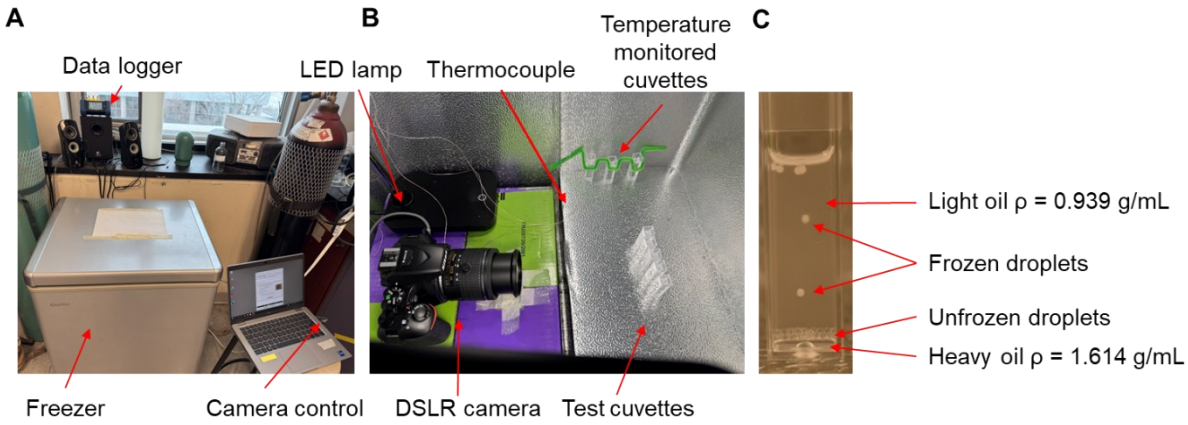

Figure 3.1 (A) Exterior of assembled assay, including the data logger, laptop, freezer, and cables utilized for camera control. **(B)** Interior of assembled freezer, including the DSLR camera, LED lights, thermocouples, temperature monitoring cuvettes and analyte cuvettes. **(C)** Prepared cuvette during cooling, including the heavy buffer oil, light oil layer as well as both frozen, and unfrozen sample droplets.

3.2 Freeze-Float Assay

To assemble our version of the Freeze-Float Assay, equipment (**Table 3.1**) was procured as similar to the equipment used by Kamijo and Derda[39] as possible. Several procedural modifications were implemented to improve the ease and reliability of data collection over the Derda assay. In our version, a data logger (with corresponding thermocouples) was utilized as opposed to a stainless-steel thermometer. The decision to use a data logger was two-fold; the use of a temperature logger allows for temperature measurement in triplicate without additional bulk within the freezer and automatically generates a spreadsheet of logged temperature data. This is preferable to the manual extraction of temperature required in the literature implementation. The low energy lamps also differed from the reference assembly, as the exact literature model was no longer available at the time of procurement. The selected lights utilize a 5 W LED lamp which was the lowest energy lamp accessible at the time of purchase. Cameras utilized in both implementations of the assay feature remote interval-capture functionality, which is operated from a basic laptop. It is worth noting that during data acquisition the camera is requited to operate below the manufacture specified operating temperature range (0 – 40 °C). This could pose long term issues with the camera sensor, internal circuitry, and battery due to accumulation of internal water. Lubricants in the lens can also be degraded during the cooling process, which would impact the ability to capture images at a high rate. The selected camera also does not provide any standard water resistance, which would have been a useful feature to consider in combating water ingress during thawing. At the time of procurement, limited

accessible camera options were rated to operate below 0 °C, but it would be a preferable option should it become available in future.

Component	Ben Lab Assay	Derda Assay
Freezer	Danby, DCF038A3SDB	Danby, DCF038A1WDB
Camera	Nikon, D5600	Canon, 5169B003
Data logger	Omega™, RDXL6SD-USB	None
Thermocouples / Thermometer	Omega™, 5SRTC-TT-K-40-72-ROHS	Traceable, 4371
Cuvettes	Fisherbrand™, 14-386-20	Fisherbrand™, 14-386-20
Emulsifier	Shin-Etsu, KF-6017	Shin-Etsu, KF-6017
Light oil	Shin-Etsu, DM-Fluid-5cs	Shin-Etsu, DM-Fluid-5cs
Heavy oil	3M™, Novec 7500	3M™, Novec 7500
Low heat lamps	Globe Electric, 12792 LED	Staples, 19639-000

Table 3.1 Components required to assemble a Freeze-Float assay; “Ben Lab Assay” components were purchased for our Freeze-Float assay (**Figure 3.1**), while the literature “Derda Assay” components are listed from Kamijo and Derda.[39]

3.2.1 Freezer validation

The literature procedure[39] pre-cools the freezer to 0 °C, loads samples, and then lowers the temperature setting on the freezer to achieve -20 °C. The freezer temperature control dial is physical and does not include any numerical markings. For consistency, our adaptation keeps the temperature setting (physical dial) consistent at half maximum. During set-up validation, there was found to be a large operator variance (5 – 20 minutes) in total time to prepare and situate cuvettes within the freezer. As preparing samples for analysis involves opening the freezer, our adaptation instead requires users to prepare and load all cuvettes at room temperature while the freezer is powered off. Once loaded, the freezer is then powered on, and cooling is initiated. This procedural change allows for the freezer to remain closed during the cooling process, limiting temperature fluctuations that could occur while assembling the samples for data collection. The temperature was measured in triplicate, with each thermocouple placed into a separate cuvette containing the same oil preparation as the imaged samples. The temperature was recorded every second, and the average temperature, as well as standard deviation (**Figure 3.2 (A)**) was calculated for each time point.

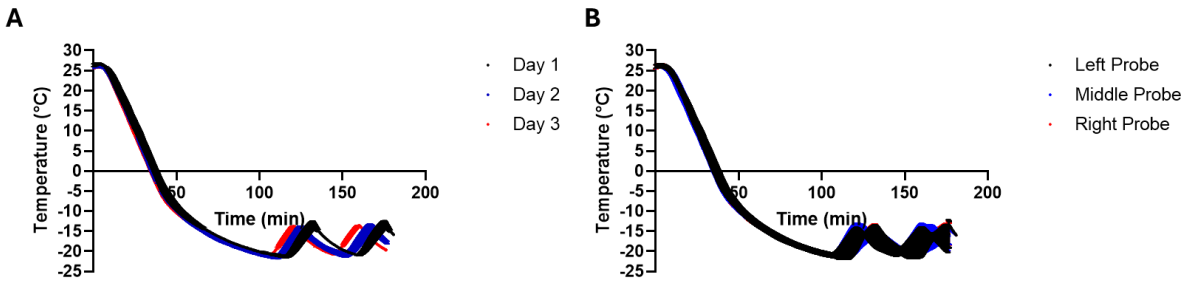

Figure 3.2 (A) Scatter plot of measured temperature as a function of time for three consecutive days. The temperature probes utilized and the position of each temperature probe was kept consistent for each day. Each datapoint represents the average temperature measured across each of the temperature probes at each time point for the given day. **(B)** The same temperature data collected for graph **(A)**, reorganized with each datapoint represents the average temperature measured from each probe measured across the three-day period.

To assess the cooling rate of the freezer, the temperature was recorded over a three-hour period on three consecutive days, utilizing the same temperature probes and orientation as would be utilized for sample analysis (**Figure 3.2**). Temperatures start at approximately 25 °C (room temperature) and once powered, the freezer motor will engage and cool the samples to approximately -21 °C. After a variable period of time, the freezer will warm to approximately -13 °C and this process will repeat. The cooling process remained consistent from initial cooling until the first warming event for each of the three days monitored (**Figure 3.2 (A)**); the time to engage the compressor, and the length of time engaged was not found to be consistent between the three days tested. As such, any data collection for this assay was to be terminated prior to motor engagement (~ -20 °C). When averaged across the three days measured, there was no meaningful difference between the temperature recorded on each of the distinct thermocouples, indicating that the differences in cuvette placement within the freezer does not have a distinct impact on the measured temperature (**Figure 3.2. (B)**).

The freezer used in our assay is not a rate-controlled freezer (RCF) and thus, the consistency of cooling needed to be examined. A standard RCF will typically have a tolerance of ± 2 °C during the cooling cycle. Our version of the Freeze-Float assay can reliably keep the standard deviation of average temperature (T_{avr}) across the three monitored cuvettes below ± 1.5 °C throughout a cooling cycle. As the cooling tolerance is typically neglected for rate-controlled freezers, the standard deviation calculated across the three thermocouples was not propagated for statistical analysis of the T_{nuc}.

To assess the degree of operator error, the average temperature (**Figure 3.3 (A)**) and standard deviation of the average temperature (**Figure 3.3 (B)**) were pooled for three different operators (Marcus Diamante N = 27, Sarah Musca (Honours student) N = 6 and, Waren Mendizza (Honours student) N = 7). The cooling rate during data collection is best fit to a one phase decay ($R^2 \geq 0.98$), where the freezer has a faster rate of cooling at warmer temperatures, slowing until a plateau at approximately -21 °C, at which time the motor re-engages, warming the freezer.

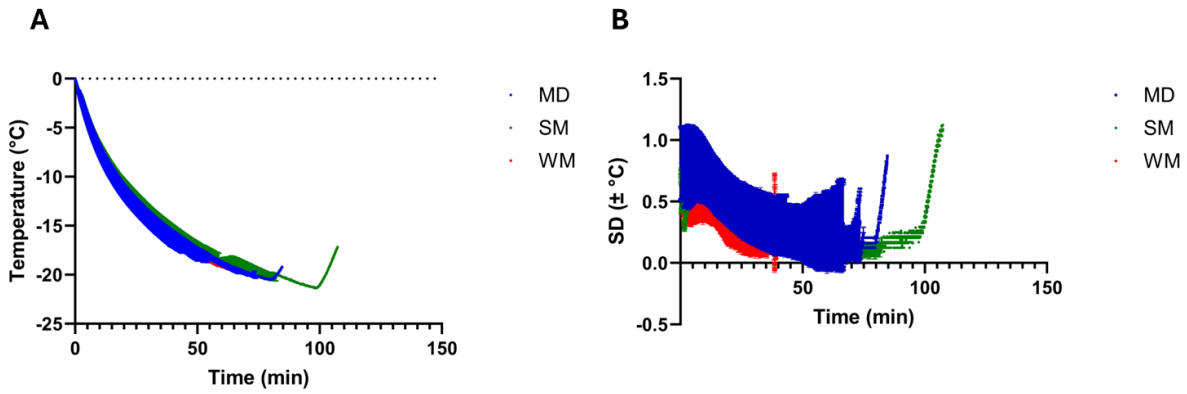

Figure 3.3 (A) Measured temperature as a function of time for three separate operators (MD N ≤ 27, SM N ≤ 6, WM N ≤ 7) during data collection runs. Presented datapoints represent the average temperature for a given time point (time collected every second following the first instance of T_{avr} 0 °C being achieved) for each data collection run. As the exact length of each run is not shared through all samples, the number of replicates utilized in the average temperature decreases as runs complete. **(B)** The standard deviation calculated across the three temperature probes measured as a function of time for the same data collection runs presented in **(A)**. Presented datapoints represent the average standard deviation for a given time point (time collected every second following the first instance of T_{avr} 0 °C being achieved) for each data collection run.

When fit to a one-phase decay (**Figure 3.3 (A)**), the individual regressions were found to be more accurate than a communal regression. Practically, the calculated cooling rates (± 9%) were found to deviate by less than 10% of the average between the three operators. The standard deviation across the three temperature probes was found to be consistent between operators, but not consistent throughout the assay run, with the T_{avr} at higher temperatures having more error than lower T_{avr} (while consistently remaining below ± 1.5 °C) (**Figure 3.3 (B)**). The use of a commercial freezer allows for intercomparison of data collected on our assay, independent of operator. However, due to the non-linear cooling rate, it is difficult to claim any measured nucleation temperature as absolute. As the cooling rate was faster at higher temperatures, less time was spent at a given temperature, and due to the stochastic nature of ice nucleation, allows for a lower probability of ice nucleation. This effect was minimized as the maximum cooling rate

achieved by our commercial freezer (~ 0.5 °C / min) would still be considered a slow cooling rate, with respect to typical cryopreservation protocol.[40]

3.2.2 Positive controls for ice nucleating agents

With the method of cooling and temperature measurement established for our Freeze-Float assay, the capacity to measure ice nucleation activity needed to be established. Two known ice nucleating agents were utilized as sources of INA activity for our Freeze-Float assay. Snomax® is a commercial ice nucleator, widely applied in the generation of snow seeding for the winter sports industry. Consisting of protein extracts from *Pseudomonas syringae*, Snomax® has been widely studied as an ice nucleating agent.[39,41,42] A sample of Snomax® was generously provided to our lab by Professor Ratmir Derda (University of Alberta). The sample was obtained by his laboratory in 2018, making our tested sample at least four years post manufacture. A 1 mg / mL solution of Snomax® in H_2O measured with our Freeze-Float assay was found to have an average nucleation temperature (T_{nuc}Avr) of - 6.0 ± 0.66 °C (n = 300), while Kamijo and Derda measured a T_{nuc}Avr of approximately - 6.9 ± 0.4 °C (n = 25) (value extracted with the use of a plot digitizer from previously reported box plot).[39] Both measurements fall within the expected range of nucleation temperature for Snomax®,[42] allowing for the use of aqueous Snomax® suspensions as a control for the promotion of ice nucleation.

The second established ice nucleating agent utilized in our Freeze-Float assay was silver iodide (AgI). Predominately used in cloud seeding,[43] AgI particles share a similar lattice structure as hexagonal ice, promoting heterogeneous ice nucleation.[44] AgI suspension in aqueous solvents have been previously utilized as a source of INA activity, most prominently in the emulsion freezing assay.[8,38,45,46] In the emulsion freezing assay, AgI particles are suspended in aqueous droplets containing the chosen solute, providing ice nucleating activity for the tested compound to act against. This is the same function that AgI suspensions in phosphate buffered saline (PBS) were used for in our Freeze-Float assay.

As the commercial freezer chosen can only reliably cool to approximately -21 °C, the use of an AgI suspension as solvent raises the nucleation temperature dramatically when compared to PBS alone. Should a compound effectively suppress ice nucleation, it is likely that nucleation will not occur (and in turn will not be measurable) without the addition of AgI particles. Our preparation of AgI suspensions followed the same process as implemented in the emulsion freezing assay,[45] generating a 50 mg / mL mixture of solid AgI in PBS, which was sonicated for at least 45 minutes in the absence of light to ensure particle dispersal; remaining large particles (≥ 11 µm) of AgI were

filtered out of suspension with filter paper, resulting in a visually homogenous AgI / PBS suspension. This AgI / PBS suspension can be utilized in place of PBS for standard solute preparation.

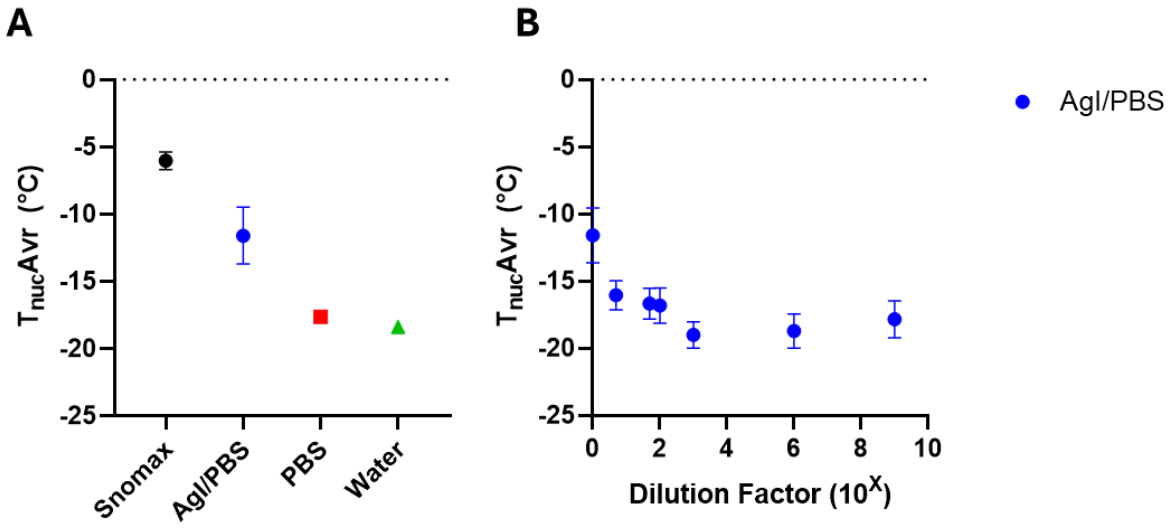

Figure 3.4 (A) Average nucleation temperature of control compounds used for the Freeze-Float assay. Positive controls ((Snomax® (n = 300) and AgI / PBS suspension (n = 89)) include pooled data from initial implementation. Standard solvents (PBS (n = 28) and H_2O (n = 16)) represent the first sample analysis for the solvent. **(B)** Average nucleation temperature of serially diluted AgI / PBS solutions (n = 18 – 30).

The preparation of AgI / PBS was found to induce ice nucleation (T_{nuc}Avr = -12 ± 2.1 °C, n = 89) when compared to standard solvents PBS (T_{nuc}Avr = -18 ± 0.70 °C, n = 28) and distilled water (T_{nuc}Avr = -18 ± 0.26 °C, n = 16) (**Figure 3.4 (A)**). The exact concentration of AgI remaining in suspension after filtration was not known. Inductively coupled plasma mass spectroscopy (ICP-MS) analysis was attempted with the University of Ottawa Geochemistry laboratory to quantify the silver and iodide quantity remaining in the filtered AgI / PBS suspension. However, a reliable digestion method for ICP-MS analysis of the AgI / PBS suspension was not successfully developed. Due to a combination of the travel time, sample processing time and sedimentation time of the suspension, reported concentrations varied dramatically between a common stock, and the analysis was not successful.

Despite not being known, the concentration on AgI remaining in AgI / PBS suspension was kept as consistent as possible. To standardize the preparation of AgI / PBS suspensions, the sonicator, filtration apparatus and SKU of filter paper were kept consistent in preparation of all AgI / PBS suspensions. To assess if there was a concentration dependence between AgI present

in the prepared suspension and T_{nuc}Avr, several dilutions of stock AgI / PBS suspension were assessed for INA activity (**Figure 3.4 (B)**). As little as a 5 fold dilution of AgI / PBS resulted in an effect on INA activity (T_{nuc}Avr = -16 ± 1.1 °C, n = 28) and a 1000 fold dilution (T_{nuc}Avr = -19 ± 1.0 °C, n = 28) resulted in nucleation similar to PBS in the absence of AgI particles. These dilutions indicate that the concentration of AgI remaining in suspension following filtration must be very low, however the removal of larger particles is vital to ensure uniform suspension.

3.3 Assessment of small molecule carbohydrate IRIs for INA activity

Many diverse investigations have been performed by the Ben laboratory exploring the structure activity relationship between small molecule carbohydrates and ice recrystallization inhibition activity.[1–4] One particular study had collaborated with Professor Takaaki Inada after a novel small molecule (**3.05**) improved the cryopreservation of red blood cells but did not possess IRI activity.[8] When examined using the emulsion freezing assay compound **3.05** (22 mM) demonstrated a high capacity to suppress AgI induced ice nucleation.[8] This was the first identified small molecule carbohydrate with notable control over ice nucleation, however a broader assessment of the INA capacity for small molecule carbohydrate derived CPAs was not performed at the time. Utilizing our large library of synthetically accessible small molecule carbohydrates of known IRI activity, an investigation was performed to assess if any IRI active small molecule carbohydrates possess the structural features required to impact ice nucleation. A range of small molecule IRIs were selected to generate a baseline assessment of the impact on ice nucleation activity, including compound **3.05** (**Figure 3.5**).

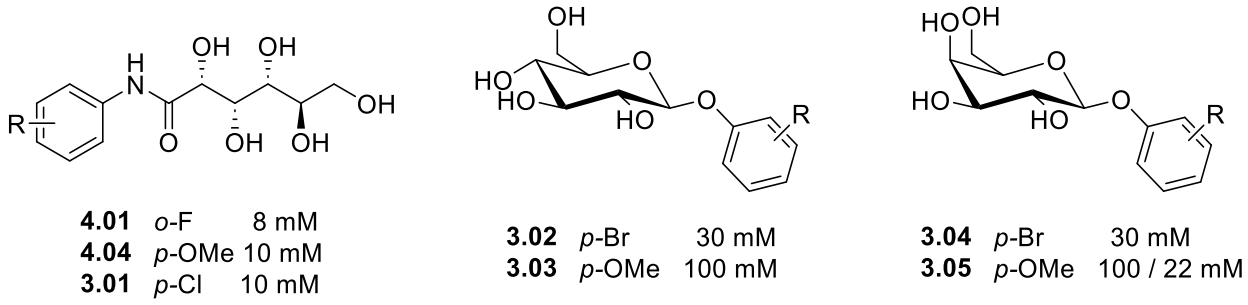

Figure 3.5 Initial compound screen of carbohydrate IRI derived molecules. Compound number, aryl substitution and concentration assessed on the modified Freeze-Float assay listed for each compound.

IRI active *N*-aryl gluconamides **4.01** and **4.04**, IRI active *O*-aryl pyranosides (**3.02** – **3.04**), as well as IRI inactive (but known ice nucleation suppressing) compound **3.05** were included in the initial compound screen. Each selected compound was assessed for INA activity in three solvents:

AgI / PBS providing the opportunity for the given compound to demonstrate the ability to suppress ice nucleation, PBS providing a direct comparison to IRI analysis preparation, and distilled water, isolating any measured INA activity to the chosen solute. Selected compounds were assessed for INA activity at the minimum concentration required to reach a rate of “zero” ice growth on the modified SCA. In testing IRI relevant compounds at IRI relevant concentrations it allows for the most direct comparison of functional requirements, but does not omit the possibility that greater INA activity may be observed at different concentrations. Compound **3.05** was tested at both the minimum concentration required to reach a rate of ice crystal growth of “zero” on the modified SCA (100 mM), and the concentration previously assessed on the emulsion freezing assay (22 mM).[8]

When investigating the average nucleation temperature of small molecule carbohydrates solvated in AgI / PBS suspension, it was evident that the INA activity of AgI was retained; the pooled average nucleation temperature of AgI / PBS solvated compounds (T_{nuc}Avr = -11 ± 1.8 °C, n = 9) being statistically warmer (One-Way ANOVA, $p < 0.0001$) than PBS (T_{nuc}Avr = -16 ± 2.0 °C, n = 9) and H_2O (T_{nuc}Avr = -15 ± 2.2 °C, n = 9) solvated compounds (**Figure 3.6 (A)**). There was not a statistical difference between the pooled set of compounds solvated in PBS or H_2O (Welch’s t-test, $\alpha = 0.05$, $p > 0.1$). When examining the average nucleation temperature of individual compounds, it was found that nucleation events occurred over a larger temperature range (absolute difference in T_{nuc} between the first and final measured nucleation event) when the solute was dissolved in H_2O ($Range_{Avr}$ = 3.5 ± 2.7 °C) when compared to PBS ($Range_{Avr}$ = 1.3 ± 1.0 °C) despite retaining a similar average nucleation temperature (**Figure 3.6 (B)**). Due to the more reliable nucleation ranges, and more direct relationship with the modified SCA, a focus was placed on the use of PBS as a solvent to complement AgI / PBS opposed to H_2O.

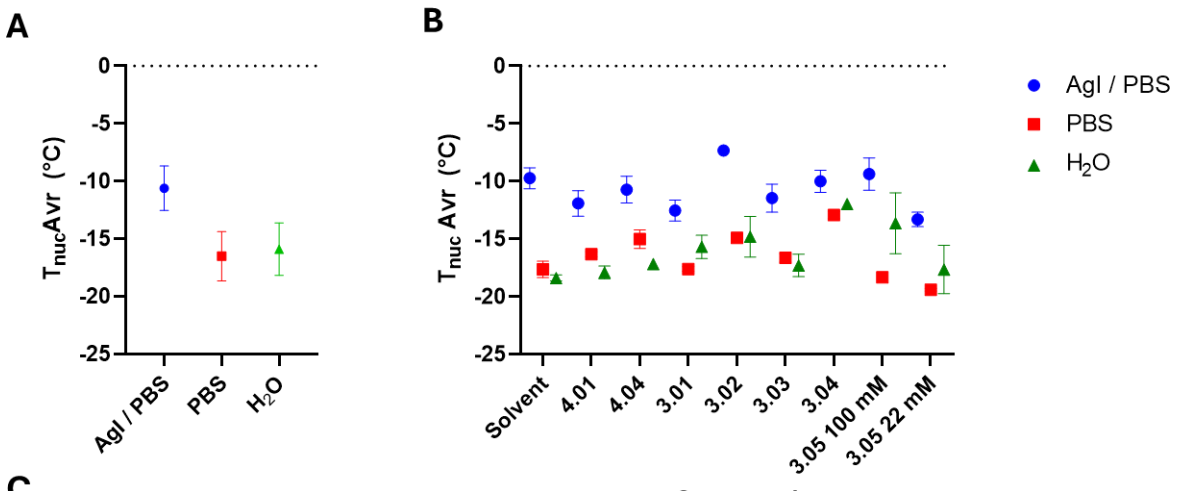

C

	AgI/PBS			PBS			H_2O		
	Mean	SD	N	Mean	SD	N	Mean	SD	N
Solvent	-9.7	0.91	30	-18	0.70	28	-18	0.26	16
4.01	-12	1.1	30	-16	0.23	27	-18	0.55	21
4.04	-11	1.2	30	-15	0.81	23	-17	0.00	7
3.01	-13	0.92	30	-18	0.19	30	-16	1.0	30
3.02	-7.3	0.02	30	-15	0.00	30	-15	1.8	30
3.03	-11	1.2	30	-17	0.37	30	-17	0.96	15
3.04	-10	0.96	30	-13	0.31	30	-12	0.00	30
3.05 100 mM	-9.4	1.4	30	-18	0.00	3	-14	2.7	18
3.05 22 mM	-13	0.63	30	-19	0.11	28	-18	2.1	5

Figure 3.6 (A) One-Way Nested ANOVA (n = 172 – 270) of average nucleation temperature for each solvent, including each analyzed compound (**Figure 3.5**) as well as the solvent alone. Error bars represent the propagated standard deviation of the pooled sample set. **(B)** Scatter plot of the average nucleation temperature calculated for each compound assessed in each solvent. Error bars represent the standard deviation of nucleation temperature for each observed nucleation event. **(C)** Table of nucleation statistics generated for the assessment of the preliminary compound screen in each of the three solvents. For each condition, 30 droplets were loaded onto the assay, and N represents the number of nucleation events observed in the analyzed cooling cycle.

When assessing small molecule carbohydrates for the ability to supress the temperature of ice nucleation, solutions were prepared with AgI / PBS suspension, and the ability for a compound to raise the nucleation temperature solutions were prepared in PBS (**Figure 3.6 (C)**). It is worth noting that visual representations, and calculated nucleation average temperatures only include nucleation events observed, and do not account for loaded droplets that do not nucleate within the cooling competency of the freezer. Should a droplet not nucleate, that indicates the nucleation temperature was lower than the temperature achievable by the freezer (~ -21 °C). As the exact temperature is not known, it could not be included as a data point. Compound **3.05** at 100 mM solvated in PBS is an example of this discrepancy, where only 3 droplets nucleated (at -18 °C),

while the remainder of the droplets remained unfrozen; the calculated average nucleation temperature is -18 °C while the real average should be below -21 °C, as 27 droplets remained unfrozen. Due to this limitation, the use of PBS solvation is not capable of accurately characterizing compounds which suppress ice nucleation. The use of AgI / PBS as a solvent is required to assess T_{nuc} suppression, while solvation in PBS can identify compounds which induce ice nucleation.

Previously assessed compound **3.05** (22 mM)[8] was found to be the most active compound at suppressing ice nucleation (**Figure 3.6 (C)**). Surprisingly, at 100 mM, **3.05** demonstrated no capacity to inhibit the ice nucleation activity of AgI (**Figure 3.6 (C)**). Traditionally when examining compounds for IRI activity there is a direct relationship between concentration and IRI activity. However, for **3.05** there may be an active window, whereby concentrations above or below a given threshold will not suppress ice nucleation. This specific observation could be justified as a function of maximum aqueous solubility. The AgI / PBS suspension prepared contains a higher concentration of solutes than PBS alone. As a result, the maximum aqueous solubility of **3.05** in AgI / PBS may be reduced, increasing the probability for precipitation during cooling, promoting heterogenous ice nucleation events.

Compounds **4.01**, **3.01** and **3.03** all suppress (Two-Way ANOVA, Tukey's PHT, $p < 0.0001$, $n = 30$) the nucleation temperature of AgI / PBS suspension when compared to the solvent alone. However, no tested analyte was capable of completely supressing the INA activity of AgI (T_{nuc} similar to PBS alone). **3.02** was identified as the only compound which statistically increased the nucleation temperature with respect to AgI / PBS alone (Two-Way ANOVA, Tukey's PHT, $p < 0.0001$, $n = 30$).

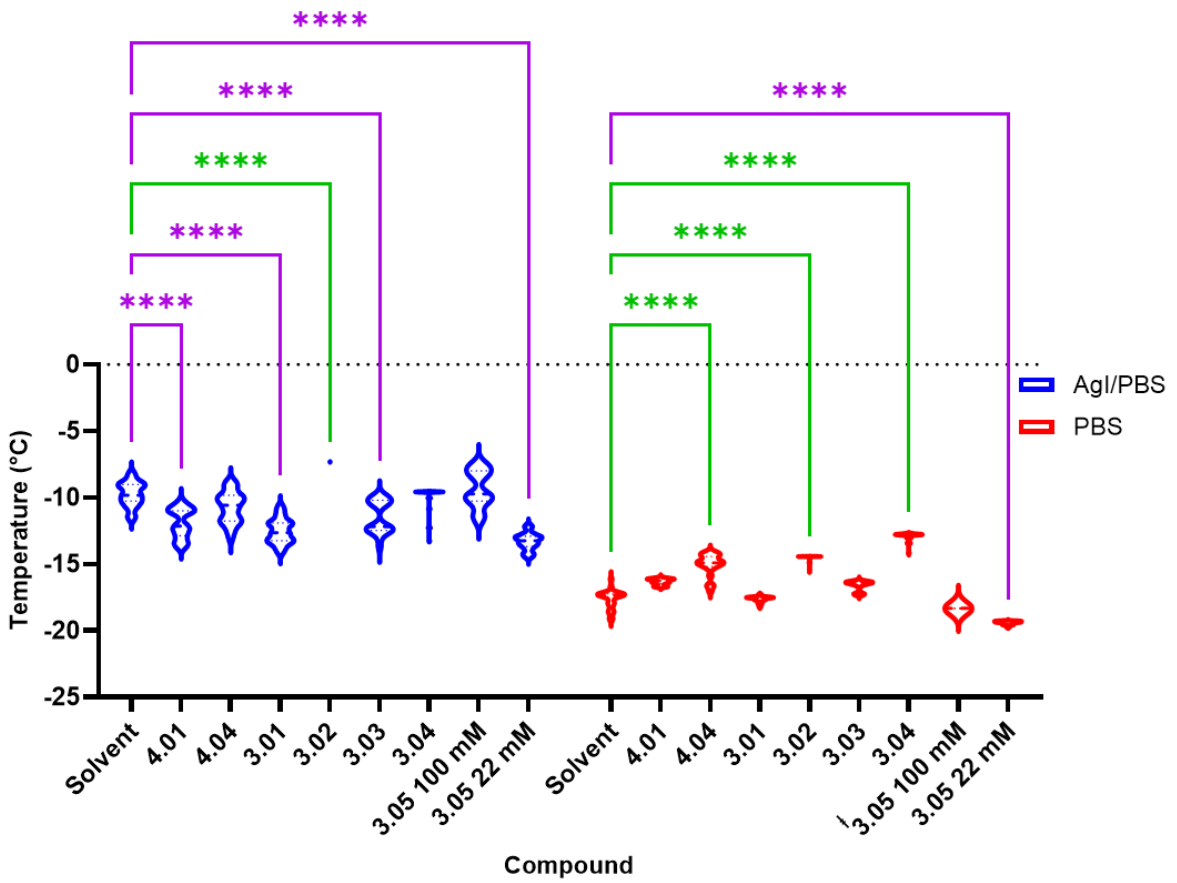

Figure 3.7 Violin plot of the nucleation temperature (T_{nuc} °C) of tested compound set (**Figure 3.5**) solvated in AgI / PBS and PBS. Significance (Two-Way ANOVA, Tukey's PHT, $p < 0.0001$, $n \geq 23$) is indicated as a significant increase in T_{nuc}Avr in green and a significant decrease in T_{nuc}Avr in purple as compared to the respective solvent alone. [t]Only 3 nucleation events were measured for compound **3.05** at 100 mM in PBS of the 30 droplets assessed.

Compounds **3.02**, **4.04,** and **3.04** were found to effectively promote ice nucleation when solvated in PBS. However, no small molecule carbohydrate assessed in PBS induced ice nucleation to a similar capacity as Snomax® or prepared AgI / PBS suspensions. Of the IRI active small molecules assessed, none possessed a promising capacity to influence ice nucleation. However, compounds **3.02** and **3.04** became of particular interest, not due to an influence on T_{nuc}, but for the extremely narrow range of nucleation events observed (**Figure 3.7**).

3.3.1 Assessment of nucleation ranges for *p*-bromophenyl substituted pyranose derivatives

As previously discussed, ice nucleation is a stochastic event dependent on the random movement of liquid water molecules. Even with known ice nucleating agents such as Snomax® or

AgI / PBS suspensions tested in our isolated hydrophobic system, ice nucleation can span several degrees (**Figure 3.8 (A)**); this is more visually apparent when represented as a violin-plot (**Figure 3.8 (B)**). The nucleation events for both Snomax® and AgI / PBS suspension occur evenly across several degrees, whereby in practical application, sample nucleation could reasonably occur at any given temperature within that range.

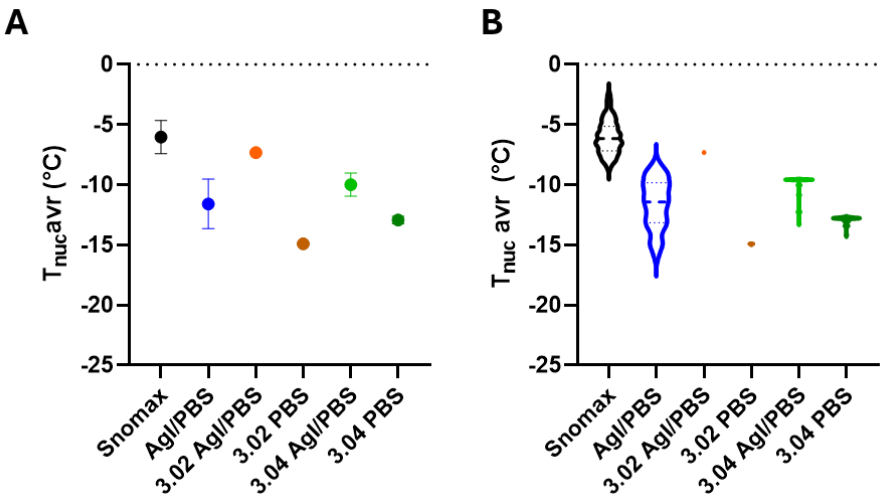

Figure 3.8 (A) Scatter plot of pooled positive controls (Snomax® (n = 300), and AgI / PBS suspension (n = 89)) as well as sample preparations of compounds **3.02** and **3.04** at 30 mM in both AgI / PBS and PBS solutions (n = 30). **(B)** The same data presented in **(A)** but presented as a violin plot, highlighting the narrow nucleation window observed with compounds **3.02** and **3.04**.

Both compounds possessing the *p*-bromophenyl moiety (**3.02**, **3.04**) demonstrated not only the ability to increase the average nucleation temperature, but to nucleate within a narrow, reliable range. Both compounds nucleated at least 90% of all loaded droplets within 90 seconds (Δ 0.3 °C), independent of chosen solvent. Specifically, compound **3.02** nucleated all 30 droplets within 10 seconds (Δ 0.06 °C) of the first observed nucleation event irrespective of the presence of AgI. Compound **3.04** shows a narrow nucleation range for the majority of droplets, however a small number (~3) of droplets did not nucleate until several minutes after the initial nucleation event.

To determine if the narrow nucleation range observed is concentration dependent, several dilutions of **3.02** and **3.04** were prepared in both AgI / PBS and PBS solvents (**Figure 3.9 (A)**). From this concentration screen, it was noted that the pooled nucleation ranges of both compounds are linearly dependent on concentration (R^2 = 0.71), independent of solvent or C_4 stereochemistry (**Figure 3.9 (A)**). This concentration dependence strongly suggests that the *β-O-*(4-bromophenol) motif is directly responsible for the observed narrow nucleation range.

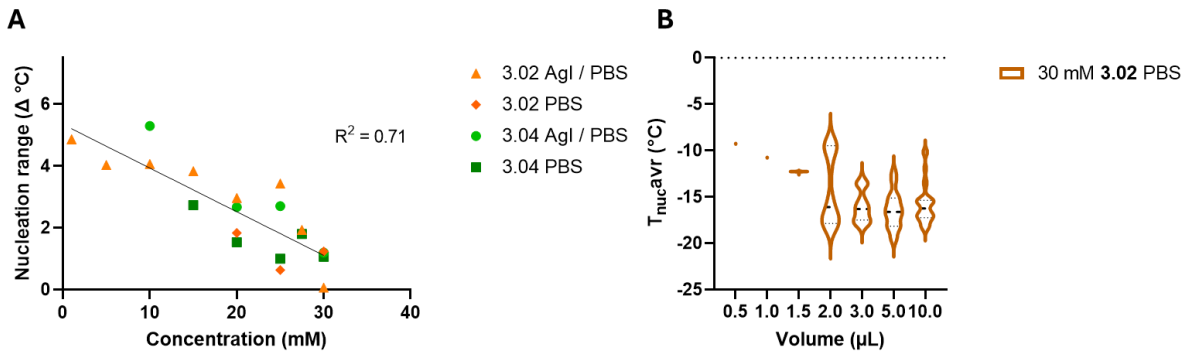

Figure 3.9 (A) Scatter plot of *O*-aryl glycosides bearing a bromine atom (*para*- position) at varying concentrations plotted against the range of measured nucleation (n = 30). Linear regression (R^2 = 0.71) is generated from the pooled set of *O*-aryl glycosides across all tested conditions. **(B)** Violin plot of 30 mM **3.02** in PBS prepared at different droplet volumes (n = 30).

As our Freeze-Float assay utilizes 1 µL droplets to maximize the sample size generated for each imaged cuvette, it could not be assumed that the narrow nucleation range observed with 1 µL droplets will scale to larger volumes. It has been reported that the nucleation properties of metallic particles in atmospheric water are dependent on droplet size;[47] this can be attributed to the dispersion of metallic particles within the water droplets, where the more disperse the particles are within a droplet, the more active nucleation sites exist and the probability of nucleation increases.[48] It was not known if this volume dependence extends to the consistency (range) of ice nucleation, or when translated to an isolated hydrophobic system.

To test this, the assay was performed with the most reliable ice nucleating compound (**3.02**) at the highest operating concentration (30 mM) in PBS (to minimize heterogeneous particles) at different droplet volumes (**Figure 3.9. (B)**). As the cuvettes utilized can only tolerate approximately 50 µL of aqueous solution in one layer across the oil interface, several cuvettes were utilized per droplet volume within the same sample acquisition to achieve the standard 30 droplet sample size (2 cuvettes for 2 µL, 3 cuvettes for 3 µL, 5 cuvettes for 5 µL, and 6 cuvettes for 10 µL). Although the standard operating procedure devised for of our Freeze-Float assay utilizes a repeater pipette, droplets exceeding 2 µL were found to break apart into several smaller droplets when ejected into the oil interface from the repeater pipette. To avoid droplet dispersal, all droplets examined in this screen were carefully loaded into the oil manually (Gilson Pipetman P2 (F144054M), or Gilson Pipetman P10 (F144055M)), ensuring the droplets remained whole. From testing with larger droplet sizes, it is clear that the reliable nucleation range observed for **3.02** is dependent on droplet volume. The narrow nucleation range is observed with 0.5 µL and 1 µL droplets, slightly expanded at 1.5 µL, and completely lost at 2 µL (**Figure 3.9 (B)**). It is worth

noting that 1 µL droplets appear circular, uniform, and evenly distributed across the cuvette (**Figure 3.10)**; however, when the droplet volume is increased beyond 2 µL the droplets widen into an oval shape and aggregate into the corners of the cuvette. The observed widening increases with respect to volume and can cause unintended contact with the plastic walls of the cuvette. Should a droplet contact the cuvette walls it can provide both a foreign nucleation surface as well as a surface to adhere to (increasing difficulty of analysis). For these reasons, we can suggest that the narrow nucleation window of **3.02** may not be scalable far beyond 1 µL testing, however it is also likely that our Freeze-Float assay is not adequately equipped for the reliable assessment of larger aqueous droplets.

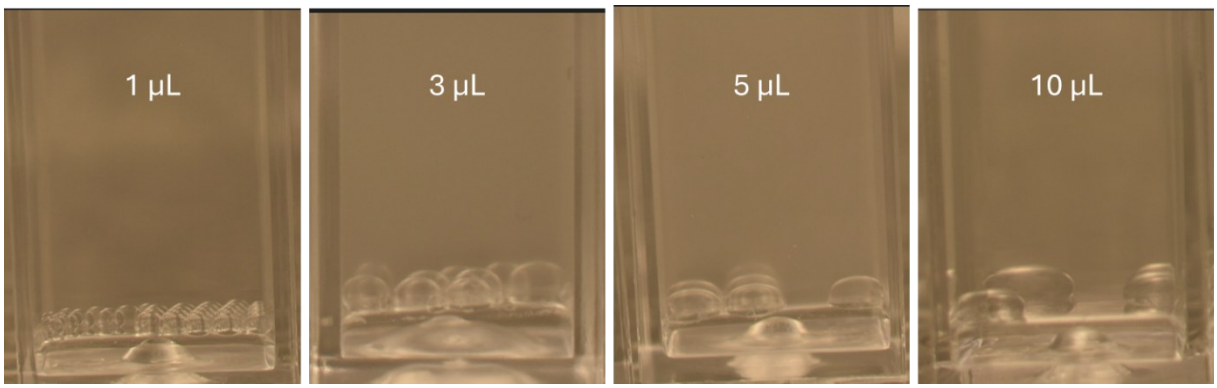

Figure 3.10 Example droplets of **3.02** dissolved in PBS loaded into the Freeze-Float assay at various droplet volumes.

As it is not known why this narrow nucleation range is observed, it can be posited based upon our observations that any *p*-bromophenol containing small molecule could also possess a similarly narrow nucleation range. The generation of numerous compounds possessing a reliable nucleation range, with a variety of ice nucleation activity could produce a useful library of small molecules that can be implemented in optimized cryopreservation protocols.

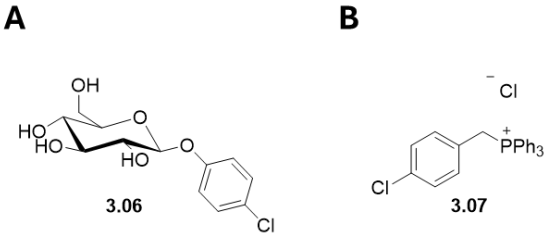

Figure 3.11 (A) *p*-Chlorophenyl pyranoside generated by Waren Mendizza for assessment of INA activity.[49] **(B)** *p*-Chlorobenzyl functionalized Wittig salt generated by Sarah Musca for assessment of INA activity.[50]

Prior to widening the scope in search of consistent ice nucleating agents, compound **3.06** (**Figure 3.11 (A)**) was generated for INA assessment by undergraduate student Waren Mendizza.[49] Demonstrating comparable nucleation activity to compounds **3.02** and **3.04**, compound **3.06** was found to have improved maximum aqueous solubility, but required higher concentrations to achieve a small nucleation range (**Figure 3.12**). The activity of compound **3.06** demonstrated that the phenomena is not limited to aryl bromides specifically, and investigation of other aryl halides could be rationalized.

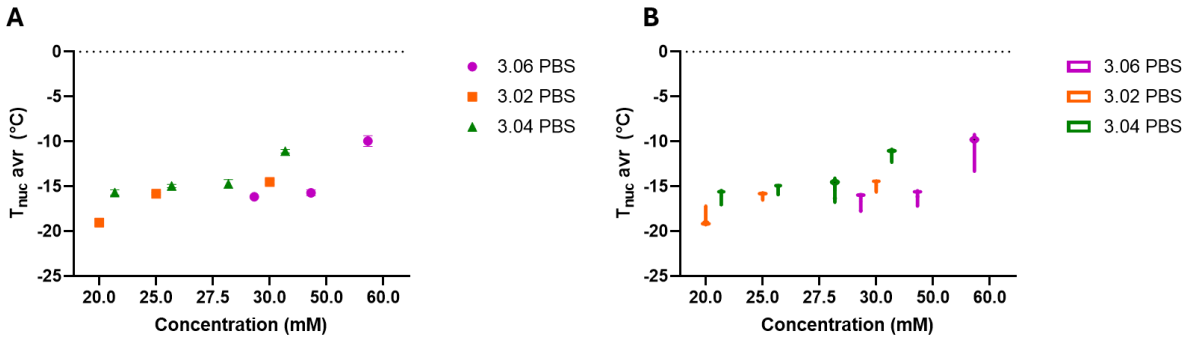

Figure 3.12 (A) Scatter plot of average nucleation temperature for *O*-(*p*-halo)-pyranosides solvated in PBS with respect to concentration (n = 30). **(B)** Violin plot of the same data presented in **(A)**, note that due to the grouped nature of data input, the x-axis depicts the concentration tested directly, and is not linearly scaled.

Undergraduate student Sarah Musca identified compound (**3.07**) from the assessment of *p*-halobenzyl Wittig salts,[50] which possessed measurable IRI activity (IC_{50} = 21 mM, **Figure 3.13 (B)**) and was capable of both suppressing ice nucleation and forcing all nucleation events to occur in a reliably narrow window (**Figure 3.13 (A)**). The identification of compound **3.07** demonstrated the importance of the *p*-chlorophenol or *p*-bromophenol motif when observing a reliable nucleation window. This finding validates the exploration of novel scaffolds to introduce *p*-haloaryl motifs to with the aim of controlling ice nucleation. When solvated in the presence of AgI, only 14 nucleation events were observed; this represents the first example of a small molecule with the capacity to inhibit ice nucleation of droplets in the presence of AgI throughout an entire cooling cycle (**Figure 3.13 (A)**). Both *p*-chloroaryl compounds (**3.06**, **3.07**) require higher concentrations to be utilized to achieve a reliable nucleation range, however the maximum aqueous solubility is higher than compounds **3.02** and **3.04**.

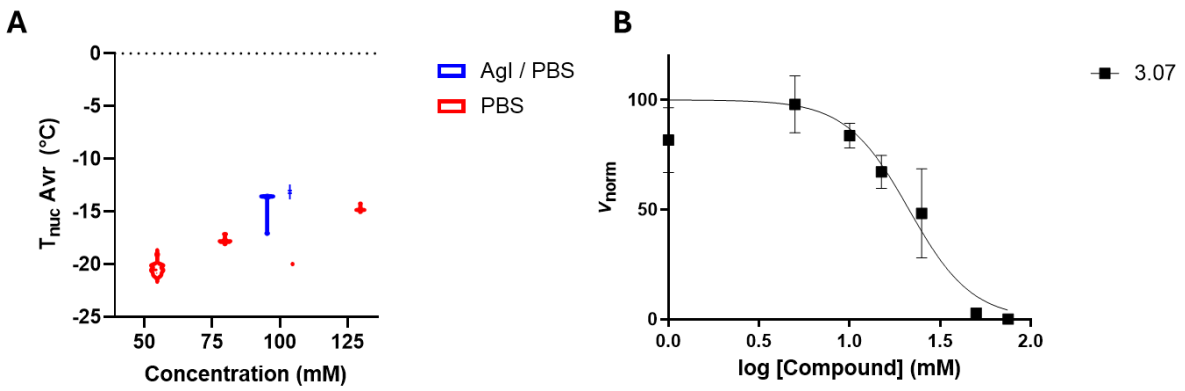

Figure 3.13 (A) Violin plot of average nucleation temperatures for compound **3.07** assessed at varying concentrations in either AgI / PBS or PBS solvent (n ≥ 29). ǂ100mM **3.07** solvated in AgI / PBS only observed 14 nucleation events. **(B)** IRI activity of compound **3.07** in PBS when assessed on the modified SCA. Four-parameter dose response curve is generated for the compound, and the resulting IC_{50} value is 21 mM.

3.4 Investigating synergy between INA and IRI activity

As both IRI activity and controlling ice nucleation are both desirable properties for the design of novel cryopreservation agents, identifying the degree of interaction between these phenomena for small molecules is important for designing small molecule CPAs. As demonstrated in **Section 3.3**, the IRI activity of a given small molecule carbohydrate played a minimal role in determining INA activity. No tested small molecule possessed similar capacity to induce ice nucleation compared to AgI or Snomax®, and the most effective ice nucleation suppression agent is the least IRI active small molecule examined.

The inability for small molecule carbohydrate IRIs to modulate ice nucleation was not unexpected, and a more extensive screen of small molecules will be required to assess structural components that correlate to ice nucleation activity. However, the ability for ice nucleation activity to influence IRI activity for small molecule carbohydrates has not been examined.

To investigate the impact of ice nucleating activity on IRI activity, each compound from the initial INA screen (**Figure 3.5**) was assessed for IRI activity in both PBS and AgI / PBS on the modified SCA[51] All compounds screened for INA activity had been previously assessed for IRI activity in PBS.[52,53] The reference PBS dose response data can be compared to the same compound solvated with AgI / PBS suspension. As previously demonstrated (**Figure 3.4 (A)**) AgI / PBS suspension possessed a measurable capacity to induce ice nucleation. The use of an INA active solvent allowed ice nucleation to be induced, without requiring structural modifications to the small molecule carbohydrates of known IRI activity. When assessed in AgI / PBS the rate of

ice crystal growth for each compound was normalized to both the PBS of the day and the AgI / PBS of the day. When normalized to PBS, any changes imparted by the presence of AgI or IRI were indicated. However, when normalized to AgI / PBS, any deviation from the reference dose response relationship was due to constructive or destructive interactions between AgI (induced ice nucleation) and the IRI since the presence of AgI particles is controlled for.

To assess the activity of AgI / PBS alone, five different preparations of AgI / PBS were assessed on the modified SCA on different days. AgI / PBS was found to have measurable IRI activity alone, with an average percent mean grain size 78 ± 5.2 % (n = 15); this means that the average ice crystal generated from AgI / PBS solution is ~ 78 % the size of the average ice crystal formed from PBS alone after annealing. This effect could implicate that the introduction of a more INA active molecule than the prepared AgI / PBS suspension (ΔT_{nuc}Avr + 6.0 °C when compared to PBS) could further inhibit the rate of ice crystal growth. This reduction in ice crystal growth could also potentially be due to the mechanical presence of insoluble particles. As the full effects of non-homogenous particles on the modified SCA are not fully understood, it is also possible that the presence of insoluble particles at the ice crystal interface could mechanically inhibit ice crystal growth. Any IRI activity measured due to the presence of physical particles are not desired for this assessment (as AgI is utilized as an ice nucleator, not an insoluble particle); normalizing IRI activity to AgI / PBS solution controls for these interactions.

As AgI / PBS suspension inherently possesses measurable IRI activity, this in turn suppresses the upper plateau of compounds tested in AgI / PBS. For analysis of AgI / PBS solvated compounds normalized to PBS, the upper plateau was fixed to equal the normalized rate of ice crystal growth for the AgI / PBS solvent prepared for the day (**Figure 3.14**).

A

Compound	IC_{50} Reference (mM)	IC_{50} Norm to PBS (mM)	IC_{50} norm to AgI/PBS (mM)
4.01	3.2	3.1	3.1
4.04	4.6*	5.3	5.2
3.01	12*	13	14
3.02	6.7	5.5	5.4
3.03	29ǂ	25	23
3.04	7.0	8.2	8.1
3.05	67	62	60

B

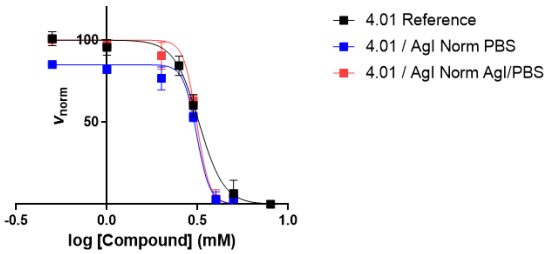

Figure 3.14 (A) Ice recrystallization inhibition activity measured for each compound. Reference values taken in the absence of AgI, IC_{50} values normalizing the rate of ice crystal growth to PBS, and IC_{50} values normalized to the AgI / PBS. **(B)** Example four-parameter dose response curve generated for model IRI compound **4.01**, treated with each of the three conditions outlined in **(A)**. *,ǂDenote reference dose-response relationships which have been previously reported.[*52ǂ53]

From the assessed compounds, there was no meaningful change in measured IRI activity through the addition of INA active AgI particles with respect to the calculated half maximal inhibitory concentrations (**Figure 3.14 (A)**). It can be visually noted (**Figure 3.14 (B)**), when examining AgI / PBS solvated compounds normalized to PBS at low compound concentrations the AgI particles lower the rate of ice crystal growth; this depression is due to the inherent IRI activity of AgI particles. This may represent a reduction in initial ice crystal grain size, however in the presence of an IRI, any change in grain size is lost during the annealing period. This was manifest by the absence of change in IC_{50} values irrespective the presence of AgI or normalization technique.

Future work is needed to confirm if the IRI activity of AgI / PBS suspension is related to INA activity or the presence of insoluble particles. This would require either the IRI assessment of several compounds of varying ice nucleating activity, or the utilization of a homogenous INA to assess in conjunction with traditional small molecule IRIs. If the reduction in mean grain size was due to the presence of a physical particle (agnostic of ice nucleation activity), this would confirm definitively that ice nucleation activity has no ability to modulate IRI activity in small molecule carbohydrates. Should the upper plateau suppression be due to ice nucleation activity, it could be possible that an alternative source of INA activity may result in improved IRI activity in the presence of a small molecule IRI.

From the work presented in this thesis, the reported correlation of IRI active macromolecules and INA[12] does not apply to small molecule IRIs. This discrepancy is likely due to difference in mechanism of IRI activity, however the utilization of small molecule IRIs at ~ 1000

times higher concentrations (wt.%) than the assessed[12] macromolecules could also limit any measurable synergy.

3.5 Conclusions

With the goal of this work to provide initial insight towards the targeted development of dual action INA – IRI active CPAs, a reliable method of measuring ice nucleation activity was implemented and the interplay between INA and IRI activity in small molecules was explored. **Section 3.2** establishes the installation of a modified version of Freeze-Float assay. The tolerance and consistency of procured equipment was assessed (**Section 3.2.1**), as well as the assessment of chosen assay controls (**Section 3.2.2**). The procured commercial freezer was found to cool consistently in an operating range of [25 °, -21 °C] (**Figure 3.2**). Temperature measurement was capable of reliably generating a standard deviation below ± 1.5 °C, remaining consistent with the tolerance found with standard controlled rate freezers (**Figure 3.3 (B)**). It is worth noting that the cooling rate of the commercial freezer was not found to be linear, decelerating as the freezer approached the lower limit of approximately -21 °C. As ice nucleation is a stochastic event, this non-linear cooling rate could bias nucleation events to the colder temperatures, as a longer period of time is spent at a given temperature; this is mitigated by the use of a slow cooling rate for the whole process (0.2 – 0.5 °C), allowing ample time at any given temperature. The selected control compounds which promote ice nucleation (1 mg / mL solution of Snomax® in water, and a filtered (≤ 11 µm) 50 mg / mL suspension of AgI in PBS) were assessed on our variation of the Freeze-Float assay (**Figure 3.4**); these assessments were found to be similar to previously published assessments of Snomax®[42] and AgI / PBS suspensions.[39]

With controls established, **Section 3.3** aimed to assess a selection of small molecule carbohydrate based compounds (**Figure 3.5**); this compound screen included IRI active *N*-aryl gluconamides (which will be investigated in more depth in **Chapter 4** and **Section 5.4.2**), IRI active *O*-aryl pyranosides, as well as IRI inactive, but known anti-ice nucleator **3.05**.[8] This screen aimed to assess the influence IRI activity has on ice nucleation. Assessment of small molecule carbohydrate compounds was performed in three solvents (water, PBS, and AgI / PBS suspension) (**Figure 3.6**), however a focus was placed upon PBS and AgI / PBS. The use of PBS more closely relates to the modified SCA utilized for IRI analysis and provides a more direct comparison to AgI / PBS (either containing INA active AgI particles in suspension, or not). This dual solvent assessment allows for PBS solvation to highlight INA active compounds, and AgI / PBS solvation to highlight compounds which suppress ice nucleation.

Little variation from the assessed solvent alone was observed for IRI active compounds assessed. Known compound **3.05** was found to be the most effective at supressing ice nucleation, and compound **3.02** was found to be the only compound which statistically increased the nucleation temperature in the presence of AgI (**Figure 3.7**). This screen indicates that there is no relationship between the IRI activity of a compound and it's capacity to influence ice nucleation in the assessed small molecules. More interestingly, *p*-bromophenol containing compounds (**3.02**, **3.04**) were found to nucleate in a very small temperature range, often having every observed nucleation event occur in one frame (one second); this nucleation range is orders of magnitude more reliable than known ice nucleating agents such as Snomax® or AgI / PBS (**Figure 3.8**). **Section 3.3.1** aimed to investigate the narrow nucleation range observed with compounds **3.02** and **3.04**; finding that this phenomenon is concentration dependent, but agnostic of carbohydrate stereochemistry (and by extension IRI activity) (**Figure 3.9 (A)**). This suggests that the *p*-bromophenol motif is the cause of the observed nucleation window opposed to the motif in conjunction with a specific carbohydrate. This finding sparked investigations performed by undergraduate students in the Ben lab, with the aim of refining the structural requirements not just for INA activity, but INA activity in a reliable temperature range. From these assessments, two model compounds were identified (**3.06** and **3.07**), which indicated that *p*-chlorophenol derivatives were also capable of reliable nucleation (at a higher concentration relative to **3.02** and **3.04**), and that the carbohydrate component is not strictly required for this phenomenon.

Section 3.4 aimed to complement **Section 3.3**, assessing the impact of ice nucleation activity to modulate measured IRI activity. As it has been previously established with IRI active macromolecules that a synergistic relationship exists,[12] it was thought that the presence of AgI particles would improve the measured IRI activity of our compound set (**Figure 3.14**). The use of an AgI / PBS suspension for this analysis was not ideal, as the effects of insoluble particles on the modified SCA are not fully known. AgI / PBS was found to possess a degree of IRI activity alone (**Figure 3.14 (B)**), however this IRI activity was ultimately overshadowed by the small molecule IRI. For all assessed compounds, the IC_{50} value was not impacted by the presence of INA active AgI particles when normalized to PBS or normalized to either solvent; this indicates there is no measurable change on the IRI activity through the introduction of INA activity. This finding reinforces that the design of small molecule and macromolecule CPAs are distinct. For small molecule carbohydrates no interaction was identified between INA and IRI activity. However, this does not preclude the possibility that the concentrations required to influence ice nucleation are not the same as required to possess IRI activity. This finding also suggests that a

dual formulation of INA and IRI active molecules may not provide synergistic benefits, but there is no evidence that any destructive interference will occur.

3.6 References

(1) Capicciotti, C. J.; Kurach, J. D. R.; Turner, T. R.; Mancini, R. S.; Acker, J. P.; Ben, R. N. Small Molecule Ice Recrystallization Inhibitors Enable Freezing of Human Red Blood Cells with Reduced Glycerol Concentrations. *Sci. Rep.* **2015**, *5* (1), 9692. https://doi.org/10.1038/srep09692.

(2) Briard, J. G.; Jahan, S.; Chandran, P.; Allan, D.; Pineault, N.; Ben, R. N. Small-Molecule Ice Recrystallization Inhibitors Improve the Post-Thaw Function of Hematopoietic Stem and Progenitor Cells. *ACS Omega* **2016**, *1* (5), 1010–1018. https://doi.org/10.1021/acsomega.6b00178.

(3) Capicciotti, C. J.; Leclère, M.; Perras, F. A.; Bryce, D. L.; Paulin, H.; Harden, J.; Liu, Y.; Ben, R. N. Potent Inhibition of Ice Recrystallization by Low Molecular Weight Carbohydrate-Based Surfactants and Hydrogelators. *Chem. Sci.* **2012**, *3* (5), 1408–1416. https://doi.org/10.1039/C2SC00885H.

(4) Briard, J. G.; Fernandez, M.; De Luna, P.; Woo, Tom. K.; Ben, R. N. QSAR Accelerated Discovery of Potent Ice Recrystallization Inhibitors. *Sci. Rep.* **2016**, *6* (1), 26403. https://doi.org/10.1038/srep26403.

(5) Tam, R. Y.; Ferreira, S. S.; Czechura, P.; Chaytor, J. L.; Ben, R. N. Hydration Index—A Better Parameter for Explaining Small Molecule Hydration in Inhibition of Ice Recrystallization. *J. Am. Chem. Soc.* **2008**, *130* (51), 17494–17501. https://doi.org/10.1021/ja806284x.

(6) Chaytor, J. L.; Tokarew, J. M.; Wu, L. K.; Leclère, M.; Tam, R. Y.; Capicciotti, C. J.; Guolla, L.; von Moos, E.; Findlay, C. S.; Allan, D. S.; Ben, R. N. Inhibiting Ice Recrystallization and Optimization of Cell Viability after Cryopreservation. *Glycobiology* **2012**, *22* (1), 123–133. https://doi.org/10.1093/glycob/cwr115.

(7) Briard, J. G.; Poisson, J. S.; Turner, T. R.; Capicciotti, C. J.; Acker, J. P.; Ben, R. N. Small Molecule Ice Recrystallization Inhibitors Mitigate Red Blood Cell Lysis during Freezing, Transient Warming and Thawing. *Sci. Rep.* **2016**, *6* (1), 23619. https://doi.org/10.1038/srep23619.

(8) Capicciotti, C. J.; Mancini, R. S.; Turner, T. R.; Koyama, T.; Alteen, M. G.; Doshi, M.; Inada, T.; Acker, J. P.; Ben, R. N. O-Aryl-Glycoside Ice Recrystallization Inhibitors as Novel Cryoprotectants: A Structure–Function Study. *ACS Omega* **2016**, *1* (4), 656–662. https://doi.org/10.1021/acsomega.6b00163.

(9) Li, Y.; Tan, J.; Li, L. Comparison of Three Methods for Cryopreservation of Human Embryonic Stem Cells. *Fertil. Steril.* **2010**, *93* (3), 999–1005. https://doi.org/10.1016/j.fertnstert.2008.10.052.

(10) Higgins, A. Z.; Cullen, D. K.; LaPlaca, M. C.; Karlsson, J. O. M. Effects of Freezing Profile Parameters on the Survival of Cryopreserved Rat Embryonic Neural Cells. *J. Neurosci. Methods* **2011**, *201* (1), 9–16. https://doi.org/10.1016/j.jneumeth.2011.06.033.

(11) Morris, G. J.; Acton, E. Controlled Ice Nucleation in Cryopreservation--a Review. *Cryobiology* **2013**, *66* (2), 85–92. https://doi.org/10.1016/j.cryobiol.2012.11.007.

(12) Mousazadehkasin, M.; Mitchell, N.; Asenath-Smith, E.; Tsavalas, J. G. Ice Nucleation Promotion Impact on the Ice Recrystallization Inhibition Activity of Polyols. *Biomacromolecules* **2023**, *24* (2), 678–689. https://doi.org/10.1021/acs.biomac.2c01120.

(13) Guerreiro, B. M.; Freitas, F.; Lima, J. C.; Silva, J. C.; Dionísio, M.; Reis, M. A. M. Demonstration of the Cryoprotective Properties of the Fucose-Containing Polysaccharide FucoPol. *Carbohydr. Polym.* **2020**, *245*, 116500. https://doi.org/10.1016/j.carbpol.2020.116500.

(14) Guerreiro, B. M.; Consiglio, A. N.; Rubinsky, B.; Powell-Palm, M. J.; Freitas, F. Enhanced Control over Ice Nucleation Stochasticity Using a Carbohydrate Polymer Cryoprotectant. *ACS Biomater. Sci. Eng.* **2022**, *8* (5), 1852–1859. https://doi.org/10.1021/acsbiomaterials.2c00075.

(15) Raymond, J. A.; DeVries, A. L. Adsorption Inhibition as a Mechanism of Freezing Resistance in Polar Fishes. *Proc. Natl. Acad. Sci.* **1977**, *74* (6), 2589–2593. https://doi.org/10.1073/pnas.74.6.2589.

(16) Meister, K.; DeVries, A. L.; Bakker, H. J.; Drori, R. Antifreeze Glycoproteins Bind Irreversibly to Ice. *J. Am. Chem. Soc.* **2018**, *140* (30), 9365–9368. https://doi.org/10.1021/jacs.8b04966.

(17) Trant, J. F.; Biggs, R. A.; Capicciotti, C. J.; Ben, R. N. Developing Highly Active Small Molecule Ice Recrystallization Inhibitors Based upon C-Linked Antifreeze Glycoprotein Analogues. *RSC Adv.* **2013**, *3* (48), 26005–26009. https://doi.org/10.1039/C3RA43835J.

(18) McMunn, L. E.; D'Costa, A. S.; Bordenave, N.; Ben, R. N. Probing the Mechanism of Action of Small-Molecule Ice Recrystallization Inhibitors Using Proton Nuclear Magnetic Resonance Relaxation. *J. Phys. Chem. Lett.* **2023**, *14* (26), 6043–6050. https://doi.org/10.1021/acs.jpclett.3c00845.

(19) Gibbs, W. J. *Gibbs G.W. - Collected Works. Thermodynamics. Volume 1-Longmans (1928).Pdf*; Longmans, Green and Co.: New York, 1928; Vol. 1.

(20) Volmer, M.; Weber, A. Keimbildung in übersättigten Gebilden. *Z. Für Phys. Chem.* **1926**, *119U* (1), 277–301. https://doi.org/10.1515/zpch-1926-11927.

(21) Becker, R.; Döring, W. Kinetische Behandlung Der Keimbildung in Übersättigten Dämpfen. *Ann. Phys.* **1935**, *416* (8), 719–752. https://doi.org/10.1002/andp.19354160806.

(22) Lin, M.; Cao, H.; Li, J. Control Strategies of Ice Nucleation, Growth, and Recrystallization for Cryopreservation. *Acta Biomater.* **2023**, *155*, 35–56. https://doi.org/10.1016/j.actbio.2022.10.056.

(23) Kojima, S.; Kaku, M.; Kawata, T.; Sumi, H.; Shikata, H.; Abonti, T. R.; Kojima, S.; Fujita, T.; Motokawa, M.; Tanne, K. Cryopreservation of Rat MSCs by Use of a Programmed Freezer with Magnetic Field. *Cryobiology* **2013**, *67* (3), 258–263. https://doi.org/10.1016/j.cryobiol.2013.08.003.

(24) Greer, N. Freezing under Pressure: A New Method for Cryopreservation. *Cryobiology* **2015**, *70* (1), 66–70. https://doi.org/10.1016/j.cryobiol.2014.12.005.

(25) Ma, Y. H.; Qin, G. F.; Li, J.; Ding, G. R.; Xu, S. L.; Zhou, Y.; Guo, G. Z. AC Electric Field Enhances Cryopreservation Efficiency of Sprague-Dawley Rat Liver During a Slow Freezing Procedure. *Biopreservation Biobanking* **2016**, *14* (1), 23–28. https://doi.org/10.1089/bio.2015.0042.

(26) Missous, G.; Thammavongs, B.; Dieuleveux, V.; Guéguen, M.; Panoff, J. M. Improvement of the Cryopreservation of the Fungal Starter *Geotrichum Candidum* by Artificial Nucleation and Temperature Downshift Control. *Cryobiology* **2007**, *55* (1), 66–71. https://doi.org/10.1016/j.cryobiol.2007.05.004.

(27) Gusta, L. V.; Wisniewski, M.; Nesbitt, N. T.; Gusta, M. L. The Effect of Water, Sugars, and Proteins on the Pattern of Ice Nucleation and Propagation in Acclimated and Nonacclimated Canola Leaves. *Plant Physiol.* **2004**, *135* (3), 1642–1653. https://doi.org/10.1104/pp.103.028308.

(28) Kasuga, J.; Arakawa, K.; Fujikawa, S. High Accumulation of Soluble Sugars in Deep Supercooling Japanese White Birch Xylem Parenchyma Cells. *New Phytol.* **2007**, *174* (3), 569–579. https://doi.org/10.1111/j.1469-8137.2007.02025.x.

(29) Galema, S. A.; Hoeiland, H. Stereochemical Aspects of Hydration of Carbohydrates in Aqueous Solutions. 3. Density and Ultrasound Measurements. *J. Phys. Chem.* **1991**, *95* (13), 5321–5326. https://doi.org/10.1021/j100166a073.
(30) Tomobe, K.; Yamamoto, E.; Yasui, M.; Yasuoka, K. Effects of Temperature, Concentration, and Isomer on the Hydration Structure in Monosaccharide Solutions. *Phys. Chem. Chem. Phys.* **2017**, *19* (23), 15239–15246. https://doi.org/10.1039/C7CP02392H.
(31) Penkov, N. V. Relationships between Molecular Structure of Carbohydrates and Their Dynamic Hydration Shells Revealed by Terahertz Time-Domain Spectroscopy. *Int. J. Mol. Sci.* **2021**, *22* (21), 11969. https://doi.org/10.3390/ijms222111969.
(32) Bakó, I.; Pusztai, L.; Pothoczki, S. Outstanding Properties of the Hydration Shell around β- D -Glucose: A Computational Study. *ACS Omega* **2024**, *9* (18), 20331–20337. https://doi.org/10.1021/acsomega.4c00798.
(33) Edelman, R.; Kusner, I.; Kisiliak, R.; Srebnik, S.; Livney, Y. D. Sugar Stereochemistry Effects on Water Structure and on Protein Stability: The Templating Concept. *Food Hydrocoll.* **2015**, *48*, 27–37. https://doi.org/10.1016/j.foodhyd.2015.01.028.
(34) Huang, H.; Yarmush, M. L.; Usta, O. B. Long-Term Deep-Supercooling of Large-Volume Water and Red Cell Suspensions via Surface Sealing with Immiscible Liquids. *Nat. Commun.* **2018**, *9* (1), 3201. https://doi.org/10.1038/s41467-018-05636-0.
(35) Isiksacan, Z.; William, N.; Senturk, R.; Boudreau, L.; Wooning, C.; Castellanos, E.; Isiksacan, S.; Yarmush, M. L.; Acker, J. P.; Usta, O. B. Extended Supercooled Storage of Red Blood Cells. *Commun. Biol.* **2024**, *7* (1), 1–9. https://doi.org/10.1038/s42003-024-06463-4.
(36) Vali, G. Supercooling of Water and Nucleation of Ice (Drop Freezer). *Am. J. Phys.* **1971**, *39* (10), 1125–1128. https://doi.org/10.1119/1.1976585.
(37) Kieft, T. L. Ice Nucleation Activity in Lichens. *Appl. Environ. Microbiol.* **1988**, *54* (7), 1678–1681. https://doi.org/10.1128/aem.54.7.1678-1681.1988.
(38) Inada, T.; Koyama, T.; Goto, F.; Seto, T. Ice Nucleation in Emulsified Aqueous Solutions of Antifreeze Protein Type III and Poly(Vinyl Alcohol). *J. Phys. Chem. B* **2011**, *115* (24), 7914–7922. https://doi.org/10.1021/jp111745v.
(39) Kamijo, Y.; Derda, R. Freeze–Float Selection of Ice Nucleators. *Langmuir* **2019**, *35* (2), 359–364. https://doi.org/10.1021/acs.langmuir.8b02902.
(40) Mazur, P.; Leibo, S. P.; Chu, E. H. Y. A Two-Factor Hypothesis of Freezing Injury: Evidence from Chinese Hamster Tissue-Culture Cells. *Exp. Cell Res.* **1972**, *71* (2), 345–355. https://doi.org/10.1016/0014-4827(72)90303-5.
(41) Li, J.; Lee, T.-C. Bacterial Ice Nucleation and Its Potential Application in the Food Industry. *Trends Food Sci. Technol.* **1995**, *6* (8), 259–265. https://doi.org/10.1016/S0924-2244(00)89110-4.
(42) Wex, H.; Augustin-Bauditz, S.; Boose, Y.; Budke, C.; Curtius, J.; Diehl, K.; Dreyer, A.; Frank, F.; Hartmann, S.; Hiranuma, N.; Jantsch, E.; Kanji, Z. A.; Kiselev, A.; Koop, T.; Möhler, O.; Niedermeier, D.; Nillius, B.; Rösch, M.; Rose, D.; Schmidt, C.; Steinke, I.; Stratmann, F. Intercomparing Different Devices for the Investigation of Ice Nucleating Particles Using Snomax® as Test Substance. *Atmospheric Chem. Phys.* **2015**, *15* (3), 1463–1485. https://doi.org/10.5194/acp-15-1463-2015.
(43) Petzold, G.; Aguilera, J. M. Ice Morphology: Fundamentals and Technological Applications in Foods. *Food Biophys.* **2009**, *4* (4), 378–396. https://doi.org/10.1007/s11483-009-9136-5.
(44) Soni, A.; Patey, G. N. Ice Nucleation by the Primary Prism Face of Silver Iodide. *J. Phys. Chem. C* **2022**, *126* (15), 6716–6723. https://doi.org/10.1021/acs.jpcc.1c10227.

(45) Koyama, T.; Inada, T.; Kuwabara, C.; Arakawa, K.; Fujikawa, S. Anti-Ice Nucleating Activity of Polyphenol Compounds against Silver Iodide. *Cryobiology* **2014**, *69* (2), 223–228. https://doi.org/10.1016/j.cryobiol.2014.07.009.
(46) Inada, T.; Koyama, T.; Tomita, H.; Fuse, T.; Kuwabara, C.; Arakawa, K.; Fujikawa, S. Anti-Ice Nucleating Activity of Surfactants against Silver Iodide in Water-in-Oil Emulsions. *J. Phys. Chem. B* **2017**, *121* (27), 6580–6587. https://doi.org/10.1021/acs.jpcb.7b02644.
(47) Mason, B. J.; Heuvel, A. P. van den. The Properties and Behaviour of Some Artificial Ice Nuclei. *Proc. Phys. Soc.* **1959**, *74* (6), 744. https://doi.org/10.1088/0370-1328/74/6/312.
(48) Genadiev, N.; Michailov, M.; Nenow, D. Ice-Nucleation Activity of AgI Particles on the Surface of Water and into the Volume. *Cryst. Res. Technol.* **1986**, *21* (10), 1253–1255. https://doi.org/10.1002/crat.2170211002.
(49) Mendizza, W.; Diamante, M. F.; Ben, R. N. Elucidating Structure Activity Relationship of Pyranoses for Ice Nucleation, 2024.
(50) Musca, S.; Diamante, M. F. Unpublished Honours Thesis, University of Ottawa, 2025.
(51) Abraham, S.; Keillor, K.; Capicciotti, C. J.; Perley-Robertson, G. E.; Keillor, J. W.; Ben, R. N. Quantitative Analysis of the Efficacy and Potency of Novel Small Molecule Ice Recrystallization Inhibitors. *Cryst. Growth Des.* **2015**, *15* (10), 5034–5039. https://doi.org/10.1021/acs.cgd.5b00995.
(52) Adam, M. K. Improving the Engraftment Activities of Cryopreserved Human Umbilical Cord Blood Through the Development of Novel Glyco(Peptide)-Based Aryl Ice Recrystallization Inhibitors, Univerity of Ottawa, 2020. http://dx.doi.org/10.20381/ruor-25034.
(53) McMunn, L. E. Unpublished PhD. Thesis, University of Ottawa, 2025.

4. Structure Function Studies of N-Aryl Gluconamide Ice Recrystallization Inhibitors (IRIs)

4.1 Introduction

First published in 2016,[1] the *N*-aryl gluconamide family of ice recrystallization inhibitors have been the most successfully applied family of small molecule IRI to date, improving post-thaw recovery and viability for a variety of cellular systems.[1–7] Consisting of a hydrophobic *N*-aryl moiety linked to a hydrophilic carbohydrate chain through an amide bond (**Figure 4.1**), the synthesis of *N*-aryl gluconamides can be achieved in one step from commercially available reagents. Due to their synthetic accessibility, a wide range of anilines have been explored in the generation of *N*-aryl gluconamides.[1,8] Even with a large library of synthetically accessible small molecules of known IRI activity, the mechanism, and structural components necessary for small molecule IRI activity remain unknown. To this point, no specific structural motif has been identified as a requirement for the IRI activity measured in small molecule *N*-aryl gluconamides.

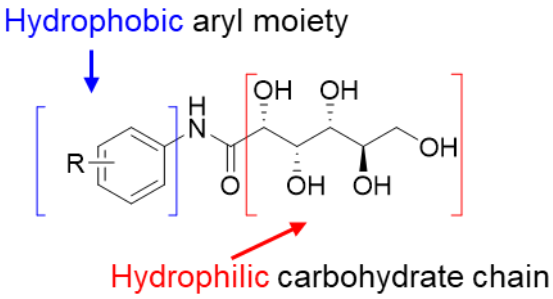

Figure 4.1 General structure of *N*-aryl gluconamides.

4.1.1 Assessment of IRI activity with the Splat Cooling Assay (SCA)

Traditionally, the IRI activity of a given molecule can be assessed through the use of the splat cooling assay (SCA).[9] With the assay, a 10 µL aqueous droplet of solvated (in phosphate buffered saline (PBS)) sample is released from a height of 2.6 meters onto an aluminum block pre-cooled to -78 °C. The frozen droplet is allowed to anneal at a constant temperature for a specific time, and the resulting ice wafer is imaged from which ice crystal size can be measured. One iteration of this assay had been employed previously by the Ben lab, which utilized a 30-minute annealing time and assessed one concentration per compound. The IRI activity of a compound assessed on the 30-minute SCA is represented as a measure of the percent mean grain size (%MGS) in comparison to PBS control. As a compound is more IRI active, it will prevent the growth of larger ice crystals during the annealing time, resulting in relatively smaller crystal sizes as compared to a less IRI active solution. The minimum concentration of D-galactose capable of measurably

reducing ice crystal growth compared to PBS, 22 mM, was chosen for assessment of compounds on the 30-minute SCA.[10] This methodology allowed for rapid screening of potential IRI active candidates, but failed to address the time and concentration dependence of ice recrystallization inhibition by small molecules.

To address these issues, a modified SCA has been developed and adopted by the Ben lab that utilizes the same basic steps as the traditional SCA, but compounds of interest are assessed at several concentrations (allowing for the generation of a dose-response relationship), and annealed for only 5-minutes.[11] The shorter annealing time still provides a predominately frozen fraction, but with a larger number of crystals generated per ice crystal wafer (approximately 200 crystals) when compared to the original implementation of the SCA (10 crystals). The assessment of compounds of interest at several concentrations, with each concentration containing more ice crystals, the modified SCA provides a more reliable assessment of compound IRI activity.

As discussed in **Section 1.3.2.1**, IRI analysis performed using the modified SCA can be represented numerically as the concentration required for 50 % inhibition of ice crystal growth (IC_{50}) with respect to PBS control, or graphically as a dose response relationship (log concentration of solute against the normalized rate of ice crystal growth) (**Figure 4.2**). IRI analysis has been performed across both iterations of the SCA in the Ben lab, resulting in a mixture of %MGS and IC_{50} values reported for any given set of compounds. Despite not allowing for a direct comparison between assays, both %MGS and IC_{50} values can be intra-compared to convey relative IRI activity information for a given compound set. A detailed explanation and procedure for the modified SCA can be found in **Appendix III**.

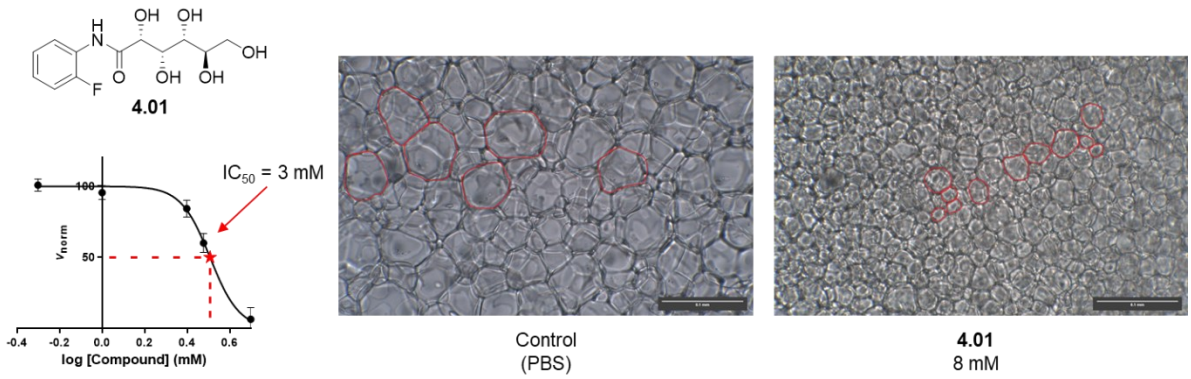

Figure 4.2 A visual representation of the data obtained through the modified SCA for the known IRI **4.01**. Ice crystal images are obtained following a 5-minute annealing period at -6.4 °C. In the absence of **4.01** (PBS control) ice crystals (examples outlined in red) grow larger than those in the presence of an 8 mM solution of **4.01**. A dose response relationship can be generated from obtained ice crystal images for a given compound (fit to a nonlinear four-parameter dose response curve) and the IC_{50} can be extracted. Ice crystal images are scaled to equivalent magnification (scale bar = 0.1 mm).

4.1.2 Prior structure function studies of small molecule carbohydrates

It has been established that a balance between hydrophobicity and hydrophilicity of a small molecule carbohydrate is required to possess IRI activity,[10,12,13] and that their mechanism of action is likely related to their ability to interact with bulk water.[14] However, without a clear understanding of why these requirements exist, or how IRIs function in solution, the ability to rationally design novel IRI active compounds is severely limited. A previous graduate student in the Ben lab, Dr. Jennie Briard, synthesized an initial library of small molecule *N*-aryl gluconamide IRIs (**Figure 4.3 (A)**).[15] From this preliminary screen, several compounds were identified (including **4.01**, **4.02**, and **4.04**) which are still utilized as cryoprotective agents a decade after initial publication (**Figure 4.3**). From this preliminary library, a computationally assisted assessment was completed, with the intension of identifying connections between structural components of small molecule IRIs and their IRI activity.[16] The generated three-dimensional Quantitative Structure-Activity Relationship (3D-QSAR) model was utilized to predict the IRI activity of several *N*-aryl gluconamides (**Figure 4.3 (B**,**C)**). With the activity threshold set at 70 % MGS,[16] the model was considered moderately accurate in predicting “active” compounds (**Figure 4.3 (B)**), although several false negatives arose from the generated set (**Figure 4.3 (C)**). Ultimately the generated 3D-QSAR model demonstrated a moderate ability to identify compounds which were IRI active at 22 mM, but failed to identify any common chemical characteristics required for IRI activity to direct future synthesis.[16]

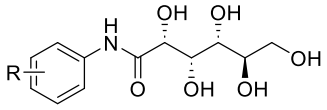

A

R = H	%MGS = 66 %
R = 2 - F	%MGS = 3 %[1]
R = 3 - F	%MGS = 10 %
R = 4 - F	%MGS = 90 %
R = 3,5 - F	%MGS = 5 %[1]
R = 3 - Br	%MGS = 75 %
R = 4 - Br	%MGS = 4 %
R = 2 - OMe	%MGS = 75 %
R = 4 - OMe	%MGS = 54 %
R = 4 - OH	%MGS = 40 %
R = 3 - COOH	%MGS = 100 %

B

R = 2,5 Cl	%MGS = 46 %
R = 4 - CH_3	%MGS = 6 %
R = 2 - OH	%MGS = 30 %
R = 3 - CF_3	%MGS = 86 %
R = 4 - CF_3	%MGS = 28 %[1]
R = 4 - OCF_3	%MGS = 14 %

C

R = 2 - Cl	%MGS = 99 %
R = 4 - Cl	%MGS = 35 %
R = 2 - CH_3	%MGS = 90 %
R = 2,6 - CH_3	%MGS = 32 %
R = 2,5 - CH_3	%MGS = 84 %

[1] - Tested at 11 mM

Figure 4.3 *N*-aryl gluconamide IRIs tested on the original 30-minute SCA, %MGS is measured at 22 mM unless otherwise specified.[15] %MGS values were extracted with the use of a plot digitizer from previously reported bar-graphs.[16] **(A)** *N*-aryl gluconamides used as the training set for 3D-QSAR model calibration. **(B)** *N*-aryl gluconamides which were predicted by the 3D-QSAR model as potentially possessing IRI activity (%MGS < 70 % at 22 mM).[16] Subsequent IRI activity measured (%MGS) is indicated beside each derivative. **(C)** *N*-aryl gluconamides which were predicted by the 3D-QSAR model to likely not be IRI active (%MGS > 70 %).[16] Subsequent IRI activity measured (%MGS) is indicated beside each derivative.

4.1.2.1 Structural modifications to small molecule pyranose IRIs

Although systematic screening of the hydrophobic component of *N*-aryl gluconamides failed to yield a tangible structural correlation, no systematic analysis of the relationship between IRI activity and hydrophilic carbohydrate component of *N*- functionalized gluconamides has been performed to date. Several modifications on the hydrophilic ring of pyranose sugars have been attempted individually.[17–21] When investigating simple monosaccahrides, previous Ben lab PhD candidate Dr. Chantelle Capicciotti discovered that modifications at the C_1 position were tolerated (resulting in compounds possessing improved IRI activity), while substitutions at the C_6 position were uniformly not tolerated.[17] It was postulated that the C_6 hydroxyl was important for both IRI activity and bulk water interactions for small molecule carbohydrates, making this position intolerant to modification. This finding was particularly impactful, as traditionally only C_2 and C_4 hydroxyls have been established as predominate factors for the hydration of a given carbohydrate.[22]

Despite the primary alcohol (C_6 position) being established as a position of importance for small molecule pyranoside IRIs,[17] it remains the second most synthetically accessible position for chemical modification beyond the anomeric C_1 hydroxyl. As a result, several attempts have been made to functionalize the C_6 position of small molecule carbohydrates. When attempting to isolate functional groups of interest for IRI activity, previous Ben lab graduate student Dr. Malay Doshi successfully synthesized an IRI active C_3-*N*-galactonamide disaccharide derivative of (**3.02**),

while the corresponding C_6 derivative resulted in no meaningful IRI activity (**Figure 4.4 (A)**).[18] Additionally, several *N*-cycloalkyl arabinose derivatives were synthesized by Dr. Doshi, which uniformly possessed lower IRI activity when compared to the corresponding *N*-cycloalkyl gluconamide derivative (**Figure 4.4 (B)**).[18]

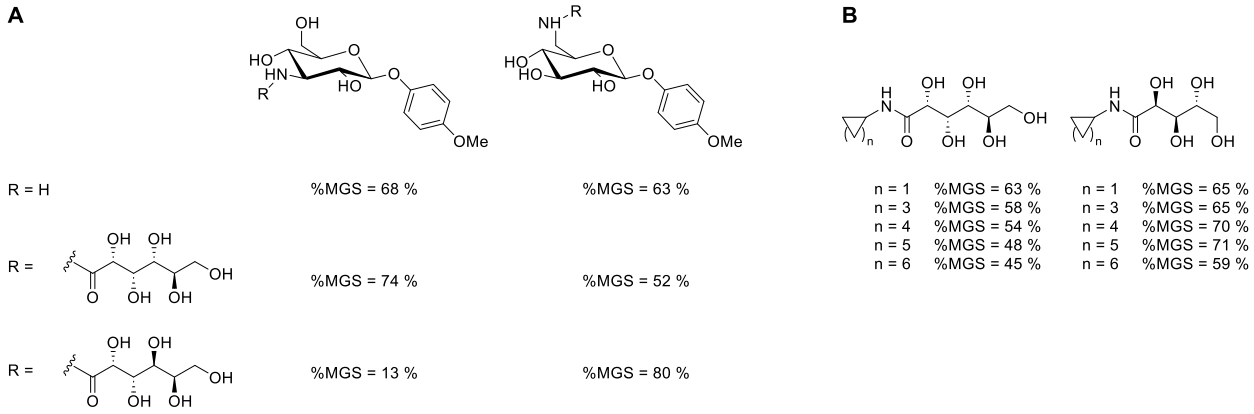

Figure 4.4 Previously synthesized[18] *N*-functionalized small molecule carbohydrates, assessed with the original 30-minute SCA, %MGS is measured at 22 mM. Listed %MGS values were extracted with the use of a plot digitizer from previously reported bar-graphs.[18] **(A)** Selected **3.02** derivatives generated, including C_3 and C_6 *N*-glycosidated glucosamine compounds. **(B)** *N*-cycloalkyl gluconamide and *N*-cycloalkyl arabinose derivatives bearing various cycloalkyl ring sizes.[18]

Previous graduate students in the Ben lab Dr. Jessica Poisson,[19] Dr. Madeleine Adam,[8] and Dr. Anna Ampaw[21] have all investigated the installation of charged functional groups onto small molecule carbohydrates (**Figure 4.5**). The addition of a charged phosphonate onto glucose resulted in an increase in IRI activity if installed at the C_1 or C_6 position.[19] This finding was not consistent when extended to IRI active *O*-aryl pyranose compounds (**3.02**, **3.03**), with the resulting C_6 phosphonate derivative not retaining IRI activity (**Figure 4.5 (B)**).[21] Similar results were obtained in the generation of C_6 ammonium salts, whereby a loss of IRI activity was observed with respect to the parent IRI active *O*-aryl gluconamide (**Figure 4.5 (B)**).[19] When investigating the installation of an azide onto a small molecule carbohydrate IRIs, Dr. Poisson systematically tested each position on the pyranose ring (**Figure 4.5 (C)**), finding no tolerance for modification at the C_2, C_4 or C_6 positions.[19] This finding agrees with the preliminary investigation of reducing sugars,[17] indicating that the C_2 and C_4 hydroxyl are important for pyranose hydration[22] as well as C_6 being important for IRI activity.

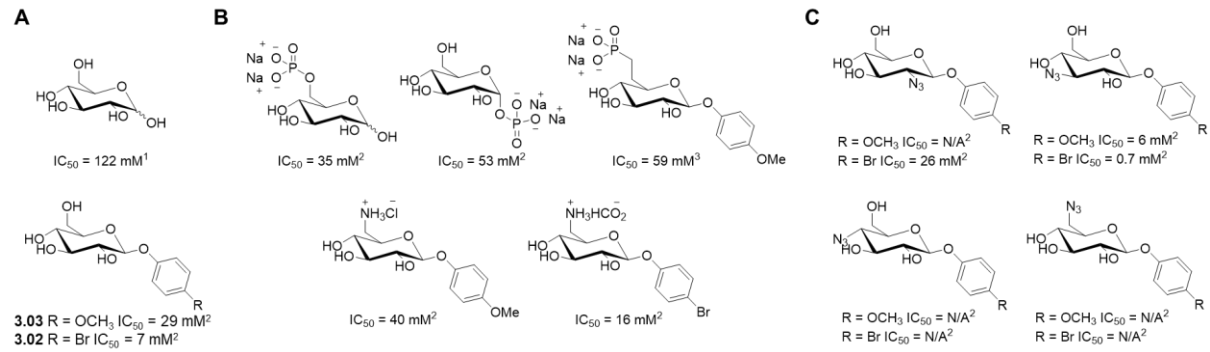

Figure 4.5 Aryl pyranose IRIs bearing various ring functionalization. IC_{50} values were obtained on the modified SCA in PBS, compounds indicated with an IC_{50} value of N/A failed to achieve a relative rate of ice crystal growth below 50% before becoming solubility limited. Author of first publication is indicated for each derivative (1[11], 2[19], 3[21]). Listed IC_{50} values were extracted with a plot digitizer from previously reported bar-graphs.[11,19,21] **(A)** Reference small molecule carbohydrates.[11,19] **(B)** Phosphonate and ammonium containing small molecule carbohydrate derivatives.[19,21] **(C)** Small molecule *O*-aryl pyranoside derived (**3.02**, **3.03**) compounds bearing an azide functional group.[19]

4.1.2.2 Structural modifications to the C_6 hydroxyl of *N*-functionalized gluconamides

The installation of charged functionality to *N*-aryl gluconamides has also been attempted, but it has been limited to the C_6 position (**Figure 4.6**).[8] All generated C_6 azide and carboxylic acid derivatives reduce IRI activity when compared to the corresponding parent *N*-aryl gluconamide (**Figure 4.6**). Subsequent attempts were not made at other positions due to the synthetic difficulty of installing modifications to *N*-functionalized gluconamides beyond the C_6 position.

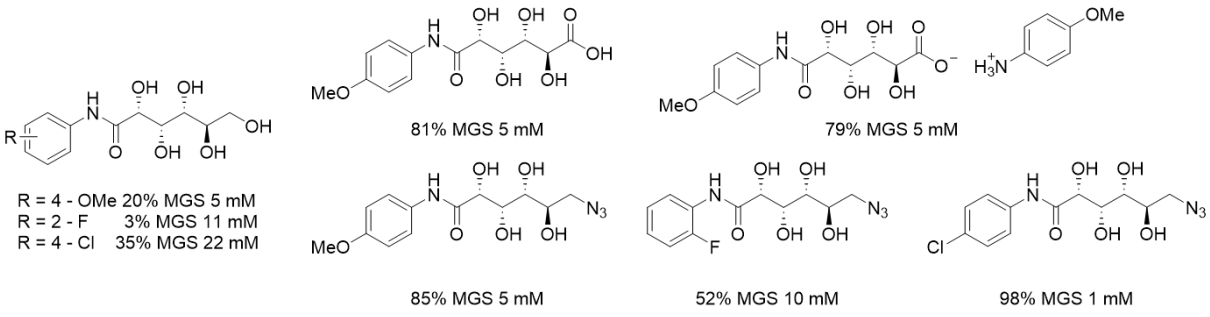

Figure 4.6. C_6-modified *N*-aryl gluconamide derivatives.[8] IRI activity was assessed on the original 30-minute SCA. Only one representative concentration was selected for representation in this figure as compound solubility and assessed concentrations varied between compounds. Listed %MGS values were extracted with the use of a plot digitizer from previously reported bar-graphs.[8]

It can be generally understood that for *O*-functionalized pyranose IRIs, modification at the C_2, C_4 and C_6 positions are not likely to be tolerated,[8,17–19,21] however it is not known if this relationship extends to *N*-functionalized gluconamides. As previous attempts to functionalize the most

synthetically accessible position (C_6) have failed, a better understanding of the positional tolerance for *N*-functionalized gluconamides is required prior to attempting synthetically difficult substitutions. Should position(s) of interest for functionalization be identified on the carbohydrate chain, it would help enable attempts to further optimize *N*-aryl gluconamides for specialized biological applications.

4.2 Individual IRI assessment of hydrophobic aniline and hydrophilic gluconic acid

It has been established that altering the choice of substituent on the aryl ring has a direct impact on measured IRI activity,[1,8] although the reason for this impact is unknown. Various IRI active *N*-aryl gluconamides have been generated utilizing either electron withdrawing (**4.01**, **4.02**) or donating (**4.04**) substituents at varying positions (*ortho*-, *meta*-, *para*-) on the aryl ring. Prior to this work, the commercial anilines utilized in the synthesis of *N*-aryl gluconamides had not been assessed for IRI activity. IRI active (**4.01**, **4.02**, **4.04**) *N*-aryl gluconamides were selected to study the positional and electronic (donating or withdrawing) importance of aryl substitution on IRI activity (**Scheme 4.1**). IRI inactive compound **4.03** was selected not only as a control for para-fluorination, but as an IRI inactive starting point, to probe for improved (measurable) IRI activity.

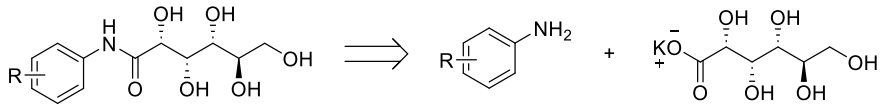

4.01 R = 2 - F IC_{50} = 3 mM
4.02 R = 3 - F IC_{50} = 7 mM
4.03 R = 4 - F IC_{50} = N/A
4.04 R = 4 - OMe IC_{50} = 5 mM

4.05 R = 2 - F IC_{50} = N/A
4.06 R = 3 - F IC_{50} = N/A
4.07 R = 4 - F IC_{50} = N/A
4.08 R = 4 - OMe IC_{50} = 24 mM

4.36 IC_{50} = 109 mM

Scheme 4.1 General figure correlating a given *N*-aryl gluconamide (**4.01** – **4.04**) to the corresponding aniline (**4.05** – **4.08**) and gluconic acid (**4.36**, assessed as the potassium salt). IC_{50} values were obtained on the modified splat cooling assay in PBS, compounds indicated with an IC_{50} value of N/A failed to achieve a relative rate of ice crystal growth below 50% before becoming solubility limited.

When decoupling the hydrophobic aniline from hydrophilic carbohydrate, there is not a clear correlation between the IRI activity of an aniline to the corresponding gluconamide (**Scheme 4.1**). All fluorinated anilines (**4.05** – **4.07**) demonstrated no measurable IRI activity, despite the corresponding *ortho*- and *meta*- gluconamides being IRI active. Interestingly, *p*-anisidine (**4.08**) did possess measurable IRI activity, however it was approximately five times lower than the corresponding gluconamide (**4.04**). As **4.08** was the only tested aniline with measurable IRI activity, it may suggest that *N*-aryl gluconamides bearing electron rich aryl rings function differently than *N*-aryl gluconamides bearing electron poor aryl rings. Gluconic acid was found to

possess IRI activity similar to glucose (IC_{50} = 122 mM),[11] which is approximately two orders of magnitude less than IRI active than compound **4.01**. It has been clearly established that a balance between hydrophobic and hydrophilic components are required for IRI activity.[10] However, the IRI activity of *p*-anisidine presents the first indication that the investigation of *N*-aryl gluconamides with differing aryl ring properties may not share structural components required for IRI activity.

4.3 Assessing relative functional importance through traditional structure function relationship investigation

Knowing that aniline or carbohydrate components alone are not responsible for the IRI activity measured for *N*-aryl gluconamides; a synthetic plan was devised to synthesize incrementally truncated derivatives of the same parent *N*-aryl gluconamide IRIs (**4.01** – **4.04**) utilized in **Section 4.2** (**Scheme 4.2**, **Section 4.3.1**). Synthetic modifications began at the C_6 position and remove one hydroxyl at a time, ending with the *N*-aryl acetamide derivative (**4.22** – **4.25**). With each modification the IRI activity was assessed, and the corresponding change in IRI activity provides insight as to the importance of the removed functional group. This approach allows for identification of positions of vital importance for IRI activity (not potential sites of modification) and positions which are not required for IRI activity (potential target sites for modification).

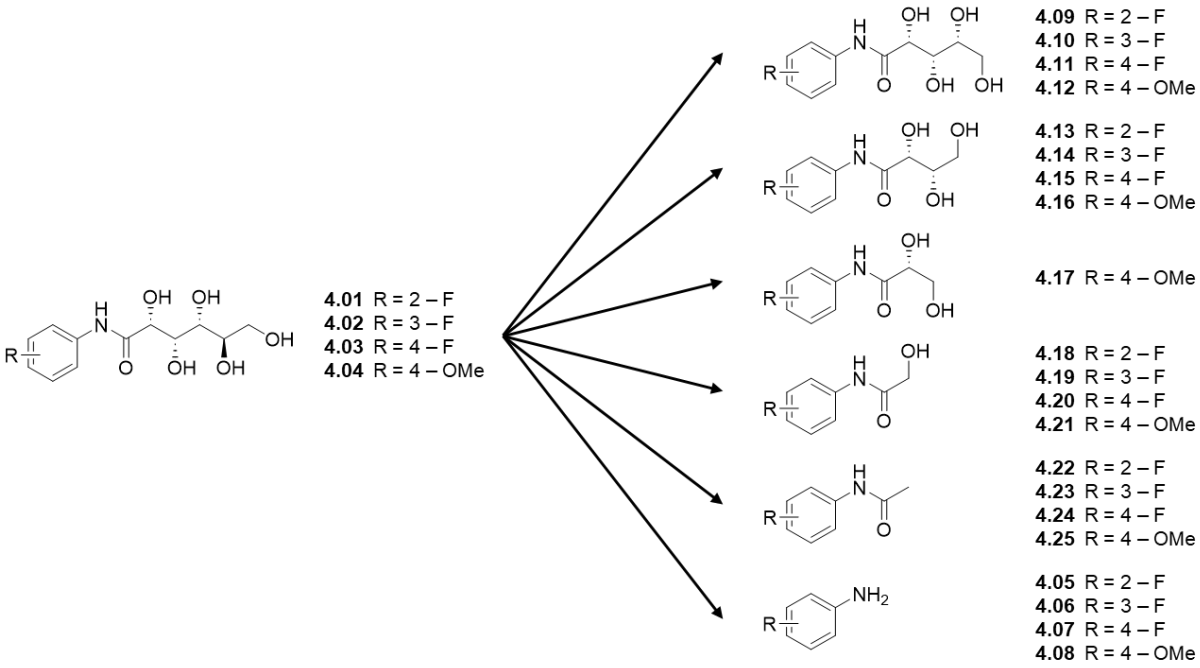

Scheme 4.2 General scheme correlating a given *N*-aryl gluconamide (**4.01** – **4.04**) to the corresponding modified derivatives. For each *N*-aryl gluconamide IRI, the corresponding *N*-aryl xylonamide (**4.09** – **4.12**), *N*-aryl threonamide (**4.13** – **4.16**), *N*-aryl propenamide (**4.17**), *N*-functionalized anilide (**4.18** – **4.21**), and *N*-aryl acetamide (**4.22** – **4.25**) are represented by the given compound number.

4.3.1 Synthetic pathway for truncated compound sets

4.3.1.1 Synthesis of reference *N*-aryl gluconamides (4.01 – 4.04)

Synthesis of parent *N*-aryl gluconamides (**4.01** – **4.04**) was achieved in one step, heating δ-gluconolactone and aniline of choice in acetic acid at 100 °C for one hour. The subsequent reaction mixture was concentrated under reduced pressure and recrystalized from 95% EtOH to afford *N*-aryl gluconamide following isolation. It is worth noting that reaction temperature must be kept at or below 100 °C, as at reflux (118 °C) the reaction mixture rapidly discoloured and yields were greatly reduced.

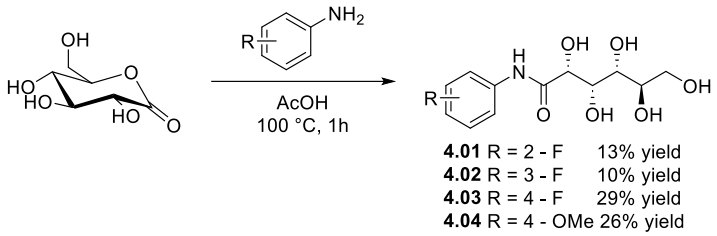

Scheme 4.3 Synthesis of *N*-aryl gluconamides from δ-D-gluconolactone adapted from previous Ben laboratory procedure.[15]

4.3.1.2 Synthesis of 4-hydoxyl containing *N*-aryl xylonamide derivatives (4.09 – 4.12)

Synthesis of *N*-aryl xylonamides (**4.09** – **4.12**) (**Scheme 4.3.1.2**) began from D-xylose. The C_1 hydroxyl was methylated under acidic conditions in methanol at reflux, allowing for the remaining hydroxyls ($C_{2\text{-}4}$) to be benzyl protected. The C_1 hydroxyl was selectively deprotected under acidic conditions, and subsequent oxidized using Albright-Goldman conditions[23] yielded 2,3,4-tri-*O*-(benzyl)-D-xylonolactone (**4.09 (i)**). The generated xylonolactone (**4.09 (i)**) was reacted with the desired aniline in acetic acid at 100 °C for one hour, yielding the 2,3,4 tri-*O*-benzyl protected xylonamide intermediate, which following deprotection (hydrogenation) yielded the desired *N*-aryl xylonaimde (**Scheme 4.4**).

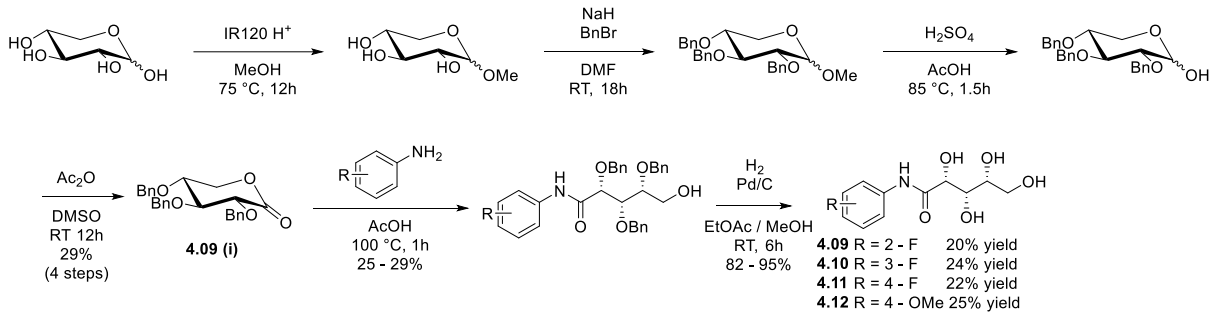

Scheme 4.4 Synthesis of *N*-aryl xylonamides from D-xylose utilizing chemical methodology adapted from literature.[24–26] Yield indicated for each derivative (**4.09** – **4.12**) are calculated starting from D-xylonolactone (**4.09 (i)**) intermediate (2 – steps).

4.3.1.3 Synthesis of 3-hydroxyl containing *N*-aryl threonaimide derivatives (4.13 – 4.16)

L-Threonamide derivatives (**4.13** – **4.16**) (**Scheme 4.5**) were synthesized starting from calcium-L-threonate, which under acidic conditions yielded 2 equivalents of L-threonolactone. The L-threonolactone was then be reacted with the corresponding aniline of choice in 100 °C acetic acid for one hour, to yield the corresponding *N*-aryl threonaomide.

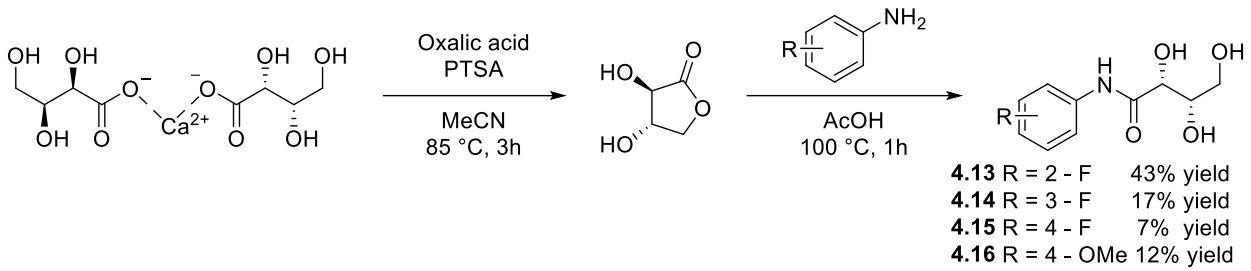

Scheme 4.5. Synthesis of *N*-aryl threonamide derivatives from calcium-L-threonate, utilizing a literature procedure for the generation of L-Threonolactone.[27]

4.3.1.4 Synthesis of *N*-aryl propenamide (4.17), *N*-aryl acetamide (4.18 – 4.25) derivatives

Synthesis of 2,3-dihydroxy-*N*-aryl-propanamides (**4.17**) involved the coupling of acryloyl chloride with the aniline of choice under basic conditions. The corresponding propenamide can then be obtained following a Sharpless asymmetric dihydroxylation,[28] utilizing AD-mix α under basic conditions. It was noted that under Sharpless conditions, the presence of an aryl fluorine was not tolerated, resulting in no reaction for *ortho*-, *meta*-, and *para*- fluorinated derivatives. *para*-Methoxy derivative **4.17** was tolerated, albeit in a poor yield (2% overall), generating the desired dihydroxy-propanamide (**4.17**). *N*-aryl-2-hydroxy-acetamides (**4.18** – **4.21**) were synthesized in one step by heating glycolic acid with the aniline of choice at 130 °C for 3 hours. Each aniline was acetylated with acetic anhydride (51 – 86%) to yield the corresponding *N*-aryl acetanilide (**4.21** – **4.25**).

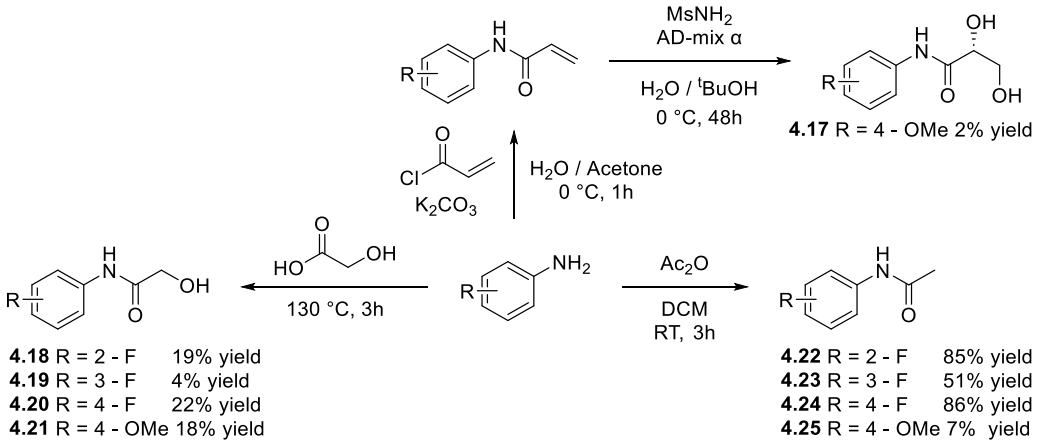

Scheme 4.6. Synthesis of *N*-aryl propenamide, *N*-functionalized anilide, and *N*-aryl acetamide derivatives from the corresponding functionalized aniline. All reaction steps are adapted from similar literature procedures.[29–31]

4.3.2 Assessing the IRI activity of *N*-(fluorophenyl) gluconamide (4.01 – 4.03) and *N*-(4-methoxyphenyl) gluconamide (4.04) derivatives

When assessing 2-Fluoro derivatives by the SCA, a large loss in IRI activity was observed with the first modification (**4.01** to **4.09**) through the relative removal of the C_6 hydroxyl (**Figure 4.7**). This loss of activity could indicate that either no modification is tolerated on the carbohydrate chain, or that the C_6 position is vital for IRI activity. A loss of activity was expected through the removal of C_6,[17,18] although the activity being lowered almost an order of magnitude was not expected. Subsequent modification to compound **4.13** (through the relative removal of the C_5-OH) resulted in another relative loss in activity (~ 2x). Due to a large loss in activity upon the first two modifications, minimal structural activity relationship information can be extracted from subsequent derivatives of **4.01**. It can be noted that for all derivatives of **4.01**, the maximum aqueous solubility was relatively improved.

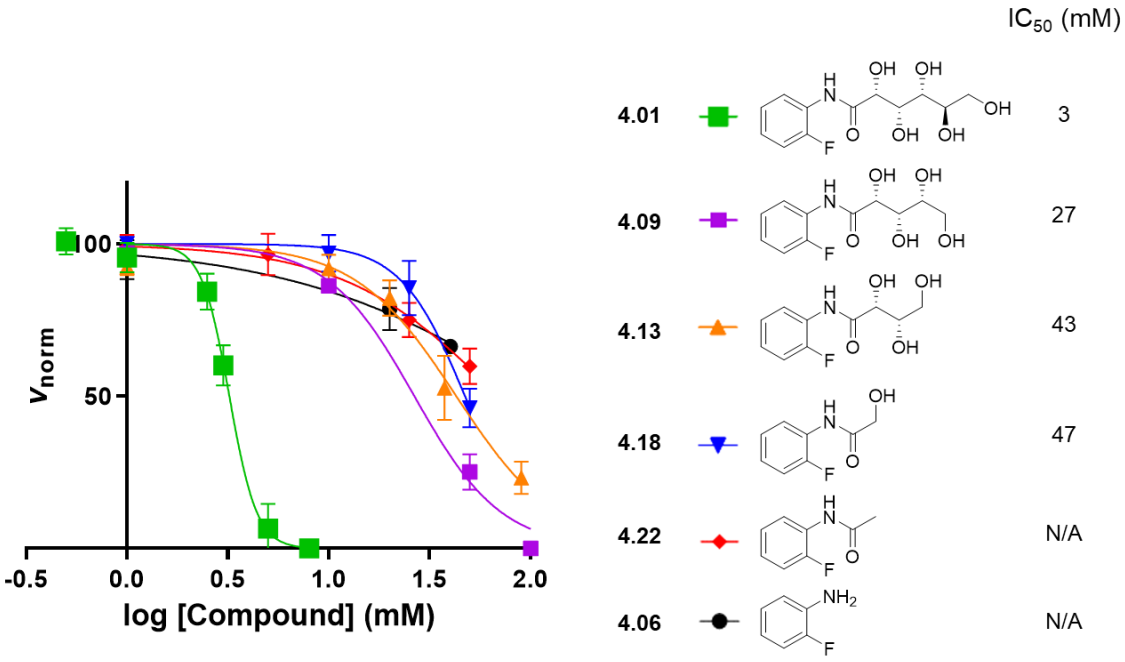

Figure 4.7 Truncated derivatives of IRI **4.01** and the four-parameter dose response curve for each compound. IC_{50} values were obtained on the modified SCA, compounds indicated with an IC_{50} value of N/A failed to achieve a relative rate of ice crystal growth below 50% before becoming solubility limited. All compounds were assessed up to the measured aqueous solubility limit in PBS at room temperature.

As observed with 2-Fluoro derivatives (**Figure 4.3.1.1**), the first 3-Fluoro derivative assessed (**4.10**) resulted in a large loss in IRI activity, and an increase in maximum aqueous solubility (**Figure 4.8**). All 3-Fluoro derivatives yield similar IRI activity and maximum aqueous solubility,

this made it difficult to draw any conclusions from modifications beyond the C_6 hydroxyl. This reinforces the hypothesis that either no modification will be tolerated to the carbohydrate chain, or the C_6 hydroxyl is essential for IRI activity.

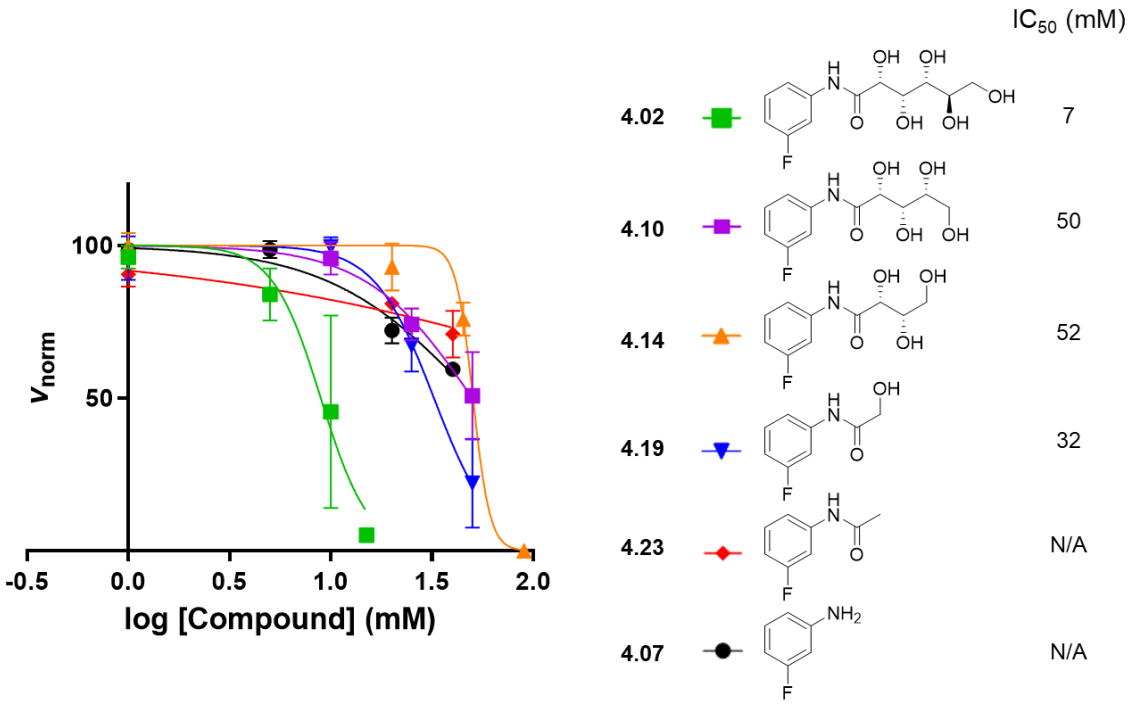

Figure 4.8 Truncated derivatives of IRI **4.02** and the four-parameter dose response curve for each compound. IC_{50} values were obtained on the modified SCA, compounds indicated with an IC_{50} value of N/A failed to achieve a relative rate of ice crystal growth below 50% before becoming solubility limited. All compounds were assessed up to the measured aqueous solubility limit in PBS at room temperature.

As compound **4.03** is not IRI active, it was expected that no 4-Fluoro derivative would be measurably IRI active. Due to the increased aqueous solubility of generated 4-Fluoro derivatives, compound **4.11** was able to reach a normalized rate of ice crystal growth of 50% (**Figure 4.9**); despite being measurable, this is a function of solvation capacity opposed to an increased IRI activity and does not convey structural information. From all fluorinated *N*-aryl gluconamides assessed (**4.01** – **4.03**), it is clear that truncation of the carbohydrate chain will not result in an increase in IRI activity. However, truncation of the gluconamide chain will result in an increase in maximum aqueous solubility with respect to the *N*-aryl gluconamide.

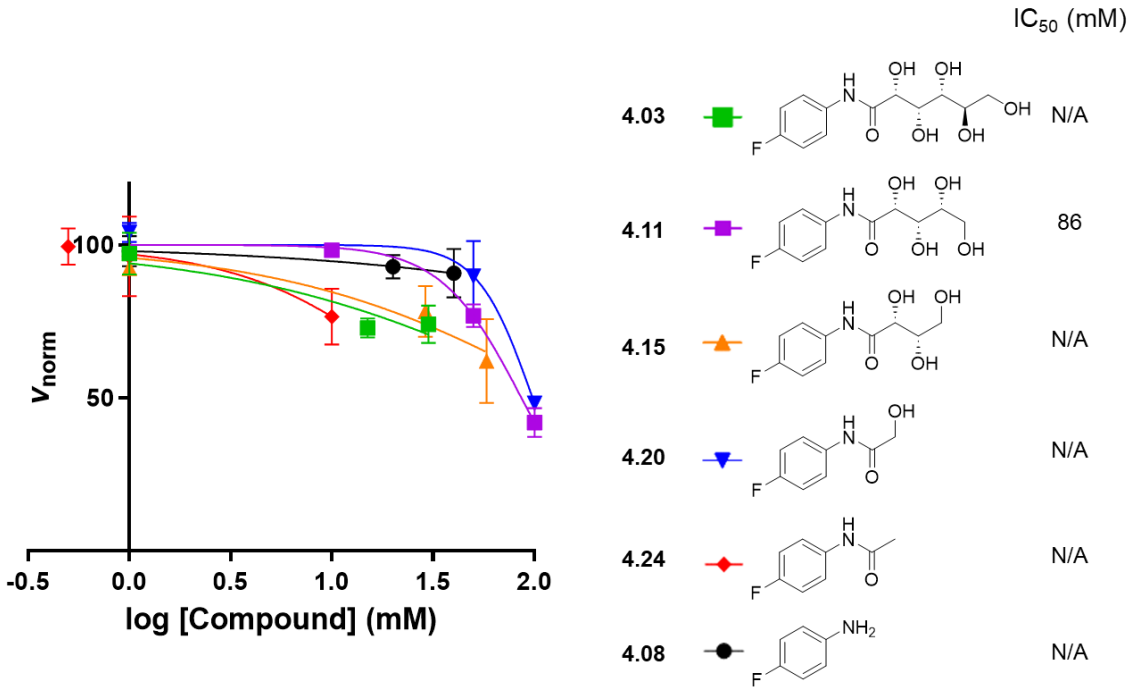

Figure 4.9 Truncated derivatives of IRI **4.03** and the four-parameter dose response curve for each compound. IC_{50} values were obtained on the modified SCA, compounds indicated with an IC_{50} value of N/A failed to achieve a relative rate of ice crystal growth below 50% before becoming solubility limited. All compounds were assessed up to the measured aqueous solubility limit in PBS at room temperature.

The IRI activity of 4-Methoxy derived molecules (**Figure 4.10**) does not resemble the assessment of 2-Fluoro derivatives (**Figure 4.7**); with measured IRI activity changing inconsistently. Notably, the L-threonamide derivative **4.16** represents the lowest activity and maximum aqueous solubility measured of any 4-Methoxy derivative assessed. This is surprising as the subsequent truncation (relative removal of the C_4 hydroxyl to generate compound **4.17**) improved IRI activity; this trend was not observed with any previous derivatives**.** The inactivity of compound **4.16** could suggest that the C_4 position of **4.04** is a target position for modification, as the relative removal of C_4 (generating **4.17**) yielded a more soluble and IRI active fragment. It is also notable that all other 4-Methoxy derivatives possessed measurable IRI activity, emphasizing the difference in assessment of *N*-aryl gluconamides bearing differing aryl substitution.

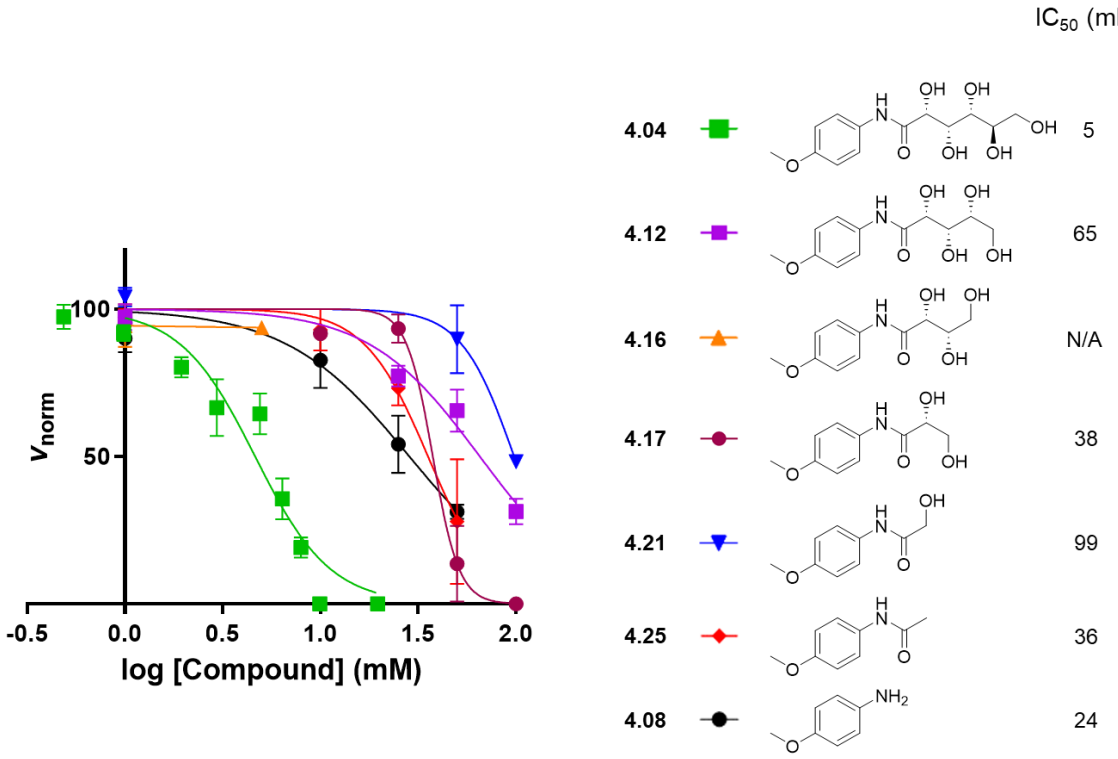

Figure 4.10 Truncated derivatives of IRI **4.04** and the four-parameter dose response curve for each compound. IC_{50} values were obtained on the modified SCA, compounds indicated with an IC_{50} value of N/A failed to achieve a relative rate of ice crystal growth below 50% before becoming solubility limited. All compounds were assessed up to the measured aqueous solubility limit in PBS at room temperature.

4.4 Assessing the functional importance of hydroxyl groups for *N*-aryl gluconamide IRIs

4.4.1 The C_4 hydroxyl

As the truncation screen employed cumulative modifications (all with the C_6 position modified), a more targeted approach is required to verify positional importance, retaining as much of the parent IRI active molecule as possible. As compound **4.16** showed a notable decrease in aqueous solubility and IRI activity (**Scheme 4.3.2.4**), the selective removal of the C_4 hydroxyl was chosen as the first targeted modification to explore for compound **4.04**. As *N*-(2-fluorophenyl)-(R)-2,3-dihydroxy-propanamide was not synthesized, the relative positional importance of C_4 was not known for **4.01**. It has been noted that 2-Fluoro and 4-Methoxy derivatives react differently to modification, for completeness, the 2-Fluoro derivative (**4.26**) was also generated.

A general synthetic pathway was devised (**Scheme 4.4.1**) to synthesize *N*-functionalized C_4-deoxy gluconamide derivatives. Starting from α-methyl-D-glucopyranoside, the C_4 and C_6 hydroxyls were benzylidene acetal protected. The C_2 and C_3 hydroxyls were subsequently benzyl

protected. The benzylidene acetal was selectively deprotected at the C_4 position through the use of iodine and sodium cyanoborohydride.[32] The C_4 hydroxyl was then activated with triflic anhydride, allowing for subsequent reduction with sodium borohydride, yielding a C_4 deoxy protected glucopyranoside (**4.26 (iv)**). The C_1 position was then deprotected under acidic conditions, allowing for subsequent oxidation under Albright-Goldman conditions to generate 2,3,6-tri-*O*-(benzyl)-4-(deoxy)-δ-gluconolactone. Installation of the chosen aniline in acetic acid at 100 °C for one hour yielded the corresponding *N*-(aryl)-2,3,6-tri-*O*-(benzyl)-gluconamide, which was deprotected through hydrogenation, yielding the corresponding *N*-(aryl)-C_4-(deoxy)-D-gluconamide (**4.26**, **4.27**) (1% overall yield).

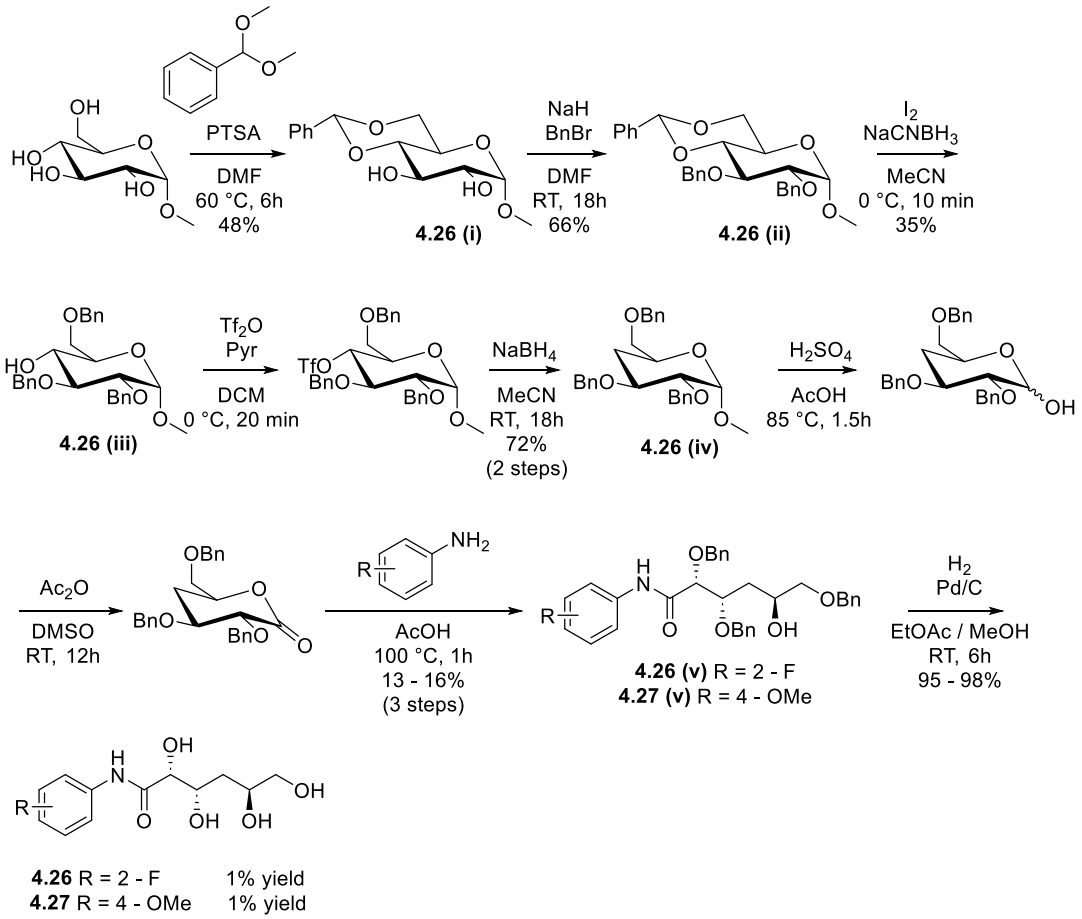

Scheme 4.7 Synthesis of C_4-deoxy-*N*-aryl gluconamide derivatives from α-methyl-D-glucopyranoside. Reaction yields are noted for each purified step, overall yield for each derivative is denoted beside the compound listing. All steps are adapted from literature examples on exact or similar substrates.[33–35]

Due to the loss in activity resulting from the addition of C_4 in **4.16** with respect to **4.17**, it was expected that the selective removal of the C_4 hydroxyl of **4.04** would result in a minimal change

in IRI activity. Unexpectedly, for the *p*-methoxy derivative (**4.27**), this targeted modification resulted in complete loss of IRI activity and a small increase in aqueous solubility with respect to **4.04** (**Scheme 4.7**). In contrast to **4.27**, compound **4.26** retained measurable IRI activity while also imparting an order of magnitude increase in aqueous solubility (**Scheme 4.7**). Compound **4.26** presents the first instance in this work of an *N*-aryl gluconamide analogue that is a viable candidate for biological testing; as the first derivative produced to retain comparable IRI activity to a traditional *N*-aryl gluconamide, compound **4.26** was of particular interest.

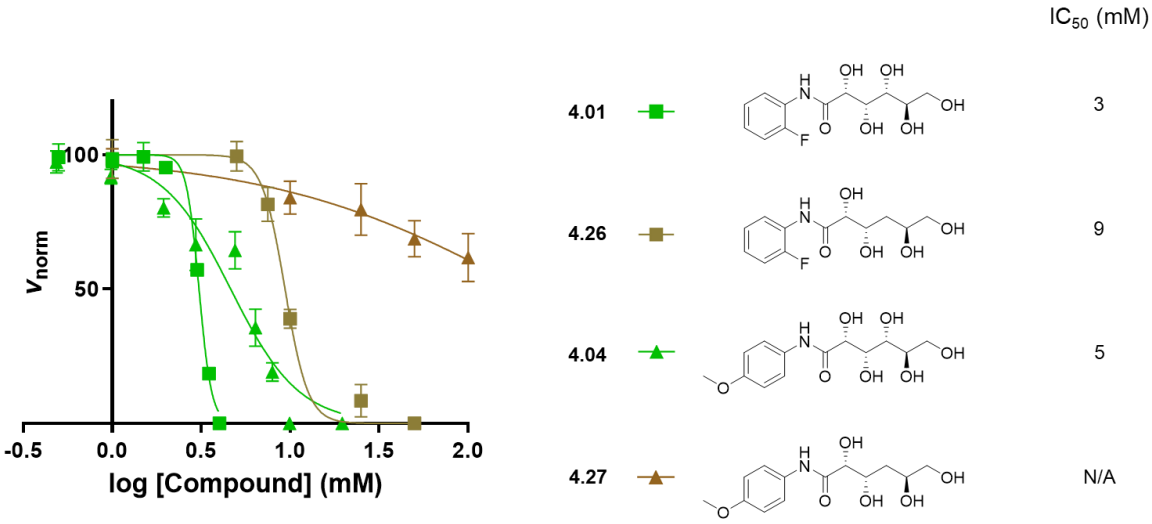

Figure 4.11 The four-parameter dose response curve for C_4-deoxy-*N*-aryl gluconamide derivatives of IRIs **4.01** and **4.04**. IC_{50} values were obtained on the modified SCA, compounds indicated with an IC_{50} value of N/A failed to achieve a relative rate of ice crystal growth below 50% before becoming solubility limited. All compounds were tested up to the measured aqueous solubility limit in PBS at room temperature.

The assessment of **4.26** indicates that **4.01** and **4.04** rely on structurally distinct components to function as an IRI, and that findings from one derivative can not reliably be extended to another. This then implies that the aryl functionality present for a given *N*-aryl gluconamide has a direct impact on the relative importance of the carbohydrate functionality present on the molecule. As **4.01** and **4.04** proved to be distinct, a focus was placed on the investigation of **4.01** as it has shown more success in biological applications.[1,3,4,7]

4.4.2 The C_6 hydroxyl

From all IRI active derivatives, a large decrease in IRI activity was observed when the C_6 hydroxyl was removed. For **4.01** specifically, there was also a subsequent decrease in activity measured through the relative removal of C_5 (**4.29**). However, as the synthesis of a C_5-deoxy

derivative would require synthetic modification to be performed on an open-chain gluconamide intermediate, an alterative strategy was devised. Synthetic modifications attempted by Dr. Anna Ampaw on a partially protected gluconamides suffered from protection group migration,[21] greatly increasing the synthetic difficulty. Rather than targeted dehydroxylation, hydroxyhexylamide derivatives were generated (**Scheme 4.8**). The generation of compounds **4.28** and **4.29** was achieved in one or two steps (respectively). This approach may be more synthetically accessible, but was reliant on the hydroxyhexylamide derivatives to retain measurable IRI activity to provide information on the structural components required for IRI activity.

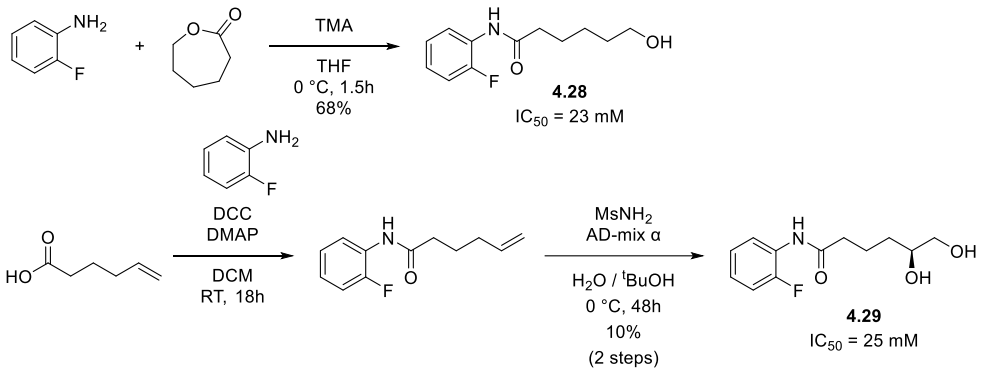

Scheme 4.8 Synthesis of *N*-(2-fluorophenyl)-(di)hydroxyhexylamide derivatives **4.28** and **4.29**. All steps are adapted from literature examples on exact or similar substrates.[36,37]

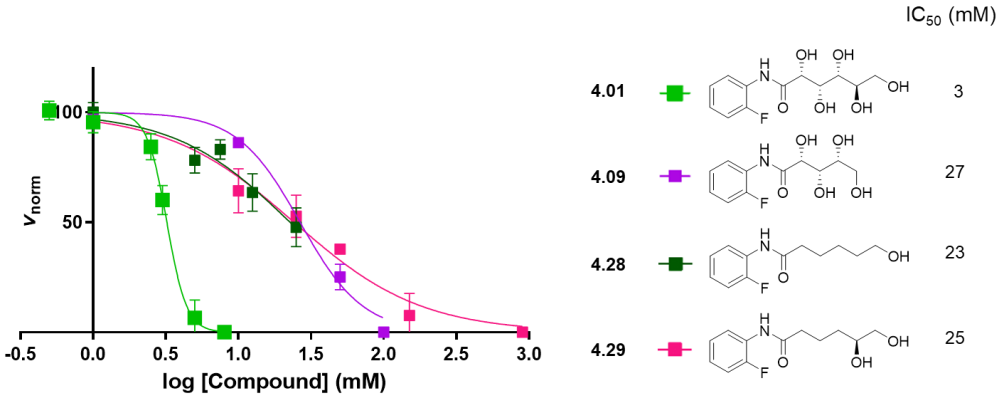

Figure 4.12 The four-parameter dose response curve for hydroxyhexylamide derivatives of **4.01**. IC_{50} values were obtained on the modified SCA. All compounds were tested up to the measured aqueous solubility limit in PBS at room temperature.

Both hydroxyhexylamide derivatives **4.28** and **4.29** possessed comparable IRI activity to **4.09** (**Figure 4.12**), while removing 3 and 2 hydroxyls respectively. Despite not being as IRI active as **4.01**, compound **4.28** retained measurable IRI activity with only the C_6 hydroxyl present. With no change in IRI activity through the relative addition of C_5-OH (**4.28** to **4.29**), it can be determined

the C_6 hydroxyl is providing the measured activity for compound **4.29**, and the C_5 hydroxyl can be identified as a potential position for modification. To better understand the role of the C_6 hydroxyl in IRI activity, the subsequent series of model compounds (**4.30** - **4.35**) were synthesized (**Scheme 4.9**).

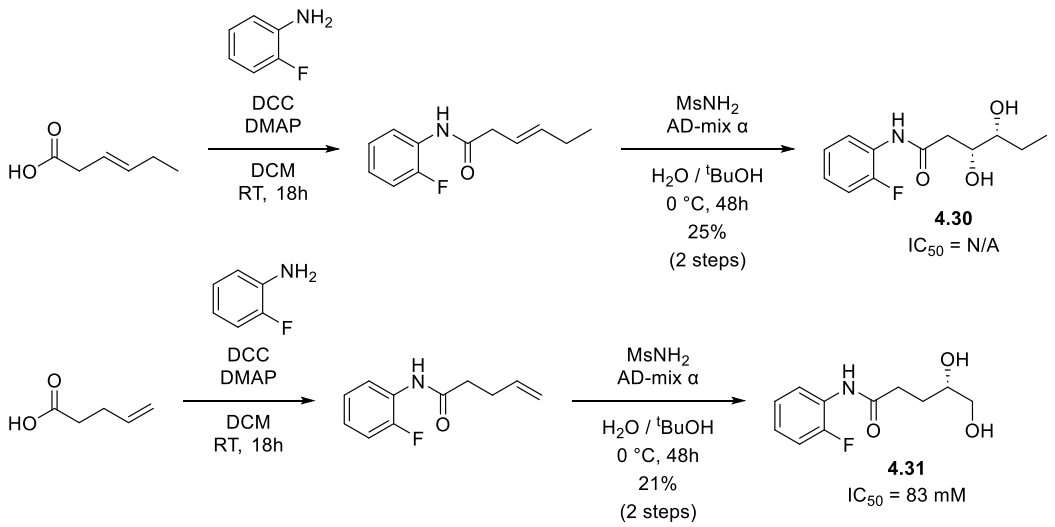

Scheme 4.9 Synthesis of 3,4-dihydroxyhexylamide (**4.30**) and 4,5-dihydroxypentamide derivatives utilizing the same synthetic pathway as outlined for **4.29** (**Scheme 4.8**). Yields for each purified reaction are listed below the reaction arrow, and IRI activity for each derivative as determined by the modified SCA is indicated below the compound identification number.

To verify the position importance, opposed to reliance solely on the number of hydroxyl groups present, compounds **4.30** and **4.31** were generated (**Scheme 4.9**) through the same synthetic process as **4.29** (**Scheme 4.8**). As the constitutional isomer of **4.29**, the IRI inactivity of compound **4.30** demonstrates the importance of a hydroxyl being present specifically at the terminal C_6 position. Similarly, compound **4.31** confirms the positional requirement is not purely terminal, but that the hydroxyl must specifically be 5 atoms away from the amide carbonyl at the C_6 position.

As the mechanism of IRI activity is thought to involve direct interaction with bulk water moleucles,[14] it is likely that the positional importance of the C_6 hydroxyl is due to the presence of a hydrogen bond donor or acceptor interaction at the specific position, or in a specific conformation. To examine the requirement of a hydrogen bond donor being present at the C_6 position, compounds **4.32** and **4.33** were generated from the alkylation (using iodomethane or 2,2-dimethoxypropane) of compounds **4.28** and **4.29** respectively (**Scheme 4.10**).

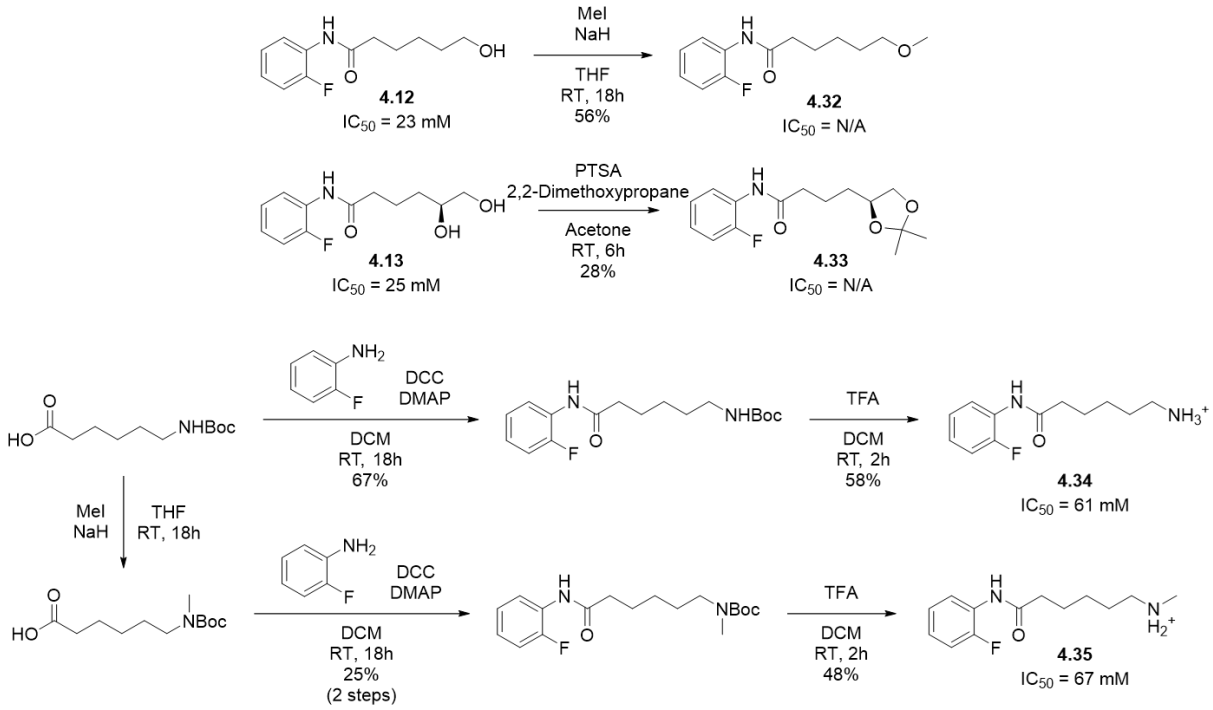

Scheme 4.10 Synthesis of terminally modified *N*-(2-flurophenyl)-hydroxyhexylamide derivatives. Yields for each purified reaction are listed below the reaction arrow, and IRI activity for each derivative as determined by the modified SCA is indicated below the compound identification number. All steps are adapted from literature examples on exact or similar substrates.[38–40]

Both terminally alkylated derivatives (**4.32**, **4.33**), result in a complete loss of IRI activity (**Scheme 4.10**). The inactivity of compound **4.32** strongly suggests the requirement of the C_6 hydroxyl to act as a hydrogen bond donor. It is worth noting that the maximum aqueous solubility of compound **4.33** dramatically reduced (15 mM) with respect to **4.29** (900 mM) but was found to be equivalent to **4.32** (15 mM). It would be expected that an increase in steric bulk and rigidity would decrease aqueous solubility, however it appears the decrease in solubility is due to the alkylation of the C_6 hydroxyl. To assess the requirement of the C_6 hydroxyl to act as a hydrogen bond acceptor, the terminal hydroxyl is replaced with a terminal ammonium (**4.34**). As the primary ammonium generated will be a worse hydrogen bond donor than the primary alcohol present in compound **4.28**, secondary ammonium **4.35** was also generated for direct comparison to **4.34** (**Scheme 4.10**). As both ammonium species are tested in pH buffered PBS (pH = 7.4), both species will carry a formal positive charge. The introduction of a cation at the C_6 position greatly increases the maximum aqueous solubility (750 mM and 200 mM when compared to respective hydroxyl species (25 mM)), but may alter the amphiphilicity, and consequentially the IRI activity. A full dose response curve and IC_{50} value was able to be generated for both charged ammonium derivatives (**Scheme 4.10**), however the activity of these species was lower than reference

hydroxyl species **4.28**. This decrease in activity is hypothesized to be due to either the inability of the charged amine species to act as a hydrogen bond acceptor, or the installation of a cation at the C_6 position. As the IRI activity of **4.35** was not improved with respect to **4.34**, it suggests that the modulation of hydrogen bond donation ability is overshadowed by either the loss of a C_6 hydrogen bond acceptor, or the introduction of a formal charge.

The model compounds generated (**Schemes 4.8** – **4.10**) establish the requirement of hydrogen bonding interactions to occur at the C_6 position for IRI activity. The ability to donate (**4.32**, **4.33**), and accept a hydrogen bond (**4.34**, **4.35**) is required for IRI activity. It is generally assumed that these hydrogen bonding interactions are occurring with bulk water, due to its large proportion relative to other molecules, however this is not directly assessed. There is also the possibility that the required hydrogen bonding interactions could be with other IRI molecules, the salts present in PBS / media solution or intramolecular. A deeper exploration of intramolecular hydrogen bonding interactions is performed in **Chapter 5** of this thesis.

4.4.3 Poly-dehydroxylation to improve aqueous solubility

Through the generation of various derivatives of **4.01**, it has been noted that every derivative of **4.01** possessed an improved aqueous solubility relative to **4.01**. This trend was highlighted by compound **4.29** which increased the aqueous solubility of **4.01** from 8 mM to approximately 900 mM through the relative removal of the C_2, C_3 and C_4 hydroxyls. Two possible explanations are posited for this observation which are not mutually exclusive; as the polyol chain present on gluconamide IRIs is more rigid than the corresponding alkyl chain, the removal of hydroxyls may allow for a conformation which is more conducive for solvation. It could also be considered that intramolecular hydrogen bonding interactions along the polyol chain outcompete interactions with bulk water, and result in less interaction with bulk water molecules. These interactions may be interrupted following the removal of a hydroxyl. An investigation as to the potential source of this phenomena is performed in **Section 5.4** of this thesis. Regardless of mechanism, this phenomena can be harnessed to modify traditionally IRI active, but aqueous solubility limited compounds (such as *N*-(octyl)-D-gluconamide) in an attempt to access a reservoir of next generation IRIs (**Chapter 5**).

4.5 Conclusions

Sections 4.2 and **4.3** attempted to examine small molecule *N*-aryl gluconamide IRIs through incremental truncation. The separation of hydrophobic aniline from hydrophilic carbohydrate (**Section 4.2**) failed to correlate the IRI activity of a given aniline to the corresponding *N*-aryl

gluconamide. The measured IRI activity of compound **4.08** provided an indication that aryl substitution may have an impact on the overall structural requirements for IRI activity in *N*-aryl gluconamides. **Section 4.3** of this chapter highlighted the importance of the C_6 hydroxyl, but following removal of the C_6 hydroxyl, IRI activity was generally not sufficient to discern meaningful information for subsequent modifications. It was further established (**Section 4.3.2**) and reinforced (**Section 4.4.1**) that differences in the *N*-aryl functionality result in differences in positional importance across the carbohydrate chain. Whereby the modification of active fluorinated *N*-aryl gluconamides (**4.01**, **4.02**) yielded similar results (**Scheme 4.3.2.1** – **4.3.2.2**), but the active *p*-methoxy derivative **4.04** did not result in any clear trend with respect to positional importance examined through truncation (**Scheme 4.3.2.4**).

To assess positional importance while maintaining the C_6 hydroxyl, the C_4 hydroxyl was identified for targeted removal due to the inactivity of compound **4.16**. The C_4 position was also selected due to the relative ease of selective dehydroxylation. **Section 4.4.1** examined the result of generated C_4-deoxy-*N*-aryl gluconamides **4.26** and **4.27**. As previously noted, it was found that differences in aryl functionality have a direct impact on the tolerance to modification. Compound **4.26** presented the first *N*-aryl gluconamide derivative with IRI activity similar to the parent compound (**4.01**), while compound **4.27** was not measurably IRI active. Following identification, the application of compound **4.26** as a next generation CPA has been performed (by other researchers) outside the scope of the work presented in this thesis; this includes characterization of physical properties and *ex vivo* assessment for the cryopreservation of biological material.

With a direct focus on compound **4.01** and the understanding that the C_6 hydroxyl is of vital importance, section **4.4.2** aimed to examine the C_6 position of **4.01**. As the positional importance of C_2, C_3 and C_5 hydroxyl for **4.01** was not clear, compound **4.28** was synthesized, with only a hydroxyl at the C_6 position. As compound **4.28** was found to have measurable IRI activity, it can serve as a starting point for the synthetic exploration of 6-hydroxyhexylamide derivatives. The relative introduction of a C_5 hydroxyl to **4.28** with the generation of **4.29** results in no change in IRI activity, indicating that the C_5 position may not be one of importance, and could be a target site of modification. To assess the positional importance of hydroxyls on compound **4.29**, compounds **4.30** and **4.31** were generated; keeping the number of hydroxyls consistent, by either shifting the diol away from the terminal position (**4.30**) or reducing the number of carbons present between the diol and amide (**4.31**). It was established that the position of the C_6 hydroxyl specifically was the important component of the IRI activity present in compounds **4.28** and **4.29**.

This importance is likely due to the C_6 hydroxyl to act as both a hydrogen bond donor (inactivity of compounds **4.32**, **4.33**) and acceptor (inactivity of compounds **4.34**, **4.35**).

Section **4.4.3** summarizes findings made throughout the chapter with respect to an unexpected increase in aqueous solubility through the relative removal of hydroxyls. It would be assumed that small molecule carbohydrates possessing a larger number of hydroxyls (which in turn have a higher number of hydrogen bond acceptors and donors), would possess the highest relative aqueous solubility. With a baseline aqueous solubility of 8 mM for compound **4.01** in PBS, every generated derivative of **4.01** possessed a higher aqueous solubility, regardless of modification. This observation was highlighted with the generation of compound **4.29** which was observed to have a maximum aqueous solubility of 900 mM in PBS. This phenomenon only applied with respect to the parent gluconamide **4.01** and can not be directly due to the relative removal of a hydroxyl, as observed with compound **4.28** possessing an aqueous solubility 36x lower than **4.29**. The source of this increase in aqueous solubility is not examined directly in this chapter but serves as inspiration for the investigation of poorly soluble *N*-alkyl gluconamides in **chapter 5**.

4.6 References

(1) Briard, J. G.; Jahan, S.; Chandran, P.; Allan, D.; Pineault, N.; Ben, R. N. Small-Molecule Ice Recrystallization Inhibitors Improve the Post-Thaw Function of Hematopoietic Stem and Progenitor Cells. *ACS Omega* **2016**, *1* (5), 1010–1018. https://doi.org/10.1021/acsomega.6b00178.

(2) Poisson, J. S.; Acker, J. P.; Briard, J. G.; Meyer, J. E.; Ben, R. N. Modulating Intracellular Ice Growth with Cell-Permeating Small-Molecule Ice Recrystallization Inhibitors. *Langmuir* **2019**, *35* (23), 7452–7458. https://doi.org/10.1021/acs.langmuir.8b02126.

(3) Jahan, S.; Adam, M. K.; Manesia, J. K.; Doxtator, E.; Ben, R. N.; Pineault, N. Inhibition of Ice Recrystallization during Cryopreservation of Cord Blood Grafts Improves Platelet Engraftment. *Transfusion (Paris)* **2020**, *60* (4), 769–778. https://doi.org/10.1111/trf.15759.

(4) Alasmar, S.; Huang, J.; Chopra, K.; Baumann, E.; Aylsworth, A.; Hewitt, M.; Sandhu, J. K.; Tauskela, J. S.; Ben, R. N.; Jezierski, A. Improved Cryopreservation of Human Induced Pluripotent Stem Cell (iPSC) and iPSC-Derived Neurons Using Ice-Recrystallization Inhibitors. *Stem Cells* **2023**, *41* (11), 1006–1021. https://doi.org/10.1093/stmcls/sxad059.

(5) Khan, S.; Poisson, J.; Davila, L.; Ben, R. N.; Courtman, D. W. Small-Molecule Ice Recrystallization Inhibitors Improve Post-Thaw Recovery of Mesenchymal Stromal Cells. *Cytotherapy* **2019**, *21* (5, Supplement), S76. https://doi.org/10.1016/j.jcyt.2019.03.477.

(6) Capicciotti, C. J.; Kurach, J. D. R.; Turner, T. R.; Mancini, R. S.; Acker, J. P.; Ben, R. N. Small Molecule Ice Recrystallization Inhibitors Enable Freezing of Human Red Blood Cells with Reduced Glycerol Concentrations. *Sci. Rep.* **2015**, *5* (1), 9692. https://doi.org/10.1038/srep09692.

(7) Waters, L.; Ben, R.; Acker, J. P.; Padula, M. P.; Marks, D. C.; Johnson, L. Characterizing the Ability of an Ice Recrystallization Inhibitor to Improve Platelet Cryopreservation. *Cryobiology* **2020**, *96*, 152–158. https://doi.org/10.1016/j.cryobiol.2020.07.003.

(8) Adam, M. K. Improving the Engraftment Activities of Cryopreserved Human Umbilical Cord Blood Through the Development of Novel Glyco(Peptide)-Based Aryl Ice Recrystallization Inhibitors, Univerity of Ottawa, 2020. http://dx.doi.org/10.20381/ruor-25034.
(9) Knight, C. A.; Hallett, J.; DeVries, A. L. Solute Effects on Ice Recrystallization: An Assessment Technique. *Cryobiology* **1988**, *25* (1), 55–60. https://doi.org/10.1016/0011-2240(88)90020-X.
(10) Tam, R. Y.; Ferreira, S. S.; Czechura, P.; Chaytor, J. L.; Ben, R. N. Hydration Index—A Better Parameter for Explaining Small Molecule Hydration in Inhibition of Ice Recrystallization. *J. Am. Chem. Soc.* **2008**, *130* (51), 17494–17501. https://doi.org/10.1021/ja806284x.
(11) Abraham, S. Development and Implementation of a Kinetic Quantitative Analysis of Novel Small Molecule Ice Recrystallization Inhibitors, University of Ottawa, 2015.
(12) Czechura, P.; Tam, R. Y.; Dimitrijevic, E.; Murphy, A. V.; Ben, R. N. The Importance of Hydration for Inhibiting Ice Recrystallization with C-Linked Antifreeze Glycoproteins. *J. Am. Chem. Soc.* **2008**, *130* (10), 2928–2929. https://doi.org/10.1021/ja7103262.
(13) Capicciotti, C. J.; Leclère, M.; Perras, F. A.; Bryce, D. L.; Paulin, H.; Harden, J.; Liu, Y.; Ben, R. N. Potent Inhibition of Ice Recrystallization by Low Molecular Weight Carbohydrate-Based Surfactants and Hydrogelators. *Chem. Sci.* **2012**, *3* (5), 1408–1416. https://doi.org/10.1039/C2SC00885H.
(14) McMunn, L. E.; D'Costa, A. S.; Bordenave, N.; Ben, R. N. Probing the Mechanism of Action of Small-Molecule Ice Recrystallization Inhibitors Using Proton Nuclear Magnetic Resonance Relaxation. *J. Phys. Chem. Lett.* **2023**, *14* (26), 6043–6050. https://doi.org/10.1021/acs.jpclett.3c00845.
(15) Briard, J. G. The Rational Design and Use of Novel Small-Molecule Ice Recrystallization Inhibitors for the Cryopreservation of Hematopoietic Stem Cells and Red Blood Cells. PhD Thesis, University of Ottawa, 2016.
(16) Briard, J. G.; Fernandez, M.; De Luna, P.; Woo, Tom. K.; Ben, R. N. QSAR Accelerated Discovery of Potent Ice Recrystallization Inhibitors. *Sci. Rep.* **2016**, *6* (1), 26403. https://doi.org/10.1038/srep26403.
(17) Capicciotti, C. J. The Rational Design of Potent Ice Recrystallization Inhibitors for Use as Novel Cryoprotectants. PhD Thesis, University of Ottawa, 2014.
(18) Doshi, M. Synthesis of Nitrogen-Containing Carbohydrate Derivatives and Their Use Toward Inhibiting Ice Recrystallization and Gas Hydrate Formation. PhD Thesis, University of Ottawa, 2016.
(19) Poisson, J. S. Synthesis and In Vitro Applications of Ice Recrystallization Inhibitors, University of Ottawa, 2019.
(20) Charlton, T. A. Synthesis of Novel Charged Ice Recrystallization Inhibitors, University of Ottawa, 2021.
(21) Ampaw, A. Addressing Solubility Limitations in Small-Molecule Ice Recrystallization Inhibitors and Evaluating Their Use in Hematopoietic Stem Cell and Red Blood Cell Cryopreservation. PhD Thesis, University of Ottawa, 2022.
(22) Galema, S. A.; Hoeiland, H. Stereochemical Aspects of Hydration of Carbohydrates in Aqueous Solutions. 3. Density and Ultrasound Measurements. *J. Phys. Chem.* **1991**, *95* (13), 5321–5326. https://doi.org/10.1021/j100166a073.
(23) Albright, J. D.; Goldman, L. Dimethyl Sulfoxide-Acid Anhydride Mixtures. New Reagents for Oxidation of Alcohols1. *J. Am. Chem. Soc.* **1965**, *87* (18), 4214–4216. https://doi.org/10.1021/ja01096a055.
(24) Paradowska, K.; Gubica, T.; Temeriusz, A.; Cyrański, M. K.; Wawer, I. 13C CP MAS NMR and Crystal Structure of Methyl Glycopyranosides. *Carbohydr. Res.* **2008**, *343* (13), 2299–2307. https://doi.org/10.1016/j.carres.2008.05.015.

(25) Underlin, E. N.; Jensen, H. H. Synthesis of Nortropane Alkaloid Calystegine B2 from Methyl α-d-Xylopyranoside. *Carbohydr. Res.* **2019**, *472*, 122–126. https://doi.org/10.1016/j.carres.2018.12.002.
(26) Tejima, S.; Ness, R. K.; Kaufman, R. L.; Fletcher, H. G. Some Partially Benzylated Pentose Derivatives. *Carbohydr. Res.* **1968**, *7* (4), 485–490. https://doi.org/10.1016/S0008-6215(00)82970-5.
(27) MARIJA, P.; YI, J.; MAHESH, R.; RENEE, D.; HERMANN, L. F. NOVEL STABILIZED NUCLEOSIDE PHOSPHATES AND ANALOGUES THEREOF. WO2024062413A1, March 28, 2024.
(28) Sharpless, K. B.; Amberg, W.; Bennani, Y. L.; Crispino, G. A.; Hartung, J.; Jeong, K. S.; Kwong, H. L.; Morikawa, K.; Wang, Z. M. The Osmium-Catalyzed Asymmetric Dihydroxylation: A New Ligand Class and a Process Improvement. *J. Org. Chem.* **1992**, *57* (10), 2768–2771. https://doi.org/10.1021/jo00036a003.
(29) Hung, J. M.; Arabshahi, H. J.; Leung, E.; Reynisson, J.; Barker, D. Synthesis and Cytotoxicity of Thieno[2,3-*b*]Pyridine and Furo[2,3-*b*]Pyridine Derivatives. *Eur. J. Med. Chem.* **2014**, *86*, 420–437. https://doi.org/10.1016/j.ejmech.2014.09.001.
(30) Chanthamath, S.; Takaki, S.; Shibatomi, K.; Iwasa, S. Highly Stereoselective Cyclopropanation of α,β-Unsaturated Carbonyl Compounds with Methyl (Diazoacetoxy)Acetate Catalyzed by a Chiral Ruthenium(II) Complex. *Angew. Chem. Int. Ed.* **2013**, *52* (22), 5818–5821. https://doi.org/10.1002/anie.201300468.
(31) Bosetti, C.; Kampasis, D.; Brinch, S. A.; Galera-Prat, A.; Karelou, M.; Dhakar, S. S.; Alaviuhkola, J.; Waaler, J.; Lehtiö, L.; Kostakis, I. K. Substitutions at the C-8 Position of Quinazolin-4-Ones Improve the Potency of Nicotinamide Site Binding Tankyrase Inhibitors. *Eur. J. Med. Chem.* **2025**, *288*, 117397. https://doi.org/10.1016/j.ejmech.2025.117397.
(32) Rao, K. V.; Patil, P. R.; Atmakuri, S.; Kartha, K. P. R. Iodine–Sodium Cyanoborohydride-Mediated Reductive Ring Opening of 4,6-*O*-Benzylidene Acetals of Hexopyranosides. *Carbohydr. Res.* **2010**, *345* (18), 2709–2713. https://doi.org/10.1016/j.carres.2010.10.013.
(33) Elchert, B.; Li, J.; Wang, J.; Hui, Y.; Rai, R.; Ptak, R.; Ward, P.; Takemoto, J. Y.; Bensaci, M.; Chang, C.-W. T. Application of the Synthetic Aminosugars for Glycodiversification: Synthesis and Antimicrobial Studies of Pyranmycin. *J. Org. Chem.* **2004**, *69* (5), 1513–1523. https://doi.org/10.1021/jo035290r.
(34) Xu, W.; Springfield, S. A.; Koh, J. T. Highly Efficient Synthesis of 1-Thioglycosides in Solution and Solid Phase Using Iminophosphorane Bases. *Carbohydr. Res.* **2000**, *325* (3), 169–176. https://doi.org/10.1016/S0008-6215(99)00327-4.
(35) Spencer, R. P.; Bae Yu, H. K.; Cavallaro, C. L.; Schwartz, J. Preparation of Aldehydo Sugars and Sugar Acids via Ozonolysis of Sugar Hydrazones. *J. Org. Chem.* **1997**, *62* (13), 4507–4509. https://doi.org/10.1021/jo970067d.
(36) Bieliauskas, A. V.; Weerasinghe, S. V. W.; Pflum, M. K. H. Structural Requirements of HDAC Inhibitors: SAHA Analogs Functionalized Adjacent to the Hydroxamic Acid. *Bioorg. Med. Chem. Lett.* **2007**, *17* (8), 2216–2219. https://doi.org/10.1016/j.bmcl.2007.01.117.
(37) Jankins, T. C.; Martin-Montero, R.; Cooper, P.; Martin, R.; Engle, K. M. Low-Valent Tungsten Catalysis Enables Site-Selective Isomerization–Hydroboration of Unactivated Alkenes. *J. Am. Chem. Soc.* **2021**, *143* (37), 14981–14986. https://doi.org/10.1021/jacs.1c07162.
(38) DONG, H.; YANG, B.; PENNINGTON, L. D.; COMER, E.; FORD, M.; AVERSA, R.; WEISS, M. M.; XIAO, Z.; THIJS, B. BCL-XL/BCL-2 DEGRADERS AND USES THEREOF. WO2023220425A1, November 16, 2023.
(39) Huang, L.-J.; Chen, S.-R.; Yuan, C.-M.; Gu, W.; Guo, B.-J.; Wang, Y.-T.; Wang, Y.; Hao, X.-J. C21-Steroidal Pregnane Sapogenins and Their Derivatives as Anti-Inflammatory Agents. *Bioorg. Med. Chem.* **2017**, *25* (13), 3512–3524. https://doi.org/10.1016/j.bmc.2017.04.045.

(40) Kawabata, E.; Kikuchi, K.; Urano, Y.; Kojima, H.; Odani, A.; Nagano, T. Design and Synthesis of Zinc-Selective Chelators for Extracellular Applications. *J. Am. Chem. Soc.* **2005**, *127* (3), 818–819. https://doi.org/10.1021/ja044697q.

5. Structure Activity Relationship of *N*-Alkyl Gluconamide Carbohydrate Chain and Ice Recrystallization Inhibition (IRI) Activity

5.1 Introduction

When first examining small molecule reducing sugars for IRI activity, a direct relationship between IRI activity and the number of water molecules a given molecule can tightly bind in solution (hydration index) was established.[1,2] It was hypothesized[3] and later supported[4] that for a compound to possess IRI activity, the hydration shell must disrupt the transfer of water molecules from bulk water to the semi-ordered quasi liquid layer; this increases the energy required for water ordering into an ice-crystal lattice, limiting ice crystal growth. Surfactants disrupt the ordering of bulk water when acting as an emulsifier,[5] starting from known surfactants,[6,7] various attempts were made to analyse the balance between hydrophobicity and hydrophilicity required for IRI activity (**Figure 5.1**).[3,8] As surfactants are generally not viable for cellular applications, a surfactant-based IRI compound would need to be IRI active well below the critical micellular concentration as to minimize disruptions to cellular membranes.[9]

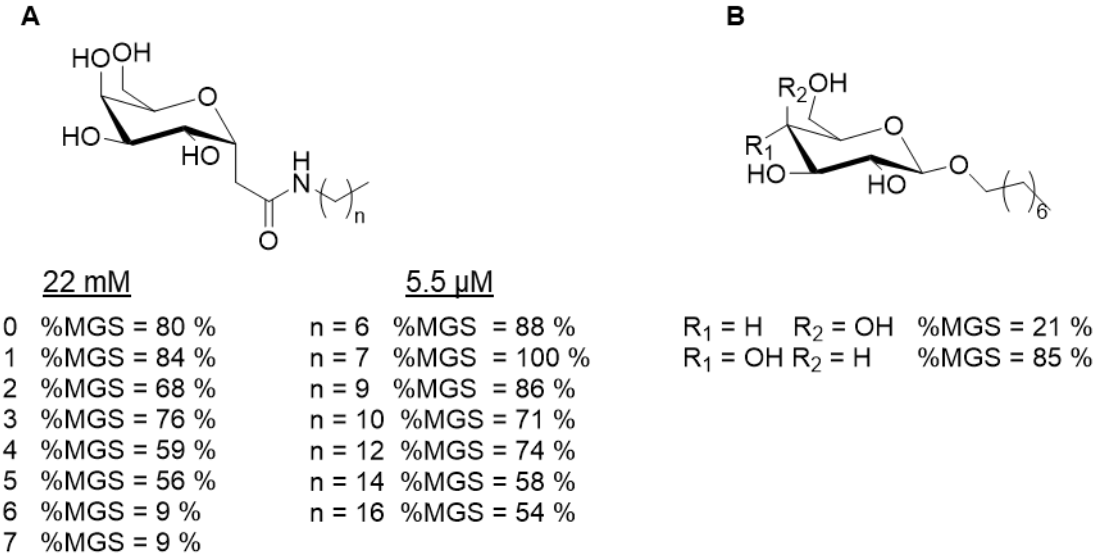

Figure 5.1 Surfactant derived IRIs tested on the original 30-minute splat cooling assay. The percent mean grain size (%MGS) is measured at 22 mM unless otherwise specified. **(A)** *N*-alkyl-2-(α-D-galactosyl)-ethylamides, assessed at either 22 mM (n = 0 – 7) or 5.5 µM (n = 6 – 16).[3] **(B)** *O*-(octyl)-β-D-pyranosides assessed for IRI activity at 22 mM.[8]

Starting from pyranose-based surfactant-derived small molecules (**Figure 5.1**), it was found that heptyl- and octyl- alkyl chains extending from the hydrophilic carbohydrate core provided adequate hydrophobicity to effectively disrupt bulk water, and subsequently provide IRI activity.[10]

Extending beyond an octyl chain resulted in a dramatic loss in aqueous solubility, not allowing for assessment at 22 mM (**Figure 5.1** (**A**)). Despite being tested at only 5.5 μM, the longest alkyl chains assessed were still able to inhibit ice recrystallization when compared to PBS. These compounds highlight the balance between the hydrophobicity required for IRI activity (to disrupt bulk water) and the hydrophilicity required to keep the compound in solution. These surfactant-derived IRIs were found to be IRI active at concentrations below the critical micelle concentration,[11] allowing for the rational use of this family of compounds in cellular applications.

Previous PhD candidates in the Ben lab, Dr. Roger Tam and Dr. Chantelle Capicciotti attempted to correlate the known hydration index of small molecule carbohydrates to the measured IRI activity.[12,13] A weak correlation ($R^2 = 0.32$) was found when examining commercial small molecule carbohydrates,[12] but an accurate measurement of the hydration index for complex synthetic carbohydrates is not readily accessible. This limits the ability to apply this method of prediction to novel small molecule IRIs. Dr. Jennie Briard (previous PhD candidate in the Ben lab) built upon these investigations, including the required balance between hydrophilic and hydrophobic components for a given molecule to possess IRI activity (**Figure 5.2**).[14] MarvinSketch™ was utilized to calculate both the polar surface area (PSA) and molecular surface area (MSA) of a given molecule, and attempts were made to correlate the ratio of PSA / MSA to the measured IRI activity.[14] In tandem, a similar analysis was performed, relating the number of carbons present in the *N*- alkylation (CH_n) to the number of hydroxyls present on a carbohydrate chain (OH) (**Figure 5.2** (**B**)).[14] This simplified CH_n / OH assessment can be completed without the need for computational software. When assessing linear *N*-alkyl gluconamide and erythronamides, a correlation was found ($R^2 > 0.8$) whereby the lower the PSA / MSA ratio, the more IRI active a compound is expected to be (**Figure 5.2** (**A**)).[14] It is notable that *N*-(hexyl)-D-gluconamide (**5.02**) was found to be a high activity outlier for this analysis, and known IRI active *N*-(octyl)-D-gluconamide (**5.04**) was omitted from this analysis due to aqueous solubility constraints.[14] From this analysis it was concluded that in general, the less polar the small molecule carbohydrate, the more IRI active it is expected to be at 22 mM. However, the most IRI active compounds (like **5.02**) require a hydrophobic component of at least 6 carbons, and a hydrophilic component of at least 4 hydroxyls.

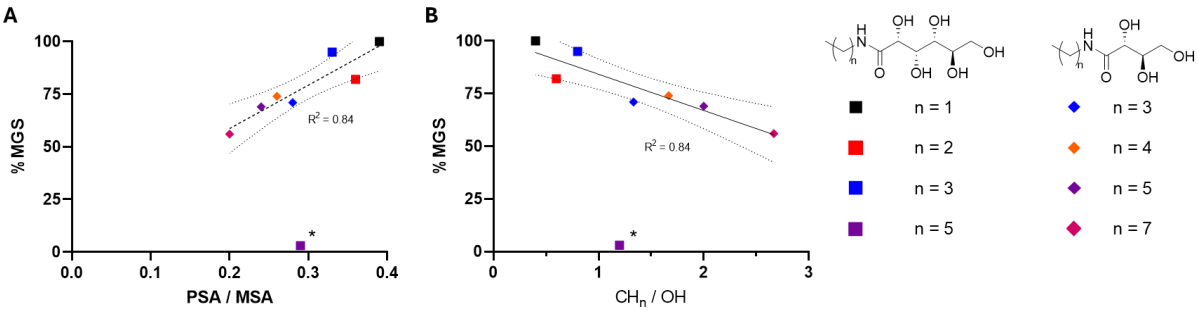

Figure 5.2 Correlation of *N*-alkyl aldonamide IRI activity (%MGS at 22 mM) and the amphiphilicity of the substrate.[14] Data points were extracted with the use of a plot digitizer from previously reported scatter plot for use of trendline generation and statistics. * *N*-hexyl-D-gluconamide was excluded from the linear regression. **(A)** Linear correlation (R^2 = 0.84) between IRI activity (%MGS) and the ratio of polar surface area to total molecular surface area (calculated by MarvinSketch™). 95 % confidence bands are indicated with dashed lines. **(B)** Linear correlation (R^2 = 0.84) between IRI activity (%MGS) and the proportion of methylene units present on the alkyl extension with respect to hydroxyls present on the carbohydrate chain. 95 % confidence bands are indicated with dashed lines.

Assessing the *N*-(cycloalkyl) aldonamides (**Figure 5.3**), no correlation (R^2 = 0.01) was found between CH_n / OH. However, a strong (R^2 = 0.98) correlation was found specifically with *N*-cycloalkyl gluconamide derivatives, whereby the larger the cycloalkyl ring, the more IRI activity was observed. For *N*-cycloalkyl arabinose derivatives, no correlation was found (R^2= 0.003), as all derivatives were similarly IRI inactive, despite alteration to alkyl ring size (**Figure 5.3**).[14] The examination of *N*-cycloalkyl gluconamides was consistent with the examination of linear *N*-alkyl gluconamides, whereby the less polar the molecule, the more IRI active it is expected to be. The broad IRI inactivity of *N*-cycloalkyl arabinose derivatives indicates that all 5 hydroxyls are required for IRI activity in *N*-alkyl gluconamides.

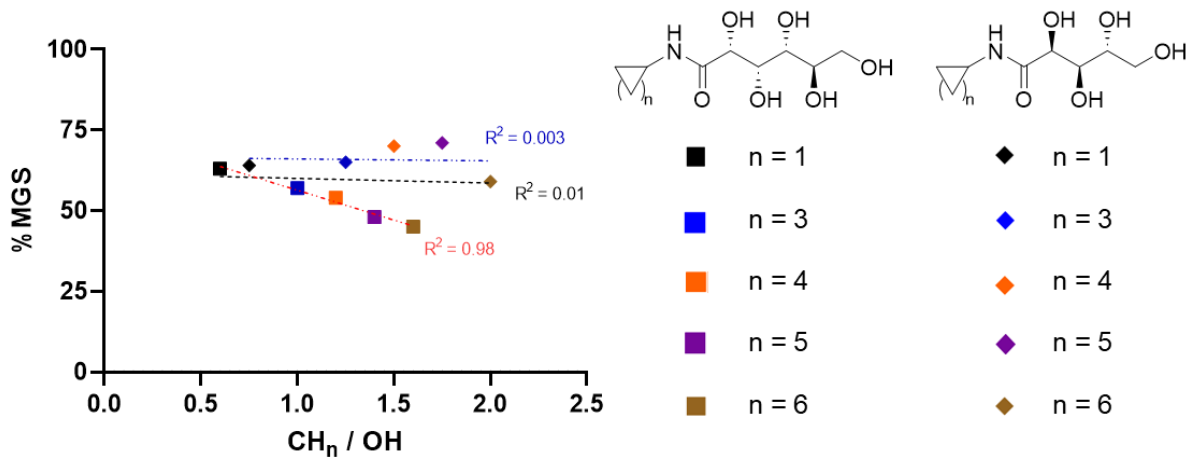

Figure 5.3 Correlation of *N*-alkyl aldonamide IRI activity (%MGS at 22 mM) against the amphiphilicity of the substrate.[14] Data points were extracted with the use of a plot digitizer from previously reported scatter plot for use of trendline generation and statistics. Linear regressions are calculated for the data set as a whole (Black trendline, R^2 = 0.01), just for *N*-cycloalkyl-D-arabinosides (Blue trendline, R^2 = 0.003), and just for *N*-cycloalkyl-D-gluconamide substrates (Red trendline, R^2 = 0.98).

N-alkyl aldonamide derivatives have been a particular focus for small molecule carbohydrate mechanistic exploration.[1,10,12,14,15] Despite this focus, and being the first class of synthetic small molecule IRIs discovered, application of this class of IRI has been limited to acellular investigations.[16] The preference against the use *N*-alkyl aldonamides is two fold: first, the potential for surfactant-like toxicity,[7,17] as the minimum micellular concentration is not known for synthetically modified derivatives. Additionally, due to the requirement of large alkyl chains, poor aqueous solubility and potential bubbling of compound in solution make *N*-alkyl aldonamides physically difficult to work with. The examination of *N*-aryl gluconamides (**Section 4.4.3**) established that the maximum aqueous solubility of a gluconamide can be increased through dehydroxylation. If this approach can be applied to *N*-alkyl gluconamides, a reservoir of next-generation IRI active small molecules may be accessible.

5.2 Assessment of small molecule *N*-alkyl gluconamide IRIs

As the assessment of *N*-alkyl derived small molecule carbohydrates has spanned two different iterations of the splat cooling assay (SCA), there is variability in the IRI assessment of key *N*-alkyl gluconamides. These compounds were first evaluated on the 30-minute SCA,[18] demonstrating unparalleled IRI activity for the time.[12,14,19] The 5-minute modified SCA has been utilized for the assessment of some linear *N*-alkyl gluconamides,[15] but no *N*-cycloalkyl gluconamides have been assessed on the 5-minute SCA. As it is difficult to reliably compare IRI activity between different

iterations of the SCA, a baseline of *N*-alkyl gluconamide IRI activity was assessed on the 5-minute modified SCA[20] prior to planning structural modifications. The commercial linear alkyl amines present in our laboratory were used to generate the corresponding *N*-alkyl gluconamides (**Figure 5.4 (A)**). Cameron Steinke (undergraduate researcher in the Ben lab) used accessible cycloalkyl amines to generate the corresponding *N*-cycloalkyl gluconamides (**Figure 5.4 (B - C)**).

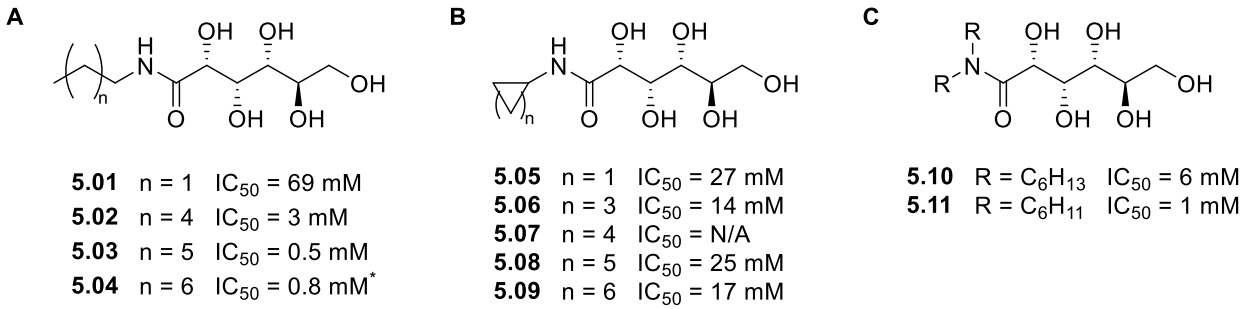

Figure 5.4 *N*-alkyl-D-gluconamide substrates assessed on the modified SCA. Compound identification number, alkyl size, and IRI activity (IC_{50} value) are indicated for each substrate. **(A)** Linear *N*-alkyl-D-gluconamides assessed for IRI activity. **(B)** *N*-cycloalkyl-D-gluconamides assessed for IRI activity. **(C)** *N,N*-dialkyl-D-gluconamides assessed for IRI activity. *The IC_{50} value of compound **5.04** is extrapolated for use as a frame of reference due to solubility limitations not allowing for a complete dose-response curve to be obtained.

The IRI assessment of linear alkyl functionalized gluconamides (**5.01** – **5.04**) reiterates the required balance of hydrophilic and hydrophobic components in small molecule carbohydrate IRIs (**Figure 5.4**). n-Hexyl-, n-heptyl- and n-octyl- functionalized derivatives (**5.02** – **5.04**) all demonstrate IRI activity comparable to model *N*-aryl gluconamide IRI **4.01** and are more IRI active than the corresponding *N*-cycloalkyl gluconamides. By contrast, *N*-propyl gluconamide (**5.01**) was found to be less IRI active than the longer alkyl chains. For linear alkyl chains there appears to be a threshold of required hydrophobicity to possess IRI activity, whereby compounds with insufficient alkyl chain length are substantially less IRI active than those with sufficient hydrophobicity. This finding matches previous assessments made on using the 30-minute SCA (**Figure 5.2**).[14] This finding is similar to previous α-*C*-linked alkyl amide derivatives (**Figure 5.1 (A)**),[3] where a roughly 6x increase in IRI activity is observed when increasing alkyl chain length from the n-hexyl- to n-heptyl- derivative, with no subsequent improvement to the n-octyl- derivative (**Figure 5.1**). Previous examinations[3] suggest that longer alkylation of linear *N*-alkyl gluconamides could uncover another threshold of improved IRI activity. However, the implementation of much longer alkyl chains would also likely be detrimental to the maximum aqueous solubility and result in more surfactant-like toxicity. For the linear alkyl gluconamides

examined, the maximum aqueous solubility was found to exponentially decay as a function of alkyl chain length (R^2 = 0.99); cycloalkyl gluconamides were also found to possess an exponential relationship between ring size and maximum aqueous solubility (R^2 = 0.98), with a plateau at approximately 30 mM (**Figure 5.5**).

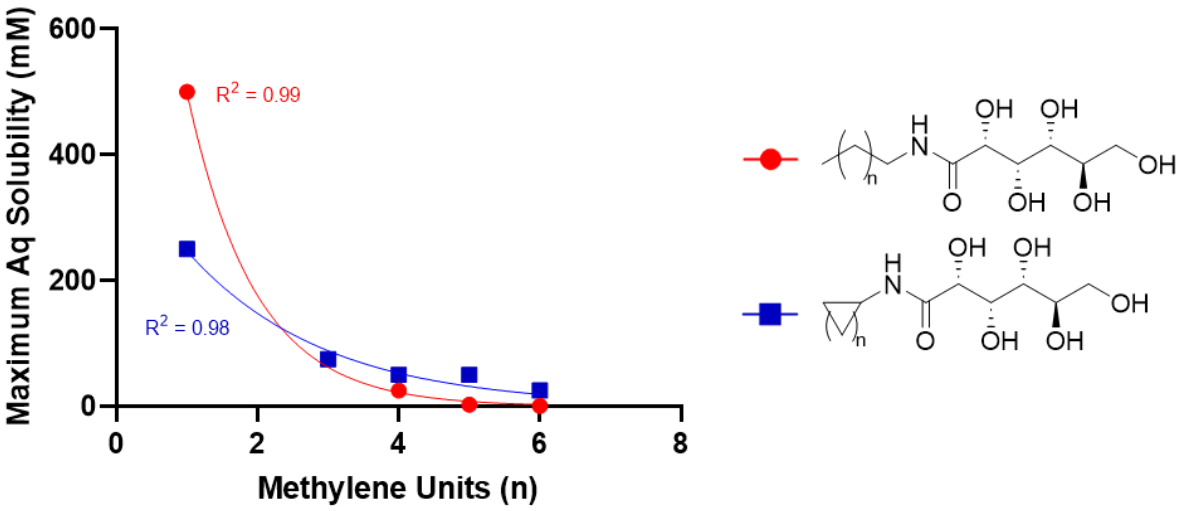

Figure 5.5 Correlation between alkyl size (n = total number of methylene units present in *N*-functionalization minus 2, as directly shown in structural representation) and apparent aqueous solubility in PBS at room temperature.

When assessing *N*-cycloalkyl gluconamides, there was no clear correlation between alkyl ring size and IRI activity (**Figure 5.4 (B)**). When compared to IRI active linear alkyl gluconamides (**5.02** – **5.04**), the corresponding cycloalkyl gluconamide derivatives (**5.07** – **5.09**) possessed at least an order of magnitude decrease in IRI activity. This assessment directly contradicts the previously reported relationship between *N*-cycloalkyl ring size and IRI activity (**Figure 5.3**).[14] This result could be attributed to the modified SCA providing a more reliable IRI analysis when compared to the original SCA iteration utilized in the Ben lab; as *N*-cycloalkyl derivatives are relatively IRI inactive, the higher resolution afforded by the modified SCA weakens the preserved relationship between *N*-cycloalkyl ring size and IRI activity. All generated cycloalkyl gluconamides possessed aqueous solubility (50 mM – 250 mM) more similar to IRI inactive *N*-propyl gluconamide (**5.01**) (500 mM) than the corresponding linear alkyl gluconamide. These findings suggest that not only is the size of the alkyl substituent of importance, but the increased degrees of rotational freedom afforded by linear alkyl substituents is influential on the activity of *N*-alkyl gluconamides.

Having established the IRI activity of *N*-alkyl gluconamide IRIs (**Figure 5.4 (A**, **B)**), the *N,N*-(dihexyl) gluconamide (**5.10**) and *N,N*-(dicyclohexyl) gluconamide (**5.11**) derivatives were synthesized (**Figure 5.4 (C)**). While keeping the hexyl motif consistent, these di-alkylated derivatives provide further insight as to the importance of both hydrophobicity and tolerance to amide alkylation for IRI activity. It has been previously established that the *N*-methylation of compound **5.04** is not tolerated.[8,12] The conclusion from this finding was that the amide hydrogen is essential for IRI activity, however di-alkylation had not been attempted with two large (≥ 6 carbon) alkyl substituents prior to this work. With respect to *N*-cyclohexyl gluconamide (**5.07**), the introduction of a second cyclohexyl moiety (compound **5.11**) was found to dramatically increase IRI activity without imparting any negative effect on maximum aqueous solubility (**Figure 5.6 (A)**). Compound **5.11** became of particular interest, possessing comparable IRI activity to any linear alkyl gluconamide tested. Compound **5.10** was also found to be IRI active, albeit with lower IRI activity with respect to **5.02**. The tolerance to *N,N*- dialkylation for both linear and cycloalkyl derivatives indicates that the amide hydrogen is not strictly required for IRI activity. The tolerance to *N*-hexyl alkylation, and intolerance to *N*-methylation[8,12] reinforces the complexities in small molecule IRI design. It can be hypothesized that the conformational change imparted by *N,N*-alkylation is detrimental to IRI activity. However, the additional hexyl moiety increased the hydrophobicity enough to overcome the detrimental conformational change, when the addition of a methyl could not.

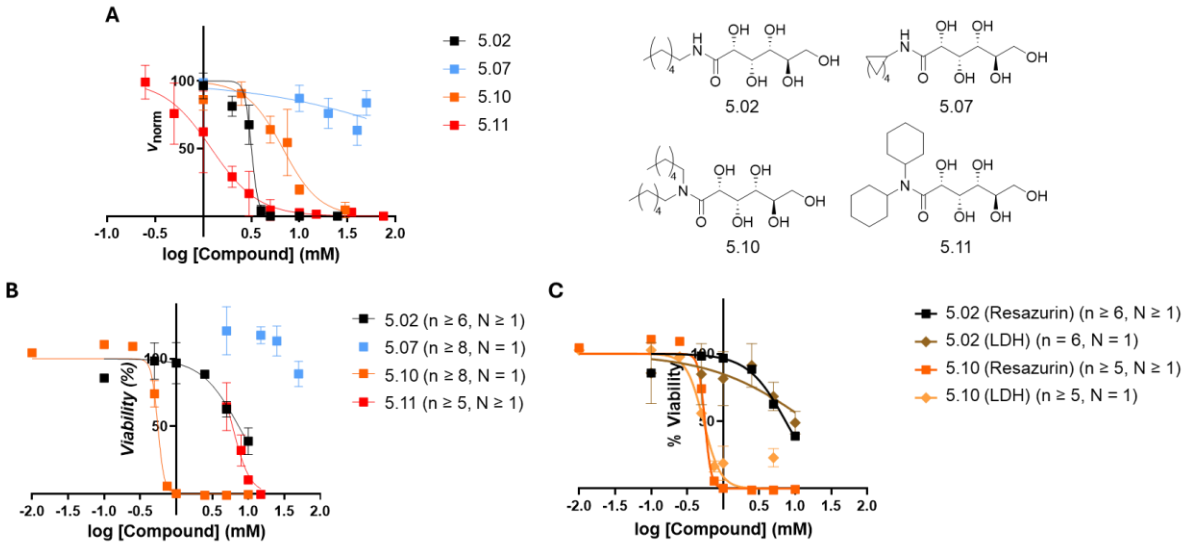

Figure 5.6 IRI activity and cytotoxicity of *N*- and *N,N*-hexyl gluconamide compounds. Technical replicates (n) are represented as the smallest number of wells utilized for a tested concentration within the sample set. **(A)** IRI activity of *N*- and *N,N*-hexyl gluconamides in PBS when assessed on the modified SCA. Dose response relationship is generated for each compound, and the resulting IC_{50} value is indicated in **Figure 5.4**. **(B)** Cellular viability of *N*- and *N,N*-hexyl gluconamides when assessed in HepG2 cells following 24-hour incubation utilizing a metabolic indicator of cellular death (the resazurin cellular viability assay). **(C)** Assessment of membrane cytotoxicity of linear *N*- and *N,N*-hexyl gluconamides, assessing cellular viability both metabolically (resazurin stain) as well as with a membrane indicator of cellular death (lactate dehydrogenase (LDH)) in HepG2 cells following 24-hour incubation.

Despite the encouraging IRI activity, the second alkyl substituent installed on compounds **5.10** and **5.11** was hypothesized to also convey a subsequent increase in cytotoxicity.[17,21] When investigating small molecule surfactants as potential IRI candidates,[8] detrimental impact to cell membranes was a primary concern.[22] To assess the degree of cytotoxicity, Cameron Steinke assessed the cytotoxicity of compounds **5.10** and **5.11** as well as the corresponding *N*-alkyl gluconamides (**5.02**, **5.07**). Two separate cytotoxicity assays were utilized: a standard resazurin based cytotoxicity assay was used to measure metabolic cell death, and a lactate dehydrogenase (LDH) cytotoxicity assay to measure the degree of cellular membrane damage. A comparison of metabolic death and membrane damage provides insight as to what proportion of measured cellular death is due to surfactant like toxicity (membrane damage). Both cytotoxicity assessments were performed with human hepatocellular carcinoma (HepG2) cells to obtain the dose-response relationship of toxicity for these compounds following 24-hour incubation (**Figure 5.6 (B - C)**). The tested 24-hour time point represents more extreme conditions than would realistically be used in practical cryopreservation applications as dosing of compound at room temperature would not

typically exceed 5 minutes. This longer incubation time represents the upper limit of cytotoxicity which would not be practically exceeded. A detailed explanation of cell culture procedures and cytotoxicity assays can be found in **Appendix III**.

When assessing metabolic cytotoxicity, dialkylation resulted in at least an order of magnitude increase in toxicity with respect to the mono-alkylated gluconamide for both linear alkyl (LD_{50} = 7.4, 0.6 mM) and cycloalkyl (LD_{50} = N/A, 6.1 mM) derivatives (**Figure 5.6 (B)**). As compound **5.07** was not cytotoxic enough to generate a LD_{50} through metabolic assessment, only the linear alkyl compounds (**5.02**, **5.10**) were assessed for membrane integrity (**Figure 5.6 (C)**). Compound **5.02** (Resazuin LD_{50} = 7.4 mM, LDH LD_{50} = 15.1 mM) demonstrated approximately half the toxicity when assessed for membrane based cellular damage when compared to general metabolic death. This suggests that for IRI active *N*-alkyl gluconamides, a portion of cell death observed metabolically may be due to membrane interactions. Compound **5.10** (resazurin LD_{50} = 0.6 mM, LDH LD_{50} = 0.5 mM) demonstrated comparable toxicity when measuring metabolic and membrane-based cell damage. This indicates that the primary mechanism of cellular damage measured for *N,N*-dialkyl gluconamides is likely surfactant-like membrane-based damage.

From this toxicity data, compound **5.10** can be excluded from future consideration as a CPA candidate, having an efficacy index (as defined as LD_{50} / IC_{50}) less than one ($EI_{\mathbf{5.10}}$ = 0.1). Despite the increase in toxicity, compound **5.11** is IRI active enough to possess a positive efficacy index ($EI_{5.11}$ = 6.1) and may be worth further biological assessment. As both alkyl moieties are required to be large to inhibit ice recrystallization, *N,N*-dialkylation presents a delicate balance between IRI activity and surfactant like toxicity. Uniformly, the introduction of a second large alkyl substituent results in increased cytotoxicity. For IRI inactive *N*-cycloalkyl gluconamides, the addition of a second large alkyl moiety was found to improve IRI activity enough to compensate for the increase in cytotoxicity. In contrast, the *N,N*-dialkylation of IRI active linear *N*-alkyl gluconamides was found to be purely detrimental, decreasing IRI activity and increasing cytotoxicity. It is important to note that the amide hydrogen is not strictly required for IRI activity, and the introduction of additional functionality at the amide position may be tolerated.

5.3 Assessment of Novel *N*-alkyl gluconamide IRIs

5.3.1 Assessing hydroxyl requirements for IRI activity in *N*-alkyl gluconamides

The IRI assessment of *N*-alkyl erythrose (3 hydroxyls) (**Figure 5.2**)[14] and arabinose (4 hydroxyls) (**Figure 4.1.3 (B)**,[19] **Figure 5.3**[14]**)** has previously been preformed using the 30-minute SCA. From these assessments, the removal of a single hydroxyl was found to decrease IRI

activity. To better understand the source of this IRI activity loss, a systematic assessment was preformed, keeping the alkyl chain consistent and incrementally removing one hydroxyl. As discussed in **Chapter 4** (**Section 4.3**), a synthetic pathway has been developed (**Schemes 4.3.1.1.1 – 4.3.1.4.1, Scheme 5.1**) to synthesize incrementally truncated derivatives of a given gluconamide IRI. To provide the highest baseline activity, the use of a heptyl- (compound **5.03**) or octyl- (compound **5.04**) chain was considered. Having established that observed trends may not be directly shared across different *N*-functionalization, an octyl chain was selected for this assessment due to the larger precedent of background biological work utilizing compound **5.04**.[16,23] The synthesis of **5.04** derivatives (**5.26** – **5.30**) followed the identical methods as described in **Chapter 4** (**Section 4.3.1**) with the exception that *N*-alkyl gluconamide **5.04** was synthesized under milder conditions (**Scheme 5.1**) than *N*-aryl gluconamides due to the use of stronger amine nucleophiles (in comparison to weaker aniline nucleophiles).

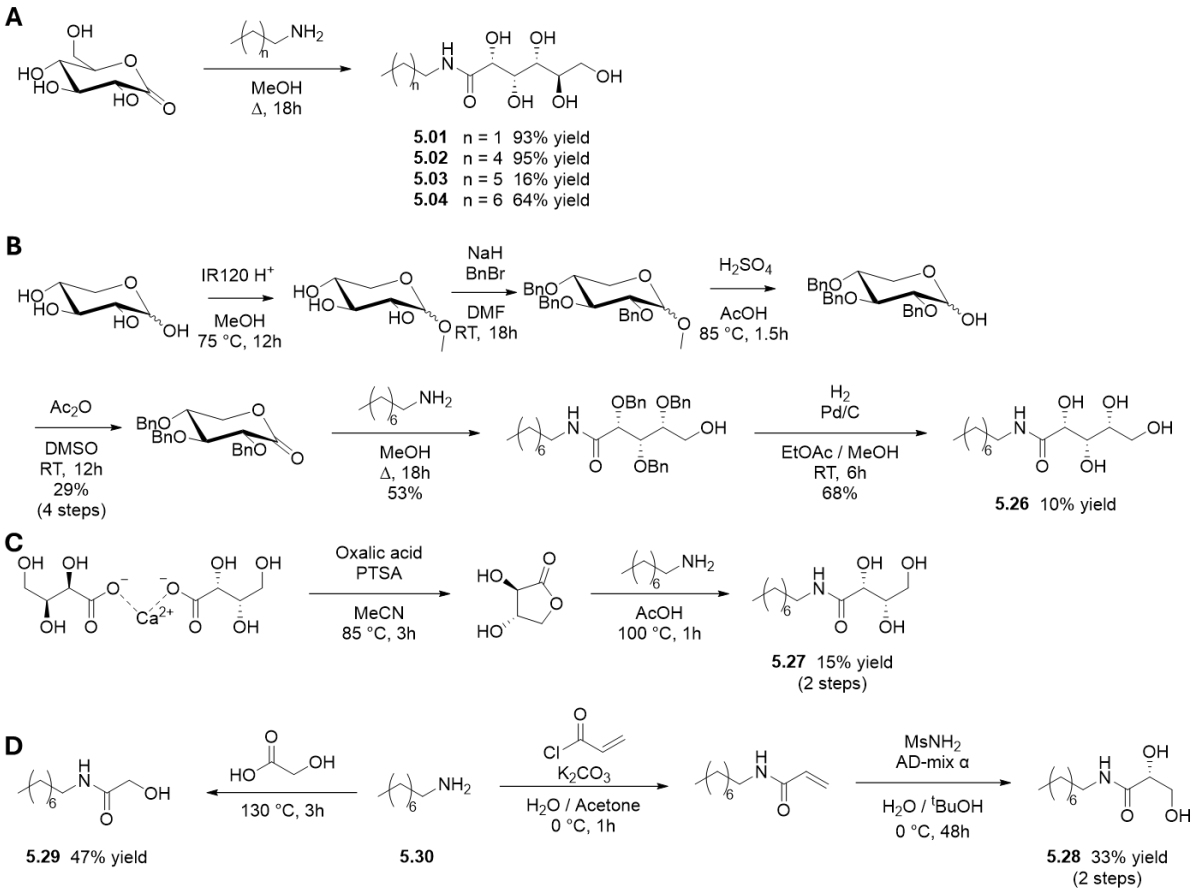

Scheme 5.1 General synthetic figure for the synthesis of modified *N*-octyl-D-gluconamide derivatives. Yields for individual steps are indicated under the respective reaction arrow. Overall yield for each compound is indicated beside the compound identification number. **(A)** Synthesis of *N*-alkyl-D-gluconamides (**5.01** – **5.04**) from commercially available D-gluconolactone. **(B)** Synthesis of *N*-octyl-D-xylonamide (**5.26**), from D-xylose through the generation of 2,3,4-tri-*O*-(benzyl)-D-xylono- δ-lactone. **(C)** Synthesis of *N*-octyl-L-threonamide (**5.27**) from calcium L-threonate, through the generation of L-threono-γ-lactone. **(D)** Synthesis of 2,3-dihydroxy-*N*-octyl-propamide (**5.28**) and 2-hydroxy-*N*-octylacetamide (**5.29**) from commercially available octylamine.

No modified n-Octyl derivative resulted in measurable IRI activity (**Figure 5.7**), but all truncated derivatives were found to possess improved maximum aqueous solubility. Similar to what was observed with aryl 2-Fluoro and 4-Methoxy derivatives (**Section 4.3.2**), little information can be directly gained from this preliminary truncation screen. Although, these findings reinforce the proposed idea (**Section 4.4.3**) that the selective removal of hydroxyls from poorly soluble gluconamide IRIs can lead to an increase in maximum aqueous solubility. It is also of note that although derivatives **5.28** – **5.30** did not possess enough aqueous solubility to obtain a full dose

response curve, they all reduced the rate of ice crystal growth below 100% at 1 mM, which has not been observed to this point by any other modified gluconamide derivative.

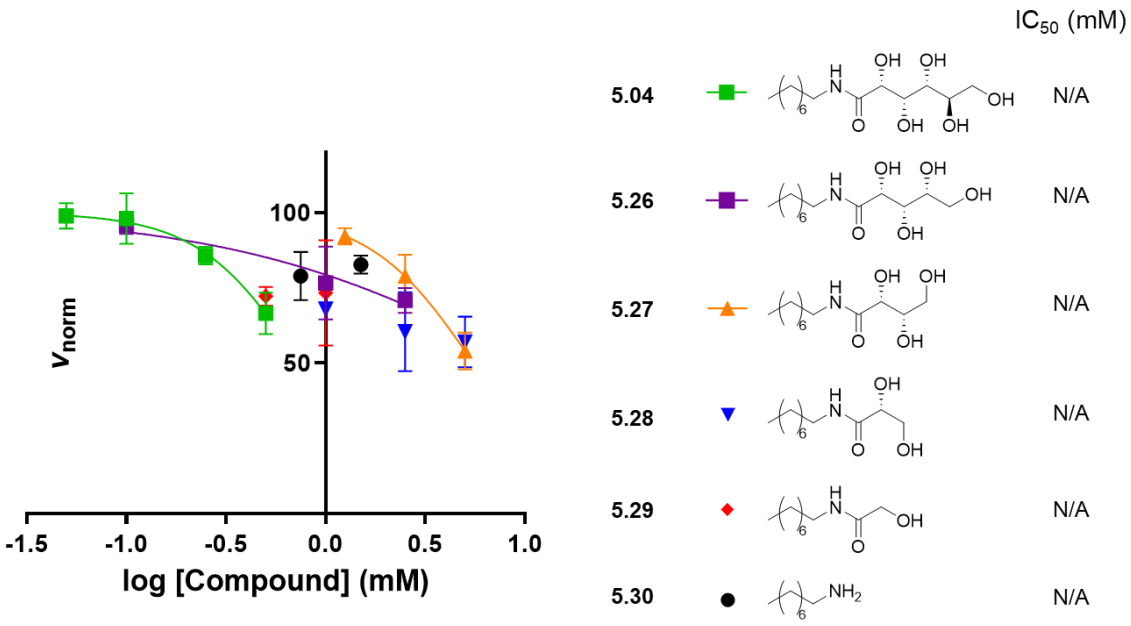

Figure 5.7 Truncated derivatives of **5.04** and the dose response curve for each compound. IC_{50} values were obtained on the modified SCA, compounds indicated with an IC_{50} value of N/A failed to achieve a relative rate of ice crystal growth below 50%. All compounds were tested up to the measured aqueous solubility limit in PBS at room temperature.

5.3.2 The importance of C_6 hydroxyl for the IRI activity of 5.04

As previously noted,[19,24] and observed with the truncation of *N*-aryl gluconamides (**Section 4.3.2**), the C_6 hydroxyl has been identified as very important for IRI activity. It has also been observed that the selective removal of hydroxyl(s) has resulted in an increase in maximum aqueous solubility for *N*-aryl gluconamides (**Section 4.4.3**); from the assessment of truncated **5.04** derivatives (**Figure 5.7**), this phenomenon appears to also apply to *N*-alkyl gluconamides. As utilized for the investigation of **4.01** (**Section 4.4.2**), the generation of *N*-alkyl 6-hydroxylhexylamide derivatives in one step from *ε*-caprolactone allows for the generation of dehydroxylated derivatives without impacting the C_6 hydroxyl (**Scheme 5.2**). As such, the 6-hydroxyhexylamide derivative of **5.04** (**5.14**) was synthesized; should the maximum aqueous solubility of **5.04** derivatives be increased, it would improve the ability to generate full dose-response relationships and subsequently compare IRI activity.

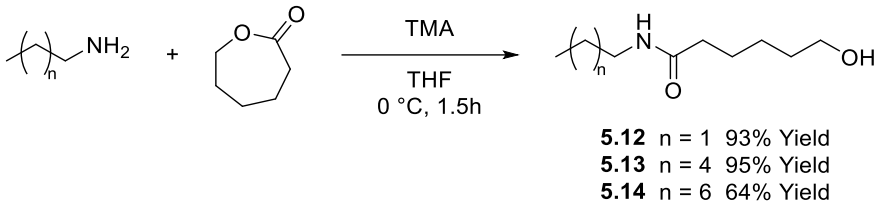

Scheme 5.2 Synthesis of *N*-alkyl-6-hydroxyhexanamide derivatives from commercially available *ε*-caprolactone and the corresponding alkyl amine.

The IRI assessment of *N*-(2-fluorophenyl)-6-hydroxyhexylamide (**4.28**) was particularly exciting, as the modified derivative retained enough IRI activity to generate a dose-response relationship (**Figure 4.12, Figure 5.8**). Compound **4.28** served as a measurably IRI active scaffold to further explore the IRI activity of *N*-aryl gluconamides. *N*-(octyl)-6-hydroxyhexylamide (**5.14**) was found to not only be measurably IRI active, but equivalent in IRI activity to parent gluconamide **5.04** (**Figure 5.8**). The generation of compound **5.14** also resulted in an order of magnitude increase in maximum aqueous solubility, allowing for a full dose-response relationship to be obtained.

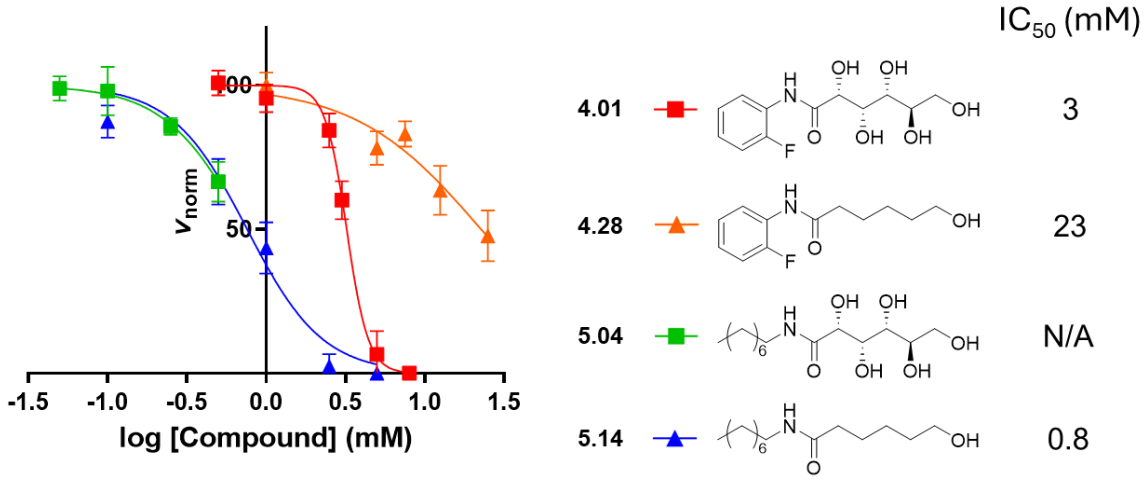

Figure 5.8 Comparison of IRI activity for *N*-functionalized gluconamide (square icon) and *N*-functionalized 6-hydroxyhexylamide derivative (triangle icon). Four-parameter dose response relationship is generated for each compound using the modified SCA.

Compound **5.14** was found to be the first *N*-functionalized gluconamide derived small molecule to possess equivalent IRI activity to the respective parent compound. This indicates that the removed functionality with respect to **5.04** ($C_{2\text{-}5}$ hydroxyls) are not strictly required for IRI activity. This finding serves as an exciting synthetically accessible functional derivative, equivalent in IRI activity to traditional *N*-alkyl gluconamides. However, this finding further complicates the

broader understanding of structural requirements for IRI activity, whereby IRI active compounds **4.01**, **4.04** and **5.04** all demonstrate distinct functional responses to the same chemical modifications. With the generation of IRI active *N,N*-dialkylated gluconamides (**5.10**, **5.11**) indicating the amide hydrogen is not strictly required, and **5.14** indicating the $C_{2\text{-}5}$ hydroxyls are not strictly required, the minimum structural requirements for the IRI activity of *N*-alkyl gluconamides must be focused at the C_6 position.

With a focus at the C_6 position of compound **5.14**, the capacity to act as a hydrogen bond donor at the C_6 position was removed through alkylation utilizing iodomethane or iodoethane in one step (**Scheme 5.3**) generating compounds **5.15** and **5.16**. In contrast to what was observed when examining *N*-aryl gluconamide **4.01**, *O*-alkylation at the C_6 position was tolerated, with compounds **5.15** (IC_{50} = 1 mM) and **5.16** (IC_{50} = 3 mM) remaining measurably IRI active. This indicates that the C_6 hydroxyl is not strictly required as a hydrogen bond donor. As the maximum aqueous solubility was reduced through *O*-alkylation, longer alkyl substituents were not assessed. However, as was observed with the *N,N*-dialkylation of compound **5.02**, it is possible that larger *O*-alkylation may be beneficial to increase IRI activity at the risk of increased surfactant like toxicity.

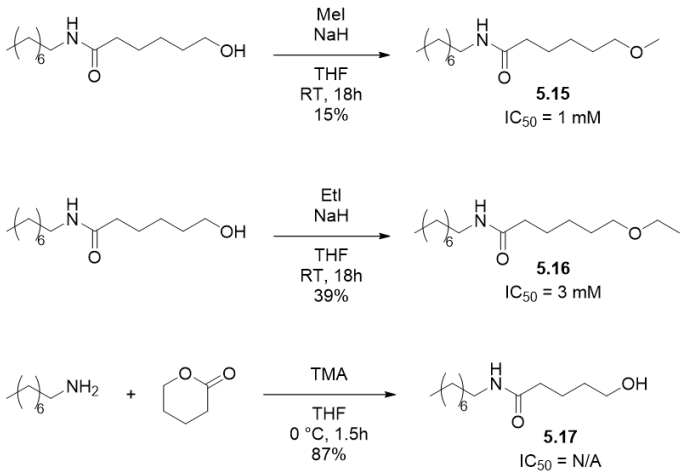

Scheme 5.3 Synthesis of C_6 modified derivatives of **5.14** starting from **5.14** itself, or commercially available reagents. Each derivative was synthesized in one step utilizing standard reaction conditions.[25–27] Yield for each reaction is indicated below the respective reaction arrow. IRI activity (IC_{50}) is indicated below each compound identification number.

Despite not being required to act as a hydrogen bond donor, generating the terminal hydroxyl at the C_5 position (**5.17**) resulted in complete loss of IRI activity; the requirement of the terminal hydroxyl to be 5 atoms away from the amide indicates that the position of the C_6 hydroxyl is

specifically required for IRI activity. This positional requirement was hypothesized to be due to either intramolecular hydrogen bonding interactions, or intermolecular interactions (with bulk water or other solutes) and is explored in further detail in **Section 5.4**.

5.3.3 Generation of next generation *N*-alkyl scaffolds

As established in **Section 4.3**, it can not be assumed that modifications of one *N*-functionalized gluconamide will directly apply to another compound within the same family. Knowing the hydrophilic / hydrophobic balance is a vital component of IRI activity,[1] an IRI active *N*-alkyl gluconamide of similar chain length to **5.04** (**5.02**) and a relatively IRI inactive *N*-alkyl gluconamide (**5.01**) were also used as a baseline to generate to 6-hydroxyhexylamide derivatives **5.12** – **5.13** (**Scheme 5.2**, **Figure 5.9**).

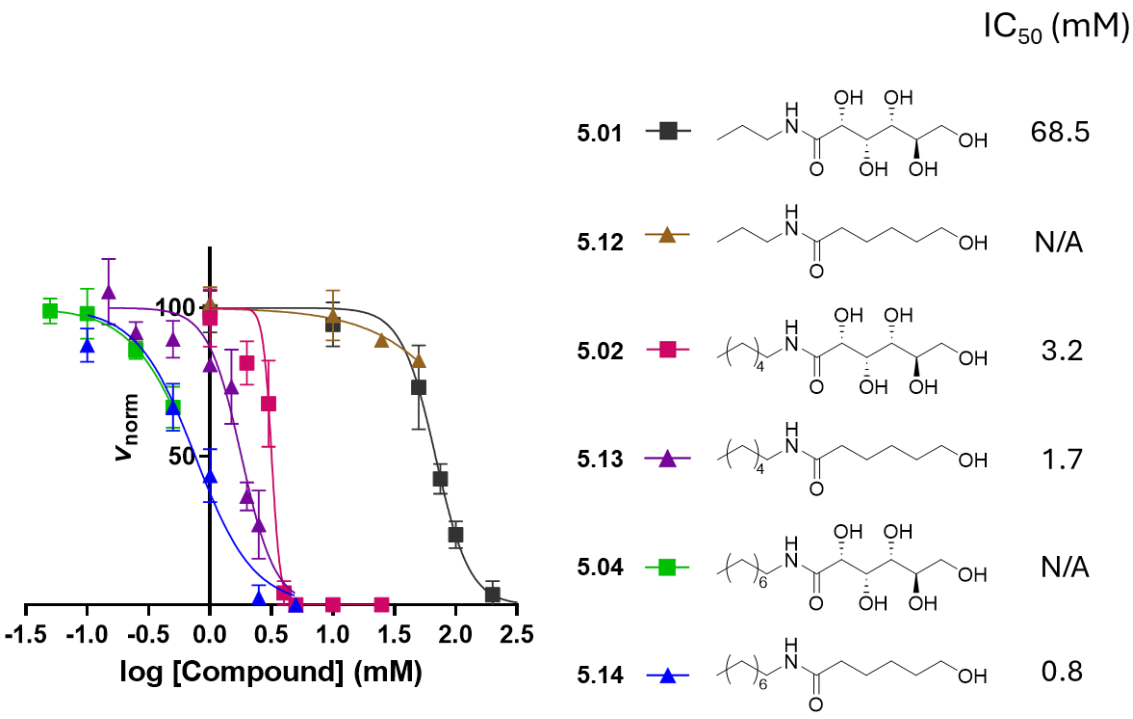

Figure 5.9 Four-parameter dose response relationships to compare *N*-alkyl gluconamides (square icons) to the respective *N*-alkyl-6-hydroxyhexanamides (triangle icons). IC_{50} values were obtained on the modified SCA, compounds indicated with an IC_{50} value of N/A failed to achieve a relative rate of ice crystal growth below 50%. All compounds were tested up to the measured aqueous solubility limit in PBS at room temperature.

When shortening the alkyl chain from eight carbons (**5.04**) to six (**5.02**), the 6-hydroxyhexylamide derivative (**5.13**) continued to demonstrate full retention of IRI activity (**Figure 5.9**). With the generation of compound **5.13**, a maximum aqueous solubility increase was not

observed (with respect to **5.02**). Interestingly, both compounds **5.13** and **5.14** share a maximum solubility of approximately 5 mM; from the investigation of *N*-alkyl gluconamides (**Figure 5.5**), it would be expected that the shorter hexyl- derivative (**5.13**) would be more soluble in aqueous media than the octyl derivative (**5.14)**. It is difficult to assess compound **5.12** due to the order of magnitude decrease in maximum aqueous solubility with respect to compound **5.01**. Unlike the uniform increase in aqueous solubility observed with the generation of dehydroxylated *N*-aryl derivatives (**Section 4.4.3**), it appears the generation of 6-hydroxyhexylamide derivatives of *N*-alkyl gluconamides will only improve the maximum aqueous solubility of poorly soluble gluconamides.

While being utilized to highlight the minimum structural features required for IRI activity in *N*-alkyl gluconamide IRIs, compounds **5.13** and **5.14** without further modification present intriguing candidates as novel CPAs, with strong IRI activity and maximum aqueous solubility. Similar to the *N,N*-dialkyl compounds **5.10** and **5.11**, there was a concern that by removing the hydrophilic $C_{2\text{-}5}$ hydroxyls of *N*-functionalized gluconamides, the cytotoxicity would greatly increase. Compounds **5.13** and **5.14** were assessed for cytotoxicity in HepG2 cells, utilizing the resazurin cellular viability assay following 24-hour incubation (**Figure 5.10**).

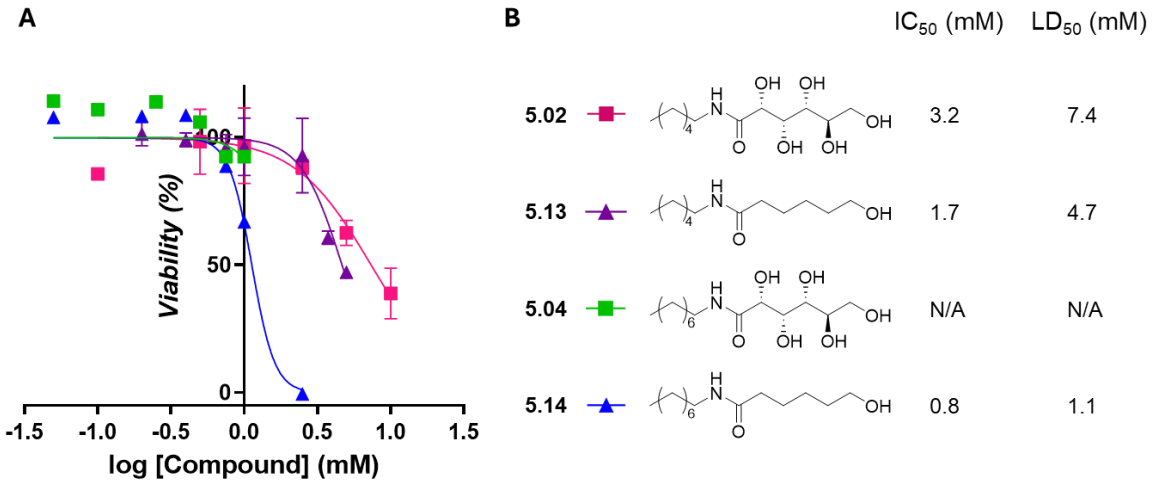

Figure 5.10 IRI activity and cytotoxicity of *N*-hexyl and *N*-octyl 6-hydroxyhexanamide derivates and the corresponding *N*-alkyl gluconamide. **(A)** Cellular viability of HepG2 cells measured metabolically with resazurin cellular viability assay following 24-hour incubation. n ≥ 5, N = 1 for *N*-hexyl compounds (**5.02**, **5.13**), n ≥ 11, N = 1 for *N*-octyl compounds (**5.04**, **5.14**). **(B)** Data summary of IRI activity (presented in **Figure 5.9**) and cellular viability. Compounds indicated with an LD_{50} value of N/A failed to achieve a relative viability below 50% prior to the maximum aqueous solubility.

In contrast to the increase in toxicity observed when comparing primary to secondary *N*-alkyl gluconamides (**Figure 5.6**), the generation of compound **5.13** does not result in an order of magnitude decrease in cellular viability with respect to compound **5.02** (**Figure 5.10**). The assessment of compound **5.14** with respect to **5.04** is difficult due to the solubility constraints of **5.04**. Both **5.13** ($EI_{5.13}$ = 2.8) and **5.14** ($EI_{5.14}$ = 1.4) exhibit measurable cytotoxicity when incubated for 24 hours, with slightly positive efficacy indexes. Without further functionalization, it is unlikely that **5.13** or **5.14** would be viable candidates for cellular application due to their cytotoxicity, however they may function as synthetically accessible scaffolds for future IRI development. The generation of synthetically accessible molecules such as **5.13** and **5.14** which possess measurable IRI activity are invaluable in attempts to explore, and ultimately better understand the mechanism(s) of IRI activity for small molecule carbohydrates.

5.4 Exploring the conformations of IRI active small molecules using computation

Throughout the modification of *N*-functionalized gluconamides (**Chapter 4**, **Chapter 5**), a number of observations have been noted with respect to the structural requirements necessary for IRI activity. Most surprisingly, it was noted that the removal of any hydroxyl(s) from an *N*-aryl gluconamide, will result in an increased maximum aqueous solubility (**Section 4.4.3**). This was also observed with the generation of 6-hydroxyhexylamide derivatives of poorly soluble *N*-alkyl gluconamide IRIs (**Section 5.3**). As the polyol chains on *N*-functionalized gluconamides are capable of forming highly stabilized linear chains, it was hypothesized that through dehydroxylation, these intramolecular hydrogen bonding interactions are disrupted. Disruption of the polyol hydrogen bonding network may allow for more hydrogen bonding interactions with bulk water and have more accessible conformations (which could be conducive to solvation).

5.4.1 Assessment of PEG functionalized derivatives

As the assumed rationale for the observed modulation of maximum aqueous solubility in simplified *N*-functionalized gluconamides is disruption of the polyol chain, a short polyethylene glycol chain (PEG) was selected as an isostere of the 6-hydroxyhexanamide alkyl chain. The PEG chain will be less rigid, with less capacity to hydrogen bond than a gluconamide chain, but more rigid and a higher capacity to hydrogen bond than an alkyl chain. Should disruption of the polyol chain be the source of improved solubility, it would be expected that the generated PEG derivatives would be highly aqueous soluble; not containing polyol intramolecular interactions, with an additional hydrogen bond donor accessible to interact with bulk water with respect to 6-hydroxyhenxylamides. Should the improved aqueous solubility be due to the ability to access a

conformation conducive to solvation, the PEG derivatives should be more soluble than gluconamides, and less soluble than 6-hydroxyhexylamides.

As no assessment had been performed on small molecule PEG containing compounds in our laboratory, **5.18** was generated in one step from commercially available m-PEG_2-amine (**Scheme 5.4**) for an accessible insight as to the IRI activity and toxicity with respect to traditional *N*-alkyl gluconamides (**Figure 5.11**).

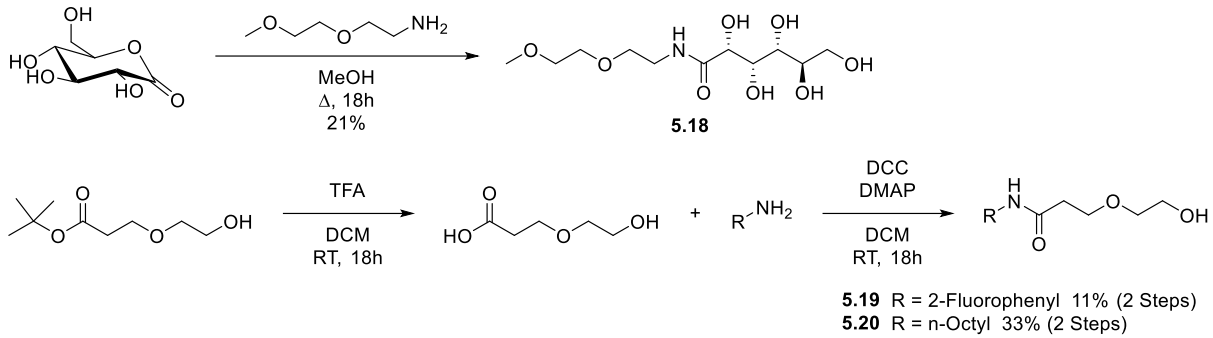

Scheme 5.4 Synthesis of gluconamide IRI PEG derivatives from commercially available gluconolactone or hydroxy-PEG_1-acid in one isolated step.

The substitution of a linear alkyl chain for a PEG chain of similar length was found to decrease IRI activity (~50x with respect to **5.03**), but an IC_{50} value (20 mM) was still able to be measured (**Figure 5.11 (A)**) due to the large increase in maximum aqueous solubility (60x with respect to **5.03**). As previously examined (**Figure 5.6**), *N*-alkyl gluconamides are found to be very IRI active, but also suffer from high degrees of cytotoxicity, specifically by membrane damage. The substitution from an unfunctionalized alkyl chain to a PEG_2 chain was found to remove any measurable cytotoxicity in HepG2 cells following a 24-hour incubation when examined with a metabolic or membrane integrity assay (**Figure 5.11 (B)**). Therefore, the introduction of heteroatoms (such as an ether) into alkyl chains may become a useful strategy in the future to mediate the poor aqueous solubility and cytotoxicity observed with highly IRI active *N*-alkyl gluconamides.

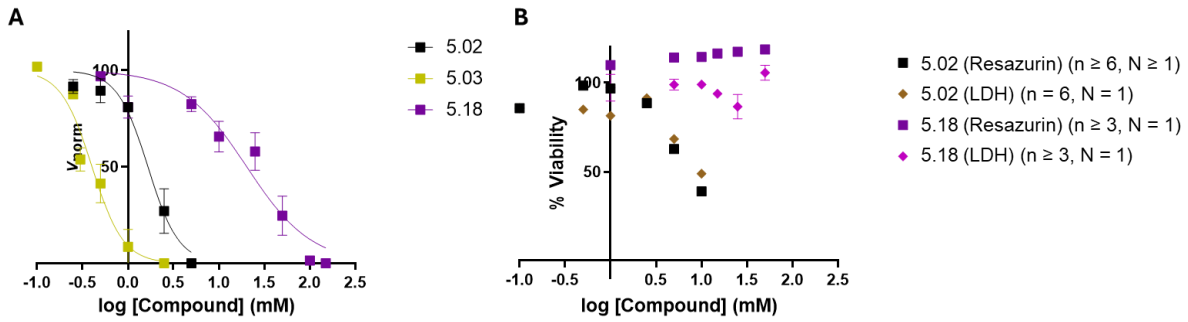

Figure 5.11 IRI activity and cytotoxicity of *N*-(2-(2-methoxyethoxy)ethyl)-gluconamide (**5.18**) and *N*-alkyl gluconamides of similar chain length. **(A)** The four-parameter dose response curve for each compound. **(B)** Cellular viability of HepG2 cells measured metabolically with resazurin cellular viability assay and by membrane integrity (LDH assay) following 24-hour incubation.

With IRI activity of a *N*-PEG_2-gluconamide (**5.18**) and *N*-alkyl 6-hydroxyhexylamides (**4.28**, **5.14**) assessed, hydroxy-PEG_1-acid was then utilized as a polyol isostere, generating compounds **5.19** and **5.20** (**Scheme 5.4**) in one step with a standard amide coupling procedure. The PEG_1 analogues were not found to possess any measurable IRI activity (**Figure 5.4.1.2**), indicating that the introduction of an ether at the C_4 position is not tolerated for IRI activity. In addition, the maximum aqueous solubility did not change through the introduction of O_4 ether. This was not an expected outcome, as it was hypothesized that by modulating the degree of available hydrogen bonding interactions with bulk water and chain rigidity the maximum aqueous solubility would be changed.

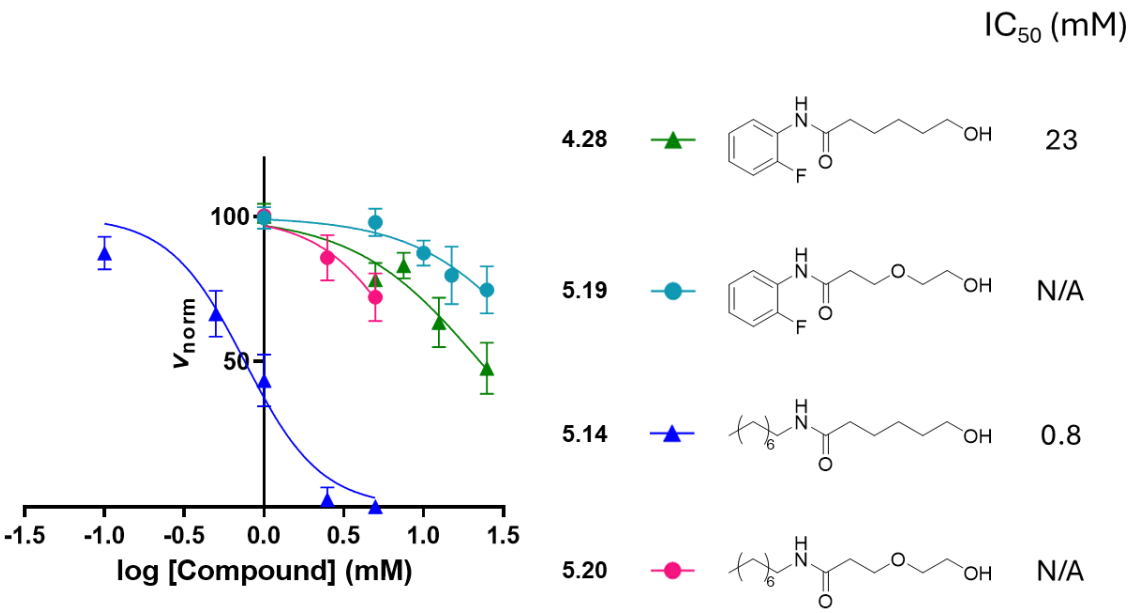

Figure 5.4.1.2 Four-parameter dose response curves to compare *N*-functionalized 6-hydroxyhexanamides (triangle icons) to the respective 3-(2-hydroxyethoxy)-*N*-functionalized propanamide (circle icons). IC_{50} values were obtained on the modified SCA, compounds indicated with an IC_{50} value of N/A failed to achieve a relative rate of ice crystal growth below 50% before becoming solubility limited. All compounds were tested up to the measured aqueous solubility limit in PBS at room temperature.

5.4.2 Computational assessment of *N*-functionalized gluconamide derivatives

One possible explanation for the lack of aqueous solubility changed with the generation of PEG_1 compounds (**5.19**, **5.20**) is that the installed O_4 ether is acting as a hydrogen bond acceptor intramolecularly, not allowing for an increase in bulk water interaction with respect to 6-hydroxyhexylamide derivatives. This could also explain the loss of IRI activity, as a stabilized intramolecular interaction could prevent compound **5.19** and **5.20** from effectively interacting with bulk water and result in a loss of IRI activity. Elucidation of this interaction became of interest; should a (or set of) conformation(s) be identified as quenching IRI activity, or impacting solvation into aqueous solution, it would be valuable to avoid for future IRI development. To help identify these potential conformations, a computational assessment of model IRI derivatives was performed.

With access to Digital Research Alliance of Canada's computational servers, geometry optimization was performed for both *N*-aryl and *N*-alkyl derivatives. Structural inputs were initially generated as 2-dimensional MDL Molfiles (.mol) in ChemDraw Prime 22. These 2D input files were imported into WebMO's online user interface (access provided by Professor Tom Woo) where a comprehensive cleanup using idealized geometry was performed, with the resulting 3-

dimensional input exported in the .XYZ format. Initial conformational assessment was performed using CREST's (Version 2.11) standard conformational search (iMTD-GC) workflow using the GFN2-xTB basis set,[28] the ALPB model of solvation,[29] and ignoring any initial topography checks prior to conformational search. This initial search provides an estimate at the lowest energy conformation of a given molecule within an implicit water shell. As open-chain carbohydrates possess over 36 atoms and over 180 degrees of rotational freedom, the chosen basis set (GFN2-xTB) provides a relatively robust assessment while still allowing calculations to complete within 48 hours. The calculations were run within an implicit shell of water at 298 K to provide data closest to what is being experimentally observed for compounds prior to freezing. Attempts were made to assess compounds utilizing explicit solvent shells or lower temperatures, however these calculations proved to require greater computational resources than was reasonably accessible. A more robust explanation as to the computational workflow utilized, as well as example input codes can be found in **Appendix III**.

With no literature precedent to guide this initial conformational analysis, the lowest energy conformer output of the CREST conformation search was accepted and used as an input for further optimization. Refined optimization was performed utilizing ORCA's[30] (Version 5.0.4) geometry optimization and vibrational frequencies functions. Standard 12-didget coordinates were extracted from the CREST optimized .XYZ files with Chemcraft and used to generate the main ASCII input file (.inp). This input file in conjunction with an initialization Bourne shell script (.sh) provide the generated input for ORCA optimization. ORCA optimization was performed utilizing Head-Gordon's fully variable DF-ωB97 DFT method,[31] the DEF2-TZVPP basis set[32] and the implicit conductor-like polarizable continuum solvent model (CPCM).[33] The ωB97 method was developed to prioritize metal-ligand binding interactions when determining stability,[31] (while not directly equivalent) it was thought that this method would be preferable to a standard hybrid method (such as B3LYP) should an explicit solvent shell be explored in future. The ORCA computational suite uses the CPCM solvation model, which generates a solvent like shell based upon the dielectric constant of your chosen solvent (in this case water), and structural computation is performed within a pocket in the center of the solvent shell. This model is crude, but presents a closer approximation to the functional solvation than calculating in gas phase. Molecular dynamic analysis utilizing an explicit water shell would be ideal for a computational assessment of model compounds. As these assessments serve only as a supplemental tool to aid experimental findings, computational assessments were limited to pre-made workflows that can be utilized with limited programming experience.

Conformational analysis was attempted for **4.01** and **5.04** as representative *N*-aryl and *N*-alkyl gluconamides respectively; the computation protocol was able to complete for **4.01**, however final optimization of **5.04** did not converge when provided with the accessible computational resources. Without having **5.04** as a frame of reference, a focus was placed on the *N*-aryl derivatives, with attempts to apply *N*-aryl computational findings to *N*-alkyl derivatives through experimental findings.

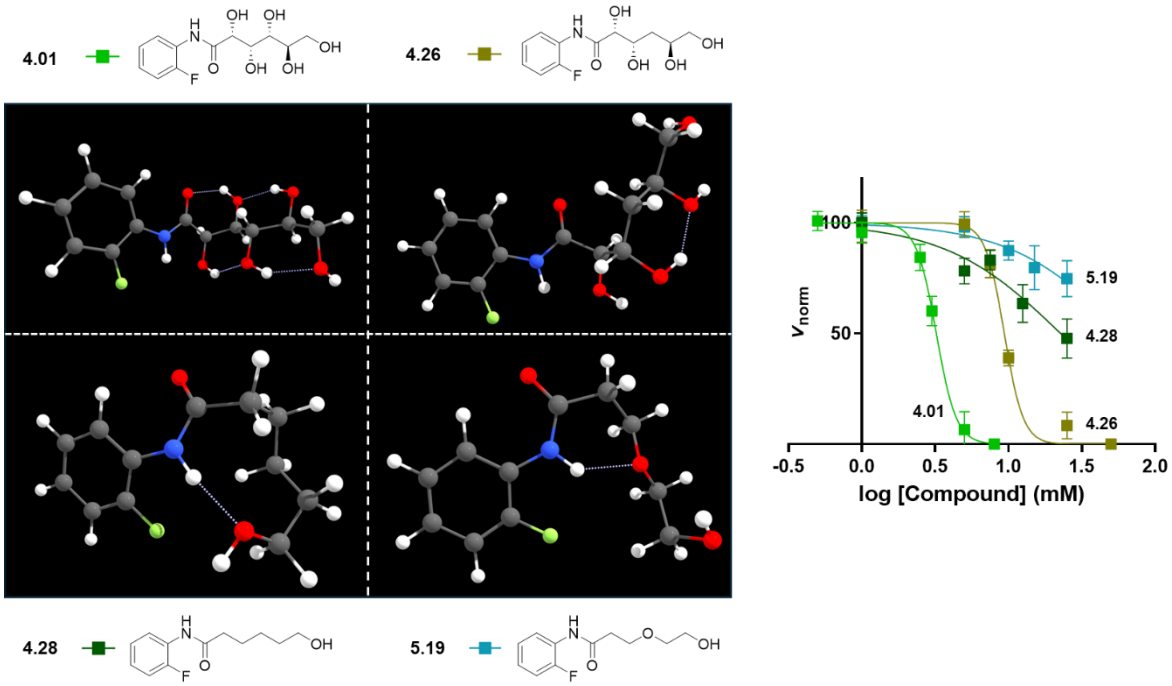

Figure 5.12 Computational assessment of **4.01** derived model compounds. Optimized geometry is visualized as ball and stick diagrams with Chemcraft software. Hydrogen bonding interactions are represented with a dashed white line (hydrogen bonding length ≤ 2.0 Å). IRI activity for each compound is represented with the four-parameter dose response curve obtained from the modified splat cooling assay.

When computing the lowest energy conformation of **4.01** (**Figure 5.12**), a preference towards intramolecular hydrogen bonding interactions (over intermolecular interactions with solvent) was observed. The inaccessibility of the carbohydrate hydroxyls to bulk water molecules is hypothesized to be the source of the hindered aqueous solubility of **4.01**. The selective removal of one hydroxyl (C_4, **4.26**) is shown to interrupt the polyol chain intramolecular hydrogen binding network, with only one intramolecular hydrogen bond formed. This disruption would allow for more hydrogen binding sites with bulk water molecules when compared to **4.01** and affords greater flexibility of the polyol chain. Highly IRI active **4.01** and **4.26** were both found to be relatively linear in their lowest energy conformation, while derivatives **4.28** and **5.19** both were found to adopt a

cyclic conformation. The measurably IRI active **4.28** adopted an NH – OC_6 9 membered ring, where the IRI inactive **5.19** utilized the introduced O_4 as a hydrogen bond acceptor, forming a more stable NH – O_4 6 membered ring. The stability of this intramolecular interaction is thought to explain the reduced IRI activity of compound **5.19** with respect to **4.28**. With a 6 membered hydrogen bonding interaction with the amide being identified as the likely intramolecular interaction of interest for compound **5.19**, several 6-hydroxyhexylamide derivatives were generated to target the formation of this conformation (**Scheme 5.5**).

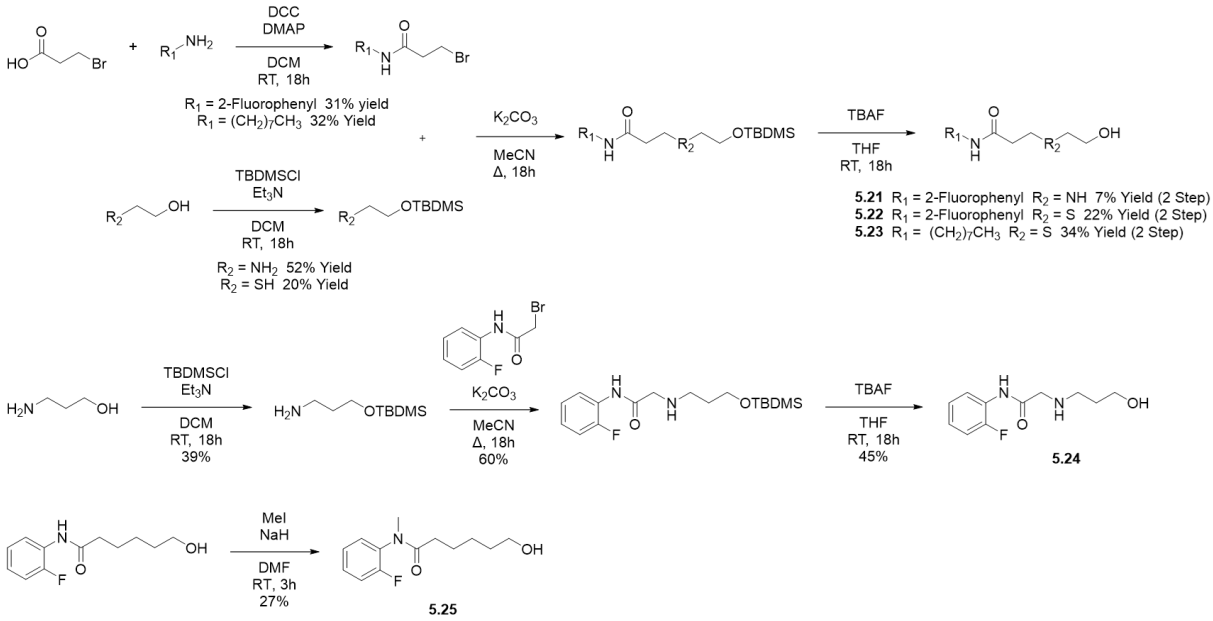

Scheme 5.5 General synthetic approach for 2-Fluoro phenyl and n-Octyl derivatives generated to probe amide – C_4 hydrogen bonding interactions. Yields for the given reaction step are indicated below the reaction arrow, or beside the compound number where applicable.

To assess the effect of heteroatom substitution at the C_4 position on the carbohydrate chain, N_4 amine and S_4 thioether derivatives were synthesized. These compounds were generated in three steps: generation of the β-halide of choice (either a derivative of **4.01** or **5.04**), coupling of the protected ethanol derivative (either ethanolamine or mercaptoethanol) with the generated β-halide, and subsequent deprotection. With the same key steps, commercially available 2-bromo-*N*-(2-fluorophenyl)acetamide was utilized to generate a N_3 amine derivative, allowing for direct comparison to the N_4 amine (**5.21**). It is worth noting that when calculating the pKa value of secondary amine derivatives (**5.21**, **5.24**) using ChemDraw 22, the N_4 secondary amine will be primarily protonated (pKa = 7.9) in PBS (buffered at pH = 7.4), while the N_3 secondary amine (pKa = 6.7) will primarily remain neutral; as a result, these compounds will be computationally assessed in their most prevalent state (charged, and neutral respectively). As both **4.28** and **5.19**

generated intramolecular ring conformations through the amide nitrogen as a hydrogen bond donor, compound **4.28** was *N*-methylated (compound **5.25**) as a control, removing the capacity for the amide nitrogen to participate in intramolecular hydrogen bonding interactions.

When substituting an O_4 ether (only hydrogen bond accepts) at the C_4 position (compound **5.19**) for a N_4 secondary ammonium (only hydrogen bond donates, compound **5.21**), a six membered ring is still observed as the lowest energy conformation (**Figure 5.13**). In contrast, when the installed secondary nitrogen is shifted to the C_3 position (**5.24**), a 9-membered ring is observed as the lowest energy conformation (**Figure 5.13**). A 9-membered ring is also observed as the lowest energy conformation when a S_4 thioether (unable to participate in hydrogen bonding interactions, compound **5.22**) is installed at the C_4 position (**Figure 5.13**). It may be worth noting that the calculated lowest energy conformation of compound **5.22** was found to generate an intramolecular hydrogen bond with the amide as a hydrogen bond donor, while **5.24** utilized a hydrogen bonding interaction with the amide carbonyl as a hydrogen bond acceptor. When the amide is methylated (**5.25**), no intramolecular ring is observed in the lowest energy conformation, forming instead a bent structure (a 80° angle is formed about the amide carbonyl) (**Figure 5.13**). Despite not forming a ring, the conformation calculated for compound **5.25** still greatly differs from the rigid linear conformation found with gluconamide IRIs (such as **4.01**). From these computed conformations, it would be expected that **5.22** and **5.24** (forming 9-membered rings) would possess IRI activity, and **5.21** (being more stabilized in a 6-membered ring), would not possess IRI activity. Compound **5.25** could provide information as to conformational tolerance, as it is not constrained into an intramolecular ring, but is not fully linear like the conformations observed with **4.01**.

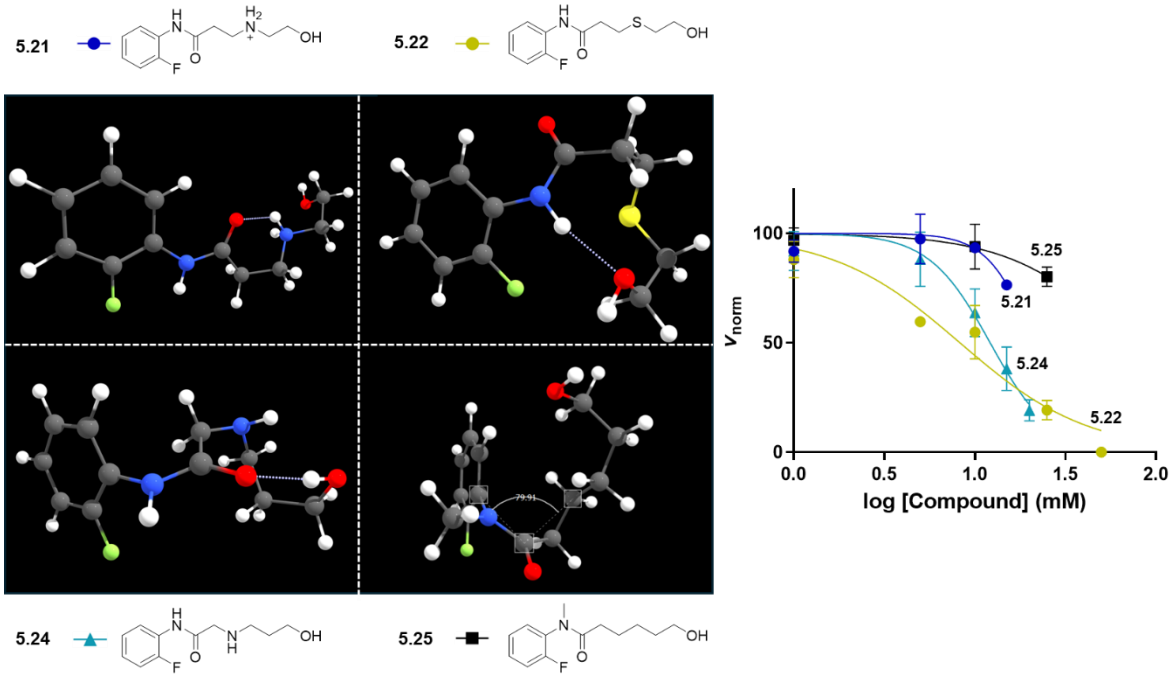

Figure 5.13 Computational assessment of compound set relating to known IRI **4.01** targeting the ability for C_4 to hydrogen bond with the amide. Each compound indicator number, legend symbol and line structure are represented above or below the respective ORCA optimized 3-dimensional structure. Optimized geometry is visualized as ball and stick diagrams with Chemcraft software. Hydrogen bonding interactions are represented with a dashed white line (hydrogen bonding length ≤ 2.0 Å). IRI activity for each compound is represented with the four-parameter dose response curve obtained from the modified SCA.

IRI assessment of compounds **5.19** and **5.21**, clearly indicate that the formation of highly stabilized 6-member intramolecular ring structures is not tolerated in 6-hydroxyhexylamide derived small molecules, as no measurable IRI activity observed. This is supported by the highly IRI active control compound **5.22** (IC_{50} = 8 mM) demonstrating tolerance to heteroatom substitution at the C_4 position as long as hydrogen bonding is not accessible. Tolerance of to the installation of a secondary amine away from the C_4 position is also demonstrated with compound **5.24** (IC_{50} = 12 mM). These observations support the hypothesis that the IRI inactivity of compound **5.18** is likely due to a highly stabilized intramolecular interaction preventing interaction with bulk water molecules. However, this does not completely explain the lack of improved aqueous solubility expected for compound **5.19** (25 mM), as neither compound **5.21** (15 mM) or **5.24** (20 mM) improve aqueous solubility with respect to **4.28** (25 mM).

Compound **5.25** was found to be IRI inactive (**Figure 5.13**), this matches the intolerance to *N*-methylation previously reported for compound **5.04**.[8,12] This finding reinforces the hypothesis

that the conformational change as a result of *N,N*- dialkylation is detrimental to IRI activity. As there are no intramolecular interactions are present in the lowest energy conformation for compound **5.25**, it highlights that both amide alkylation and the formation of a 6-membered intramolecular ring are separate conformations which negatively impact IRI activity. As the ability to overcome the negative impact of *N,N*-dialkylation was established through the use of two large alkyl groups (compound **5.11**); it is possible that further functionalization (such as the installation of non-hydrogen bonding heteroatoms) could result in an IRI active derivative, despite the formation of an intramolecular 6-membered ring.

When assessing the lowest energy conformation of *N*-alkyl derivatives, it is difficult to confidently define a single conformation as being the lowest energy. When performing a conformational search on compound **5.14**, the CREST optimized geometry (**Figure 5.14**) was reported as a total Gibbs energy of -756.0004614 E_h. When selecting for the lowest energy conformation containing an intramolecular ring (structure +22, +0.95 kcal / mol with respect to the optimized structure), the final optimized structure was calculated to have a total Gibbs energy of -756.000546 E_h; this translates to a Δ 0.05 kcal / mol difference in energies with respect to the CREST optimized structure and the formation of a 9-membered ring. The lack of differentiation between two different optimized conformations of the same molecule suggests either there is not one specific conformation representing a global minima, or the computational approach employed is not able to accurately identify it. When attempting to optimize the 22nd best conformer found for *N*-aryl gluconamide (**4.01**) for comparison, calculations could not converge, indicating no minima was found and the submitted conformation could not be optimized.

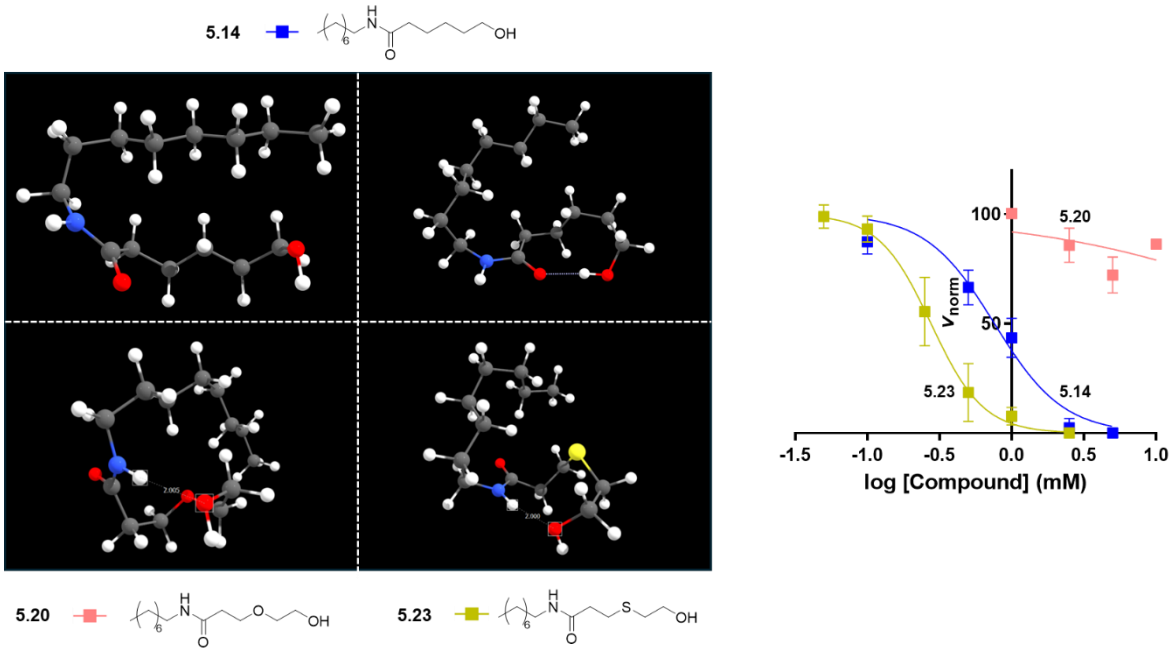

Figure 5.14 Computational assessment of compound set relating to **5.14**, targeting the tolerance for hydrogen bond acceptor at the C_4 position. Compound **5.14** is represented in both the lowest energy CREST optimized geometry (Left), as well as the lowest energy conformation found by CREST to contain an intramolecular 9-membered ring (Right). Optimized geometry is visualized as ball and stick diagrams with Chemcraft software. Hydrogen bonding interactions are represented with a dashed white line (hydrogen bonding length ≤ 2.0 Å). The distance between N-**H** and C_6-**O**H is indicated (in white text, Å) for compounds **5.20** and **5.23** to highlight the similarities between conformations. IRI activity for each compound is represented with the four-parameter dose response curve obtained from the modified SCA.

Computational assessment of compounds **5.20** and **5.23** further complicate the investigation of *N*-alkyl gluconamides; both compounds were found to have virtually identical lowest energy conformations, but vastly different IRI activities (**Figure 5.14**). When assessed for IRI activity, **5.23** was found to be one of the most active compounds tested within this work (IC_{50} = 0.3 mM) with an improved maximum aqueous solubility (2.5 mM) with respect to **5.04** (0.5 mM). By contrast, compound **5.20** was found to be IRI inactive. This experimental assessment matches the intolerance to the introduction of a hydrogen bonding heteroatom at the C_4 position observed with *N*-aryl derivatives (**5.19**, **5.21**). However, due to the size and degrees of freedom afforded by long unsaturated alkyl chains, it is unlikely that any given structural optimization with the given computational power will find the global minima, or in turn identify a common active conformation. Despite the inability to effectively utilize the implemented computational approach for *N*-alkyl gluconamides, the assessed tolerance to modification and generation of compound **5.23** represent an exciting progression in the development of small molecule IRIs.

5.5 Conclusions

Section 5.2 aimed to standardize the assessment of *N*-alkyl gluconamide IRIs on the modified SCA. The assessment of linear *N*-alkyl gluconamides (**Figure 5.4 (A)**) reinforced the established[1] requirement for a balance between hydrophilic and hydrophobic components. The smaller alkyl substituent (**5.01**) was found to be an order of magnitude less IRI active than derivatives bearing a longer alkyl chain (**5.02** – **5.04**). In direct contrast, the *N*-cycloalkyl gluconamide derivates assessed were found to have no correlation between alkyl ring size and IRI activity (**Figure 5.4 (B)**). The restricted degrees of rotational freedom for *N*-cycloalkyl derivatives is thought to play a role in the reduced IRI activity, whereby increasing the size of the cycloalkyl does not meaningfully increase the disruption of bulk water. It was noted that both linear and cyclic alkyl gluconamide derivatives demonstrate an inverse exponential relationship between alkyl size and maximum aqueous solubility (**Figure 5.5**). *N*-cycloalkyl gluconamides were found to possess a solubility plateau beyond a 6-membered ring (at approximately 30 mM), while linear *N*-alkyl derivatives were found to decrease exponentially beyond a 6-membered chain.

N,N-dialkyl gluconamide derivatives (**5.10**, **5.11**) were found to be highly IRI active (**Figure 5.6 (A)**), while retaining comparable maximum aqueous solubility when compared to the respective mono-alkylated counterpart. This finding contradicts the previously reported IRI inactivity of *N*-methylated **5.04**; it is hypothesized that *N,N*-dialkylation is detrimental to IRI activity, but the installation of a larger (hexyl opposed to methyl) alkyl group compensates for the conformational change, resulting in IRI activity. Despite the promising IRI activity, it was hypothesized that the generated *N,N*-dialkyl gluconamide derivatives would be prohibitively toxic to cellular membranes. All hexyl functionalized gluconamides (**5.02**, **5.07**, **5.10**, **5.11**) were assessed for cytotoxicity in HepG2 cells following 24-hour incubation. Using a metabolic indicator of cellular viability (resazurin), *N,N*-dialkylation was found to drastically increase the measured cytotoxicity with respect to the monoalkylated derivative (**Figure 5.3.2 (B)**). To confirm that the observed cell death was more accurately caused by cell membrane damage, a membrane-based indicator of cellular death (LDH) was utilized. With the metabolic and membrane-based indicators of cellular death producing the same LD_{50} values for compound **5.10**, the observed cytotoxicity was very likely due to damage to the cellular membrane (**Figure 5.6 (C)**).

From the assessment of *N*-alkyl gluconamides, a general baseline for IRI activity (~1 mM) and aqueous solubility (≤ 10 mM) was established for the family of small molecule IRIs. It was established that *N,N*-dialkylation can be tolerated with respect to IRI activity, but the increase in hydrophobicity was found to also impart surfactant-like membrane toxicity. Compound **5.11** was

identified as a highly active novel IRI with a positive efficacy index ($EI_{\mathbf{5.11}}$ = 6.1) and outstanding aqueous solubility (75 mM). It is worth noting that the application of compound **5.11** should be avoided for any biological applications where membrane instability is a prime concern (such as red blood cells or spermatozoa[34]), but could otherwise be a promising CPA candidate.

Compound **5.04** was chosen for structure activity relationship examination following a process similar to the investigation of compound **4.01** described in **Chapter 4**. The selection of compound **5.04** was due to a larger library of precedent work. Investigation first focused on the incremental truncation of the carbohydrate chain (**Scheme 5.1**), resulting in a set of modified **5.04** derivatives which consisted of an *N*-octyl chain and incrementally less hydroxyls (**Figure 5.7**). No correlation was evident when examining the incremental truncation of **5.04**; both IRI activity and maximum aqueous solubility were variable, resulting in no compound possessing a complete dose-response relationship (**Figure 5.7**). It was noted that all **5.04** derivatives improved upon the maximum aqueous solubility. The direct modification to *N*-alkyl-6-hydroxyhexanamide (**5.14**) was attempted. Having established precedent that the C_6 position is not tolerant to functionalization, it was reasoned that some IRI activity may be retained through the retention of only the C_6 hydroxyl. Serendipitously, it was found that compound **5.14** possessed improved aqueous solubility with respect to **5.04**, with complete retention of IRI activity (**Figure 5.8**).

The generation of compound **5.14** invigorated the examination of *N*-alkyl gluconamides, providing a scaffold molecule that possessed minimal required functionality. *O*-alkylation at the C_6 position was found to also be tolerated (**Scheme 5.3**), but the generation of a C_5 primary hydroxyl was not found to be tolerated. The retention of IRI activity when generating 6-hydroxyhexylamide derivatives was found to not be exclusive to *N*-octyl functionalization, as compound **5.13** demonstrated equivalent IRI activity to fully furnished **5.02**. Similar to the generation of compounds **5.10** and **5.11**, it was hypothesized that the modification to *N*-alkyl-6-hydroxylhexylamides would also impart an increase in cytotoxicity. Instead, it was determined that this was not the case, and that 6-hydroxylhexylamide derivatives possessed similar cytotoxicity (measured metabolically) to the reference gluconamides. IRI active 6-hydroxyhexylamide derivatives **5.13**, **5.14** present exciting scaffolds for future IRI development.

Section 5.4 aimed to leverage computational analysis of the model compounds generated in **Chapter 4** and **Chapter 5** to help rationalize the experimental trends presented. Specifically, the increased aqueous solubility as a result of dehydroxylation was of particular interest. It was reasoned that the removal of one or more hydroxyl from the polyol chain will interrupt the intramolecular hydrogen bonding network as well as increase the flexibility of the carbohydrate

chain. The lowest energy conformation calculated for compound **4.26** (with respect to **4.01**) highlights the loss of intramolecular hydrogen bonding interactions along the polyol chain (**Figure 5.12**). The assessment of PEG derivatives (**5.19**, **5.20**) aimed to provide an isostere between polyol chain and alkyl chain with respect to capacity to hydrogen bond, and flexibility. Through the generation of PEG_1 IRI derivatives (**5.19**, **5.20**) IRI activity was lost, and no change in aqueous solubility was observed with respect to 6-hydroxyhexylamide derivatives (**Figure 5.4.1.2**). The computational assessment of these PEG_1 derivatives suggested the O_4 ether is likely interacting with the intramolecular amide opposed to interacting with bulk water (**Figure 5.12**), which would rationalize these observations.

The lowest energy conformation obtained for compound **5.19** was of particular interest (**Figure 5.12**), whereby the formation of a stabilized intramolecular ring appeared to impact the resulting IRI activity. To assess the impact of heteroatom substitution targeting the formation of intramolecular hydrogen bonding interactions, a series of molecules were generated (**Scheme 5.5**). The installation of a N_4 ammonium (**5.21**) was generated to allow for the amide to act as a hydrogen bond acceptor when forming an intramolecular 6-membered ring. S_4 thioether (**5.22**) and N_3 amine (**5.24**) derivatives were generated as controls, incorporating a heteroatom without the capacity to generate highly stabilizing hydrogen bonding interactions. The capacity to form of a stable 6-membered ring (**5.19**, **5.21**) was found to result in no measurable IRI activity (**Figure 5.13**). Control compounds **5.22** and **5.24** were both found to be comparatively IRI active to hit compound **4.26** (**Chapter 4**), demonstrating not only a tolerance, but a preference for heteroatom functionalization for 6-hydroxyhexylamide derivatives. This highly suggests that it is the formation of a highly stabilized intramolecular ring which is negatively impacting IRI activity.

The assessment of methylated derivative **5.25** reinforces the hypotheses that amide methylation results in a conformational change which is detrimental to IRI activity; this conformation being distinct from the stabilized intramolecular interactions hypothesized to quench IRI activity in compounds **5.19** and **5.21**. As was demonstrated with compound **5.11** (**Figure 5.6**), it may be possible to overcome this IRI inactive conformation with further derivatization, but the formation of highly stabilized intramolecular interactions should be avoided if possible in future hydroxyhexylamide IRI development.

Computational assessments were focused exclusively on *N*-aryl functionalized molecules as the computational workflow utilized (**Appendix III**) was not capable of reliably resolving *N*-alkyl derived compounds. *N*-alkyl 6-hydroxyhexylamide derivatives are equally chemically accessible as *N*-aryl derivatives, allowing for the targeted assessment of *N*-octyl O_4 ether (**5.20**) and S_4

thioether (**5.23**) derivatives for direct comparison to *N*-(2-flurophenyl) counterparts (**5.19**, **5.22** respectively). As observed with *N*-aryl derivatives, an on-off relationship was observed, whereby the O_4 ether resulted in no measurable IRI activity, and the S_4 thioether was not only IRI active, but the most IRI active small molecule derivative characterized to date (**Figure 5.14**). It would be suspected that this relationship mirrors the computational assessment of *N*-aryl derivatives (whereby a highly stabilizing intramolecular interaction quenches the IRI activity of **5.20**) but can not be verified computationally with the utilized workflow. Further work will be required to assess rationale as to the increase in IRI activity observed through the introduction of an N_3 amine or S_4 thioether. From this work a novel set of highly synthetically flexible IRI active molecules have been identified. Moving forward, biological assessment (cytotoxicity, functional application) of 6-hydrohexylamide derivatives (**5.22**, **5.23** in particular) is required to assess the practical impact of this work for the development of novel small molecule CPAs.

5.6 References

(1) Tam, R. Y.; Ferreira, S. S.; Czechura, P.; Chaytor, J. L.; Ben, R. N. Hydration Index—A Better Parameter for Explaining Small Molecule Hydration in Inhibition of Ice Recrystallization. *J. Am. Chem. Soc.* **2008**, *130* (51), 17494–17501. https://doi.org/10.1021/ja806284x.

(2) Czechura, P.; Tam, R. Y.; Dimitrijevic, E.; Murphy, A. V.; Ben, R. N. The Importance of Hydration for Inhibiting Ice Recrystallization with C-Linked Antifreeze Glycoproteins. *J. Am. Chem. Soc.* **2008**, *130* (10), 2928–2929. https://doi.org/10.1021/ja7103262.

(3) Trant, J. F.; Biggs, R. A.; Capicciotti, C. J.; Ben, R. N. Developing Highly Active Small Molecule Ice Recrystallization Inhibitors Based upon C-Linked Antifreeze Glycoprotein Analogues. *RSC Adv.* **2013**, *3* (48), 26005–26009. https://doi.org/10.1039/C3RA43835J.

(4) McMunn, L. E.; D'Costa, A. S.; Bordenave, N.; Ben, R. N. Probing the Mechanism of Action of Small-Molecule Ice Recrystallization Inhibitors Using Proton Nuclear Magnetic Resonance Relaxation. *J. Phys. Chem. Lett.* **2023**, *14* (26), 6043–6050. https://doi.org/10.1021/acs.jpclett.3c00845.

(5) De, S.; Malik, S.; Ghosh, A.; Saha, R.; Saha, B. A Review on Natural Surfactants. *RSC Adv.* **2015**, *5* (81), 65757–65767. https://doi.org/10.1039/C5RA11101C.

(6) Ollivon, M.; Eidelman, O.; Blumenthal, R.; Walter, A. Micelle-Vesicle Transition of Egg Phosphatidylcholine and Octylglucoside. *Biochemistry* **1988**, *27* (5), 1695–1703. https://doi.org/10.1021/bi00405a047.

(7) Lorber, B.; Bishop, J. B.; DeLucas, L. J. Purification of Octyl β-d-Glucopyranoside and Re-Estimation of Its Micellar Size. *Biochim. Biophys. Acta BBA - Biomembr.* **1990**, *1023* (2), 254–265. https://doi.org/10.1016/0005-2736(90)90421-J.

(8) Capicciotti, C. J.; Leclère, M.; Perras, F. A.; Bryce, D. L.; Paulin, H.; Harden, J.; Liu, Y.; Ben, R. N. Potent Inhibition of Ice Recrystallization by Low Molecular Weight Carbohydrate-Based Surfactants and Hydrogelators. *Chem. Sci.* **2012**, *3* (5), 1408–1416. https://doi.org/10.1039/C2SC00885H.

(9) Henriksen, J. R.; Andresen, T. L.; Feldborg, L. N.; Duelund, L.; Ipsen, J. H. Understanding Detergent Effects on Lipid Membranes: A Model Study of Lysolipids. *Biophys. J.* **2010**, *98* (10), 2199. https://doi.org/10.1016/j.bpj.2010.01.037.

(10) Liu, S.; Ben, R. N. C-Linked Galactosyl Serine AFGP Analogues as Potent Recrystallization Inhibitors. *Org. Lett.* **2005**, *7* (12), 2385–2388. https://doi.org/10.1021/ol050677x.
(11) Chong, T. T.; Hashim, R.; Bryce, R. A. Molecular Dynamics Simulation of Monoalkyl Glycoside Micelles in Aqueous Solution: Influence of Carbohydrate Headgroup Stereochemistry. *J. Phys. Chem. B* **2006**, *110* (10), 4978–4984. https://doi.org/10.1021/jp056851g.
(12) Capicciotti, C. J. The Rational Design of Potent Ice Recrystallization Inhibitors for Use as Novel Cryoprotectants. PhD Thesis, University of Ottawa, 2014.
(13) Tam, R. Y. Studies Into the Structural Features of C-Linked Antifreeze Glycoprotein Analogues Responsible for Ice-Recrystallization Inhibition Activity. PhD Thesis, University of Ottawa, 2011.
(14) Briard, J. G. The Rational Design and Use of Novel Small-Molecule Ice Recrystallization Inhibitors for the Cryopreservation of Hematopoietic Stem Cells and Red Blood Cells. PhD Thesis, University of Ottawa, 2016.
(15) Newell, K. Enabling the Effective Transport of RNA Oligonucleotide Constructs and RNA Viruses: Preservation and Stabilization of Viruses Using Ice Recrystallization Inhibitors. Unpublished Honours Thesis, University of Ottawa, 2021.
(16) Balcerzak, A. K. Elucidating the Key Structural Features of Carbohydrates and Surfactants Necessary for Inhibiting Ice Recrystallization. PhD Thesis, University of Ottawa, 2014.
(17) Hildreth, J. E. K. *N* - D -Gluco- *N* -Methylalkanamide Compounds, a New Class of Non-Ionic Detergents for Membrane Biochemistry. *Biochem. J.* **1982**, *207* (2), 363–366. https://doi.org/10.1042/bj2070363.
(18) Knight, C. A.; Hallett, J.; DeVries, A. L. Solute Effects on Ice Recrystallization: An Assessment Technique. *Cryobiology* **1988**, *25* (1), 55–60. https://doi.org/10.1016/0011-2240(88)90020-X.
(19) Doshi, M. Synthesis of Nitrogen-Containing Carbohydrate Derivatives and Their Use Toward Inhibiting Ice Recrystallization and Gas Hydrate Formation. PhD Thesis, University of Ottawa, 2016.
(20) Abraham, S.; Keillor, K.; Capicciotti, C. J.; Perley-Robertson, G. E.; Keillor, J. W.; Ben, R. N. Quantitative Analysis of the Efficacy and Potency of Novel Small Molecule Ice Recrystallization Inhibitors. *Cryst. Growth Des.* **2015**, *15* (10), 5034–5039. https://doi.org/10.1021/acs.cgd.5b00995.
(21) Baron, C.; Thompson, T. E. Solubilization of Bacterial Membrane Proteins Using Alkyl Glucosides and Dioctanoyl Phosphatidylcholine. *Biochim. Biophys. Acta BBA - Biomembr.* **1975**, *382* (3), 276–285. https://doi.org/10.1016/0005-2736(75)90270-9.
(22) Capicciotti, C. J.; Kurach, J. D. R.; Turner, T. R.; Mancini, R. S.; Acker, J. P.; Ben, R. N. Small Molecule Ice Recrystallization Inhibitors Enable Freezing of Human Red Blood Cells with Reduced Glycerol Concentrations. *Sci. Rep.* **2015**, *5* (1), 9692. https://doi.org/10.1038/srep09692.
(23) Ghobadloo, S. M.; Balcerzak, A. K.; Gargaun, A.; Muharemagic, D.; Mironov, G. G.; Capicciotti, C. J.; Briard, J. G.; Ben, R. N.; Berezovski, M. V. Carbohydrate-Based Ice Recrystallization Inhibitors Increase Infectivity and Thermostability of Viral Vectors. *Sci. Rep.* **2014**, *4* (1), 5903. https://doi.org/10.1038/srep05903.
(24) Ampaw, A.; Charlton, T. A.; Briard, J. G.; Ben, R. N. Designing the next Generation of Cryoprotectants – From Proteins to Small Molecules. *Pept. Sci.* **2019**, *111* (1), e24086. https://doi.org/10.1002/pep2.24086.
(25) Helquist, P. Process for 1,10-Phenanthroline Ligands. US6730788B1, May 4, 2004.
(26) Drouin, A.; Winter, D. K.; Pichette, S.; Aubert-Nicol, S.; Lessard, J.; Spino, C. Photochemical Rearrangement of N-Mesyloxylactams: Stereospecific Formation of N-Heterocycles. *J. Org. Chem.* **2011**, *76* (1), 164–169. https://doi.org/10.1021/jo101805q.

(27) Singh, M. K.; Waybright, J.; Zhang, Q. A Facile Method to Enable a Model Phospholipid Cell-Permeable and Photoactivatable. *Tetrahedron* **2017**, *73* (26), 3677–3683. https://doi.org/10.1016/j.tet.2017.04.026.
(28) Bannwarth, C.; Ehlert, S.; Grimme, S. GFN2-xTB—An Accurate and Broadly Parametrized Self-Consistent Tight-Binding Quantum Chemical Method with Multipole Electrostatics and Density-Dependent Dispersion Contributions. *J. Chem. Theory Comput.* **2019**, *15* (3), 1652–1671. https://doi.org/10.1021/acs.jctc.8b01176.
(29) Ehlert, S.; Stahn, M.; Spicher, S.; Grimme, S. Robust and Efficient Implicit Solvation Model for Fast Semiempirical Methods. *J. Chem. Theory Comput.* **2021**, *17* (7), 4250–4261. https://doi.org/10.1021/acs.jctc.1c00471.
(30) Neese, F. The ORCA Program System. *WIREs Comput. Mol. Sci.* **2012**, *2* (1), 73–78. https://doi.org/10.1002/wcms.81.
(31) Chai, J.-D.; Head-Gordon, M. Long-Range Corrected Hybrid Density Functionals with Damped Atom–Atom Dispersion Corrections. *Phys. Chem. Chem. Phys.* **2008**, *10* (44), 6615–6620. https://doi.org/10.1039/B810189B.
(32) Hellweg, A.; Rappoport, D. Development of New Auxiliary Basis Functions of the Karlsruhe Segmented Contracted Basis Sets Including Diffuse Basis Functions (Def2-SVPD, Def2-TZVPPD, and Def2-QVPPD) for RI-MP2 and RI-CC Calculations. *Phys. Chem. Chem. Phys.* **2014**, *17* (2), 1010–1017. https://doi.org/10.1039/C4CP04286G.
(33) Barone, V.; Cossi, M. Quantum Calculation of Molecular Energies and Energy Gradients in Solution by a Conductor Solvent Model. *J. Phys. Chem. A* **1998**, *102* (11), 1995–2001. https://doi.org/10.1021/jp9716997.
(34) Giraud, M. N.; Motta, C.; Boucher, D.; Grizard, G. Membrane Fluidity Predicts the Outcome of Cryopreservation of Human Spermatozoa. *Hum. Reprod.* **2000**, *15* (10), 2160–2164. https://doi.org/10.1093/humrep/15.10.2160.

6. Conclusions and future work

6.1 Conclusions

The goal of this thesis was to identify and explore novel modifications towards the development of next-generation cryoprotective agents (CPAs). To achieve this goal, the decades of previous CPA characterization performed by the Ben lab was leveraged. Utilizing compounds of known ice recrystallization inhibition (IRI) activity, an underexplored cryopreservation phenomena (ice nucleation activity (INA)) was examined in **Chapter 3**; while introspective assessments of established families of small molecule carbohydrate IRIs were explored in **Chapter 4** and **Chapter 5**. From this work, novel applications, novel IRI active derivatives, and furthered structural understanding of small molecule carbohydrate CPAs was obtained.

Objective 1 of this thesis was to identify the relationship between INA and IRI activity. This involved the assessment of INA activity for small molecule carbohydrates of known IRI activity. In complement, IRI activity in the presence of INA active silver iodide (AgI) particles on the modified splat cooling assay (SCA) was also assessed. The small molecule carbohydrates possessing IRI activity were not found to strongly influence ice nucleation temperature when compared to traditional INAs. IRI inactive **3.05** was identified as the most active suppressor of ice nucleation, which coincides with the previous assessment of **3.05** utilizing the emulsion freezing assay. The IRI assessment of small molecule carbohydrates was found to be agnostic of the presence of INA active AgI particles. These findings together suggest that for small molecule carbohydrates, the phenomena of INA and IRI are not related. This finding does not coincide with the synergistic relationship reported in IRI active macromolecules but also does not indicate any antagonistic interactions.

During the INA assessment of small molecule carbohydrates, it was noted that *p*-bromophenyl containing compounds (**3.02** and **3.04**) reliably nucleated all samples within a narrow range (within approximately 10 seconds). This narrow range of nucleation was only observed for compounds **3.02** and **3.04**, while known ice nucleator Snomax® was found to nucleate over the course of several minutes. With assistance from Waren Mendizza (Honours student) and Sarah Musca (Honours student), *p*-chloroaryl containing compounds **3.06** and **3.07** were also identified as reliably nucleating ice in a narrow range. It was noted that the concentration of compound required for a narrow nucleation range was found to be higher in *p*-chloroaryl containing compounds than *p*-bromophenyl containing compounds. As a charged Wittig salt, compound **3.07** demonstrated

that the observed narrow nucleation range is dependent on the *p*-haloaryl present, opposed to the carbohydrate moiety.

While assessing known small molecule carbohydrate IRIs for INA activity, **Objective 2** of this thesis examined the pharmacophore of *N*-aryl gluconamides. To assess the positional importance for each hydroxyl present on the carbohydrate chain, a synthetic scheme was devised to generate incrementally truncated derivatives. Starting with the most successful *N*-aryl gluconamide identified to date (**4.01**), the importance of aryl fluorine regiochemistry was determined through examination of compounds **4.02** and **4.03**. The impact of electron density at the aryl moiety was examined with compound **4.04**. The incremental truncation of IRI active aryl-fluorinated derivatives (**4.01**, **4.02**) indicated that the C_6 hydroxyl is strictly required, as all derivatives without the C_6 hydroxyl were found to be IRI inactive. The modification of IRI inactive **4.03** did not yield any IRI active derivatives. However, the incremental modification of **4.04** did not yield any consistent trend as IRI activity and maximum aqueous solubility fluctuated from one derivative to the next. Compound **4.16** was identified as being particularly IRI inactive, with compound **4.17** (subsequent truncation of compound **4.16**, with the relative removal of the C_4 hydroxyl) being measurably IRI active.

From the information gathered through incremental truncation, the structural requirements for IRI activity were further examined through the selective removal of a hydroxyl identified as less important for IRI activity. The C_4 hydroxyl was selected due to the relative synthetic ease and poor IRI activity of compound **4.16**. The generated C_4-deoxy derivative of **4.01** (**4.26**) did retain measurable IRI activity, while also imparting a ten-fold increase in aqueous solubility. In contrast, the C_4-deoxy derivative of **4.04** (**4.27**) did not yield an IRI active derivative. This finding was surprising as the C_4 position was selected from the screening of **4.04** derivatives, and this finding suggests that a change in aryl substitution directly impacts the positional importance of the carbohydrate polyol chain. As aryl substitution was found to vary the structural components required for IRI activity, a focus was placed directly on the model *N*-aryl gluconamide **4.01**.

As the initial modifications (removal of the C_6 hydroxyl) resulted in a large loss in IRI activity, the C_6 position was identified as a requirement for IRI activity. To probe the functional requirement of the C_6 hydroxyl, *N*-(2-fluorophenyl)-6-hydroxyhexylamide (**4.28**) was synthesized, containing only one hydroxyl, at the C_6 position. As compound **4.28** was found to be measurably IRI active, it provided a baseline for targeted modifications to the C_6 hydroxyl. Selective modification at the C_6 position, removing the ability for **4.28** derivatives to participate in hydrogen bonding interactions resulted in a loss of measurable IRI activity. Moving the hydroxyl from the C_6 position was also

found to negatively impact IRI activity. The intolerance to C_6 modification implies that the C_6 hydroxyl is required to be present with the capacity to participate in hydrogen bonding interactions.

During the generation of *N*-aryl gluconamide analogs, it was noted that through the relative removal of one or more hydroxyls, the maximum aqueous solubility improved with respect to the parent *N*-aryl gluconamide. This unexpected finding prompted **Objective 3** of this thesis: to identify the structural components required for IRI activity in *N*-alkyl gluconamides and generate novel IRI active derivatives with improved aqueous solubility. *N,N*-dialkyl derivatives **5.10** and **5.11** were identified as compounds of interest, possessing similar IRI activity to *N*-alkyl derivatives **5.02** – **5.04** with improved maximum aqueous solubility. These *N,N*-dialkyl derivatives demonstrated a tolerance to amide alkylation, in contrast to previously reported intolerance to amide methylation. With highly hydrophobic functionalization, compounds **5.10** and **5.11** were also identified as being highly cytotoxic (specifically causing membrane instability). These compounds demonstrated the first example of the amide hydrogen not being required for IRI activity and highlight the challenging balance between IRI activity and surfactant-like cytotoxicity for *N*-alkyl gluconamides.

To examine the positional importance of hydroxyls on the *N*-alkyl gluconamide polyol chain, *N*-Octyl gluconamide (**5.04**) was selected for incremental truncation, following the same methodology utilized in **Objective 2**. No derivative of **5.04** was found to be measurably IRI active. However, every derivative improved the maximum aqueous solubility with respect to **5.04**. As the C_6 hydroxyl was identified as a position of importance for compound **4.01**, compound **5.14** was generated, containing only one hydroxyl, at the C_6 position. Compound **5.14** measured equivalent IRI activity as **5.04** while imparting a ten fold increase in aqueous solubility. **5.14** was found to be tolerant to *O*-alkylation, but not to a change in primary hydroxyl position. This indicates that the IRI activity measured in **5.04** is not dependent on the $C_{2\text{-}5}$ hydroxyls or for the C_6 hydroxyl to act as a hydrogen bond donor. When applied to *N*-alkyl gluconamides of differing chain length, IRI activity was not decreased through the generation of 6-hydroxyhexylamide derivatives. However, an increase in maximum aqueous solubility was not observed for derivatives of shorter alkyl chain length. Unlike the *N,N*-dialkyl derivatives assessed, the modification from gluconamide to 6-hydroxyhexylamide did not impart a prohibitive increase in cytotoxicity.

Despite being utilized in the generation of novel *N*-alkyl gluconamide derivatives, it was not known why the targeted removal of hydroxyls generally imparted an increase in aqueous solubility; as these modifications lowered the total number of hydrogen bond donors and acceptors present on the molecule, it was assumed to decrease aqueous solubility. One possible

rationale was that through the removal of a hydroxyl, interactions between the polyol chain was disrupted. To assess this hypothesis, polyethylene glycol (PEG) chains were utilized as an isostere to the polyol chain or alkyl chain. Regardless of *N*-functionalization, the installation of O_4 ether was found to remove IRI activity. This complete loss in IRI activity prompted the computational assessment of model compounds generated during **Objective 2** and **Objective 3** to assess the lowest energy conformation in aqueous solution.

Utilizing Digital Research Alliance of Canada's computational servers, a conformation search was performed on compounds generated during **Objective 2** and **Objective 3**, with the lowest energy conformer being optimized at a higher level of theory. As there was no literature precedent for *N*-functionalized gluconamide structural conformations, the computational analysis performed were utilized only to help direct the targeted synthetic assessments. From the conformation searches performed, two observations were made: gluconamides are highly stabilized by intramolecular hydrogen bonding interactions along the polyol chain, and the installation of an O_4 ether allows for a highly stabilized intramolecular hydrogen bonding interaction with the amide hydrogen. The former observation aids in explaining the increase in aqueous solubility observed, whereby interrupting the intramolecular polyol hydrogen bonding interactions hydroxyls present are more likely to interact with bulk water. The ladder observation was of particular interest, as it was not known if the 6-hydroxyhexylamide derivatives would be tolerant to chain substitution. Upon examination, the *N*-functionalized 6-hydroxyhexylamide scaffold was found to benefit from chain substitution, as long hydrogen bonding interactions were not accessible at the C_4 position. In the process, compounds **5.22**, **5.23** and **5.24** were identified as highly IRI active small molecules, with compound **5.23** being the most IRI active carbohydrate derived small molecule assessed to date.

6.2 Future work

The work presented in this thesis continues to advance the functional understanding of small molecule CPAs, unfortunately the collective understanding of these compounds and their application are not complete. **Chapter 3** of this thesis suggests that the phenomena of INA and IRI activity do not interact for small molecule carbohydrates. This finding should be examined with other sources of ice nucleation activity, which are ideally both homogenous and biocompatible. The work presented in **Chapter 3** also identified small molecules capable of reliably inducing ice nucleation in a very narrow temperature range. All compounds assessed with a narrow nucleation range bore a *p*-halogenated aryl motif, further examination is required to identify the structural tolerance of this observation. The importance of halogen stereochemistry, tolerance to poly-

halogenation, and importance of aromaticity are valuable investigations. Compound **3.07** demonstrates that the small molecule does not need to be a carbohydrate to nucleate ice in a narrow range, justifying the examination of a myriad of CPA relevant small molecule scaffolds. Once a catalog of compounds of known INA activity is obtained, the translation from isolated hydrophobic droplet to cellular media is required. The assessment of not only the capacity to influence ice nucleation, but the functional impact of ice nucleation temperature on post-thaw recovery, viability, and functionality will be instrumental to establishing small molecule INA development and implementation as CPAs.

The work presented in **Chapter 4** and **Chapter 5** of this thesis highlight a collection of observations related to the structural tolerance of *N*-functionalized gluconamide derived small molecules. As the mechanism of action for these CPAs is not fully understood, it is difficult to state definitively that the synthetic tolerance of one small molecule IRI directly translates to another. Broadly, from the examinations preformed, *N*-aryl gluconamides are less tolerant to modification when compared to *N*-alkyl gluconamides. With scaffolds **4.28** and **5.14** identified, it may be more amenable to develop functionalized 6-hydroxyhexylamide derived IRIs opposed to traditional gluconamides. Translation from positive *in vitro* activity to *ex vivo* cryopreservation outcomes will be vital to the future development of 6-hydroxyhexylamide derived IRIs. Compounds **4.26**, **5.23**, and **5.25** all represent intriguing CPA candidates, however, without a clearer mechanistic understanding of IRI activity, the development of novel small molecule IRIs will remain restricted. The use of live cell imaging or molecular dynamics simulations may be required to eventually elucidate the mechanism(s) of small molecule IRI activity, with both approaches posing extreme difficulty for the target system at this time.

Appendices

Appendix I. Contribution to original research

1. Implementation of the Freeze-Float assay in the Ben laboratory as described in **Chapter 3**. INA assessment of compounds **3.01** – **3.05**, **4.01**, **4.04**, and synthesis of compounds **3.02**, **3.04**, **4.01**, **4.04**. Assessment of IRI activity of small molecule carbohydrates (**3.01** – **3.05**, **4.01**, **4.04**) in the presence of INA active AgI / PBS suspension. The INA assessment of compounds **4.01** and **4.04** in AgI / PBS was performed with Ellyssa Walsh. The physical implementation of equipment and assessment of generated operating procedures was performed with assistance from Ellyssa Walsh and Leah McMunn. Samples of compounds **3.01**, **3.03** and **3.05** were graciously provided by Dr. Madeline Adam (previous Ben lab member).
2. Assessment of small molecule compounds containing a *p*-halogenated aryl motif which were identified and assessed as possessing the capacity to induce ice nucleation in a reliably narrow temperature range. This includes the acquisition of dose-response relationship of compounds **3.02**, **3.04**, **3.06**, **3.07**. The synthesis of compound **3.06** was performed with Warren Mendizza, and the synthesis and INA analysis of compound **3.07** was performed with Sarah Musca.
3. Synthesis and IRI assessment of *N*-aryl gluconamide IRIs through systematic modification as presented in **Chapter 4**. This includes derivatives possessing a truncated polyol chain (**4.09** – **4.25**), selectively dehydroxylated derivatives (**4.26** – **4.30**), and C_6 modified derivatives (**4.31** – **4.35**). IRI assessment of anilines (**4.05** – **4.08**).
4. Synthesis and IRI assessment of *N*-(cyclo)alkyl gluconamide derivatives as described in **Chapter 5**. This includes linear (**5.01** – **5.04**), cycloalkyl (**5.05** – **5.09**) and *N,N*-di(cyclo)alkyl (**5.10**, **5.11**) derivatives. Synthesis and IRI assessment of *N*-alkyl gluconamides through systematic modification (**5.12** – **5.17**, **5.27** – **5.29**). The generation and IRI assessment of compounds **5.05** – **5.11** was performed with Cameron Steinke.
5. Computational assessment of small molecule carbohydrates presented in **Chapters 3** – **5** was performed through access to the Digital Research Alliance of Canada's computational servers. Initial guidance for computational assessments was provided by Leah McMunn (who received initial guidance from Professor Fabien Gagosz) as to operation procedures and variable selection. Synthesis and IRI analysis of computationally targeted **4.01** and **5.04** derivatives (**5.19** – **5.27**).

6. Assessment of cytotoxicity (Resazurin or LDH viability assay) presented in **Chapter 5** was performed with guidance from Leah McMunn. The assessment of compounds **5.02**, **5.13** and **5.14** utilizing the Resazurin cellular viability assay. The assessment of compounds **5.07**, **5.10**, and **5.11** utilizing the Resazurin cellular viability assay was performed with Cameron Steinke. The assessment of compound **5.18** and all assessments made with the LDH cellular viability assay were performed with Leah McMunn.

Appendix II. Thesis and non-thesis related publications and presentations

Publications relating to described work in thesis

1. **Diamante, M. F.**; Walsh, E. M; Ben, R. N. Interaction between Ice Recrystallization Inhibition Activity and Ice Nucleation Activity in Small Molecule Carbohydrates. In preparation.
2. **Diamante, M. F.**; Steinke, C. S.; McMunn, L. E.; Ben, R. N. Generation of Next Generation Small Molecule *N*-alkyl Gluconamide Derived Ice Recrystallization Inhibitors. In preparation.

Patents relating to described work in thesis

1. Ben, R. N,; **Diamante, M.** Small Molecule Ice Recrystallization Inhibitors and Methods of Use Thereof. International Patent PCT/CA2024/050977, July 24th 2024.
2. Ben, R. N,; **Diamante, M.**; Paquette, A. Tertiary Amide Aldonamide Based Ice Recrystallization Inhibition Compounds and Compositions and Uses Thereof for Cryopreservation. U.S. Patent US63/725006, November 23rd 2024.

Presentations relating to described work in thesis

1. **Diamante, M. F.***; Ben, R. N. ASSESSING KEY STRUCTURAL ATTRIBUTES FOR CONTROLLING ICE GROWTH IN N-FUNCTIONALIZED GLUCONAMIDES.; **CSC 2025**; Ottawa, ON; June 15th – June 19th, 2025
2. **Diamante, M. F.***; Ben, R. N. Controlling Ice Growth – From Ice Recrystallization to Nucleation; Society for Cryobiology webinar series; Online; November 11th, 2023
3. **Diamante, M. F.***; Walsh, E. M. Ben, R. N.; Identifying the Key Structural Attributes Necessary for IRI Activity in *N*- Functionalized Gluconamides; **Cryobiology 2023**; Minneapolis, MN, USA; July 24th – July 28th, 2023. https://doi.org/10.1016/j.cryobiol.2023.104648

4. **Diamante, M. F.**[*]; Walsh, E. M.; Ben, R. N. Identifying the Key Structural Attributes Necessary for IRI Activity in Aryl Gluconamides; **Cryobiology 2022**; Dublin, Ireland; July 18th – July 22nd, 2022. https://doi.org/10.1016/j.cryobiol.2022.11.099
5. **Diamante, M. F.**[*]; Walsh, E. M.; Ben, R. N. Identifying the Key Structural Attributes Necessary for IRI Activity in Fluorinated Aldonamides.; **CSC 2021**; Online; August 13th – August 20th, 2021
6. **Diamante, M. F.**[*]; Ben, R. N.; Identifying the Key Structural Attributes Necessary for IRI Activity in Fluorinated Aldonamides; **Extreme Cryo 2021**; Online, March 27th, 2021

Presentations relating to non-thesis work

1. Walsh, E. M. [*]; **Diamante, M. F.**; Ben. R. N. Optimizing alkylated ammonium-based compounds for ICE recrystallization inhibition (IRI) activity; **Cryobiology 2023**; Minneapolis, MN, USA; July 24th – July 28th, 2023. https://doi.org/10.1016/j.cryobiol.2023.104609

Appendix III. Experimental methods

Computational assessment of lowest energy conformers

Two-dimensional structures of the target molecule were generated using ChemDraw Prime 22 (version 22.0.0)[2] and exported as a MDL Molfile (.mol) to be interpreted by software (either WebMO online user interface (version 18.1.00e),[3] or Avogadro molecular editor (version 1.99.0)[4]) capable of generating 3-dimensional coordinate structures. Once imported into a 3-dimensional editor, a crude geometry optimization was performed based upon idealized geometry. The prepared initial 3-dimensional structure was then exported as a .XYZ file, containing the atomic coordinates of the input in a plain-text format, serving as one half of the initial optimization input. Initial conformational analysis was performed with Conformer-Rotamer Ensemble Sampling Tool (CREST) (version 2.11)[5,6] through the use of Digital Research Alliance of Canada computational servers. To command the CREST software suite, a Bourne shell script (.sh) was generated with the MobaXterm (version 24.1)[7] office MobaTextEditor; the required support software (GNU Compiler Collection (GCC) version 10.2.0),[8] specified software environment (StdEnv/2020), computational workflow (iMTD-GC),[5] method (GFN2-xTB),[9] solvation model (ALPB),[10] and any additional preferences (such as ignoring initial topography checks) were indicated in the .sh command file (**Figure A1**).

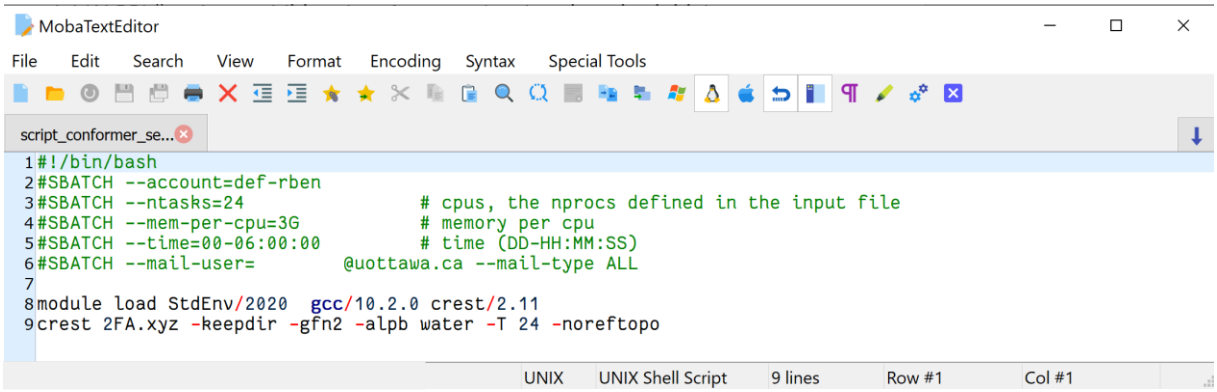

Figure A1 Example shell script input for the CREST conformation search of compound **4.01** .xyz input file.

Both structural information and command script were uploaded to a general use compute server (Digital Research Alliance of Canada) and allowed to run until completion (3 – 24 hours). Once the initial conformation search was completed, the “crest_best.xyz” file was retrieved, as well as “crest_conformers.xyz” representing the single best optimized structure, and the conformers considered during the optimization process respectively. The crest_best.xyz file was visualized with ChemCraft visualizer (version 1.8 build 763bt)[11] and the atomic coordinates were extracted in a 12-didget format. The extracted coordinates, along with computational method (ωB97),[12] basis set (DEF2-TZVPP),[13] and solvation model (CPCM)[14] were used to generate an ASCII input file (.inp) which is used as the main input for final geometry optimization through ORCA (version 5.0.4) (**Figure A2(A)**).[15,16] The selected support software (GCC version 10.3.0,[8] message passing library (openmpi version 4.1.1)[17]), operating environment (StdEnv/2020), and version of ORCA (5.0.4) were specified in a generated shell script (.sh) (**Figure A2(B)**).

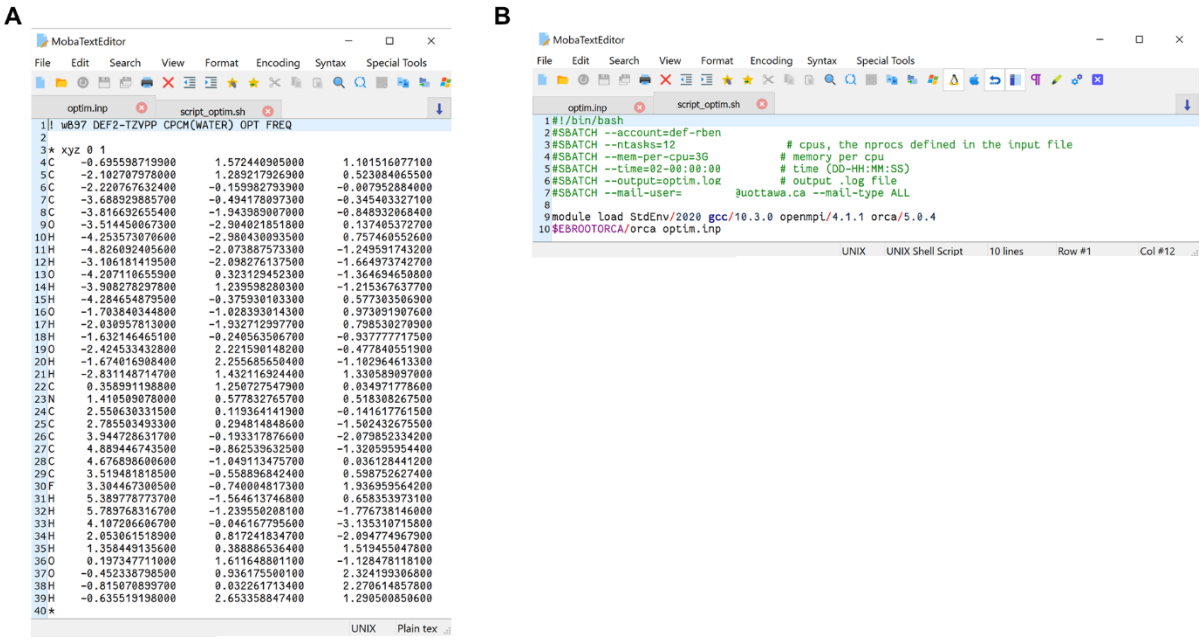

Figure A2 (A) Example structural input file for the ORCA optimization of compound **4.01** which was extracted following CREST optimization (**Figure A1**). **(B)** Example shell script used in conjunction with the structural input file to direct the ORCA optimization suite.

Once generated, the input (.inp) and configuration script (.sh) were uploaded to Digital Research Alliance of Canada server and allowed to process until completion (12 – 36 hours). Once the geometry optimization and frequency calculations were complete, “optim.xyz” and “optim_traj.xyz” were downloaded, containing the final optimized structure and the conformations assessed to obtain the final structure respectively. The data log “optim.log” was also downloaded, as it contains the final calculated energies for the optimized structure. Figures presented in this thesis were visualized with ChemCraft,[11] using the “CPK coloring 1” display preset.

Modified splat cooling assay

The target analyte was dissolved into phosphate buffered saline (PBS) at the highest concentration assessed for the given day. Subsequent concentrations were generated by serial dilutions in PBS. Once solvated, 10 µL of solution was dropped (Gilson, Pipetman P10, F144055M) from a height of 2 m onto an aluminum block (which was pre-cooled with a bed of dry ice for at least 15 minutes). The droplet was rapidly frozen, generating an ice crystal wafer which was then transported into a Peltier thermoelectric cooler (Alpha Omega Instruments, S3 Series 800 temperature controller) on a glass coverslip (Fisherbrand™, FIS12-545-80) using pre-cooled metal tweezers. The ice wafer was allowed to anneal at - 6.7 °C for five minutes. Following the annealing time, the Peltier unit was moved under a camera (Nikon, custom implementation) fitted

microscope and illuminated (OSRAM GmbH, HLX64250). Several ice crystal images were captured (NIS-Elements D (Version 5.30.01, B1541)), with the clearest image being selected for analysis during subsequent data processing steps. Each concentration was assessed in triplicate, generating three distinct ice crystal wafers, and subsequent ice crystal images for analysis.

Analysis of generated ice crystal images was performed with ImageJ (Version 1.53e), whereby the boundary for each distinct ice crystal was defined (with the polygon selection tool) and logged into the region of interest (ROI) manager. The area of selected ice crystals was measured in pixel^2 and converted to mm^2 with a fixed scalar ratio (1 mm : 3775 pixel). A list of crystal areas was imported into a pre-prepared automated excel spread sheet, which sorts each crystal area into a defined bin; any crystal below 0.001mm^2 included in “bin 1” and could be reasonably formed instantaneously upon freezing (no growth during annealing time). Subsequent bins consist of crystals with areas > 0.001mm^2, and are considered to only exist as a function of ice recrystallization during the annealing period. The proportion of crystals (and the proportional ice crystal area) which are not in bin 1 was calculated and used to generate the rate of ice crystal growth observed over the 5-minute annealing period. Growth for a given concentration was then normalized to the rate of ice crystal growth calculated for the PBS control of the day and presented as a normalized rate (v_{norm}). From this analysis, a concentration which achieves an ice crystal growth rate of zero (every crystal was smaller than 0.001 mm^2), was considered to have completely halted recrystallization during the annealing period.

The calculated normalized rates for each concentration of an assessed compound were imported into an X-Y data table in GraphPad Prism 9.0.0 (build 121). The data was then fit to a four-parameter dose response relationship: $Y = P_L + \frac{(P_T - P_L)}{\left(1+10^{\left((Log\ IC_{50} - X) * HillSlope\right)}\right)}$, whereby P_T and P_L are defined as the upper and lower plateau. P_T is fixed to $v_{norm} = 100$, and P_L is fixed to $v_{norm} = 0$ when calculating the dose response relationship.

Freeze-Float ice nucleation activity assay

The desired quantity ((number of cuvettes * 3 mL) + 1 mL) of silicon (light) oil (Shin-Etsu, DM-Fluid-5cs) was transferred into a 50 mL Falcon tube (FroggaBio, TB50-25) using an Eppendorf pipette (Gilson, Pipetman P5000, F144066). 1 % (V / V) emulsifier (Shin-Etsu, KF-6017) was added to the silicon oil using an Eppendorf pipette (Gilson, Pipetman P1000, F144059M), the Falcon tube was then closed tightly and sealed (Bemis™, Parafilm® type M). The sealed Falcon tube was placed securely on a rotor (Thermo Scientific™, 88882003) and allowed to mix at 50

RPM for one hour. For the use of AgI / PBS suspension, 50 mg / mL solid AgI (Millipore Sigma, 99.999%, 204404) was measured into a round bottom flask containing the requisite volume of PBS. The round bottom flask was then immediately sealed with a rubber stopper and wrapped in aluminum foil; the sealed flask was clamped into an ultrasonic cleaner (Branson, B1510R-MT) for 45 minutes at 40 kHz. Immediately following sonication, the AgI / PBS slurry was poured through filter paper (Whatman™ 1, pore size 11 µm) into a glass vial wrapped in aluminum foil.

Target sample preparation follows the same general procedure as the modified splat cooling assay, whereby the compound of interest was weighed into a clean glass vial, and solvent (PBS or AgI / PBS) was added with an Eppendorf pipette (Gilson, Pipetman P1000, F144059M). Solvation may be aided with the application of heat (Black+Decker, HG1300), or by agitation on the rotor. Preparation of Snomax® positive control follows the same procedure, however distilled water was utilized as solvent, and no heating was allowed to assist solvation.

Once the mixing of the light oil – emulsifier solution was complete, cuvettes (Fisherbrand™, 14-386-20) were prepared first with 200 µL of heavy oil (3M™, Novec 7500), and then 3 mL of 1 % emulsifier – light oil solution. Three cuvettes were then transferred into the freezer (Danby DCF038A3SDB) for use in temperature monitoring. The working benchtop space was covered in damp paper towel prior to sample loading to minimize static electricity. A repeater pipette (Eppendorf®, Repeater®, E3x) was then used to load 30 1 µL droplets of sample solution into the light oil layer. It is worth noting that the surface tension of aqueous solution is sufficient to be retained at the end of the pipette tip (Eppendorf®, Combitips® advanced, 0030089405); each droplet needed to be gently touched to the oil surface to facilitate transfer of a whole droplet into the oil layer. Once placed, the cuvette was then transferred (with extreme care as to not agitate) into the center of the freezer. Once all samples were installed, the LED lights (Globe Electric, 12792 LED) were turned on, and the camera (Nikon, D5600) was positioned in front of the sample cuvettes. A USB-C cable was used to connect the camera to a laptop (Dell, Latitude 5420) running Nikon Camera Control Pro (Version 2.25.0). With the laptop settled, the temperature logger (Omega™, RDXL6SD-USB) was powered on, ensuring the time and date are set to match the laptop exactly. Thermocouples (Omega™, 5SRTC-TT-K-40-72-ROHS) were attached to the temperature logger, and the ends were then placed into the 3 temperature cuvettes. Once completely assembled (should take no more than 5 minutes after the completion of light oil mixing), the freezer was closed and powered on (with power dial at half-maximum). Once the coldest thermocouple reads a temperature of 2 °C, temperature was logged at one-second intervals and saved to a SD-card installed in the temperature logger. Using Nikon Camera Control

Pro, the camera field of view was focused on the center cuvette, and images were captured automatically at a set interval (either 1 or 5 seconds). Once all samples have completely nucleated or the temperature measured - 20 °C on all thermocouples, the image and temperature acquisition was stopped, and the freezer was then unplugged. All samples and consumables were discarded, and data (temperature spreadsheet and images) are extracted from respective devices for analysis.

Analysis of collected data was performed with a semi-automated excel spreadsheet, whereby the temperature data was imported, allowing for automatic recall of the average temperature for a given time point. The maximum standard deviation calculated for all collected time points was identified; if < 1.5 °C, analysis can proceed, if ≥ 1.5 °C the collected data was discarded, and the assessment is re-attempted once the system equilibrates back to room temperature. Images were analyzed for ice nucleation events (initial change in opacity is ideal, as it precedes floating by a few seconds), with the time of each event (the creation time of the image) input as a nucleation event on the analysis spreadsheet. Once all nucleation events are logged, statistical analysis can be performed using GraphPad Prism 9.0.0 (build 121).

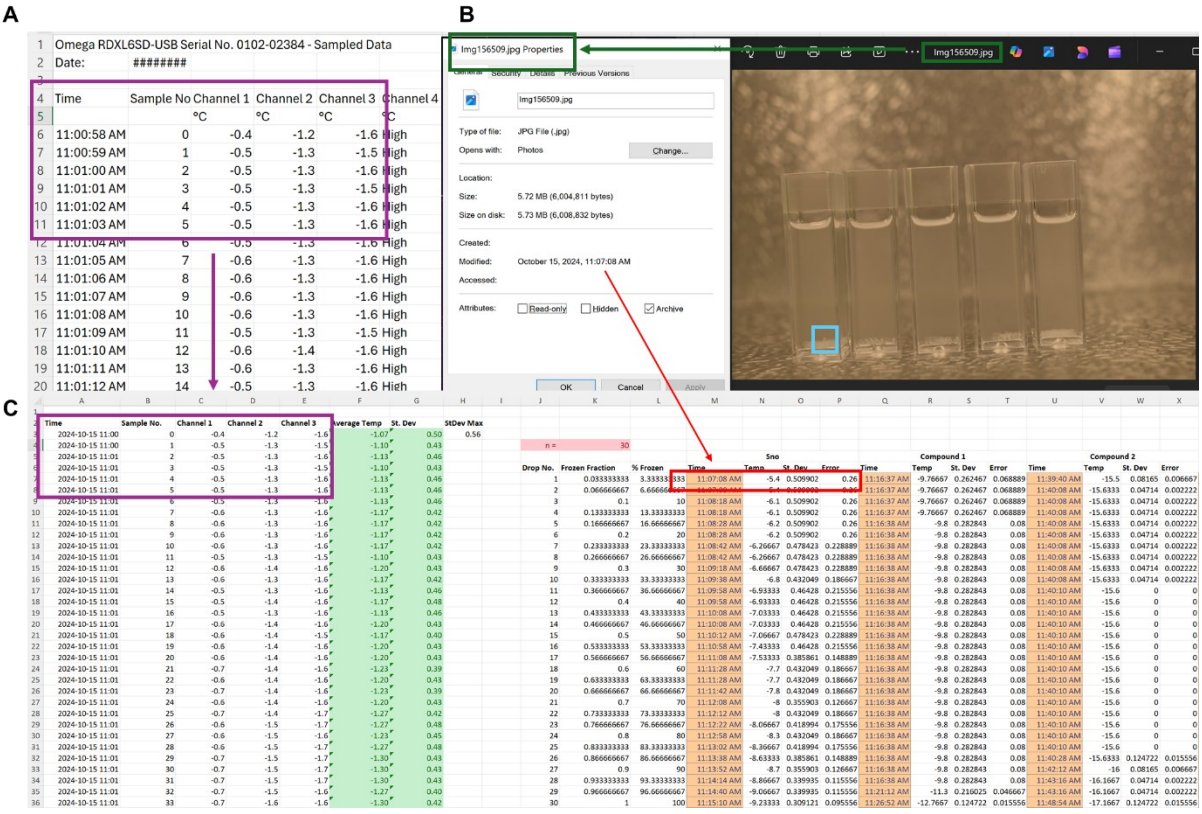

Figure A3 Example workflow for analysis of ice nucleation events. **(A)** Automatically generated spreadsheet obtained from temperature logger. Time, sample number, and channel temperatures are copied from this sheet into the analysis sheet. **(B)** Identification of a nucleation event (outlined with a light blue box), whereby the image creation date is extracted, and used to denote a nucleation event on the analysis sheet (highlighted in red). **(C)** Example analysis sheet, containing temperature data (purple box), whereby the input of a given time (red box) will automatically report the temperature logged at that time. Average nucleation temperature can be extracted from each measured nucleation event.

General cell culture for HepG2 cells

HepG2 cells (human hepatocellular carcinoma cells, ATCC, HB-8065) were cultured in 75 cm^2 flasks (Corning®, CLS-3275) at an initial seeding density of 1.0 x 10^6 cells / mL using Minimum's Essential Medium (MEM, Gibco, 11095080) supplemented with 10 % Fetal Bovine Serum (FBS, Gibco, 10082147), 1 % penicillin-streptomycin (Pen-Strep, Hyclone 100X solution, SV30010), 1 % non-essential amino acids (NEAA, Sigma, M7145), and 0.1 % 1 M sodium pyruvate. The cultured cells were incubated at 37 °C with 5 % CO_2. Cell media was changed every 48 – 72 hours. Once cells reached 80 – 85 % confluency they were washed with Dulbecco's phosphate-buffered saline (DPBS without Ca^{2+} or Mg^{2+}, Gibco, 14190144), then incubated with Accutase (Sigma, A6964) for 15 minutes to detach the cells from the flask. Cells were pelleted by

centrifugation and resuspended in fresh MEM. A hemocytometer was used to obtain a live cell count by using the Trypan blue (Sigma, T8154) exclusion assay. Cells were replated into 75 cm^2 flasks if passaged or used as described below for cytotoxicity assays.

Resazurin Cytotoxicity assay with HepG2 Cells

To assess cytotoxicity by the Resazurin assay, a 96-well plate (Corning®, clear flat-bottom, CLS-3596) was plated with 10,000 cultured HepG2 cells (passage 8 to 13) in 100 µL MEM per well. The plate was incubated at 37 °C and 5 % CO_2 for 24 hours to ensure cell attachment. The media was then aspirated and replaced with 100 µL MEM supplemented with the target compound at the desired concentrations for testing (n ≥ 3 wells per concentration). A set of wells were reserved as blanks with no cells, containing only 100 µL MEM. A set of wells were reserved as the positive control, where the cells were exposed to 100 µL MEM alone. A set of wells were reserved as the negative control, where the cells were exposed to 100 µL MEM containing 1 % Triton-X-100 (Sigma, X100). The plate was incubated with compound for 24 hours at 37 °C at 5 % CO_2. Following incubation, 10 µL of 498 µM resazurin (CAS 62758-13-8) in sterile DPBS was added to each well in the dark. The plate was incubated in the dark at 37 °C in 5 % CO_2 for 4 hours and then fluorescence was recorded by a SpectraMax Absorbance microplate reader using 530 nm as the excitation wavelength and 590 nm as the emission wavelength. The average fluorescence reading from the blank wells was subtracted from all other wells. The metabolic activity for a given test condition was presented as viability (%) normalized to the average of the positive control.

LDH Cytotoxicity assay with HepG2 Cells

Cytotoxicity by lactate dehydrogenase (LDH) assay was assessed using the Pierce LDH Cytotoxicity Assay kit by ThermoFisher Scientific (#88954). A 96-well plate (Corning®, clear flat-bottom, CLS-3596) was plated with 7,500 cultured HepG2 cells (passage 8 to 13) in 100 µL MEM per well. The plate was incubated at 37 °C and 5 % CO_2 for 24 hours to ensure cell attachment. The media was then aspirated and replaced with 100 µL MEM supplemented with the target compound at the desired concentrations for testing (n ≥ 3 wells per concentration). A set of wells were reserved as blanks with no cells, containing only 100 µL MEM. A set of wells were reserved as the positive (spontaneous LDH release) control, where the cells were exposed to 100 µL MEM alone. A set of wells were reserved as the negative (maximum LDH release) control, where the cells were exposed to 100 µL MEM and 10 µL of lysis buffer. The plate was incubated with compound for 24 hours at 37 °C at 5 % CO_2. Following incubation, the cell culture plate was gently agitated and 50 µL of each well's supernatant was transferred to a new 96-well plate (Corning®,

clear flat-bottom, CLS-3596). To the new 96-well plate, 50 µL of the reaction mixture (made from 600 µL of assay buffer + 11.4 mL of substrate stock solution) was added to each well. The plate was gently mixed and then incubated for 30 minutes at room temperature protected from light. After incubation, 50 µL of stop solution was added to each sample well. The plate was gently mixed and then the absorbance of each well was read (within 1 – 2 hours of stop solution addition) by a SpectraMax Absorbance microplate reader at 490 nm and 680 nm wavelengths. The average absorbance reading from blank wells was subtracted from all other wells. The absorbance reading of given test condition was presented as viability (%) calculated using the below formula.

$$\%\ Cytotoxicity = \frac{compound\ treated\ LDH\ activity - spontaneous\ LDH\ activity}{maximum\ LDH\ activity - spontaneous\ LDH\ activity}(100\%)$$

General experimental for chemical synthesis

Chemical reagents were purchased from commercial sources and utilized without further purification unless otherwise stated. Reactions were monitored utilizing thin-layer chromatography (TLC) (SiliaPlate, Aluminum backed, 200 µm, 60 F_{254}) and visualized with ultra-violet lamp (Entela, UVGL-58, 254 nm). TLC visualization agents (Orcinol, *p*-Anisaldehyde, $KmnO_4$) were prepared according to literature,[18] and utilized as required. Flash chromatography was performed utilizing SiliFlash® P60 silica gel and compressed air. Choice of flash column eluent is denoted as a volume / volume percentage of polar component (EtOAc or MeOH) to non-polar component (Hexanes or EtOAc); for example, “30 % EtOAc : Hex” represents a 30 % V / V mixture of EtOAc in hexanes utilized as eluent. The utilization of eluent gradients is denoted with the hyphenated V / V percentages utilized throughout the flash column progress; for example, “30 – 70 % EtOAc : Hex” represents the utilization of a 30 % V / V EtOAc in hexanes solution utilized as the initial eluent, which was transitioned to 70 % V / V EtOAc in hexanes during the flash column progress. All flash column chromatography was performed using a MeOH wash following perceived completion; this wash resulted in the generation of a bulk MeOH fraction which is referred to as the “flush”.

Anhydrous conditions were performed using flame-dried glassware under a positive pressure of Argon (Messer Canada Inc., 100052); oven dried (110 °C) long-needles (VWR International Co., 89234224, 12”, 18G) were utilized for the transfer of air sensitive reagents. Anhydrous solvents were either obtained from solvent purification system (LC Technology Solutions, SPBT-1) (toluene, acetonitrile, dichloromethane) or charged with furnace dried (400 °C) 4 Å molecular sieves (Sigma-Aldrich, beads 1.6 – 2.6 mm, 208604) which were equilibrated to room temperature under high-vacuum and stored under argon atmosphere (THF, DMF).

Nuclear magnetic resonance (NMR) spectroscopy characterization was performed using a Bruker AVANCE II 400 spectrometer (400 MHz ^{1}H, 100 MHz ^{13}C); all NMR measurements were performed at room temperature utilizing pre-designed acquisition work-flows. Deuterated solvents utilized for NMR spectroscopy include: acetone (acetone-d_6), chloroform ($CDCl_3$), deuterium oxide (D_2O), dimethyl sulfoxide (DMSO-d_6) and methanol (MeOD). All deuterated solvents were purchased from ACP Chemicals Inc. and used without further purification. Chemical shifts are reported in ppm utilizing the residual solvent peak as an internal calibrant. Splitting patterns are defined as follows: singlet – s, doublet – d. triplet – t, quartet – q, quintet – quint, multiplet – m, broad singlet – br. Low resolution mass spectrometry (LRMS) was performed by the John L. Holmes mass spectrometry facility, utilizing electro-spray ionization and time of flight mass analyzer (Waters™, Synapt G1). Compounds **3.01**, **3.03**, and **3.05** were graciously provided by previous graduate student Madeleine Adam upon completion of their doctoral degree,[19] spectral data was collected prior to assay use.

Synthesis and characterization of chemical compounds

***N*-(4-chlorophenyl)-D-gluconamide** (**3.01**)

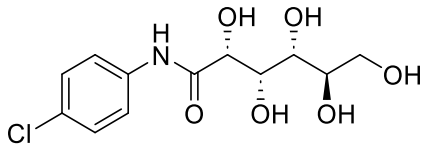

3.01

^{1}H NMR (400 MHz, $(CD_3)_2SO$): *δ* 9.68 (s, 1H), 7.76 – 7.69 (m, 2H), 7.34 – 7.28 (m, 2H), 5.70 (d, *J* = 5.1 Hz, 1H), 4.57 (d, *J* = 4.3 Hz, 1H), 4.52 (m, 2H), 4.34 (t, *J* = 5.6 Hz, 1H), 4.14 (t, *J* = 4.2 Hz, 1H), 4.02 – 3.94 (m, 1H), 3.60 – 3.52 (m, 1H), 3.51 – 3.43 (m, 2H), 3.40 – 3.31 (m, 1H). **^{13}C NMR** (100 MHz, $(CD_3)_2SO$): *δ* 172.27, 138.02, 128.90 (2 X CH), 127.41, 121.66 (2 X CH), 74.69, 72.67, 71.99, 70.79, 63.74.

4-Bromophenyl-β-D-glucopyranoside (3.02)

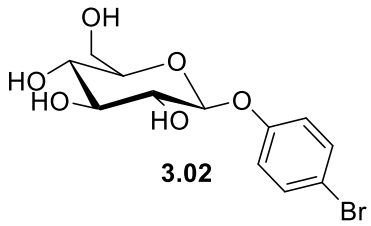

3.02

To a flame-dried flask under inert atmosphere containing 4 Å molecular sieves, penta-*O*-(acetyl)glucoside (2 g, 1 eq), and 4-bromophenol (1.77 g, 2 eq) were dissolved in anhydrous DCM (10 mL, 0.5 M). The reaction flask was cooled in a water / ice bath for 5 minutes before being charged with $BF_3 \bullet OEt_2$ (1.3 mL, 2 eq). The reaction mixture was allowed to warm to room temperature and stir under an inert atmosphere overnight (18 h). The reaction was diluted with DCM (20 mL) and quenched with excess saturated sodium bicarbonate solution. The organic phase was extracted three times with brine, dried with Na_2SO_4 and concentrated under reduced pressure. The crude solid was subjected to flash column chromatography (15% EtOAc : Hexanes) and concentrated *in vacuo* affording a white solid (1.06 g). β-*O*-(4-bromophenol)-2,3,4,6-tetra-*O*-(acetyl)glucoside (1.06 g, 1 eq), was dissolved in MeOH (11 mL, 0.2 M) and brought to a basic pH (> 12) with 1M NaOMe (0.2 mL, 0.1 eq). The reaction was allowed to stir for one hour and then was acidified (pH 4 – 5) with MeOH washed IR 120 H^+ Resin. The heterogenous mixture was filtered through celite and concentrated under reduced pressure, to afford a white solid (0.66 g, 39 % over two steps). **^{1}H NMR** (400 MHz, $(CD_3)_2SO$): *δ* 7.45 – 7.39 (m, 2H), 6.98 – 6.92 (m, 2H), 5.32 (d, *J* = 4.5 Hz, 1H), 5.09 (d, *J* = 4.1 Hz, 1H), 5.02 (d, *J* = 5.0 Hz, 1H), 4.81 (d, *J* = 7.4, 1H), 4.54 (t, *J* = 5.7 Hz, 2H), 3.67 – 3.60 (m, 1H), 3.41 (q, *J* = 11.8 Hz, 1H), 3.29 – 3.25 (m, 1H), 3.23 – 3.15 (m, 2H), 3.14 – 3.06 (m, 1H). **^{13}C NMR** (100 MHz, $(CD_3)_2SO$) : *δ* 157.14, 132.54 (2 X CH), 118.98 (2 X CH), 113.72, 100.83, 77.52, 76.97, 73.63, 70.08, 61.10. LRMS (ESI): *m/z* calcd. For $C_{12}H_{15}BrO_6$ [M+2 Na] = 359.0; found, 359.1.

4-Methoxyphenyl-β-D-glucopyranoside (3.03)

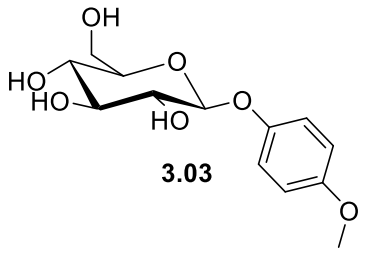

3.03

^{1}H NMR (400 MHz, $(CD_3)_2SO$): *δ* 6.97 – 6.91 (m, 2H), 6.84 – 6.78 (m, 2H), 5.26 (d, *J* = 4.9 Hz, 1H), 5.05 (d *J* = 4.7 Hz, 1H), 4.99 (d, *J* = 5.2 Hz, 1H), 4.67 (d *J* = 7.4 Hz, 1H), 4.55 (t, *J* = 5.8 Hz, 1H), 3.69 – 3.61 (m, 4H), 3.42 (q, *J* = 11.9 Hz, 1H), 3.26 – 3.06 (m, 4H). **^{13}C NMR** (100 MHz, $(CD_3)_2SO$): *δ* 154.72, 151.95, 118.03 (2 X CH), 114.84 (2 X CH), 101.96, 77.45, 77.07, 73.75, 70.23, 61.22, 55.80.

4-Bromophenyl-β-D-galactopyranoside (3.04)

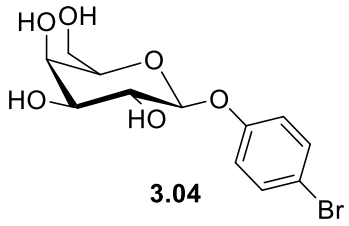

3.04

To a flame-dried flask under inert atmosphere containing 4 Å molecular sieves, penta-*O*-(acetyl)galactopyranoside (2 g, 1 eq), and 4-bromophenol (1.77 g, 2 eq) were dissolved in anhydrous DCM (10 mL, 0.5 M). The reaction flask was cooled in a water / ice bath for 5 minutes before being charged with BF_3•OEt_2 (1.3 mL, 2 eq). The reaction mixture was allowed to warm to room temperature and stir under an inert atmosphere overnight (18 h). The reaction was diluted with DCM (20 mL), and quenched with excess saturated sodium bicarbonate solution. The organic phase was extracted three times with brine, dried with Na_2SO_4 and concentrated under reduced pressure. The crude solid was subjected to flash column chromatography (15% EtOAc : Hexanes) and concentrated *in vacuo* affording a white solid (1.87 g). β-*O*-(4-bromophenyl)-2,3,4,6-tetra-*O*-(acetyl)galactopyranoside (1.87 g, 1 eq), was dissolved in MeOH (19 mL, 0.2 M) and brought to a basic pH (> 12) with 1M NaOMe (0.4 mL, 0.1 eq). The reaction was allowed to stir for one hour, and then acidified (pH 4 – 5) with MeOH washed IR 120 H^+ Resin. The heterogenous mixture was filtered through celite and concentrated under reduced pressure, to afford a white solid (1.12 g, 65 % over two steps). **^{1}H NMR** (400 MHz, $(CD_3)_2SO$): *δ* 7.45 – 7.39 (m, 2H), 6.98 – 6.92 (m, 2H),

5.15 (d, *J* = 5.1 Hz, 1H), 4.85 (d, *J* = 5.6 Hz, 1H), 4.77 (d, *J* = 7.7 Hz, 1H), 4.62 (t, *J* = 5.5 Hz, 1H), 4.48 (d, *J* = 4.6 Hz, 1H), 3.65 (t, *J* = 4.0 Hz, 1H), 3.55 – 3.39 (m, 4H), 3.38 – 3.33 (m, 1H). **^{13}C NMR** (100 MHz, $(CD_3)_2SO$): *δ* 157.22, 132.52 (2 X CH), 119.00 (2 X CH), 113.63, 101.46, 75.99, 73.67, 70.66, 68.54, 60.78. LRMS (ESI): *m/z* calcd. For $C_{12}H_{15}BrO_6$ [M+2 Na] = 359.0; found, 359.1.

4-Methoxyphenyl-β-D-galactopyranoside (3.05)

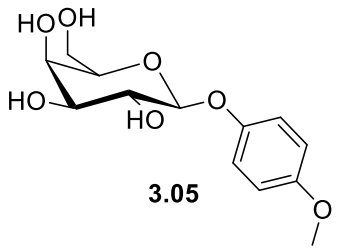

3.05

^{1}H NMR (400 MHz, $(CD_3)_2SO$): *δ* 6.96 – 6.91 (m, 2H), 6.83 – 6.78 (m, 2H), 5.32 – 4.66 (m, 2H), 4.63 (d, *J* = 7.7 Hz, 1H), 4.61 – 4.27 (m, 2H), 3.66 (s, 3H), 3.64 (d, *J* = 3.3 Hz, 1H), 3.54 – 3.42 (m, 4H), 3.34 (dd, *J* = 9.5, 3.3 Hz, 1H). **^{13}C NMR** (100 MHz, $(CD_3)_2SO$): *δ* 154.67, 152.03, 118.08 (2 X CH), 114.83 (2 X CH), 102.59, 75.88, 73.75, 70.82, 68.61, 60.86, 55.77.

4-Chlorophenyl-β-D-glucopyranoside (3.06)

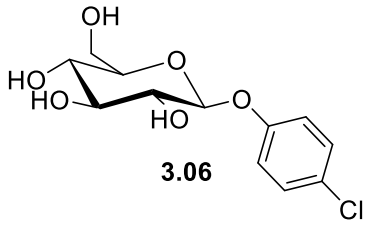

3.06

To a flame-dried flask under inert atmosphere containing 4 Å molecular sieves, penta-*O*-(acetyl)glucoside (1 g, 1 eq), and 4-chlorophenol (0.46 g, 2 eq) were dissolved in anhydrous DCM (7 mL, 0.5 M). The reaction flask was cooled in a water / ice bath for 5 minutes before being charged with BF_3•OEt_2 (0.6 mL, 2 eq). The reaction mixture was allowed to warm to room temperature and stir under an inert atmosphere overnight (18 h). The reaction was diluted with DCM (20 mL) and quenched with excess saturated sodium bicarbonate solution. The organic phase was extracted three times with brine, dried with Na_2SO_4 and concentrated under reduced pressure. The crude solid was subjected to flash column chromatography (30% EtOAc : Hexanes) and concentrated *in vacuo* to afford a white solid (695 mg). β-*O*-(4-chlorophenyl)-2,3,4,6-tetra-*O*-(acetyl)glucoside (695 mg, 1 eq), was dissolved in MeOH (0.5 mL, 0.6 M) and brought to a basic

pH (> 12) with 1M NaOMe (0.1 eq). The reaction was allowed to stir for one hour and then acidified (pH 4 – 5) with MeOH washed IR 120 H^+ Resin. The heterogenous mixture was filtered through celite and concentrated under reduced pressure, affording a white solid (318 mg, 43 %) **^{1}H NMR** (400 MHz, $(CD_3)_2SO$): *δ* 7.32 – 7.28 (m, 2H), 7.03 – 6.99 (m, 2H), 5.31 (d, *J* = 4.9 Hz, 1H), 5.08 (d, *J* = 4.7 Hz, 1H), 5.01 (d, *J* = 5.3 Hz, 1H), 4.81 (d, *J* = 7.4 Hz, 1H), 4.54 (t, *J* = 5.8 Hz, 1H), 3.68 – 3.60 (m, 1H), 3.41 (quint, *J* = 6.0 Hz, 1H), 3.29 – 3.07 (m, 4H). **^{13}C NMR** (100 MHz, $(CD_3)_2SO$): *δ* 156.71, 129.63 (2 X CH), 125.93, 118.48 (2 X CH), 100.94, 77.52, 76.98, 73.64, 70.10, 61.10. LRMS (ESI): *m/z* calcd. For $C_{12}H_{15}ClO_6$ [M+ Na] = 313.0; found, 313.1.

4-Chlorobenzyl(triphenyl)phosphonium chloride (3.07)

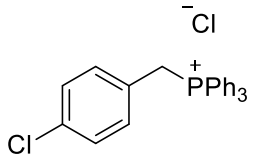

3.07

To a round-bottom flask, 4-chlorobenzyl chloride (1 g, 1 eq), PPh_3 (1.95 g, 1.2 eq) and toluene (15 mL, 0.4 M) were added. A water condenser was added to the reaction flask, and the toluene was heated to reflux. The reaction was allowed to stir overnight, after-which the reaction flask was removed from heat and allowed to cool to room temperature. The resulting white precipitate was filtered through filter paper and rinsed with Et_2O. The isolated solid was dried under vacuum, yielding a white crystalline solid (1.09 g, 41 %). **^{1}H NMR** (400 MHz, $CDCl_3$): *δ* 7.80 – 7.67 (m, 9H), 7.60 – 7.53 (m, 6H), 7.12 – 7.07 (m, 2H), 7.03 – 6.97 (m, 2H), 5.66 (d, *J* = 14.9 Hz, 2H). **^{13}C NMR** (100 MHz, $CDCl_3$): *δ* 134.83 (d, *J* = 3.0 Hz, 3x CH), 134.50 (d, *J* = 9.9 Hz, 6x CH), 134.29 (d, *J* = 4.7 Hz), 133.10 (d, *J* = 5.5 Hz, 2 X CH), 130.09 (d, *J* = 12.6 Hz, 6x CH), 128.77 (d, *J* = 3.4 Hz, 2 X CH), 126.36 (d, *J* = 8.8 Hz), 117.83 (d, *J* = 85.6 Hz), 29.66 (d, *J* = 46.5 Hz). LRMS (ESI): *m/z* calcd. For $C_{25}H_{21}ClP^+$ [M+ Na] = 387.11; found, 387.16.

***N*-(2-Fluorophenyl)-D-gluconamide (4.01)**

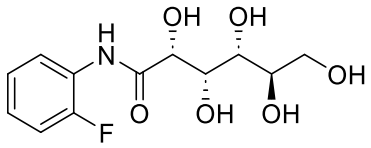

4.01

D-(+)-δ-Gluconolactone (5 g, 1 eq), was dissolved in acetic acid (140 mL, 0.2 M) and 2-fluoroaniline (3 mL, 1.1 eq) was added. A water condenser was equipped to the stirring flask, and

the reaction was brought to 100 °C. The reaction was allowed to stir for one hour, then was removed from heat, allowed to cool to room temperature, and concentrated under reduced pressure. The crude oil was recrystalized from 95 % EtOAc until pure white solid was obtained (1.02 g, 13 %). **^{1}H NMR** (400 MHz, $(CD_3)_2SO$): *δ* 9.17 (br, 1H), 8.09 (dt, *J* = 8.0, 1.9, 1H), 7.28 – 7.20 (m, 1H), 7.17 – 7.06 (m, 2H), 5.93 (d, *J* = 4.9 Hz, 1H), 4.65 (d, *J* = 7.3 Hz, 1H), 4.60 (dd, *J* = 9.1, 5.6 Hz, 2H), 4.37 (t, *J* = 5.6 Hz, 1H), 4.21 (dd, *J* = 4.7, 1.4 Hz, 1H), 3.99 (dt, *J* = 7.2, 3.0 Hz, 1H), 3.60 – 3.44 (m, 3H), 3.40 – 3.36 (m, 1H). **^{13}C NMR** (100 MHz, $(CD_3)_2SO$): *δ* 172.0, 153.01 (d, *J* = 243.2 Hz), 126.40 (d, *J* = 10.6 Hz), 125.82 (d, *J* = 7.6 Hz), 125.00 (d, *J* = 3.4 Hz), 122.50, 115.69 (d, *J* = 19.1 Hz), 74.41, 72.66, 72.03, 70.70, 63.73. NMR analysis matches reference spectra.[20]

***N*-(3-Fluorophenyl)-D-gluconamide (4.02)**

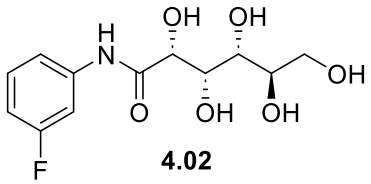

4.02

D-(+)-δ-Gluconolactone (5 g, 1 eq), was dissolved in acetic acid (56 mL, 0.5 M) and 3-fluoroaniline (3 mL, 1.1 eq) was added. A water condenser was equipped to the stirring flask, and the reaction was brought to 100 °C. The reaction was allowed to stir for one hour, then was removed from heat, allowed to cool to room temperature, and concentrated under reduced pressure. The crude oil was recrystalized from 95% EtOAc until pure white solid was obtained (0.82 g, 10 %). **^{1}H NMR** (400 MHz, $(CD_3)_2SO$): *δ* 9.73 (br, 1H), 7.68 (dt, *J* = 11.8, 2.2 Hz, 1H), 7.47 (dd, *J* = 8.2, 1.3 Hz, 1H), 7.29 (dd, *J* = 8.2, 7.0 Hz, 1H), 6.84 (dd, *J* = 8.4, 2.2 Hz, 1H), 5.73 (d, *J* = 5.2 Hz, 1H), 4.59 (d, *J* = 5.1 Hz, 1H), 4.57 – 4.51 (m, 2H), 4.16 (dd, *J* = 5.0, 1.2 Hz, 1H), 4.01 – 3.96 (m, 1H), 3.60 – 3.53 (m, 1H), 3.51 – 3.44 (m, 2H), 3.43 – 3.38 (m, 1H). **^{13}C NMR** (100 MHz, $(CD_3)_2SO$): *δ* 172.49, 162.58 (d, *J* = 240.8 Hz), 140.79 (d, *J* = 11.2 Hz), 130.62 (d, *J* = 9.4 Hz), 115.85 (d, *J* = 2.5 Hz), 110.26 (d, *J* = 21.1 Hz), 106.82 (d, *J* = 28.3 Hz), 74.69, 72.63, 71.99, 70.81, 63.73. LRMS (ESI): *m/z* calcd. For $C_{12}H_{16}FNO_6$ [M+ Na] = 312.3; found, 312.1.

***N*-(4-Fluorophenyl)-D-gluconamide (4.03)**

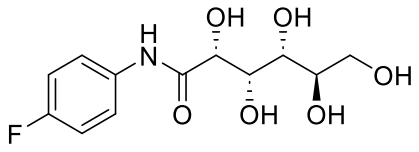

4.03

D-(+)-δ-Gluconolactone (1 g, 1 eq), was dissolved in acetic acid (11 mL, 0.5 M) and 4-fluoroaniline (0.7 mL, 1.1 eq) was added. A water condenser was equipped to the stirring flask, and the reaction was brought to 100 °C. The reaction was allowed to stir for one hour, then was removed from heat, allowed to cool to room temperature, and concentrated under reduced pressure. The crude oil was recrystalized from 95% EtOAc until pure white solid was obtained (0.44 g, 29 %). **^{1}H NMR** (400 MHz, $(CD_3)_2SO$): *δ* 9.63 (br, 1H), 7.78 – 7.71 (m, 2H), 7.18 – 7.10 (m, 2H), 5.70 (d, *J* = 5.2 Hz, 1H), 4.61 (d, *J* = 4.8 Hz, 1H), 4.59 – 4.54 (m, 2H), 4.39 (t, *J* = 5.6 Hz, 1H), 4.20 (t, *J* = 4.0 Hz, 1H), 4.06 – 4.00 (m, 1H), 3.65 – 3.58 (m, 1H), 3.57 – 3.50 (m, 2H), 3.46 – 3.43 (m, 1H). **^{13}C NMR** (100 MHz, $(CD_3)_2SO$): *δ* 170.91, 157.43 (d, *J* = 239.8 Hz), 134.46 (d, *J* = 2.4 Hz), 120.82 (d, *J* = 7.7 Hz, 2 X CH), 114.47 (d, *J* = 22.2 Hz, 2 X CH), 73.56, 71.68, 70.95, 69.73, 62.71. NMR analysis matches reference spectra.[20]

***N*-(4-Methoxyphenyl)-D-gluconamide (4.04)**

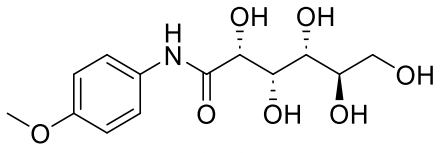

4.04

D-(+)-δ-Gluconolactone (5 g, 1 eq), was dissolved in acetic acid (140 mL, 0.2 M) and *p*-anisidine (3.8 g, 1.1 eq) was added. A water condenser was equipped to the stirring flask, and the reaction was brought to 100 °C. The reaction was allowed to stir for one hour, then was removed from heat, allowed to cool to room temperature, and concentrated under reduced pressure. The crude oil was recrystalized from 95% EtOAc until pure white solid was obtained (2.15 g, 26 %). **^{1}H NMR** (400 MHz, $(CD_3)_2SO$): *δ* 9.37 (br, 1H), 7.60 – 7.55 (m, 2H), 6.86 – 6.81 (m, 2H), 5.62 (d, *J* = 5.2 Hz, 1H), 4.56 (d, *J* = 5.2 Hz, 1H), 4.52 – 4.46 (m, 2H), 4.33 (t, *J* = 5.7 Hz, 1H), 4.10 (dd, *J* = 5.2, 1.4 Hz, 1H), 3.99 – 3.94 (m, 1H), 3.68 (s, 3H), 3.58 – 3.52 (m, 1H), 3.50 – 3.45 (m, 2H), 3.39 – 3.35 (m, 1H). **^{13}C NMR** (100 MHz, $(CD_3)_2SO$): *δ* 171.46, 155.74, 132.21, 121.53, 114.13, 74.58, 72.76, 71.99, 70.73, 63.77, 55.61. LRMS (ESI): *m/z* calcd. For $C_{13}H_{19}NO_7$ [M+ Na] = 324.3; found, 324.1.

Synthesis of *N*-aryl xylonamide derivatives (4.09 – 4.12)

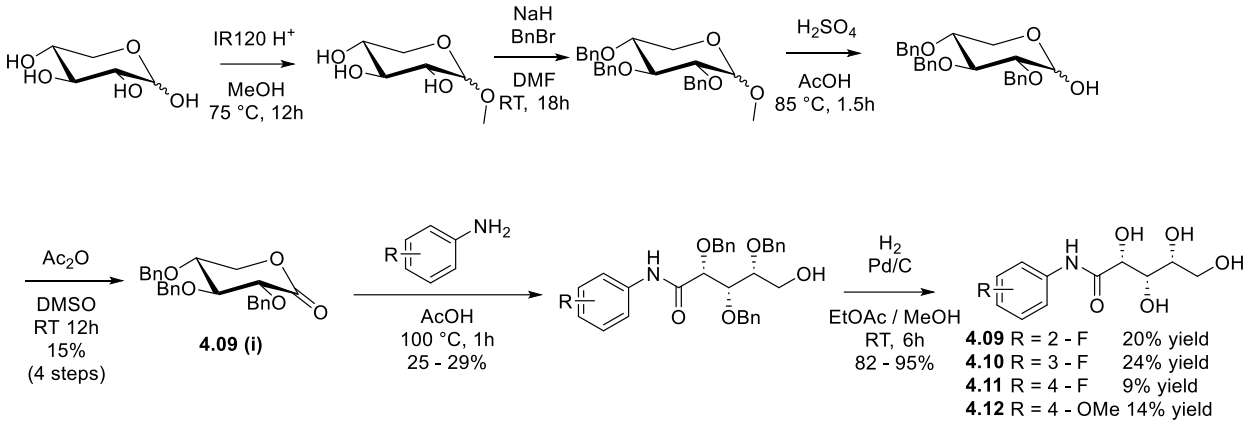

2,3,4-tri-(*O*-benzyl)-D-xylono-δ-lactone (4.09 (i))

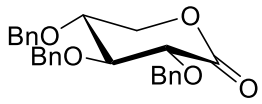

4.09 (i)

To a flame-dried round-bottom flask under an atmosphere of argon, D-Xylose (10 g, 1 eq), IR120 H^+ resin (10 g, 1 g / g) and MeOH (133 mL, 0.5 M) were added. The round bottom flask was equipped with a water condenser and allowed to reflux for 18 hours. The reaction flask was removed from heat and allowed to cool to room temperature; once cool, the slurry was filtered through celite and concentrated under reduced pressure. The resulting orange oil was recrystalized with 95 % EtOH until an off-yellow oil was obtained as a mixture of α / β anomers (7.25 g). The resulting Methyl-D-xylonopyranoside (7.25 g, 1 eq) was transferred into a flame-dried round bottom flask and placed under an atmosphere of argon. DMF (109 mL, 15 mL / g) was added, and the oil was stirred 10 minutes to homogenise. The reaction flask was placed into a water / ice bath, and NaH (60 % suspension in mineral oil) (7.95 g, 4.5 eq) was added portion-wise to the reaction flask and allowed to homogenise completely. BnBr (24 mL, 4.5 eq) was added to reaction flask dropwise, ensuring no film of NaH / mineral oil suspension forms at the surface of the reaction mixture. Once the addition of BnBr was complete, the reaction was removed from the water / ice bath and allowed to stir at room temperature 18 hours. Once complete, the crude mixture was concentrated to a thick oil under reduced pressure; the crude mixture was added directly onto silica gel and purified by flash column chromatography (30 % EtOAc : Hex). The isolated sample was concentrated under reduced pressure, yielding a mixture of α / β anomers as a clear oil (6.3 g). 2,3,4-tri-*O*-(Benzyl)-methyl-D-xylonopyranoside (6.3 g, 1 eq) was dissolved

in AcOH (101 mL, 7 mL / mmol), and 3 M H_2SO_4 (12 mL, 2.5 eq) was added to the reaction flask. The reaction flask was equipped with a water condenser and brought to 80 °C, being allowed to stir for 100 minutes. The reaction flask was then removed from heat and allowed to cool to room temperature. The reaction mixture was diluted with DCM and the organic phase was extracted with water (3 X 50 mL), dried with Na_2SO_4, filtered through cotton and concentrated under reduced pressure to yield a crude oil (8.18 g). The crude 2,3,4-tri-*O*-(Benzyl)-D-glucopyranoside (8.18 g, 1 eq) was dried under high vacuum for 8 hours, after-which, the oil was dissolved in DMSO (49 mL, 0.4 M) and charged with Ac_2O (31 mL, 17 eq). The reaction mixture was allowed to stir at room temperature overnight, after-which the reaction mixture was poured into water (100 mL) and diluted with DCM (150 mL). The organic phase was washed with brine (3 X 50 mL), dried with Na_2SO_4, filtered through cotton, and concentrated under reduced pressure. The crude oil was added onto silica gel for purification by flash silica column chromatography (15 – 30 % EtOAc : Hex), the title product precipitated out of solution on column, allowing for retrieval with MeOH flushing. 5.38 g (29 % over four steps) of product was isolated as a white solid. **^{1}H NMR** (400 MHz, $CDCl_3$): *δ* 7.41 – 7.37 (m, 2H), 7.35 – 7.22 (m, 13H), 5.01 (d, *J* = 11.6 Hz, 1H), 4.64 (d, *J* = 11.6 Hz, 2H), 4.58 – 4.47 (m, 3H), 4.41 – 4.35 (m, 1H), 4.30 – 4.25 (m, 1H), 4.12 (d, *J* = 6.6 Hz, 1H), 3.87 (ddt, *J* = 6.6, 2.1, 0.6 Hz, 1H), 3.74 (dt, *J* = 3.3, 2.1 Hz, 1H). **^{13}C NMR** (100 MHz, $CDCl_3$): *δ* 137.06 (2 X C), 128.57 (2 X CH), 128.51 (2 X CH), 128.48 (2 X CH), 128.34 (2 X CH), 128.07 (3 X CH), 127.95 (2 X CH), 127.78 (2 X CH), 81.34, 78.09, 75.16, 73.31, 72.76, 70.57, 65.67. Note: ^{13}C sample too dilute for **C**=O to appear in spectra. LRMS (ESI): *m/z* calcd. For $C_{26}H_{26}O_5$ [M+ Na] = 441.5, found, 441.2.

***N*-(2-Fluorophenyl)-D-xylonamide (4.09)**

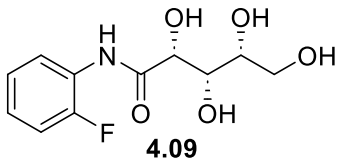

4.09

2,3,4-tri-(*O*-benzyl)-D-glucono-δ-lactone (0.4 g, 1 eq) was dissolved in AcOH (2 mL, 0.5 M) and 2-fluoroaniline (90 µL, 1 eq) was added to the reaction flask. A water condenser was equipped to the reaction flask, the reaction was brought to 100 °C and allowed to stir for one hour. The reaction flask was then removed from heat, and allowed to cool to room temperature. The reaction solution was concentrated under reduced pressure and added onto silica for purification by silica flash column chromatography (30 % EtOAc : Hex). The desired benzylated intermediate was isolated as a yellow oil (140 mg). 2,3,4-tri-*O*-(benzyl)-*N*-(2-fluorophenyl)-D-xylonamide (140 mg, 1 eq) was

transferred to a hydrogenation flask with EtOAc (2.6 mL, 0.1 M) and MeOH (2.6 mL, 0.1 M). Pd/C (10 wt% on activated carbon support) (28 mg, 0.1 eq) was added to the hydrogenation flask, and the air was purged from the system through water aspiration. A hydrogen balloon was attached to the hydrogenation flask, and the reaction was placed under an atmosphere of hydrogen; the hydrogenation flask was purged of gas and replaced with fresh hydrogen gas every hour. Once the reaction was deemed complete (6 hours) the reaction mixture was filtered through celite and concentrated under reduced pressure to yield the desired product as a white solid (47 mg, 19 % over two steps). **^{1}H NMR** (400 MHz, $(CD_3)_2SO$): *δ* 9.18 (br, 1H), 8.12 (dt, *J* = 8.0, 1.9 Hz, 1H), 7.25 (ddd, *J* = 11.3, 7.9, 1.7 Hz, 1H), 7.18 – 7.06 (m, 2H), 5.95 (d, *J* = 5.4 Hz, 1H), 4.72 – 4.65 (m, 2H), 4.63 (t, *J* = 5.4 Hz, 1H), 4.18 (dd, *J* = 5.2, 2.2 Hz, 1H), 3.84 – 3.78 (m, 1H), 3.62 – 3.54 (m, 1H), 3.51 – 3.43 (m, 1H), 3.42 – 3.35 (m, 1H). **^{13}C NMR** (100 MHz, $(CD_3)_2SO$): *δ* 172.19, 126.48, 125.15, 125.04, 122.31, 115.80, 115.61, 73.15, 73.07, 71.95, 62.69. LRMS (ESI): *m/z* calcd. For $C_{11}H_{14}FNO_5$ [M+ Na] = 282.2, found, 282.2.

***N*-(3-Fluorophenyl)-D-xylonamide (4.10)**

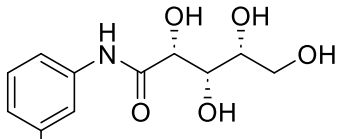

4.10

2,3,4-tri-(*O*-benzyl)-D-glucono-δ-lactone (0.4 g, 1 eq) was dissolved in AcOH (2 mL, 0.5 M) and 3-fluoroaniline (100 µL, 1 eq) was added to the reaction flask. A water condenser was equipped to the reaction flask the reaction is brought to 100 °C and allowed to stir for one hour. The reaction flask was then removed from heat and allowed to cool to room temperature. The reaction solution was concentrated under reduced pressure and added onto silica for purification by silica flash column chromatography (10 % EtOAc : Hex). The desired benzylated intermediate was isolated as a yellow oil (149 mg). 2,3,4-tri-*O*-(benzyl)-*N*-(3-fluorophenyl)-D-xylonamide (149 mg, 1 eq) was transferred to a hydrogenation flask with EtOAc (3 mL, 0.1 M) and MeOH (3 mL, 0.1 M). Pd/C (10 wt% on activated carbon support) (30 mg, 0.1 eq) was added to the hydrogenation flask, and the air was purged from the system through water aspiration. A hydrogen balloon was attached to the hydrogenation flask, and the reaction was placed under an atmosphere of hydrogen; the hydrogenation flask was purged of gas and replaced with new hydrogen gas every hour. Once the reaction was deemed complete (5 hours) the reaction mixture was filtered through celite and concentrated under reduced pressure to yield the desired product as a white solid (60 mg, 24 %

over two steps). **^{1}H NMR** (400 MHz, $(CD_3)_2SO$): *δ* 9.72 (br, 1H), 7.70 (dt, *J* = 11.9, 2.2 Hz, 1H), 7.49 (dd, *J* = 8.2, 1.1 Hz, 1H), 7.33 – 7.26 (m, 1H), 6.84 (dd, *J* = 8.3, 2.2 Hz, 1H), 5.68 (d, *J* = 5.8 Hz, 1H), 4.65 (d, *J* = 5.0 Hz, 1H), 4.62 – 4.53 (m, 2H), 4.12 (q, *J* = 2.8 Hz, 1H), 3.82 – 3.76 (m, 1H), 3.60 – 3.53 (m 1H), 3.51 – 3.43 (m, 1H), 3.41 – 3.35 (m, 1H). **^{13}C NMR** (100 MHz, $(CD_3)_2SO$): *δ* 172.73, 140.87 (d, *J* = 11.1 Hz), 130.63 (d, *J* = 5.3 Hz), 115.79, 110.17 (d, *J* = 21.1 Hz), 106.67 (d, *J* = 26.3 Hz), 73.31, 73.17, 72.05, 62.76. LRMS (ESI): *m/z* calcd. For $C_{11}H_{14}FNO_5$ [M+ Na] = 282.2, found, 282.2.

***N*-(4-Fluorophenyl)-D-xylonamide (4.11)**

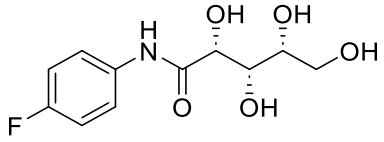

4.11

2,3,4-tri-(*O*-benzyl)-D-glucono-δ-lactone (0.4 g, 1 eq) was dissolved in AcOH (2 mL, 0.5 M) and 4-fluoroaniline (100 µL, 1 eq) was added to the reaction flask. A water condenser was equipped to the reaction flask the reaction is brought to 100 °C and allowed to stir for one hour. The reaction flask was then removed from heat and allowed to cool to room temperature. The reaction solution was concentrated under reduced pressure and placed onto silica for purification by silica flash chromatography (10 - 30 % EtOAc : Hex). The desired benzylated intermediate was isolated as an off-yellow solid (383 mg). 2,3,4-tri-*O*-(benzyl)-*N*-(4-fluorophenyl)-D-xylonamide (383 mg, 1 eq) was transferred to a hydrogenation flask with EtOAc (7 mL, 0.1 M) and MeOH (7 mL, 0.1 M). Pd/C (10 wt% on activated carbon support) (77 mg, 0.1 eq) was added to the hydrogenation flask, and the air was purged from the system through water aspiration. A hydrogen balloon was attached to the hydrogenation flask, and the reaction was placed under an atmosphere of hydrogen; the hydrogenation flask was purged of gas and replaced with new hydrogen gas every hour. Once the reaction was deemed complete (4.5 hours) the reaction mixture was filtered through celite and concentrated under reduced pressure to yield the desired product as a white solid (55 mg, 22 % over two steps). **^{1}H NMR** (400 MHz, $(CD_3)_2SO$): *δ* 9.58 (br, 1H), 7.75 – 7.69 (m, 2H), 7.14 – 7.06 (m, 2H), 5.68 – 5.60 (m, 1H), 4.68 – 4.61 (m, 1H), 4.50 – 4.52 (m, 2H), 4.13 – 4.08 (m, 1H), 3.82 – 3.76 (m, 1H), 3.60 – 3.52 (m, 1H), 3.51 – 3.42 (m, 1H), 3.41 – 3.34 (m, 1H). **^{13}C NMR** (100 MHz, $(CD_3)_2SO$): *δ* 172.18, 158.52 (d, *J* = 239.8 Hz), 135.52, 121.91 (d, *J* = 7.7 Hz, 2 X CH), 115.60 (d, *J* = 22.2 Hz, 2 X CH), 73.25, 73.20, 72.01, 62.78. LRMS (ESI): *m/z* calcd. For $C_{11}H_{14}FNO_5$ [M+ Na] = 282.2, found, 282.1.

***N*-(4-Methoxyphenyl)-D-xylonamide (4.12)**

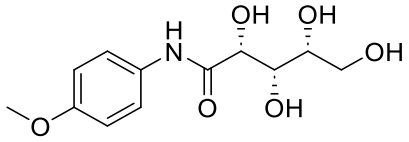

4.12

2,3,4-tri-(*O*-benzyl)-D-glucono-δ-lactone (0.4 g, 1 eq) was dissolved in AcOH (2 mL, 0.5 M) and *p*-anisidine (118 mg, 1 eq) was added to the reaction flask. A water condenser was equipped to the reaction flask, the reaction was brought to 100 °C and allowed to stir for one hour. The reaction flask was then removed from heat and allowed to cool to room temperature. The reaction solution was concentrated under reduced pressure and placed onto silica for purification by silica flash chromatography (30 % EtOAc : Hex). The desired benzylated intermediate was isolated as a red solid (275 mg). 2,3,4-tri-*O*-(benzyl)-*N*-(4-methoxy)-D-xylonamide (275 mg, 1 eq) was transferred to a hydrogenation flask with EtOAc (5 mL, 0.1 M) and MeOH (5 mL, 0.1 M). Pd/C (10 wt% on activated carbon support) (47 mg, 0.1 eq) was added to the hydrogenation flask, and the air was purged from the system through water aspiration. A hydrogen balloon was attached to the hydrogenation flask, and the reaction was placed under an atmosphere of hydrogen; the hydrogenation flask was purged of gas and replaced with new hydrogen gas every hour. Once the reaction was deemed complete (6 hours) the reaction mixture was filtered through celite and concentrated under reduced pressure to yield the desired product as a white solid (63 mg, 25 % over two steps). **^{1}H NMR** (400 MHz, $(CD_3)_2SO$): *δ* 9.36 (br, 1H), 7.61 – 7.56 (m, 2H), 6.87 – 6.81 (m, 2H), 5.57 (d, *J* = 5.8 Hz, 1H), 4.62 (d, *J* = 5.0 Hz, 1H), 4.56 (t, *J* = 5.4 Hz, 1H), 4,53 (d, *J* = 6.7 Hz, 1H), 4.08 (dd, *J* = 5.9, 2.8 Hz, 1H), 3.82 – 3.76 (m, 1H), 3.68 (s, 3H), 3.59 – 3,52 (m, 1H), 3.50 – 3.42 (m, 1H), 3.41 – 3,34 (m, 1H). **^{13}C NMR** (100 MHz, $(CD_3)_2SO$): *δ* 171.64, 155.71, 132.29, 121.41 (2 X CH), 114.14 (2 X CH), 73.24, 73.21, 71.95, 62.80, 55.61. LRMS (ESI): *m/z* calcd. For $C_{12}H_{17}NO_6$ [M+ Na] = 294.3, found, 294.2.

***N*-(2-Fluorophenyl)-L-threonamide (4.13)**

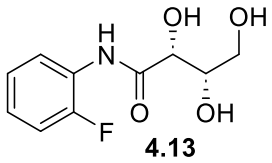

4.13

Calcium-L-threonate (1 g, 1 eq), oxalic acid (0.29 g, 1 eq), PTSA (9 mg, 3 mg / mmol) and acetonitrile (6 mL, 0.6 M) were added into a flame-dried round bottom flask which had been placed under an atmosphere of argon. The reaction flask was equipped with a water condenser and brought to reflux. The reaction was allowed to reflux until complete (3 hours), after-which the reaction flask was removed from heat and allowed to cool to room temperature. The crude slurry was filtered through celite and the remaining liquid was co-evaporated with EtOAc (3 X 50 mL) to dryness under reduced pressure, to yield L-threonolactone as an off-white solid (0.41 g). Once sufficiently dried under high-vacuum L-threonolactone (0.41 g, 1 eq) was suspended in acetic acid (17 mL, 0.2 M) and charged with 2-fluoroaniline (0.3 mL, 1 eq). The reaction flask was equipped with a water condenser and brought to 100 °C. The reaction was allowed to stir at 100 °C for one hour, after-which the reaction flask was removed from heat and allowed to cool to room temperature. The resulting brown mixture was concentrated under reduced pressure and added onto silica gel for purification by silica flash column chromatography (50 – 100 % EtOAc : Hex). The isolated product was concentrated under reduced pressure, then recrystalized from EtOAc : Hexanes; the resulting solid was filtered, washed with Et_2O and dried under reduced pressure. The desired product was obtained as a red solid (0.33 g, 43 %). **^{1}H NMR** (400 MHz, $(CD_3)_2SO$): *δ* 9.17 (br, 1H), 8.14 (dt, *J* = 8.0, 1.9 Hz, 1H), 7.25 (ddd, *J* = 11.4, 7.9, 1.6 Hz, 1H), 7.18 – 7.06 (m, 2H), 5.94 (d, *J* = 6.6 Hz, 1H), 4.74 (d, *J* = 6.8 Hz, 1H), 4.67 (dd, *J* = 5.4, 1.0 Hz, 1H), 4.13 (dd, *J* = 6.5, 2.1 Hz, 1H), 3.82 – 3.75 (m, 1H), 3.46 – 3.34 (m, 2H). **^{13}C NMR** (100 MHz, $(CD_3)_2SO$): *δ* 172.69, 153.16 (*J* = 243.1 Hz), 126.43 (*J* = 10.5 Hz), 125.05 (*J* = 3.7 Hz, 2 X CH), 122.13, 115.69 (*J* = 19.1 Hz), 72.53, 72.00, 62.31. LRMS (ESI): *m/z* calcd. For $C_{10}H_{12}FNO_4$ [M+ Na] = 252.1, found, 252.1.

***N*-(3-Fluorophenyl)-L-threonamide (4.14)**

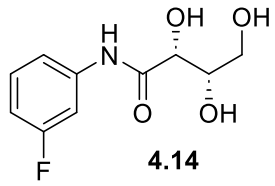

4.14

Calcium-L-threonate (1 g, 1 eq), oxalic acid (0.28 g, 1 eq), PTSA (10 mg, 3 mg / mmol) and acetonitrile (6 mL, 0.6 M) were added into a flame-dried round bottom flask which had been placed under an atmosphere of argon. The reaction flask was equipped with a water condenser and brought to reflux. The reaction was allowed to reflux until complete (3 hours), after-which the reaction flask was removed from heat and allowed to cool to room temperature. The crude slurry was filtered through celite and the remaining liquidwas co-evaporated with EtOAc (3 X 50 mL) to dryness under reduced pressure, to yield L-threonolactone as an off-white solid (0.6 g). Once sufficiently dried under high-vacuum L-threonolactone (0.6 g, 1 eq) was suspended in acetic acid (25 mL, 0.2 M) and charged with 3-fluoroaniline (0.5 mL, 1 eq). The reaction flask was equipped with a water condenser and brought to 100 °C. The reaction was allowed to stir at 100 °C for one hour, after-which the reaction flask was removed from heat and allowed to cool to room temperature. The resulting brown mixture was concentrated under reduced pressure and placed onto silica gel for purification by silica flash column chromatography (50 – 100 % EtOAc : Hex). The isolated product was concentrated under reduced pressure, then recrystalized from EtOAc : Hexanes; the resulting solid was filtered, washed with Et_2O and dried under reduced pressure. The desired product was obtained as an off-white solid (58 mg, 17 %). **^{1}H NMR** (400 MHz, $(CD_3)_2SO$): *δ* 9.71 (br, 1H), 7.70 (dt, *J* = 11.9, 2.2 Hz, 1H), 7.48 (dd, *J* = 8.2, 1.8 Hz, 1H), 7.33 – 7.25 (m, 1H), 6.84 (dt, *J* = 8.5, 2.6 Hz, 1H), 5.55 (d, *J* = 6.8 Hz, 1H), 4.67 (d, *J* = 6.4 Hz, 1H), 4.64 (dd, *J* = 6.3, 1.4 Hz, 1H), 4.07 (dd, *J* = 6.8, 2.0 Hz, 1H), 3.84 – 3.76 (m, 1H), 3.46 – 3.38 (m, 1H), 3.37 – 3.34 (m, 1H). **^{13}C NMR** (100 MHz, $(CD_3)_2SO$): *δ* 173.21, 162.71 (d, *J* = 240.8 Hz), 140.79 (d, *J* = 11.2 Hz), 130.59 (d, *J* = 9.5 Hz), 115.74 (d, *J* = 2.6 Hz), 110.22 (d, *J* = 21.1 Hz), 106.66 (d, *J* = 26.3 Hz), 72.64, 72.21, 62.46. LRMS (ESI): *m/z* calcd. For $C_{10}H_{12}FNO_4$ [M+ Na] = 252.1, found, 252.1.

***N*-(4-Fluorophenyl)-L-threonamide (4.15)**

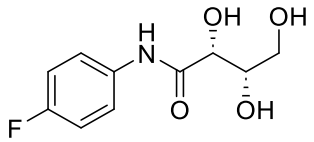

4.15

Calcium-L-threonate (2 g, 1 eq), oxalic acid (0.58 g, 1 eq), PTSA (19 mg, 3 mg / mmol) and acetonitrile (11 mL, 0.6 M) were added into a flame-dried round bottom flask which had been placed under an atmosphere of argon. The reaction flask was equipped with a water condenser and brought to reflux. The reaction was allowed to reflux until complete (3 hours), after-which the reaction flask was removed from heat and allowed to cool to room temperature. The crude slurry was filtered through celite and the remaining liquid was co-evaporated with EtOAc (3 X 50 mL) to dryness under reduced pressure to yield L-threonolactone as an off-white solid. Once sufficiently dried under high-vacuum L-threonolactone (0.7 g, 1 eq) was suspended in acetic acid (32 mL, 0.2 M) and charged with 4-fluoroaniline (0.6 mL, 1 eq). The reaction flask was equipped with a water condenser and brought to 100 °C. The reaction was allowed to stir at 100 °C for one hour, after-which the reaction flask was removed from heat and allowed to cool to room temperature. The resulting brown mixture was concentrated under reduced pressure and added onto silica gel for purification by silica flash chromatography (50 – 100 % EtOAc : Hex). The column flush (MeOH) was concentrated under reduced pressure to yield an off-brown solid which when recrystalized with EtOAc yielded the title compound as a white solid following filtration and concentration (104 mg, 7 %). **^{1}H NMR** (400 MHz, $(CD_3)_2SO$): *δ* 9.63 (br, 1H), 7.80 – 7.71 (m, 2H), 7.14 (t, *J* = 8.9 Hz, 2H), 5.59 (s, 1H), 4.77 – 4.63 (m, 2H), 4,16 – 4.09 (m, 1H), 3.89 – 3,82 (m, 1H), 3.54 – 3.45 (m, 1H), 3.44 – 3.40 (m, 1H). **^{13}C NMR** (100 MHz, $(CD_3)_2SO$): *δ* 171.57, 157.32 (d, *J* = 239.7 Hz), 134.47 (d, *J* = 2.4 Hz), 120.63 (d, *J* = 7.6 Hz, 2 X CH), 114.49 (d, *J* = 22.1 Hz, 2 X CH), 71.60, 71.06, 61.46. LRMS (ESI): *m/z* calcd. For $C_{10}H_{12}FNO_4$ [M+ H] = 252.1, found, 252.1.

***N*-(4-Methoxyphenyl)-L-threonamide (4.16)**

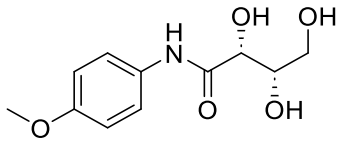

4.16

Calcium-L-threonate (1 g, 1 eq), oxalic acid (0.28 g, 1 eq), PTSA (10 mg, 3 mg / mmol) and acetonitrile (6 mL, 0.6 M) were added into a flame-dried round bottom flask which had been placed

under an atmosphere of argon. The reaction flask was equipped with a water condenser and brought to reflux. The reaction was allowed to reflux until complete (3 hours), after-which the reaction flask was removed from heat and allowed to cool to room temperature. The crude slurry iwas filtered through celite and the remaining liquid was co-evaporated with EtOAc (3 X 50 mL) to dryness under reduced pressure to yield L-threonolactone as an off-white solid (0.62 g). Once sufficiently dried under high-vacuum L-threonolactone (0.62 g, 1 eq) was suspended in methanol (26 mL, 0.2 M) and charged with *p*-anisidine (0.64 g, 1 eq). The reaction flask was equipped with a water condenser and brought to reflux. The reaction was allowed to stir at reflux overnight, after-which the reaction flask was removed from heat and allowed to cool to room temperature. The resulting brown mixture was concentrated under reduced pressure, and placed onto silica gel for purification by silica flash column chromatography (50 – 100 % EtOAc : Hex). The isolated product was concentrated under reduced pressure, then recrystalized from 99 % EtOH; the resulting solid was filtered, washed with Et_2O and dried under reduced pressure. The desired product was obtained as a yellow solid (93 mg, 12 %). **^{1}H NMR** (400 MHz, D_2O): *δ* 7.25 – 7.20 (m, 2H), 6.89 – 6.84 (m, 2H), 4.19 (d, *J* = 2.3 Hz, 1H), 3.98 – 3.93 (m, 1H), 3.68 (s, 3H), 3.62 – 3.51 (m, 2H). **^{13}C NMR** (100 MHz, D_2O): *δ* 173.61, 156.82, 129.14, 124.60 (2 X CH), 114.38 (2 X CH), 72.10, 71.56, 62.23, 56.48. LRMS (ESI): *m/z* calcd. For $C_{11}H_{15}NO_5$ [M+ H] = 242.1, found, 242.1.

***N*-(4-Methoxyphenyl)-(R)-2,3-dihydroxy-propanamide (4.17)**

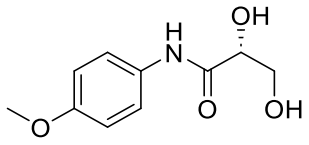

4.17

To a flame dried round bottom flask under an argon atmosphere, K_2CO_3 (1.12 g, 2 eq), water (2 mL, 0.25 mL / mmol K_2CO_3), and acetone (8 mL, 2 mL / mmol aniline) were added. The reaction flask was placed in a water / ice bath and allowed to cool for 5 minutes. Acryloyl chloride (0.65 mL, 2 eq) was added to the flask slowly, followed by the portion-wise addition of *p*-anisidine (0.5 g, 1 eq). The reaction was allowed to stir in the ice bath until complete (1 hour). The reaction was diluted with excess DCM (50 mL), filtered through celite, and the organic phase was extracted with brine (3 X 50 mL). The resulting organic phase was dried with Na_2SO_4, filtered through cotton and concentrated under reduced pressure. Crude *N*-(4-Methoxyphenyl)acrylamide (0.85 g, 1 eq) was obtained as a clear oil and was suspended in ^{t}BuOH (30 mL, 0.16 M) and water (30 mL, 0.16 M). AD-mix-α (6.7 g, 1.4 g / mmol) and methanesulfonamide (0.43 g, 0.09 g / mmol) were added to the reaction flask, and it was allowed to stir at room temperature until complete (4 days). The

reaction was quenched with saturated Na_2SO_3, diluted with EtOAc, and the organic phase was washed with brine (3 X 100 mL). The resulting organic phase was dried with Na_2SO_4, filtered through cotton and concentrated under reduced pressure. The crude solid was dissolved in minimal eluent (30 % EtOAc : Hex) and purified with silica flash column chromatography (30 – 50 – 90 % EtOAc : Hex). The desired product was obtained as a white solid after concentrating under reduced pressure (20 mg, 2 % over two steps). **^{1}H NMR** (400 MHz, (MeOD): *δ* 7.49 – 7.44 (m, 2H), 6.88 – 6.84 (m, 2H), 4.14 (dd, *J* = 5.1, 1.5 Hz, 1H), 3.83 – 3.76 (m, 1H), 3.75 (s, 3H). **^{13}C NMR** (100 MHz, (MeOD): *δ* 171.61, 156.81, 130.52, 121.88 (2 X CH), 113.56 (2 X CH), 73.10, 63.94, 54.45. LRMS (ESI): *m/z* calcd. For $C_{10}H_{13}NO_4$ [M+ Na] = 234.2, found, 234.2.

***N*-(2-Fluorophenyl)-2-hydroxyacetamide (4.18)**

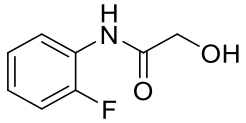

4.18

Glycolic acid (0.55 g ,1eq) and 2-fluoroaniline (0.7 mL, 1 eq) were added into a round-bottom flask equipped with a water condenser. The reaction flask was brought to 130 °C and allowed to stir until completion (3 hours). The reaction flask was removed from heat and allowed to cool to room temperature. 2-fluoroaniline was removed under reduced pressure, to afford the title product as a white solid (0.16 g, 19 %). **^{1}H NMR** (400 MHz, $CDCl_3$): *δ* 8.66 (br, 1H), 6.25 (t, *J* = 7.9 Hz, 1H), 7.14 – 7.02 (m, 3H), 4.24 (s, 3H). **^{13}C NMR** (100 MHz, $CDCl_3$): *δ* 170.18, 152.76 (d, *J* = 244.3 Hz), 125.36 (d, *J* = 10.3 Hz), 125.05 (d, *J* = 7.7 Hz), 124.60 (d, *J* = 3.7 Hz), 121.82, 115.03 (d, *J* = 19.1 Hz), 62.67. LRMS (ESI): *m/z* calcd. For $C_8H_8FNO_2$ [M+ Na] = 192.2, found, 192.1.

***N*-(3-Fluorophenyl)-2-hydroxyacetamide (4.19)**

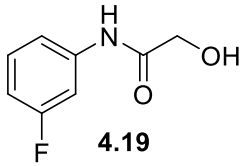

4.19

Glycolic acid (0.55 g ,1eq) and 3-fluoroaniline (0.7 mL, 1 eq) were added into a round-bottom flask equipped with a water condenser. The reaction flask was brought to 130 °C and allowed to stir until completion (3.5 hours). The reaction flask was removed from heat and allowed to cool to room temperature. 3-Fluoroaniline was removed under reduced pressure to afford the title product as a white solid (45 mg, 4 %). **^{1}H NMR** (400 MHz, $CDCl_3$): *δ* 8.59 (br, 1H), 7.45 (dt, *J* = 10.7, 2.0

Hz, 1H), 7.27 – 7.19 (m, 1H), 7.17 – 7.12 (m, 1H), 6.80 (dt, *J* = 8.3, 1.8 Hz, 1H), 4.18 (s, 2H). **^{13}C NMR** (100 MHz, $CDCl_3$): *δ* 170.47, 162.90 (d, *J* = 245.2 Hz), 138.29 (d, *J* = 10.7 Hz), 130.24 (d, *J* = 9.3 Hz), 115.32 (d, *J* = 3.0 Hz), 111.67 (d, *J* = 21.3 Hz), 107.53 (d, *J* = 26.2 Hz), 62.36. LRMS (ESI): *m/z* calcd. For $C_8H_8FNO_2$ [M+ Na] = 192.2, found, 192.2.

***N*-(4-Fluorophenyl)-2-hydroxyacetamide (4.20)**

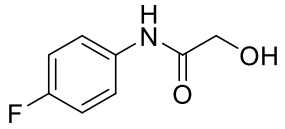

4.20

Glycolic acid (0.56 g ,1 eq) and 4-fluoroaniline (0.7 mL, 1 eq) were added into a round-bottom flask equipped with a water condenser. The reaction flask was brought to 130 °C and allowed to stir until completion (3 hours). The reaction flask was removed from heat and allowed to cool to room temperature. 4-Fluoroaniline was removed under reduced pressure, to afford the title product as a blue / green solid (0.27 g, 22 %). **^{1}H NMR** (400 MHz, $CDCl_3$): *δ* 8.36 (br, 1H), 7.52 – 7.46 (m, 2H), 7.05 – 6.97 (m, 2H), 4.21 (s, 2H). **^{13}C NMR** (100 MHz, $CDCl_3$): *δ* 169.55, 159.89 (d, *J* = 244.2 Hz), 132.94 (d, *J* = 2.8 Hz), 121.82 (d, *J* = 7.9 Hz, 2 X CH), 115.85 (d, *J* = 22.6 Hz, 2 X CH), 62.45. LRMS (ESI): *m/z* calcd. For $C_8H_8FNO_2$ [M+ Na] = 192.2, found, 192.1.

***N*-(4-Methoxyphenyl)-2-hydroxyacetamide (4.21)**

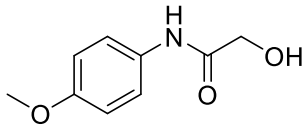

4.21

Glycolic acid (0.31 g ,1 eq) and *p*-anisidine (0.5 g, 1 eq) were added into a round-bottom flask equipped with a water condenser. The reaction flask was brought to 130 °C and allowed to stir until completion (3 hours). The reaction flask was removed from heat and allowed to cool to room temperature. The crude mixture was purified with silica flash column chromatography (50 – 70 % EtOAc : Hex), yielding the title compound as a white solid after concentration under reduced pressure (0.12 g, 18 %). **^{1}H NMR** (400 MHz, $CDCl_3$): *δ* 8.34 (br, 1H), 7.43 – 7.37 (m, 2H), 6.86 – 6.81 (m, 2H), 4.14 (s, 2H), 3.75 (s, 3H). **^{13}C NMR** (100 MHz, $CDCl_3$): *δ* 169.90, 156.78, 129.93, 121.86 (2 X CH), 114.26 (2 X CH), 62.37, 55.48. NMR analysis matches reference spectra.[21]

***N*-(2-Fluorophenyl)-acetamide (4.22)**

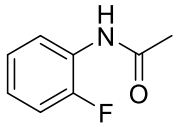

4.22

To a flamed-dried round-bottom flask placed under an atmosphere of argon, 2-fluoroaniline (0.5 mL, 1 eq) and DCM (13 mL, 0.4 M) were added, followed by Ac_2O (0.58 mL, 1.2 eq). The reaction was allowed to stir at room temperature until complete (3 hours). The reaction was quenched with the addition of excess saturated Na_2CO_3 and excess DCM (50 mL). The organic phase was washed with brine (3 X 50 mL), dried with Na_2SO_4, filtered through cotton and concentrated under reduced pressure. The title compound was obtained as a white solid (0.59 g, 74 %). **^{1}H NMR** (400 MHz, $CDCl_3$): *δ* 8.09 (t, *J* = 8.5 Hz, 1H), 8.03 (br, 1H), 7.04 – 6.92 (m, 3H), 2.13 (s, 3H). **^{13}C NMR** (100 MHz, $CDCl_3$): *δ* 169.12, 152.93 (d, *J* = 244.0 Hz), 126.24 (d, *J* = 10.6 Hz), 124.67 (d, *J* = 7.6 Hz), 124.34 (d, *J* = 3.6 Hz), 122.71, 114.91(d, *J* = 19.4 Hz), 24.19. NMR analysis matches reference spectra.[22]

***N*-(3-Fluorophenyl)-acetamide (4.23)**

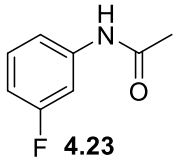

4.23

To a flamed-dried round-bottom flask placed under an atmosphere of argon, 3-fluoroaniline (0.5 mL, 1 eq) and DCM (13 mL, 0.4 M) were added, followed by Ac_2O (0.59 mL, 1.2 eq). The reaction was allowed to stir at room temperature until complete (3 hours). The reaction was quenched with the addition of excess saturated Na_2CO_3 and excess DCM (50 mL). The organic phase was washed with brine (3 X 50 mL), dried with Na_2SO_4, filtered through cotton and concentrated under reduced pressure. The title compound was obtained as a white solid (0.36 g, 51 %). **^{1}H NMR** (400 MHz, $CDCl_3$): *δ* 8.81 (br, 1H), 7.48 (dt, *J* = 11.0, 2.4 Hz, 1H), 7.22 – 7.12 (2H), 6.75 (tt, *J* = 6.9, 2.2 Hz, 1H), 2.14 (s, 3H). **^{13}C NMR** (100 MHz, $CDCl_3$): *δ* 169.67, 162.55 (d, *J* = 244.3 Hz), 139.63 (d, *J* = 10.8 Hz),129.92 (d, *J* = 9.4 Hz), 115.70 (d, *J* = 2.8 Hz), 111.02 (d, *J* = 21.3 Hz), 107.86 (d, *J* = 26.1 Hz), 24.31. NMR analysis matches reference spectra.[23]

***N*-(4-Fluorophenyl)-acetamide (4.24)**

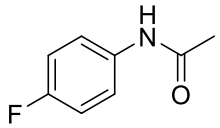

4.24

To a flamed-dried round-bottom flask placed under an atmosphere of argon, 4-fluoroaniline (0.5 mL, 1 eq) and DCM (13 mL, 0.4 M) were added, followed by Ac_2O (0.6 mL, 1.2 eq). The reaction was allowed to stir at room temperature until complete (3 hours). The reaction was quenched with the addition of excess saturated Na_2CO_3 and excess DCM (50 mL). The organic phase was washed with brine (3 X 50 mL), dried with Na_2SO_4, filtered through cotton and concentrated under reduced pressure. The title compound was obtained as a white solid (0.69 g, 86 %). **^{1}H NMR** (400 MHz, $CDCl_3$): *δ* 7.51 (br, 1H), 7.46 – 7.39 (m, 2H), 7.01 – 6.93 (m, 2H), 2.13 (s, 3H). **^{13}C NMR** (100 MHz, $CDCl_3$): *δ* 168.48, 159.31 (d, *J* = 243.5 Hz), 133.88 (d, *J* = 2.8 Hz), 121.88 (d, *J* = 7.9 Hz), 155.52 (d, *J* = 22.5 Hz), 24.34. LRMS (ESI): *m/z* calcd. For C_8H_8FNO [M+ Na] = 176.2, found, 176.2.

***N*-(4-Methoxyphenyl)-acetamide (4.25)**

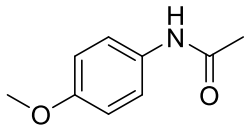

4.25

To a flamed-dried round-bottom flask placed under an atmosphere of argon, *p*-anisidine (0.5 g, 1 eq) and DCM (10 mL, 0.4 M) were added, followed by Ac_2O (0.46 mL, 1.2 eq). The reaction was allowed to stir at room temperature until complete (3.5 hours). The reaction was quenched with the addition of excess saturated Na_2CO_3 and excess DCM (50 mL). The organic phase was washed with brine (3 X 50 mL), dried with Na_2SO_4, filtered through cotton and concentrated under reduced pressure. The title was compound obtained as a white solid (50 mg, 7 %). **^{1}H NMR** (400 MHz, $CDCl_3$): *δ* 8.00 (br, 1H), 7.38 – 7.33 (m, 2H), 6.81 – 6.76 (m, 2H), 3.73 (s, 3H), 2.07 (s, 3H). **^{13}C NMR** (100 MHz, $CDCl_3$): *δ* 168.82, 156.40, 131.19, 122.13 (2 X CH), 114.05 (2 X CH), 55.46, 24.12. NMR analysis matches reference spectra.[24]

Synthesis of C_4-deoxy glucoamide derivatives (4.26, 4.27)

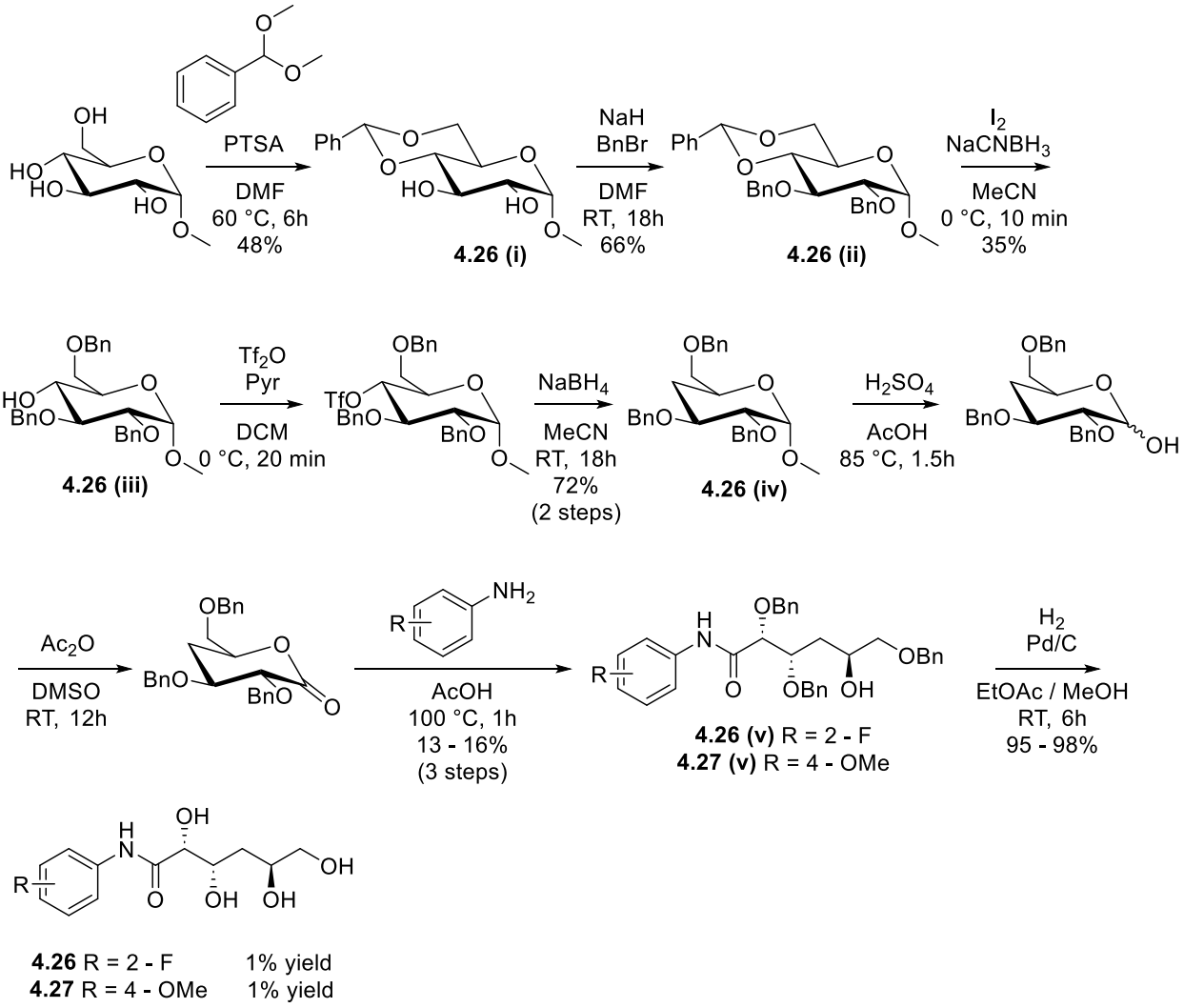

4,6-*O*-(benzylidene)-1-*O*-(methyl)-α-D-glucopyranoside (4.26 (i))

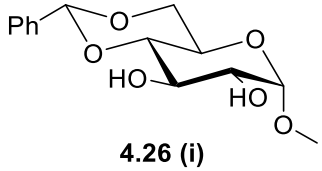

4.26 (i)

To a fame-dried round-bottom flask placed under argon atmosphere, α-methyl glucose (7.5 g, 1 eq), PTSA (0.67 g, 0.1 eq), benzaldehyde dimethyl acetal (6.5 mL, 1.1 eq) and DMF (77 mL, 0.5 M) were added. A water condenser was attached to the reaction flask, and the temperature was raised to 60 °C. The reaction was allowed to stir at 60 °C until complete (5 hours). The reaction mixture was diluted with EtOAc (150 mL) and the organic phase was washed with brine (3 X 100

mL), dried with Na_2SO_4, filtered through cotton and concentrated under reduced pressure. The crude mixture was recrystalized from DCM / Hexanes to yield the title product as a white crystalline solid (6.05 g, 55%). **^{1}H NMR** (400 MHz, $(CD_3)_2SO$): *δ* 7.42 – 7.38 (m, 2H), 7.36 – 7.31 (m, 3H), 5.53 (s, 1H), 5.16 (d, *J* = 5.1 Hz, 1H), 4.99 (d, *J* = 6.7 Hz, 1H), 4.59 (d, *J* = 3.7 Hz, 1H), 4.13 (dd, *J* = 9.8, 4.7 Hz, 1H), 3.65 (t, *J* = 10.1 Hz, 1H),3.58 – 3.49 (m, 2H), 3.37 – 3.31 (m, 2H), 3.28 (s, 3H). **^{13}C NMR** (100 MHz, $(CD_3)_2SO$): *δ* 138.29, 129.31, 128.49 (2 X CH), 126.86 (2 X CH), 101.31, 101.01, 81.81, 72.88, 70.35, 68.64, 62.85, 55.22. LRMS (ESI): *m/z* calcd. For $C_{14}H_{18}O_6$ [M+ Na] = 305.3, found, 305.2.

2,3-*O*-(benzyl)-4,6-(benzylidene)-1-*O*-(methyl)-α-D-glucopyranoside (4.26 (ii))

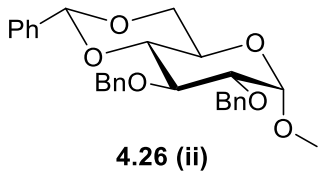

4.26 (ii)

To a flame-dried round-bottom flask placed under an atmosphere of argon **4.26(i)** (1.13 g, 1 eq) was dissolved in DMF (40 mL, 0.1 M). The reaction flask was placed in a water / ice bath and allowed to cool for 5 minutes. NaH (60 % mineral oil suspension) (0.48 g, 3 eq) was added to the flask portion-wise, ensuring adequate stirring for homogeneity. BnBr (1.4 mL, 3 eq) was added dropwise to the reaction mixture, and the resulting solution was allowed to stir overnight at room temperature. Once complete, the reaction mixture was diluted with DCM (100 mL) and the organic phase was washed with brine (3 X 50 mL), dried with Na_2SO_4, filtered through cotton and concentrated under reduced pressure. The dried organic phase was purified by silica flash chromatography (5 – 30 % EtOAc : Hex). The desired product was isolated as a white solid after concentration under reduced pressure (0.81 g, 44 %). **^{1}H NMR** (400 MHz, $CDCl_3$): *δ* 7.50 – 7.46 (m, 2H), 7.41 – 7.25 (m, 13H), 5.54 (s, 1H), 4.94 – 4.80 (m, 3H), 4.69 (d, *J* = 12.2 Hz, 1H), 4.59 (d, *J* = 3.7 Hz, 1H), 4.26 (dd, *J* = 10.1, 4.7 Hz, 1H), 4.04 (t, *J* = 9.3 Hz, 1H), 3.87 – 3.78 (m, 1H), 3.70 (t, *J* = 10.2 Hz, 1H), 3.63 – 3.53 (m, 2H), 3.39 (s, 3H). **^{13}C NMR** (100 MHz, $CDCl_3$): *δ* 138.74, 138.17, 137.42, 128.94, 128.48 (2 X CH), 128.34 (2 X CH), 128.25 (2 X CH), 128.16 (2 X CH), 128.06 (2 X CH), 127.95, 127.62, 126.05, 101.28, 99.26, 82.15, 79.18, 78.63, 75.38, 73.82, 69.08, 62.34, 55.38. LRMS (ESI): *m/z* calcd. For $C_{28}H_{30}O_6$ [M+ Na] = 485.5, found, 485.5.

2,3,6-Tri-*O*-(benzyl)-1-*O*-(methyl)-α-D-glucopyranoside (4.26 (iii))

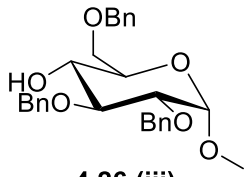

4.26 (iii)

To a flame-dried round-bottom flask placed under an atmosphere of argon is charged with 4 Å molecular sieves and allowed to equilibrate to room temperature under high vacuum. The reaction flask was removed vacuum, and an atmosphere of argon is restored. **4.26 (ii)** (1.46 g, 1 eq) and MeCN (7.5 mL, 2 mL / 100 mg acetal) were added to the reaction flask. $NaCNBH_3$ (0.99 g, 5 eq) was added to the reaction flask and allowed to stir for 5-minutes. The reaction flask was placed into a water / ice bath and I_2 chips (2.8 g, 3.5 eq) were added portion-wise. The reaction was allowed to stir for 10-minutes from the first addition of I_2 (total addition performed in less than one minute). The reaction mixture was removed from the water / ice bath and filtered through celite. Excess DCM (50 mL) was added to the reaction mixture, and the organic phase was washed with brine (3 X 50 mL), dried with Na_2SO_4, filtered through cotton and concentrated under reduced pressure. The crude mixture was purified by silica flash column chromatography (30 % EtOAc : Hex), to yield the title product as a clear oil after concentration under reduced pressure (0.51 g, 35 %). **^{1}H NMR** (400 MHz, $CDCl_3$): *δ* 7.38 – 7.22 (m, 15H), 4.99 (d, *J* = 11.4 Hz, 1H), 4.78 – 4.49 (m, 6H), 3.77 (t, *J* = 9.1 Hz, 1H), 3.72 – 3.64 (m, 3H), 3.59 (t, *J* = 9.1 Hz, 1H), 3.52 (dd, *J* = 9.6, 3.6 Hz, 1H), 3.37 (s, 3H), 2.30 (br, OH). **^{13}C NMR** (100 MHz, $CDCl_3$): *δ* 138.81, 138.06, 138.01, 128.61 (2 X CH), 128.49 (2 X CH), 128.38 (2 X CH), 128.15 (2 X CH), 128.02 (2 X CH), 127.98, 127.87, 127.66, 127.64 (2 X CH), 98.21, 81.47, 79.59, 75.45, 73.59, 73.18, 70.72, 69.88, 69.47, 55.27. Note: ^{1}H and ^{13}C spectra contain residual EtOAc from flash column purification. LRMS (ESI): *m/z* calcd. For $C_{28}H_{32}O_6$ [M+ Na] = 487.6, found, 487.2.

2,3,6-Tri-*O*-(benzyl)-4-deoxy-1-*O*-(methyl)-α-D-glucopyranoside (4.26 (iv))

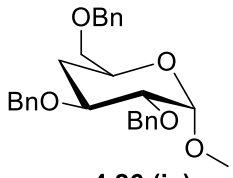

4.26 (iv)

To a flame-dried round-bottom flask placed under an atmosphere of argon, **4.26 (iii)** (0.5 g, 1 eq), pyridine (0.26 mL, 3 eq) and DCM (4 mL, 0.3 M) were added. The reaction flask was placed into

a water / ice bath and allowed to stir for 5 minutes. Tf_2O (0.3 mL, 1.5 eq) was added dropwise to the reaction mixture over the course of 5 minutes. The reaction was allowed to stir at room temperature until complete (20 minutes), after-which the reaction mixture was diluted with EtOAc (50 mL), poured into water (50 mL), and the organic phase was extracted with brine (2 X 50 mL). The resulting organic phase was dried with Na_2SO_4, filtered through cotton and concentrated under reduced pressure. Once sufficiently dried under high vacuum, the crude 2,3,6-Tri-*O*-(benzyl)-4-*O*-(trifluoromethanesulfonate)-1-*O*-(methyl)-α-D-glucopyranoside (0.64 g, 1eq) was placed under an atmosphere of argon and solvated in MeCN (54 mL, 0.02 M). $NaBH_4$ (0.33 g, 8 eq) was added to the reaction flask, and the resulting slurry was allowed to stir overnight. Once complete, the reaction was diluted with EtOAc (100 mL) and the organic phase was washed with brine (3 X 100 mL), dried with Na_2SO_4, filtered through cotton and concentrated under reduced pressure. The crude mixture was purified with silica flash chromatography (10 % EtOAc : Hex), to yield the title product as a clear oil following concentration under reduced pressure (0.35 g, 72% over two steps). **^{1}H NMR** (400 MHz, $CDCl_3$): *δ* 7.38 – 7.23 (m, 15H), 4.83 (d, *J* = 12.2 Hz, 1H), 4.74 (d, *J* = 11.8 Hz, 1H), 4.67 (dd, *J* = 12.6, 4.6 Hz, 1H), 4.54 (s, 2H), 3.96 – 3.87 (m, 2H), 3.49 – 3.43 (m, 3H), 3.37 (s, 3H), 2.05 (dd, *J* = 12.8, 7.4 Hz, 1H), 1.50 (q, *J* = 12.1 Hz, 1H). **^{13}C NMR** (100 MHz, $CDCl_3$): *δ* 138.91, 138.56, 138.12, 128.38 (4x, CH), 128.06 (2 X, CH), 127.74, 127.65 (4x, CH), 127.62 (3 X, CH), 127.51, 99.07, 80.47, 75.32, 73.42, 73.33, 72.52, 72.42, 66.74, 55.19, 33.96. LRMS (ESI): *m/z* calcd. For $C_{28}H_{32}O_5$ [M+ Na] = 471.6, found, 471.3.

***N*-(2-Fluorophenyl)-2,3,6-tri-*O*-(benzyl)-4-deoxy-D-gluconamide (4.26 (v))**

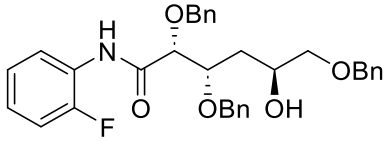

4.26 (v)

4.26(iv) (1.08 g, 1 eq) was dissolved in AcOH (17 mL, 7 mL / mmol), and 3 M H_2SO_4 (2 mL, 2.5 eq) was added to the reaction flask. The reaction flask was equipped with a water condenser and brought to 80 °C, being allowed to stir for 100 minutes. The reaction flask was then removed from heat and allowed to cool to room temperature. The reaction mixture was diluted with DCM and the organic phase extracted with water (3 X 25 mL), dried with Na_2SO_4, filtered through cotton and concentrated under reduced pressure to yield a crude oil (0.96 g). The crude 2,3,6-tri-*O*-(Benzyl)-4-(deoxy)-D-glucopyranoside (0.96 g, 1 eq) was placed under high vacuum for 8 hours, after-which, the oil was dissolved in DMSO (5.5 mL, 0.4 M) and charged with Ac_2O (3.5 mL, 17

eq). The reaction mixture was allowed to stir at room temperature overnight, after-which the reaction mixture was poured into water (50 mL) and diluted with DCM (75 mL). The organic phase was washed with brine (3 X 50 mL), dried with Na_2SO_4, filtered through cotton and concentrated under reduced pressure to yieldd 2,3,6-tri-*O*-(Benzyl)-4-(deoxy)-D-glucono-γ-lactone as a clear oil (0.87 g, 0.2 g reserved for alternate reaction). To a round-bottom flask, 2,3,6-tri-*O*-(Benzyl)-4-(deoxy)-D-glucono-γ-lactone (0.67 g, 1 eq), 2-fluoroaniline (0.15 mL, 1 eq) and AcOH (3 mL, 0.5 M) were added, and a water condenser is equipped. The reaction flask was brought to 100 °C and allowed to stir for one hour, after-which the reaction flask was removed from heat, and allowed to cool to room temperature. The resulting slurry was concentrated under reduced pressure, and purified by silica flash column chromatography (10 – 50 % EtOAc : Hex) to afford the title intermediate as a white solid (0.14 g, 14 % over three steps). **^{1}H NMR** (400 MHz, $CDCl_3$): *δ* 8.77 (br, 1H), 8.34 (dt, *J* = 8.0, 1.4 Hz, 1H), 7.38 – 7.26 (m, 10H), 7.20 – 7.16 (m, 4H), 7.15 – 7.04 (m, 3H), 4.73 (d, *J* = 11.4 Hz, 1H), 4.58 (d, *J* = 11.4 Hz, 1H), 4.56 (s, 2H), 4.52 (s, 2H), 4.22 – 4.17 (m, 1H), 4.03 (d, *J* = 3.1 Hz, 1H), 4.00 – 3.93 (m, 1H), 3.46 (dd, *J* = 9.4, 3.2 Hz, 1H), 3.29 (dd, *J* = 9.4, 7.6 Hz, 1H), 2.29 (br, OH), 1.82 – 1.73 (m, 1H), 1.64 – 1.55 (m, 1H). Note: Residual EtOAc is present in ^{1}H spectrum from flash column chromatography. ^{13}C spectrum was not acquired for this intermediate.

***N*-(4-Methoxyphenyl)-2,3,6-tri-*O*-(benzyl)-4-deoxy-D-gluconamide (4.27 (v))**

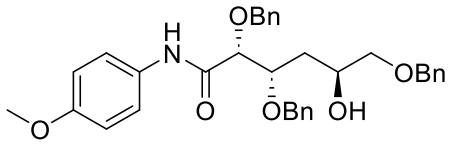

4.27 (v)

4.26(iv) (0.35 g, 1 eq) was dissolved in AcOH (5.5 mL, 7 mL / mmol), and 3 M H_2SO_4 (0.65 mL, 2.5 eq) was added to the reaction flask. The reaction flask was equipped with a water condenser and brought to 80 °C, being allowed to stir for 100 minutes. The reaction flask was then removed from heat and allowed to cool to room temperature. The reaction mixture was diluted with DCM and the organic phase extracted with water (3 X 25 mL), dried with Na_2SO_4, filtered through cotton and concentrated under reduced pressure to yield a crude oil (0.28 g). The crude 2,3,6-tri-*O*-(benzyl)-4-(deoxy)-D-glucopyranoside (0.28 g, 1 eq) was placed under high vacuum for 8 hours, after-which, the oil was dissolved in DMSO (2 mL, 0.4 M) and charged with Ac_2O (1 mL, 17 eq). The reaction mixture was allowed to stir at room temperature overnight, after-which the reaction mixture was poured into water (50 mL) and diluted with DCM (75 mL). The organic phase was

washed with brine (3 X 50 mL), dried with Na_2SO_4, filtered through cotton and concentrated under reduced pressure to yield 2,3,6-tri-*O*-(benzyl)-4-(deoxy)-D-glucono-γ-lactone as a clear oil (0.30 g). To a round-bottom flask, 2,3,6-tri-*O*-(benzyl)-4-(deoxy)-D-glucono-γ-lactone (0.30 g, 1 eq), *p*-anisidine (95 mg, 1.1 eq) and AcOH (1.4 mL, 0.5 M) were added, and a water condenser was equipped. The reaction flask was brought to 100 °C and allowed to stir for one hour, after-which the reaction flask was removed from heat and allowed to cool to room temperature. The resulting slurry was concentrated under reduced pressure and purified by silica flash column chromatography (30 % EtOAc : Hex) to afford the title intermediate as a white solid (67 mg, 15 % over three steps). **^{1}H NMR** (400 MHz, $CDCl_3$): *δ* 8.33 (br, 1H), 7.40 – 7.35 (m, 2H), 7.35 – 7.27 (m, 10H), 7.21 – 7.15 (m, 2H), 6.87 – 6.82 (m, 2H), 4.69 (d, *J* = 11.5 Hz, 1H), 4.59 (d, *J* = 11.5 Hz, 1H), 4.54 (s, 2H), 4.52 (s, 2H), 4.22 – 4.16 (m, 1H), 4.00 (d, *J* = 2.9 Hz, 1H), 3.98 – 3.92 (m, 1H), 3.78 (s, 3H), 3.46 (dd, *J* = 9.4, 3.2 Hz, 1H), 3.30 (dd, *J* = 9.4, 1.9 Hz, 1H), 2.31 (br, OH), 1.84 – 1.74 (m, 1H), 1.61 – 1.53 (m, 1H). **^{13}C NMR** (100 MHz, $CDCl_3$): *δ* 168.92, 156.47, 137.93, 137.86, 136.59, 130.50, 128.70 (4x CH), 128.50 (3 X CH), 128.41 (2 X CH), 128.33 (2 X CH), 127.84, 127.80, 127.77 (2 X CH), 121.26 (2 X CH), 114.18 (2 X CH), 62.71, 77.25, 77.18, 74.74, 74.40, 74.22, 73.34, 67.19, 55.52, 35.24.

***N*-(2-Flurophenyl)-4-deoxy-D-gluconamide (4.26)**

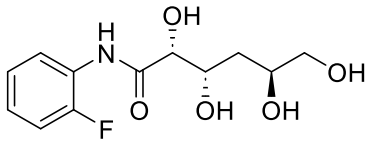

4.26

To a hydrogenation flask, **4.26 (v)** (0.14 g, 1 eq), EtOAc (2.5 mL, 0.1 M) and MeOH (2.5 mL, 0.1 M) were added, followed by Pd/C (10 wt% on activated carbon support) (27 mg, 0.1 eq). The air was purged from the system through water aspiration. A hydrogen balloon was attached to the hydrogenation flask, and the reaction was placed under an atmosphere of hydrogen; the hydrogenation flask was purged of atmosphere and replaced with hydrogen gas every hour. Once the reaction was deemed complete (10 hours) the reaction mixture was filtered through celite and concentrated under reduced pressure to yield the desired product as a white solid (72 mg, 93 %). **^{1}H NMR** (400 MHz, D_2O): *δ* 8 7.45 (dt, *J* = 7.9, 1.6 Hz, 1H), 7.24 – 7.17 (m, 1H), 7.15 – 7.08 (m, 2H), 4.16 – 4.11 (m, 2H), 3.81 – 3.73 (m, 1H), 3.50 (dd, *J* = 11.7, 4.0 Hz, 1H), 3.38 (dd, *J* = 11.7, 7.1 Hz, 1H), 1.72 – 1.63 (m, 1H), 1.54 – 1.44 (m, 1H). **^{13}C NMR** (100 MHz, D_2O): *δ* 174.17, 128.23 (d, *J* = 7.9 Hz), 126.29, 124.62 (d, *J* = 3.8 Hz), 116.00 (d, *J* = 19.5 Hz), 74.85, 68.59, 68.38, 65.95,

35.95. Note: ^{13}C NMR too dilute for **C**-F doublet to be displayed. LRMS (ESI): *m/z* calcd. For $C_{12}H_{16}FNO_5$ [M+ Na] = 296.3, found, 296.1.

***N*-(4-Methoxyphenyl)-4-deoxy-D-gluconamide (4.27)**

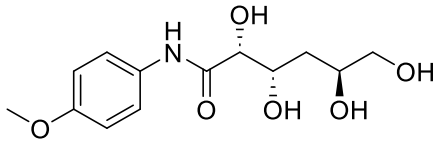

4.27

To a hydrogenation flask, **4.27 (v)** (61 mg, 1 eq), EtOAc (1.2 mL, 0.1 M) and MeOH (1.2 mL, 0.1 M) were added, followed by Pd/C (10 wt% on activated carbon support) (13 mg, 0.1 eq). The air was purged from the system through water aspiration. A hydrogen balloon was attached to the hydrogenation flask, and the reaction was placed under an atmosphere of hydrogen; the hydrogenation flask was purged of atmosphere and replaced with hydrogen gas every hour. Once the reaction was deemed complete (6 hours) the reaction mixture was filtered through celite and concentrated under reduced pressure to yield the desired product as a white solid (37 mg, 99 %). **^{1}H NMR** (400 MHz, $(CD_3)_2SO$): *δ* 9.36 (br, 1H), 7.59 – 7.54 (m, 2H), 6.86 – 6.80 (m, 2H), 5.49 – 5,41 (m, 1H), 4.46 (t, *J* = 5.9 Hz, 1H), 4.42 – 4.35 (m, 2H), 4.04 – 3.97 (m, 1H), 3.82 – 3.78 (m, 1H), 3.68 (s, 3H), 3.63 – 3.55 (m, 1H), 1.63 – 1.54 (m, 1H), 1.33 – 1.23 (m, 1H). Note: Due to lack of compound, ^{13}C spectrum too dilute to process. LRMS (ESI): *m/z* calcd. For $C_{13}H_{19}NO_6$ [M+ Na] = 308.3, found, 308.1.

***N*-(2-Fluorophenyl)-6-hydroxyhexylamide (4.28)**

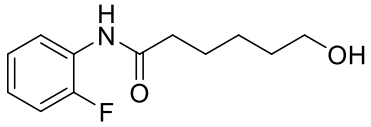

4.28

To a flame-dried round-bottom flask under an atmosphere of argon, ε-caprolactone (0.5 mL, 1 eq) and THF (45 mL, 0.1 M) were added. The reaction flask was placed into a water / ice bath and allowed to cool for 5 minutes. TMA (2M solution in toluene) (4.5 mL, 2 eq) was added to the solution dropwise followed by the careful addition of 2-fluoroaniline (0.9 mL, 2 eq). The reaction flask was removed from the water / ice bath and allowed to stir at room temperature until complete (2 hours). The reaction was quenched with the slow addition of 1 M HCl solution (50 mL) and allowed to stir for 30 minutes. The reaction mixture was diluted with Et_2O (150 mL), the organic

phase was washed with brine (3 X 100 mL), dried with Na_2SO_4, filtered through cotton, and concentrated under reduced pressure. The crude mixture was purified with silica flash chromatography (30 – 50 % EtOAc : Hex), to yield the title product as a white solid after concentration under reduced pressure (0.69 g, 68 %). **^{1}H NMR** (400 MHz, $CDCl_3$): *δ* 8.31 (t, *J* = 7.6 Hz, 1H), 7.35 (br, 1H), 7.13 – 6.98 (m, 3H), 3.66 (q, *J* = 6.3 Hz, 2H), 2.41 (t, *J* = 7.4 Hz, 2H), 1.76 (quint, *J* = 7.6 Hz, 2H), 1.65 – 1.56 (m, 2H), 1.51 – 1.43 (m, 2H). **^{13}C NMR** (100 MHz, $CDCl_3$): *δ* 171.20, 126.40, 124.63 (d, *J* = 3.7 Hz), 124.17 (d, *J* = 7.5 Hz), 121.70, 114.73 (d, *J* = 19.4 Hz), 62.63, 37.63, 32.30, 25.33, 25.08. Note: 13C spectrum not concentrated enough to automatically peak pick **C** – F doublet (152.16 (d, *J* = 245.9)). LRMS (ESI): *m/z* calcd. For $C_{12}H_{16}FNO_2$ [M+ Na] = 248.3, found, 248.1.

***N*-(2-Fluorophenyl)-(S)-5,6-dihydroxyhexylamide (4.29)**

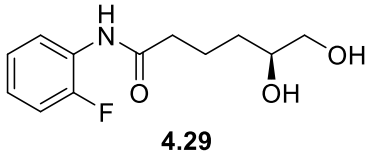

4.29

To a flame-dried round-bottom flask under an atmosphere of argon 5-hexenoic acid (0.5 mL, 1 eq), 2-fluoroaniline (0.48 mL, 1.1 eq), and DCM (14 mL, 0.33 M) were added. DMAP (60 mg, 0.1 eq) was added to the reaction flask, and the flask is placed into a water / ice bath. DCC (1.4 g, 1.5 eq) was added portion-wise to the reaction flask, after complete addition, the reaction flask was removed from the water / ice bath and allowed to stir at room temperature until complete (24 hours). Excess DCM (50 mL) was added, the organic phase was extracted with 1 M HCl (3 X 50 mL), saturated sodium bicarbonate (3 X 50 mL) then brine (2 X 50 mL). The resulting organic phase was dried with Na_2SO_4, filtered through cotton and concentrated under reduced pressure. Crude mixture was purified with silica flash column chromatography (10 % EtOAc : Hex), to yield *N*-(2-fluorophenyl)-hex-5-enamide (0.23 g) as a white solid after concentration under reduced pressure. Once sufficiently dried, *N*-(2-fluorophenyl)-hex-5-enamide (0.23 g, 1 eq) was suspended in ^{t}BuOH (7 mL, 0.16 M) and water (7 mL, 0.16 M). Methanesulfonamide (0.1 g, 90 mg / mmol) and AD-mix-α (1.54 g, 1.4 g / mmol) were added to the reaction flask. The reaction was allowed to stir until complete (5 days). Once complete, the reaction was quenched with the addition of saturated Na_2SO_3 (50 mL) and diluted with the addition of EtOAc (50 mL). The organic phase was extracted with brine (3 X 50 mL), dried with Na_2SO_4, filtered through cotton, and concentrated under reduced pressure. The crude slurry was purified with silica flash column chromatography (EtOAc – 10% MeOH : EtOAc), to yield the title compound as a white solid

following concentration under reduced pressure (0.11 g, 10 % two steps). **^{1}H NMR** (400 MHz, $(CD_3)_2SO$): *δ* 9.60 (br, 1H), 7.86 – 7.79 (m, 1H), 7.23 – 7.16 (m, 1H), 7.13 – 7.06 (m, 2H), 4.47 – 4.38 (m, 2H), 3.38 (sept, *J* = 4.3 Hz, 1H), 3.28 – 3.16 (m, 2H), 2.40 – 2.26 (m, 2H), 1.76 – 1.63 (m, 1H), 1.60 – 1.49 (m, 1H), 1.48 – 1.38 (m, 1H), 1.26 – 1.16 (m, 1H). **^{13}C NMR** (100 MHz, $(CD_3)_2SO$): *δ* 172.20, 154.00 (d, *J* = 244.8 Hz), 126.74 (d, *J* = 11.6 Hz), 125.54 (d, *J* = 7.4 Hz), 124.84, 124.70 (d, *J* = 3.5 Hz), 115.89 (d, *J* = 19.5 Hz), 71.38, 68.40, 36.44, 33.41, 22.09. LRMS (ESI): *m/z* calcd. For $C_{12}H_{16}FNO_3$ [M+ Na] = 264.3, found, 264.1.

***N*-(2-Fluorophenyl)-(R,R)-3,4-dihydroxyhexylamide (4.30)**

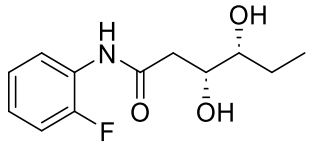

4.30

To a flame-dried round-bottom flask under an atmosphere of argon, 3-hexenoic acid (1 mL, 1 eq), 2-fluoroaniline (0.9 mL, 1.1 eq), and DCM (26 mL, 0.33 M) were added. DMAP (0.1 g, 0.1 eq) was added to the reaction flask, and the flask was placed into a water / ice bath. DCC (2.6 g, 1.5 eq) was added portion-wise to the reaction flask, after complete addition, the reaction flask was removed from the water / ice bath and allowed to stir at room temperature until complete (18 hours). Excess DCM (100 mL) was added, the organic phase was then extracted with 1 M HCl (3 X 75 mL), saturated sodium bicarbonate (3 X 75 mL) then brine (2 X 75 mL). The resulting organic phase was dried with Na_2SO_4, filtered through cotton and concentrated under reduced pressure. Crude mixture was purified with silica flash column chromatography (10 % EtOAc : Hex), to yield *N*-(2-fluorophenyl)-hex-3-enamide (0.63 g) as a clear oil after concentration under reduced pressure. Once sufficiently dried, *N*-(2-fluorophenyl)-hex-3-enamide (0.63 g, 1 eq) was suspended in ^{t}BuOH (19 mL, 0.16 M) and water (19 mL, 0.16 M). Methanesulfonamide (0.27 g, 90 mg/mmol) and AD-mix-α (4.23 g, 1.4 g/mmol) were added to the reaction flask. The reaction was allowed to stir until complete (3 days). Once complete, the reaction was quenched with the addition of saturated Na_2SO_3 (100 mL) and diluted with the addition of EtOAc (100 mL). The organic phase was extracted with brine (3 X 100 mL), dried with Na_2SO_4, filtered through cotton, and concentrated under reduced pressure. The crude slurry was purified with silica flash column chromatography (50 % EtOAc : Hex), to yield the title compound as a white solid following concentration under reduced pressure (0.51 g, 25 % two steps). **^{1}H NMR** (400 MHz, $(CD_3)_2SO$): *δ* 9.60, 7.91 (dt, *J* = 5.1, 1.9 Hz, 1H), 7.23 – 7.16 (m, 1H), 7.13 – 7.04 (m, 2H), 4.66 (d, *J* = 5.7

Hz, 1H), 4.40 (d, *J* = 6.0 Hz, 1H), 3.82 (sext, *J* = 5.4 Hz, 1H), 3.20 (sext, *J* = 5.4 Hz, 1H), 2.53 – 2.36 (m, 3H), 1.53 – 1.41 (m, 1H), 1.31 – 1.18 (m, 1H), 0.86 (t, *J* = 7.4 Hz, 3H). **^{13}C NMR** (100 MHz, $(CD_3)_2SO$): *δ* 171.18, 153.74 (d, *J* = 244.4 Hz), 126.78 (d, *J* = 11.4 Hz), 125.28 (d, *J* = 7.6 Hz), 124.70 (d, *J* = 3.5 Hz), 124.26, 115.18 (d, *J* = 19.5 Hz), 74.88, 70.71, 40.30, 25.33, 11.17. LRMS (ESI): *m/z* calcd. For $C_{12}H_{16}FNO_3$ [M+ Na] = 264.3, found, 264.0.

***N*-(2-Fluorophenyl)-(S)-4,5-dihydroxypentylamide (4.31)**

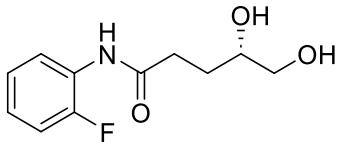

4.31

To a flame-dried round-bottom flask under an atmosphere of argon 4-pentenoic acid (1.5 mL, 1 eq), 2-fluoroaniline (1.6 mL, 1.1 eq), and DCM (45 mL, 0.33 M) were added. DMAP (0.18 g, 0.1 eq) was added to the reaction flask, and the flask was placed into a water / ice bath. DCC (4.6 g, 1.5 eq) was added portion-wise to the reaction flask, after the complete addition, the reaction flask was allowed to stir at room temperature until complete (18 hours). Excess DCM (100 mL) was added, the organic phase was then extracted with 1 M HCl (3 X 100 mL), saturated sodium bicarbonate (3 X 100 mL) then brine (2 X 100 mL). The resulting organic phase was dried with Na_2SO_4, filtered through cotton and concentrated under reduced pressure. Crude mixture was purified with silica flash column chromatography (10 % EtOAc : Hex), to yield *N*-(2-fluorophenyl)-pent-4-enamide (1.32 g) as a white solid after concentration under reduced pressure. Once sufficiently dried, *N*-(2-fluorophenyl)-pent-4-enamide (1.32 g, 1 eq) was suspended in ^{t}BuOH (43 mL, 0.16 M) and water (43 mL, 0.16 M). Methanesulfonamide (0.6 g, 90 mg/mmol) and AD-mix-α (9.6 g, 1.4 g/mmol) were added to the reaction flask. The reaction was allowed to stir until complete (7 days). Once complete, the reaction was quenched with the addition of saturated Na_2SO_3 (150 mL) and diluted with the addition of EtOAc (150 mL). The organic phase was extracted with brine (3 X 100 mL), dried with Na_2SO_4, filtered through cotton, and concentrated under reduced pressure. The crude slurry was purified with silica flash column chromatography (EtOAc – 10% MeOH : EtOAc), to yield the title compound as a white solid following concentration under reduced pressure (0.7 g, 21 % two steps). **^{1}H NMR** (400 MHz, $(CD_3)_2SO$): *δ* 9.62 (br, 1H), 7.85 – 7.77 (m, 1H), 7.22 – 7.15 (m, 1H), 7.12 – 7.05 (m, 2H), 4.51 (d, *J* = 5.0 Hz, 1H), 4.48 (t, *J* = 5.7 Hz, 1H), 3.04 (sept, *J* = 4.3 Hz, 1H), 3.29 – 3.18 (m, 2H), 2.50 – 2.33 (m, 2H), 1.81 – 1.70 (m, 1H), 1.53 – 1.42 (m, 1H). **^{13}C NMR** (100 MHz, $(CD_3)_2SO$): *δ* 172.40, 152.96, 126.75 (d, *J* =

11.6 Hz), 125.48, 124.87, 124.67 (d, *J* = 3.6 Hz), 115.89 (d, *J* = 19.5 Hz), 71.09, 66.24, 32.71, 29.75. Note: ^{13}C Spectrum reported as peak-picked with the range define tool, sample too dilute to automatically detect peaks at 155.31 and 125.56; reported singlets 152.96, and 125.48 would be doublets (due to ^{19}F coupling) in a more concentrated sample. LRMS (ESI): *m/z* calcd. For $C_{11}H_{15}FNO_3$ [M+ Na] = 251.1, found, 251.1.

***N*-(2-Fluorophenyl)-6-Methoxyhexylamide (4.32)**

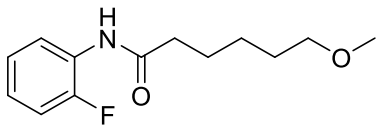

4.32

To a flame-dried round-bottom flask under an atmosphere of argon, 6-methoxy hexanoic acid (0.5 mL, 1 eq), 2-fluoroaniline (0.3 mL, 1.1 eq), and DCM (9 mL, 0.33 M) were added, and the reaction flask is placed in a water / ice bath. DMAP (37 mg, 0.1 eq) was added to the reaction flask followed by the portion-wise addition of DCC (0.93 g, 1.5 eq). The reaction was allowed to stir at room temperature until complete (22 hours), after-which the reaction was diluted with DCM (50 mL). The organic phase was washed with 1 M HCl (3 X 50 mL), saturated sodium bicarbonate (3 X 50 mL) and brine (2 X 50 mL). The resulting organic phase was dried with Na_2SO_4, filtered through cotton and concentrated under reduced pressure. The crude mixture was purified with silica flash column chromatography (10 – 30 % EtOAc : Hex), to isolate the title compound as a white solid following concentration under reduced pressure (0.4 g, 56 %). **^{1}H NMR** (400 MHz, $CDCl_3$): *δ* 8.27 (t, *J* = 8.0 Hz, 1H), 7.43 (br, 1H), 7.11 – 6.96 (m, 3H), 3.36 (dt, *J* = 6.4, 1.4 Hz, 2H), 3.30 (d, *J* = 1.8 Hz, 3H), 2.38 (t, *J* = 7.5 Hz, 2H), 1.73 (quint, *J* = 7.8 Hz, 2H), 1.63 – 1.54 (m, 2H), 1.47 – 1.37 (m, 2H). **^{13}C NMR** (100 MHz, $CDCl_3$): *δ* 171.31, 152.37 (d, *J* = 242.8 Hz), 126.43 (d, *J* = 9.9 Hz), 124.56 (d, *J* = 3.7 Hz), 124.16 (d, *J* = 7.6 Hz), 121.84, 114.75 (d, *J* = 19.3 Hz), 72.53, 58.56, 37.63, 29.33, 25.79, 25.30. LRMS (ESI): *m/z* calcd. For $C_{13}H_{18}FNO_2$ [M+ Na] = 262.3, found, 262.1.

N-(2-Fluorophenyl)-(S)-5,6-*O*-(isopropylidene)-hexylamide (4.33)

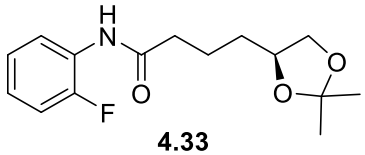

4.33

To a flame-dried round-bottom flask under an atmosphere of argon, **4.29** (0.26 g, 1 eq), 2,2-DMP (0.15 mL, 1.1 eq), PTSA (9 mg, 0.05 eq) and acetone (0.5 mL, 1.8 M) were added. The reaction was allowed to stir at room temperature until complete (5 hours), after-which the crude mixture was concentrated under reduced pressure. The resulting slurry was purified with silica flash column chromatography (10 – 30 % EtOAc : Hex) affording the title compound as a clear oil following concentration under reduced pressure (84 mg, 31 %).**^{1}H NMR** (400 MHz, $CDCl_3$): *δ* 8.26 (t, *J* = 8.1 Hz, 1H), 7.51 (br, 1H), 7.12 – 6.97 (m, 3H), 4.09 (quint, *J* = 6.9 Hz, 1H), 4.05 – 3.99 (m, 1H), 3.50 (t, *J* = 7.5 Hz, 1H), 2.45 (t, *J* = 7.3 Hz, 2H), 1.89 – 1.75 (m, 2H), 1.68 – 1.59 (m, 2H), 1.38 (s, 3H), 1.33 (s, 3H). **^{13}C NMR** (100 MHz, $CDCl_3$): *δ* 171.02, 152.23 (*J* = 242.8 Hz), 126.31 (*J* = 10.1 Hz), 124.57 (*J* = 3.7 Hz), 124.28 (*J* = 7.7 Hz), 121.91, 114.79 (*J* = 19.3 Hz), 108.95, 75.89, 69.34, 37.26, 32.52, 26.90, 25.73, 22.03. LRMS (ESI): *m/z* calcd. For $C_{15}H_{20}FNO_3$ [M+ Na] = 304.3, found, 304.1.

Synthesis of N_6 amine derivatives of compound 4.28

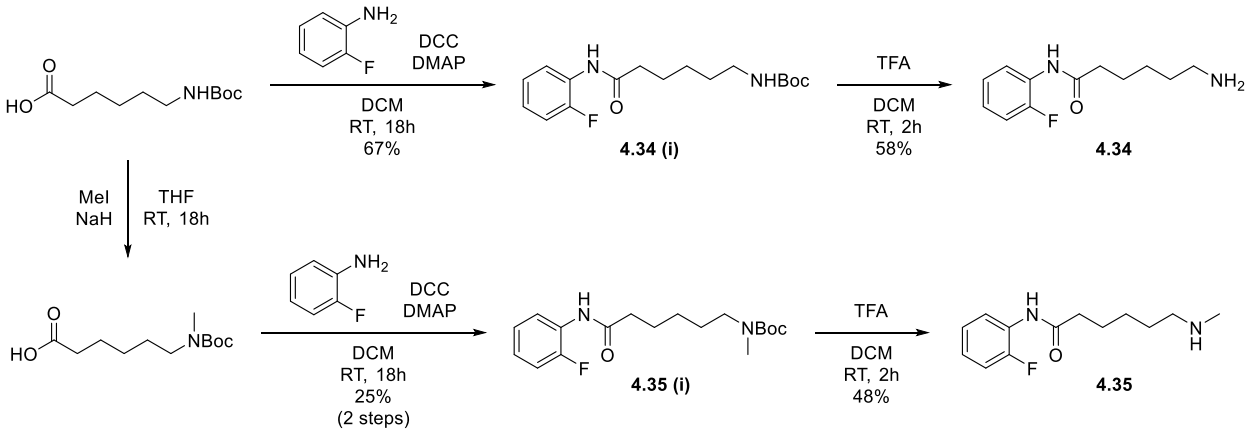

tert-Butyl-(6-oxo-6-(2-fluorophenylamino)hexyl)carbamate (4.34 (i))

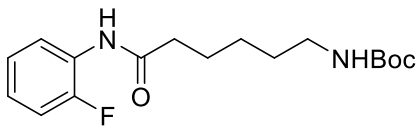

4.34 (i)

To a flame-dried round-bottom flask under an atmosphere of argon, Boc-6-Ahx-OH (0.5 g, 1 eq), 2-fluoroaniline (0.2 mL, 1 eq), DIPEA (1.5 mL, 4 eq), and DMF (3 mL, 0.7 M) were added. HBTU (0.9 g, 1.1 eq) was then added, and the reaction was allowed to stir at room temperature until complete (26 hours). Once complete, EtOAc (50 mL) was added, and the organic phase was washed with brine (3 X 50 mL), dried with Na_2SO_4, filtered through cotton and concentrated under reduced pressure. The crude mixture was purified with silica flash column chromatography (20 – 30 % EtOAc : Hex), to yield the title compound as a white solid following concentration under reduced pressure (0.36 g, 52 %). **^{1}H NMR** (400 MHz, $CDCl_3$): *δ* 8.09 (t, *J* = 8.0 Hz, 1H), 7.91 (br, 1H), 7.02 – 6.89 (m, 3H), 4.84 – 4.72 (m, 1H), 3.04 – 2.94 (m, 2H), 2.32 (t, *J* = 7.5 Hz, 2H), 1.62 (quint, *J* = 7.5 Hz, 2H), 1.43 – 1.36 (m, 2H), 1.33 (s, 9H), 1.30 – 1.23 (m, 2H). **^{13}C NMR** (100 MHz, $CDCl_3$): *δ* 171.69, 156.10, 152.86 (d, *J* = 243.7 Hz), 126.27 (d, *J* = 10.5 Hz), 124.44 (d, *J* = 7.6 Hz), 124.32 (d, *J* = 3.6 Hz), 122.58, 114.85 (d, *J* = 19.4 Hz), 78.87, 40.28, 37.13, 29.72, 28.37 (3 X CH_3), 26.27, 25.07. LRMS (ESI): *m/z* calcd. For $C_{17}H_{25}FN_2O_3$ [M+ Na] = 347.2, found, 347.2.

6-Amino-*N*-(2-fluorophenyl)-hexamide (4.34)

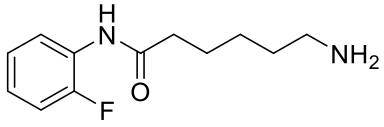

4.34

To a flame-dried round-bottom flask under an atmosphere of argon, **4.34 (i)** (0.36 g, 1 eq), TFA (0.4 mL, 5 eq) and DCM (11 mL, 0.1 M) were added. The reaction was allowed to stir at room temperature until complete (3 hours). The reaction mixture was concentrated under reduced pressure, and added onto silica for purification by flash column chromatography (30 – 50 – 90 % EtOAc : Hex). The title product was isolated as a white solid following concentration under reduced pressure (47 mg, 19 %). **^{1}H NMR** (400 MHz, $((CD_3)_2CO)$: *δ* 8.22 – 8.13 (m, 1H), 7.16 – 7.04 (m, 3H), 3.76 (t, *J* = 7.5 Hz, 2H), 2.54 – 2.46 (m, 2H), 2.08 – 2.06 (m, 2H), 1.85 (quint, *J* = 7.4 Hz, 2H), 1.72 (quint, *J* = 7.4 Hz, 2H), 1.54 – 1.44 (m, 2H). **^{13}C NMR** (100 MHz, $((CD_3)_2CO)$: *δ* 171.34, 152.04, 127.00 (d, *J* = 11.1 Hz), 124.29 (d, *J* = 7.3 Hz), 124.13 (d, *J* = 3.7 Hz), 123.07, 114.92 (d, *J* = 19.6 Hz), 46.93, 35.82, 26.83, 25.73, 24.58. LRMS (ESI): *m/z* calcd. For $C_{12}H_{17}FN_2O$ [M+ Na] = 247.1, found, 247.1.

tert-Butyl-(6-oxo-6-(2-Fluorophenylamino)hexyl)-*N*-(methyl)carbamate (4.35 (i))

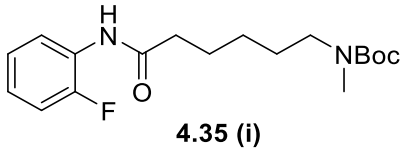

4.35 (i)

To a flame-dried round-bottom flask under an atmosphere of argon, 6-(tert-butoxycarbonylamino)hexanoic acid (0.5 g, 1 eq) and THF (5 mL, 0.4 M) were added. The reaction flask was placed in a water / ice bath, and NaH (60 % suspension in mineral oil) (0.35 g, 4 eq) was added potion-wise, followed by the dropwise addition of MeI (0.4 mL, 3 eq). The reaction was removed from the water / ice bath and allowed to stir at room temperature until complete (18 hours). Once complete, the reaction mixture was poured into saturated NH_4Cl (50 mL) and diluted with EtOAc (50 mL). The organic phase was washed with brine (3 X 50 mL), dried with Na_2SO_4, filtered through cotton, and concentrated under reduced pressure, yielding 6-(tert-butoxycarbonyl(methyl)amino)hexanoic acid as a yellow oil (0.3 g). To a flame-dried round-bottom flask under an atmosphere of argon, 6-(tert-butoxycarbonyl(methyl)amino)hexanoic acid (0.3 g, 1 eq), 2-fluoroaniline (0.12 mL, 1.1 eq), and DCM (4 mL, 0.33 M) were added, the reaction flask was then placed in a water / ice bath. DMAP (15 mg, 0.1 eq) was added to the reaction flask followed by the portion-wise addition of DCC (0.37 g, 1.5 eq). The reaction was allowed to stir at room temperature until complete (22 hours), after-which the reaction is diluted with DCM (50 mL). The organic phase was washed with 1 M HCl (3 X 50 mL), saturated sodium bicarbonate (3 X 50 mL) and brine (2 X 50 mL). The resulting organic phase is dried with Na_2SO_4, filtered through cotton and concentrated under reduced pressure. The crude mixture was purified with silica flash column chromatography (20 – 50 % EtOAc : Hex), isolating the title compound as a clear oil following concentration under reduced pressure (0.19 g, 47 %). **^{1}H NMR** (400 MHz, $CDCl_3$): δ 8.19 (t, J = 7.8 Hz, 1H), 7.64 (br, 1H), 7.08 – 6.91 (m, 3H), 3.17 – 3.09 (m, 2H), 2.76 (s, 3H), 2.40 – 2.30 (m, 2H), 1.74 – 1.64 (m, 2H), 1.51 – 1.43 (m, 2H), 1.37 (s, 9H), 1.33 – 1.26 (m, 2H). **^{13}C NMR** (100 MHz, $CDCl_3$): δ 171.40, 155.79, 152.91 (d, J = 243.1 Hz), 126.34 (d, J = 10.2 Hz), 124.44 (d, J = 3.5 Hz), 123.27 (d, J = 7.4 Hz), 122.13, 114.76 (d, J = 19.3 Hz), 79.14, 37.45, 33.94, 32.66, 30.87, 28.42, 26.25, 25.18.

6-(Methylamino)-*N*-(2-fluorophenyl)-hexanamide (4.35)

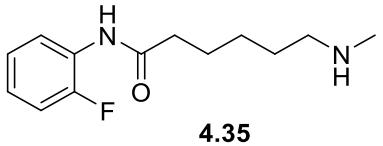

4.35

To a flame-dried round-bottom flask under an atmosphere of argon, **4.35 (i)** (0.19 g, 1 eq), TFA (0.2 mL, 5 eq) and DCM (6 mL, 0.1 M) were added. The reaction was allowed to stir at room temperature until complete (3 hours). The reaction mixture was concentrated under reduced pressure, and added onto silica for purification by flash column chromatography (20 – 50 % EtOAc : Hex – 10 % MeOH : EtOAc). The title product was isolated as a clear oil following concentration under reduced pressure (66 mg, 48 %). **^{1}H NMR** (400 MHz, $(CD_3)_2SO$): *δ* 9.66 (br ,1H), 8.27 (br, 2H), 7.89 – 7.80 (m, 1H), 7.27 – 7.19 (m, 1H), 7.17 – 7.12 (m, 2H), 2.87 (t, *J* = 7.6 Hz, 2H), 2.54 (s, 3H), 2.39 (t, *J* = 7.3 Hz, 2H), 1.65 – 1.53 (m, 4H), 1.40 – 1.30 (m, 2H). **^{13}C NMR** (100 MHz, $(CD_3)_2SO$): *δ* 170.80, 152.35 125.53 (d, *J* = 11.6 Hz), 124.61, 123.79, 123.66, 114.82 (d, *J* = 19.5 Hz), 47.56, 34.84, 31.91, 24.87, 24.67, 23.94. Please note, **C**-F (152.35) and *o*-**C**-H (125.53) peaks are picked manually due to low sample concentration. LRMS (ESI): *m/z* calcd. For $C_{13}H_{19}FN_2O$ [M+ Na] = 239.2, found, 239.2.

***N*-(Propyl)-D-gluconamide (5.01)**

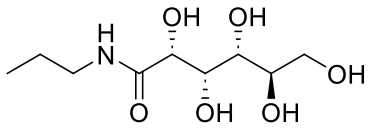

5.01

Glucono-δ-lactone (3 g, 1 eq), propylamine (1.4 mL, 1 eq) and MeOH (67 mL, 0.25 M) were added to a round-bottom flask. A water condenser was equipped, and the reaction was brought to reflux. The reaction was allowed to stir at reflux overnight, after-which it was removed from heat, and allowed to cool to room temperature. The crude mixture was concentrated under vacuum to afford the title compound as a white solid (3.69 g, 92 %). **^{1}H NMR** (400 MHz, $(CD_3)_2SO$): *δ* 7.58 (t, *J* = 5.9 Hz, 1H), 5.33 (d, *J* = 4.1 Hz, 1H), 4.52 (br, 1H), 4.45 (d, *J* = 1.8 Hz, 1H), 4.37 (d, *J* = 7.0 Hz, 1H), 4.31 (br, 1H), 3.97 – 3.91 (m, 1H), 3.89 – 3.82 (m, 1H), 3.57 – 3.50 (m, 1H), 3.46 – 3.39 (m, 2H), 3.36 – 3.28 (m, 1H), 3.07 – 2.93 (m, 2H), 1.38 (sext, *J* = 7.3 Hz, 2H), 0.78 (t, *J* = 7.4 Hz, 3H). **^{13}C NMR** (100 MHz, $(CD_3)_2SO$): *δ* 172.77, 74.11, 72.86, 71.92, 70.56, 63.81, 40.45, 22.86, 11.78. LRMS (ESI): *m/z* calcd. For $C_9H_{19}NO_6$ [M+ Na] = 260.2, found, 260.1.

***N*-(Hexyl)-D-gluconamide (5.02)**

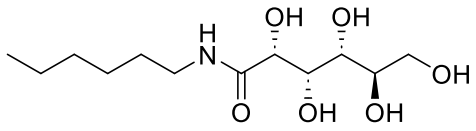

5.02

Glucono-δ-lactone (2.69 g, 1 eq), hexylamine (2.0 mL, 1 eq) and MeOH (61 mL, 0.25 M) were added to a round-bottom flask. A water condenser was equipped, and the reaction was brought to reflux. The reaction was allowed to stir at reflux overnight, after-which it was removed from heat, and allowed to cool to room temperature. The crude mixture was concentrated under vacuum to afford the title compound as a white solid (4.02 g, 95 %). **^{1}H NMR** (400 MHz, $(CD_3)_2SO$): *δ* 7.60 (t, *J* = 5.9 Hz, 1H), 5.36 (d, *J* = 3.4 Hz, 1H), 4.54 (d, *J* = 2.7 Hz, 1H), 4.48 (d, *J* = 3.7 Hz, 1H), 4.40 (d, *J* = 7.1 Hz, 1H), 4.34 (br, 1H), 3.99 – 3.94 (m, 1H), 3.91 – 3.85 (m, 1H), 3.57 (d, *J* = 10.7 Hz, 1H), 3.50 – 3.42 (m, 2H), 3.40 – 3.32 (m, 2H), 3.13 – 2.99 (m, 2H), 1.44 – 1.34 (m, 2H), 1.31 – 1.18 (m, 6H), 0.85 (t, *J* = 6.7 Hz, 3H). **^{13}C NMR** (100 MHz, $(CD_3)_2SO$): *δ* 172.69, 74.09, 72.87, 71.94, 70.57, 63.84, 38.70, 31.50, 29.59, 26.49, 26.49, 22.53, 14.40. LRMS (ESI): *m/z* calcd. For $C_{12}H_{25}NO_6$ [M+ Na] = 302.3, found, 302.2.

***N*-(Heptyl)-D-gluconamide (5.03)**

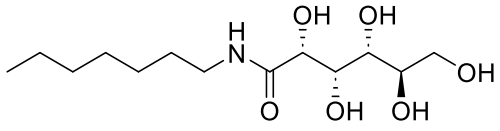

5.03

Glucono-δ-lactone (1.2 g, 1 eq), heptylamine (1.0 mL, 1 eq) and MeOH (27 mL, 0.25 M) were added to a round-bottom flask. A water condenser was equipped, and the reaction was brought to reflux. The reaction was allowed to stir at reflux overnight, after-which it was removed from heat, and allowed to cool to room temperature. The crude mixture was recrystallized from 99 % EtOH and concentrated under vacuum to afford the title compound as a white solid (0.32 g, 16 %). **^{1}H NMR** (400 MHz, $(CD_3)_2SO$): *δ* 7.56 (t, *J* = 5.9 Hz, 1H), 5.31 (d, *J* = 5.1 Hz, 1H), 4.50 (d, *J* = 5.0 Hz, 1H), 4.44 (d, *J* = 5.4 Hz, 1H), 4.35 (d, *J* = 7.2 Hz, 1H), 4.30 (t, *J* = 5.7 Hz, 1H), 3.95 – 3.90 (m, 1H), 3.88 – 3.82 (m, 1H), 3.56 – 3.50 (m, 1H), 3.46 – 3.38 (m, 2H), 3.10 – 2.95 (m, 2H), 1.41 – 1.32 (m, 2H), 1.28 – 1.14 (m, 8H), 0.82 (t, *J* = 7.0 Hz, 3H). **^{13}C NMR** (100 MHz, $(CD_3)_2SO$): *δ* 172.69, 74.09, 72.86, 71.94, 70.57, 63.84, 38.70, 31.72, 29.63, 28.91, 26.79, 22.53, 14.44. LRMS (ESI): *m/z* calcd. For $C_{13}H_{27}NO_6$ [M+ H] = 294.4, found, 294.2.

***N*-(Octyl)-D-gluconamide (5.04)**

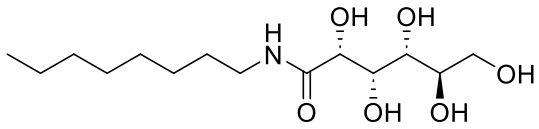

5.04

Glucono-δ-lactone (4.3 g, 1 eq), octylamine (4.0 mL, 1 eq) and MeOH (90 mL, 0.25 M) were added to a round-bottom flask. A water condenser was equipped, and the reaction was brought to reflux. The reaction was allowed to stir at reflux overnight, after-which it was removed from heat, and allowed to cool to room temperature. The crude mixture was concentrated under vacuum to afford the title compound as a white solid (4.7 g, 63 %). **^{1}H NMR** (400 MHz, $(CD_3)_2SO$): *δ* 7.61 (t, *J* = 6.0 Hz, 1H), 5.36 (d, *J* = 5.0 Hz, 1H), 4.55 (d, *J* = 5.0 Hz, 1H), 4.48 (d, *J* = 5.3 Hz, 1H), 4.40 (d, *J* = 7.2 Hz, 1H), 3.45 (t, *J* = 5.7 Hz, 1H), 4.00 – 3.95 (m, 1H), 3.92 – 3.87 (m, 1H), 3.62 – 3.55 (m, 1H), 3.51 – 3.43 (m, 2H), 3.40 – 3.33 (m, 3H), 3.14 – 2.99 (m, 2H), 1.45 – 1.35 (m, 2H), 1.31 – 1.19 (m, 10H), 0.86 (t, *J* = 6.6 Hz, 3H). **^{13}C NMR** (100 MHz, $(CD_3)_2SO$): *δ* 172.69, 74.09, 72.86, 71.94, 70.57, 63.84, 38.70, 31.72, 29.63, 28.93, 26.79, 22.54, 14.43. LRMS (ESI): *m/z* calcd. For $C_{14}H_{29}NO_6$ [M+ Na] = 330.4, found, 330.2.

***N*-(Cyclopropyl)-D-gluconamide (5.05)**

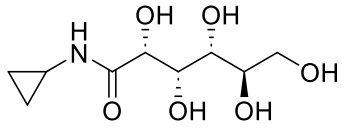

5.05

Glucono-δ-lactone (1.9 g, 1 eq), cyclopropylamine (0.75 mL, 1 eq) and MeOH (43 mL, 0.25 M) were added to a round-bottom flask. A water condenser was equipped, and the reaction was brought to reflux. The reaction was allowed to stir at reflux overnight, after-which it was removed from heat, and allowed to cool to room temperature. The crude mixture was concentrated under vacuum to afford the title compound as a white solid (1.74 g, 73 %). **^{1}H NMR** (400 MHz, $(CD_3)_2SO$): *δ* 7.50 (d, *J* = 4.5 Hz, 1H), 5.23 (d, *J* = 5.1 Hz, 1H), 4.50 (d, *J* = 4.9 Hz, 1H), 4.42 (d, *J* = 5.3 Hz, 1H), 4.37 (d, *J* = 7.1 Hz, 1H), 4.30 (t, *J* = 5.7 Hz, 1H), 3.91 (t, *J* = 4.1 Hz, 1H), 3.88 – 3.82 (m, 1H), 3.56 – 3.50 (m, 1H), 3.46 – 3.37 (m, 2H), 3.36 – 3.33 (m, 1H), 2.66 – 2.58 (m, 1H), 0.59 – 0.52 (m, 2H), 0.49 – 0.40 (m, 2H). **^{13}C NMR** (100 MHz, $(CD_3)_2SO$): *δ* 174.19, 74.01, 72.68, 71.93, 70.61, 63.81, 22.67, 6.15, 5.98. LRMS (ESI): *m/z* calcd. For $C_9H_{17}NO_6$ [M+ Na] = 258.2, found, 258.1.

***N*-(Cyclopentyl)-D-gluconamide (5.06)**

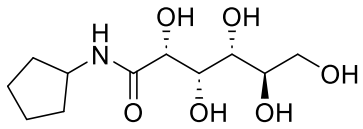

5.06

Glucono-δ-lactone (1.35 g, 1 eq), cyclopentylamine (0.75 mL, 1 eq) and MeOH (30 mL, 0.25 M) were added to a round-bottom flask. A water condenser was equipped, and the reaction was brought to reflux. The reaction was allowed to stir at reflux overnight, after-which it was removed from heat, and allowed to cool to room temperature. The crude mixture was concentrated under vacuum to afford the title compound as a white solid (1.54 g, 77 %). **^{1}H NMR** (400 MHz, $(CD_3)_2SO$): *δ* 7.37 (d, *J* = 7.7 Hz, 1H), 5.30 (d, *J* = 5.3 Hz, 1H), 4.50 (d, *J* = 4.9 Hz, 1H), 4.42 (d, *J* = 5.2 Hz, 1H), 4.37 (d, *J* = 7.2 Hz, 1H), 4.30 (t, *J* = 5.7 Hz, 1H), 3.98 (q, *J* = 7.2 Hz, 1H), 3.94 – 3.90 (m, 1H), 3.87 – 3.82 (m, 1H), 3.57 – 3.50 (m, 1H), 3.47 – 3.38 (m, 2H), 3.36 – 3.33 (m, 1H), 1.80 – 1.69 (m, 2H), 1.65 – 1.54 (m, 2H), 1.50 – 1.31 (m, 4H). **^{13}C NMR** (100 MHz, $(CD_3)_2SO$): *δ* 172.34, 74.03, 72.83, 71.92, 70.57, 63.82, 50.40, 32.69, 32.62, 23.93, 23.90. LRMS (ESI): *m/z* calcd. For $C_{11}H_{21}NO_6$ [M+ Na] = 286.3, found, 286.2.

***N*-(Cyclohexyl)-D-gluconamide (5.07)**

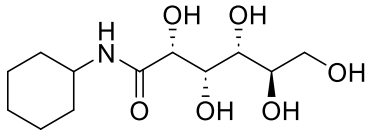

5.07

Glucono-δ-lactone (1.00 g, 1 eq), cyclohexylamine (0.64 mL, 1 eq) and MeOH (23 mL, 0.25 M) were added to a round-bottom flask. A water condenser was equipped, and the reaction was brought to reflux. The reaction was allowed to stir at reflux overnight, after-which it was removed from heat, and allowed to cool to room temperature. The crude mixture was concentrated under vacuum to afford the title compound as a white solid (1.17 g, 75 %). **^{1}H NMR** (400 MHz, $(CD_3)_2SO$): *δ* 7.28 (d, *J* = 8.3 Hz, 1H), 5.32 (d, *J* = 5.2 Hz, 1H), 4.50 (d, *J* = 5.0 Hz, 1H), 4.42 (d, *J* = 5.3 Hz, 1H), 4.38 (d, *J* = 7.2 Hz, 1H), 4.30 (t, *J* = 3.4 Hz, 1H), 3.93 – 3.89 (m, 1H), 3.86 – 3.82 (m, 1H), 3.58 – 3.48 (m, 2H), 3.46 – 3.38 (m, 2H), 3.36 – 3.33 (m, 1H), 1.70 – 1.58 (m, 4H), 1.51 (d, *J* = 12.8 Hz, 1H), 1.29 – 1.01 (m, 5H). **^{13}C NMR** (100 MHz, $(CD_3)_2SO$): *δ* 171.86, 73.98, 72.81, 71.90, 70.58, 63.82, 47.63, 21.74, 21.73, 25.61, 25.08 (2 X, CH_2). LRMS (ESI): *m/z* calcd. For $C_{12}H_{23}NO_6$ [M+ Na] = 300.3, found, 300.1.

***N*-(Cycloheptyl)-D-gluconamide (5.08)**

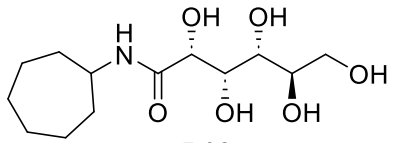

5.08

Glucono-δ-lactone (1.05 g, 1 eq), cycloheptylamine (0.75 mL, 1 eq) and MeOH (42 mL, 0.25 M) were added to a round-bottom flask. A water condenser was equipped, and the reaction was brought to reflux. The reaction was allowed to stir at reflux overnight, after-which it was removed from heat, and allowed to cool to room temperature. The crude mixture was recrystallized from MeOH then concentrated under vacuum to afford the title compound as a white solid (1.13 g, 66 %). **^{1}H NMR** (400 MHz, $(CD_3)_2SO$): *δ* 7.31 (d, *J* = 6.4 Hz, 1H), 5.32 (d, *J* = 5.2 Hz, 1H), 4.50 (d, *J* = 5.1 Hz, 1H), 4.41 (d, *J* = 5.4 Hz, 1H), 4.38 (d, *J* = 7.2 Hz, 1H), 4.30 (t, *J* = 5.7 Hz, 1H), 3.91 (dd, *J* = 5.0, 1.2 Hz, 1H), 3.87 – 3.82 (m, 1H), 3.76 – 3.66 (m, 1H), 3.56 – 3,49 (m, 1H), 3.47 – 3.38 (m, 2H), 3.37 – 3.33 (m, 1H), 1.76 – 1,66 (m, 2H), 1.60 – 1.29 (m, 10H). **^{13}C NMR** (100 MHz, $(CD_3)_2SO$): *δ* 171.52, 73.97, 72.83, 71.91, 70.57, 63.82, 49.81, 34.75, 34.68, 28.10, 28.02, 24.25 (2 X CH_2). LRMS (ESI): *m/z* calcd. For $C_{13}H_{25}NO_6$ [M+ Na] = 314.3, found, 314.2.

***N*-(Cyclooctyl)-D-gluconamide (5.09)**

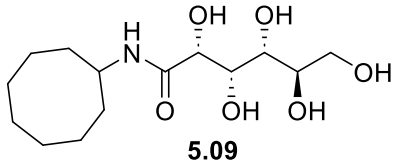

5.09

Glucono-δ-lactone (0.97 g, 1 eq), 185cyclooctylamine (0.75 mL, 1 eq) and MeOH (22 mL, 0.25 M) were added to a round-bottom flask. A water condenser was equipped, and the reaction was brought to reflux. The reaction was allowed to stir at reflux overnight, after-which it was removed from heat, and allowed to cool to room temperature. The crude mixture was concentrated under vacuum to afford the title compound as a white solid (0.80 g, 48 %). **^{1}H NMR** (400 MHz, $(CD_3)_2SO$): *δ* 7.30 (d, *J* = 8.2 Hz, 1H), 5.33 (d, *J* = 4.7 Hz, 1H), 4.52 (d, *J* = 3.4 Hz, 1H), 4.44 (d, *J* = 3.5 Hz, 1H), 4.40 (d, *J* = 7.1 Hz, 1H), 4.35 – 4.30 (m, 1H), 3.94 – 3.89 (m, 1H), 3.86 – 3.81 (m, 1H), 3.79 – 3.71 (m, 1H), 3.53 (d, *J* = 10.3 Hz, 1H), 3.45 – 3.40 (m, 2H), 1.68 – 1.32 (m, 15H). **^{13}C NMR** (100 MHz, $(CD_3)_2SO$): *δ* 171.51, 73.99, 72.83, 71.89, 70.58, 63.81, 48.68, 32.13, 32.00, 27.27, 27.18, 25.49, 23.89, 23.77. LRMS (ESI): *m/z* calcd. For $C_{14}H_{27}NO_6$ [M+ Na] = 328.4, found, 328.8.

***N,N*-(Dihexyl)-D-gluconamide (5.10)**

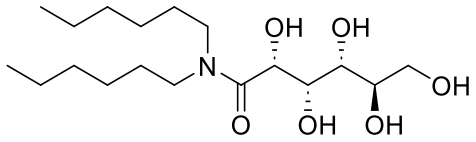

5.10

Glucono-δ-lactone (1.14 g, 1 eq), dihexylamine (1.5 mL, 1 eq) and MeOH (26 mL, 0.25 M) were added to a round-bottom flask. A water condenser was equipped, and the reaction was brought to reflux. The reaction was allowed to stir at reflux overnight, after-which it was removed from heat, and allowed to cool to room temperature. The crude mixture was concentrated under vacuum to afford the title compound as a white solid (1.30 g, 56 %). **^{1}H NMR** (400 MHz, $(CD_3)_2SO$): *δ* 3.78 – 3.75 (m, 1H), 3.63 (d, *J* = 4.2 Hz, 1H), 3.52 (dd, *J* = 10.9, 3.2 Hz, 1H), 3.45 – 3.37 (m, 2H), 3.29 (q, *J* = 4.9 Hz, 1H), 2.79 – 2.72 (m, 4H), 1.57 – 1,49 (m, 4H), 1.30 – 1.16 (m, 12H), 0.83 (t, *J* = 6.4 Hz, 6H). **^{13}C NMR** (100 MHz, $(CD_3)_2SO$): *δ* 176.27, 73.26, 72.85, 72.03, 71.10, 64.10, 47.29 (2 X CH_2), 31.24 (2 X CH_2), 26.24 (2 X CH_2), 26.20 (2 X CH_2), 22.38 (2 X CH_2), 14.32 (2 X CH_3). LRMS (ESI): *m/z* calcd. For $C_{18}H_{37}NO_6$ [M+ Na] = 386.5, found, 386.3.

***N,N*-(Dicyclohexyl)-D-gluconamide (5.11)**

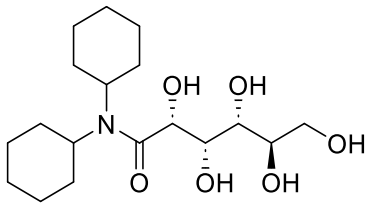

5.11

Glucono-δ-lactone (0.67 g, 1 eq), dicyclohexylamine (0.75 mL, 1 eq) and MeOH (15 mL, 0.25 M) were added to a round-bottom flask. A water condenser was equipped, and the reaction was brought to reflux. The reaction is allowed to stir at reflux overnight, after-which it is removed from heat, and allowed to cool to room temperature. The crude mixture was recrystallized from MeOH, then concentrated under vacuum to afford the title compound as a white solid (1.11 g, 82 %). **^{1}H NMR** (400 MHz, $(CD_3)_2SO$): *δ* 3.76 (dd, *J* = 4.4, 2.2, 1H), 3.61 (d, *J* = 4.4, 1H), 3.52 (dd, *J* = 10.9, 3.3 Hz, 1H), 3.47 – 3.37 (m, 1H), 3.31 – 3.26 (m, 1H), 3.01 – 2.90 (m, 2H), 1.98 – 1.86 (m, 4H), 1.75 – 1.63 (m, 4H), 1.56 (d, *J* = 12.2 Hz, 2H), 1.28 – 1.14 (m, 8H), 1.11 – 0.98 (m, 2H). **^{13}C NMR** (100 MHz, $(CD_3)_2SO$): *δ* 175.77, 73.19, 72.81, 72.04, 71.21, 64.12, 52.44 (2 X CH_2), 29.73 (2 X CH_2), 25.41 (2 X CH_2), 24.53 (6x CH_3).

***N*-(Propyl)-6-hydroxyhexanamide (5.12)**

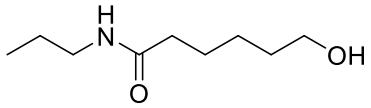

5.12

To a flame-dried round bottom flask under an atmosphere of argon, ε-caprolactone (1 mL, 1 eq), propylamine (1.5 mL, 2 eq) and THF (90 mL, 0.1 M) were added. The reaction flask was placed in a water / ice bath and allowed to cool for 5 minutes. A 2 M solution of TMA in toluene (9 mL, 2 eq) was added to the reaction flask dropwise. The reaction flask was removed from the water / ice bath and allowed to stir at room temperature until complete (1.5 hours). The reaction was stopped with the addition of excess 1 M HCl (100 mL) and diluted with Et_2O (150 mL). The organic phase was washed with brine (3 X 100 mL), dried with Na_2SO_4, filtered through cotton and concentrated under reduced pressure to yield the title compound as a clear oil (0.22 g, 14 %). **^{1}H NMR** (600 MHz, $CDCl_3$): *δ* 6.18 (br, 1H), 3.58 (t, *J* = 6.5 Hz, 2H), 3.15 (q, *J* = 7.0 Hz, 2H), 3.07 (br, 1H), 2.15 (t, *J* = 7.8 Hz, 2H), 1.62 (quint, *J* = 7.6 Hz, 2H), 1.54 (quint, *J* = 7.2 Hz, 2H), 1.48 (hept, *J* = 7.2 Hz, 2H), 1.39 – 1.32 (m, 2H), 0.88 (t, *J* = 7.4 Hz, 3H). **^{13}C NMR** (150 MHz, $CDCl_3$): *δ* 173.44, 62.16, 41.20, 36.55, 32.22, 25.43, 25.37, 22.77, 11.35. LRMS (ESI): *m/z* calcd. For $C_9H_{19}NO_2$ [M+ Na] = 196.3, found, 196.1.

***N*-(Hexyl)-6-hydroxyhexanamide (5.13)**

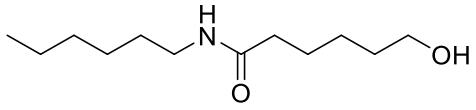

5.13

To a flame-dried round bottom flask under an atmosphere of argon, ε-caprolactone (1 mL, 1 eq), hexylamine (2.4 mL, 2 eq) and THF (90 mL, 0.1 M) were added. The reaction flask was placed in a water / ice bath and allowed to cool for 5 minutes. A 2 M solution of TMA in toluene (9 mL, 2 eq) was added to the reaction flask dropwise. The reaction flask was removed from the water / ice bath and allowed to stir at room temperature until complete (1.5 hours). The reaction was stopped with the addition of excess 1 M HCl (100 mL) and diluted with Et_2O (150 mL). The organic phase was washed with brine (3 X 100 mL), dried with Na_2SO_4, filtered through cotton and concentrated under reduced pressure. The resulting oil was purified with silica flash column chromatography (10 – 30 % EtOAc : Hex) to yield the title compound as a white solid following concentration (1.39 g, 72 %). **^{1}H NMR** (400 MHz, $CDCl_3$): *δ* 6.67 (br, 1H), 3.44 (t, *J* = 6.5 Hz, 2H),

3.26 (s, 1H), 3.04 (q, *J* = 6.1 Hz, 2H), 2.04 (t, *J* = 7.5 Hz, 2H), 1.49 (quint, *J* = 7.5 Hz, 2H), 1.41 (quint, *J* = 7.0 Hz, 2H), 1.34 (quint, *J* = 7.1 Hz, 2H), 1.27 – 1,19 (m, 2H), 1.18 – 1.08 (m, 6H), 0.73 (t, *J* = 7.0 Hz, 3H). **^{13}C NMR** (100 MHz, $CDCl_3$): *δ* 173.77, 61.85, 39.49, 36.37, 32.10, 31.41, 29.36, 26.54, 25.46, 25.31, 22.46, 13.90. LRMS (ESI): *m/z* calcd. For $C_{12}H_{25}NO_2$ [M+ Na] = 238.3, found, 238.2.

***N*-(Octyl)-6-hydroxyhexanamide (5.14)**

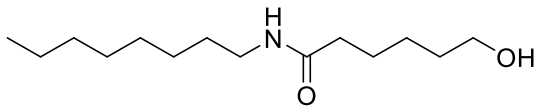

5.14

To a flame-dried round bottom flask under an atmosphere of argon, ε-caprolactone (1 mL, 1 eq), octylamine (2.8 mL, 2 eq) and THF (85 mL, 0.1 M) were added. The reaction flask was placed in a water / ice bath and allowed to cool for 5 minutes. A 2 M solution of TMA in toluene (8.5 mL, 2 eq) was added to the reaction flask dropwise. The reaction flask was removed from the water / ice bath and allowed to stir at room temperature until complete (1.5 hours). The reaction was stopped with the addition of excess 1 M HCl (100 mL) and diluted with Et_2O (150 mL). The organic phase was washed with brine (3 X 100 mL), dried with Na_2SO_4, filtered through cotton and concentrated under reduced pressure. The resulting oil was purified with silica flash column chromatography (10 – 30 – 100 % EtOAc : Hex) to yield the title compound as a white solid following concentration (2.14 g, 99 %). **^{1}H NMR** (400 MHz, $CDCl_3$): *δ* 5.98 (br, 1H), 3.57 (t, *J* = 6.5 Hz, 2H), 3.18 – 3.03 (m, 3H), 2.11 (dd, *J* = 8.4, 0.6 Hz, 2H), 1.59 (quint, *J* = 7.5 Hz, 2H), 1.51 (quint, *J* = 6.9 Hz, 2H), 1.41 (quint, *J* = 6.8 Hz, 2H), 1.37 – 1.27 (m, 2H), 1.26 – 1.14 (m, 10H), 0.81 (t, *J* = 7.0 Hz, 3H). **^{13}C NMR** (100 MHz, $CDCl_3$): *δ* 173.31, 62.22, 39.55, 36.59, 32.23, 31.77, 29.58, 29.26, 29.20, 26.94, 25.40, 25.37, 22.61, 14.07. LRMS (ESI): *m/z* calcd. For $C_{14}H_{29}NO_2$ [M+ Na] = 266.4, found, 266.1.

***N*-(Octyl)-6-methoxyhexanamide (5.15)**

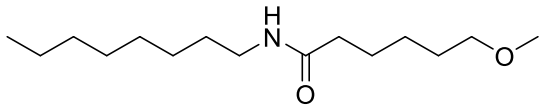

5.15

To a flame-dried round bottom flask under an atmosphere of argon in a water / ice bath **5.14** (1 g, 1 eq) and DMF (17 mL, 0.24 M) were added. 60 % suspension of NaH in mineral oil (0.20 g,

1.2 eq) was added to the reaction mixture slowly, followed by the dropwise addition of MeI (0.3 mL, 1.2). The reaction flask was removed from the water / ice bath and allowed to stir at room temperature until complete (3 hours). The reaction was stopped with the addition of excess saturated NH_4Cl and diluted with EtOAc (50 mL). The organic phase was washed with brine (3 x 50 mL), dried with Na_2SO_4, filtered through cotton and concentrated under reduced pressure. The resulting oil was purified with flash column chromatography (50 – 100 % EtOAc : Hex) yielding the title compound as a white solid following concentration under reduced pressure (0.15 g, 15 %). **^{1}H NMR** (400 MHz, $CDCl_3$): *δ* 5.98 (br, 1H), 3.26 (t, *J* = 6.5 Hz, 2H), 3.25 (s, 3H), 3.11 (q, *J* = 7.0 Hz, 2H), 2.07 (t, *J* = 7.8 Hz, 2H), 1.54 (quart, *J* = 7.5 Hz, 2H), 1.48 (quart, *J* = 7.0 Hz, 2H), 1.38 (quart, *J* = 6.7 Hz, 2H), 1.32 – 1.24 (m, 2H), 1.23 – 1.10 (m, 10H), 0.77 (t, *J* = 6.7 Hz, 3H). **^{13}C NMR** (100 MHz, $CDCl_3$): *δ* 172.93, 72.52, 58.43, 39.44, 36.58, 31.73, 29.60, 29.29, 29.23, 29.16, 26.91, 25.80, 25.59, 22.57, 14.00. Note: ^{1}H and ^{13}C spectra contain residual EtOAc from flash column purification. LRMS (ESI): *m/z* calcd. For $C_{15}H_{31}NO_2$ [M+ Na] = 280.4, found, 280.2.

***N*-(Octyl)-6-ethoxyhexanamide (5.16)**

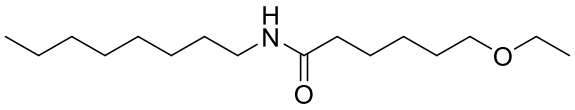

5.16

To a flame-dried round bottom flask under an atmosphere of argon in a water / ice bath **5.14** (0.19 g, 1 eq) and DMF (3 mL, 0.24 M) were added. 60 % suspension of NaH in mineral oil (37 mg, 1.2 eq) was added to the reaction mixture slowly, followed by the dropwise addition of iodoethane (0.1 mL, 1.2 eq). The reaction flask was removed from the water / ice bath and allowed to stir at room temperature until complete (24 hours). The reaction was stopped with the addition of excess saturated NH_4Cl and diluted with EtOAc (50 mL). The organic phase was washed with brine (3 x 50 mL), dried with Na_2SO_4, filtered through cotton and concentrated under reduced pressure. The resulting oil was purified with flash column chromatography (10 – 50 – 100 % EtOAc : Hex) to yield the title compound as a white solid following concentration under reduced pressure (80 mg, 39 %). **^{1}H NMR** (400 MHz, $CDCl_3$): *δ* 5.68 (br, 1H), 3.40 (q, *J* = 7.0 Hz, 2H), 3.34 (t, *J* = 6.5 Hz, 2H), 3.16 (q, *J* = 6.9 Hz, 2H), 2.11 (t, *J* = 7.6 Hz, 2H), 1.65 – 1.49 (m, 4H), 1.42 (quint, *J* = 6.8 Hz, 2H), 1.36 – 1.29 (m, 2H), 1.27 – 1.17 (m, 10H), 1.13 (t, *J* = 7.0 Hz, 3H), 0.86 – 0.78 (m, 3H). **^{13}C NMR** (100 MHz, $CDCl_3$): *δ* 172.91, 70.40, 66.05, 39.48, 36.72, 31.76, 29.65, 29.49, 29.25, 29.19, 26.92, 25.90, 25.63, 22.61, 15.20, 14.05. LRMS (ESI): *m/z* calcd. For $C_{16}H_{33}NO_2$ [M+ Na] = 294.4, found, 294.2.

***N*-(Octyl)-5-hydroxypentanamide (5.17)**

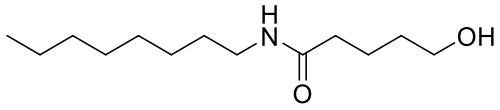

5.17

To a flame-dried round bottom flask under an atmosphere of argon, δ-valerolactone (0.75 mL, 1 eq), octylamine (2.7 mL, 2 eq) and THF (81 mL, 0.1 M) were added. The reaction flask was placed in a water / ice bath and allowed to cool for 5 minutes. A 2 M solution of TMA in toluene (8 mL, 2 eq) was added to the reaction flask dropwise. The reaction flask was removed from the water / ice bath and allowed to stir at room temperature until complete (1.5 hours). The reaction was stopped with the addition of excess 1 M HCl (100 mL) and diluted with Et_2O (150 mL). The organic phase was washed with brine (3 X 100 mL), dried with Na_2SO_4, filtered through cotton and concentrated under reduced pressure to yield the title compound as a white solid (1.68 g, 87 %). **^{1}H NMR** (400 MHz, $CDCl_3$): *δ* 5.78 (br, 1H), 3.60 (t, *J* = 6.2 Hz, 2H), 3.19 (q, *J* = 7.1 Hz, 2H), 2.67 (br, 1H), 2.18 (t, *J* = 7.3 Hz, 2H), 1.71 (quart, *J* = 7.2 Hz, 2H), 1.60 – 1.52 (m, 2H), 1.49 – 1.41 (m, 2H), 1.30 – 1.17 (m, 10H), 0.84 (t, *J* = 6.7 Hz, 3H). **^{13}C NMR** (100 MHz, $CDCl_3$): *δ* 173.22, 61.93, 39.61, 36.09, 31.99, 31.79, 29.61, 29.26, 29.21, 26.94, 22.63, 21.76, 14.09. LRMS (ESI): *m/z* calcd. For $C_{13}H_{27}NO_2$ [M+ Na] = 252.4, found, 252.2.

***N*-(2-(2-Methoxy-ethoxy)-ethyl)-D-gluconamide (5.18)**

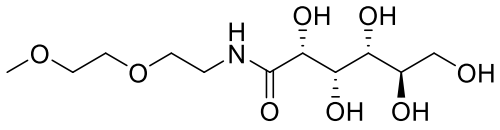

5.18

Glucono-δ-lactone (1.49 g, 1 eq), 2-(2-methoxyethoxy)ethanamine (1 g, 1 eq) and MeOH (34 mL, 0.25 M) were added to a round-bottom flask. A water condenser was equipped, and the reaction was brought to reflux. The reaction was allowed to stir at reflux overnight, after-which it was removed from heat, and allowed to cool to room temperature. The crude mixture was concentrated under vacuum and the crude slurry was recrystallized from 99 % EtOH, which following filtration and evaporation of residual solvent, yielded the title compound as a low melting point white solid (0.54 g, 22 %). **NMR** (400 MHz, $(CD_3)_2SO$): *δ* 7.60 (t, *J* = 5.8 Hz, 1H), 5.43 (d, *J* = 4.9 Hz, 1H), 4.54 (br, 1H), 4.48 (br, 1H), 4.42 (d, *J* = 7.2 Hz, 1H), 4.34 (t, *J* = 5.5 Hz, 1H), 3.99 (t, *J* = 4.1 Hz, 1H), 3.92 – 3.87 (m, 1H), 3.57 (dd, *J* = 10.8, 4.0 Hz, 1H), 3.53 – 3.49 (m, 2H), 3.48

– 3,45 (m, 2H), 3.44 – 3.40 (m, 4H), 3.39 – 3.37 (m, 1H), 3.31 – 3.17 (m, 5H). **^{13}C NMR** (100 MHz, $(CD_3)_2SO$): *δ* 173.01, 73.96, 72.77, 71.95, 71.69, 70.53, 69.83, 69.37, 63.81, 58.55, 38.58. LRMS (ESI): *m/z* calcd. For $C_{11}H_{23}NO_8$ [M+ H] = 298.2, found, 298.2.

3-(2-Hydroxy-ethoxy)-*N*-(2-fluorophenyl)-propamide (5.19)

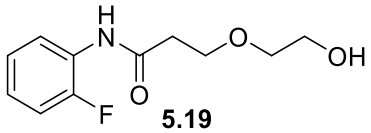

5.19

To a flame-dried round bottom flask under an atmosphere of argon, 3-(2-hydroxyethoxy)propanoic acid (0.35 g, 1 eq), 2-fluoroaniline (0.25 mL, 1 eq), DIPEA (1.8 mL, 4 eq) and DMF (3.8 mL, 0.7 M) were added. HBTU (1.1 g, 1.1 eq) was added potion wise, and the reaction was allowed to stir at room temperature until completion (22 hours). The reaction was diluted with EtOAc (50 mL), and the organic phase was washed with brine (3 x 50 mL). The resulting organic phase was dried with Na_2SO_4, filtered through cotton and concentrated under reduced pressure. The crude oil was placed onto silica and purified with silica flash column chromatography (20 – 50 % EtOAc : Hex) to afford the title compound as a clear oil (49 mg, 9 %). **^{1}H NMR** (400 MHz, $CDCl_3$): *δ* 8.51 (br, 1H), 8.27 (dt, *J* = 8.1, 1.5 Hz, 1H), 7.11 – 6.96 (m, 3H), 3.81 (t, *J* = 5.4 Hz, 2H), 3.78 (t, *J* = 2.4 Hz, 2H), 3.63 (t, *J* = 4.8 Hz, 2H), 2.76 (s, 1H), 2.67 (t, *J* = 5.9 Hz, 2H). **^{13}C NMR** (100 MHz, $CDCl_3$): *δ* 169.96, 152.35 (d, *J* = 242.7 Hz), 126.46 (d, *J* = 10.2 Hz), 124.60 (d, *J* = 3.6 Hz), 124.26 (d, *J* = 7.8 Hz), 121.86, 114.76 (d, *J* = 19.3 Hz), 72.51, 66.79, 61.65, 37.89. LRMS (ESI): *m/z* calcd. For $C_{11}H_{14}FNO_3$ [M+ Na] = 250.2, found, 250.1.

3-(2-Hydroxy-ethoxy)-*N*-(octyl)-propamide (5.20)

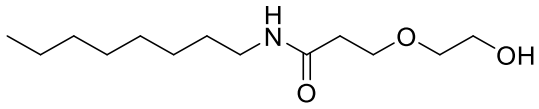

5.20

To a flame-dried round bottom flask under an atmosphere of argon, 3-(2-hydroxyethoxy)propanoic acid (0.2 g, 1 eq), octylamine (0.25 mL, 1 eq), DIPEA (1 mL, 4 eq) and DMF (2 mL, 0.7 M) were added. HBTU (0.6 g, 1.1 eq) was added potion wise, and the reaction was allowed to stir at room temperature until completion (22 hours). The reaction was diluted with EtOAc (50 mL), and the organic phase was washed with brine (3 x 50 mL). The resulting organic phase was dried with Na_2SO_4, filtered through cotton and concentrated under reduced pressure. The crude oil was placed onto silica and purified with silica flash column chromatography (30 –

70 % EtOAc : Hex) to afford the title compound as a pale orange solid (122 mg, 33 %). **^{1}H NMR** (400 MHz, $CDCl_3$): δ 6.58 (br, 1H), 3.78 – 3.51 (m, 6H), 3.16 (q, J = 6.4 Hz, 2H), 2.48 (tt, J = 18.0, 5.4 Hz 2H), 1.50 – 1.35 (m, 2H), 1.29 – 1.13 (m, 10H), 0.82 (t, J = 6.5 Hz, 3H). **^{13}C NMR** (100 MHz, $CDCl_3$): δ 172.27, 71.79, 66.98, 61.45, 39.79, 36.09, 31.78, 29.28, 29.25, 29.22, 26.95, 22.62, 14.08. LRMS (ESI): *m/z* calcd. For $C_{13}H_{27}NO_3$ [M+ Na] = 268.2, found, 268.2.

Synthesis of C_4 substituted derivatives of 6-hydroxyhexanamide derivatives (5.21 – 5.23)

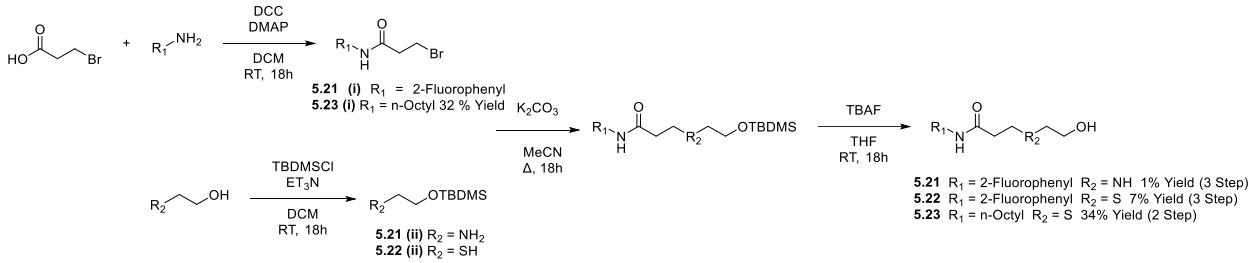

3-Bromo-*N*-(octyl)propenamide (5.23 (i))

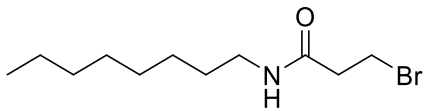

5.23 (i)

To a flame-dried round bottom flask under an atmosphere of argon, 3-bromopropanoic acid (1 g, 1 eq), octylamine (1.2 mL, 1.1 eq), DMAP (80 mg, 0.1 eq) and DCM (20 mL, 0.33 M) were added. The reaction flask was placed in a water / ice bath and allowed to cool for 5-minutes. DCC (2 g, 1.5 eq) was added portion-wise, the reaction was removed from the water / ice bath and allowed to stir at room temperature until complete (18 hours). The reaction mixture was filtered through a bed of celite, washed with DCM (3 x 50 mL), and the collected organic phase was washed with saturated NH_4Cl (3 X 50 mL), saturated sodium bicarbonate (3 x 50 mL) and brine (2 x 50 mL). The subsequent organic phase was dried with Na_2SO_4, filtered through cotton, and concentrated under reduced pressure. The crude oil was purified with silica flash column chromatography (50 % EtOAc : Hex) to yield the title compound as a white solid following concentration under reduced pressure (0.56 g, 32 %). **^{1}H NMR** (400 MHz, $CDCl_3$): δ 6.96 (t, J = 5.2 Hz, 1H), 3.51 (t, J = 6.7 Hz, 2H), 3.12 (q, J = 6.0 Hz, 2H), 2.68 (t, J = 6.7 Hz, 2H), 1.46 – 1.36 (m, 2H), 1.27 – 1.07 (m, 11H), 0.75 (t, J = 6.9 Hz, 3H). **^{13}C NMR** (100 MHz, $CDCl_3$): δ 169.95, 39.73, 39.47, 31.73, 29.47, 29.24, 29.17, 27.79, 26.93, 22.57, 14.01. LRMS (ESI): *m/z* calcd. For $C_{11}H_{22}BrNO$ [M+ Na] = 286.1, found, 286.1.

2-((tert-Butyldimethylsilyl)oxy)ethanamine (5.21 (ii))

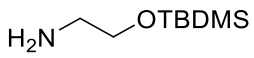

5.21 (ii)

To a flame-dried flask under an atmosphere of argon, ethanolamine (1 mL, 1 eq), Et_3N (2.5 mL, 1.1 eq) and DCM (25 mL, 0.67 M) were added. A glass vial was flame-dried and placed under argon, it was charged with TBDMSCl (2.5 g, 1 eq) and DCM (5 mL, 3.3 M). Both reaction flask, and vial were allowed to mix until homogenous, after-which the TBDMSCl / DCM solution was added to the reaction mixture dropwise. The reaction was allowed to stir at room temperature overnight. The reaction mixture was washed with saturated sodium bicarbonate (3 x 50 mL) and brine (2 x 50 mL), the resulting organic phase was dried with Na_2SO_4, filtered through cotton, and concentrated under reduced pressure. The crude oil was purified with silica flash column chromatography (5 % EtOAc : Hex) to afford the title compound as a clear oil after concentration under reduced pressure (1.5 g, 52 %). **^{1}H NMR** (400 MHz, $CDCl_3$): *δ* 4.29 (br, 2H), 3.44 (t, *J* = 5.4 Hz, 2H), 2.57 (t, *J* = 5.4 Hz, 2H), 0.66 (s, 9H), -0.17 (s, 6H). Note: residual TBDMSOH is present in the sample, and removed in subsequent reactions. LRMS (ESI): *m/z* calcd. For $C_8H_{21}NOSi$ [M+ Na] = 198.1, found, 198.1.

2-((tert-Butyldimethylsilyl)oxy)ethane-1-thiol (5.22 (ii))

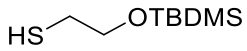

5.22 (ii)

To a flame-dried flask under an atmosphere of argon, β-mercaptoethanol (1 mL, 1 eq), imidazole (2.4 g, 2.5 eq) and DCM (6 mL, 2.5 M) were added. A glass vial was flame-dried and placed under argon, it was charged with TBDMSCl (2.35 g, 1 eq) and DCM (3 mL, 4.7 M). Both reaction flask, and vial were allowed to mix until homogenous, after-which the TBDMSCl / DCM solution was added to the reaction mixture dropwise. The reaction was allowed to stir at room temperature overnight. The reaction mixture was washed with saturated sodium bicarbonate (3 x 50 mL) and brine (2 x 50 mL), the resulting organic phase was dried with Na_2SO_4, filtered through cotton, and concentrated under reduced pressure. The crude oil was purified with silica flash column chromatography (5 % EtOAc : Hex) to afford the title compound as a clear oil after concentration under reduced pressure (0.23 g, 6 %). **^{1}H NMR** (400 MHz, $CDCl_3$): *δ* 3.70 (t, *J* = 6.4 Hz, 2H), 2.60 (dt, *J* = 8.3, 6.4 Hz, 2H), 1.51 (t, *J* = 8.3 Hz, 1H), 0.88 (s, 9H), 0.05 (s, 6H). **^{13}C NMR** (100 MHz,

$CDCl_3$): δ 65.06, 27.31, 25.89 (3 X CH_3), 18.32, -5.26 (2 X CH_3). LRMS (ESI): *m/z* calcd. for disulfide $C_{16}H_{38}O_2S_2Si_2$ [M+ Na] = 405.8, found, 405.2.

3-(2-Hydroxy-ethylamine)-*N*-(2-fluorophenyl)-propamide (5.21)

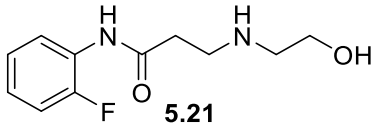

5.21

To a flame-dried round bottom flask under an atmosphere of argon, 3-bromopropanoic acid (1.5 g, 1 eq), 2-fluoroaniline (1 mL, 1.1 eq), DMAP (120 mg, 0.1 eq) and DCM (30 mL, 0.33 M) were added. The reaction flask was placed in a water / ice bath and allowed to cool for 5 minutes. DCC (3 g, 1.5 eq) was added portion-wise, the reaction was removed from the water / ice bath and allowed to stir at room temperature until complete (18 hours). The reaction mixture was filtered through a bed of celite, washed with DCM (3 x 50 mL), and the collected organic phase is washed with saturated NH_4Cl (3 X 50 mL), saturated sodium bicarbonate (3 x 50 mL) and brine (2 x 50 mL). The subsequent organic phase was dried with Na_2SO_4, filtered through cotton, and concentrated under reduced pressure. The crude oil was purified with silica flash column chromatography (10 – 30 % EtOAc : Hex) to yield 3-bromo-*N*-(2-fluorophenyl)propenamide as a white solid following concentration under reduced pressure (0.26 g). To a flame-dried round bottom flask under an atmosphere of argon, 3-bromo-*N*-(2-fluorophenyl)propenamide (0.26 g, 1 eq), **5.21 (ii)** (0.2 g, 1.05 eq), K_2CO_3 (0.18 g, 1.25 eq) and MeCN (3 mL, 0.4 M) were added. A water condenser was equipped, and the reaction solution was brought to reflux. The reaction was allowed to proceed at reflux until complete (22 hours). The reaction flask was removed from heat and allowed to cool to room temperature. The reaction mixture was diluted with EtOAc (50 mL), and washed with KH_2PO_4 (50 mL). The resulting organic phase was washed with brine (3 x 50 mL), dried with Na_2SO_4, filtered through cotton, and concentrated under reduced pressure. The crude oil was placed onto silica and purified with silica flash column chromatography (10 – 50 % EtOAc : Hex), yielding a clear oil (72 mg) after concentration under reduced pressure. 3-(2-(tert-Butyldimethylsilyl)oxy)-ethylamine)-*N*-(2-fluorophenyl)-propamide (72 mg, 1 eq) was suspended in THF (0.7 mL, 0.33 M) and 1 M TBAF in THF (0.44 mL, 2 eq) was added. The reaction was allowed to stir at room temperature until complete (20 hours). The reaction mixture was concentrated under reduced pressure and purified by silica flash column chromatography (50 – 100 % EtOAc : Hex – 20 % MeOH : EtOAc) to yield the title compound as a white solid after concentration under reduced pressure (36 mg, 1 % over three steps). **^{1}H NMR** (400 MHz, $CDCl_3$):

δ 10.54 (br, 1H), 8.33 (dt, *J* = 8.1, 1.6 Hz, 1H), 7.12 – 6.95 (m, 3H), 3.78 (t, *J* = 5.0 Hz, 2H), 3.02 (t, *J* = 5.9 Hz, 2H), 2.85 (t, *J* = 5.1 Hz, 2H), 2.55 (t, *J* = 5.9 Hz, 2H). **^{13}C NMR** (100 MHz, $CDCl_3$): *δ* 171.07, 152.39 (d, *J* = 242.9 Hz), 126.92 (d, *J* = 10.5 Hz), 124.54 (d, *J* = 3.5 Hz), 123.80 (d, *J* = 7.7 Hz), 121.79, 114.71 (d, *J* = 19.2 Hz), 61.37, 50.88, 45.06, 36.31. LRMS (ESI): *m/z* calcd. For $C_{11}H_{15}FN_2O_2$ [M+ H] = 227.1, found, 227.1.

3-(2-Hydroxy-ethanethiol)-*N*-(2-fluorophenyl)-propamide (5.22)

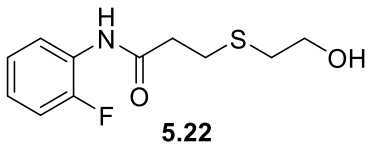

5.22

To a flame-dried round bottom flask under an atmosphere of argon, 3-bromopropanoic acid (1 g, 1 eq), 2-fluoroaniline (0.7 mL, 1.1 eq), DMAP (80 mg, 0.1 eq) and DCM (20 mL, 0.33 M) were added. The reaction flask was placed in a water / ice bath and allowed to cool for 5 minutes. DCC (2 g, 1.5 eq) was added portion-wise, the reaction was removed from the water / ice bath and allowed to stir at room temperature until complete (18 hours). The reaction mixture was filtered through a bed of celite, washed with DCM (3 x 50 mL), and the collected organic phase is washed with saturated NH_4Cl (3 X 50 mL), saturated sodium bicarbonate (3 x 50 mL) and brine (2 x 50 mL). The subsequent organic phase was dried with Na_2SO_4, filtered through cotton, and concentrated under reduced pressure. The crude oil was purified with silica flash column chromatography (10 – 30 % EtOAc : Hex) to yield 3-Bromo-*N*-(2-fluorophenyl)propenamide as a white solid following concentration under reduced pressure (0.46 g). To a flame-dried round bottom flask under an atmosphere of argon, 3-Bromo-*N*-(2-fluorophenyl)propenamide (0.46 g, 1 eq), **5.22 (ii)** (0.37 g, 1.05 eq), K_2CO_3 (0.32 g, 1.25 eq) and MeCN (5 mL, 0.4 M) were added. A water condenser was equipped, and the reaction solution was brought to reflux. The reaction was allowed to proceed at reflux until complete (21 hours). The reaction flask was removed from heat and allowed to cool to room temperature. The reaction mixture was diluted with EtOAc (50 mL) and washed with KH_2PO_4 (50 mL). The resulting organic phase was washed with brine (3 x 50 mL), dried with Na_2SO_4, filtered through cotton, and concentrated under reduced pressure. The crude oil was placed onto silica and purified with silica flash column chromatography (10 – 30 % EtOAc : Hex), yielding a clear oil (0.33 g) after concentration under reduced pressure. 3-(2-(tert-Butyldimethylsilyl)oxy)-ethanethiol)-*N*-(2-fluorophenyl)-propamide (0.33 g, 1 eq) was suspended in THF (2 mL, 0.33 M) and 1 M TBAF in THF (1.4 mL, 2 eq) was added. The reaction was allowed to stir at room temperature until complete (18 hours). The reaction mixture was concentrated

under reduced pressure and placed onto silica for purification by silica flash column chromatography (50 % EtOAc : Hex) to yield the title compound as a clear oil after concentration under reduced pressure (103 mg, 7 % over three steps). **^{1}H NMR** (400 MHz, $CDCl_3$): *δ* 8.18 (dt, *J* = 8.5, 0.9 Hz, 1H), 8.00 (br, 1H), 7.10 – 6.94 (m, 3H), 3.73 (t, *J* = 5.9 Hz, 2H), 2.92 (br, 1H), 2.88 (t, *J* = 7.0 Hz, 2H), 2.71 (t, *J* = 5.9 Hz, 2H), 2.67 (t, *J* = 7.0 Hz, 2H). **^{13}C NMR** (100 MHz, $CDCl_3$): *δ* 169.96, 152.68 (d, *J* = 243.7 Hz), 126.00 (d, *J* = 10.4 Hz), 124.76 (d, *J* = 7.7 Hz), 124.54 (d, *J* = 3.6 Hz), 122.36, 114.95 (d, *J* = 15.3 Hz), 61.02, 37.66, 35.38, 27.40. LRMS (ESI): *m/z* calcd. For $C_{11}H_{14}FNO_2S$ [M+ H] = 244.1, found, 244.1.

3-(2-Hydroxy-ethanethiol)-*N*-(octyl)-propamide (5.23)

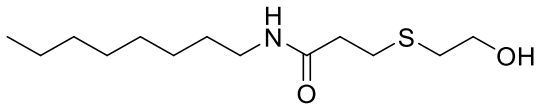

5.23

To a flame-dried round bottom flask under an atmosphere of argon, **5.23 (i)** (0.29 g, 1 eq), **5.22 (ii)** (0.23 g, 1.05 eq), K_2CO_3 (0.19 g, 1.25 eq) and MeCN (3 mL, 0.4 M) were added. A water condenser was equipped, and the reaction solution was brought to reflux. The reaction was allowed to proceed at reflux until complete (21 hours). The reaction flask was removed from heat and allowed to cool to room temperature. The reaction mixture was diluted with EtOAc (50 mL), and washed with KH_2PO_4 (50 mL). The resulting organic phase was washed with brine (3 x 50 mL), dried with Na_2SO_4, filtered through cotton, and concentrated under reduced pressure. The crude oil was placed onto silica and purified with silica flash column chromatography (10 – 30 % EtOAc : Hex), yielding a clear oil (0.23 g) after concentration under reduced pressure. 3-(2-(tert-Butyldimethylsilyl)oxy)-ethanethiol)-*N*-(octyl)-propamide (0.23 g, 1 eq) was suspended in THF (2 mL, 0.33 M) and 1 M TBAF in THF (1.2 mL, 2 eq) was added. The reaction was allowed to stir at room temperature until complete (17 hours). The reaction mixture was concentrated under reduced pressure and placed onto silica for purification by silica flash column chromatography (50 - 100 % EtOAc : Hex) to yield the title compound as a white solid after concentration under reduced pressure (99 mg, 34 % over two steps). **NMR** (400 MHz, $(CD_3)_2SO$): *δ* 7.80 (t, *J* = 5.0 Hz, 1H), 4.75 (t, *J* = 5.5 Hz, 1H), 3.47 (q, *J* = 6.9 Hz, 2H), 2.98 (q, *J* = 6.7 Hz, 2H), 2.64 (t, *J* = 7.3 Hz, 2H), 2.51 (t, *J* = 7.0 Hz, 2H), 2.27 (t, *J* = 7.3 Hz, 2H), 1.38 – 1.29 (m, 2H), 1.26 – 1.16 (m, 10H), 0.82 (t, *J* = 6.9 Hz, 3H). **^{13}C NMR** (100 MHz, $CDCl_3$): *δ* 170.65, 61.32, 38.93, 36.49, 34.30, 31.70, 29.55, 29.18, 29.13, 27.95, 26.86, 22.56, 14.43. LRMS (ESI): *m/z* calcd. For $C_{13}H_{27}NO_2S$ [M+ Na] = 284.2, found, 284.2.

Synthesis of N_3 amine derivative of 4.28

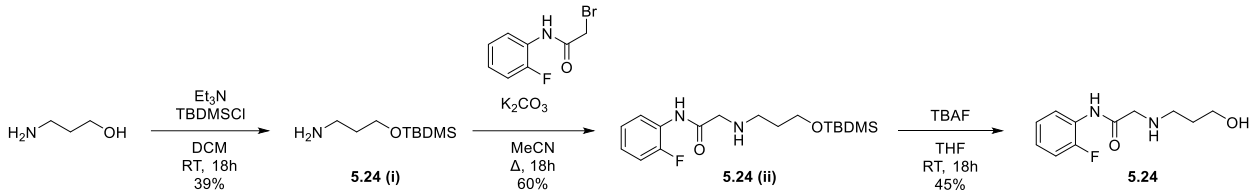

2-((tert-Butyldimethylsilyl)oxy)propanamine (5.24 (i))

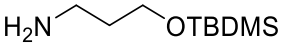

5.24 (i)

To a flame-dried flask under an atmosphere of argon, 3-aminopropanol (1 mL, 1 eq), Et_3N (2 mL, 1.1 eq) and DCM (20 mL, 0.67 M) were added. A glass vial was flame-dried and placed under argon, it was charged with TBDMSCl (1.98 g, 1 eq) and DCM (4 mL, 3.3 M). Both reaction flask, and vial were allowed to mix until homogenous, after-which the TBDMSCl / DCM solution was added to the reaction mixture dropwise. The reaction was allowed to stir at room temperature overnight. The reaction mixture was washed with saturated sodium bicarbonate (3 x 50 mL) and brine (2 x 50 mL), the resulting organic phase was dried with Na_2SO_4, filtered through cotton, and concentrated under reduced pressure to afford the title compound as a clear oil (1.66 g, 39 %). **^{1}H NMR** (400 MHz, $CDCl_3$): δ 3.57 (t, J = 6.1 Hz, 2H), 2.68 (t, J = 6.8 Hz, 2H), 1.80 (br, 2H), 1.55 (quint, J = 6.4 Hz, 2H), 0.77 (s, 9H), -0.07 (s, 6H). **^{13}C NMR** (100 MHz, $CDCl_3$): δ 61.11, 39.23, 35.97, 25.84 (3 X CH_3), 18.17, -5.46 (2 X CH_3). NMR analysis matches reference spectra.[25]

tert-Butyl-(3-((2-oxo-2-(2-fluorophenylamino)ethyl)amino)propyl)-carbonate (5.24 (ii))

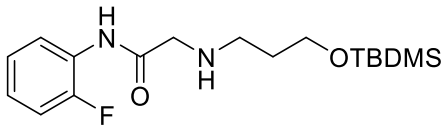

5.24 (ii)

To a flame-dried round bottom flask under an atmosphere of argon, **5.25 (i)** (0.6 g, 1.05 eq), 2-bromo-*N*-(2-fluorophenyl)acetamide (0.7 g, 1 eq), K_2CO_3 (0.55 g, 1.25 eq) and MeCN (7.5 mL, 0.4 M) were added. A water condenser was equipped, and the reaction solution was brought to reflux. The reaction was allowed to proceed at reflux until complete (22 hours). The reaction flask was removed from heat, and allowed to cool to room temperature. The reaction mixture was diluted with EtOAc (50 mL), and washed with KH_2PO_4 (50 mL). The resulting organic phase was

washed with brine (3 x 50 mL), dried with Na_2SO_4, filtered through cotton, and concentrated under reduced pressure. The crude oil was placed onto silica and purified with silica flash column chromatography (30 % EtOAc : Hex), yielding a clear oil (0.65 g, 63 %). **^{1}H NMR** (400 MHz, $CDCl_3$): *δ* 9.71 (br, 1H), 8.36 (dt, *J* = 8.1, 1.4 Hz, 1H), 7.14 – 6.98 (m, 3H), 3.72 (t, *J* = 6.0 Hz, 2H), 3.40 (s, 2H), 2.78 (t, *J* = 6.5 Hz, 2H), 1.73 (quart, *J* = 6.3 Hz, 2H), 0.85 (s, 9H), 0.03 (s, 6H). **^{13}C NMR** (100 MHz, $CDCl_3$): *δ* 170.17, 152.47 (d, *J* = 243.7 Hz), 126.27 (d, *J* = 10.2 Hz), 124.52 (d, *J* = 7.7 Hz), 124.12 (d, *J* = 7.6 Hz), 121.26, 114.83 (d, *J* = 19.0 Hz), 61.63, 53.21, 47.92, 32.67, 25.88 (3 X CH_3), 18.25, -5.41 (2 X CH_3).

2-(3-hydroxypropylamino)-*N*-(2-fluorophenyl)acetamide (5.24)

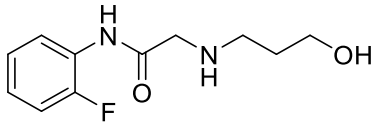

5.24

To a flame-dried round bottom flask under an atmosphere of argon **5.25 (ii)** (30.6 mg, 1 eq) was suspended in THF (0.3 mL, 0.33 M) and 1 M TBAF in THF (0.2 mL, 2 eq) was added. The reaction was allowed to stir at room temperature over night. The reaction mixture was concentrated under reduced pressure and placed onto silica for purification by silica flash column chromatography (50 – 70 % EtOAc : Hex) to yield the title compound as a white solid after concentration under reduced pressure (9.1 mg, 45 %). **^{1}H NMR** (400 MHz, $CDCl_3$): *δ* 9.67 (br, 1H), 8.34 (dt, *J* = 8.1, 1.6 Hz, 1H), 7.13 – 7.00 (m, 3H), 3.80 (t, *J* = 6.0 Hz, 2H), 3.44 (s, 2H), 2.84 (t, *J* = 6.5 Hz, 2H), 1.78 (quart, *J* = 6.2 Hz, 2H). **^{13}C NMR** (100 MHz, $CDCl_3$): *δ* 169.84, 152.63 (d, *J* = 243.5 Hz), 126.11 (d, *J* = 10.1 Hz), 124.59 (d, *J* = 3.6 Hz), 124.31 (d, *J* = 7.6 Hz), 121.41, 114.86 (d, *J* = 19.1 Hz), 61.50, 53.18, 47.89, 32.24. LRMS (ESI): *m/z* calcd. For $C_{11}H_{15}FN_2O_2$ [M+ Na] = 249.2, found, 249.1.

***N*-(2-Fluorophenyl)-*N*-(methyl)-6-hydroyhexanamide (5.25)**

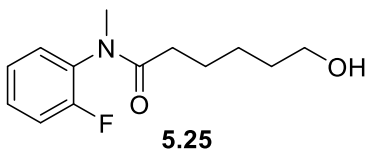

5.25

To a flame-dried round bottom flask under an atmosphere of argon, **4.28** (0.92 g, 1 eq) and DMF (17 mL, 0.24 M) were added. The reaction flask was placed into a water / ice bath and allowed to cool for 5 minutes. 60% suspension of NaH in mineral oil (0.2 g, 1.2 eq) followed by MeI (0.31

mL, 1.2 eq) were added and the reaction flask was removed from the water / ice bath and allowed to stir until completion (4 hours). The reaction mixture was diluted with EtOAc (50 mL) and quenched with the addition of saturated NH_4Cl (50 mL). The organic phase was washed with brine (3 x 50 mL), dried with Na_2SO_4, filtered through cotton and concentrated under reduced pressure. The resulting crude oil was placed onto silica and purified with silica flash column chromatography (50 % EtOAc : Hex) to afford the title compound as a yellow oil following concentration under reduced pressure (0.26 g, 27 %). **^{1}H NMR** (400 MHz, $CDCl_3$): *δ* 7.32 – 7.24 (m, 1H), 7.18 – 7.07 (m, 3H), 3.49 (t, *J* = 6.5 Hz, 2H), 3.14 (s, 3H), 2.58 (br, 1H), 1.98 (t, *J* = 7.8 Hz, 2H), 1.50 (quat, *J* = 8.0 Hz, 2H), 1.40 (quat, *J* = 7.0 Hz, 2H), 1.24 – 1.14 (m, 2H). **^{13}C NMR** (100 MHz, $CDCl_3$): *δ* 173.44, 157.90 (d, *J* = 249.8 Hz), 131.44 (d, *J* = 13.1 Hz), 129.82 (d, *J* = 7.8 Hz), 129.63, 125.14 (d, *J* = 4.0 Hz), 116.93 (d, *J* = 20.1 Hz), 62.25, 36.43, 33.44, 32.24, 25.26, 24.73. LRMS (ESI): *m/z* calcd. For $C_{13}H_{18}FNO_2$ [M+ Na] = 262.3, found, 262.1.

***N*-(Octyl)-D-xylonamide (5.26)**

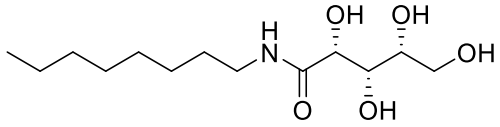

5.26

2,3,4-tri-(*O*-benzyl)-D-glucono-δ-lactone (0.22 g, 1 eq) was dissolved in MeOH (3 mL, 0.5 M) and octylamine (100 µL, 1 eq) was added to the reaction flask. A water condenser was equipped to the reaction flask, the reaction was brought to reflux and allowed to stir for overnight. The reaction flask was then removed from heat and allowed to cool to room temperature. The reaction solution was concentrated under reduced pressure affording the benzylated intermediate isolated as a yellow oil (40 mg). 2,3,4-tri-*O*-(benzyl)-*N*-(octyl)-D-xylonamide (40 mg, 1 eq) was transferred to a hydrogenation flask with EtOAc (0.8 mL, 0.1 M) and MeOH (0.8 mL, 0.1 M). Pd/C (10 wt% on activated carbon support) (8 mg, 0.1 eq) was added to the hydrogenation flask, and the air was purged from the system through water aspiration. A hydrogen balloon was attached to the hydrogenation flask, and the reaction was placed under an atmosphere of hydrogen; the hydrogenation flask was purged of atmosphere and replaced with hydrogen gas every hour. Once the reaction was deemed complete (5 hours) the reaction mixture was filtered through celite and concentrated under reduced pressure to yield the desired product as a white solid (30 mg, 21 % over two steps). **^{1}H NMR** (400 MHz, $(CD_3)_2SO$): *δ* 7.54 (t, *J* = 5.9 Hz, 1H), 5.27 (br, 1H), 4.64 – 4.28 (m, 3H), 3.90 (d, *J* = 2.6 Hz, 1H), 3.70 – 3.63 (m, 1H), 3.56 – 3.48 (m, 1H), 3.45 – 3.38 (m, 1H), 3.36 – 3.33 (m, 1H), 3.10 – 2.95 (m, 2H), 1.36 (t, *J* = 6.5 Hz, 2H), 1.28 – 1.15 (m, 10H), 0.87

– 0.78 (m, 3H). **^{13}C NMR** (100 MHz, $(CD_3)_2SO$): *δ* 172.81, 73.23, 72.75, 71.73, 62.80, 38.73, 31.73, 29.66, 29.24, 29.15, 26.84, 22.57, 14.43. LRMS (ESI): *m/z* calcd. For $C_{13}H_{27}NO_5$ [M+ Na] = 300.4, found, 300.2.

***N*-(Octyl)-L-threonamide (5.27)**

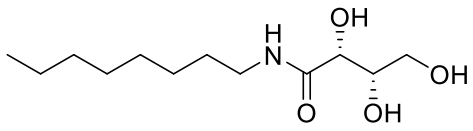

5.27

Calcium-L-threonate (2 g, 1 eq), oxalic acid (0.58 g, 1 eq), PTSA (19 mg, 3 mg / mmol) and acetonitrile (11 mL, 0.6 M) were added into a flame dried round-bottom flask which had been placed under an atmosphere of argon. The reaction flask was equipped with a water condenser and brought to reflux. The reaction was allowed to reflux until complete (3 hours), after-which the reaction flask was removed from heat and allowed to cool to room temperature. The crude slurry was filtered through celite and the remaining liquid was co-evaporated with EtOAc (3 X 50 mL) to dryness under reduced pressure, yielding L-threonolactone as an off-white solid (1.58 g). Once sufficiently dried under high-vacuum L-threonolactone (1.58 g, 1 eq) was suspended in acetic acid (65 mL, 0.2 M) and charged with octylamine (2.2 mL, 1 eq). The reaction flask was equipped with a water condenser and brought to 100 °C. The reaction was allowed to stir at 100 °C for one hour, after-which the reaction flask was removed from heat and allowed to cool to room temperature. The resulting brown mixture was concentrated under reduced pressure, and placed onto silica gel for purification by silica flash column chromatography (EtOAc). The isolated product was concentrated under reduced pressure, then recrystalized from EtOAc : Hexanes; the resulting solid was filtered, washed with Et_2O and dried under reduced pressure. The desired product is obtained as a white solid (0.23 g, 14 %). **^{1}H NMR** (400 MHz, $(CD_3)_2SO$): *δ* 7.53 (t, *J* = 5.8 Hz, 1H), 5.10 (d, *J* = 6.8 Hz, 1H), 4.52 (dd, *J* = 6.2, 1.1 Hz, 1H), 4.42 (d, *J* = 6.6 Hz, 1H), 3.84 (dd, *J* = 6.9, 2.2 Hz, 1H), 3.68 (ddd, *J* = 7.1, 6.8, 2.3 Hz, 1H), 3.39 – 3.33 (m, 1H), 3.29 – 3.23 (m, 1H), 3.10 – 2.96 (m, 2H), 1.36 (t, *J* = 6.5 Hz, 2H), 1.28 – 1.14 (m, 10H), 0.82 (t, *J* = 7.0 Hz, 3H). **^{13}C NMR** (100 MHz, $(CD_3)_2SO$): *δ* 173.19, 72.46, 71.57, 62.63, 38.72, 31.73, 29.70, 29.23, 29.15, 26.83, 22.57, 14.44. LRMS (ESI): *m/z* calcd. For $C_{12}H_{25}NO_4$ [M+ Na] = 270.3, found, 270.1.

***N*-(Octyl)-(R)-2,3-dihydroxy-propanamide (5.28)**

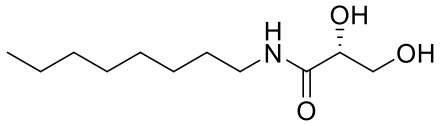

5.28

To a flame dried round bottom flask under an argon atmosphere, K_2CO_3 (2.5 g, 2 eq), water (4.5 mL, 0.25 mL / mmol K_2CO_3), and acetone (18 mL, 2 mL / mmol aniline) were added. The reaction flask was placed in a water / ice bath and allowed to cool for 5 minutes. Acryloyl chloride (1.5 mL, 2 eq) was added to the flask slowly, followed by the portion-wise addition of octylamine (1.5 mL, 1 eq). The reaction was allowed to stir in the ice bath until complete (1 hour). The reaction was diluted with excess DCM (50 mL), filtered through celite, and the organic phase was extracted with brine (3 X 50 mL). The resulting organic phase was dried with Na_2SO_4, filtered through cotton and concentrated under reduced pressure. Crude *N*-(octylamine)acrylamide (2.1 g, 1 eq) was obtained as a clear oil and was suspended in ^{t}BuOH (71 mL, 0.16 M) and water (71 mL, 0.16 M). AD-mix-α (15.8 g, 1.4 g / mmol) and methanesulfonamide (1.0 g, 0.09 g / mmol) were added to the reaction flask, and it was allowed to stir at room temperature until complete (4 days). The reaction was quenched with saturated Na_2SO_3, diluted with EtOAc, and the organic phase was washed with brine (3 X 100 mL). The resulting organic phase was dried with Na_2SO_4, filtered through cotton and concentrated under reduced pressure. The crude solid was dissolved in minimal eluent (30 % EtOAc : Hex) and purified with silica flash column chromatography (50 % EtOAc : Hex). The desired product was obtained as an off-white solid after concentrating under reduced pressure (0.6 g, 33 % over two steps). **^{1}H NMR** (400 MHz, $CDCl_3$): *δ* 6.83 (br, 1H), 4.14 (t, *J* = 5.0 Hz, 1H), 3.87 – 3.78 (m, 2H), 3.30 – 3.20 (m, 2H), 1.54 – 1.45 (m, 2H), 1.32 – 1.18 (m, 10H), 0.86 (t, *J* = 6.7 Hz, 3H). **^{13}C NMR** (100 MHz, $CDCl_3$): *δ* 172.03, 72.06, 64.26, 39.31, 31.79, 29.47, 29.24, 29.20, 26.89, 22.65, 14.10. LRMS (ESI): *m/z* calcd. For $C_{11}H_{23}NO_3$ [M+ Na] = 240.3, found, 240.2.

***N*-(Octyl)-2-hydroxyacetamide (5.29)**

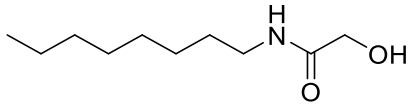

5.29

Glycolic acid (0.46 g ,1 eq) and octylamine (1 mL, 1 eq) were added into a round-bottom flask equipped with a water condenser. The reaction flask was brought to 130 °C and allowed to stir until completion (3 hours). The reaction flask was removed from heat and allowed to cool to room temperature. Aniline was removed under reduced pressure, to afford the title product as a white solid (0.54 g, 47 %). **^{1}H NMR** (400 MHz, $CDCl_3$): *δ* 6.83 (br, 1H), 4.50 (br, 1H), 3.99 (s, 2H), 3.22 (q, *J* = 6.9 Hz, 2H), 1.48 (quint, *J* = 6.8 Hz, 2H), 1.34 – 1.16 (m, 10H), 0.84 (t, *J* = 6.7 Hz, 3H). **^{13}C NMR** (100 MHz, $CDCl_3$): *δ* 172.39, 61.98, 39.06, 31.78, 29.48, 29.24, 29.19, 26.90, 22.63, 14.07. LRMS (ESI): *m/z* calcd. For $C_{10}H_{21}NO_2$ [M+ Na] = 210.3, found, 210.1.

References

(1) Capicciotti, C. J.; Mancini, R. S.; Turner, T. R.; Koyama, T.; Alteen, M. G.; Doshi, M.; Inada, T.; Acker, J. P.; Ben, R. N. O-Aryl-Glycoside Ice Recrystallization Inhibitors as Novel Cryoprotectants: A Structure–Function Study. *ACS Omega* **2016**, *1* (4), 656–662. https://doi.org/10.1021/acsomega.6b00163.

(2) ChemDraw Prime 22. https://revvitysignals.com/products/research/chemdraw.

(3) WebMO. https://www.webmo.net/.

(4) Avogadro. https://avogadro.cc/.

(5) Pracht, P.; Bohle, F.; Grimme, S. Automated Exploration of the Low-Energy Chemical Space with Fast Quantum Chemical Methods. *Phys. Chem. Chem. Phys.* **2020**, *22* (14), 7169–7192. https://doi.org/10.1039/C9CP06869D.

(6) Grimme, S. Exploration of Chemical Compound, Conformer, and Reaction Space with Meta-Dynamics Simulations Based on Tight-Binding Quantum Chemical Calculations. *J. Chem. Theory Comput.* **2019**, *15* (5), 2847–2862. https://doi.org/10.1021/acs.jctc.9b00143.

(7) MobaXterm. https://mobaxterm.mobatek.net/.

(8) GCC, the GNU Compiler Collection. https://gcc.gnu.org/.

(9) Bannwarth, C.; Ehlert, S.; Grimme, S. GFN2-xTB—An Accurate and Broadly Parametrized Self-Consistent Tight-Binding Quantum Chemical Method with Multipole Electrostatics and Density-Dependent Dispersion Contributions. *J. Chem. Theory Comput.* **2019**, *15* (3), 1652–1671. https://doi.org/10.1021/acs.jctc.8b01176.

(10) Ehlert, S.; Stahn, M.; Spicher, S.; Grimme, S. Robust and Efficient Implicit Solvation Model for Fast Semiempirical Methods. *J. Chem. Theory Comput.* **2021**, *17* (7), 4250–4261. https://doi.org/10.1021/acs.jctc.1c00471.

(11) Andrienko, G. A. Chemcraft - Graphical Software for Visualization of Quantum Chemistry Computations. https://www.chemcraftprog.com.

(12) Chai, J.-D.; Head-Gordon, M. Long-Range Corrected Hybrid Density Functionals with Damped Atom–Atom Dispersion Corrections. *Phys. Chem. Chem. Phys.* **2008**, *10* (44), 6615–6620. https://doi.org/10.1039/B810189B.

(13) Hellweg, A.; Rappoport, D. Development of New Auxiliary Basis Functions of the Karlsruhe Segmented Contracted Basis Sets Including Diffuse Basis Functions (Def2-SVPD, Def2-TZVPPD, and Def2-QVPPD) for RI-MP2 and RI-CC Calculations. *Phys. Chem. Chem. Phys.* **2014**, *17* (2), 1010–1017. https://doi.org/10.1039/C4CP04286G.
(14) Barone, V.; Cossi, M. Quantum Calculation of Molecular Energies and Energy Gradients in Solution by a Conductor Solvent Model. *J. Phys. Chem. A* **1998**, *102* (11), 1995–2001. https://doi.org/10.1021/jp9716997.
(15) Neese, F. The ORCA Program System. *WIREs Computational Molecular Science* **2012**, *2* (1), 73–78. https://doi.org/10.1002/wcms.81.
(16) Neese, F. Software Update: The ORCA Program System—Version 5.0. *WIREs Computational Molecular Science* **2022**, *12* (5), e1606. https://doi.org/10.1002/wcms.1606.
(17) A High Performance Message Passing Library. https://www.open-mpi.org/.
(18) Cai, L. Thin Layer Chromatography. *Current Protocols Essential Laboratory Techniques* **2014**, *8* (1), 6.3.1-6.3.18. https://doi.org/10.1002/9780470089941.et0603s08.
(19) Adam, M. K. Improving the Engraftment Activities of Cryopreserved Human Umbilical Cord Blood Through the Development of Novel Glyco(Peptide)-Based Aryl Ice Recrystallization Inhibitors, Univerity of Ottawa, 2020. http://dx.doi.org/10.20381/ruor-25034.
(20) Briard, J. G. The Rational Design and Use of Novel Small-Molecule Ice Recrystallization Inhibitors for the Cryopreservation of Hematopoietic Stem Cells and Red Blood Cells. PhD Thesis, University of Ottawa, 2016.
(21) Radhakrishna, V. Y.; Khatik, G. L.; Vijaya, B. S.; Nair, V. A. A Mild and Eco-Friendly, One-Pot Synthesis of 2-Hydroxy-N-Arylacetamides from 2-Chloro-N-Arylacetamides. Research Square August 17, 2023. https://doi.org/10.21203/rs.3.rs-3251914/v1.
(22) Wu, Q.; Ma, Z.; Li, R.; Shang, R.; An, Z.; Liu, Y.; Huang, Q.; Qi, Z. Synthesis of Amides via TBN-Induced Oxidation Cross-Coupling of Acetonitrile and N-Sulfinylanilines. *Synthetic Communications* **2025**, *55* (9), 652–660. https://doi.org/10.1080/00397911.2025.2494245.
(23) Nie, Q.; Yi, F.; Huang, B.; Cai, M. Efficient Heterogeneous Gold(I)-Catalyzed Direct C(Sp2)–C(Sp) Bond Functionalization of Arylalkynes through a Nitrogenation Process to Amides. *Advanced Synthesis & Catalysis* **2017**, *359* (22), 3968–3976. https://doi.org/10.1002/adsc.201700783.
(24) Xiang, S.-K.; Zhang, D.-X.; Hu, H.; Shi, J.-L.; Liao, L.-G.; Feng, C.; Wang, B.-Q.; Zhao, K.-Q.; Hu, P.; Yang, H.; Yu, W.-H. Synthesis of N-Arylamides by Copper-Catalyzed Amination of Aryl Halides with Nitriles. *Advanced Synthesis & Catalysis* **2013**, *355* (8), 1495–1499. https://doi.org/10.1002/adsc.201300189.
(25) Lan, C. B.; Auclair, K. Organocatalytic Hat Trick: 1,5,7-Triazabicyclo[4.4.0]Dec-5-Ene (TBD)-Catalyzed Synthesis of Cyclic Imides via an Amidation–Cyclization–Elimination Cascade. *J. Org. Chem.* **2025**, *90* (1), 700–708. https://doi.org/10.1021/acs.joc.4c02649.

Appendix IV. Nuclear magnetic spectra

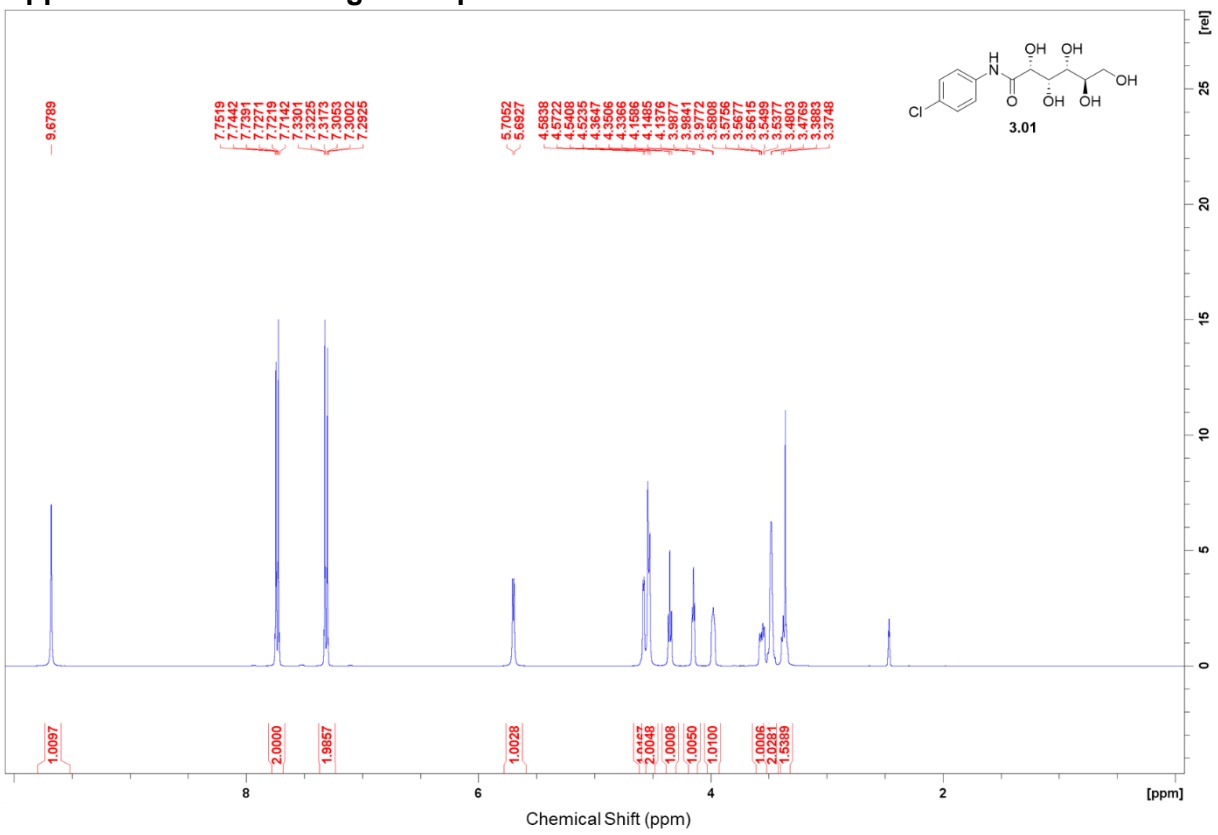

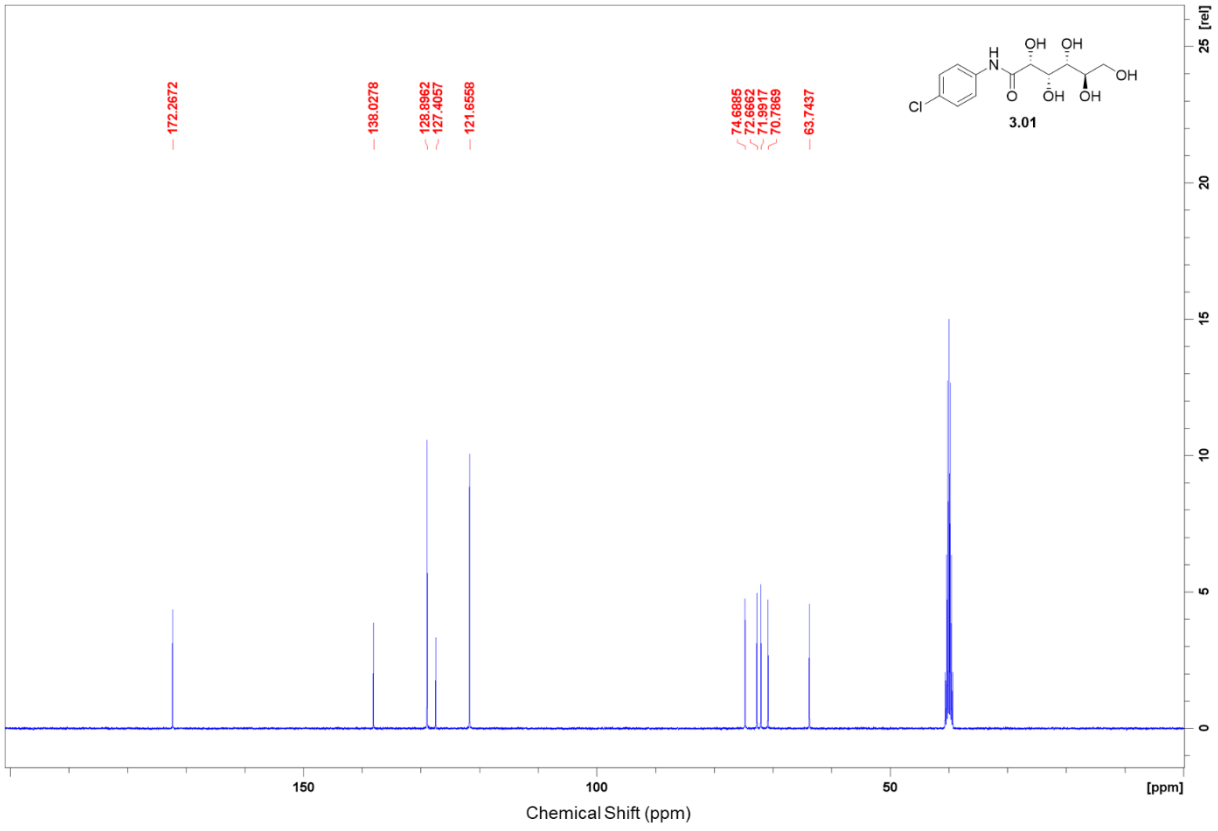

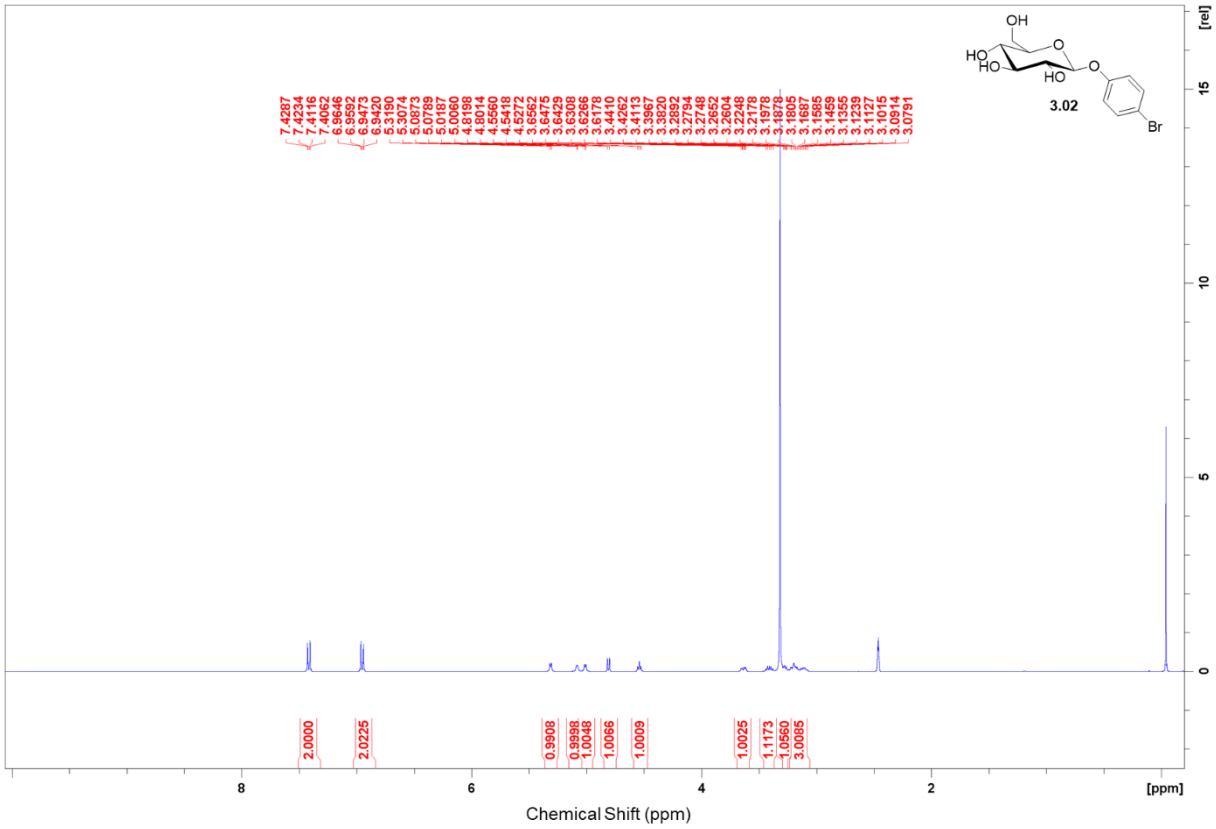
OH
HO
HO
HO
O
O
3.02
Br
7.4287
7.4234
7.4116
7.4062
6.9646
6.9592
6.9473
6.9420
5.3190
5.3074
5.0873
5.0789
5.0187
5.0060
4.8198
4.8014
4.5560
4.5418
4.5272
3.6562
3.6475
3.6429
3.6308
3.6266
3.6178
3.4410
3.4262
3.4113
3.3967
3.3820
3.2892
3.2754
3.2748
3.2652
3.2604
3.2248
3.2178
3.1978
3.1878
3.1805
3.1687
3.1585
3.1469
3.1355
3.1239
3.1127
3.1015
3.0914
3.0791
2.0000
2.0225
0.9908
0.9986
1.0048
1.0066
1.0009
1.0025
1.1173
1.0560
3.0085
[rel]
15
10
5
0
8
6
4
2
[ppm]
Chemical Shift (ppm)

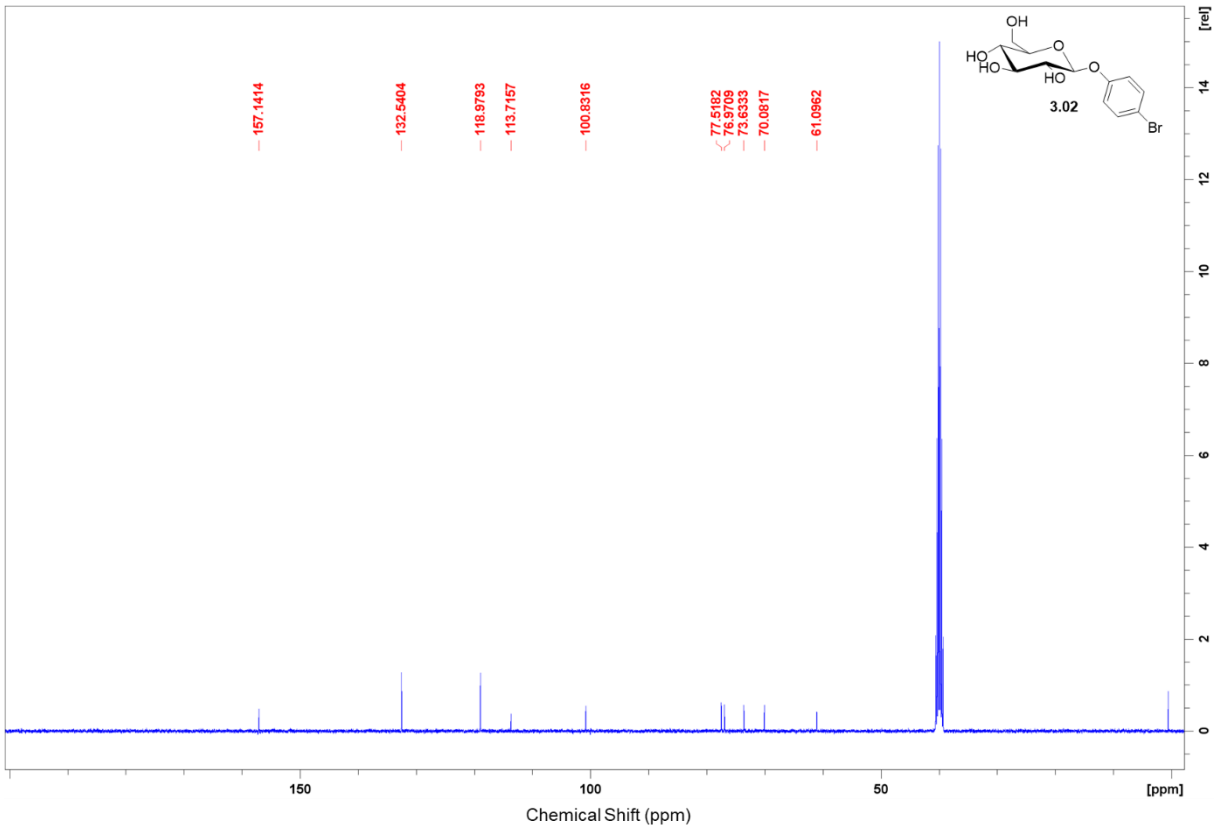
OH
HO
HO
HO
O
O
3.02
Br
157.1414
132.5404
118.9793
113.7157
100.8316
77.5182
76.9709
73.6333
70.0817
61.0962
[rel]
14
12
10
8
6
4
2
0
150
100
50
[ppm]
Chemical Shift (ppm)

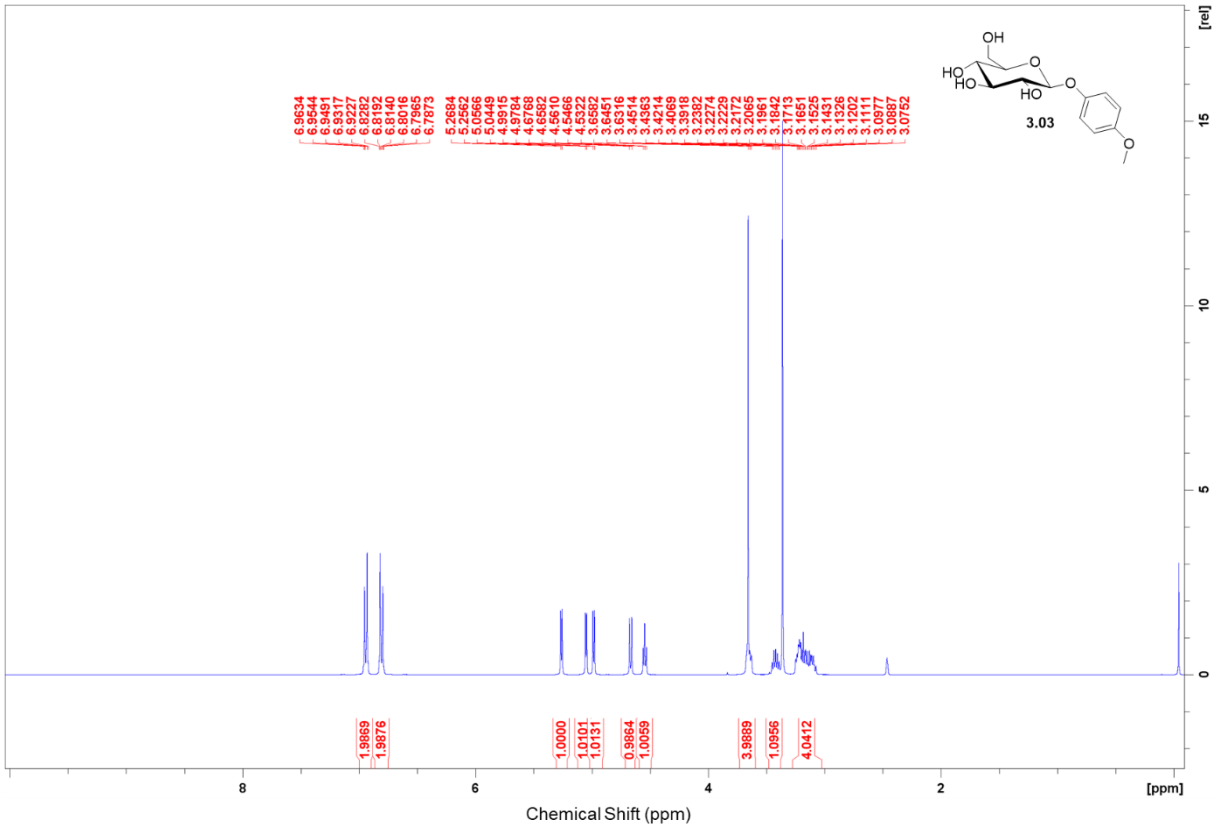
6.9634
6.9544
6.9491
6.9437
6.9327
6.9277
6.8282
6.8192
6.8140
6.8016
6.7965
6.7873
5.2684
5.2582
5.0566
5.0449
4.9915
4.9784
4.6768
4.6582
4.5610
4.5466
4.5322
3.6582
3.6451
3.6316
3.4554
3.4453
3.4214
3.4069
3.3918
3.2382
3.2274
3.2229
3.2172
3.2065
3.1961
3.1842
3.1713
3.1651
3.1525
3.1431
3.1326
3.1202
3.1111
3.0977
3.0887
3.0752
1.9869
1.9876
1.0000
1.0101
1.0131
0.9864
1.0059
3.9889
1.0956
4.0412
OH
HO
HO
HO
O
O
O
3.03
[rel]
[ppm]
Chemical Shift (ppm)

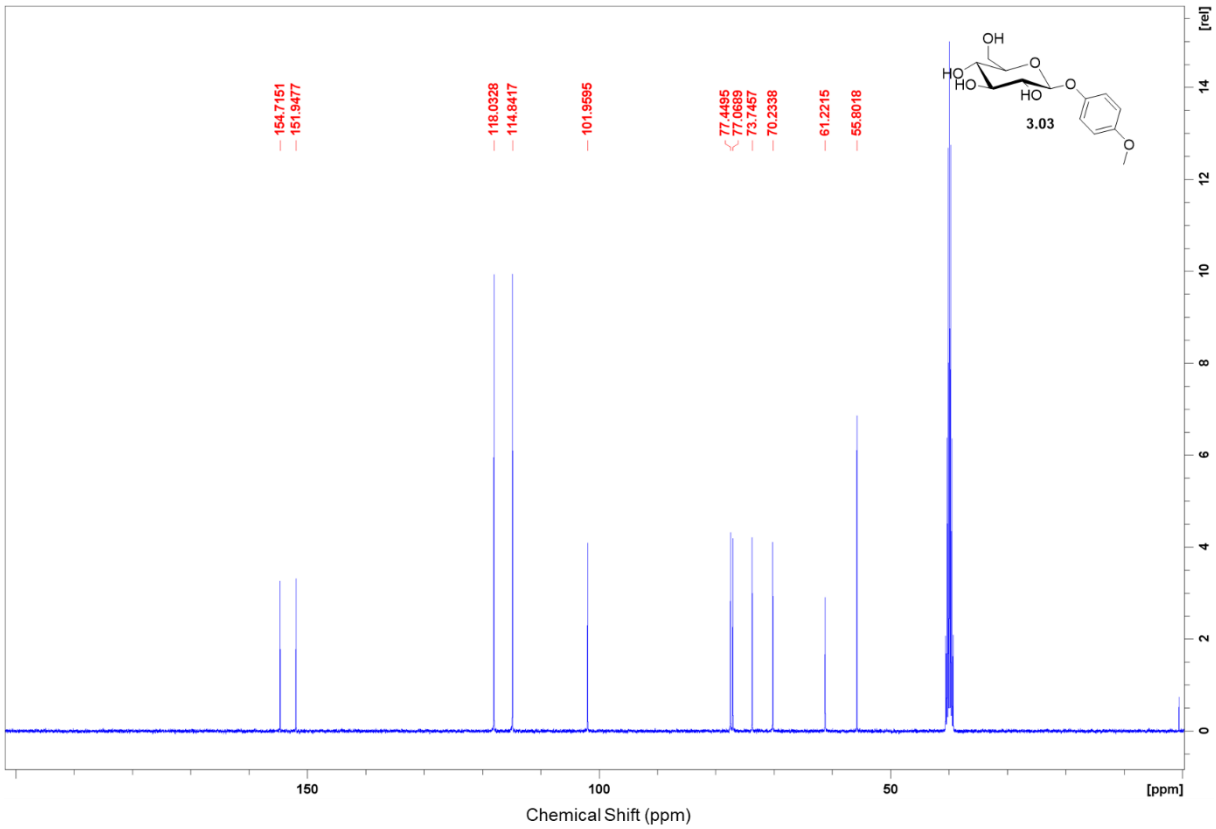
154.7151
151.9477
118.0328
114.8417
101.9595
77.4495
77.0689
73.7457
70.2338
61.2215
55.8018
OH
HO
HO
HO
O
O
O
3.03
[rel]
[ppm]
Chemical Shift (ppm)

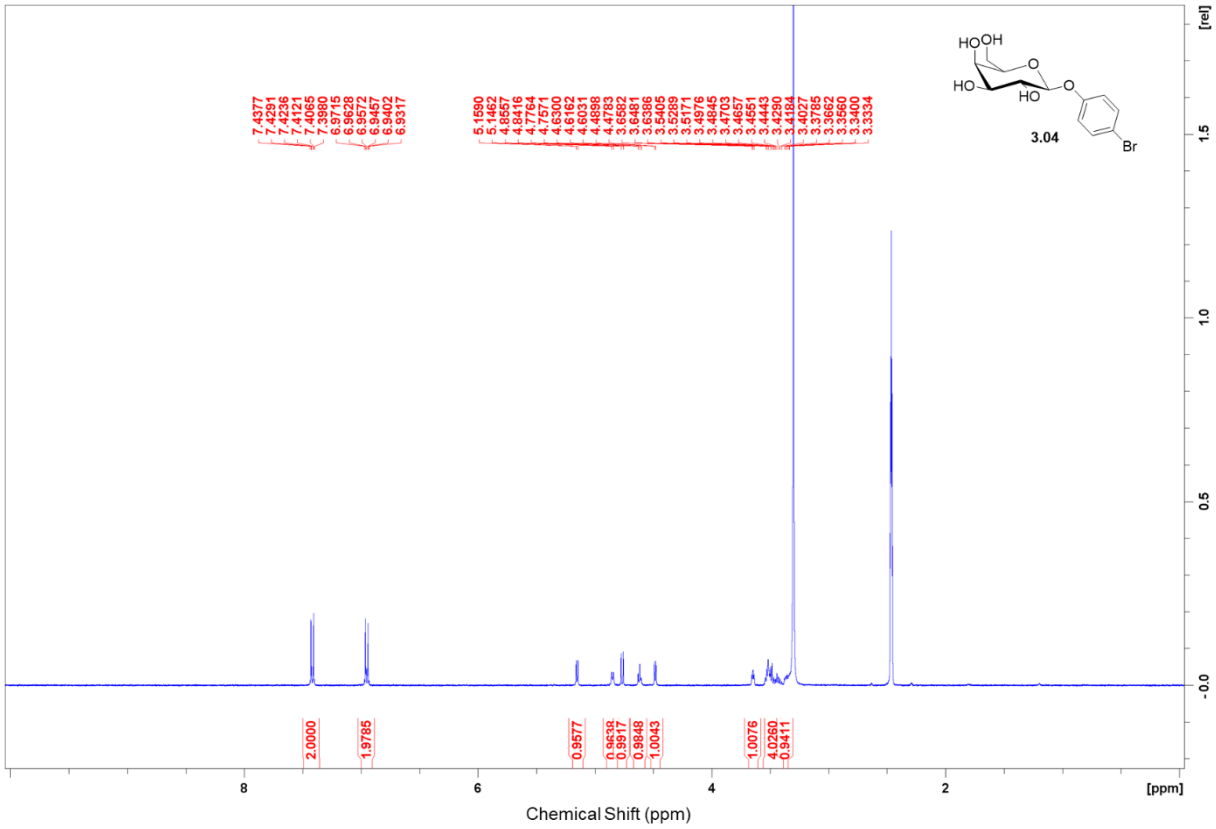
7.4377
7.4291
7.4236
7.4121
7.4065
7.3980
6.9715
6.9628
6.9572
6.9457
6.9402
6.9317
5.1690
5.1462
4.9557
4.8416
4.7764
4.7571
4.6300
4.6162
4.6031
4.4898
4.4783
3.6582
3.6481
3.6386
3.6065
3.6009
3.5171
3.4976
3.4845
3.4703
3.4657
3.4551
3.4443
3.4290
3.4184
3.4027
3.3785
3.3662
3.3550
3.3400
3.3334
2.0000
1.9785
0.9577
0.9638
0.9917
0.9848
1.0043
1.0076
4.0260
0.9411
3.04
Br
[rel]
[ppm]
Chemical Shift (ppm)

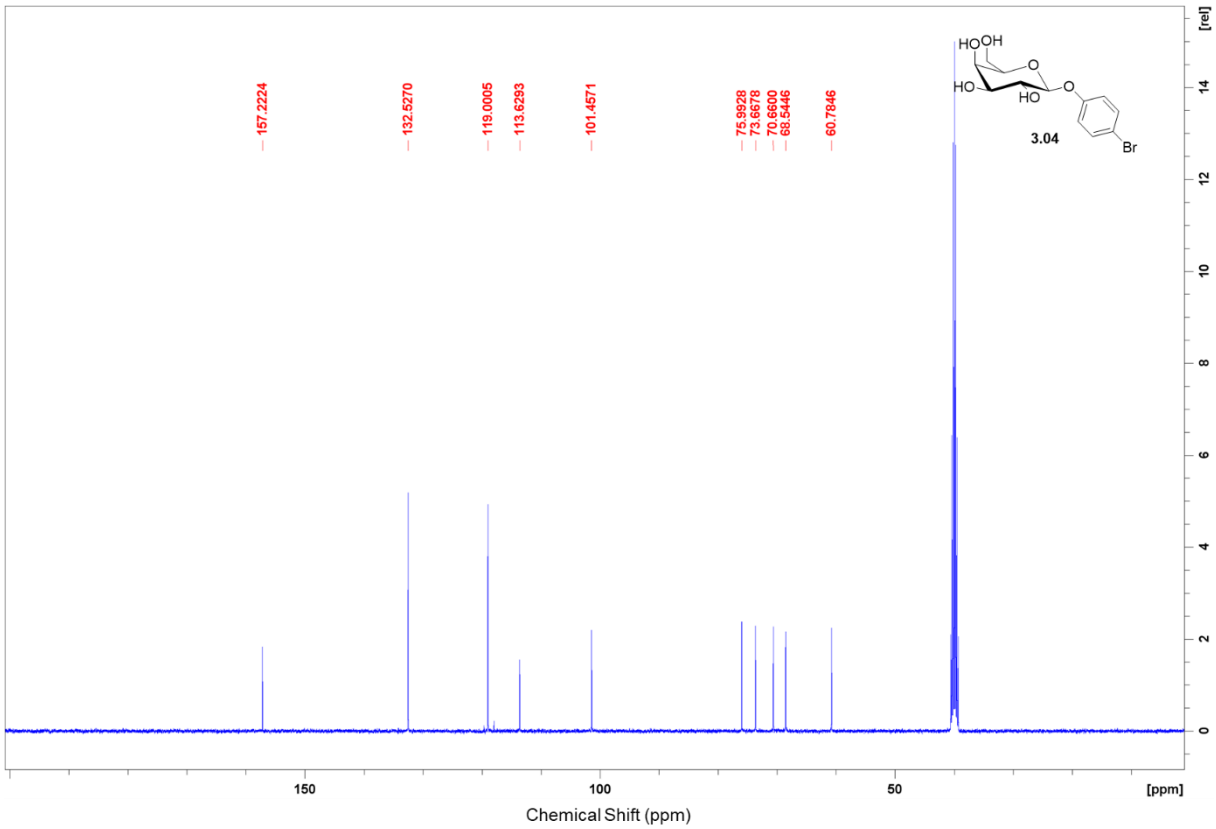
157.2224
132.5270
119.0005
113.6283
101.4571
75.9928
73.6678
70.6600
68.5446
60.7846
3.04
Br
[rel]
[ppm]
Chemical Shift (ppm)

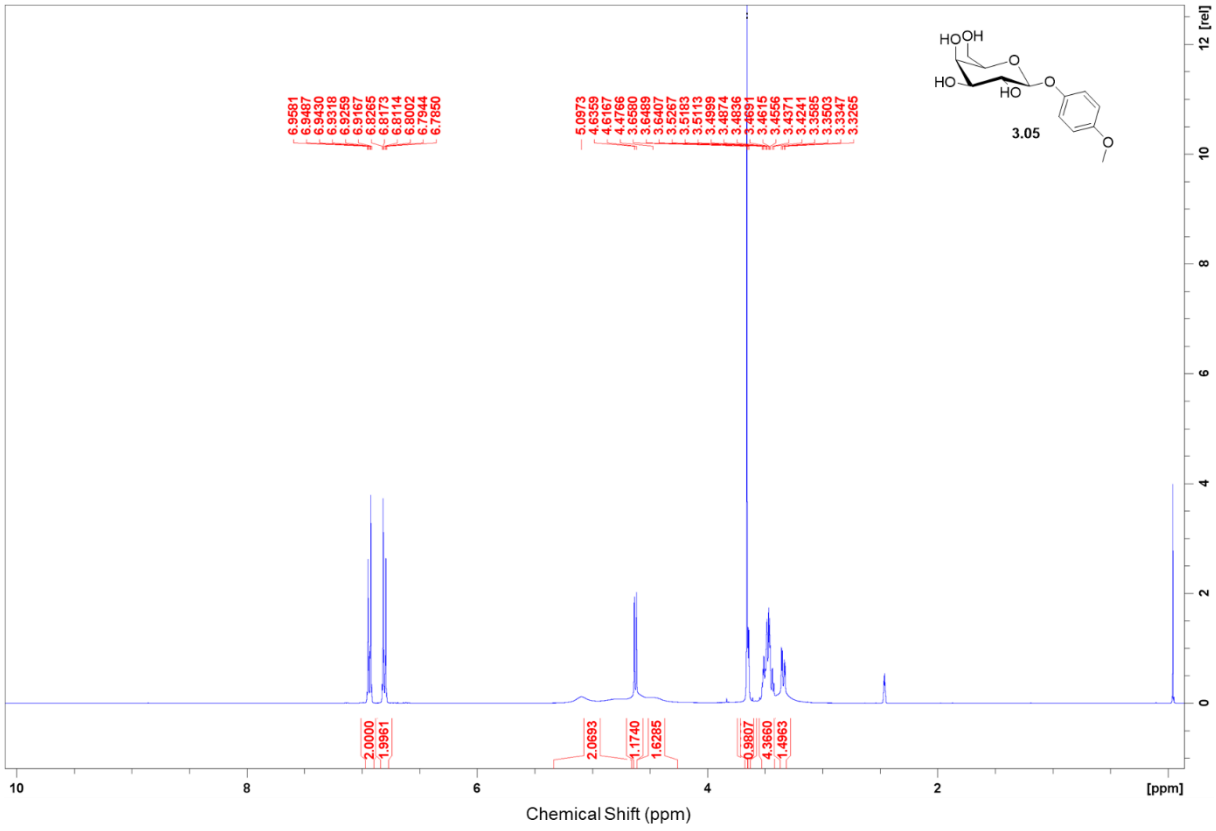
6.9581
6.9487
6.9430
6.9318
6.9259
6.9167
6.8265
6.8173
6.8114
6.8002
6.7944
6.7850
5.0973
4.6359
4.6167
4.4766
4.4580
4.4469
4.4407
3.5267
3.5183
3.5113
3.4999
3.4874
3.4836
3.4691
3.4615
3.4556
3.4371
3.4241
3.3665
3.3563
3.3347
3.3265
2.0000
1.9961
2.0693
1.1740
1.6285
0.9807
4.3660
1.4963
HO
OH
O
HO
HO
O
O
3.05
12 [rel]
10
8
6
4
2
0
10
8
6
4
2
[ppm]
Chemical Shift (ppm)

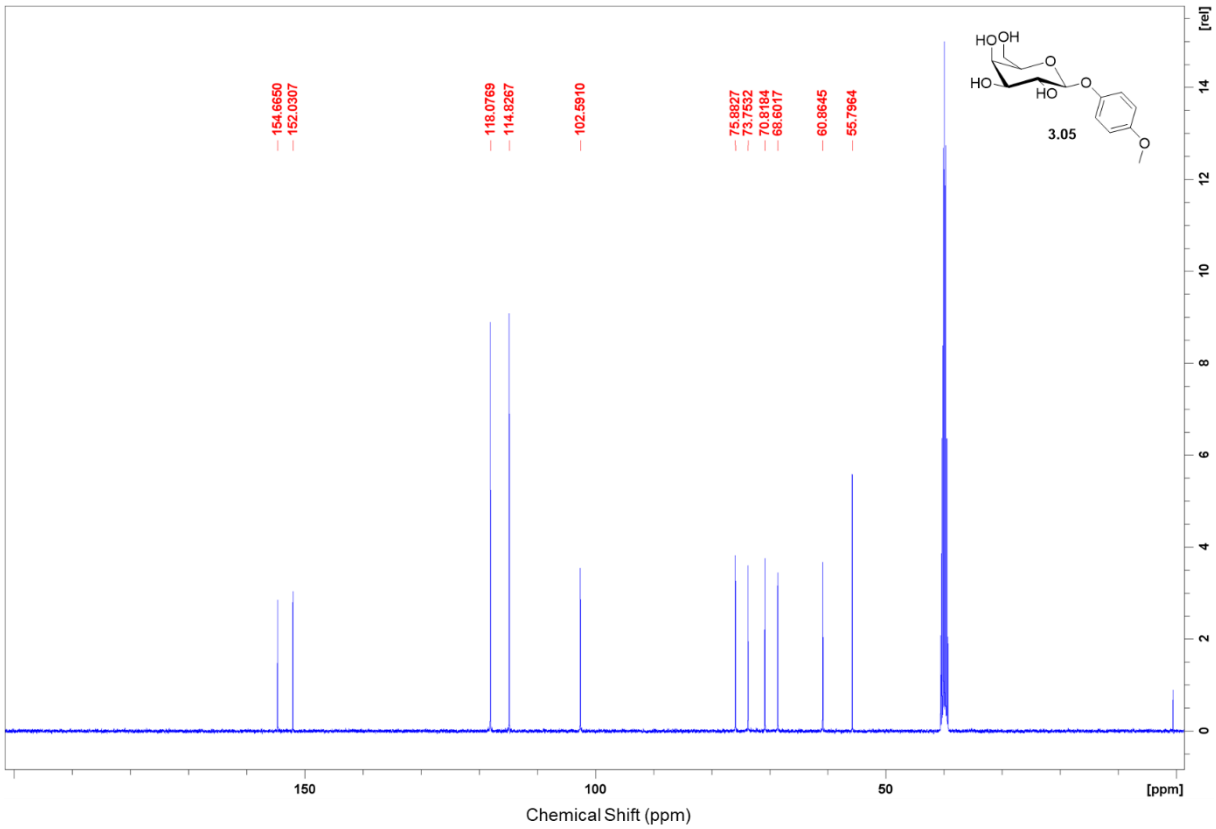
154.6650
152.0307
118.0769
114.8267
102.5910
75.8827
73.7532
70.8184
68.6017
60.8645
55.7964
HO
OH
O
HO
HO
O
O
3.05
[rel]
14
12
10
8
6
4
2
0
150
100
50
[ppm]
Chemical Shift (ppm)

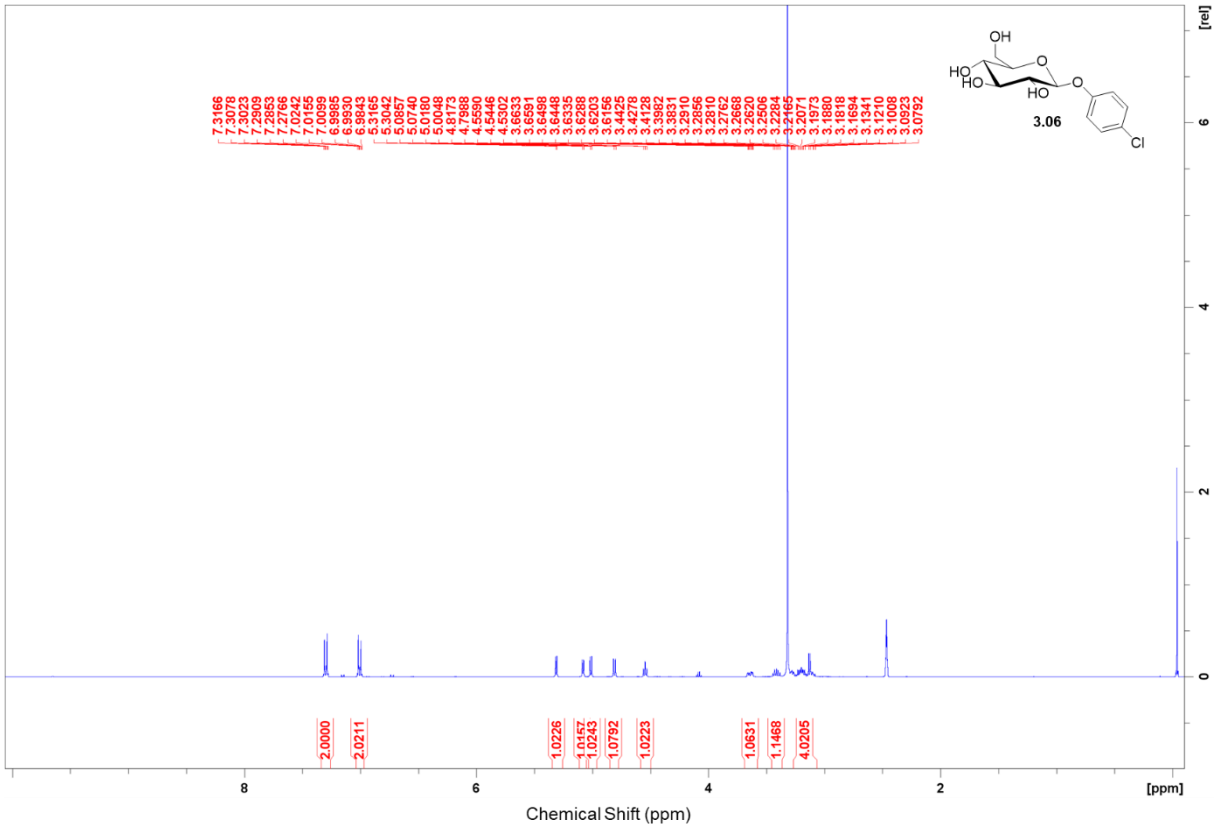
7.3166
7.3078
7.3023
7.2909
7.2853
7.2766
7.2742
7.0145
7.0099
6.9985
6.9930
6.9843
5.3165
5.3042
5.0857
5.0740
5.0180
5.0048
4.9173
4.7988
4.6590
4.5446
4.5302
3.6633
3.6591
3.6498
3.6448
3.6335
3.6288
3.6203
3.6156
3.4425
3.4278
3.4128
3.3982
3.3831
3.2910
3.2856
3.2810
3.2762
3.2668
3.2620
3.2506
3.2284
3.2165
3.2071
3.1973
3.1880
3.1818
3.1694
3.1341
3.1210
3.1008
3.0923
3.0792
OH
HO
HO
HO
O
O
Cl
3.06
2.0000
2.0211
1.0226
1.0157
1.0243
1.0792
1.0223
1.0631
1.1468
4.0205
8
6
4
2
[ppm]
[rel]
Chemical Shift (ppm)

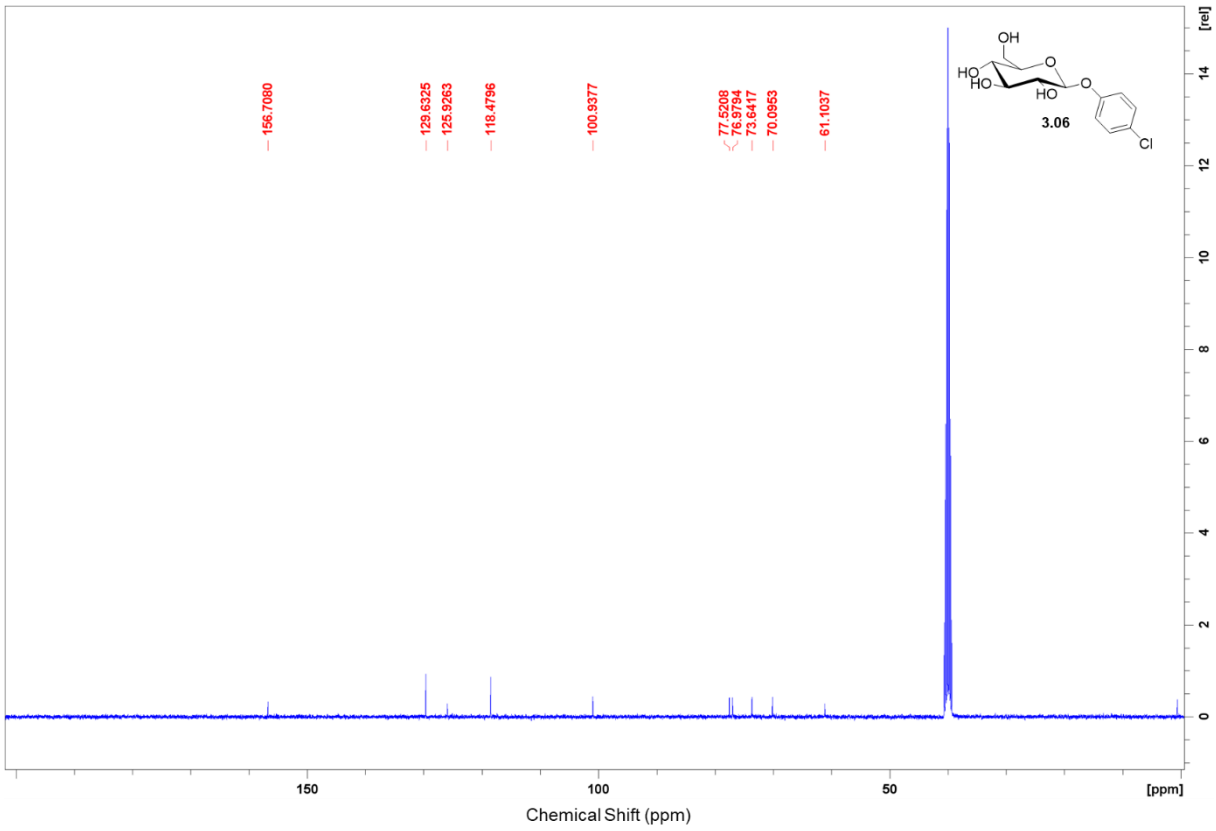
156.7080
129.6325
125.9263
118.4796
100.9377
77.5208
76.9794
73.6417
70.0953
61.1037
OH
HO
HO
HO
O
O
Cl
3.06
150
100
50
[ppm]
[rel]
Chemical Shift (ppm)

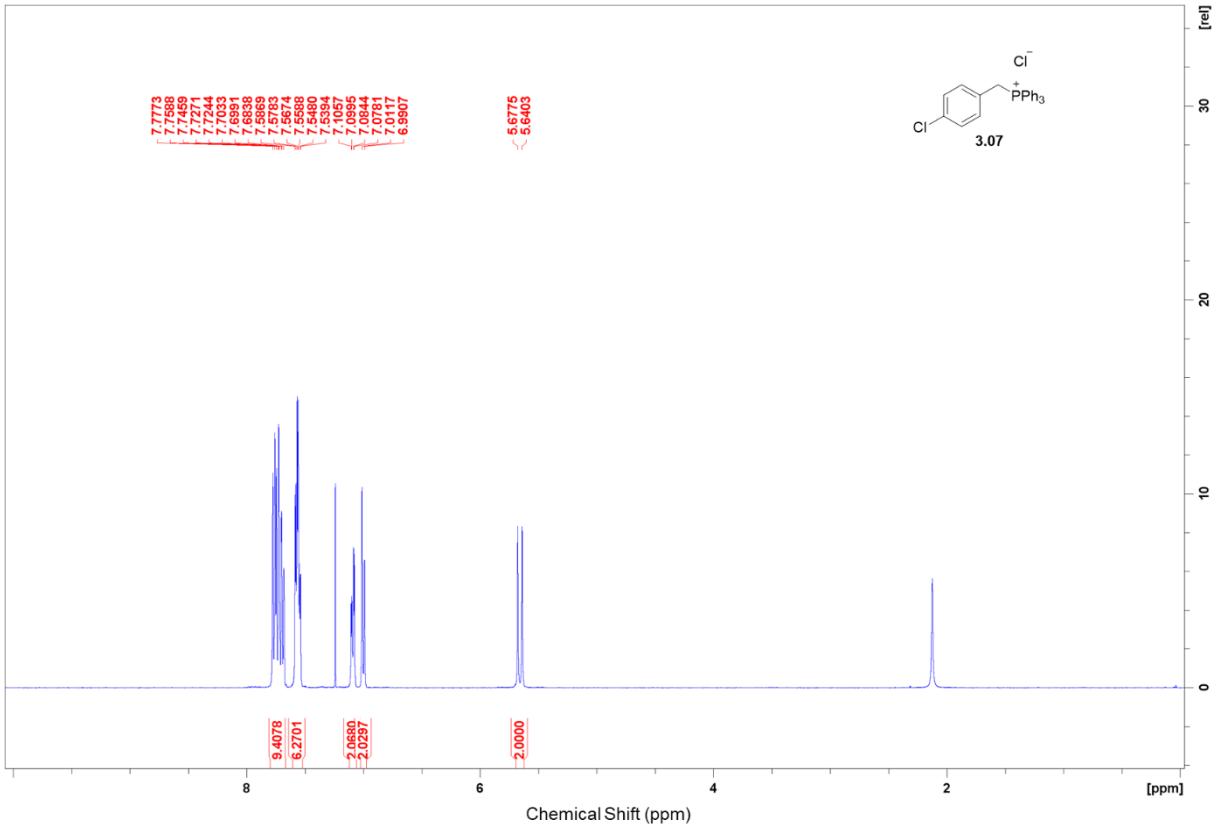
7.7773
7.7568
7.7489
7.7271
7.7244
7.7033
7.6991
7.6838
7.5869
7.5783
7.5674
7.5588
7.5480
7.5394
7.1057
7.0995
7.0844
7.0781
7.0117
6.9907
5.6775
5.6403
9.4076
6.2701
2.0680
2.0297
2.0000
Cl⁻
PPh3
Cl
3.07
[rel]
[ppm]
Chemical Shift (ppm)

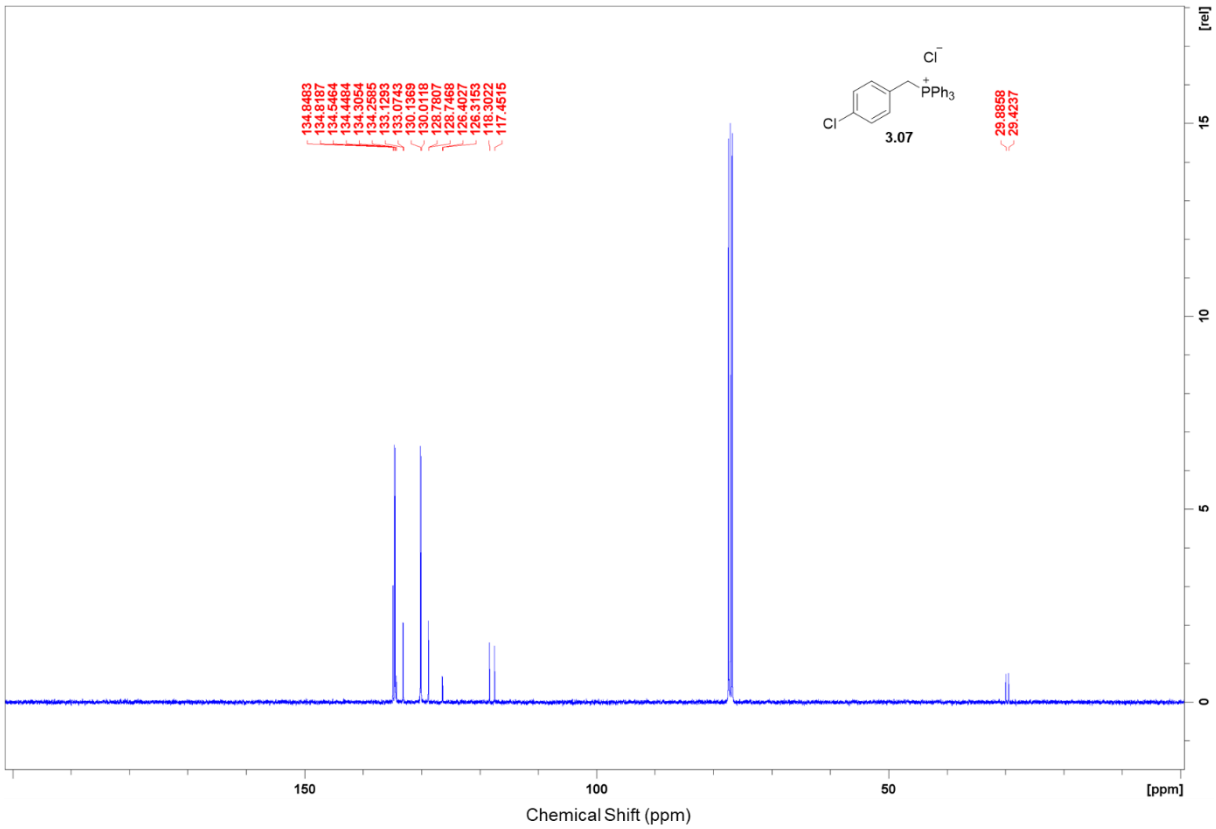
134.8483
134.8187
134.5464
134.4484
134.3054
134.2585
133.1283
133.0743
130.1369
130.0116
128.7497
128.6468
126.4027
126.3153
118.3022
117.4515
29.8858
29.4237
Cl⁻
PPh3
Cl
3.07
[rel]
[ppm]
Chemical Shift (ppm)

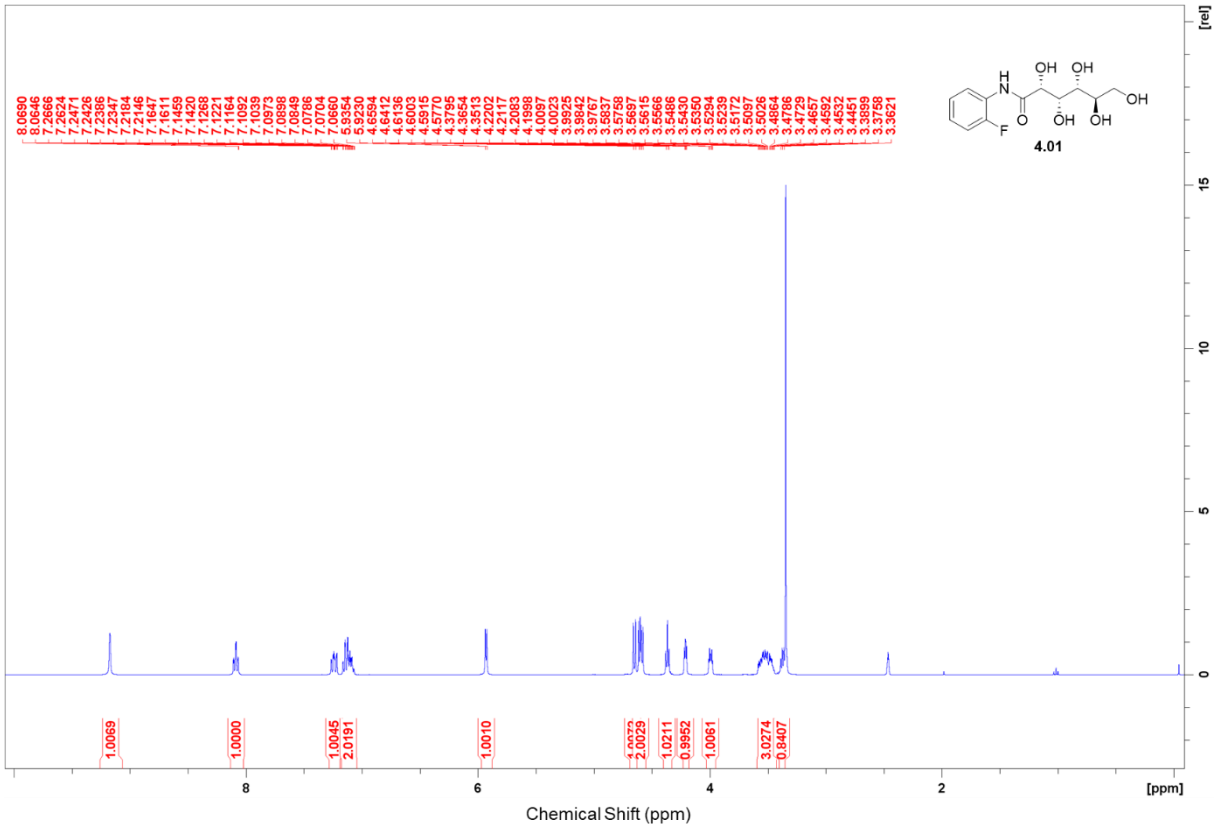
8.0690
8.0646
7.2666
7.2624
7.2471
7.2426
7.2306
7.2247
7.2194
7.2146
7.1647
7.1611
7.1459
7.1420
7.1268
7.1221
7.1164
7.1092
7.1039
7.0973
7.0898
7.0849
7.0786
7.0704
7.0660
5.9354
5.9230
4.6594
4.6412
4.6136
4.6003
4.5915
4.5770
4.3755
4.3654
4.3513
4.2202
4.2117
4.2083
4.1998
4.0097
4.0023
3.9925
3.9842
3.9767
3.5837
3.5758
3.5697
3.5615
3.5566
3.5486
3.5430
3.5350
3.5294
3.5239
3.5172
3.5097
3.5026
3.4864
3.4796
3.4629
3.4567
3.4492
3.4532
3.4451
3.3899
3.3758
3.3621
1.0069
1.0000
1.0045
2.0191
1.0010
4.0037
2.0029
1.0211
0.9952
1.0061
3.0274
0.8407
8
6
4
2
[ppm]
[rel]
0
5
10
15
OH
OH
OH
OH
OH
H
N
O
F
4.01
Chemical Shift (ppm)

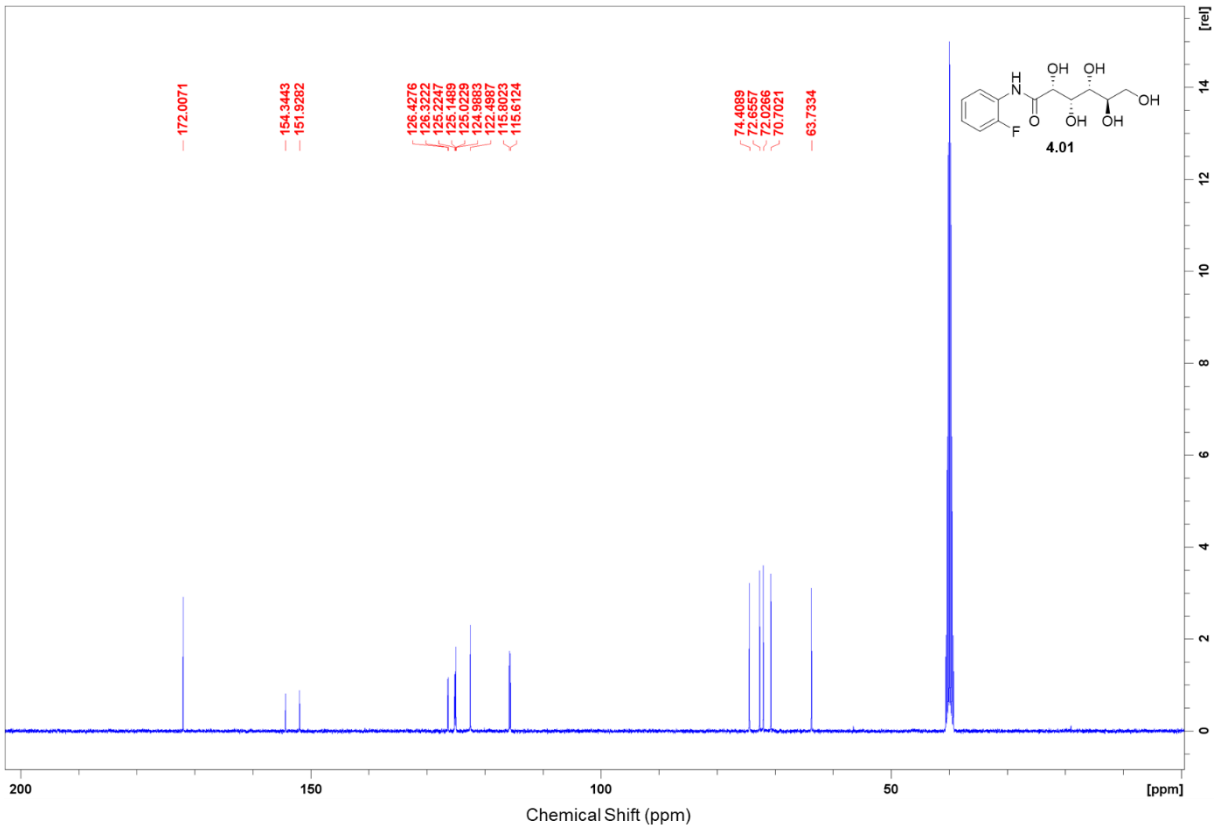
172.0071
154.3443
151.9282
126.4276
126.3222
125.2247
125.1469
125.0223
123.9683
122.4987
115.8023
115.6124
74.4089
72.6557
72.0266
70.7021
63.7334
200
150
100
50
[ppm]
[rel]
0
2
4
6
8
10
12
14
OH
OH
OH
OH
OH
H
N
O
F
4.01
Chemical Shift (ppm)

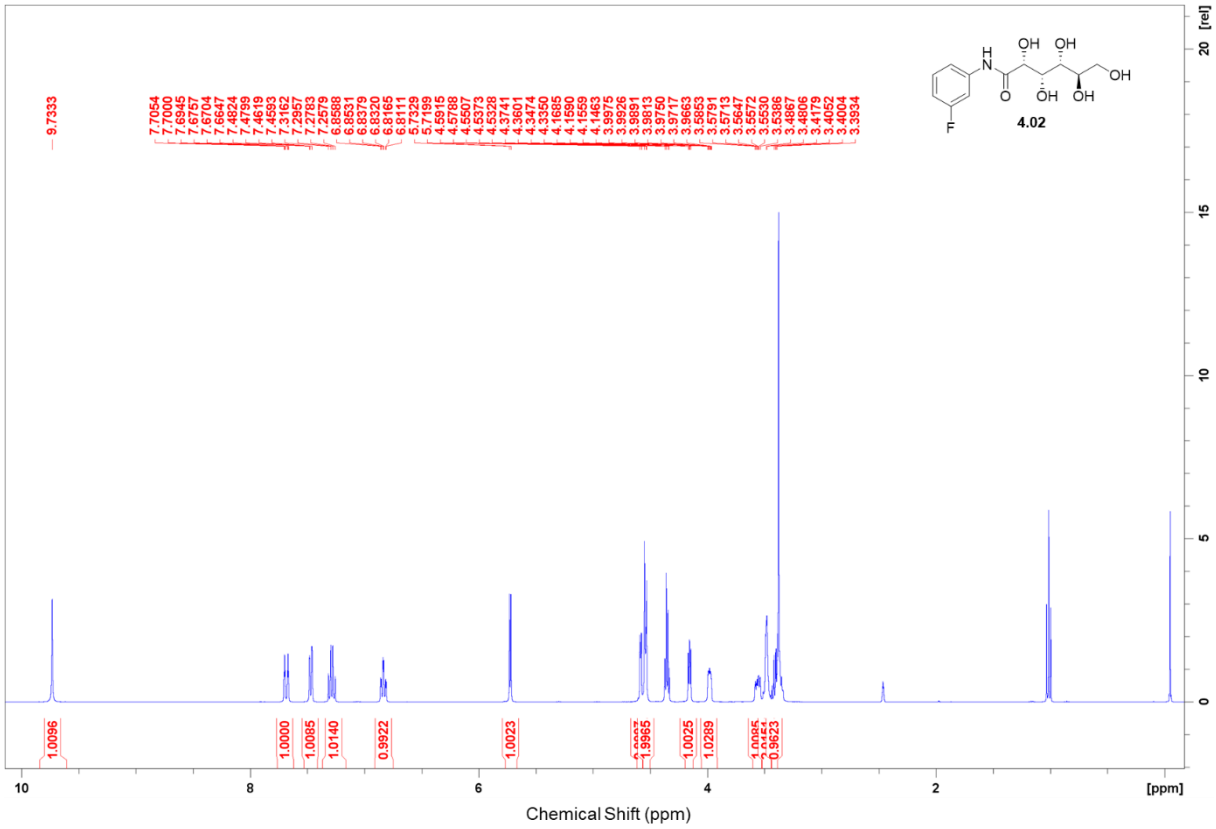
9.7333
7.7054
7.7000
7.6945
7.6757
7.6704
7.6647
7.4824
7.4799
7.4619
7.4593
7.3162
7.2957
7.2703
7.2678
6.6588
6.6531
6.6379
6.6320
6.6165
6.6111
5.7329
5.7199
4.6915
4.6788
4.6507
4.6373
4.6228
4.3741
4.3601
4.3474
4.3350
4.1685
4.1590
4.1559
4.1463
3.9975
3.9926
3.9891
3.9813
3.9750
3.9717
3.9663
3.5853
3.5791
3.5713
3.5647
3.5572
3.5530
3.5386
3.4887
3.4806
3.4179
3.4052
3.4004
3.3934
1.0096
1.0000
1.0085
1.0140
0.9922
1.0023
2.9955
1.0025
1.0289
1.0095
2.0154
0.9623
OH
OH
OH
OH
OH
F
4.02
10
8
6
4
2
[ppm]
Chemical Shift (ppm)
[rel]
20
15
10
5
0

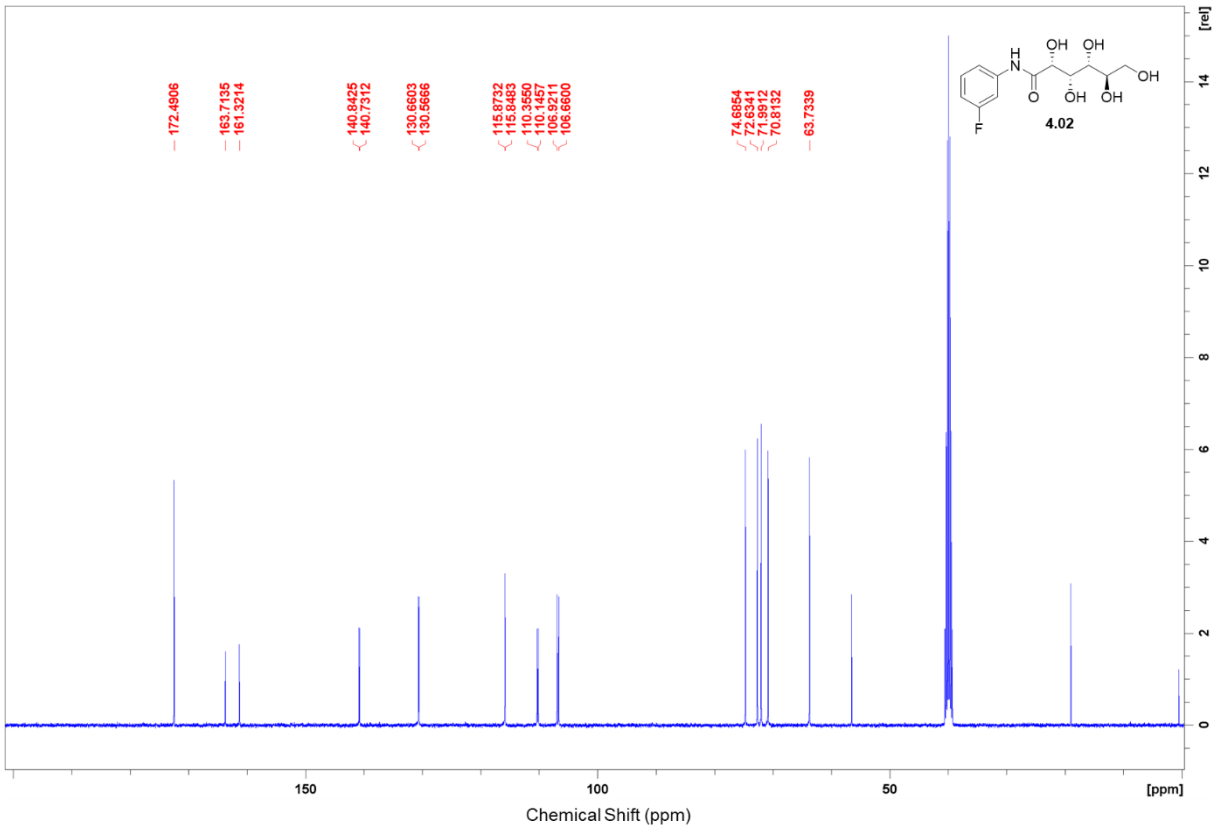
172.4906
163.7135
161.3214
140.8425
140.7312
130.6603
130.5666
115.8732
115.8483
110.3550
110.1457
106.9211
106.6600
74.6854
72.6341
71.9912
70.8132
63.7339
OH
OH
OH
OH
OH
F
4.02
150
100
50
[ppm]
Chemical Shift (ppm)
[rel]
14
12
10
8
6
4
2
0

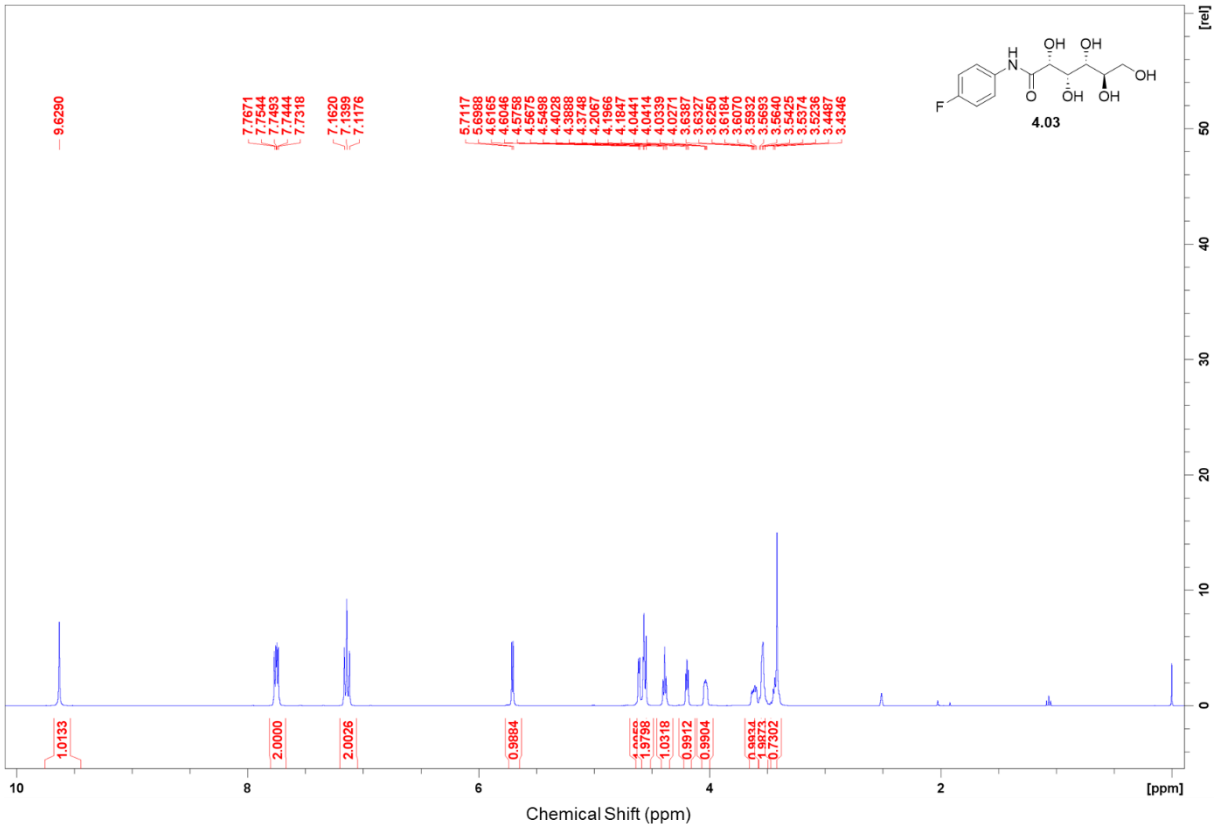
9.6290
7.7671
7.7544
7.7493
7.7444
7.7318
7.1620
7.1399
7.1176
5.7117
5.6988
4.6165
4.6046
4.5758
4.5675
4.5498
4.4028
4.3888
4.3748
4.2067
4.1966
4.1847
4.0441
4.0414
4.0039
4.0271
3.6387
3.6327
3.6250
3.6184
3.6070
3.5932
3.5693
3.5640
3.5425
3.5374
3.5236
3.4497
3.4346
1.0133
2.0000
2.0026
0.9884
1.0318
0.9912
0.9904
0.7302
4.03
[rel]
[ppm]
Chemical Shift (ppm)

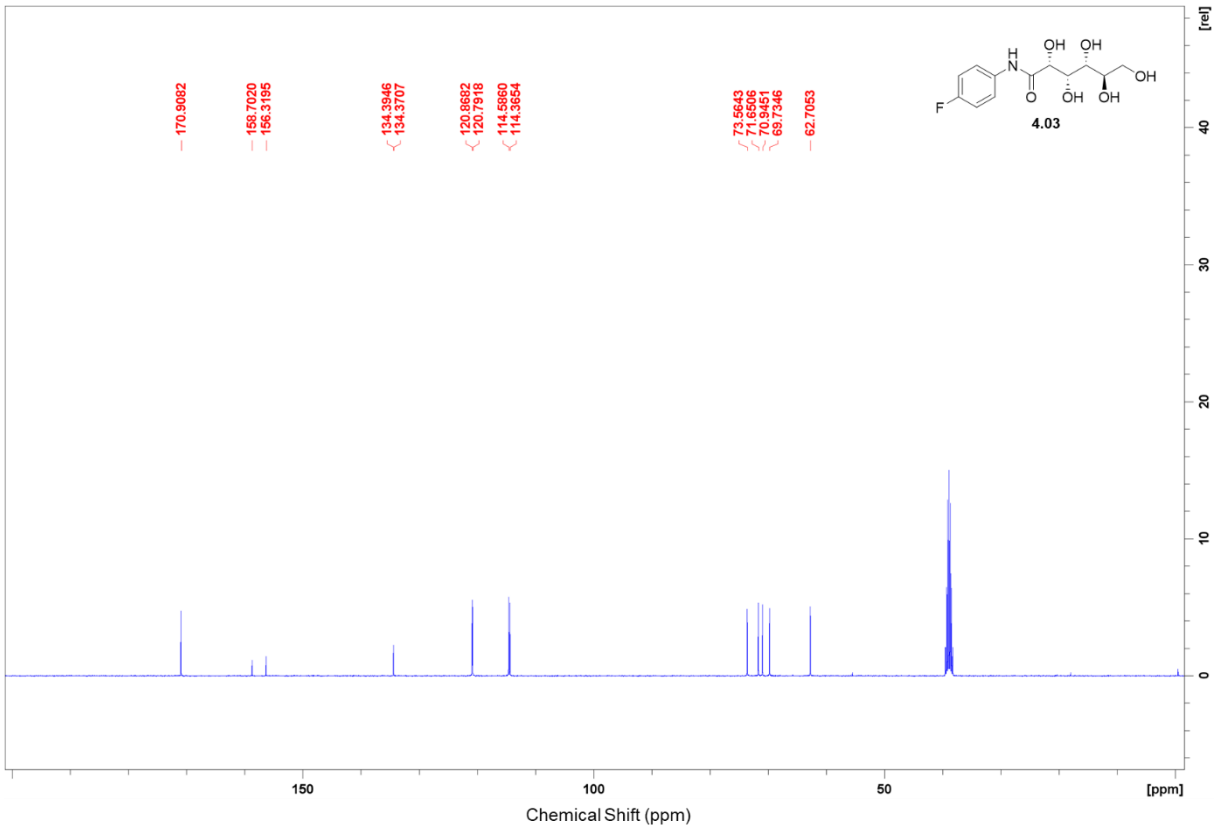
170.9082
158.7020
156.3195
134.3946
134.3707
120.8682
120.7918
114.5860
114.3654
73.5643
71.6506
70.9451
69.7346
62.7053
4.03
[rel]
[ppm]
Chemical Shift (ppm)

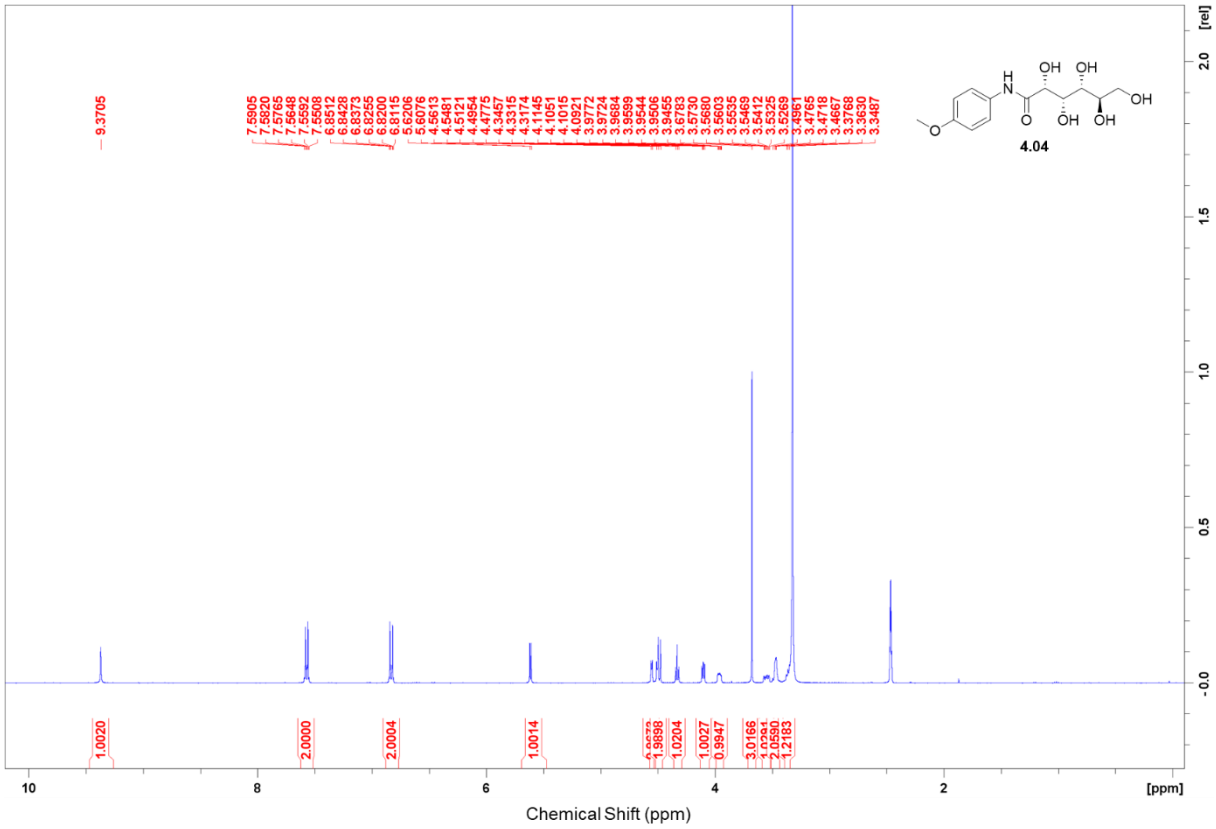
9.3705
7.5905
7.5820
7.5765
7.5648
7.5592
7.5508
6.8512
6.8428
6.8373
6.8255
6.8200
6.8115
5.6076
4.5613
4.5481
4.5121
4.4954
4.4775
4.3457
4.3315
4.3174
4.1145
4.1051
4.1015
4.0921
3.9772
3.9724
3.9684
3.9599
3.9544
3.9506
3.9455
3.6783
3.5730
3.5680
3.5603
3.5535
3.5469
3.5412
3.5325
3.5269
3.4981
3.4765
3.4718
3.4667
3.3768
3.3630
3.3487
1.0020
2.0000
2.0004
1.0014
1.9698
1.0204
1.0027
0.9947
3.0166
1.0291
2.0590
1.2183
OH
OH
OH
OH
OH
N
H
O
O
4.04
[rel]
2.0
1.5
1.0
0.5
-0.0
10
8
6
4
2
[ppm]
Chemical Shift (ppm)

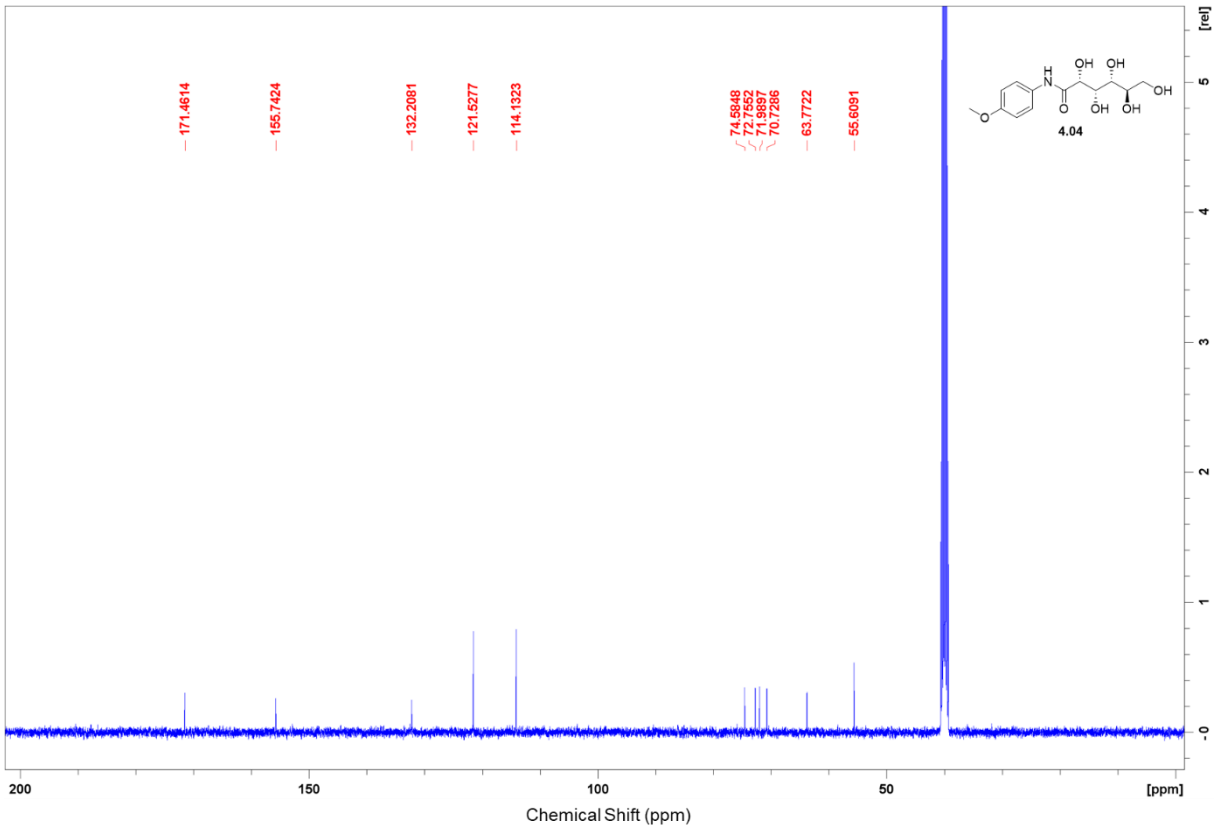
171.4614
155.7424
132.2081
121.5277
114.1323
74.5848
72.7552
71.9897
70.7286
63.7722
55.6091
OH
OH
OH
OH
OH
N
H
O
O
4.04
[rel]
5
4
3
2
1
-0
200
150
100
50
[ppm]
Chemical Shift (ppm)

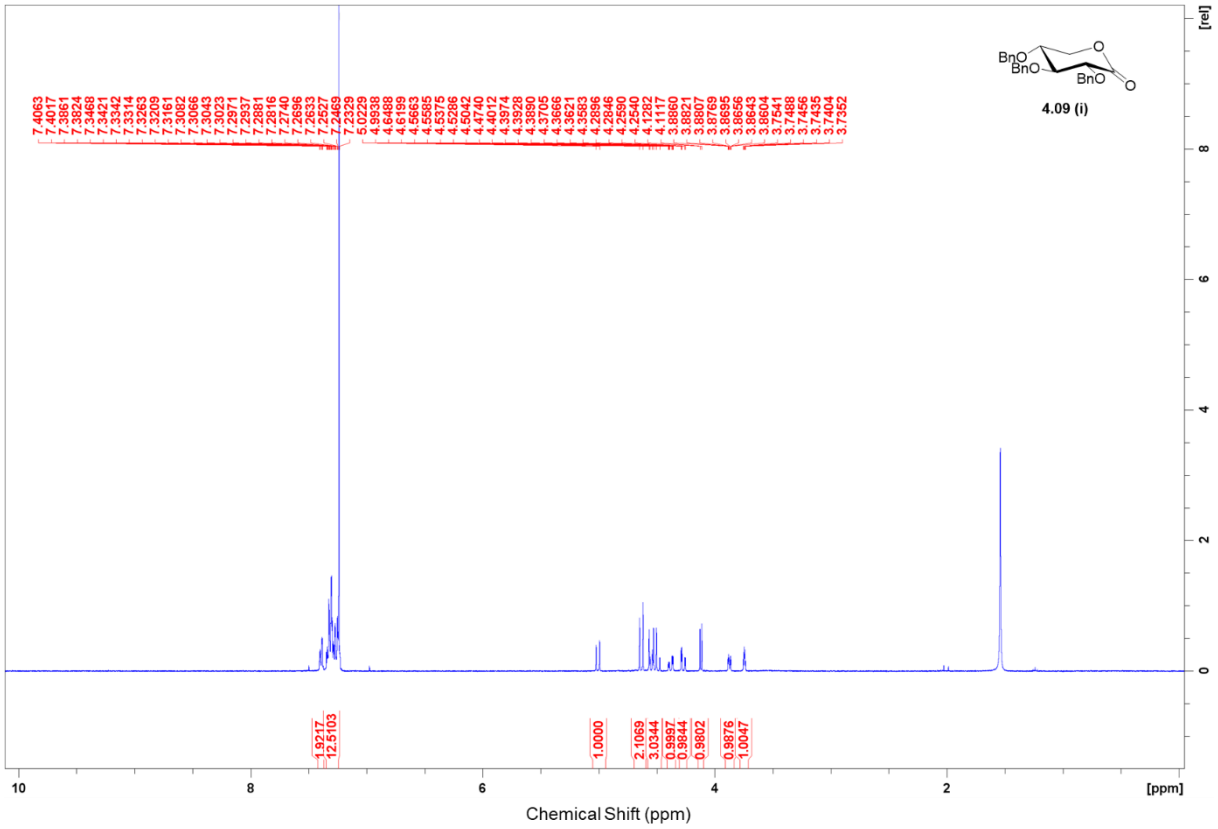
4.09 (i)
Chemical Shift (ppm)

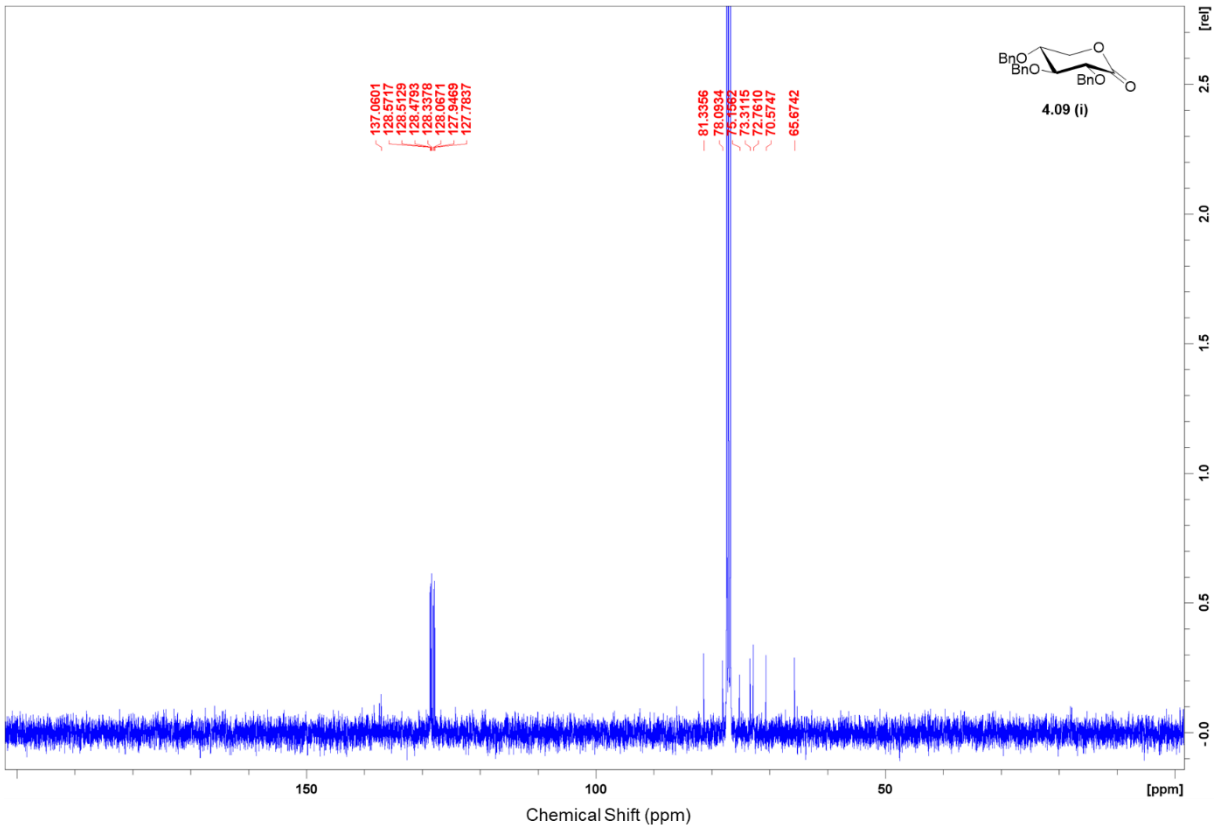
4.09 (i)
Chemical Shift (ppm)

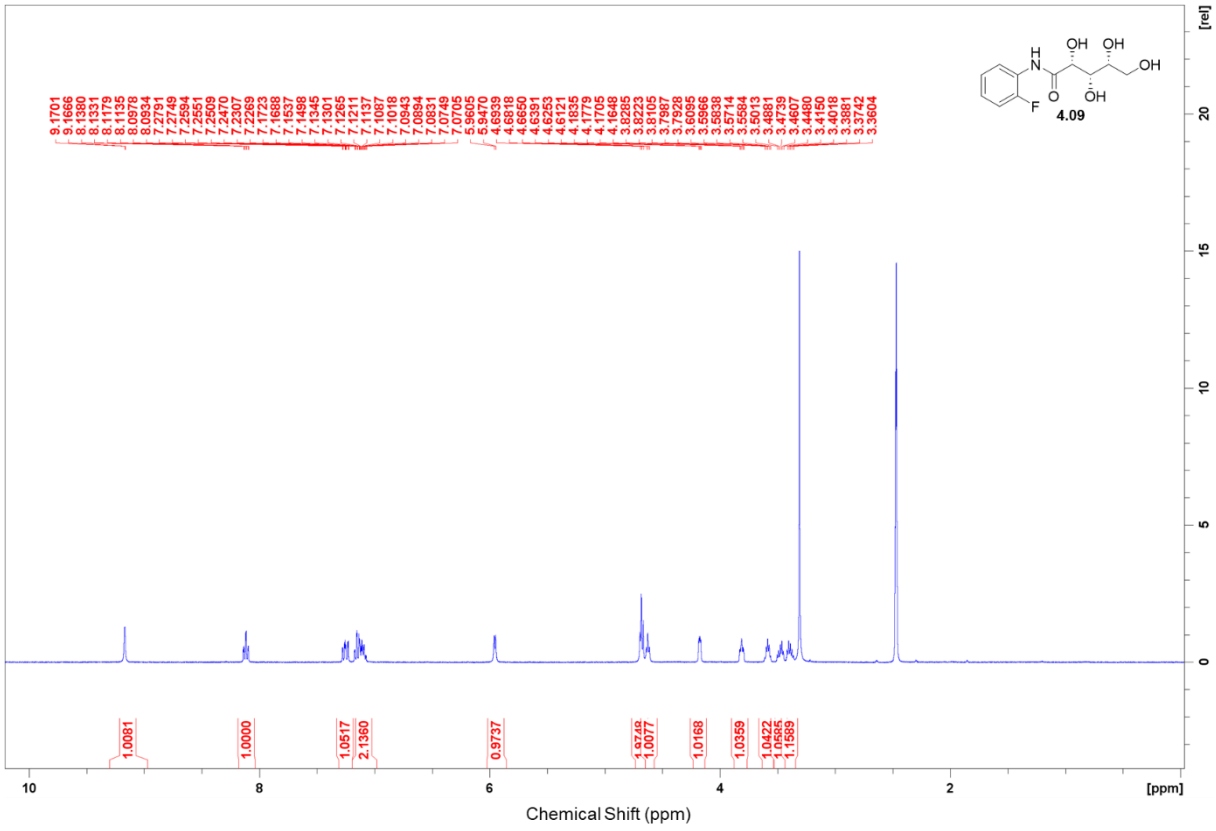
9.1701
9.1666
8.1380
8.1331
8.1179
8.1135
8.0978
8.0934
7.2791
7.2749
7.2694
7.2651
7.2509
7.2470
7.2307
7.2269
7.1723
7.1688
7.1537
7.1498
7.1345
7.1301
7.1265
7.1211
7.1137
7.1097
7.1018
7.0943
7.0894
7.0831
7.0749
7.0705
5.9605
5.9470
4.6939
4.6818
4.6650
4.6391
4.6253
4.6121
4.1835
4.1779
4.1705
4.1648
3.8285
3.8223
3.8105
3.7987
3.7928
3.6085
3.5986
3.5938
3.5714
3.5584
3.5013
3.4881
3.4739
3.4607
3.4480
3.4150
3.4018
3.3881
3.3742
3.3604
1.0081
1.0000
1.0517
2.1360
0.9737
1.9748
1.0077
1.0168
1.0359
1.0422
1.0585
1.1589
10
8
6
4
2
[ppm]
[rel]
20
15
10
5
0
OH
OH
OH
OH
N
H
O
F
4.09
Chemical Shift (ppm)

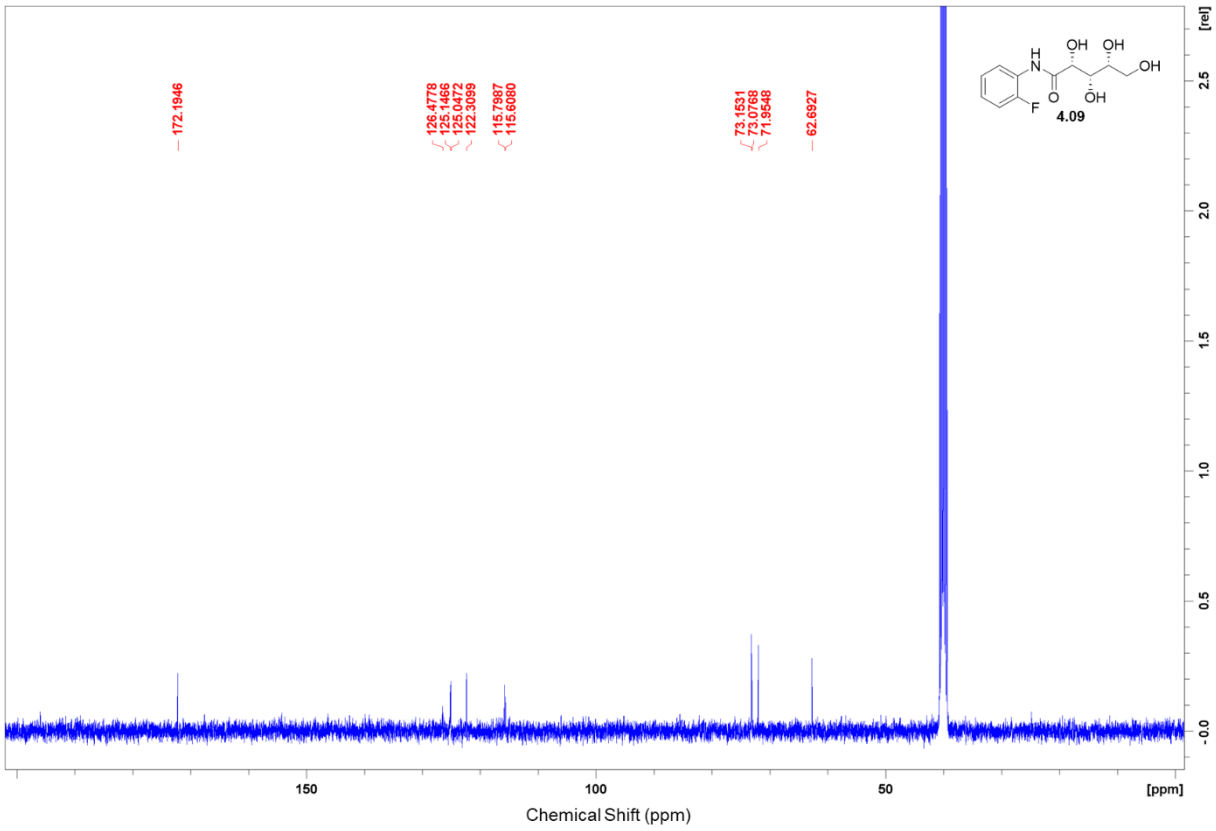
172.1946
126.4778
125.1466
125.0472
122.3099
115.7987
115.6080
73.1531
73.0768
71.9548
62.6927
150
100
50
[ppm]
[rel]
2.5
2.0
1.5
1.0
0.5
-0.0
OH
OH
OH
OH
N
H
O
F
4.09
Chemical Shift (ppm)

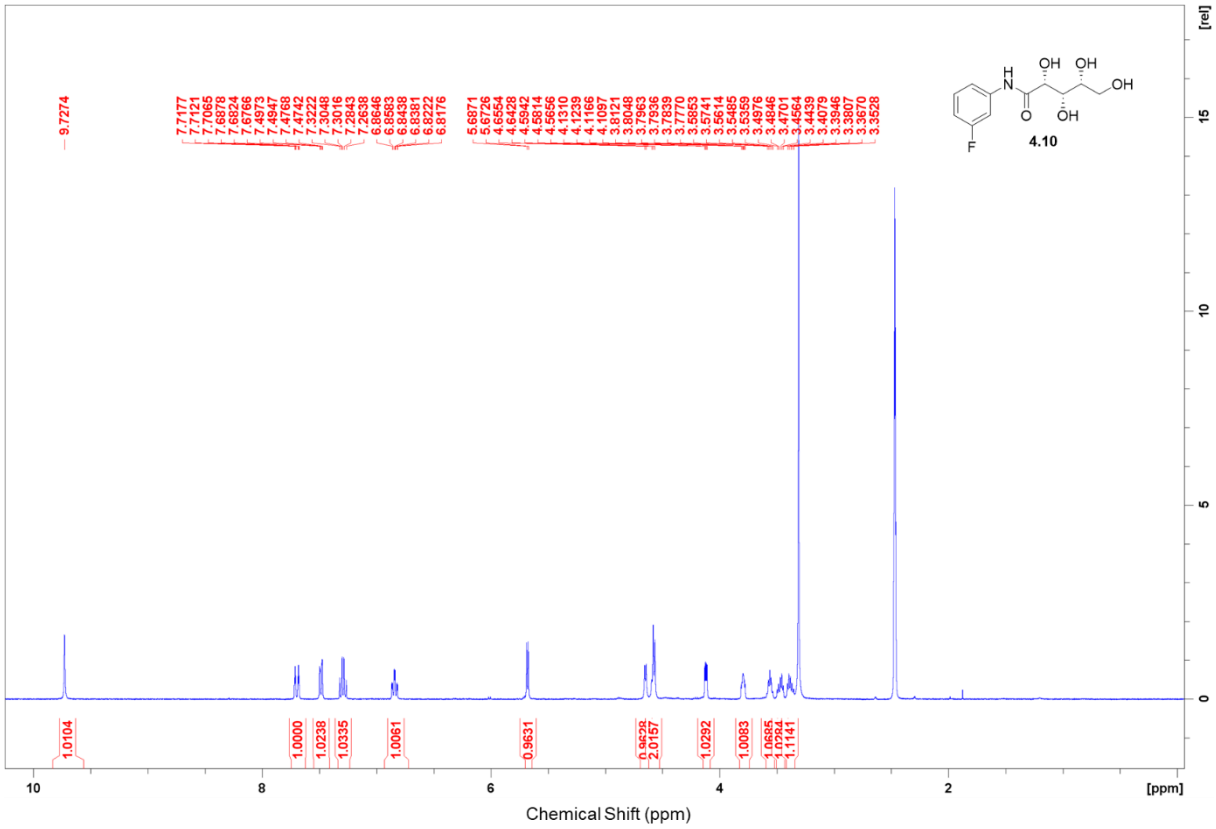
9.7274
7.7177
7.7121
7.7065
7.6878
7.6824
7.6766
7.4973
7.4947
7.4768
7.4742
7.3222
7.3048
7.3016
7.2943
7.2638
6.8646
6.8583
6.8438
6.8381
6.8222
6.8176
5.6871
5.6726
4.6554
4.6428
4.6342
4.6314
4.6266
4.1310
4.1239
4.1156
4.1097
3.8121
3.8048
3.7963
3.7936
3.7839
3.7770
3.5863
3.5741
3.5614
3.5485
3.5359
3.4876
3.4846
3.4701
3.4564
3.4439
3.4079
3.3946
3.3807
3.3670
3.3528
1.0104
1.0000
1.0238
1.0335
1.0061
0.9631
0.9629
2.0157
1.0292
1.0083
1.0685
1.0284
1.1141
4.10
[rel]
[ppm]
Chemical Shift (ppm)

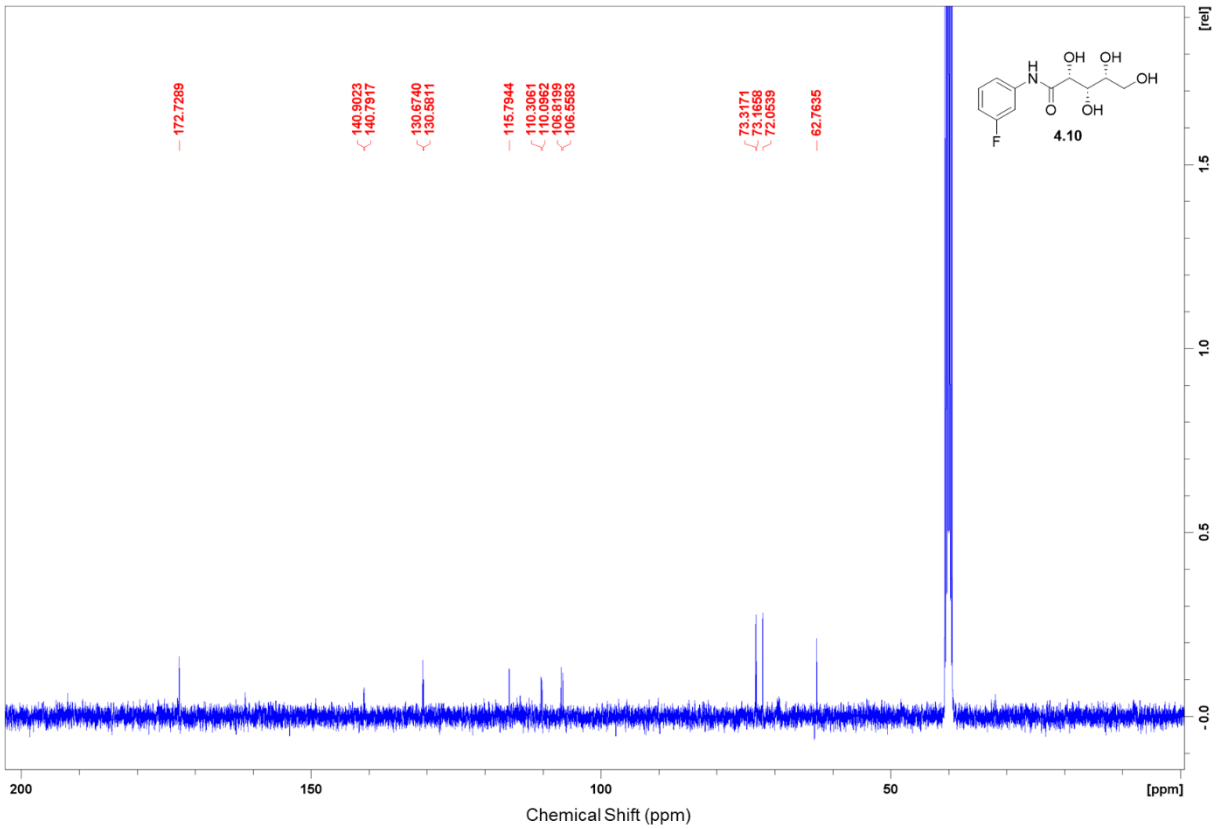
172.7289
140.9023
140.7917
130.6740
130.5811
115.7944
110.3061
110.0962
106.8199
106.5583
73.3171
73.1658
72.0539
62.7635
4.10
[rel]
[ppm]
Chemical Shift (ppm)

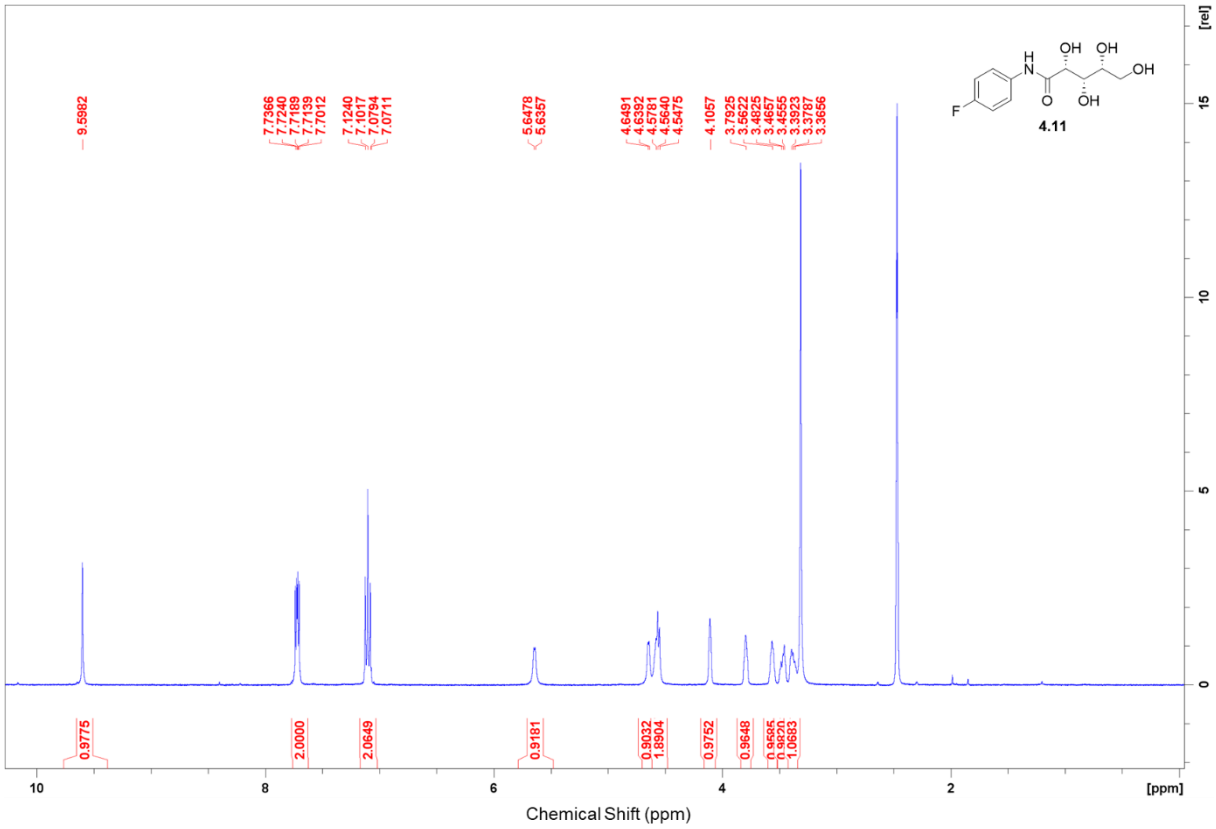
9.5982
7.7366
7.7240
7.7189
7.7139
7.7012
7.1240
7.1017
7.0794
7.0711
5.6478
5.6357
4.6491
4.6392
4.5781
4.5640
4.5475
4.1057
3.7925
3.5622
3.4825
3.4657
3.4555
3.3923
3.3787
3.3656
0.9775
2.0000
2.0649
0.9181
0.9032
1.8904
0.9752
0.9648
0.9585
0.9420
1.0683
10
8
6
4
2
[ppm]
[rel]
15
10
5
0
OH
OH
OH
OH
N
H
O
F
4.11
Chemical Shift (ppm)

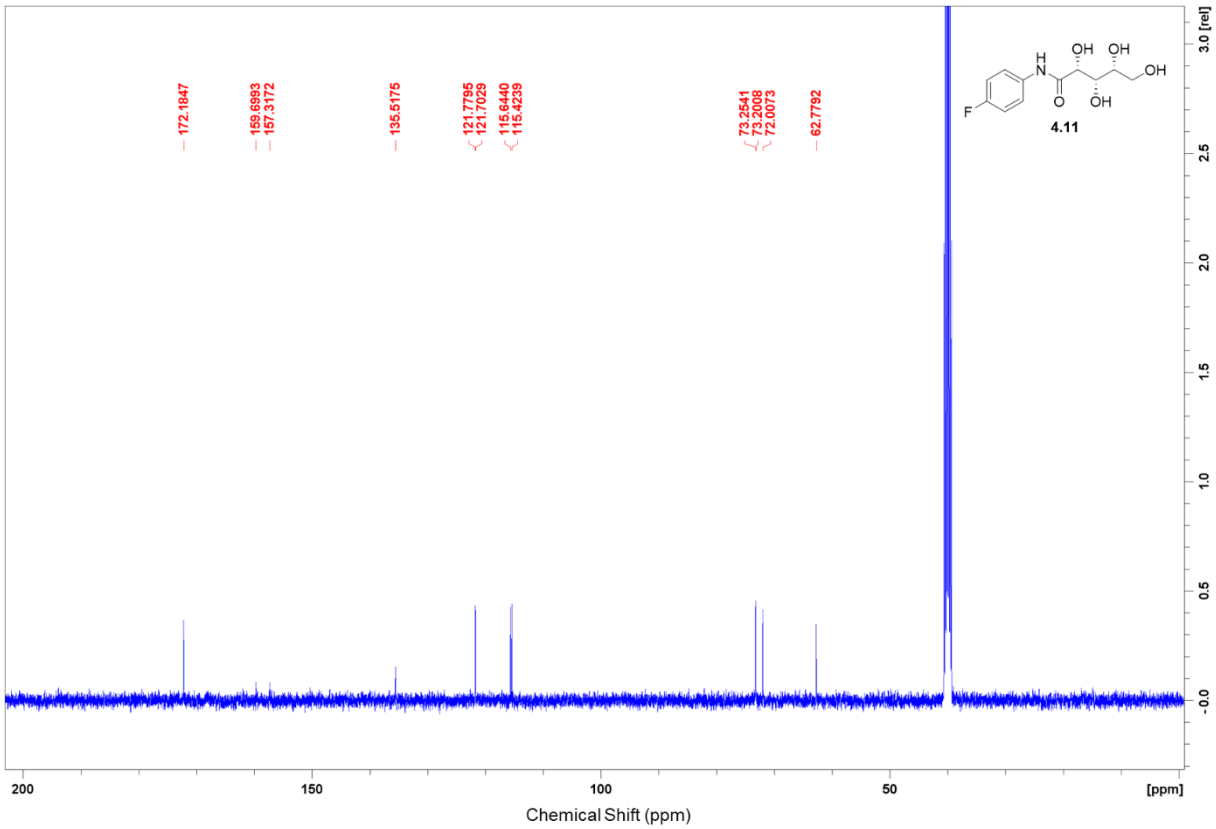
172.1847
159.6993
157.3172
135.5175
121.7795
121.7029
115.6440
115.4239
73.2541
73.2008
72.0073
62.7792
200
150
100
50
[ppm]
3.0 [rel]
2.5
2.0
1.5
1.0
0.5
-0.0
OH
OH
OH
OH
N
H
O
F
4.11
Chemical Shift (ppm)

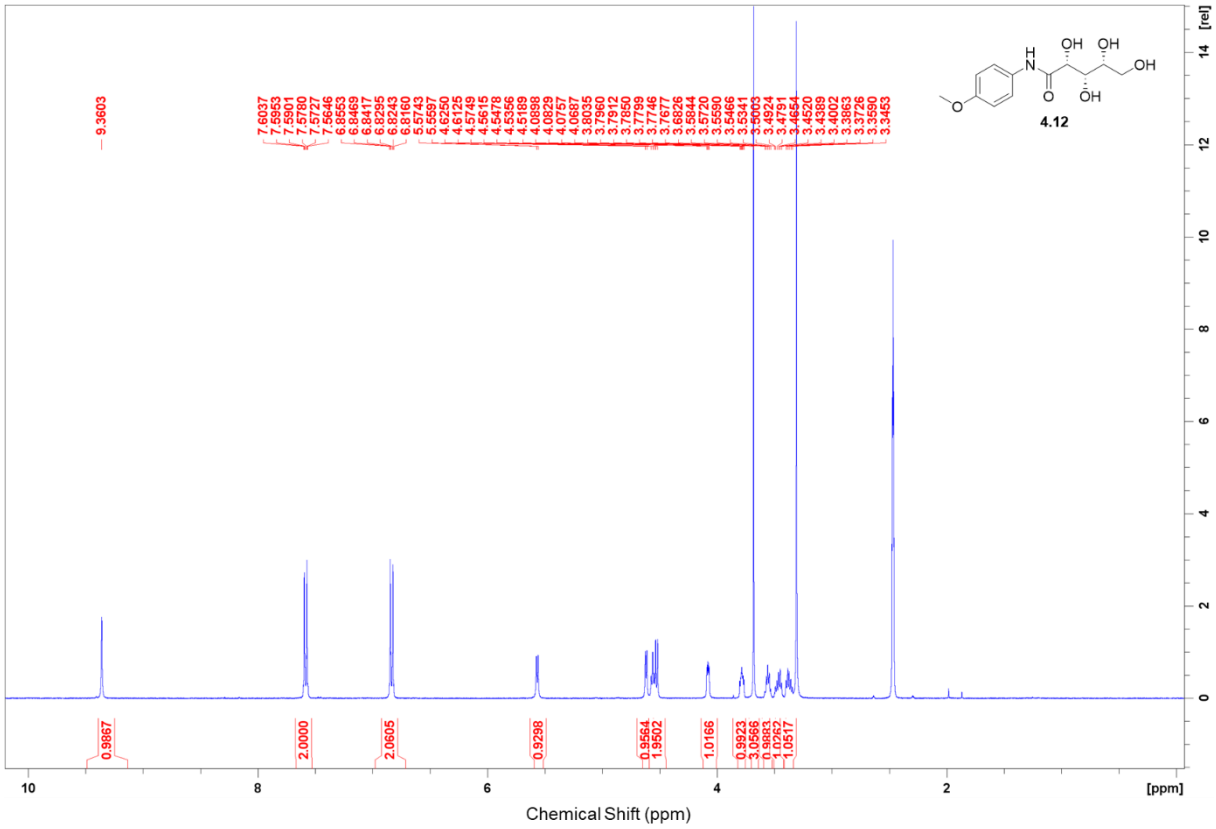
9.3603
7.6037
7.5953
7.5901
7.5780
7.5727
7.5646
6.8553
6.8469
6.8447
6.8295
6.8243
6.8160
5.5743
5.5597
4.6250
4.6125
4.5749
4.5615
4.5478
4.5356
4.5189
4.0898
4.0829
4.0757
4.0687
3.8035
3.7960
3.7912
3.7850
3.7799
3.7746
3.7677
3.6826
3.5844
3.5720
3.5590
3.5446
3.5341
3.5003
3.4924
3.4791
3.4654
3.4520
3.4389
3.4002
3.3863
3.3726
3.3590
3.3453
0.9867
2.0000
2.0605
0.9298
0.9564
1.9502
1.0166
0.9923
3.0566
0.9883
1.0252
1.0517
OH
OH
OH
OH
4.12
[rel]
[ppm]
Chemical Shift (ppm)

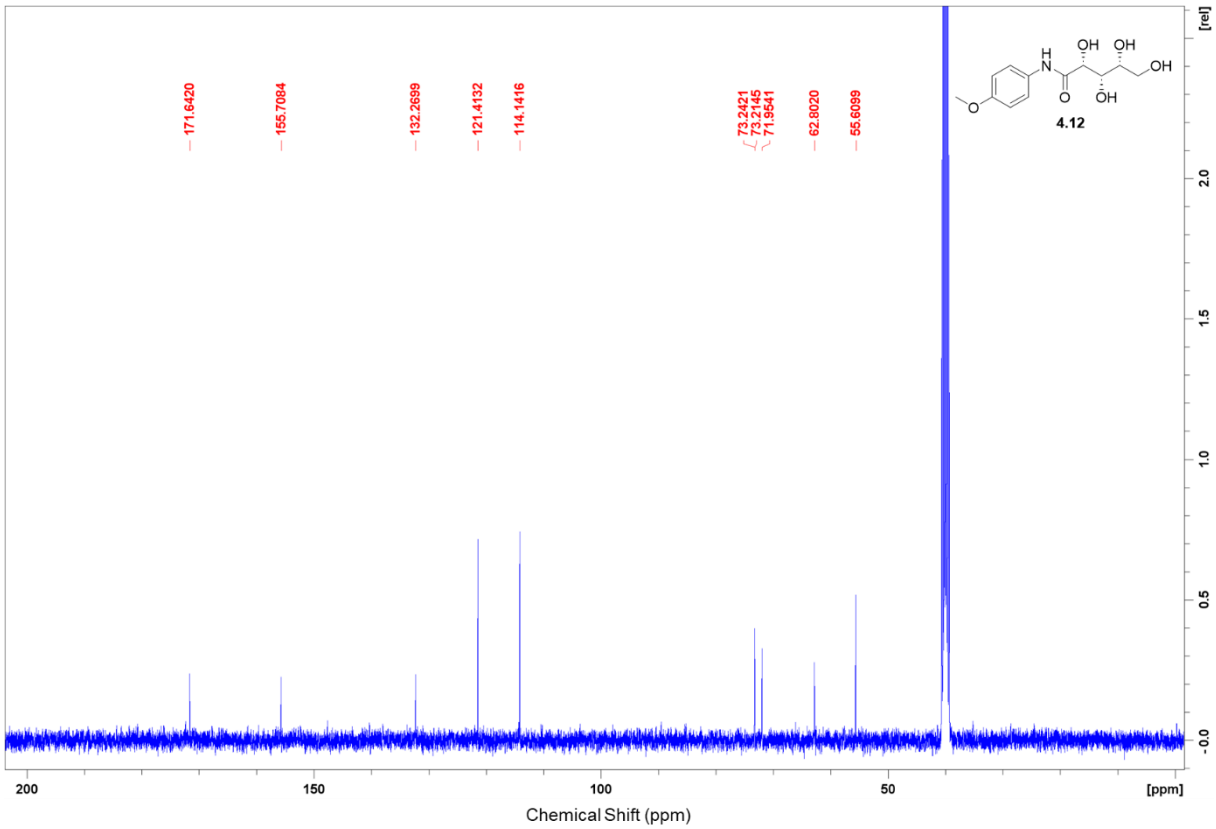
171.6420
155.7084
132.2699
121.4132
114.1416
73.2421
73.2145
71.9541
62.8020
55.6099
OH
OH
OH
OH
4.12
[rel]
[ppm]
Chemical Shift (ppm)

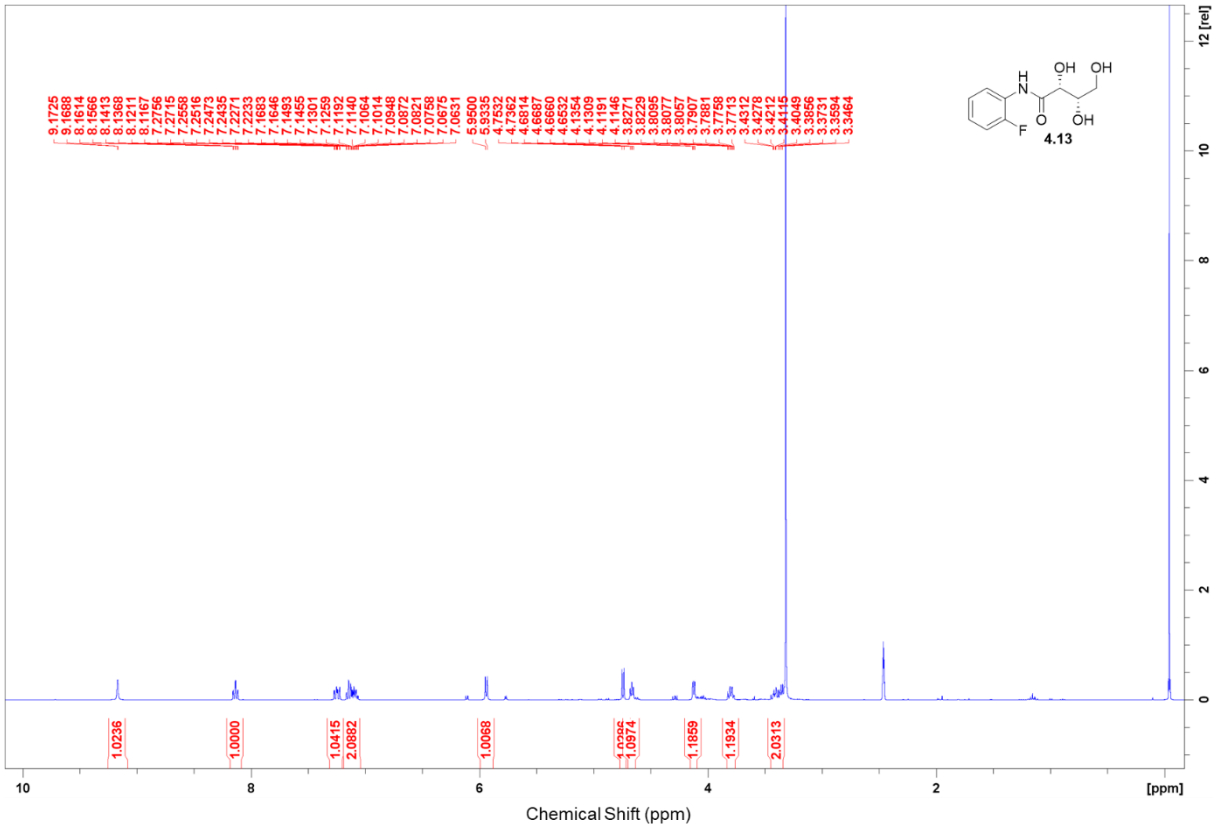
9.1725
9.1688
8.1614
8.1566
8.1413
8.1368
8.1211
8.1167
7.2756
7.2715
7.2658
7.2516
7.2473
7.2435
7.2271
7.2233
7.1683
7.1646
7.1493
7.1455
7.1301
7.1259
7.1192
7.1140
7.1064
7.1014
7.0948
7.0872
7.0821
7.0758
7.0675
7.0631
5.9500
5.9335
4.7632
4.7362
4.6814
4.6687
4.6680
4.6552
4.1354
4.1309
4.1191
4.1146
3.8271
3.8229
3.8095
3.8077
3.8057
3.7907
3.7881
3.7758
3.7713
3.4372
3.4278
3.4212
3.4115
3.4049
3.3856
3.3731
3.3594
3.3464
OH
OH
OH
N
H
O
F
4.13
1.0236
1.0000
1.0415
2.0882
1.0068
1.0392
1.0974
1.1859
1.1934
2.0313
12 [rel]
10
8
6
4
2
0
10
8
6
4
2
[ppm]
Chemical Shift (ppm)

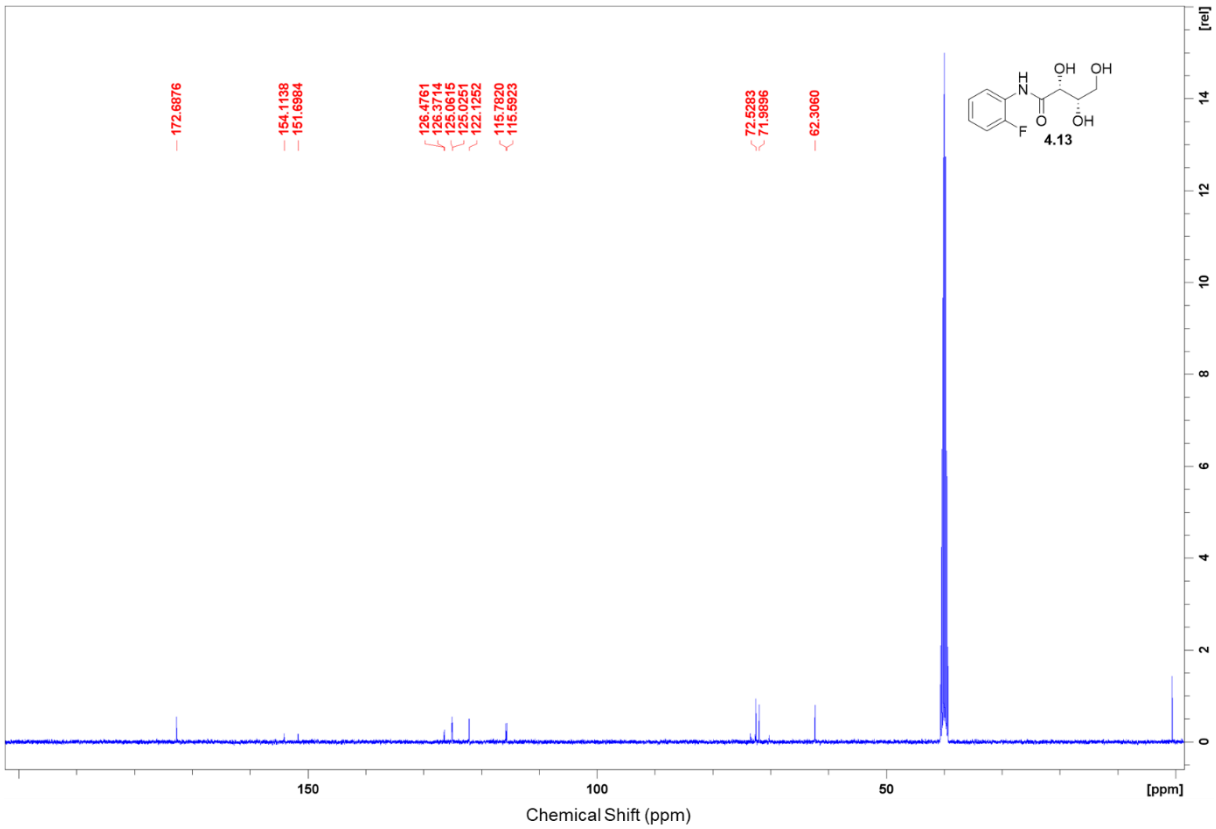
172.6876
154.1138
151.6984
126.4761
126.3714
125.0615
125.0251
122.1252
115.7820
115.5923
72.5283
71.9896
62.3060
OH
OH
OH
N
H
O
F
4.13
[rel]
14
12
10
8
6
4
2
0
150
100
50
[ppm]
Chemical Shift (ppm)

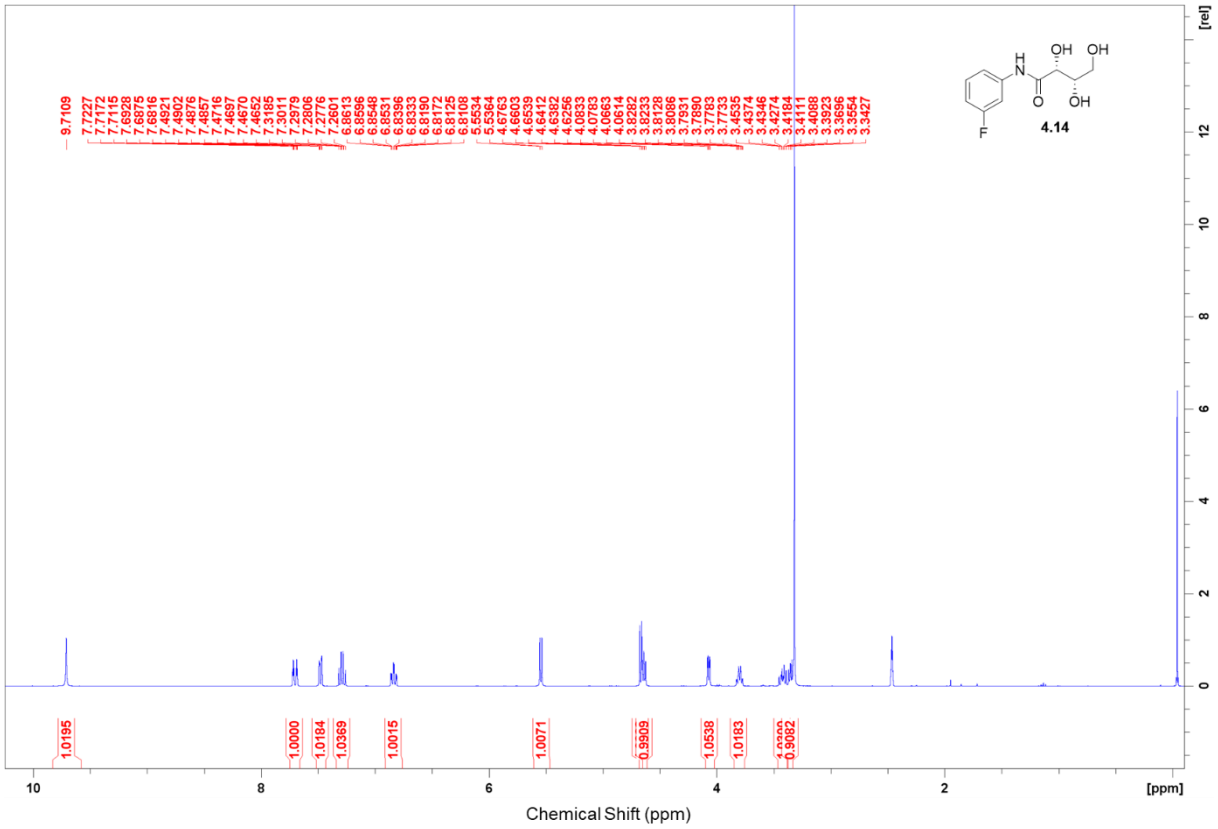
9.7109
7.7227
7.7172
7.7115
7.6928
7.6875
7.6816
7.4921
7.4902
7.4876
7.4857
7.4716
7.4697
7.4670
7.4652
7.3165
7.3011
7.2979
7.2806
7.2776
7.2601
6.8613
6.8596
6.8548
6.8531
6.8396
6.8333
6.8190
6.8172
6.8125
6.8109
5.5534
5.5384
4.6763
4.6603
4.6539
4.6412
4.6382
4.6256
4.0833
4.0783
4.0663
4.0614
3.9232
3.9233
3.8128
3.8086
3.7931
3.7890
3.7783
3.7733
3.4535
3.4374
3.4346
3.4274
3.4184
3.4141
3.4098
3.3923
3.3696
3.3554
3.3427
1.0195
1.0000
1.0184
1.0369
1.0015
1.0071
0.9905
1.0538
1.0183
0.9082
OH
OH
OH
N
H
O
F
4.14
10
8
6
4
2
[ppm]
[rel]
Chemical Shift (ppm)

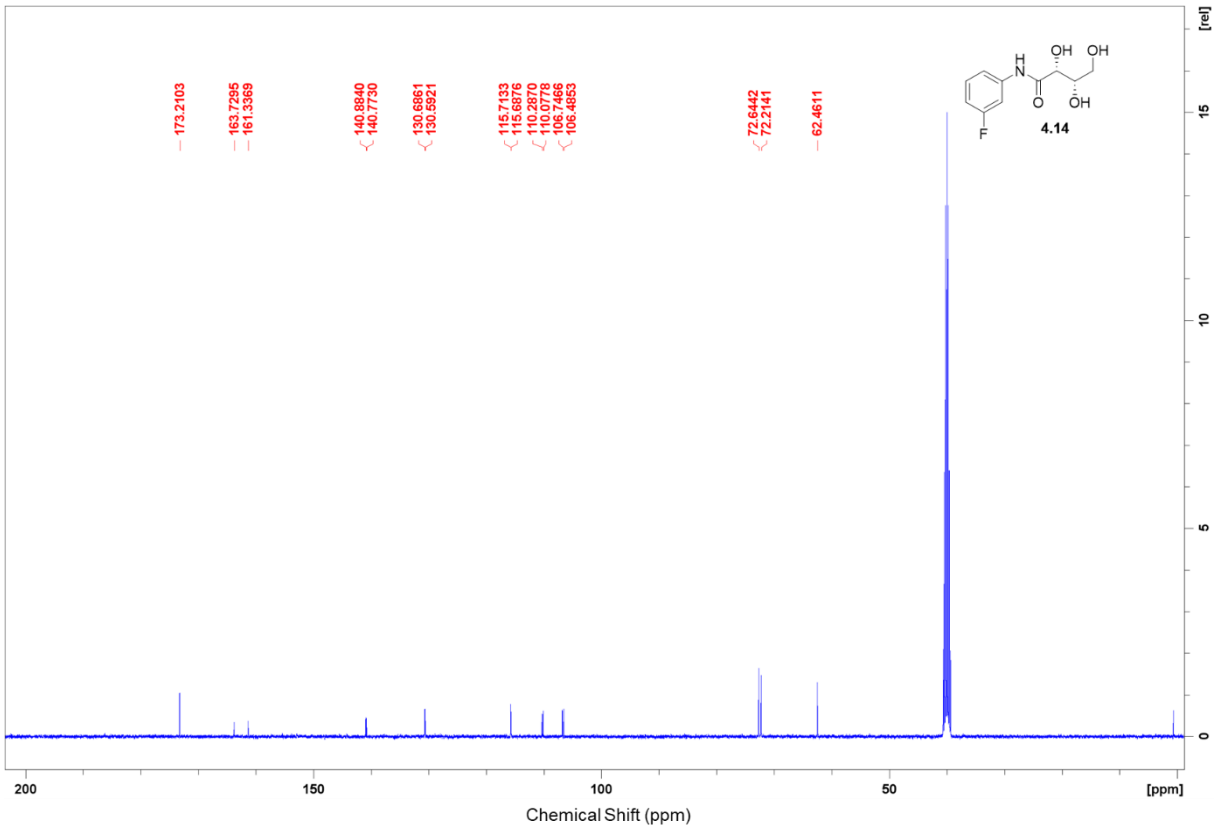
173.2103
163.7295
161.3369
140.8840
140.7730
130.6861
130.5921
115.7133
115.6876
110.2870
110.0778
106.7466
106.4853
72.6442
72.2141
62.4611
OH
OH
OH
N
H
O
F
4.14
200
150
100
50
[ppm]
[rel]
Chemical Shift (ppm)

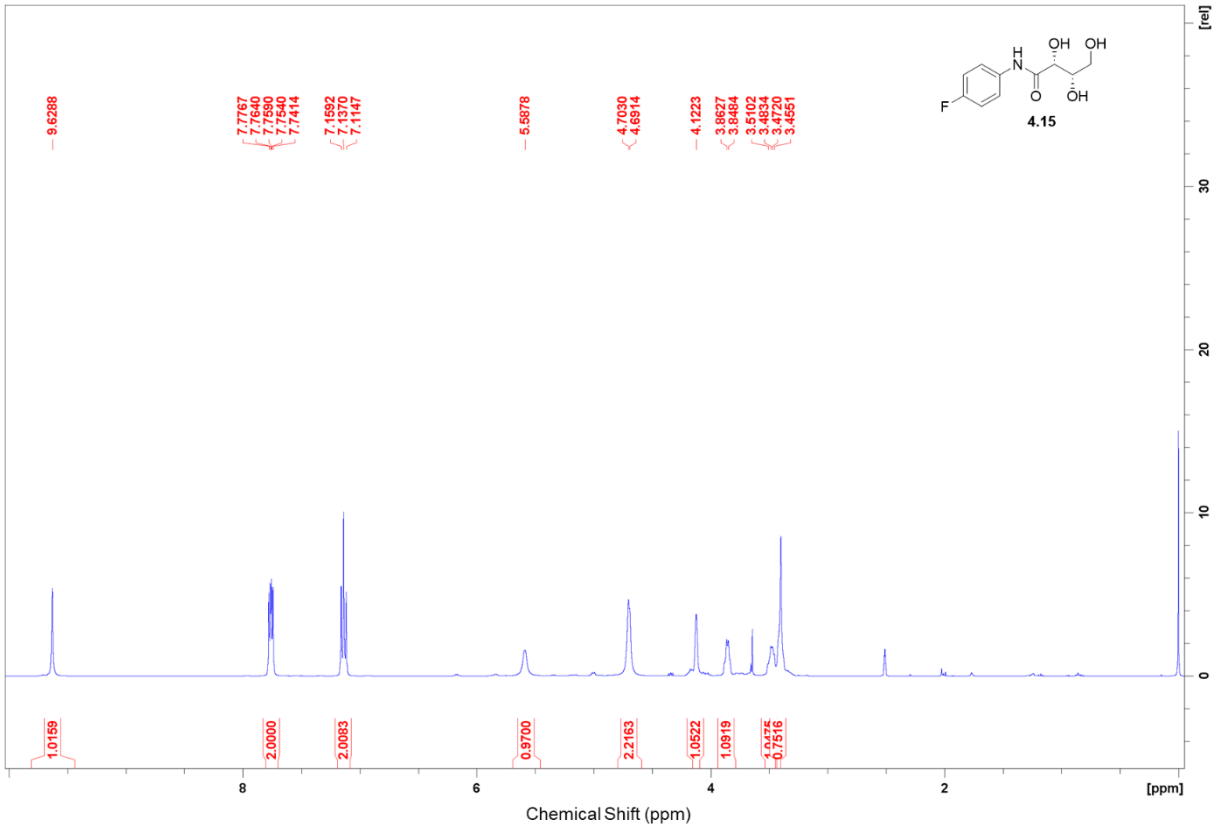
9.6288
7.7767
7.7640
7.7590
7.7540
7.7414
7.1592
7.1370
7.1147
5.5878
4.7030
4.6914
4.1223
3.8627
3.8484
3.5102
3.4834
3.4720
3.4551
1.0159
2.0000
2.0083
0.9700
2.2163
1.0522
1.0919
0.7516
4.15
[rel]
[ppm]
Chemical Shift (ppm)

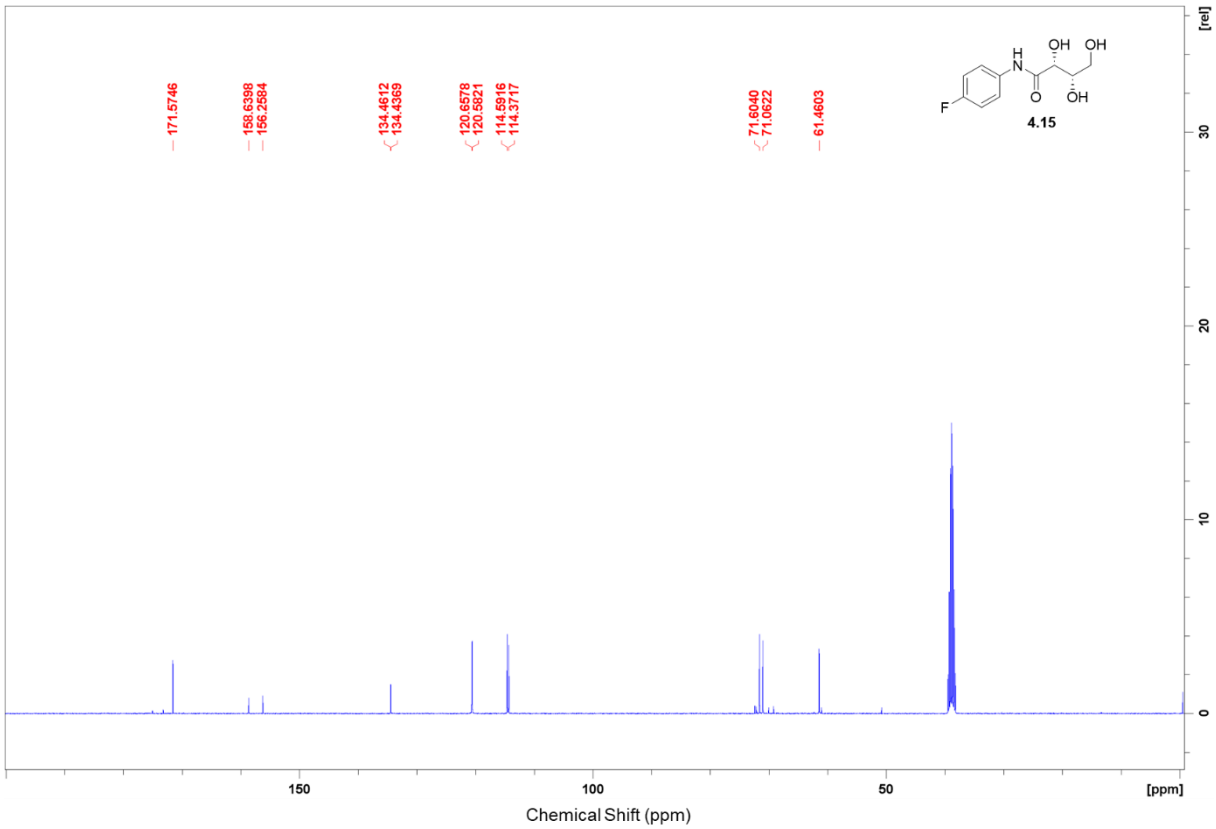
171.5746
158.6398
156.2584
134.4612
134.4369
120.6578
120.5821
114.5916
114.3717
71.6040
71.0622
61.4603
4.15
[rel]
[ppm]
Chemical Shift (ppm)

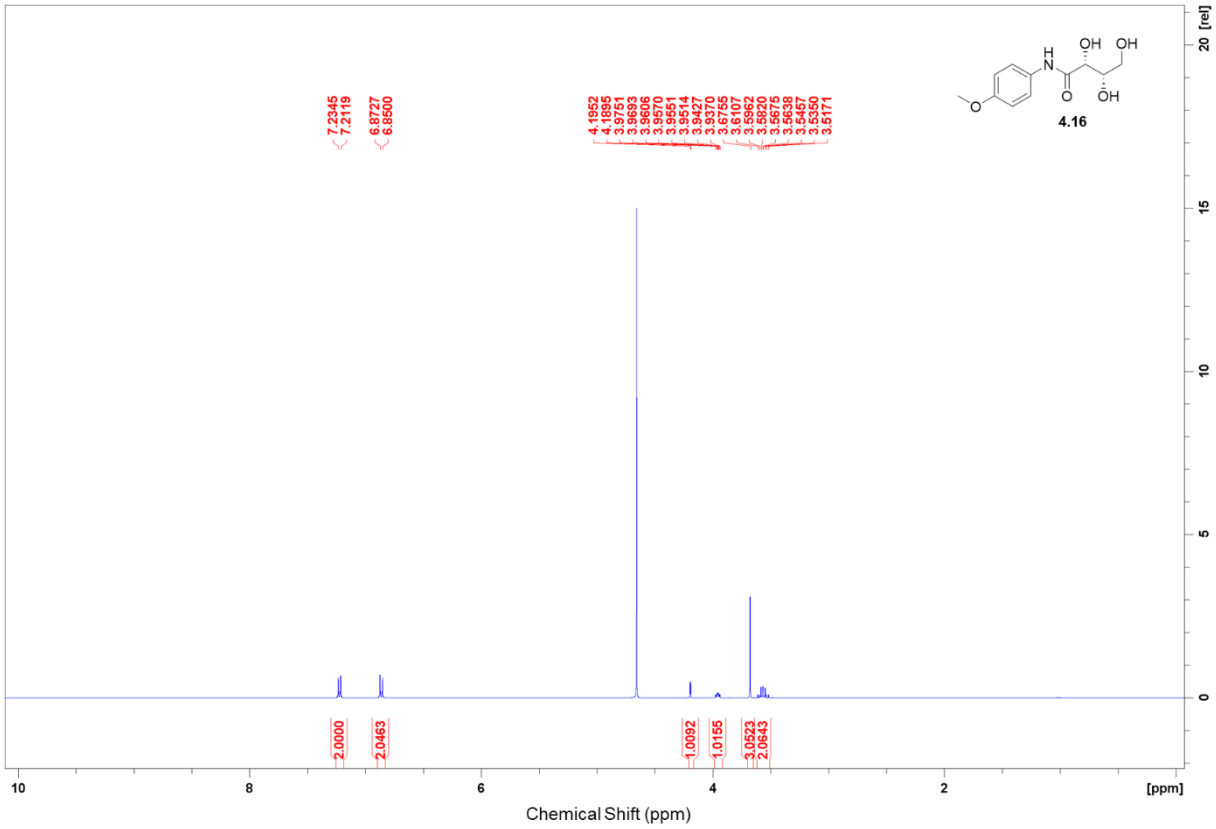
7.2345
7.2119
6.8727
6.8500
4.1952
4.1895
3.9751
3.9693
3.9626
3.9570
3.9551
3.9514
3.9427
3.9370
3.6755
3.6107
3.5962
3.5820
3.5675
3.5638
3.5457
3.5350
3.5171
2.0000
2.0463
1.0092
1.0155
3.0523
2.0643
OH
OH
OH
N
H
O
O
4.16
10
8
6
4
2
[ppm]
Chemical Shift (ppm)
20
15
10
5
0
[rel]

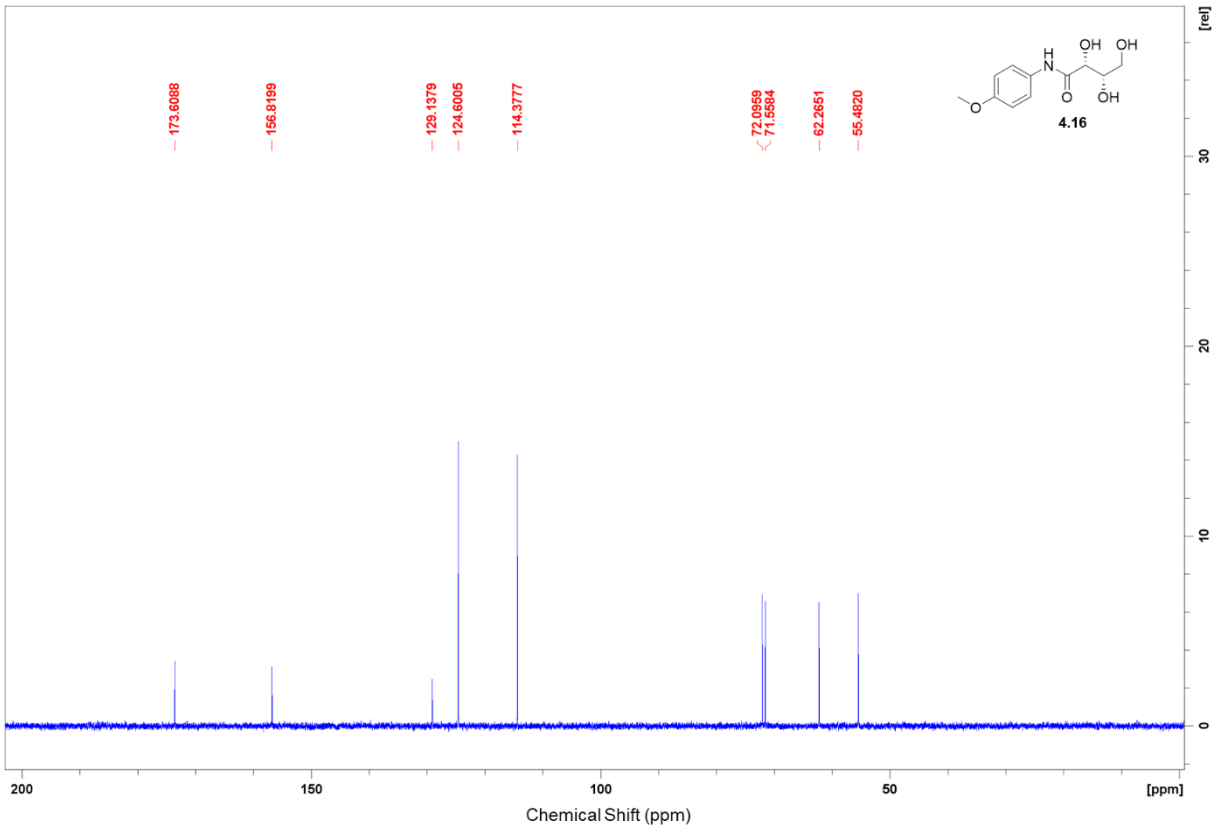
173.6088
156.8199
129.1379
124.6005
114.3777
72.0959
71.5584
62.2651
55.4820
OH
OH
OH
N
H
O
O
4.16
200
150
100
50
[ppm]
Chemical Shift (ppm)
30
20
10
0
[rel]

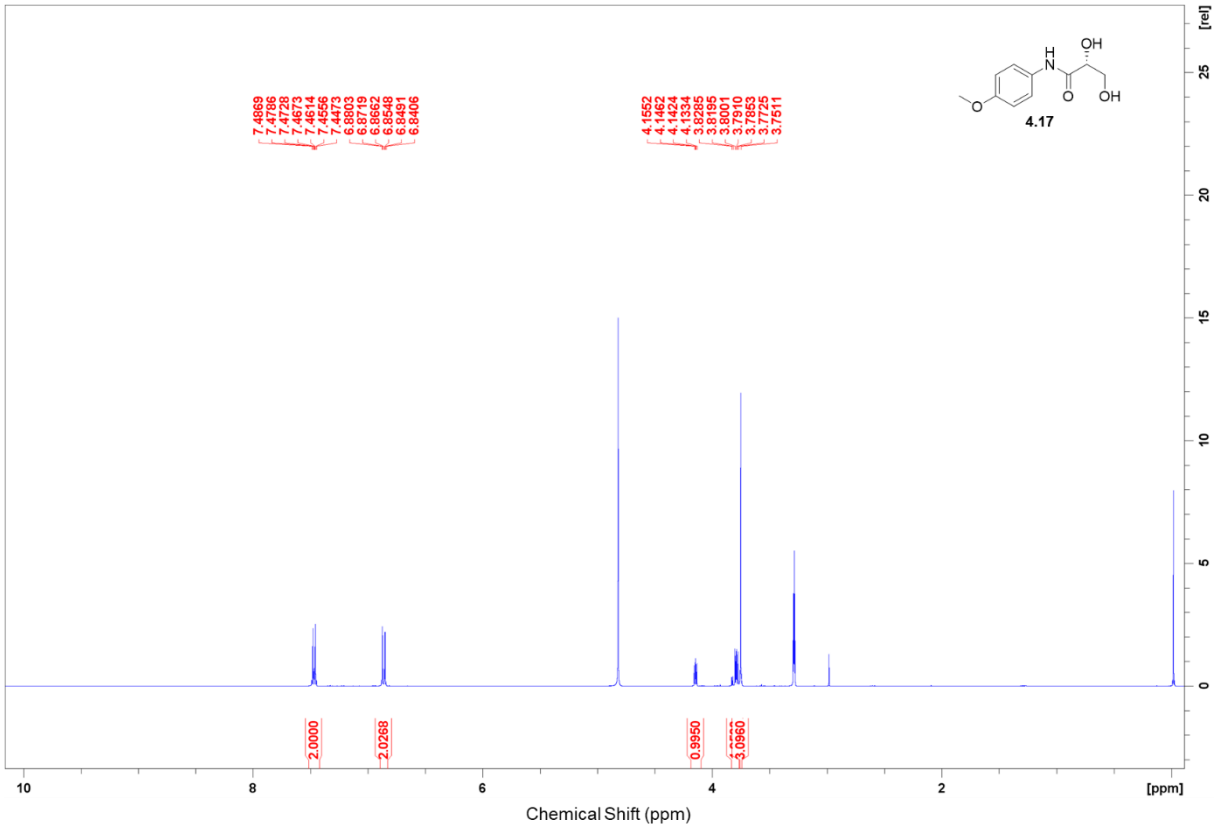
7.4869
7.4786
7.4728
7.4673
7.4614
7.4556
7.4473
6.8803
6.8719
6.8662
6.8548
6.8491
6.8406
4.1552
4.1492
4.1434
4.1334
3.8285
3.8195
3.8001
3.7910
3.7853
3.7725
3.7511
2.0000
2.0268
0.9950
3.0960
4.17
[rel]
[ppm]
Chemical Shift (ppm)

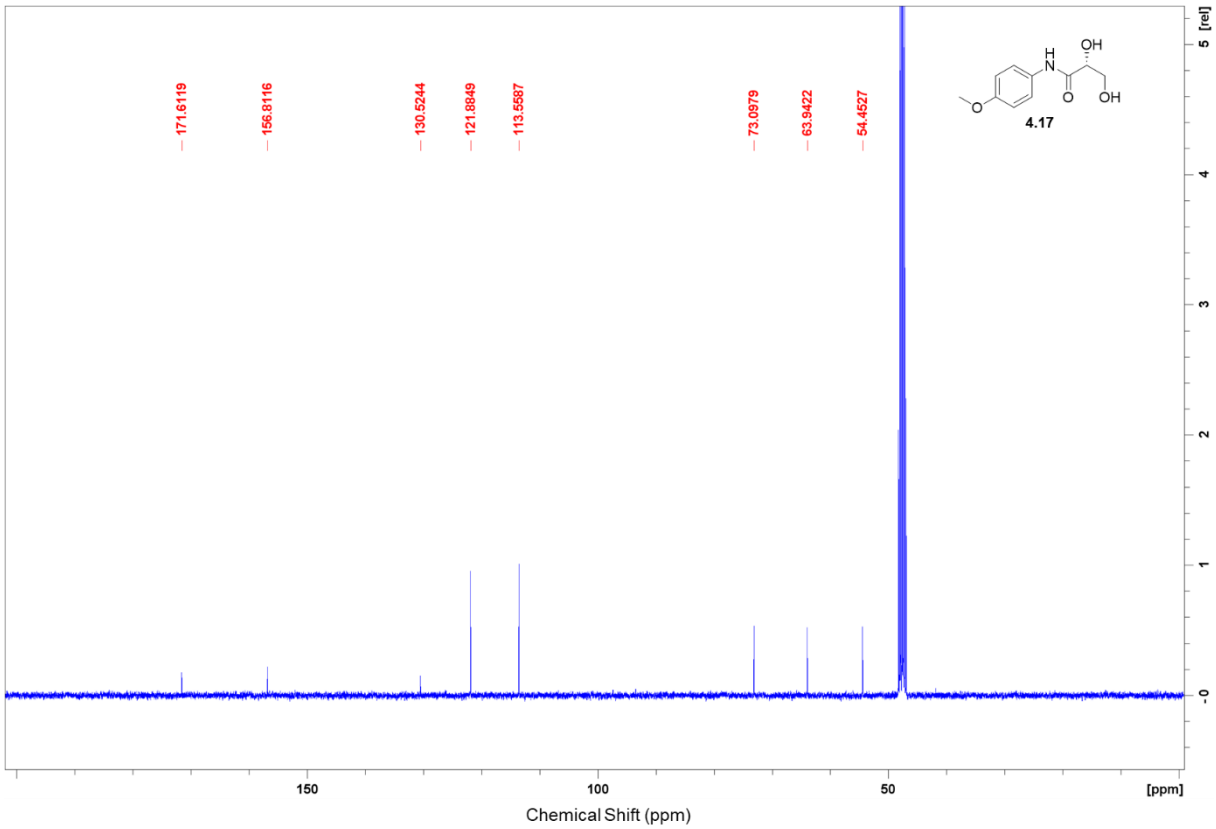
171.6119
156.8116
130.5244
121.8849
113.5587
73.0979
63.9422
54.4527
4.17
[rel]
[ppm]
Chemical Shift (ppm)

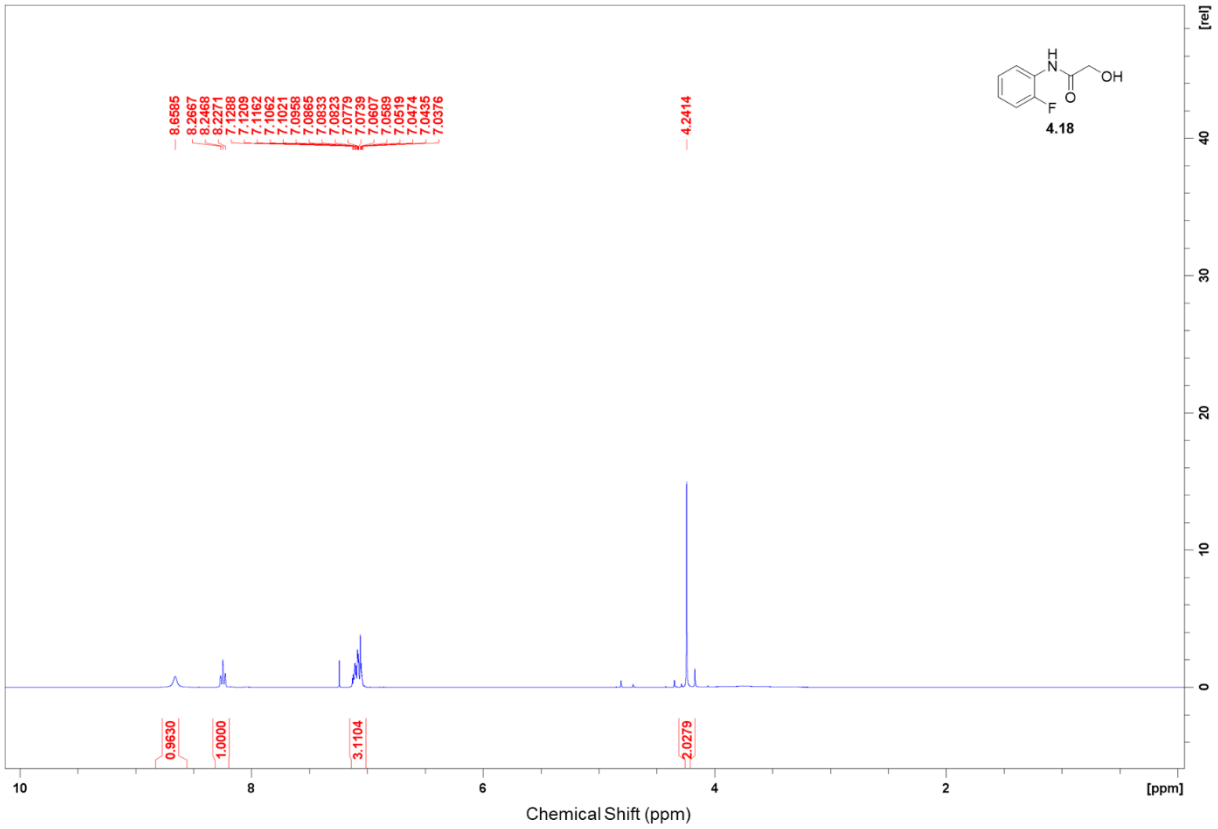
8.6585
8.2667
8.2468
8.2271
7.1288
7.1209
7.1162
7.1062
7.1021
7.0968
7.0865
7.0833
7.0823
7.0779
7.0739
7.0607
7.0589
7.0519
7.0474
7.0435
7.0376
4.2414
0.9630
1.0000
3.1104
2.0279
10
8
6
4
2
[ppm]
Chemical Shift (ppm)
[rel]
0
10
20
30
40
OH
F
4.18

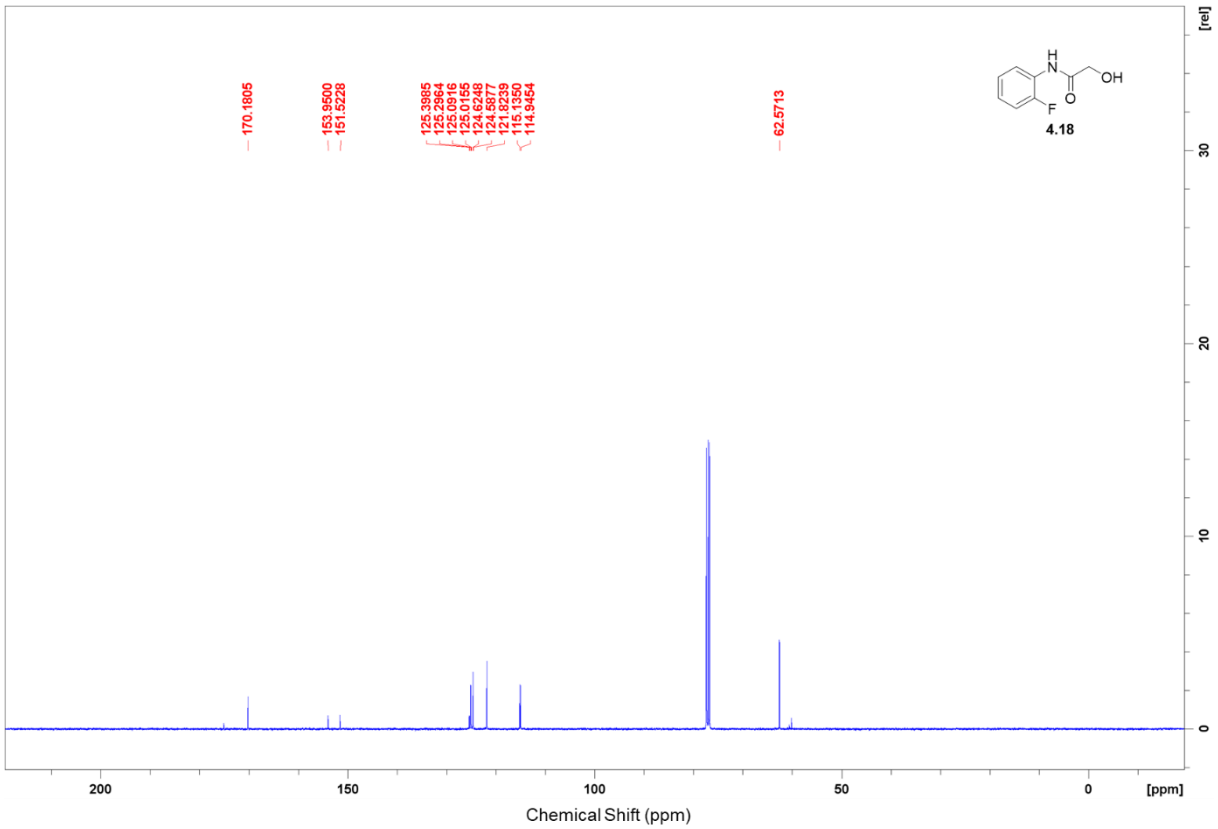
170.1805
153.9500
151.5228
125.3985
125.2964
125.0916
125.0155
124.6977
124.6046
121.8239
115.1350
114.9454
62.5713
200
150
100
50
0
[ppm]
Chemical Shift (ppm)
[rel]
0
10
20
30
OH
F
4.18

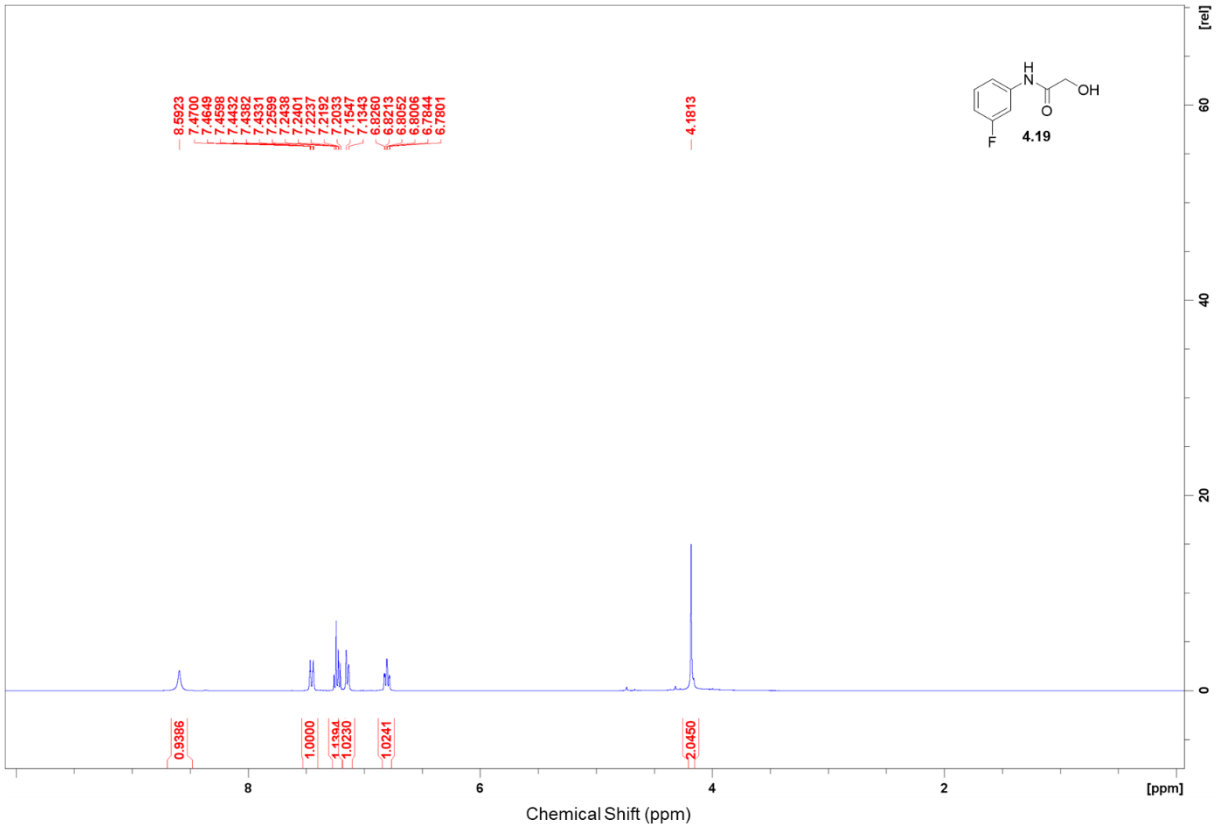
8.5923
7.4700
7.4649
7.4598
7.4432
7.4382
7.4331
7.2599
7.2438
7.2401
7.2237
7.2192
7.2033
7.1547
7.1343
6.8260
6.8213
6.8052
6.8006
6.7844
6.7801
4.1813
0.9386
1.0000
1.1394
1.0230
1.0241
2.0450
4.19
[rel]
[ppm]
Chemical Shift (ppm)

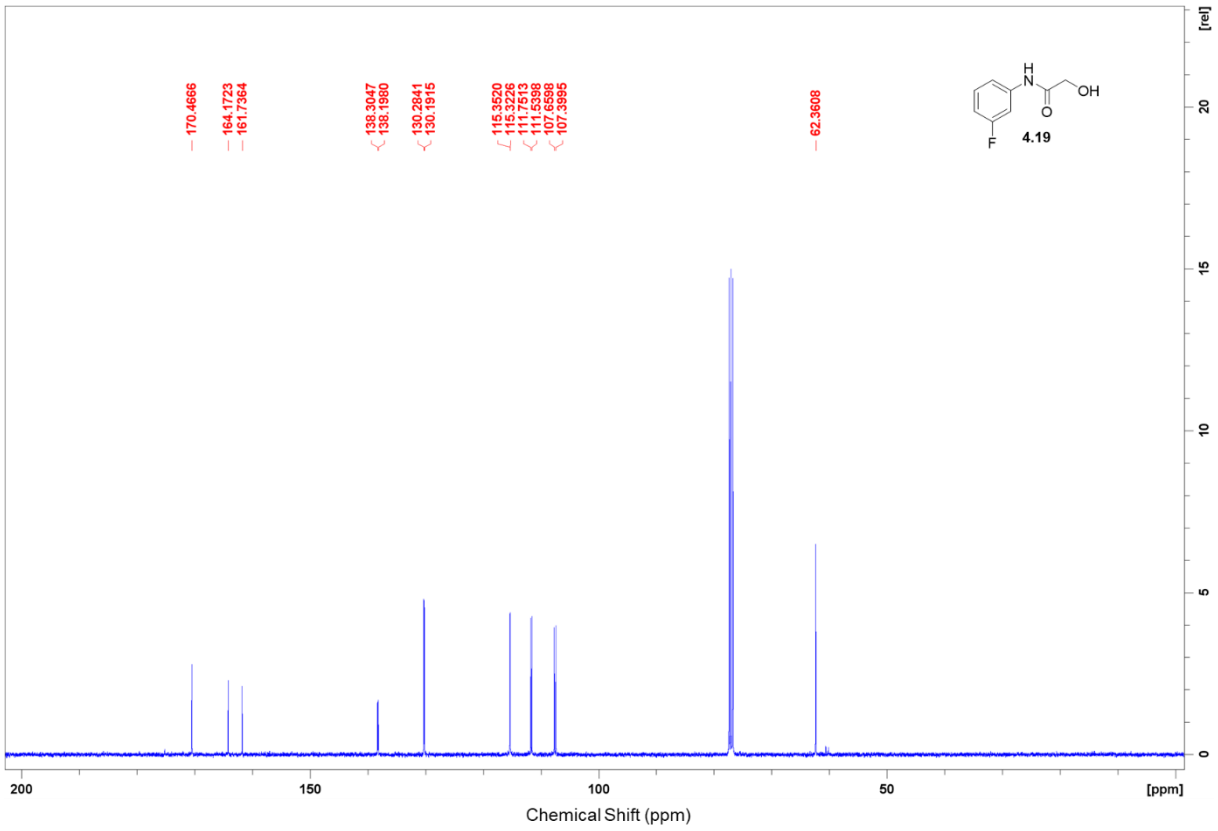
170.4666
164.1723
161.7364
138.3047
138.1980
130.2841
130.1915
115.3520
115.3226
111.7513
111.5398
107.6586
107.3995
62.3608
4.19
[rel]
[ppm]
Chemical Shift (ppm)

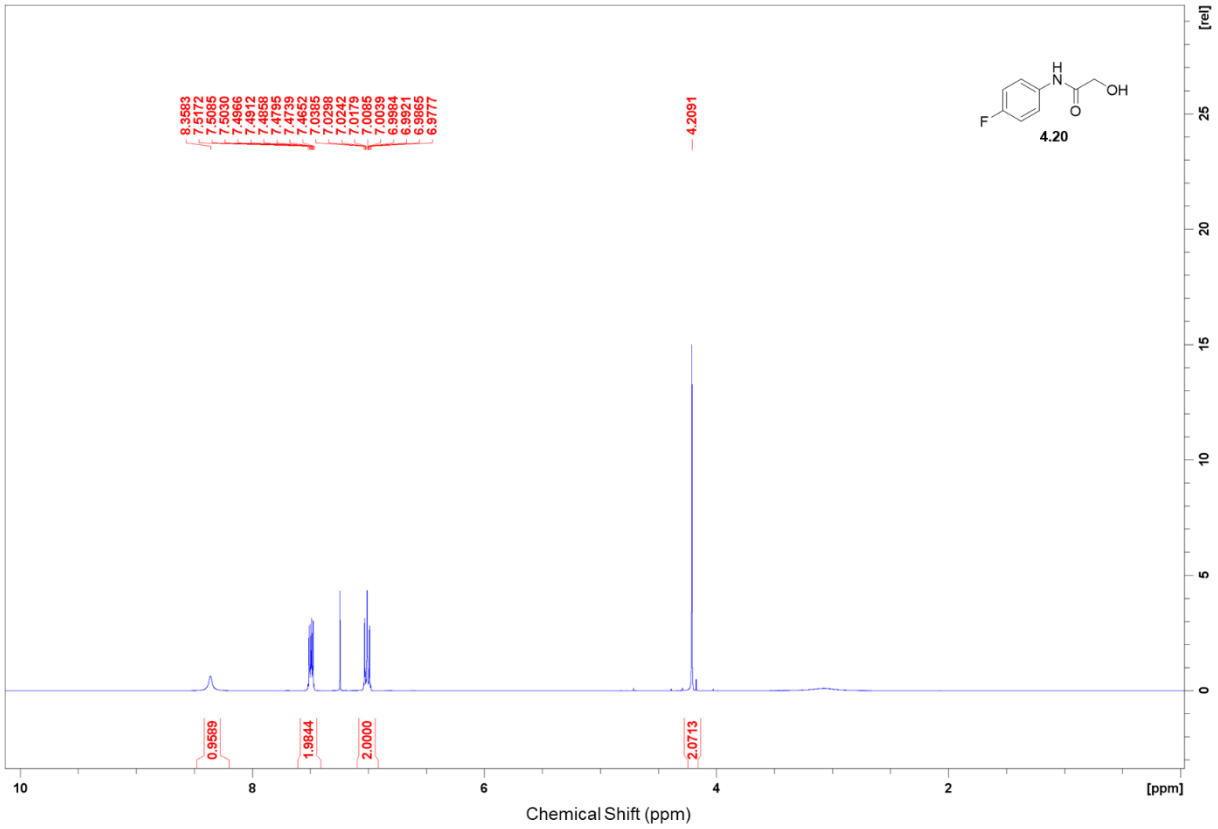
8.3593
7.5172
7.5085
7.5030
7.4966
7.4912
7.4858
7.4795
7.4739
7.4652
7.0385
7.0298
7.0242
7.0179
7.0085
7.0039
6.9994
6.9921
6.9865
6.9777
4.2091
0.9589
1.9844
2.0000
2.0713
10
8
6
4
2
[ppm]
[rel]
Chemical Shift (ppm)
4.20

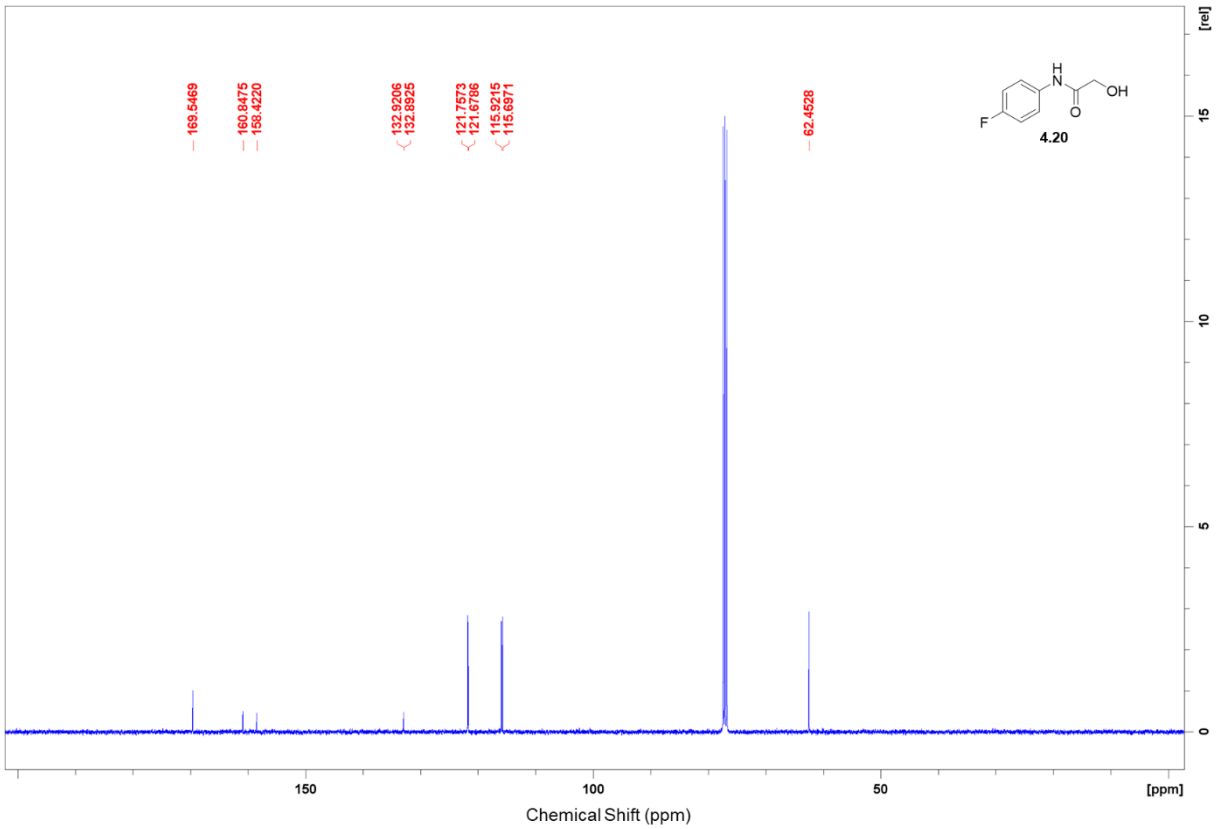
169.5469
160.8475
158.4220
132.9206
132.8925
121.7573
121.6786
115.9215
115.6971
62.4528
150
100
50
[ppm]
[rel]
Chemical Shift (ppm)
4.20

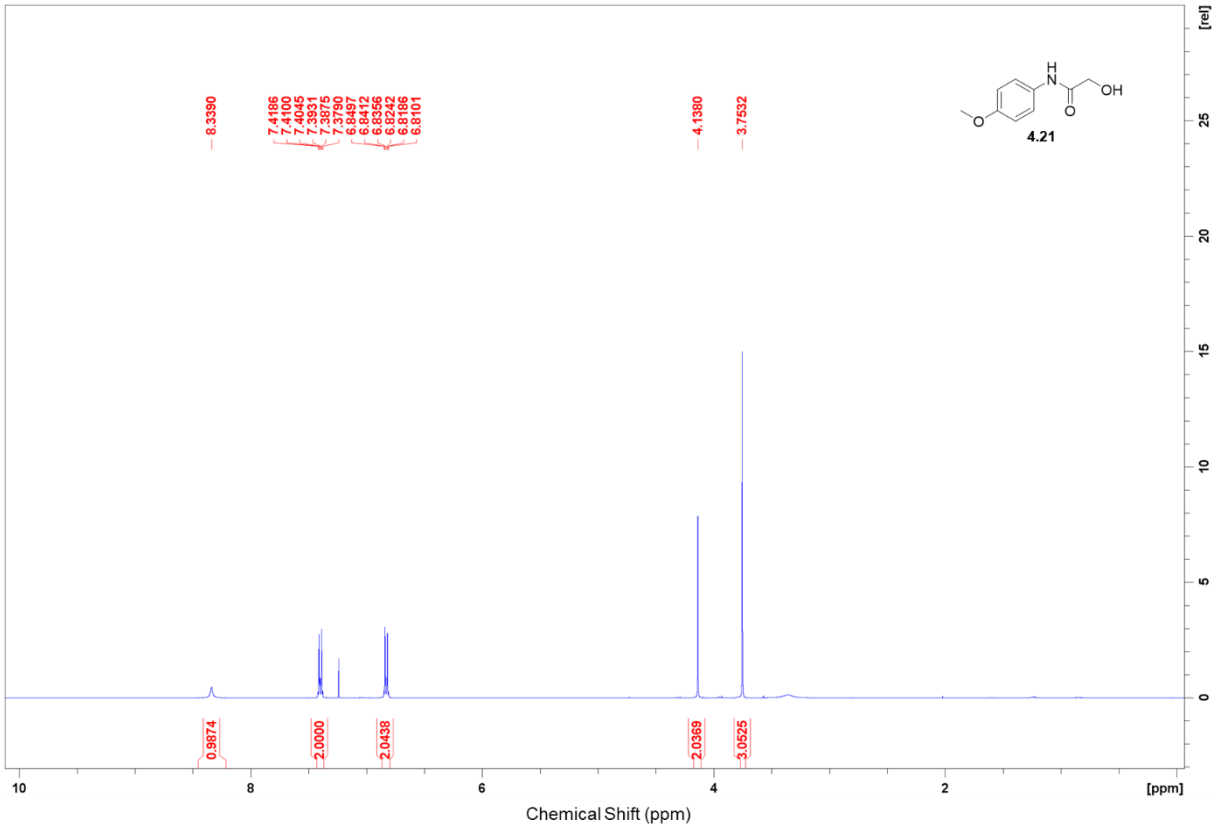
8.3390
7.4186
7.4100
7.4045
7.3931
7.3875
7.3790
7.3497
6.8412
6.8356
6.8242
6.8186
6.8101
4.1380
3.7532
0.9874
2.0000
2.0438
2.0369
3.0525
4.21
OH
[rel]
[ppm]
Chemical Shift (ppm)

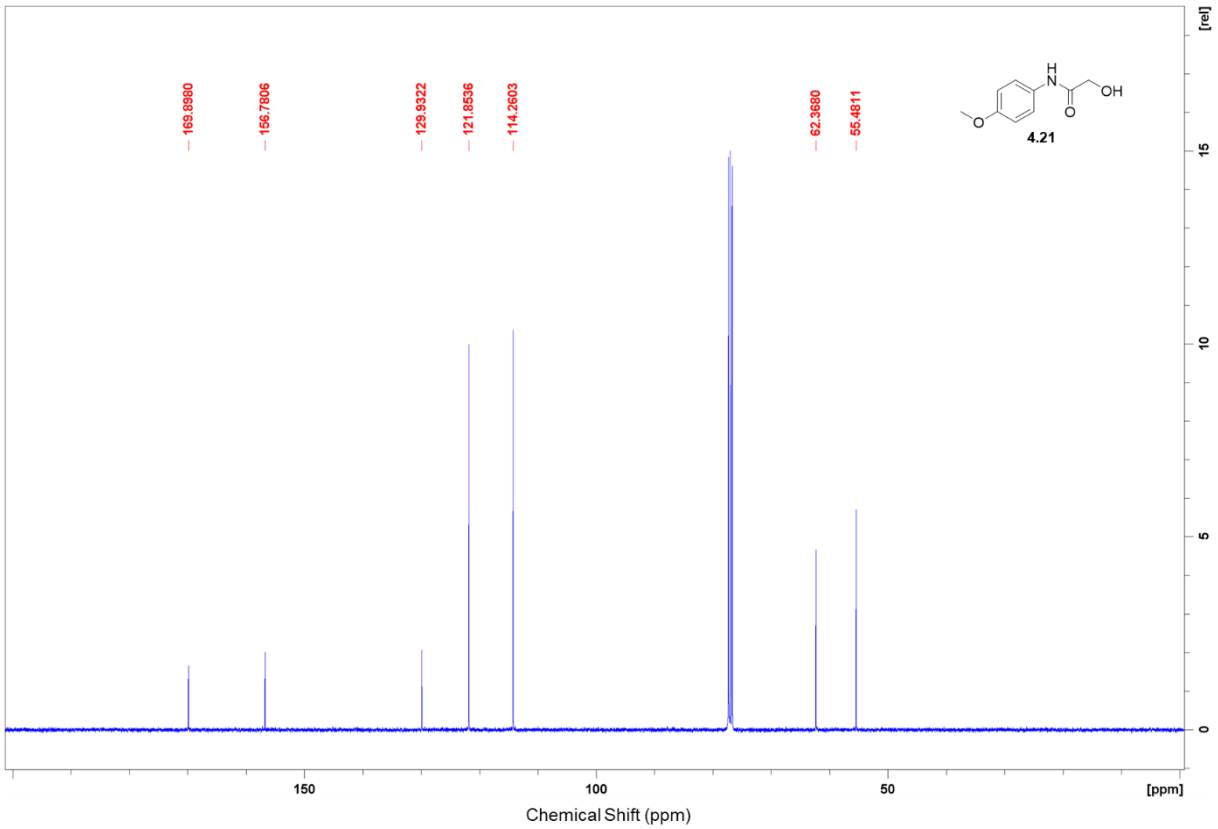
169.8980
156.7806
129.9322
121.8536
114.2603
62.3680
55.4811
4.21
OH
[rel]
[ppm]
Chemical Shift (ppm)

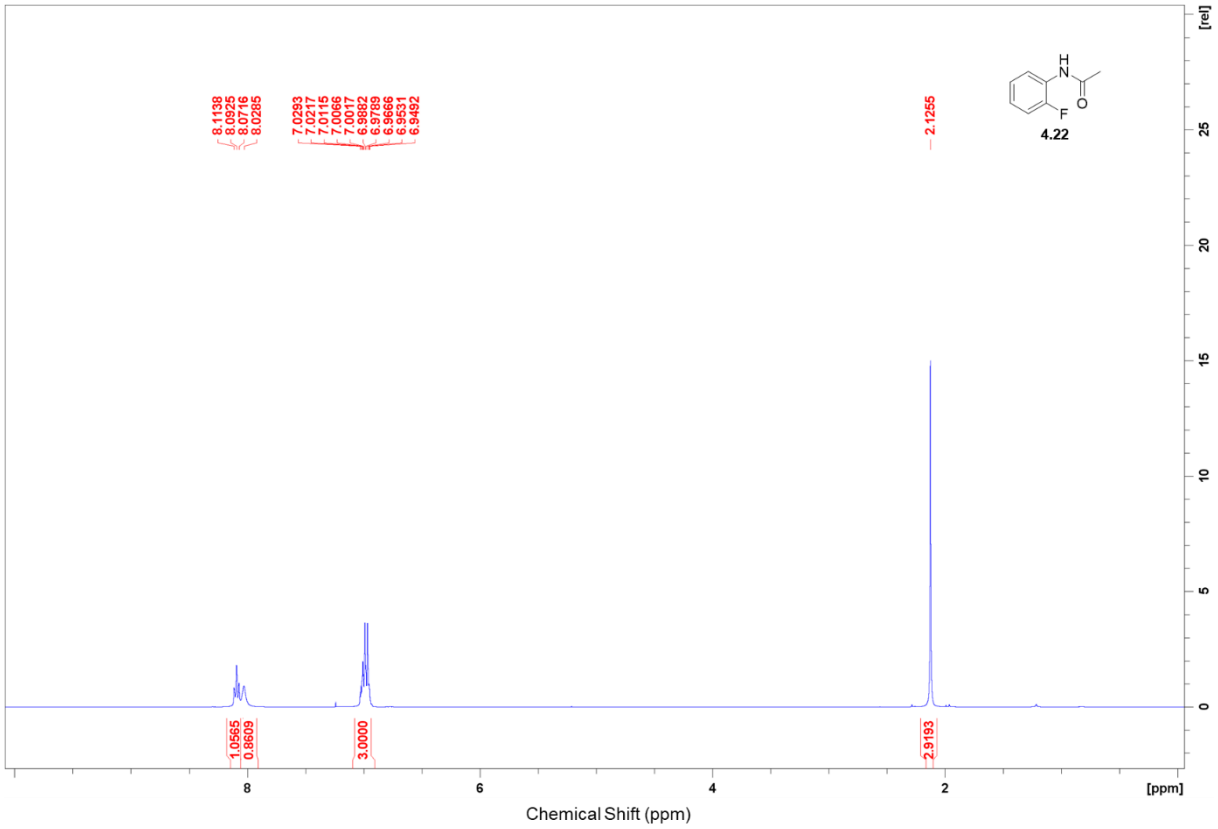
8.1138
8.0925
8.0716
8.0285
7.0293
7.0217
7.0115
7.0066
7.0017
6.9882
6.9789
6.9666
6.9531
6.9492
2.1255
4.22
1.0565
0.8609
3.0000
2.9193
[rel]
[ppm]
Chemical Shift (ppm)

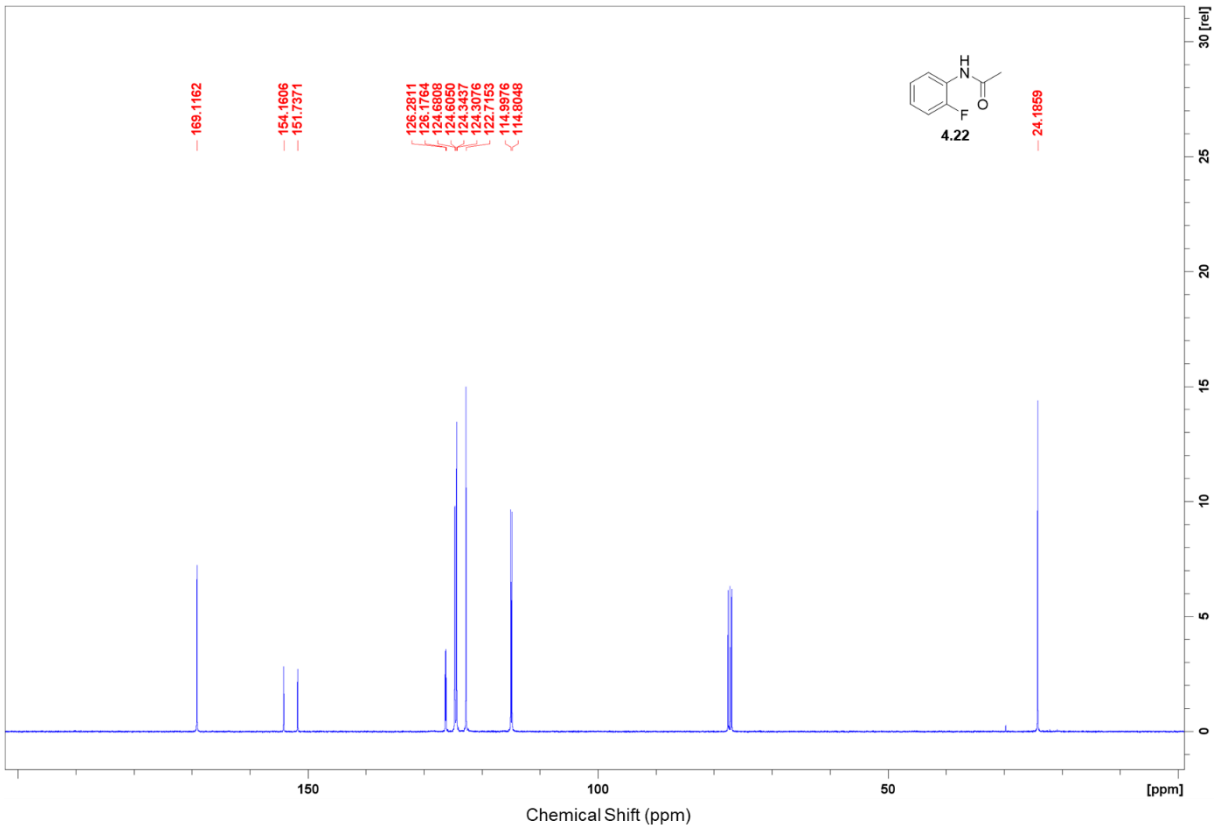
169.1162
154.1606
151.7371
126.2811
126.1764
124.6806
124.5450
124.4497
124.3076
122.7153
114.9976
114.8048
24.1659
4.22
[rel]
[ppm]
Chemical Shift (ppm)

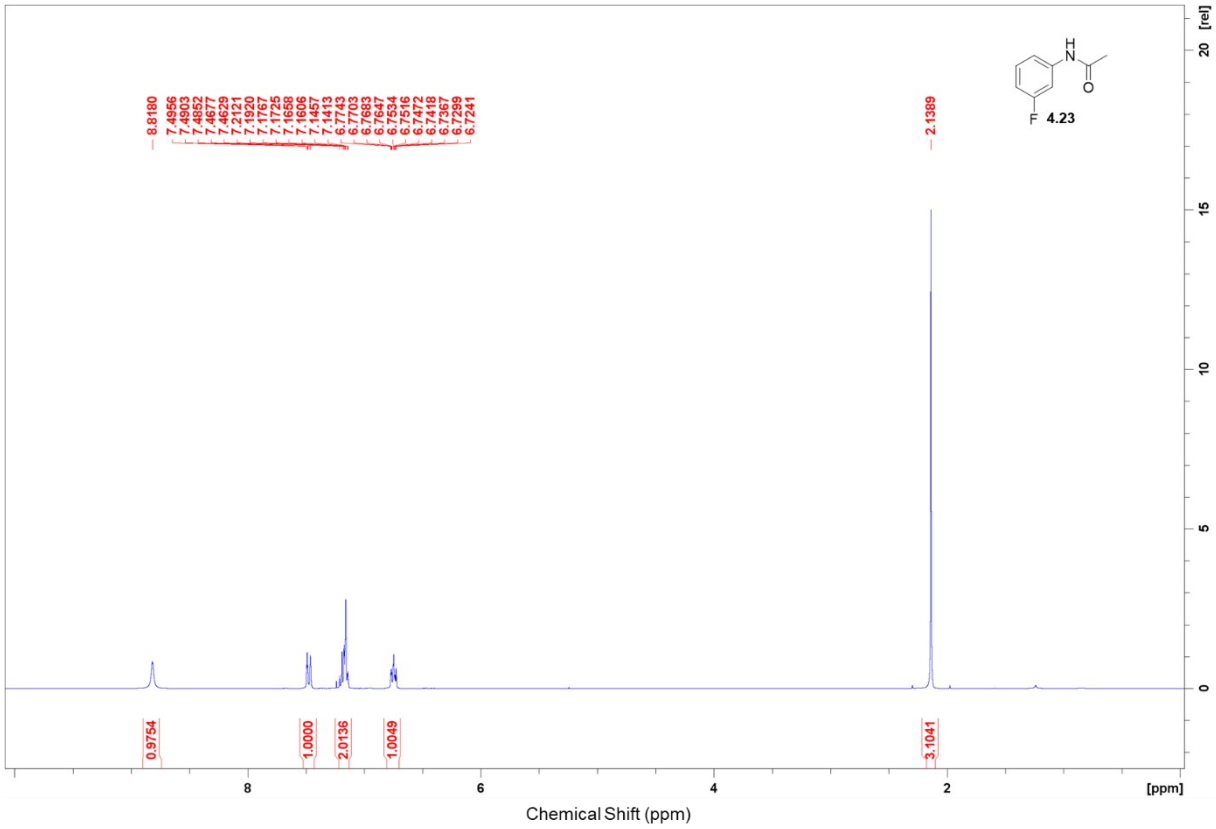
8.8180
7.4956
7.4863
7.4672
7.4677
7.4629
7.2121
7.1920
7.1767
7.1725
7.1658
7.1606
7.1457
7.1413
6.7743
6.7703
6.7663
6.7637
6.7534
6.7516
6.7472
6.7418
6.7367
6.7299
6.7241
2.1389
F 4.23
0.9754
1.0000
2.0136
1.0049
3.1041
[rel]
[ppm]
Chemical Shift (ppm)

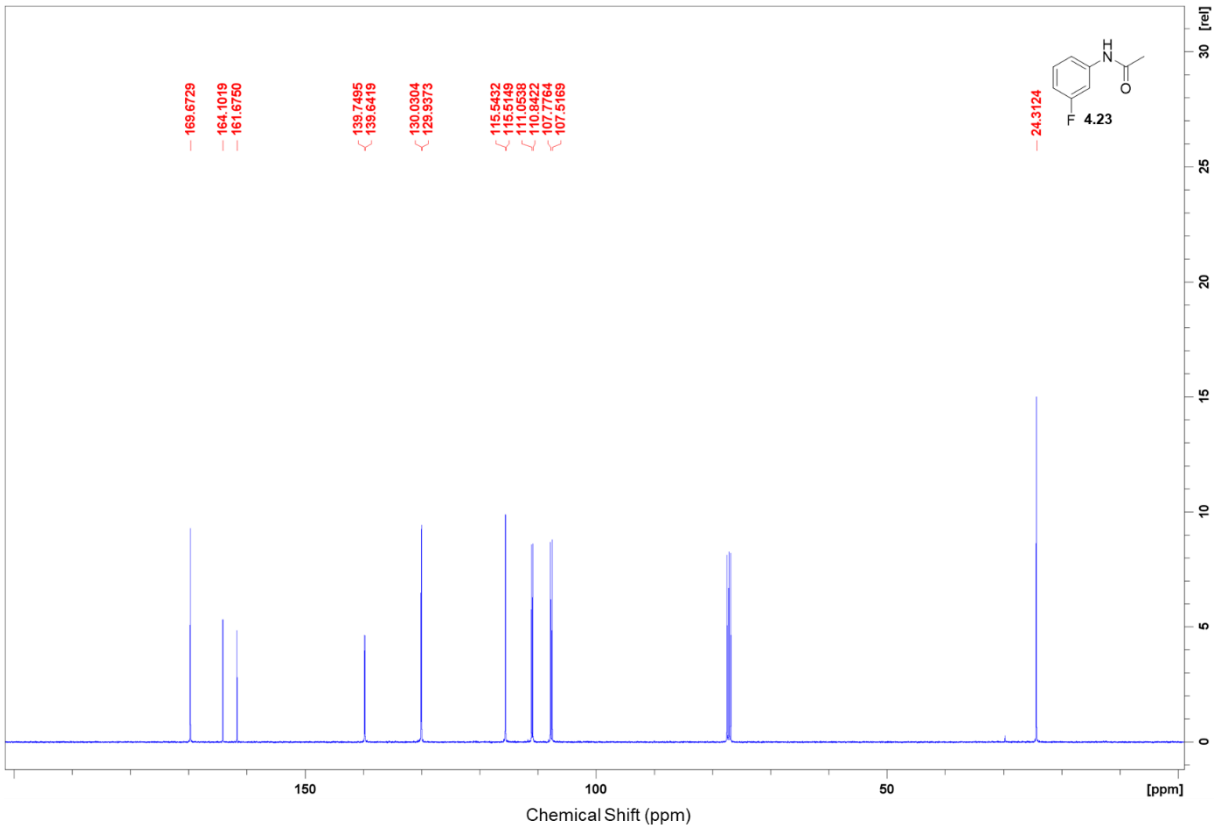
169.6729
164.1019
161.6750
139.7495
139.6419
130.0304
129.9373
115.5432
115.5149
111.0538
110.8422
107.7764
107.5189
24.3124
F 4.23
[rel]
[ppm]
Chemical Shift (ppm)

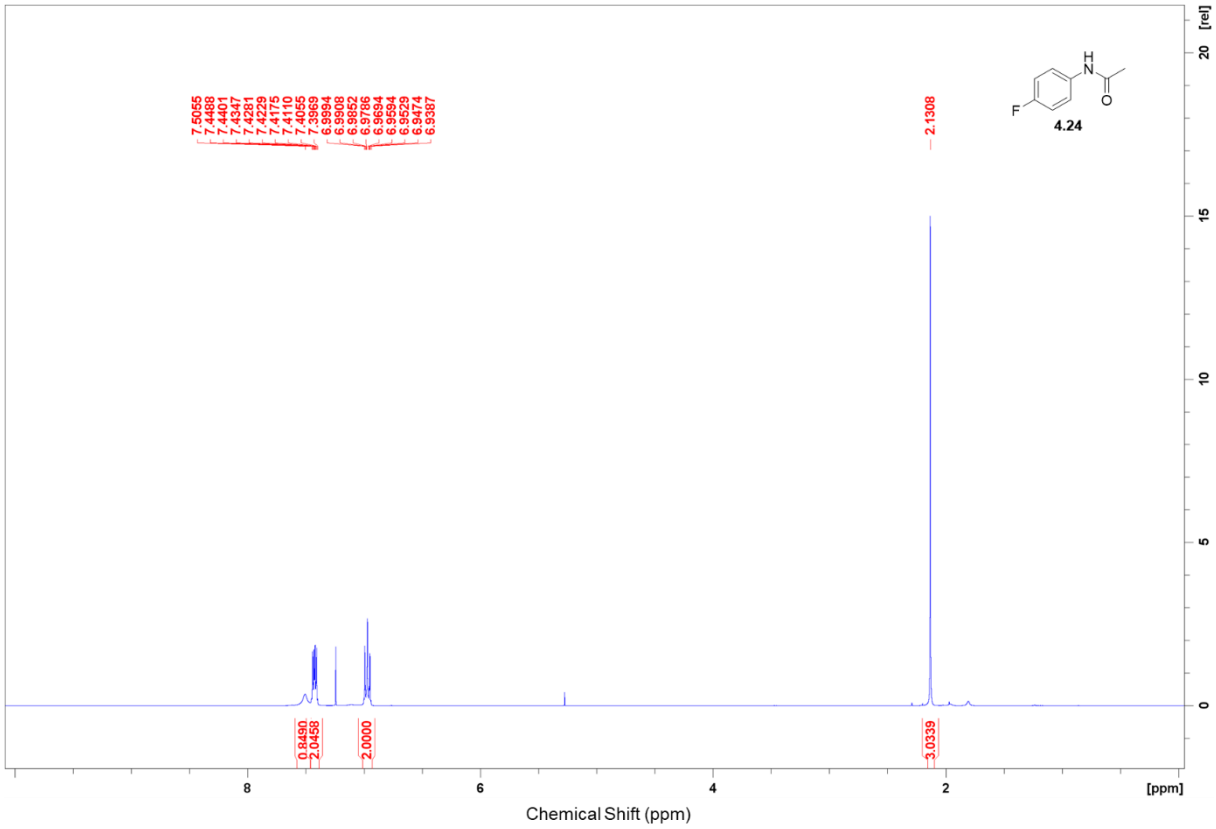
7.5055
7.4488
7.4401
7.4347
7.4281
7.4229
7.4175
7.4110
7.4055
7.3969
6.8994
6.8908
6.8852
6.8795
6.8694
6.8584
6.8529
6.8474
6.8387
2.1308
0.8490
2.0458
2.0000
3.0339
4.24
[rel]
[ppm]
Chemical Shift (ppm)

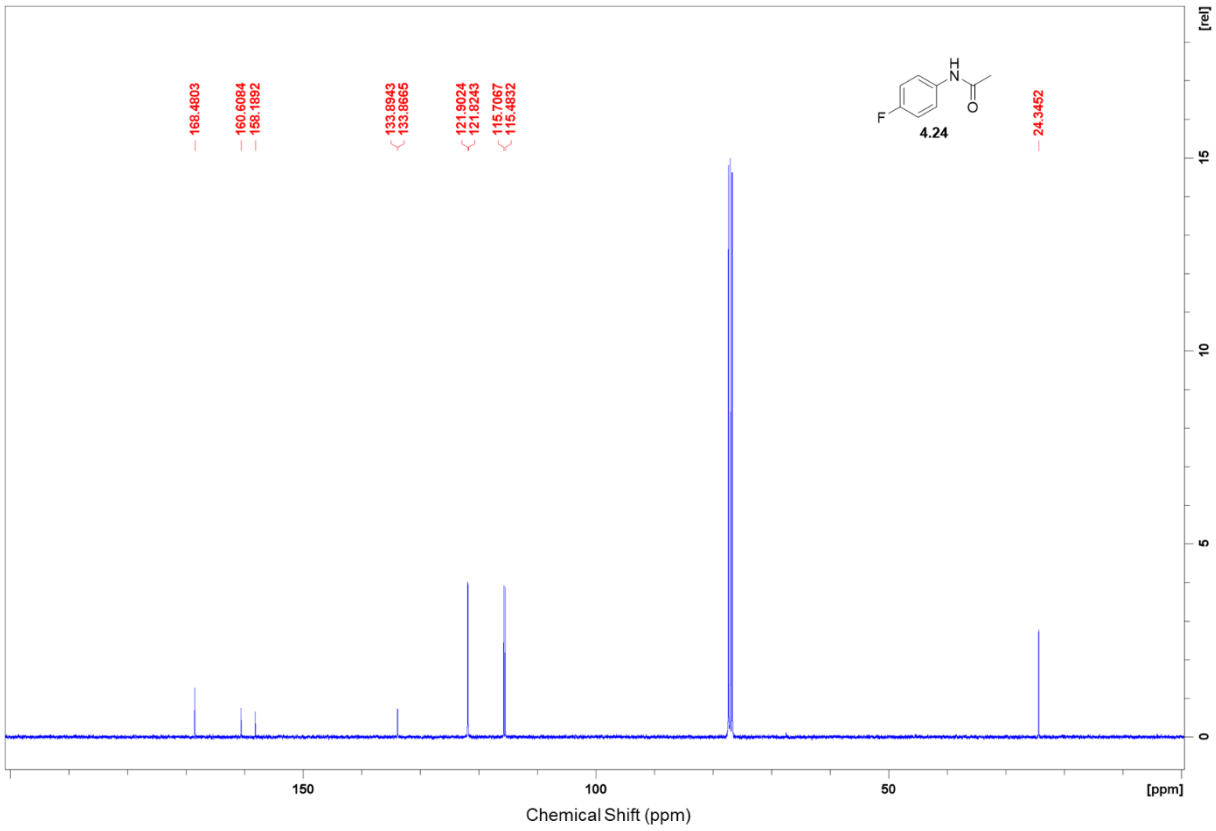
168.4803
160.6084
158.1692
133.8943
133.8665
121.9024
121.8243
115.7067
115.4832
24.3452
4.24
[rel]
[ppm]
Chemical Shift (ppm)

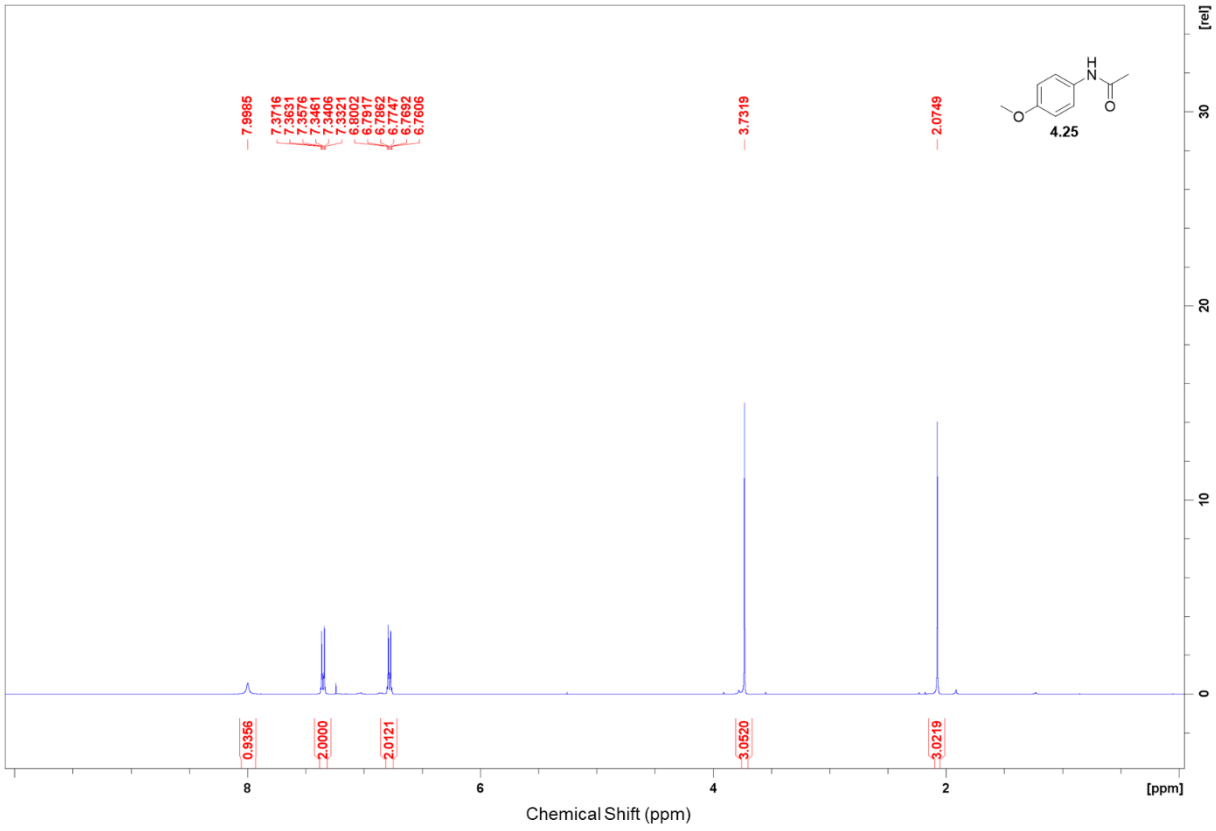
7.9985
7.3716
7.3631
7.3576
7.3461
7.3406
7.3321
6.8002
6.7947
6.7902
6.7747
6.7692
6.7606
3.7319
2.0749
4.25
0.9356
2.0000
2.0121
3.0520
3.0219
[rel]
[ppm]
Chemical Shift (ppm)

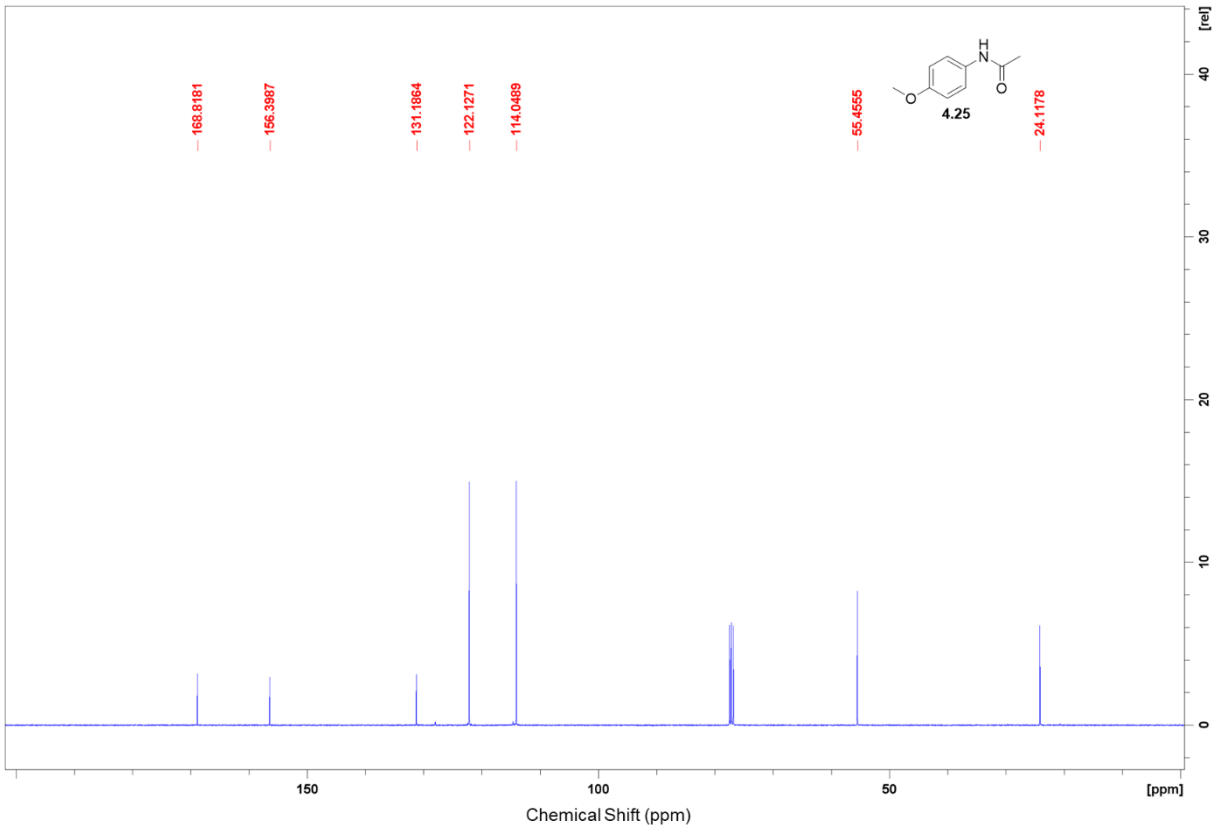
168.8181
156.3987
131.1864
122.1271
114.0489
55.4555
24.1178
4.25
[rel]
[ppm]
Chemical Shift (ppm)

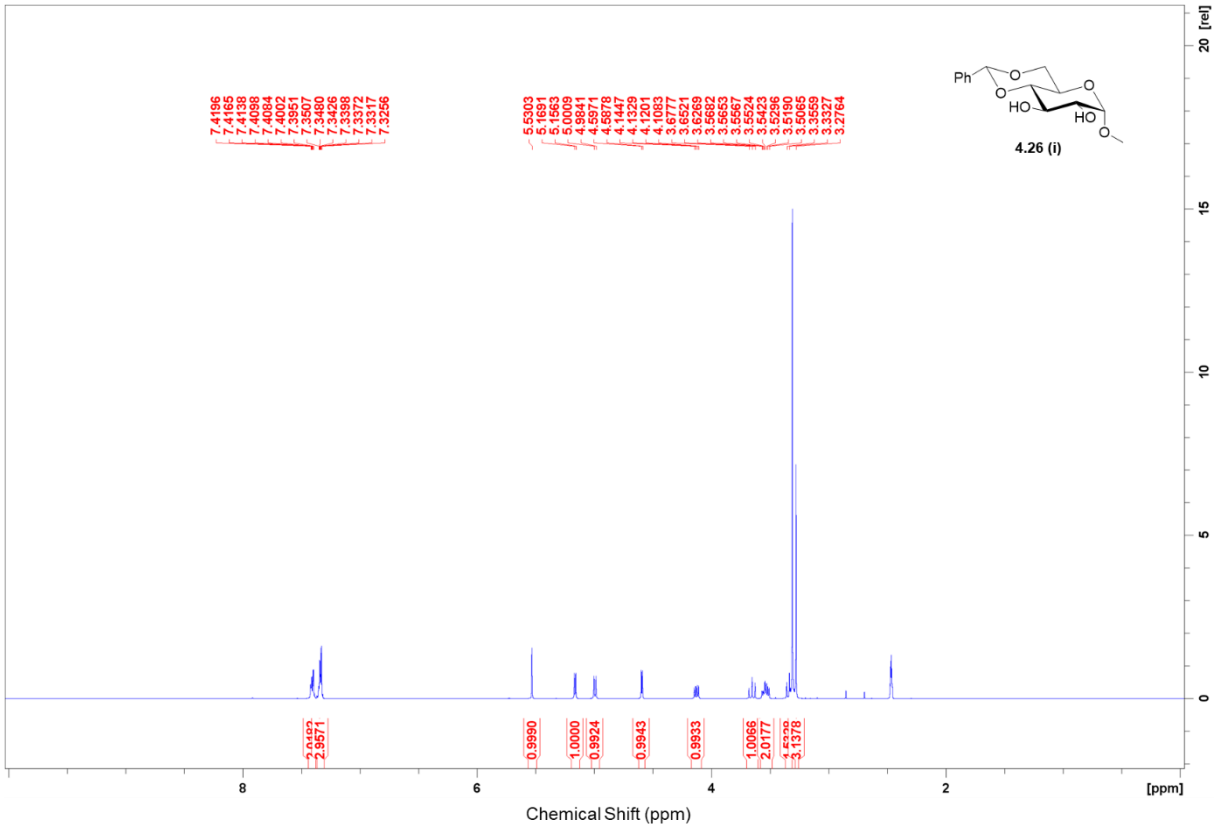
7.4196
7.4165
7.4138
7.4098
7.4064
7.4002
7.3951
7.3507
7.3480
7.3426
7.3398
7.3372
7.3317
7.3256
5.5303
5.1691
5.1563
5.0009
4.9841
4.9571
4.8878
4.1447
4.1229
4.1201
4.1083
3.6777
3.6521
3.6269
3.5682
3.5653
3.5667
3.5524
3.5423
3.5296
3.5180
3.5065
3.3569
3.3327
3.2764
Ph
O
HO
HO
4.26 (i)
0.9990
1.0000
0.9924
0.9943
0.9933
1.0066
2.0177
3.1378
[rel]
20
15
10
5
0
8
6
4
2
[ppm]
Chemical Shift (ppm)

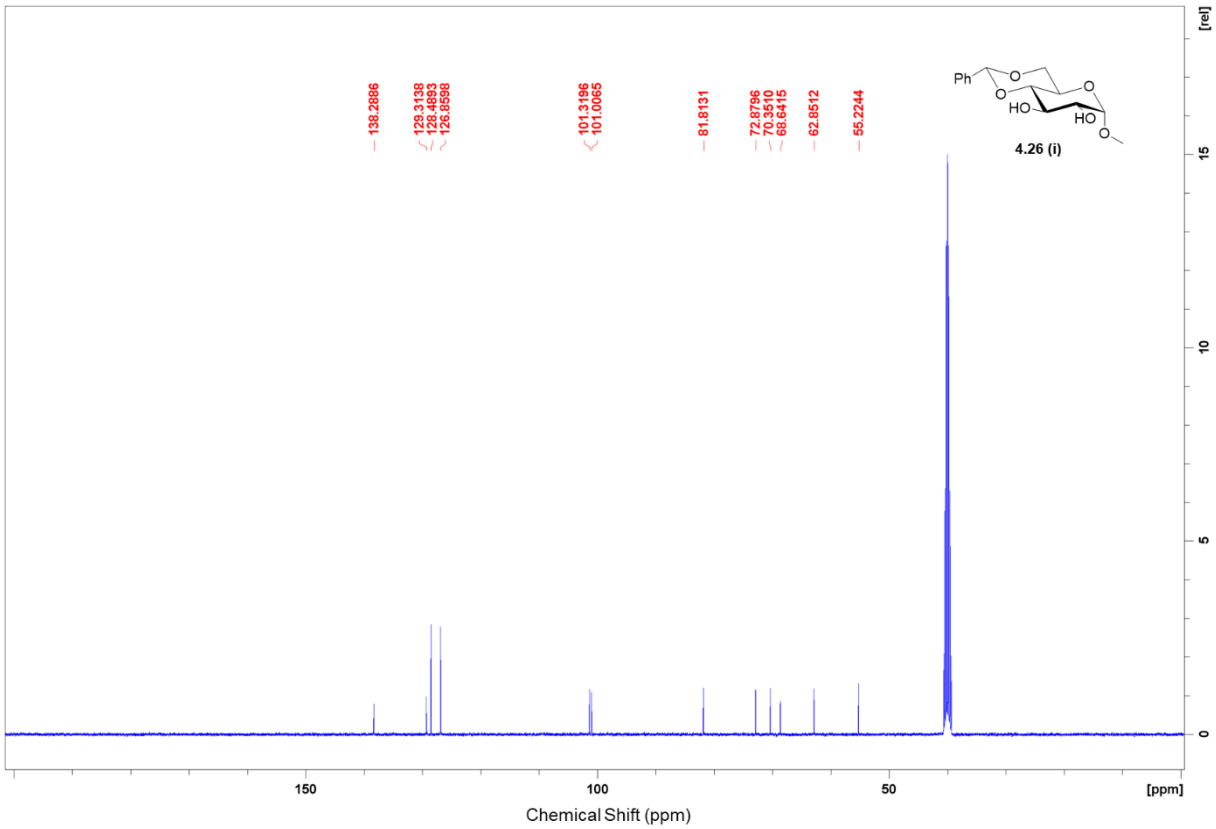
138.2886
129.3138
128.4883
126.8598
101.3196
101.0065
81.8131
72.8796
70.3510
68.6415
62.8512
55.2244
Ph
O
HO
HO
4.26 (i)
[rel]
15
10
5
0
150
100
50
[ppm]
Chemical Shift (ppm)

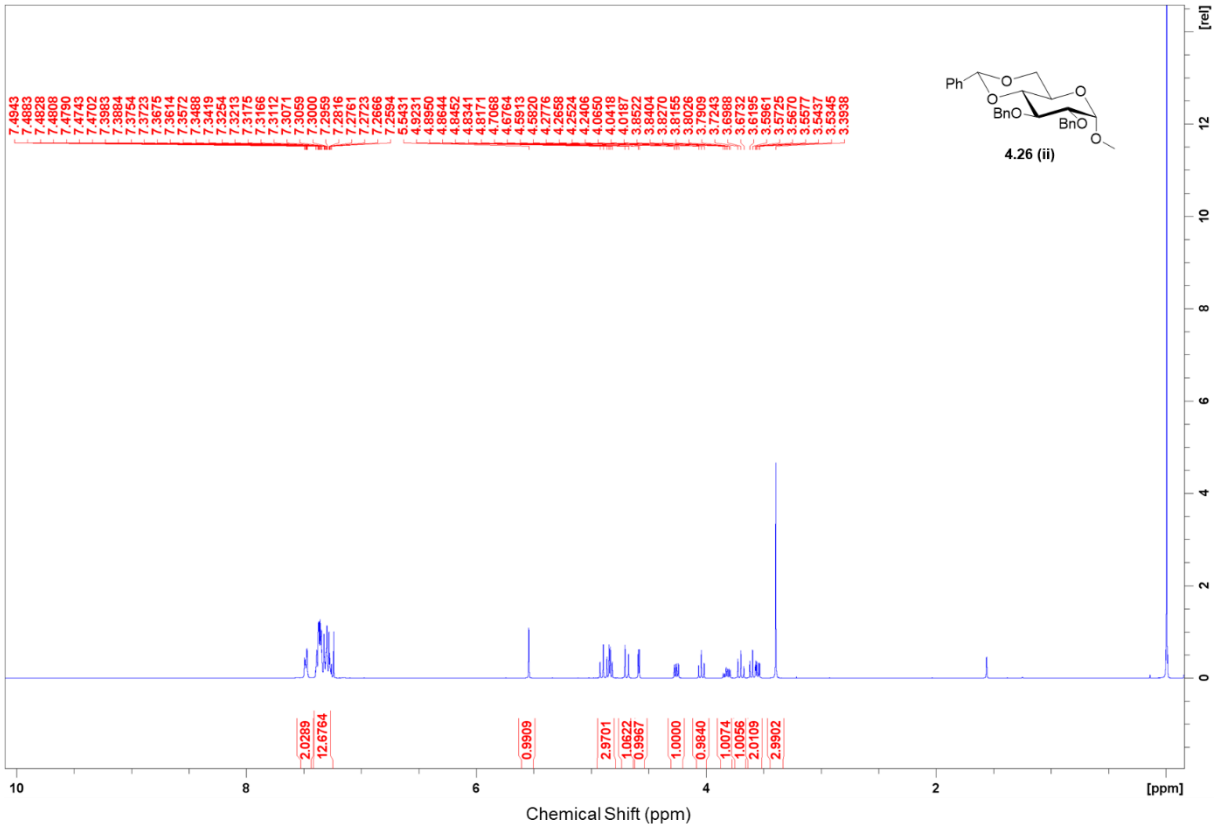
7.4943
7.4883
7.4828
7.4808
7.4790
7.4743
7.4702
7.3983
7.3884
7.3754
7.3723
7.3675
7.3614
7.3572
7.3488
7.3419
7.3254
7.3213
7.3175
7.3166
7.3112
7.3071
7.3059
7.3000
7.2959
7.2816
7.2761
7.2723
7.2666
7.2594
5.5431
4.9231
4.8950
4.8644
4.8452
4.8341
4.8171
4.7068
4.6764
4.6613
4.6520
4.2776
4.2658
4.2524
4.2406
4.0650
4.0418
4.0187
3.8522
3.8404
3.8270
3.8155
3.7926
3.7849
3.7243
3.6988
3.6732
3.6195
3.5961
3.5725
3.5670
3.5577
3.5437
3.5345
3.3938
Ph
BnO
BnO
4.26 (ii)
2.0289
12.6764
0.9909
2.9701
1.0622
0.9967
1.0000
0.9840
1.0074
1.0056
2.0109
2.9902
[rel]
[ppm]
Chemical Shift (ppm)

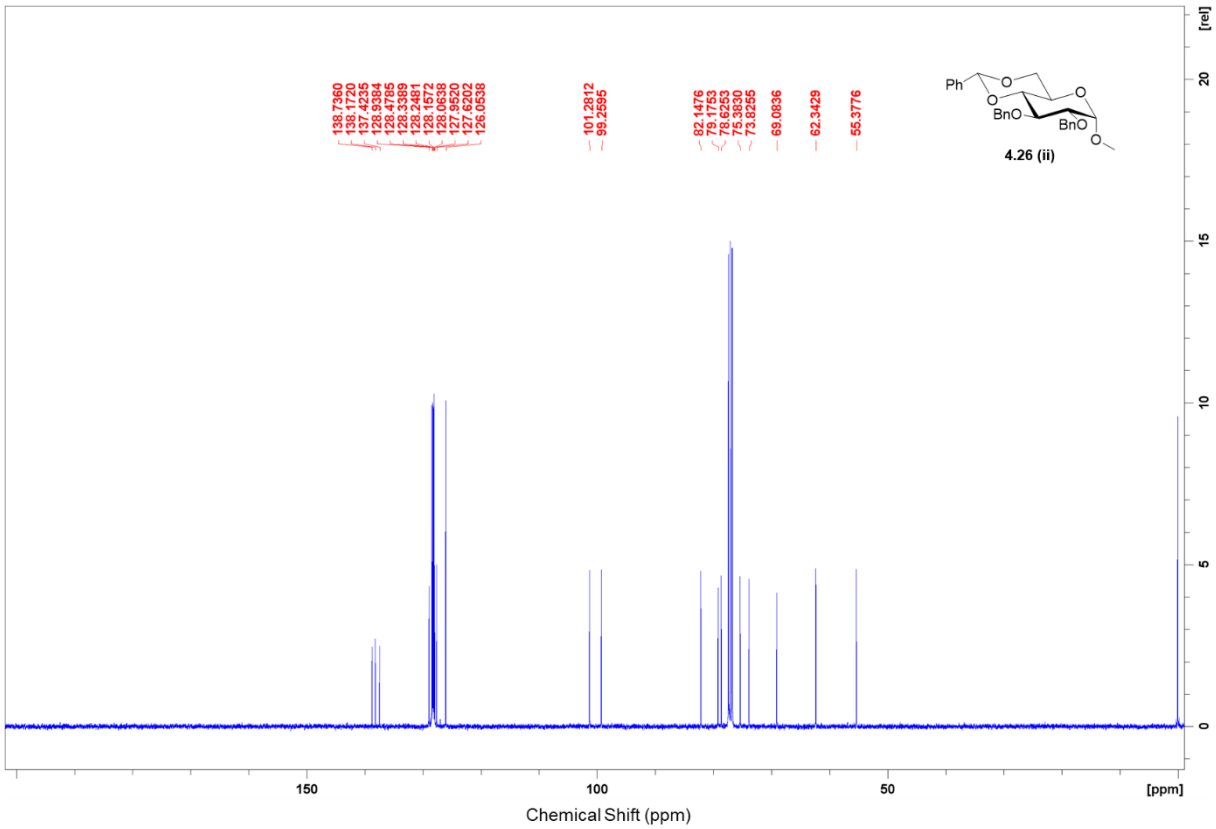
138.7360
138.1720
137.4235
128.9384
128.4785
128.3389
128.2481
128.1572
128.0638
127.9520
127.6202
126.0538
101.2812
99.2595
82.1476
79.1753
78.6253
75.3830
73.8255
69.0836
62.3429
55.3776
Ph
BnO
BnO
4.26 (ii)
[rel]
[ppm]
Chemical Shift (ppm)

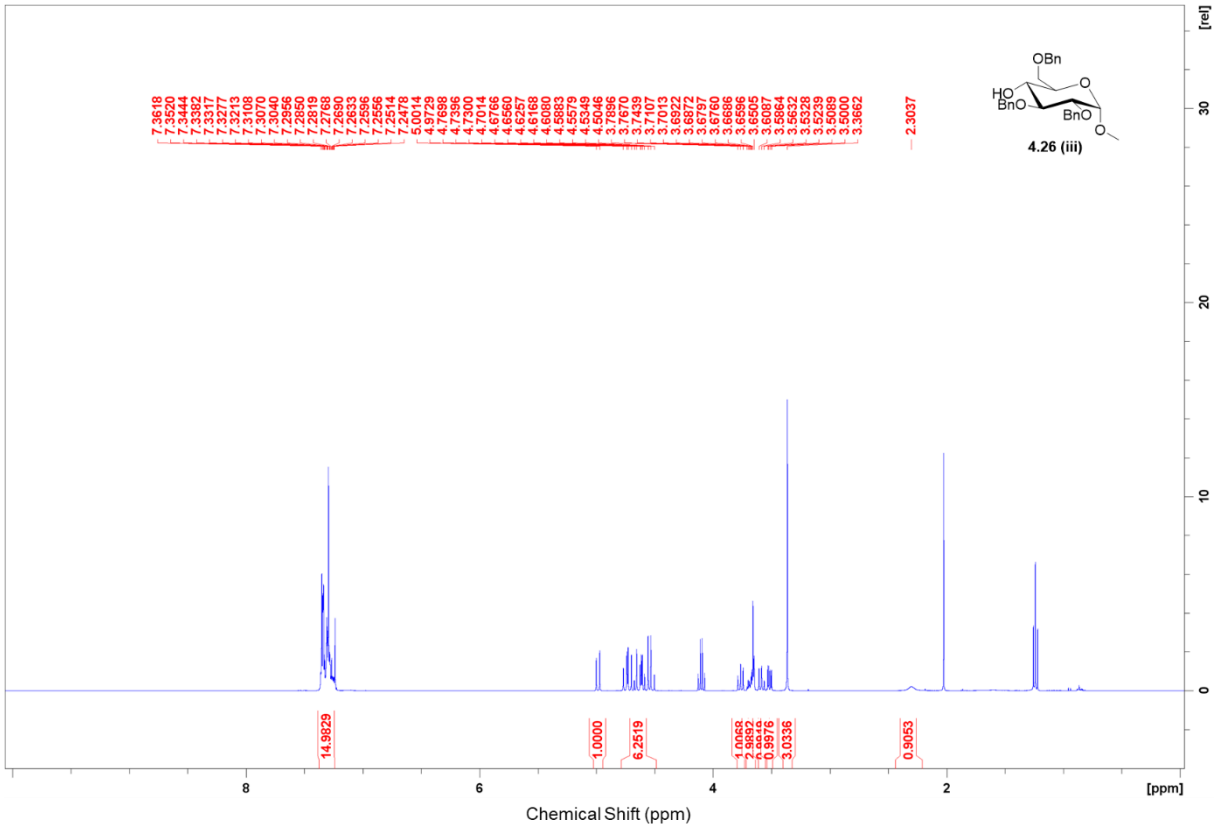
7.3618
7.3520
7.3444
7.3382
7.3317
7.3277
7.3213
7.3108
7.3070
7.3040
7.2956
7.2850
7.2819
7.2768
7.2690
7.2633
7.2596
7.2556
7.2514
7.2478
5.0014
4.9729
4.7698
4.7396
4.7300
4.7014
4.6766
4.6560
4.6357
4.6168
4.6080
4.5883
4.5579
4.5349
4.5046
3.7896
3.7670
3.7439
3.7107
3.7013
3.6922
3.6872
3.6757
3.6750
3.6686
3.6596
3.6505
3.6087
3.5984
3.5632
3.5328
3.5239
3.5089
3.5000
3.3662
2.3037
OBn
HO
BnO
BnO
O
O
4.26 (iii)
14.9829
1.0000
6.2519
1.0068
2.9892
2.0414
0.9976
3.0336
0.9053
[rel]
30
20
10
0
8
6
4
2
[ppm]
Chemical Shift (ppm)

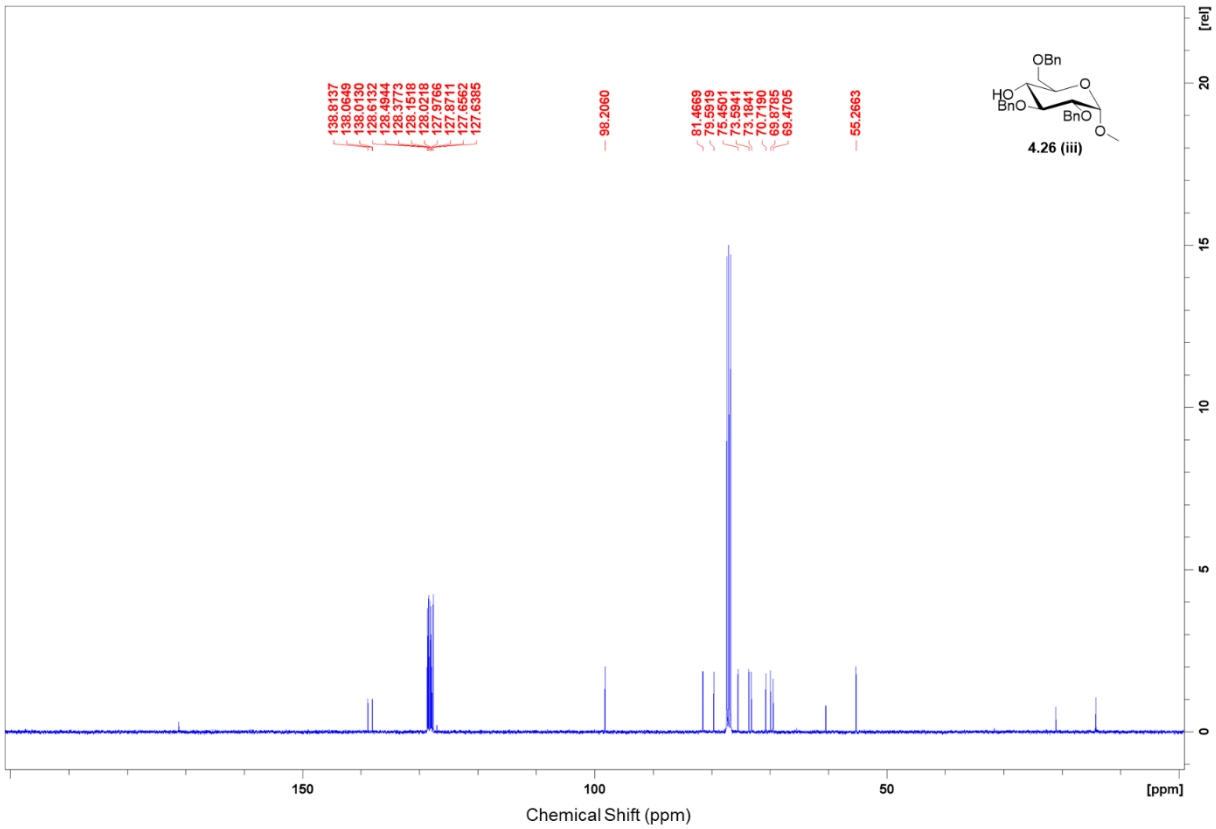
138.8137
138.0649
138.0130
128.6132
128.4944
128.3773
128.1518
128.0218
127.9766
127.8741
127.6552
127.6385
98.2060
81.4669
79.5919
75.4501
73.5941
73.1841
70.7190
69.8785
69.4705
55.2663
OBn
HO
BnO
BnO
O
O
4.26 (iii)
[rel]
20
15
10
5
0
150
100
50
[ppm]
Chemical Shift (ppm)

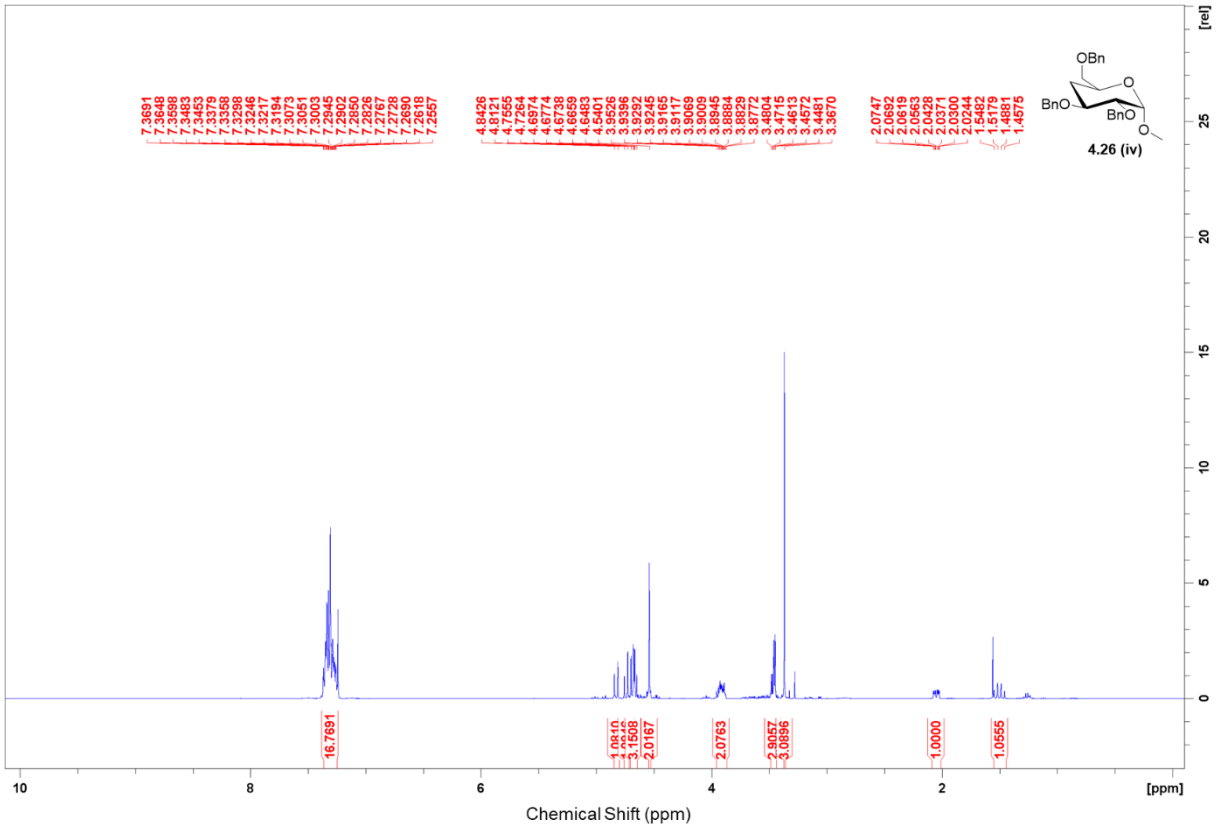
7.3691
7.3648
7.3588
7.3483
7.3453
7.3379
7.3358
7.3298
7.3246
7.3217
7.3194
7.3073
7.3051
7.3003
7.2945
7.2902
7.2850
7.2826
7.2797
7.2728
7.2680
7.2618
7.2557
4.8426
4.8121
4.7565
4.7394
4.6974
4.6774
4.6738
4.6659
4.6483
4.5401
3.9526
3.9396
3.9292
3.9245
3.9165
3.9117
3.9069
3.9049
3.8945
3.8884
3.8829
3.8772
3.4804
3.4715
3.4613
3.4572
3.4481
3.3670
2.0747
2.0692
2.0619
2.0563
2.0428
2.0371
2.0340
2.0244
1.5482
1.5179
1.4881
1.4575
OBn
BnO
BnO
O
O
4.26 (iv)
16.7691
1.0810
1.0446
3.1508
2.0167
2.0763
2.9057
3.0895
1.0000
1.0555
[rel]
25
20
15
10
5
0
10
8
6
4
2
[ppm]
Chemical Shift (ppm)

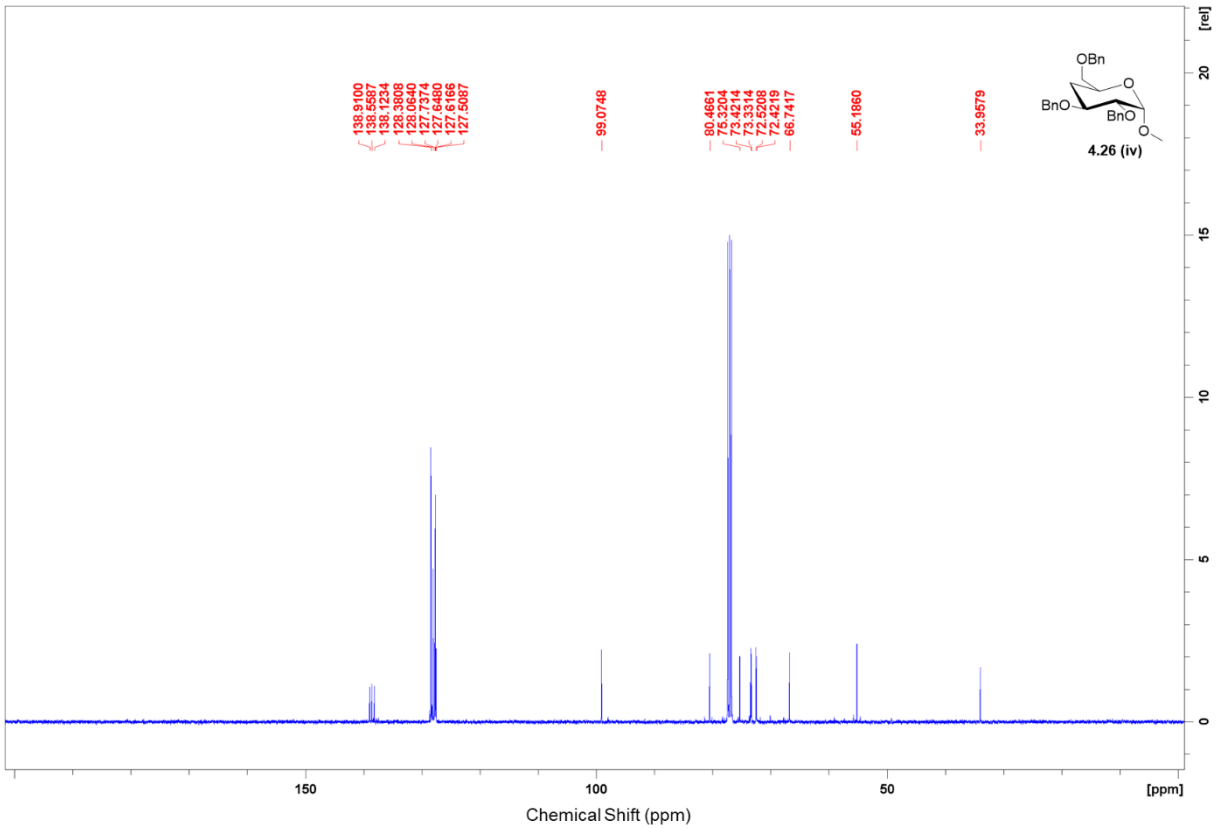
138.9100
138.5587
138.1234
128.3808
128.0640
127.7374
127.6480
127.6166
127.5087
99.0748
80.4661
75.3204
73.4214
73.3314
72.5208
72.4219
66.7417
55.1860
33.9579
OBn
BnO
BnO
O
O
4.26 (iv)
[rel]
20
15
10
5
0
150
100
50
[ppm]
Chemical Shift (ppm)

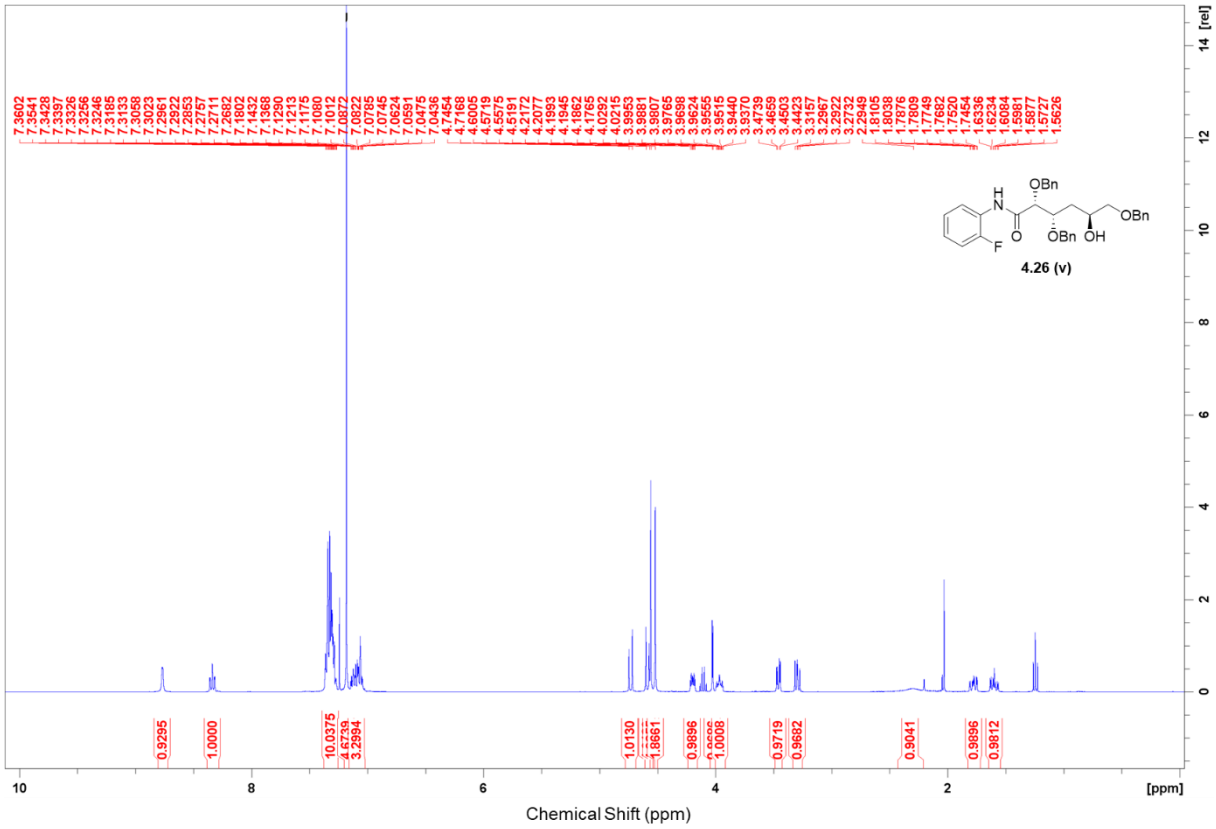
4.26 (v)
Chemical Shift (ppm)
[ppm]
[rel]

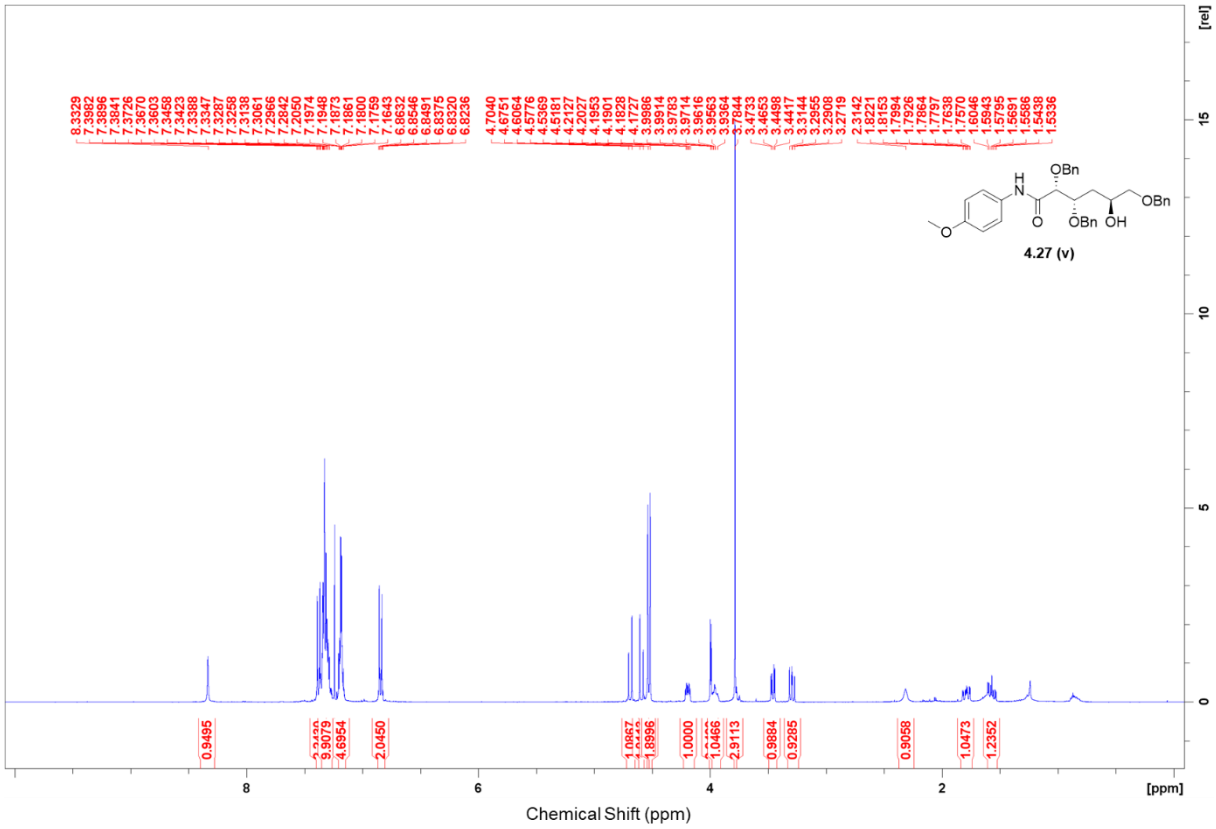
[rel]
[ppm]
Chemical Shift (ppm)
4.27 (v)

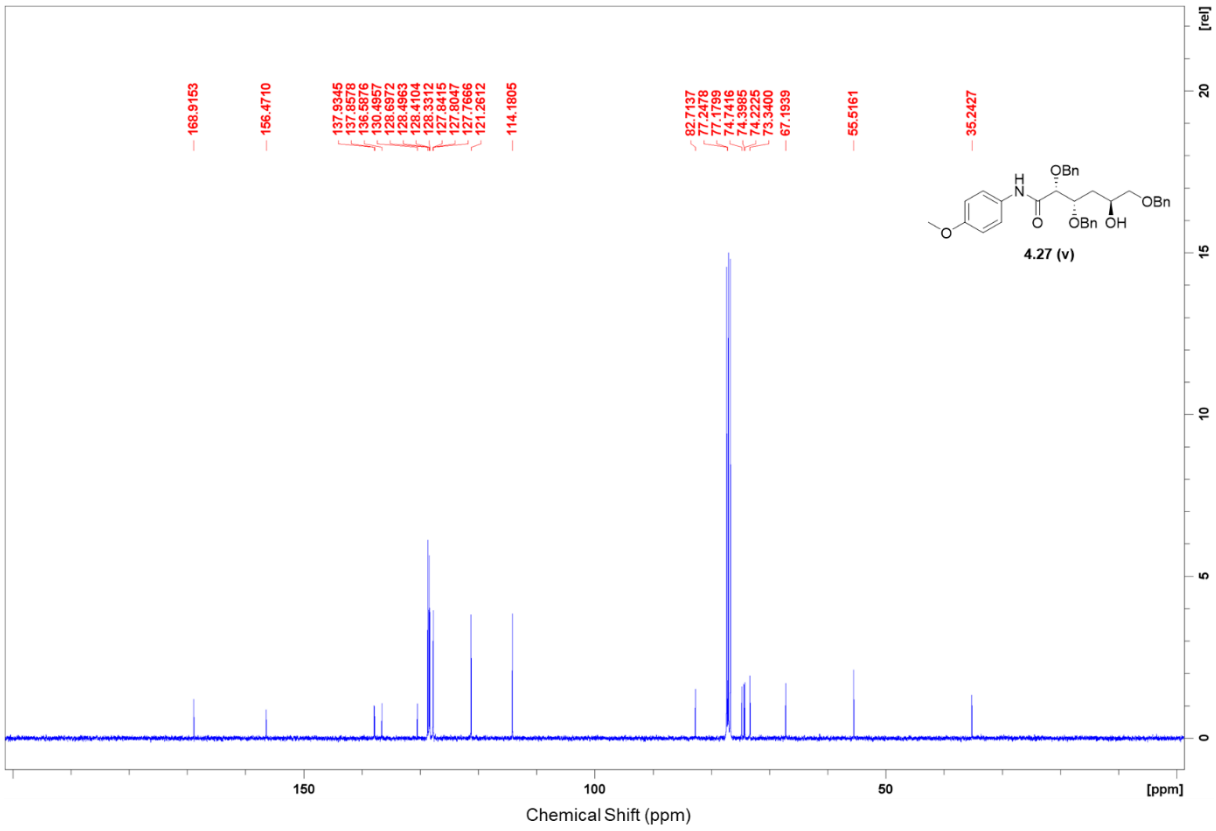
[rel]
[ppm]
Chemical Shift (ppm)
4.27 (v)

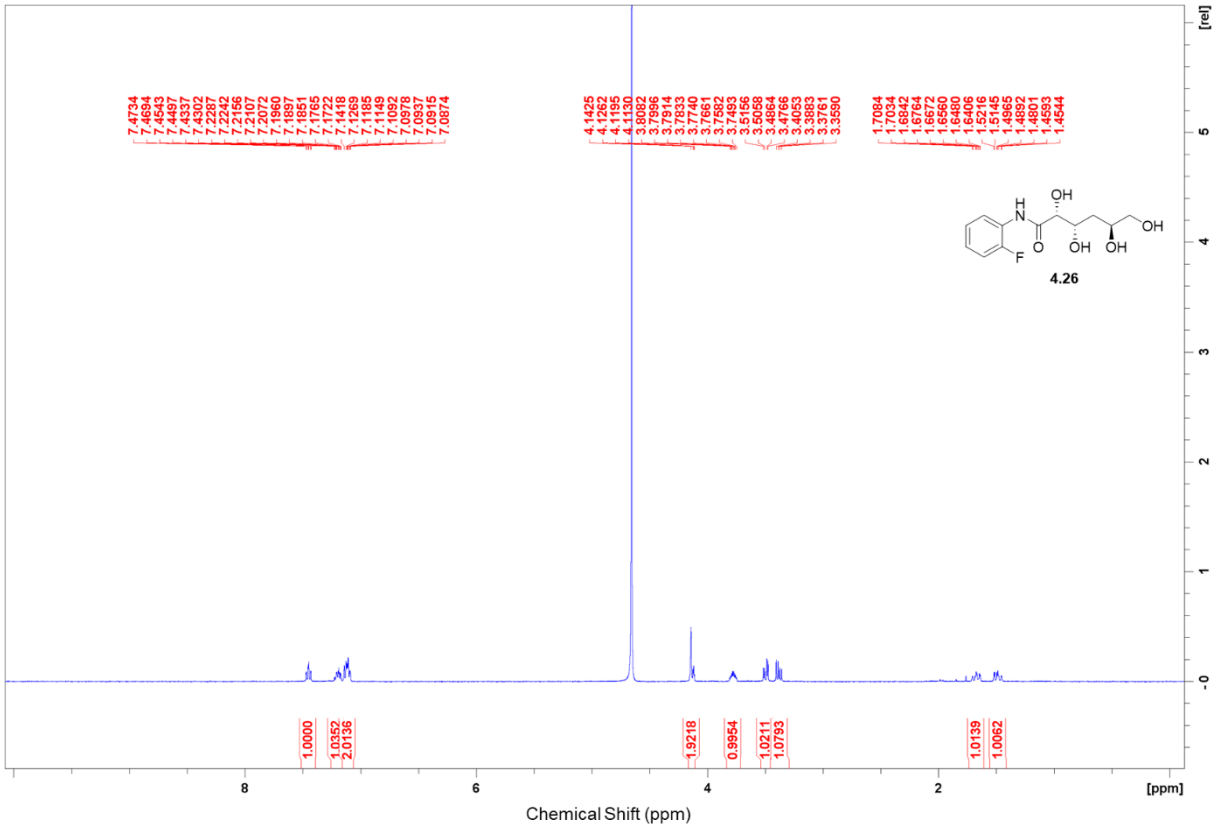
7.4734
7.4694
7.4543
7.4497
7.4337
7.4302
7.2287
7.2242
7.2156
7.2107
7.2072
7.1960
7.1897
7.1851
7.1765
7.1722
7.1418
7.1289
7.1165
7.1149
7.1092
7.0978
7.0937
7.0915
7.0874
4.1425
4.1262
4.1195
4.1130
3.8082
3.7996
3.7914
3.7833
3.7740
3.7681
3.7582
3.7493
3.5156
3.5068
3.4954
3.4766
3.4053
3.3883
3.3761
3.3590
1.7084
1.7034
1.6842
1.6764
1.6672
1.6560
1.6480
1.6406
1.6316
1.5145
1.4965
1.4892
1.4801
1.4593
1.4544
1.0000
1.0352
2.0136
1.9218
0.9954
1.0211
1.0793
1.0139
1.0062
OH
H
N
O
F
OH
OH
OH
4.26
[rel]
[ppm]
Chemical Shift (ppm)

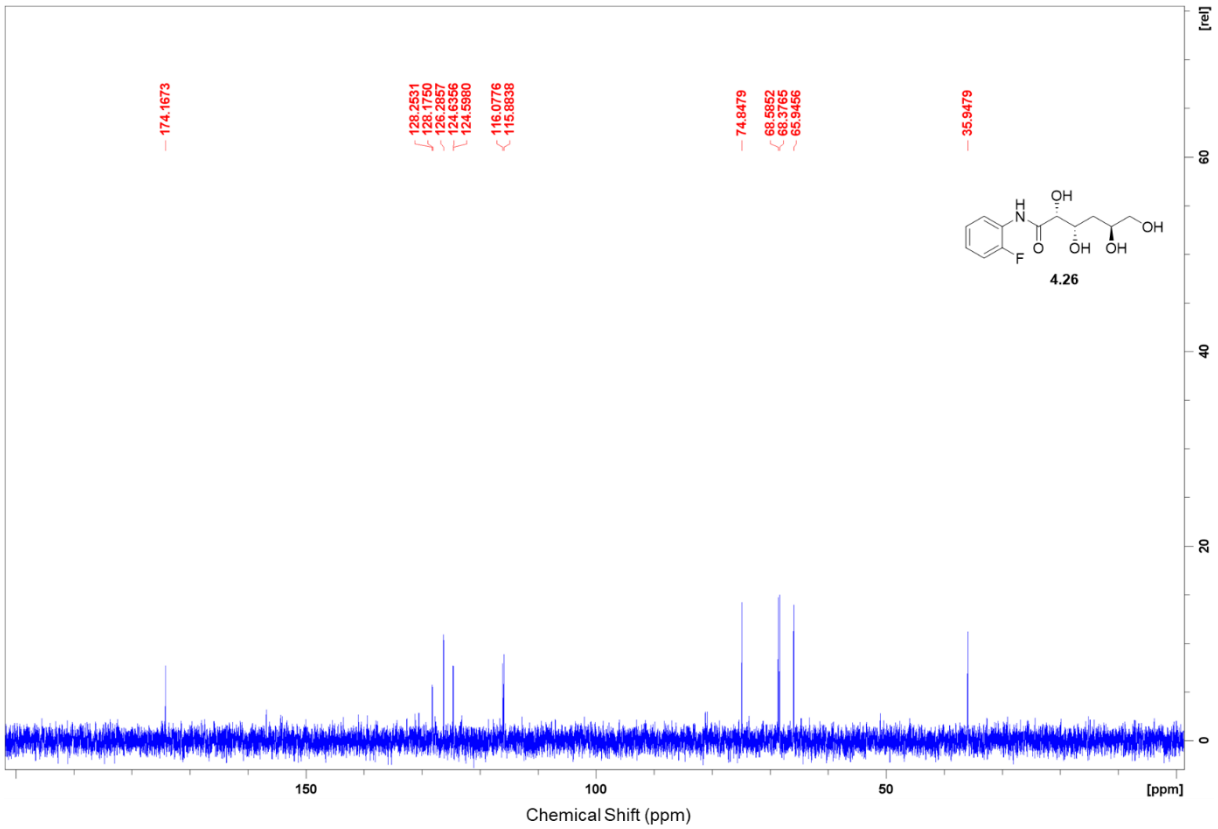
174.1673
128.2531
128.1750
126.2857
124.6356
124.5980
116.0776
115.8838
74.8479
68.5852
68.3765
65.9456
35.9479
OH
H
N
O
F
OH
OH
OH
4.26
[rel]
[ppm]
Chemical Shift (ppm)

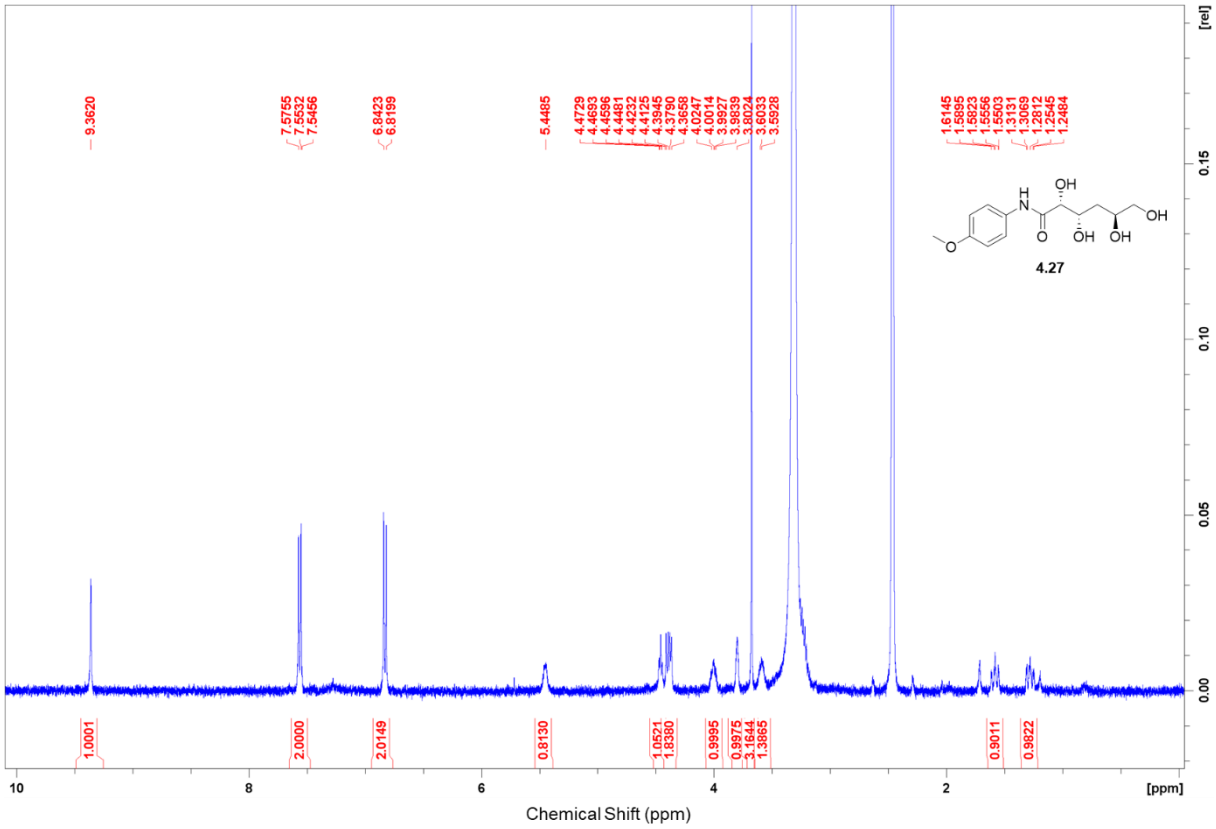
9.3620
7.5755
7.5532
7.5456
6.8423
6.8199
5.4485
4.4729
4.4693
4.4596
4.4491
4.4372
4.4125
4.3945
4.3790
4.3658
4.0247
4.0014
3.9927
3.9839
3.8024
3.6033
3.5928
1.6145
1.5895
1.5823
1.5556
1.5503
1.3131
1.3069
1.2812
1.2545
1.2484
1.0001
2.0000
2.0149
0.8130
1.0521
1.8380
0.9995
0.9975
3.1644
1.3865
0.9011
0.9822
[rel]
0.15
0.10
0.05
0.00
10
8
6
4
2
[ppm]
Chemical Shift (ppm)
OH
H
N
OH
O
OH
OH
O
4.27

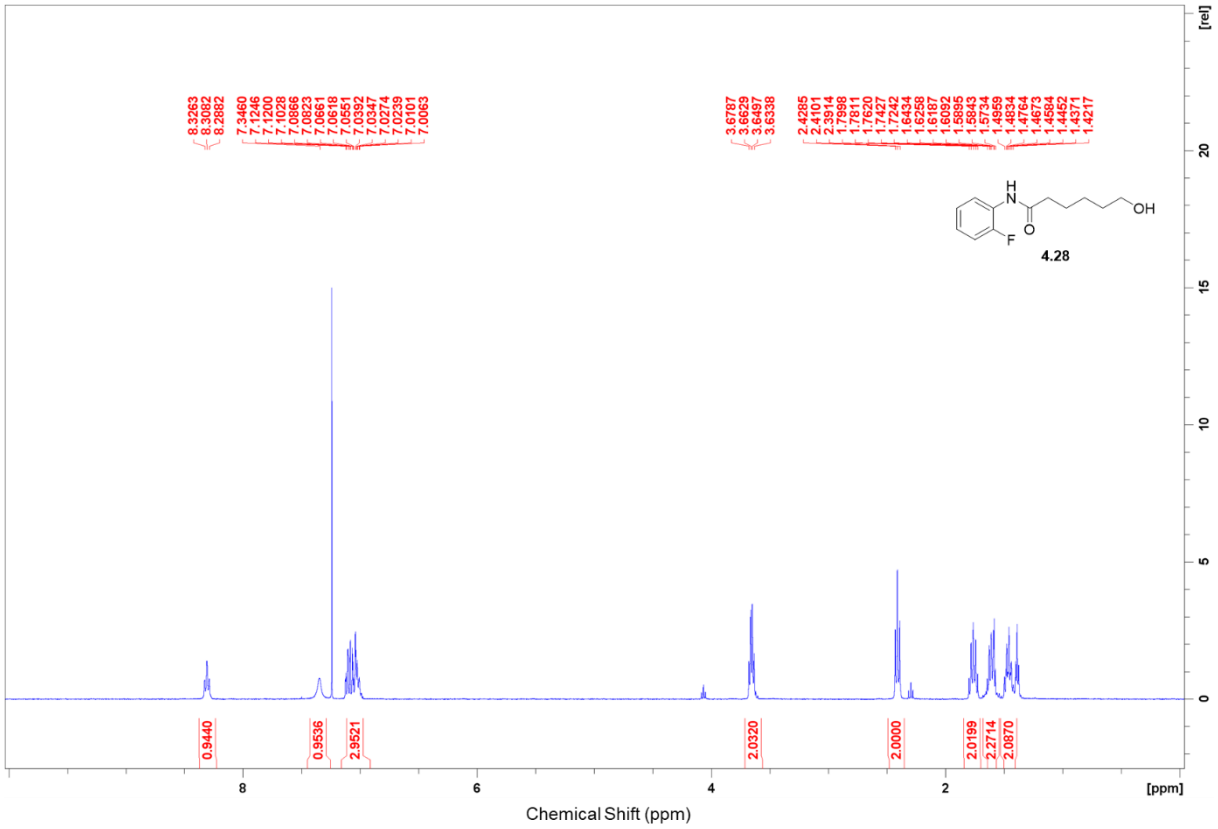
8.3263
8.3082
8.2882
7.3460
7.1246
7.1020
7.1028
7.0866
7.0823
7.0661
7.0618
7.0551
7.0392
7.0347
7.0274
7.0239
7.0101
7.0063
3.6787
3.6629
3.6497
3.6338
2.4285
2.4101
2.3914
2.3898
1.7811
1.7620
1.7427
1.7242
1.6434
1.6258
1.6187
1.6092
1.5895
1.5843
1.5734
1.4959
1.4754
1.4734
1.4673
1.4584
1.4452
1.4371
1.4217
0.9440
0.9536
2.9521
2.0320
2.0000
2.0199
2.2714
2.0870
4.28
[rel]
[ppm]
Chemical Shift (ppm)

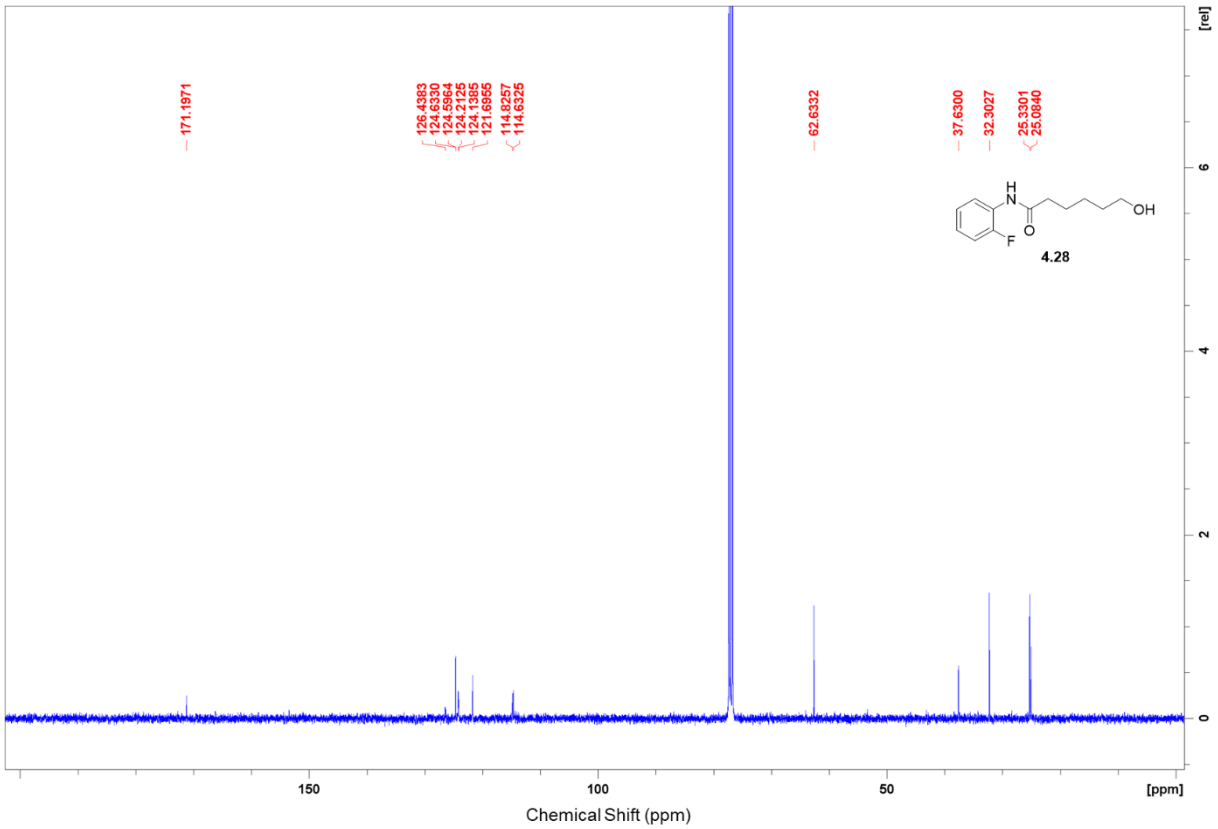
171.1971
126.4383
124.6330
124.5964
124.2125
124.1385
121.6955
114.8257
114.6325
62.6332
37.6300
32.3027
25.3301
25.0840
4.28
[rel]
[ppm]
Chemical Shift (ppm)

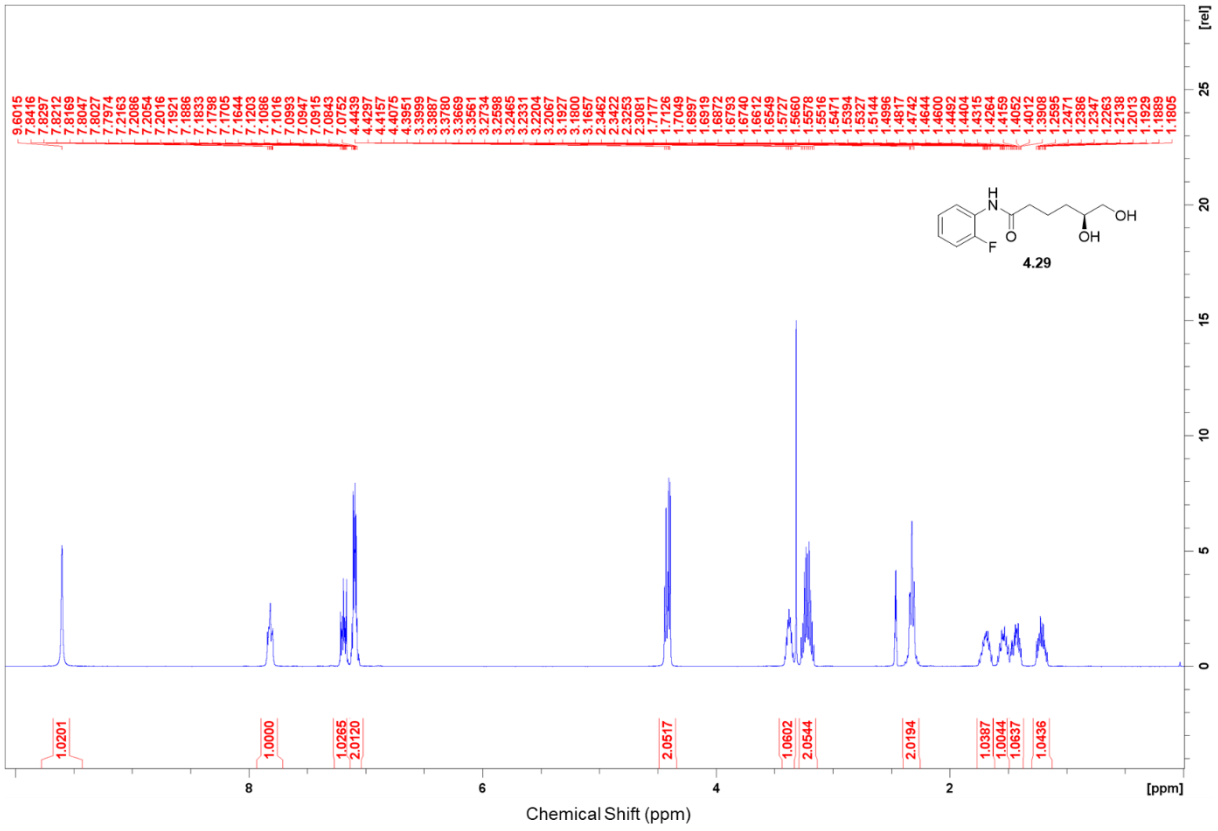
[rel]
25
20
15
10
5
0
9.6015
7.8446
7.8237
7.8212
7.8169
7.8047
7.8027
7.7974
7.7163
7.2086
7.2054
7.2016
7.1921
7.1886
7.1833
7.1798
7.1705
7.1644
7.1203
7.1086
7.1016
7.0993
7.0947
7.0915
7.0843
7.0752
4.4439
4.4297
4.4157
4.4075
4.3951
3.3999
3.3887
3.3780
3.3669
3.3561
3.2734
3.2698
3.2485
3.2331
3.2204
3.2067
3.1927
3.1800
3.1657
2.3462
2.3422
2.3253
2.3081
1.7177
1.7126
1.7049
1.6897
1.6819
1.6872
1.6793
1.6740
1.6612
1.6549
1.5727
1.5660
1.5578
1.5516
1.5471
1.5394
1.5327
1.5144
1.4896
1.4817
1.4742
1.4644
1.4600
1.4492
1.4404
1.4315
1.4264
1.4159
1.4062
1.4012
1.3908
1.2595
1.2471
1.2386
1.2347
1.2263
1.2138
1.2013
1.1929
1.1889
1.1805
H
N
O
F
OH
OH
4.29
1.0201
1.0000
1.0265
2.0120
2.0517
1.0602
2.0544
2.0194
1.0387
1.0044
1.0637
1.0436
8
6
4
2
[ppm]
Chemical Shift (ppm)

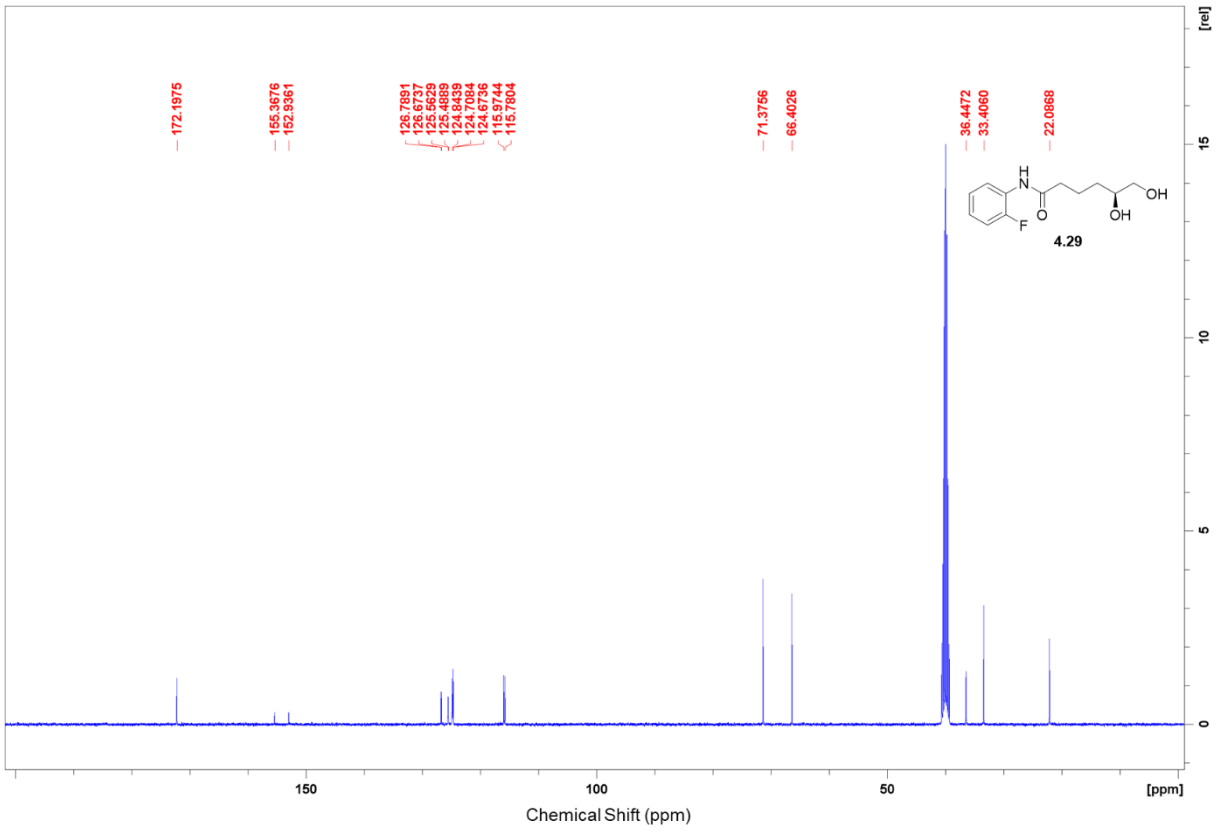
[rel]
15
10
5
0
172.1975
155.3676
152.9361
126.7891
126.6737
125.5629
125.4889
124.8439
124.7084
124.6736
115.9744
115.7804
71.3756
66.4026
36.4472
33.4060
22.0668
H
N
O
F
OH
OH
4.29
150
100
50
[ppm]
Chemical Shift (ppm)

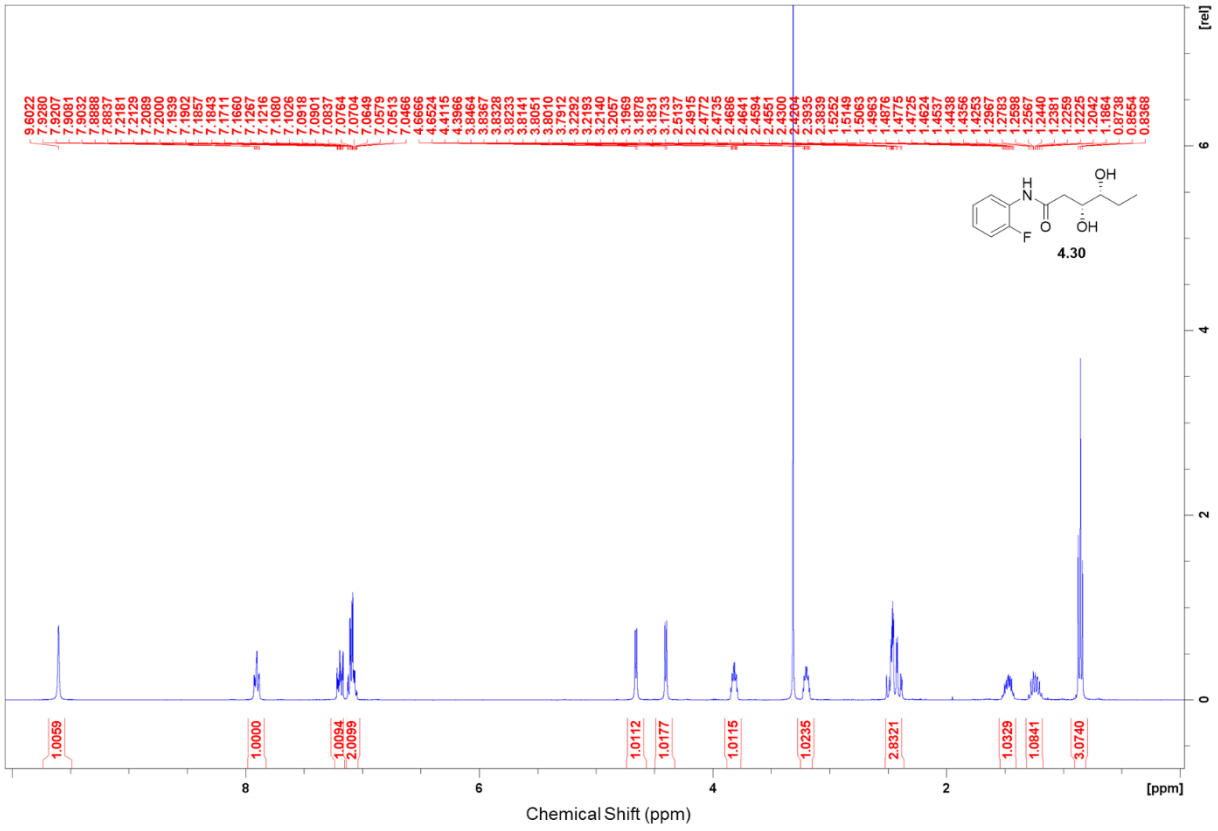
9.6022
7.9260
7.9207
7.9081
7.9032
7.8888
7.8837
7.2181
7.2129
7.2089
7.2000
7.1939
7.1902
7.1857
7.1843
7.1711
7.1660
7.1267
7.1216
7.1080
7.1026
7.0918
7.0901
7.0837
7.0764
7.0704
7.0649
7.0573
7.0513
7.0466
4.6666
4.6524
4.4115
4.3966
3.8464
3.8367
3.8328
3.8233
3.8141
3.8051
3.7910
3.7912
3.2292
3.2193
3.2140
3.2057
3.1969
3.1878
3.1831
3.1733
2.5137
2.4915
2.4772
2.4735
2.4686
2.4641
2.4554
2.4551
2.4300
2.4204
2.3935
2.3839
1.5252
1.5149
1.5063
1.4963
1.4876
1.4775
1.4723
1.4624
1.4537
1.4438
1.4356
1.4253
1.2967
1.2783
1.2698
1.2567
1.2440
1.2381
1.2259
1.2225
1.2042
1.1864
0.8738
0.8554
0.8368
OH
N
H
O
OH
F
4.30
1.0059
1.0000
1.0094
2.0099
1.0112
1.0177
1.0115
1.0235
2.8321
1.0329
1.0841
3.0740
8
6
4
2
[ppm]
[rel]
Chemical Shift (ppm)

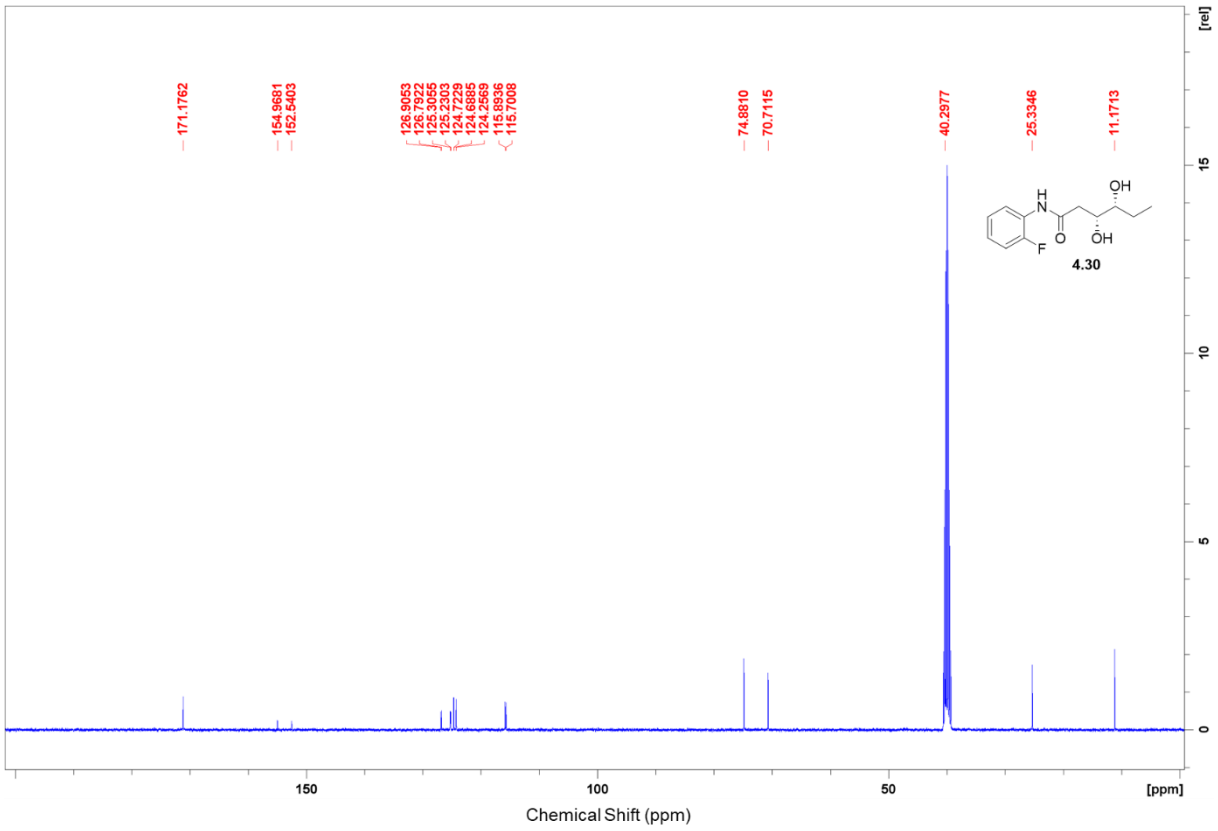
171.1762
154.9681
152.5403
126.9053
126.7922
125.3055
125.2303
124.7229
124.6885
124.2569
115.8936
115.7008
74.8810
70.7115
40.2977
25.3346
11.1713
OH
N
H
O
OH
F
4.30
150
100
50
[ppm]
[rel]
Chemical Shift (ppm)

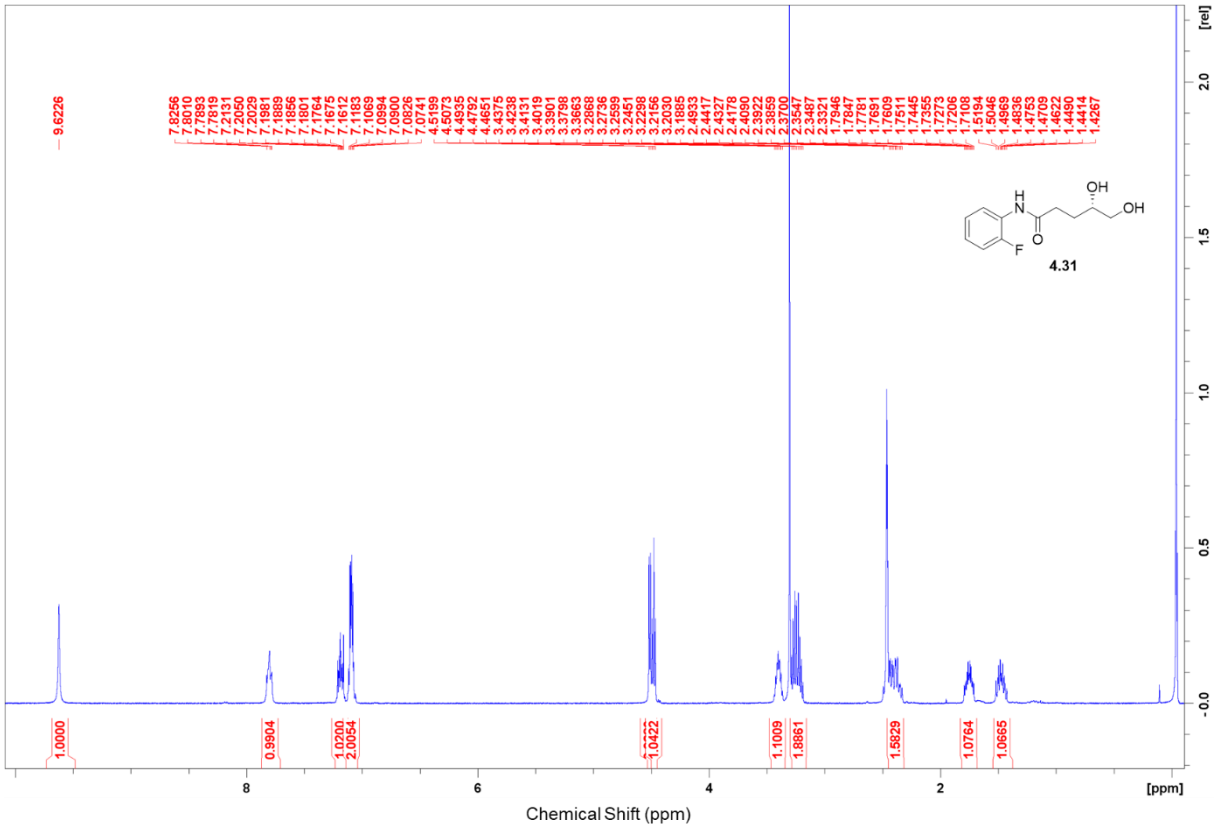
9.6226
7.8256
7.8010
7.7893
7.7619
7.7151
7.2150
7.2029
7.1981
7.1889
7.1856
7.1801
7.1764
7.1675
7.1612
7.1183
7.1069
7.0994
7.0900
7.0726
7.0741
4.5199
4.5073
4.4935
4.4792
4.4651
3.4375
3.4238
3.4131
3.4019
3.3901
3.3798
3.3663
3.3568
3.2736
3.2599
3.2451
3.2298
3.2156
3.2030
3.1885
2.4933
2.4417
2.4327
2.4178
2.4090
2.3922
2.3868
2.3700
2.3547
2.3487
2.3321
1.7946
1.7847
1.7781
1.7691
1.7609
1.7511
1.7445
1.7325
1.7253
1.7206
1.7108
1.5194
1.5046
1.4969
1.4836
1.4753
1.4709
1.4622
1.4490
1.4414
1.4267
1.0000
0.9904
1.0200
2.0054
1.0422
1.1009
1.8861
1.5829
1.0764
1.0665
OH
OH
H
N
O
F
4.31
[rel]
[ppm]
Chemical Shift (ppm)

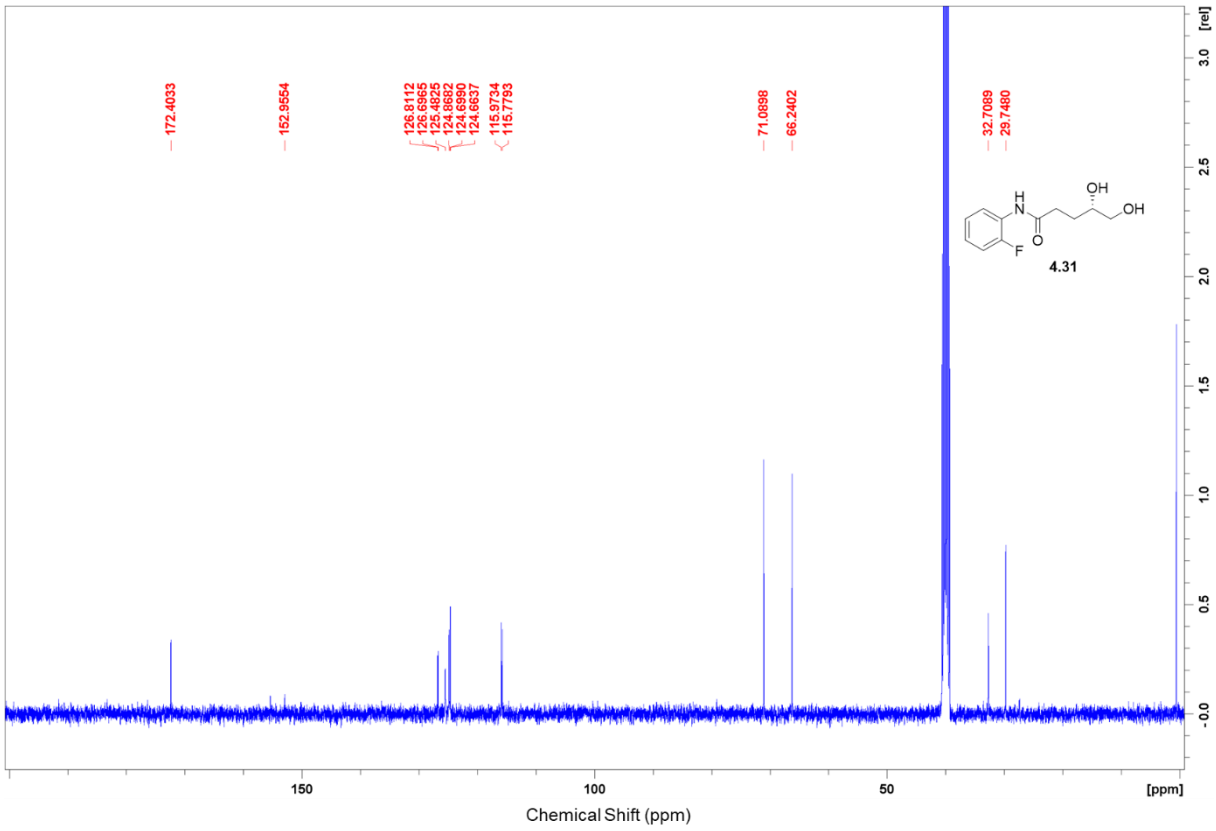
172.4033
152.9554
126.8112
126.6955
126.4825
124.8662
124.6990
124.6637
115.9734
115.7793
71.0898
66.2402
32.7089
29.7480
OH
OH
H
N
O
F
4.31
[rel]
[ppm]
Chemical Shift (ppm)

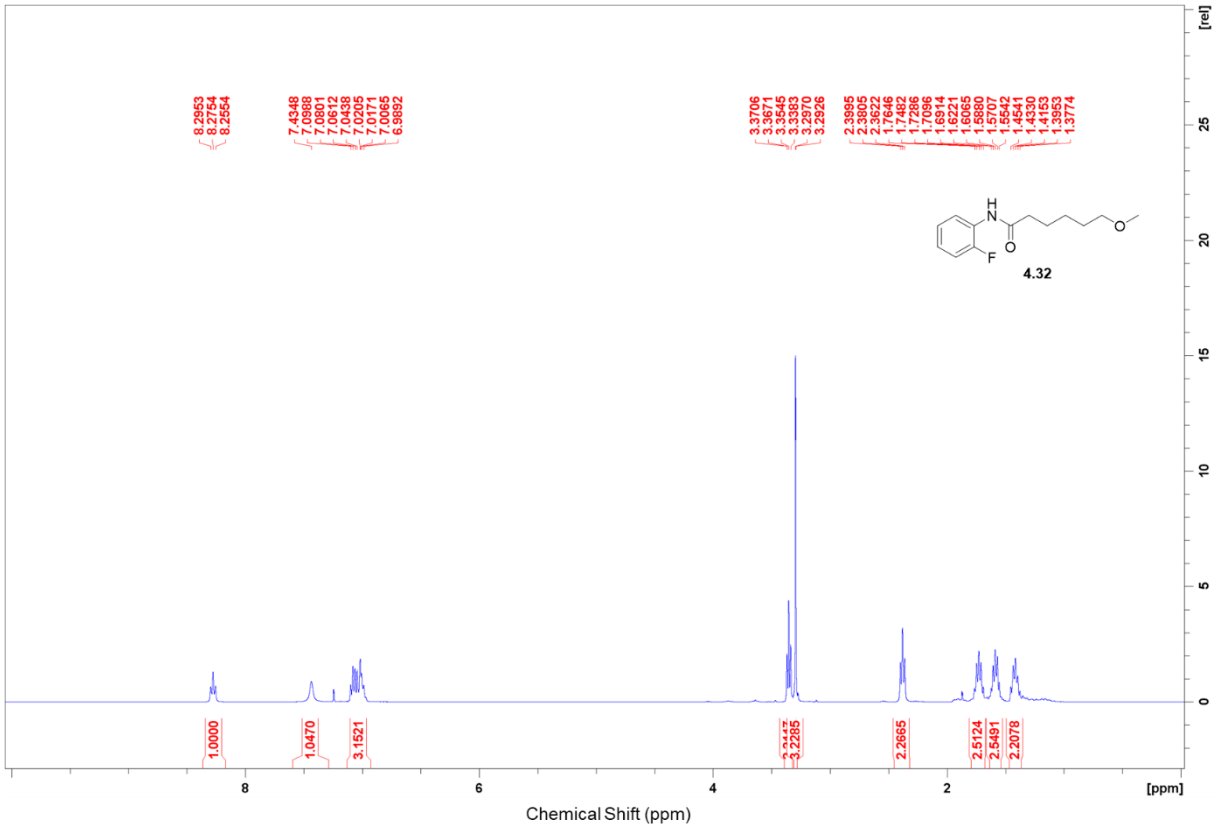
8.2953
8.2754
8.2554
7.4348
7.0988
7.0801
7.0612
7.0438
7.0205
7.0171
7.0065
6.9892
3.3706
3.3671
3.3545
3.3383
3.2970
3.2926
2.3995
2.3805
2.3622
1.7646
1.7482
1.7286
1.7096
1.6914
1.6221
1.6065
1.5880
1.5707
1.5542
1.4541
1.4330
1.4153
1.3953
1.3774
4.32
1.0000
1.0470
3.1521
3.2285
2.2665
2.5124
2.5491
2.2078
[rel]
[ppm]
Chemical Shift (ppm)

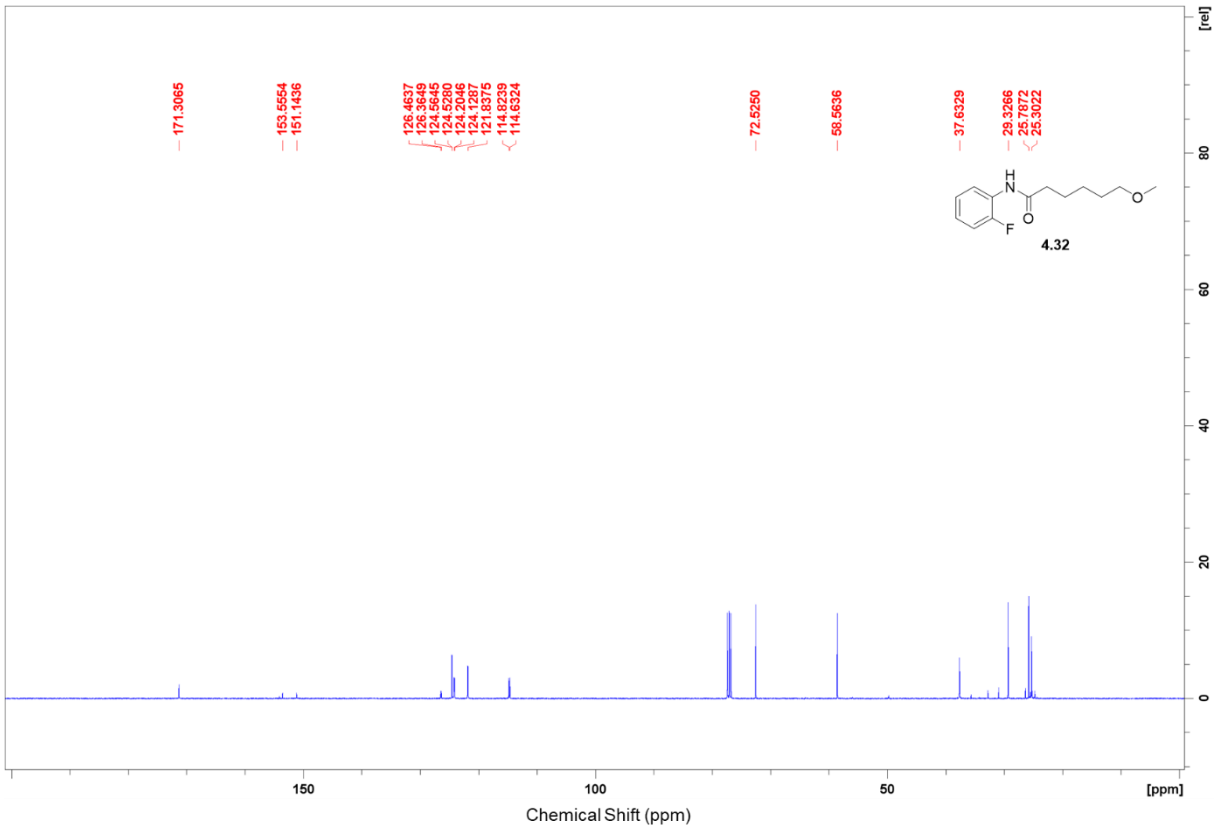
171.3065
153.5554
151.1436
126.4637
126.3649
124.5645
124.5280
124.2046
124.1287
121.8375
114.8239
114.6324
72.5250
58.5636
37.6329
29.3266
25.7872
25.3022
4.32
[rel]
[ppm]
Chemical Shift (ppm)

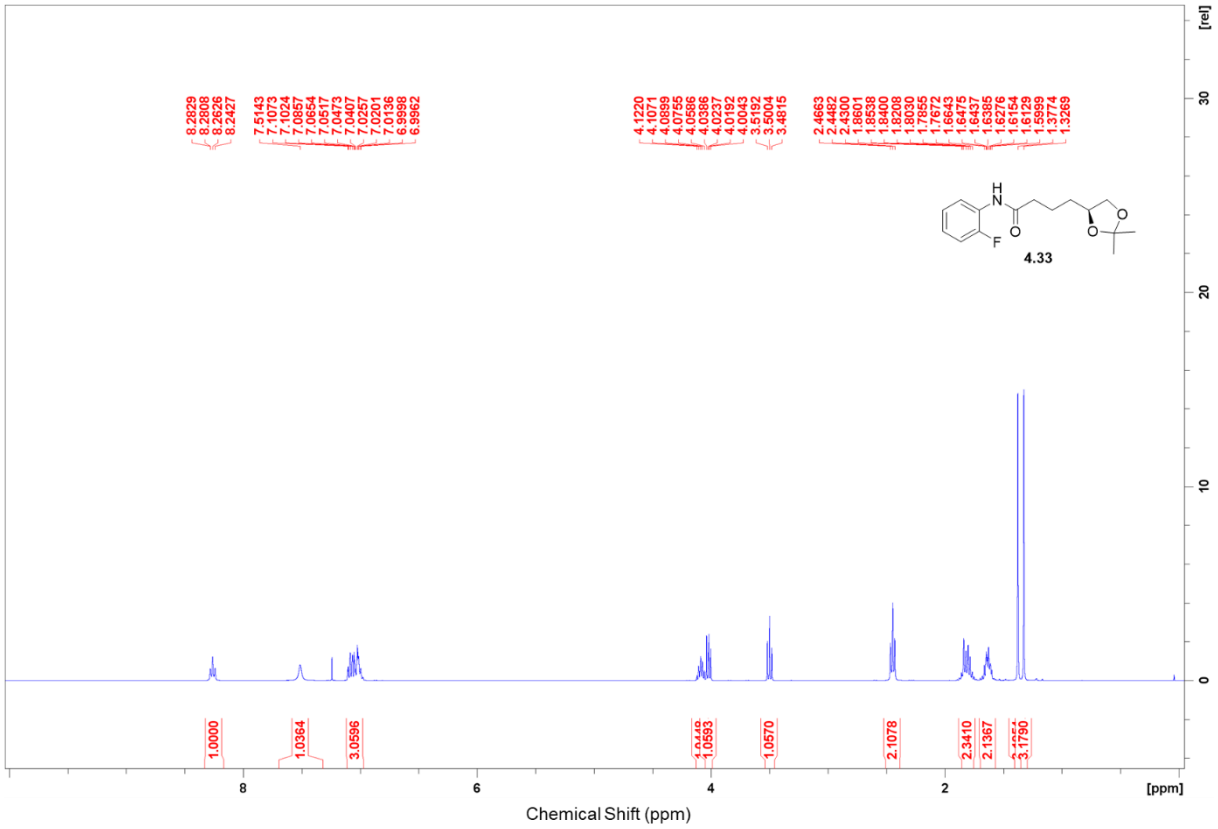
8.2829
8.2808
8.2626
8.2427
7.5143
7.1073
7.1024
7.0857
7.0654
7.0477
7.0473
7.0407
7.0257
7.0201
7.0136
6.9998
6.9962
4.1220
4.1071
4.0899
4.0755
4.0586
4.0386
4.0237
4.0132
4.0043
3.5192
3.5004
3.4815
2.4663
2.4482
2.4300
1.8801
1.8658
1.8440
1.8208
1.8030
1.7855
1.7672
1.6643
1.6475
1.6437
1.6385
1.6276
1.6154
1.6129
1.5999
1.3774
1.3269
4.33
1.0000
1.0364
3.0596
1.0446
1.0593
1.0570
2.1078
2.3410
2.1367
3.1250
3.1790
[rel]
[ppm]
Chemical Shift (ppm)

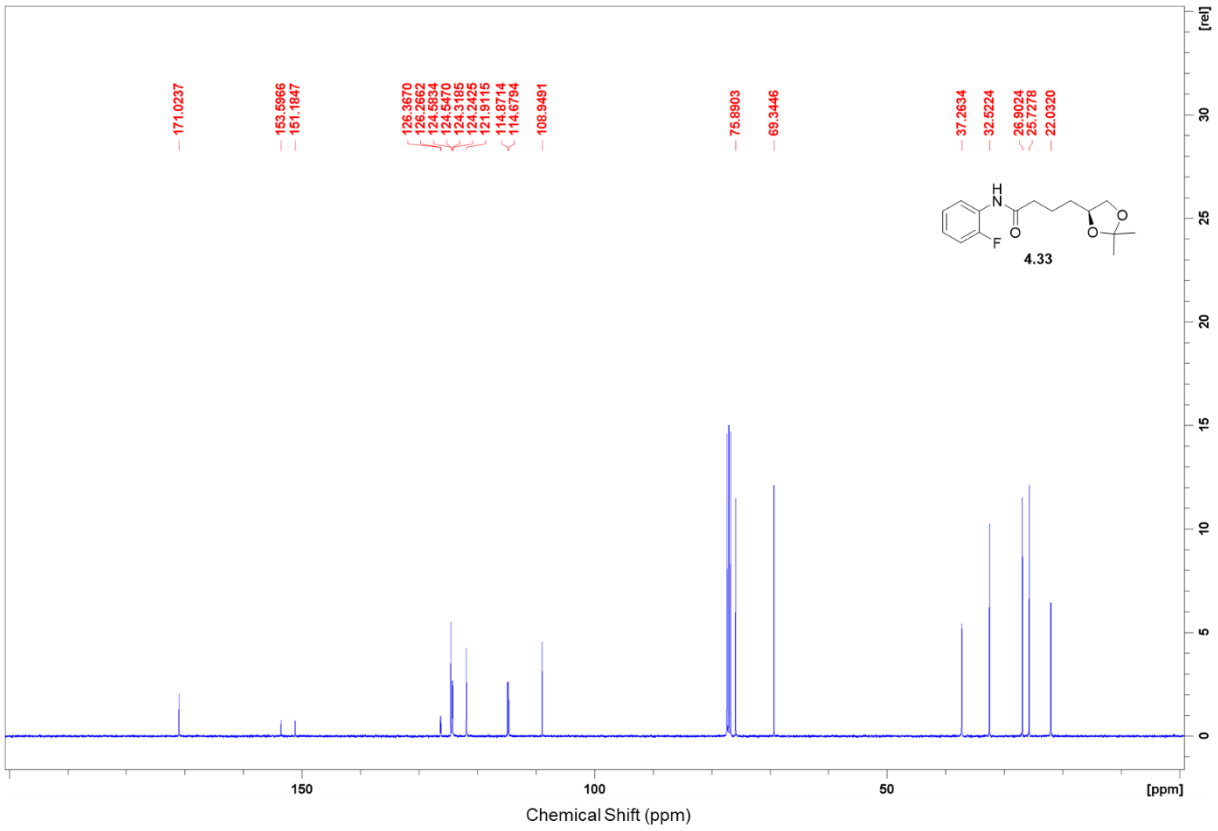
171.0237
153.5966
151.1847
126.3670
126.2662
124.5834
124.5470
124.3185
124.2425
121.9115
114.8714
114.6794
108.9491
75.8903
69.3446
37.2634
32.5224
26.9024
25.7278
22.0320
4.33
[rel]
[ppm]
Chemical Shift (ppm)

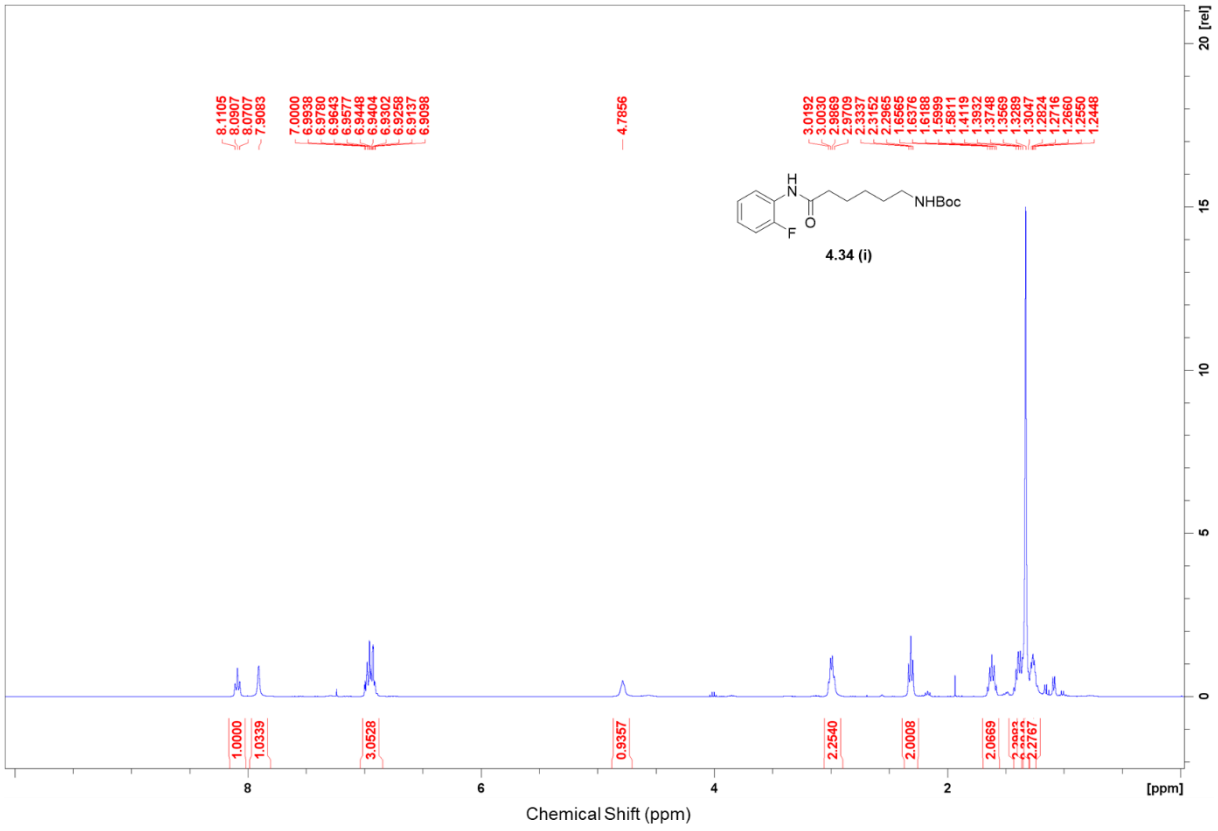
8.1105
8.0907
8.0707
7.9083
7.0000
6.9938
6.9780
6.9643
6.9577
6.9448
6.9404
6.9302
6.9258
6.9137
6.9098
4.7856
3.0192
3.0030
2.9869
2.9709
2.3337
2.3152
2.2985
1.6565
1.6376
1.6198
1.5989
1.5811
1.4119
1.3932
1.3748
1.3569
1.3289
1.3047
1.2824
1.2716
1.2660
1.2550
1.2448
NHBoc
4.34 (i)
1.0000
1.0339
3.0528
0.9357
2.2540
2.0006
2.0669
2.2767
[rel]
[ppm]
Chemical Shift (ppm)

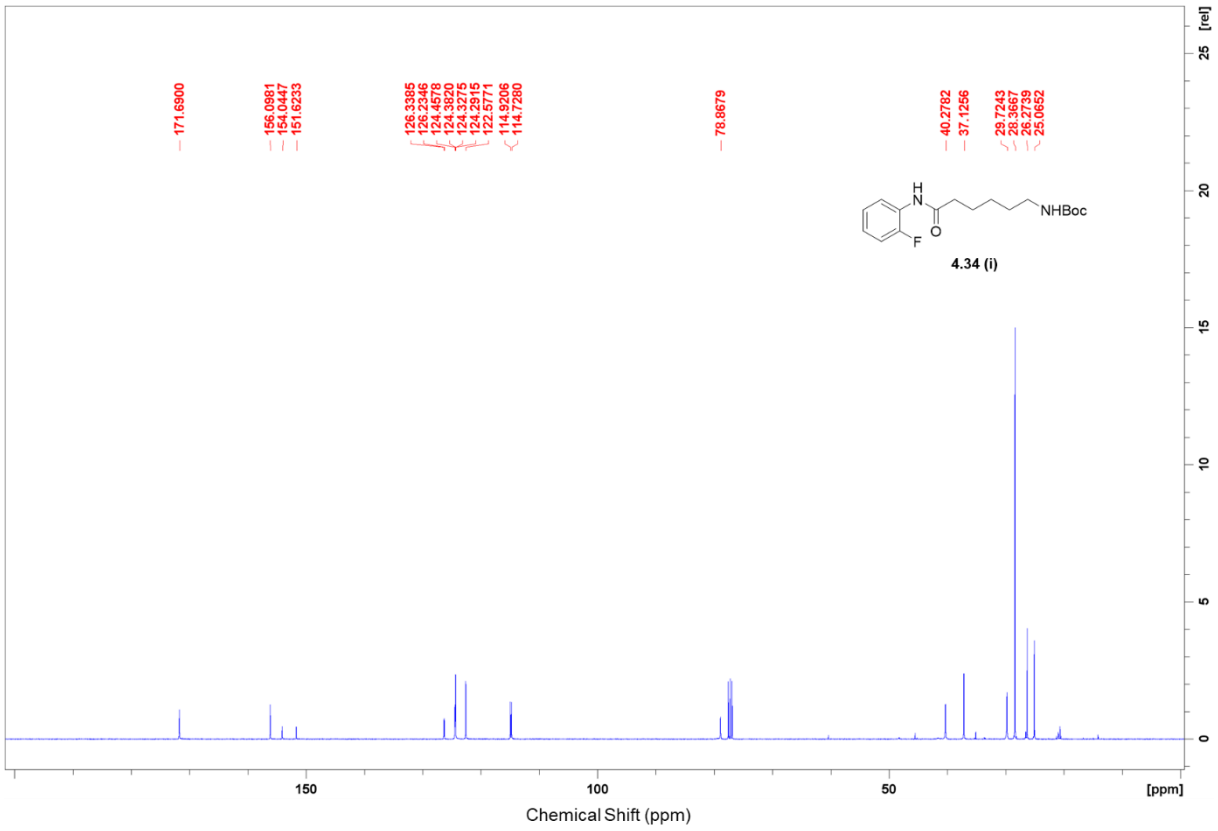
171.6900
156.0981
154.0447
151.6233
126.3385
126.2346
124.4578
124.4370
124.3275
124.2915
122.5771
114.9206
114.7280
78.8679
40.2782
37.1256
29.7243
28.3667
26.2739
25.0652
NHBoc
4.34 (i)
[rel]
[ppm]
Chemical Shift (ppm)

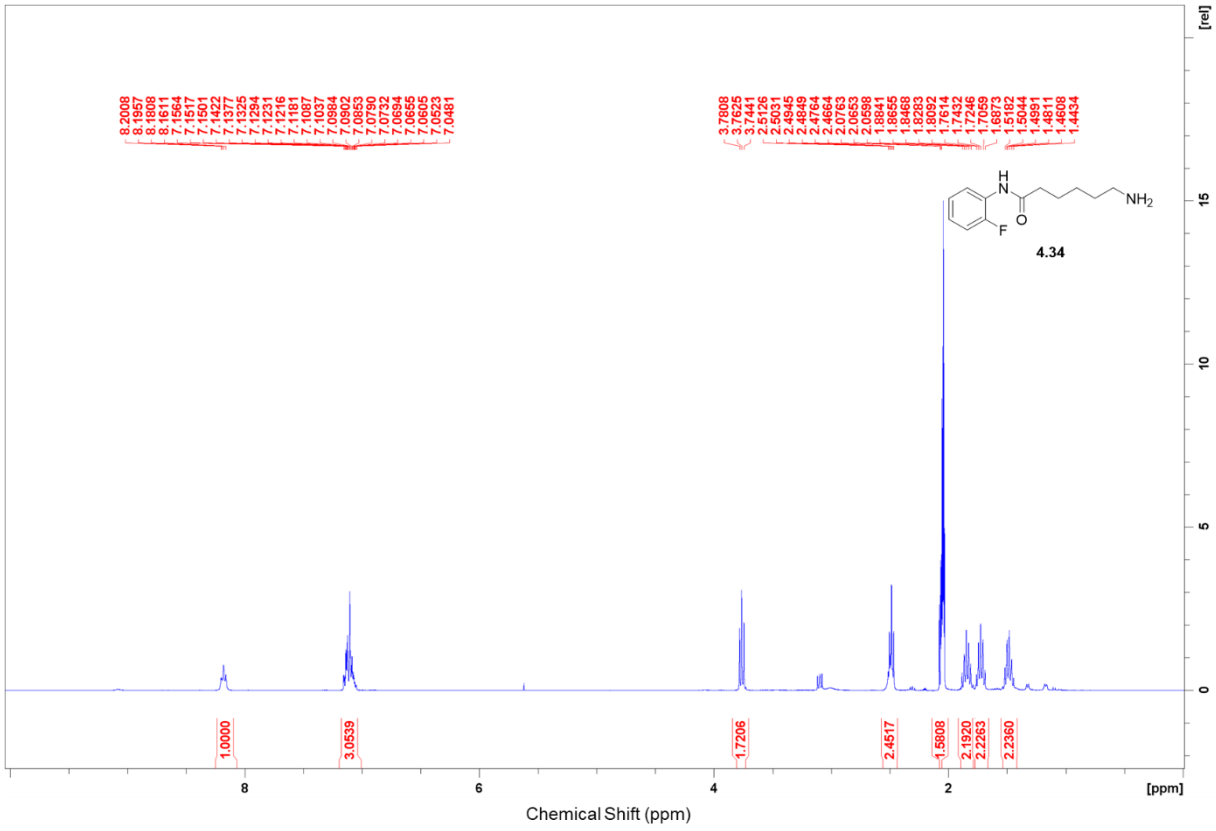
8.2008
8.1957
8.1808
8.1611
7.1564
7.1517
7.1501
7.1422
7.1377
7.1325
7.1234
7.1231
7.1216
7.1181
7.1087
7.1037
7.0984
7.0902
7.0853
7.0790
7.0732
7.0694
7.0655
7.0605
7.0523
7.0461
3.7808
3.7625
3.7441
2.5126
2.5031
2.4945
2.4849
2.4764
2.4664
2.0763
2.0653
2.0598
1.8841
1.8655
1.8468
1.8283
1.8092
1.7614
1.7432
1.7246
1.7059
1.6873
1.6512
1.5044
1.4991
1.4811
1.4608
1.4434
1.0000
3.0539
1.7206
2.4517
1.5808
2.1920
2.2263
2.2360
8
6
4
2
[ppm]
[rel]
15
10
5
0
Chemical Shift (ppm)
4.34

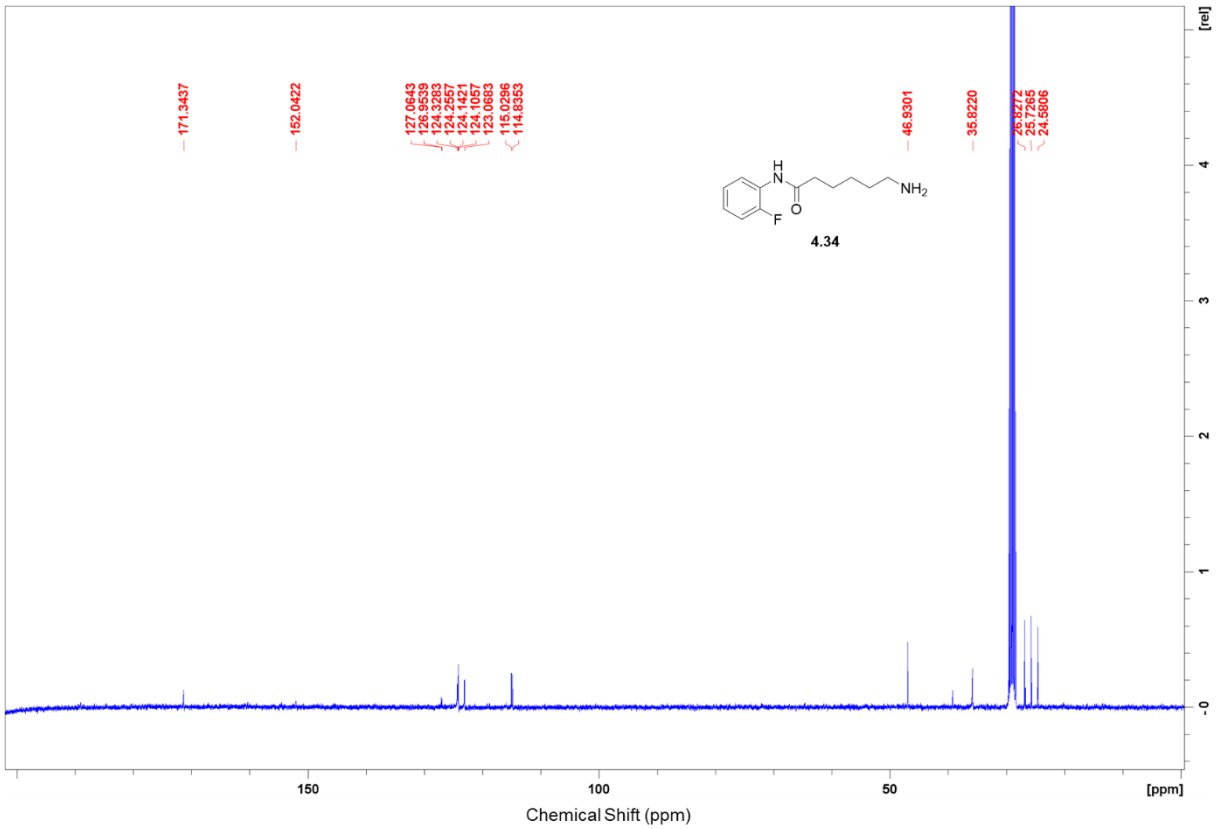
171.3437
152.0422
127.0643
126.9539
124.2263
124.2057
124.1421
124.1057
123.0683
115.0296
114.8353
46.9301
35.8220
26.8272
25.7265
24.5806
150
100
50
[ppm]
[rel]
4
3
2
1
-0
Chemical Shift (ppm)
4.34

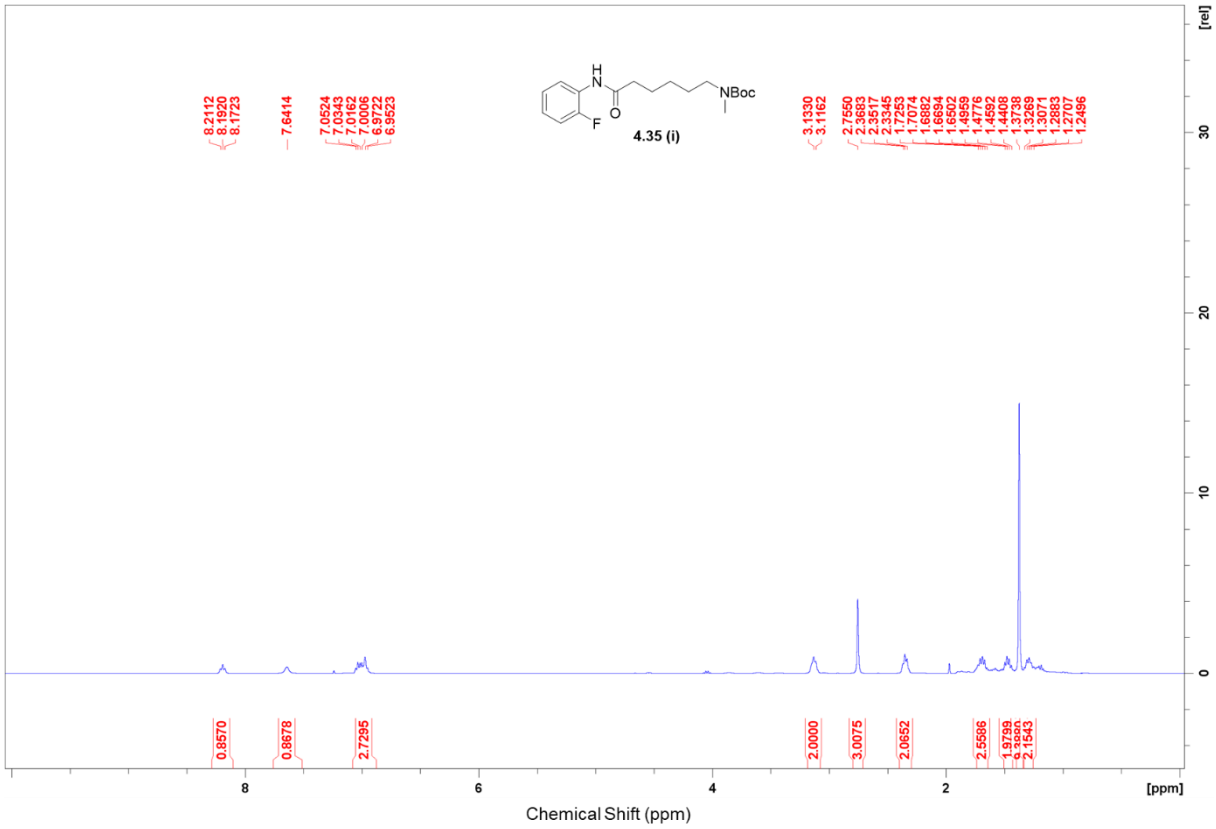
8.2112
8.1920
8.1723
7.6414
7.0524
7.0343
7.0162
7.0006
6.9722
6.9523
3.1330
3.1162
2.7550
2.3683
2.3517
2.3345
1.7253
1.7074
1.6892
1.6694
1.6502
1.4959
1.4776
1.4592
1.4408
1.3738
1.3269
1.3071
1.2883
1.2707
1.2496
4.35 (i)
NBoc
H
N
O
F
0.6570
0.8678
2.7295
2.0000
3.0075
2.0652
2.5586
1.9799
2.1543
[rel]
[ppm]
Chemical Shift (ppm)

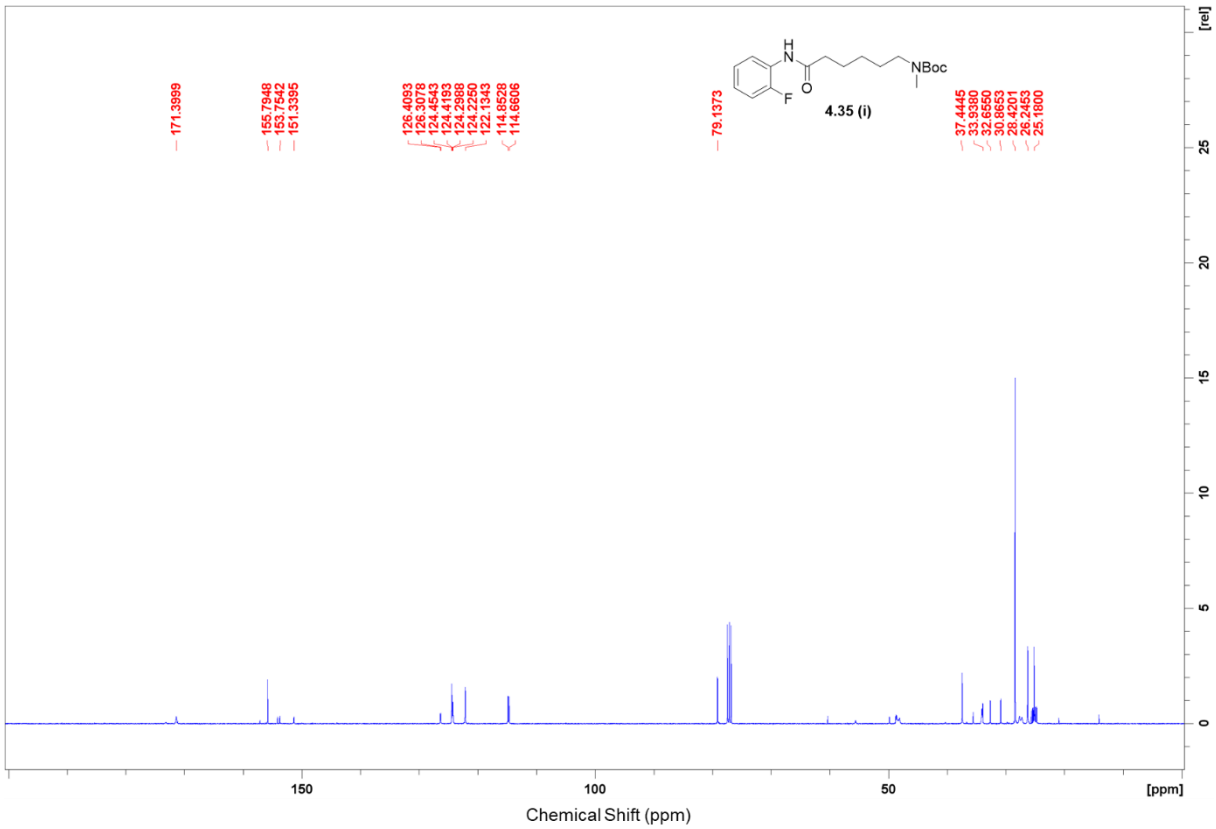
171.3999
155.7948
153.7542
151.3395
126.4083
126.3078
124.4543
124.4193
124.2988
124.2250
122.1343
114.8528
114.6606
79.1373
37.4445
33.9380
32.6550
30.8653
28.4201
26.2453
25.1600
4.35 (i)
NBoc
H
N
O
F
[rel]
[ppm]
Chemical Shift (ppm)

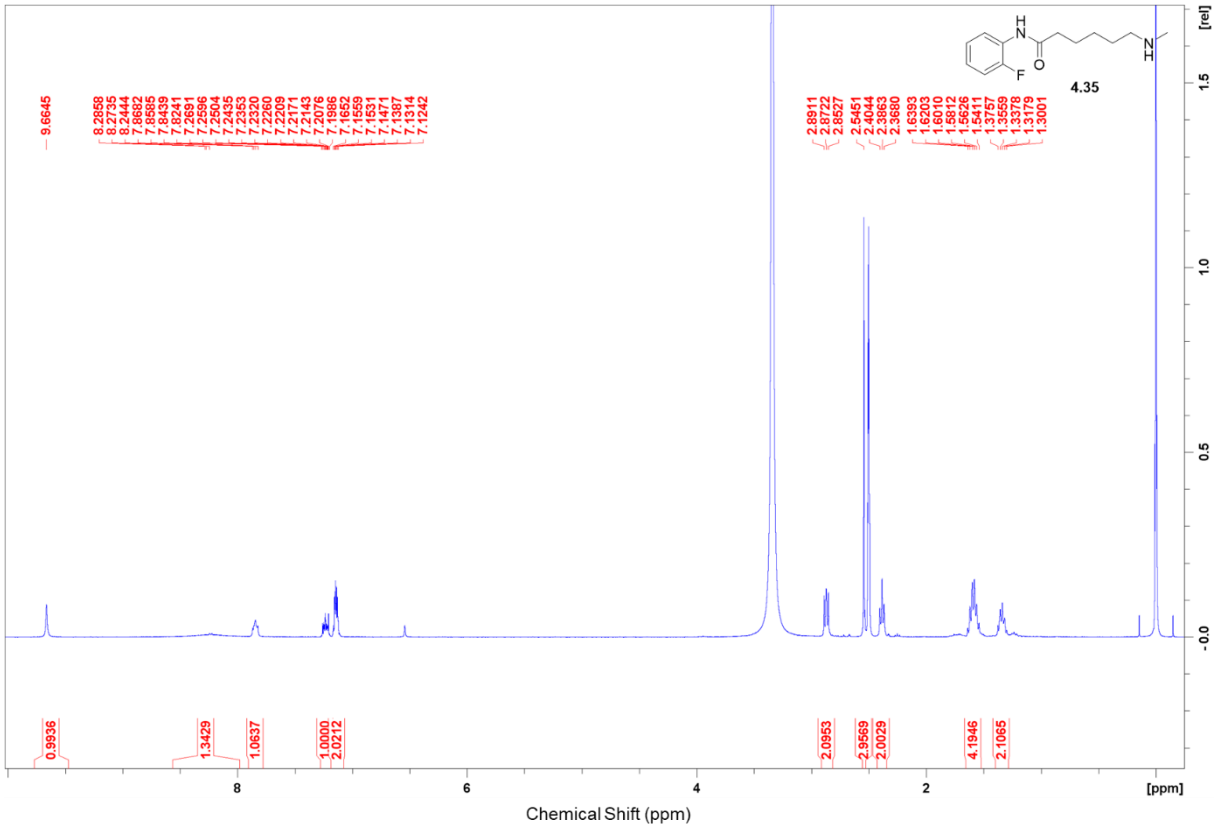
4.35
9.6645
8.2858
8.2735
8.2444
7.8682
7.8585
7.8439
7.8241
7.2691
7.2596
7.2504
7.2435
7.2353
7.2260
7.2209
7.2171
7.2143
7.2076
7.1986
7.1652
7.1559
7.1531
7.1471
7.1387
7.1314
7.1242
2.8911
2.8722
2.8527
2.5451
2.4044
2.3963
2.3680
1.6393
1.6203
1.6010
1.5812
1.5626
1.5411
1.3757
1.3559
1.3378
1.3179
1.3001
0.9936
1.3429
1.0637
1.0000
2.0212
2.0953
2.9569
2.0029
4.1946
2.1065
[rel]
[ppm]
Chemical Shift (ppm)

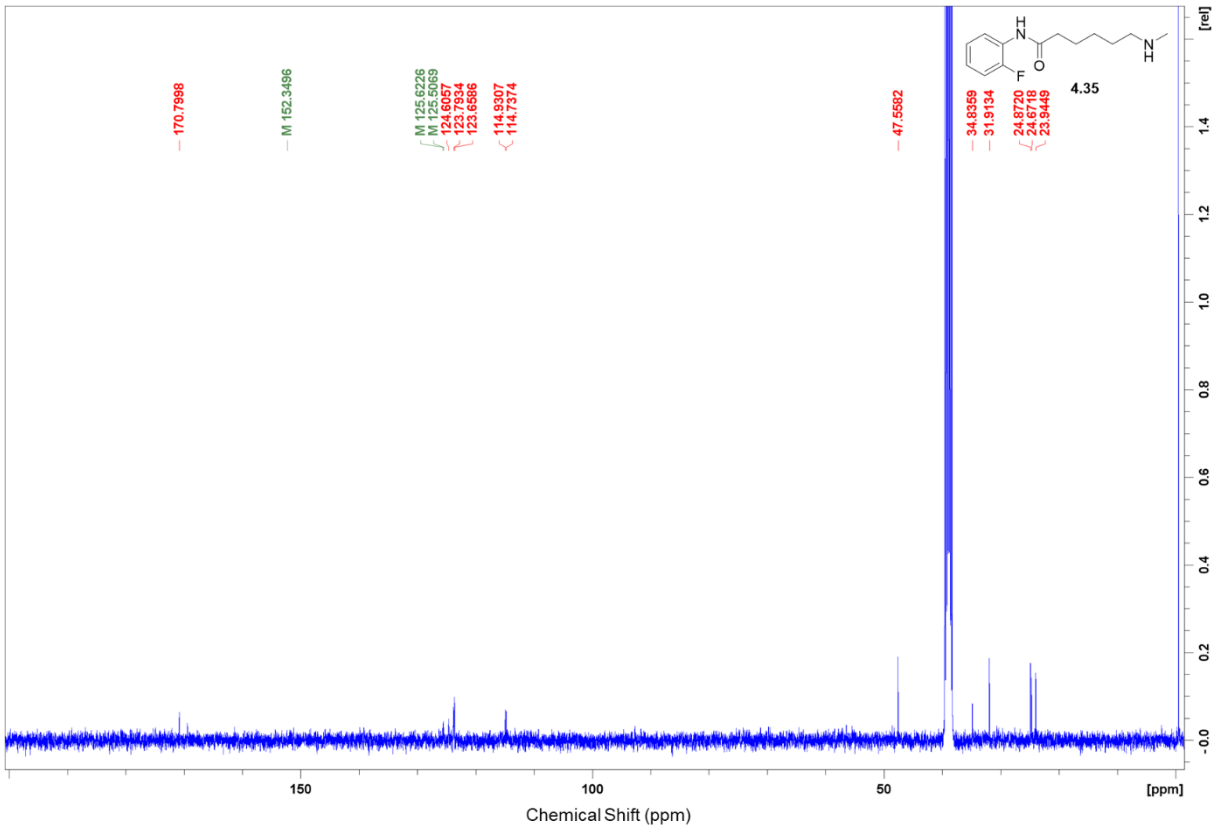
4.35
170.7988
M 152.3496
M 125.6226
M 125.5069
124.6057
123.7934
123.6586
114.9307
114.7374
47.5582
34.8359
31.9134
24.8720
24.6718
23.9449
[rel]
[ppm]
Chemical Shift (ppm)

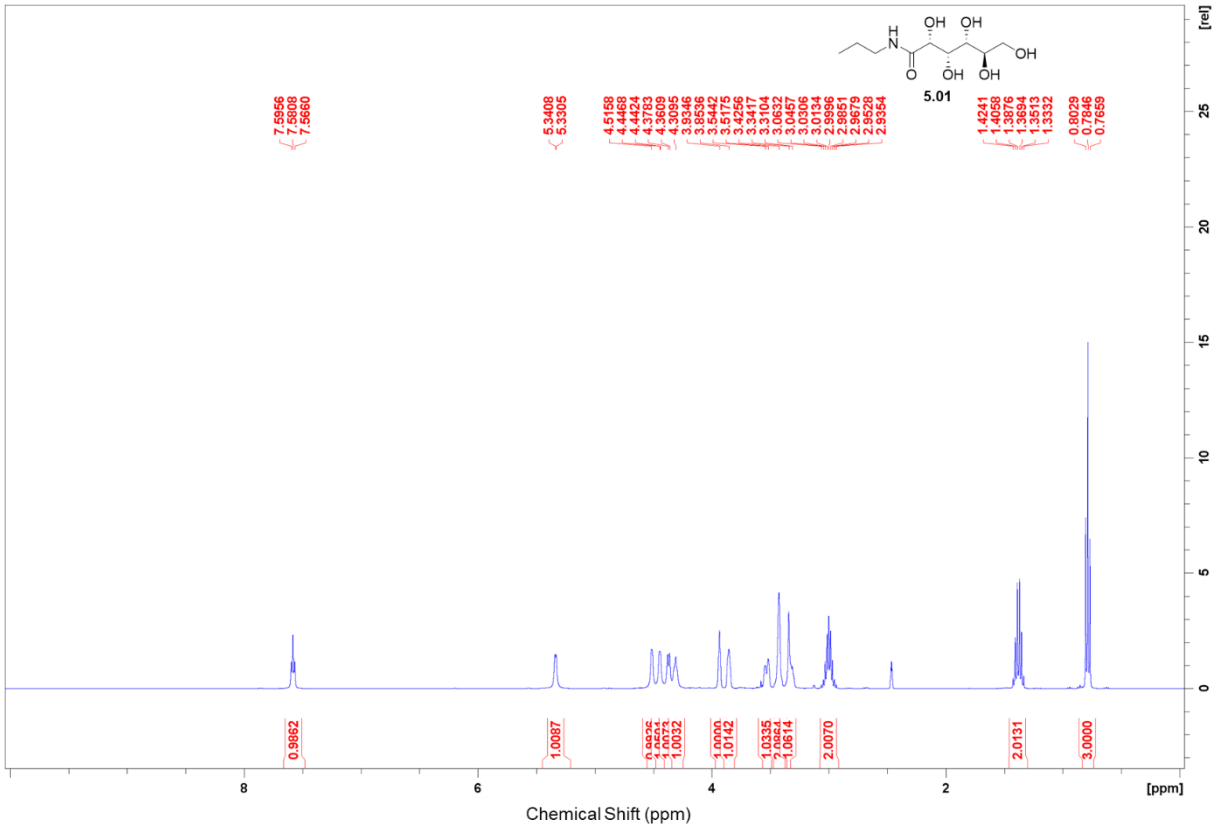
5.01
7.5956
7.5808
7.5660
5.3408
5.3305
4.5158
4.4468
4.4424
4.3783
4.3609
4.3095
4.3046
3.8536
3.5442
3.5175
3.4256
3.3417
3.3104
3.0632
3.0457
3.0306
3.0134
2.9896
2.9651
2.9579
2.9528
2.9354
1.4241
1.4076
1.3878
1.3684
1.3513
1.3332
0.8029
0.7846
0.7659
0.9862
1.0087
1.0335
2.0131
3.0000
2.0070
Chemical Shift (ppm)
[rel]
[ppm]

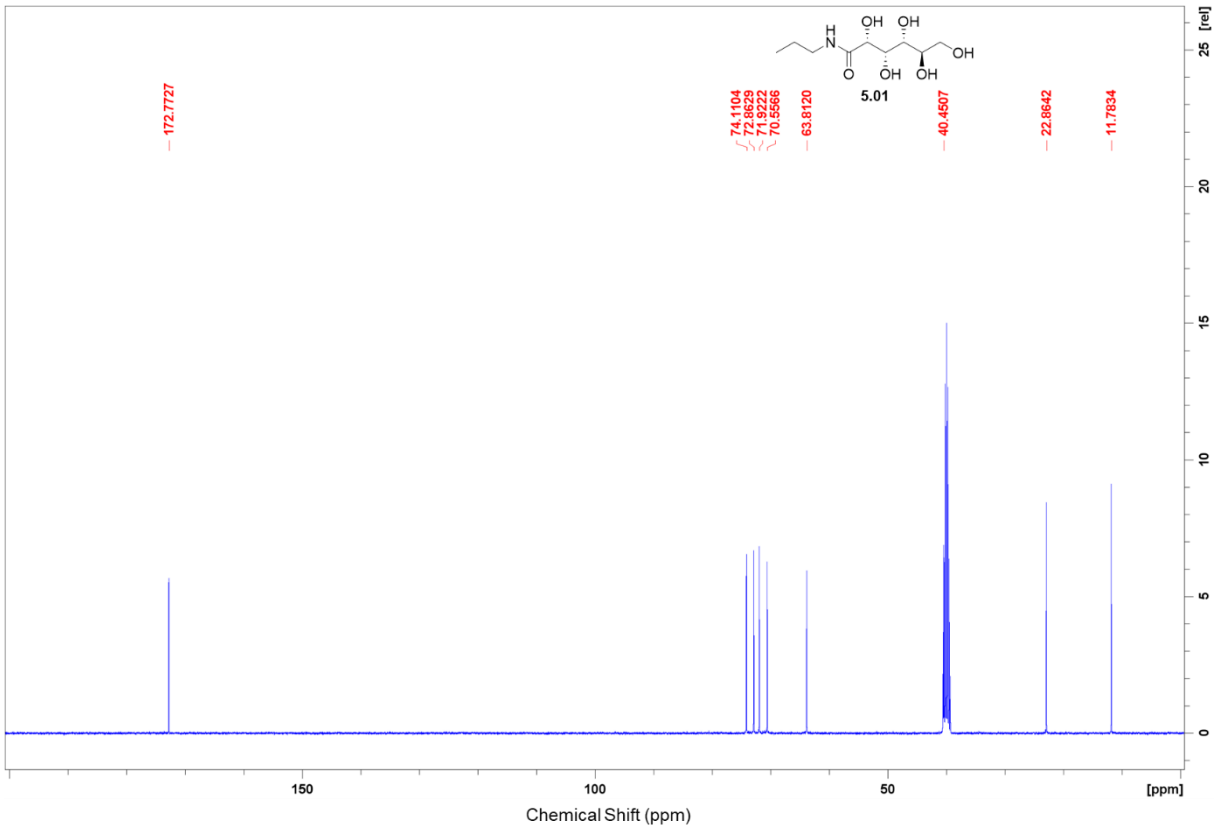
5.01
172.7727
74.1104
72.8629
71.9222
70.5566
63.8120
40.4607
22.8642
11.7834
Chemical Shift (ppm)
[rel]
[ppm]

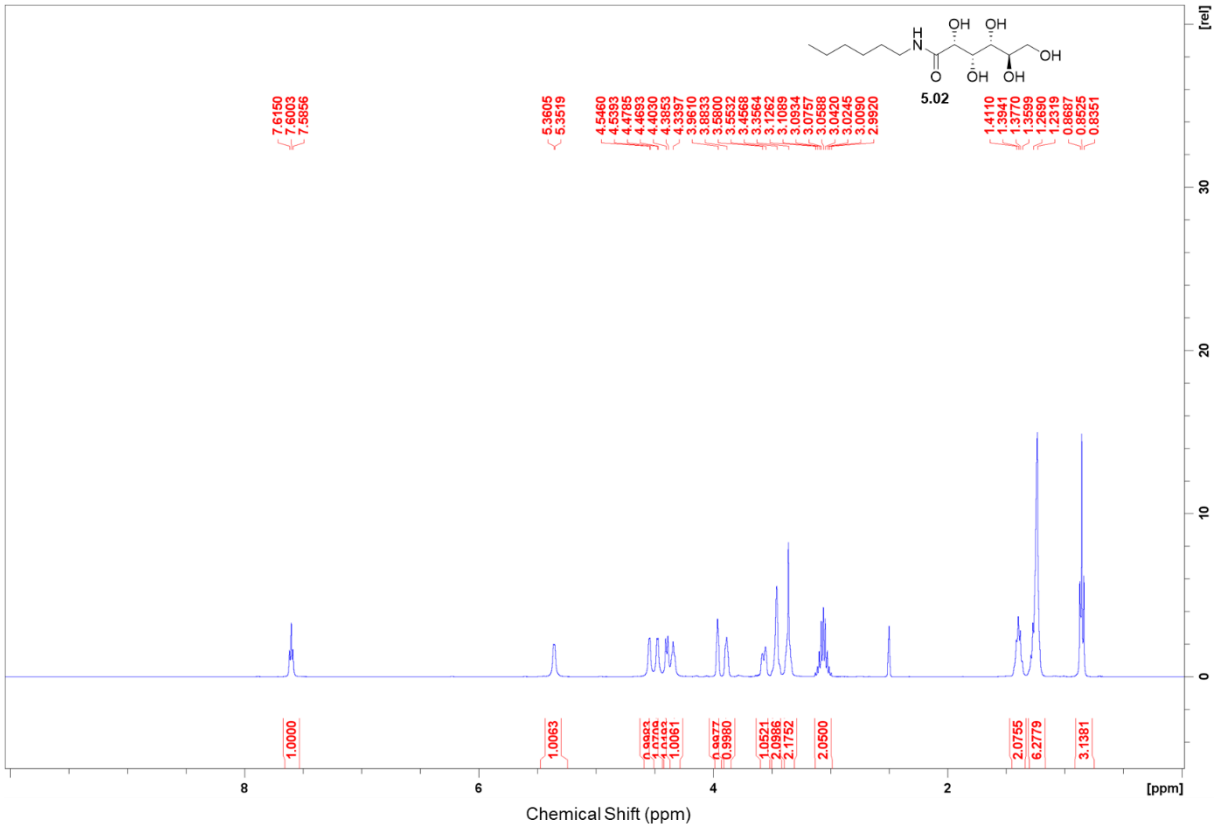
5.02
7.6150
7.6003
7.5856
5.3605
5.3519
4.5460
4.5393
4.4785
4.4693
4.4030
4.3853
4.3397
3.9610
3.8833
3.8800
3.4552
3.4468
3.3564
3.1262
3.1089
3.0934
3.0757
3.0588
3.0420
3.0245
3.0090
2.9920
1.4110
1.3941
1.3770
1.3589
1.2690
1.2319
0.8687
0.8525
0.8351
1.0000
1.0063
0.9980
1.0521
2.0988
2.1752
2.0500
2.0755
6.2779
3.1381
[rel]
[ppm]
Chemical Shift (ppm)

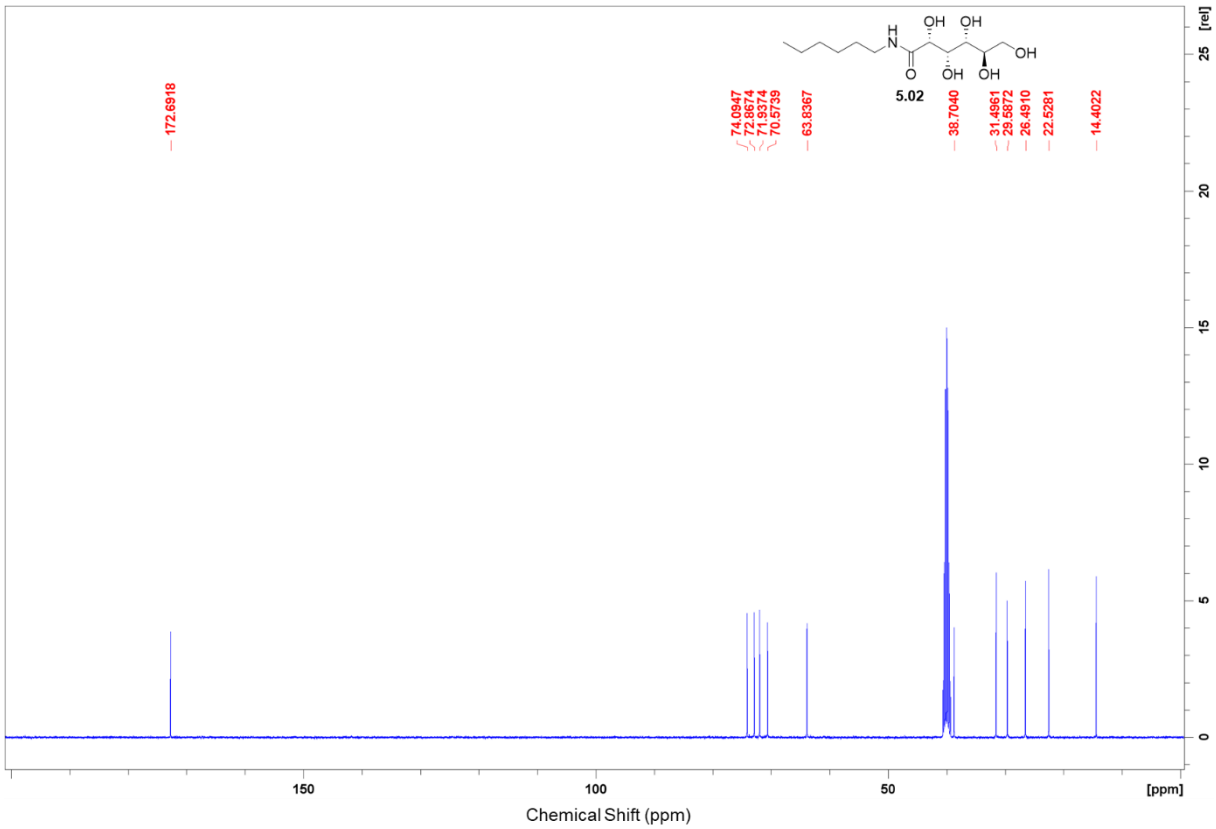
5.02
172.6918
74.0947
72.8674
71.9374
70.5739
63.8367
38.7040
31.4961
29.5872
28.4910
22.5281
14.4022
[rel]
[ppm]
Chemical Shift (ppm)

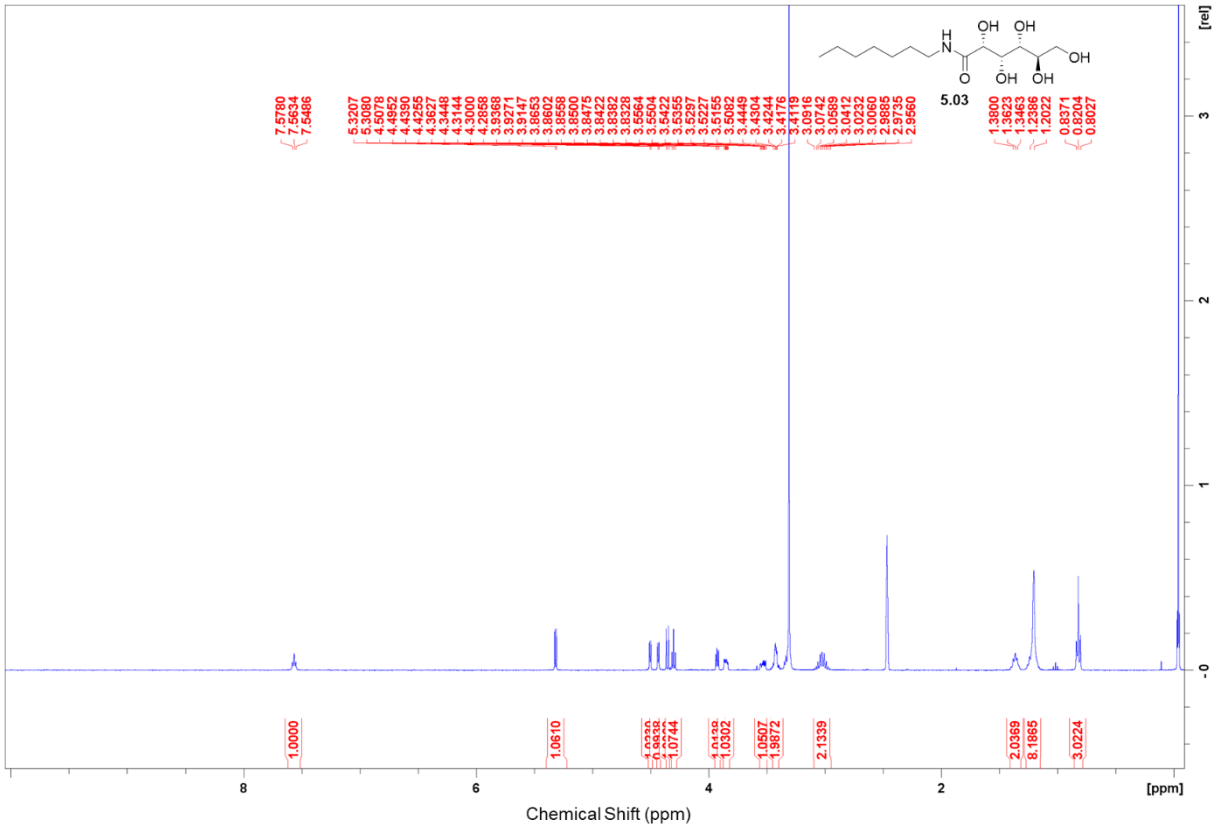
5.03
Chemical Shift (ppm)
[rel]
[ppm]

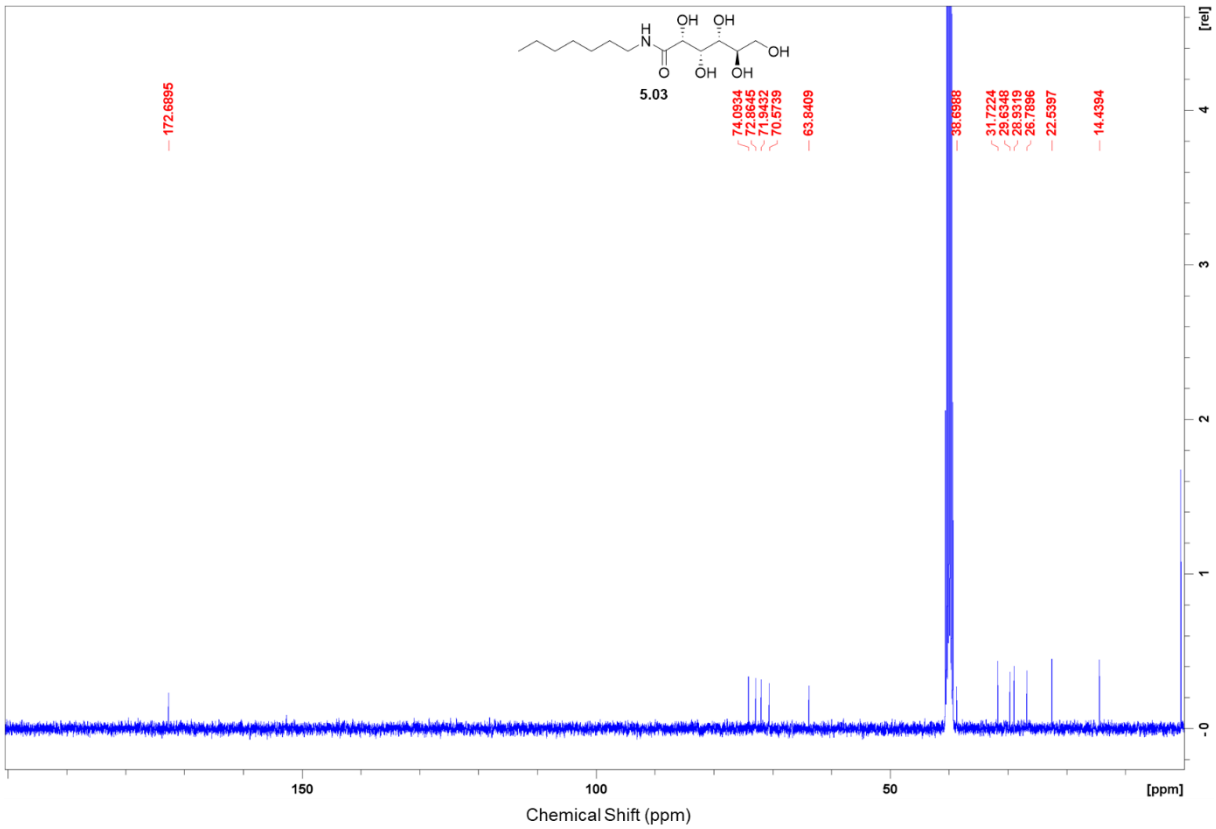
5.03
Chemical Shift (ppm)
[rel]
[ppm]

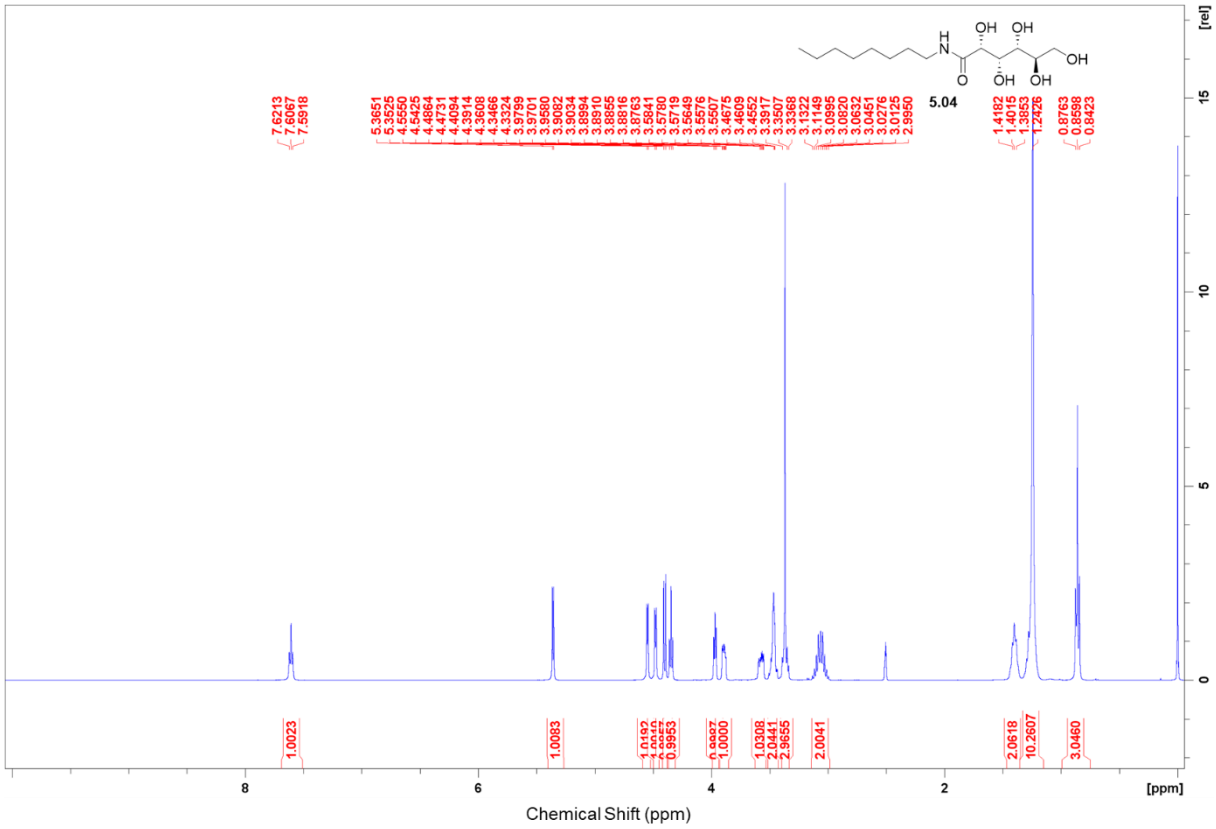
5.04
Chemical Shift (ppm)

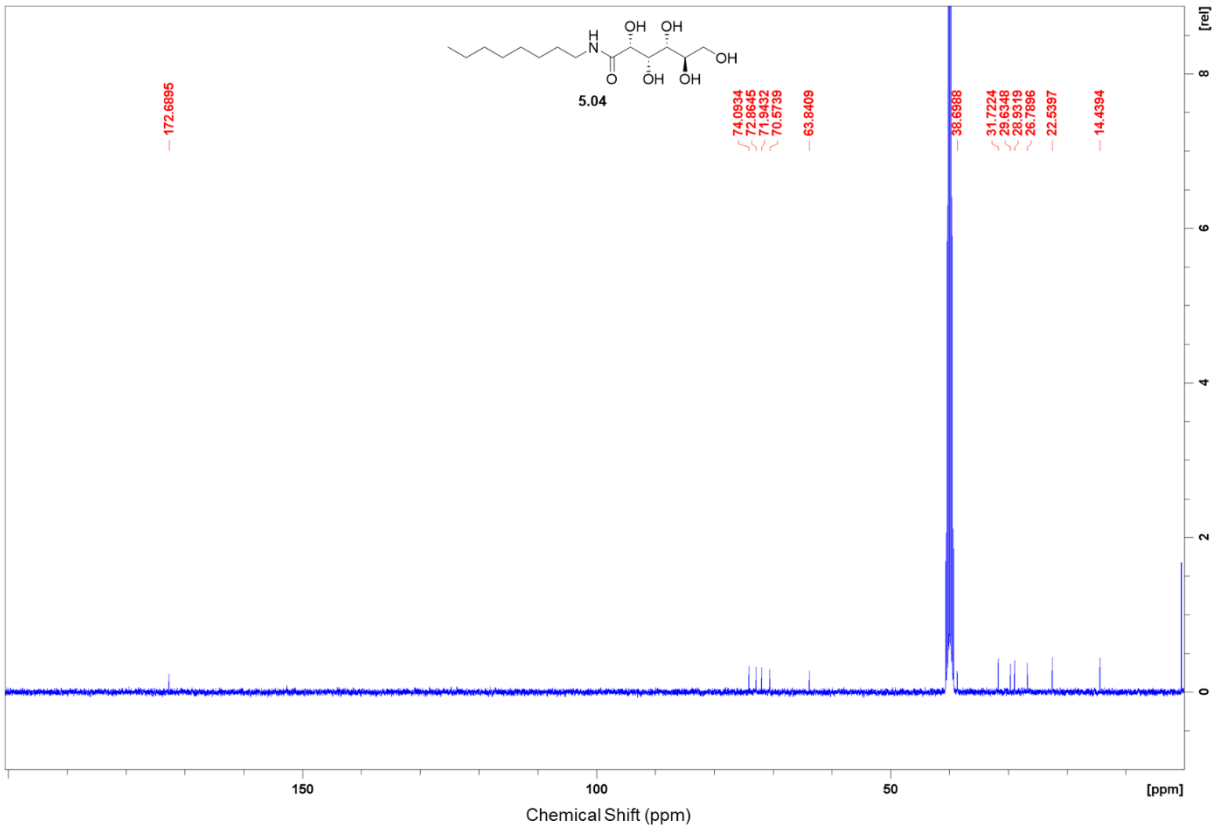
5.04
Chemical Shift (ppm)

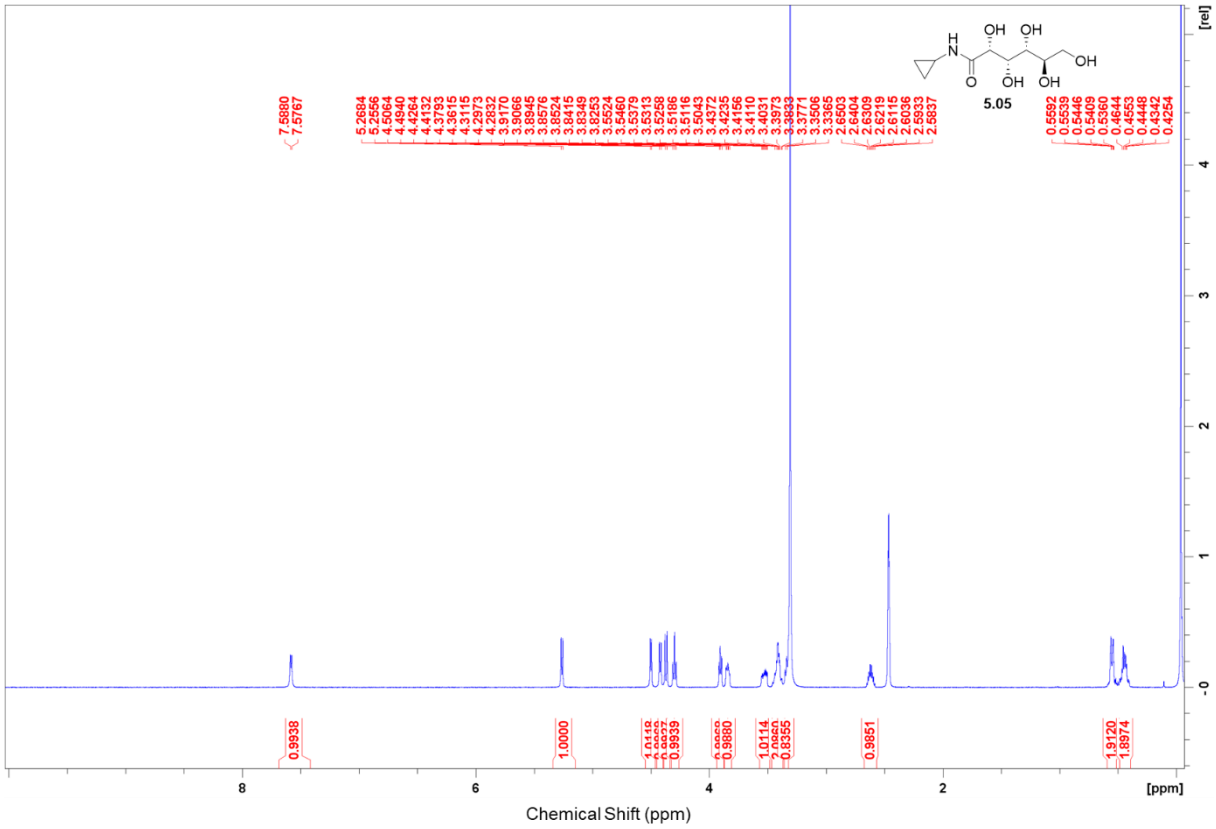
5.05
Chemical Shift (ppm)

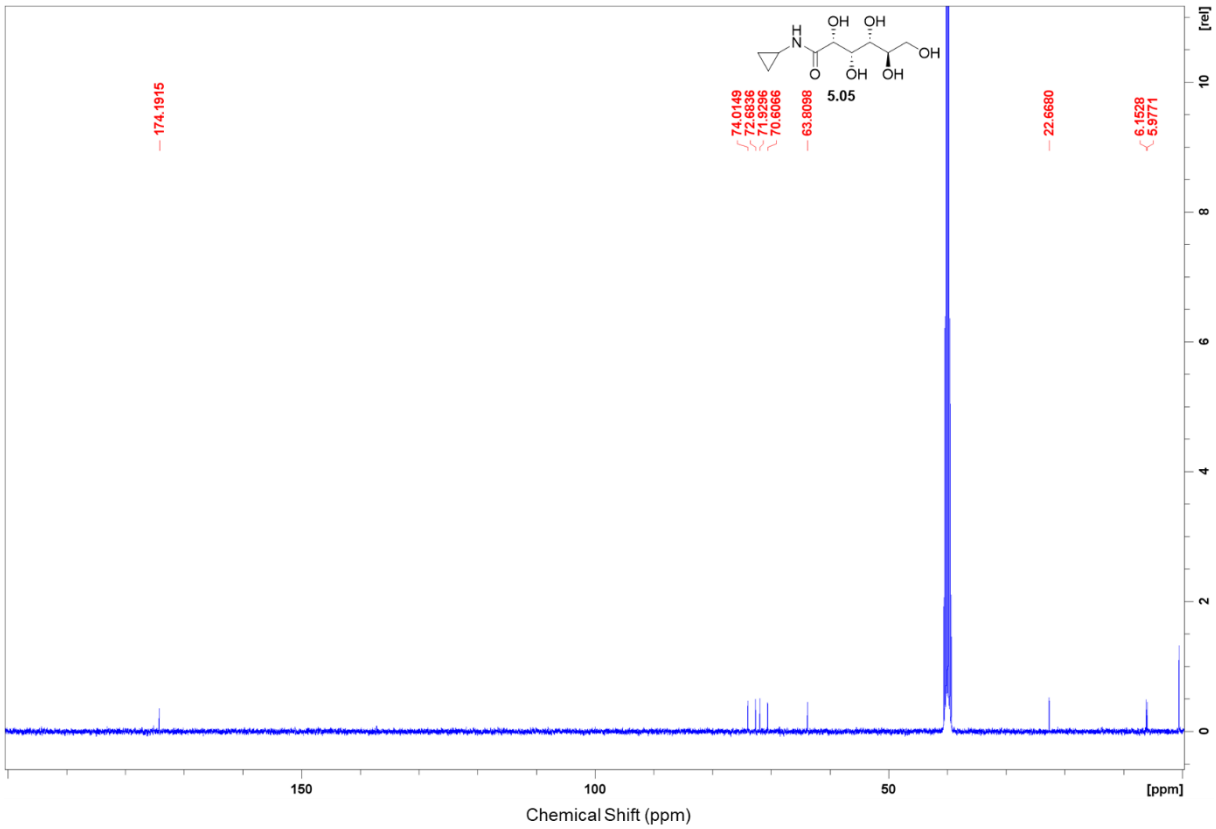
5.05
Chemical Shift (ppm)

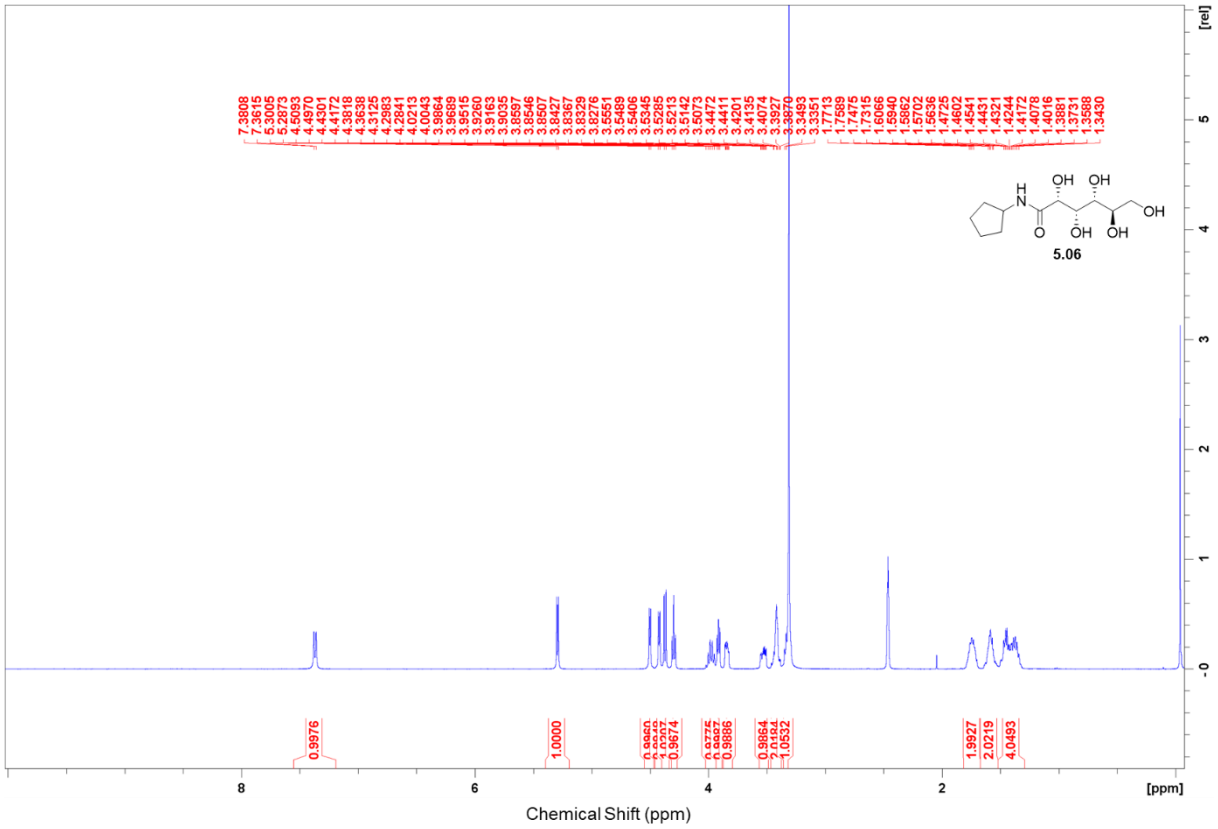
7.3808
7.3615
5.3005
5.2873
4.4993
4.4970
4.4301
4.4172
4.3818
4.3638
4.3125
4.2983
4.2841
4.0213
4.0043
3.9864
3.9689
3.9555
3.9260
3.9163
3.9035
3.8597
3.8546
3.8507
3.8427
3.8367
3.8329
3.8276
3.5551
3.5489
3.5406
3.5345
3.5295
3.5213
3.5142
3.5073
3.4472
3.4411
3.4201
3.4135
3.4074
3.3927
3.3870
3.3493
3.3351
3.3253
1.7569
1.7475
1.7315
1.6066
1.5940
1.5862
1.5702
1.5636
1.4725
1.4602
1.4541
1.4431
1.4321
1.4244
1.4172
1.4078
1.4016
1.3881
1.3731
1.3588
1.3430
OH
OH
OH
OH
OH
H
N
O
5.06
0.9976
1.0000
0.9674
0.9886
0.9864
2.0194
1.0532
1.9927
2.0219
4.0493
[rel]
[ppm]
Chemical Shift (ppm)

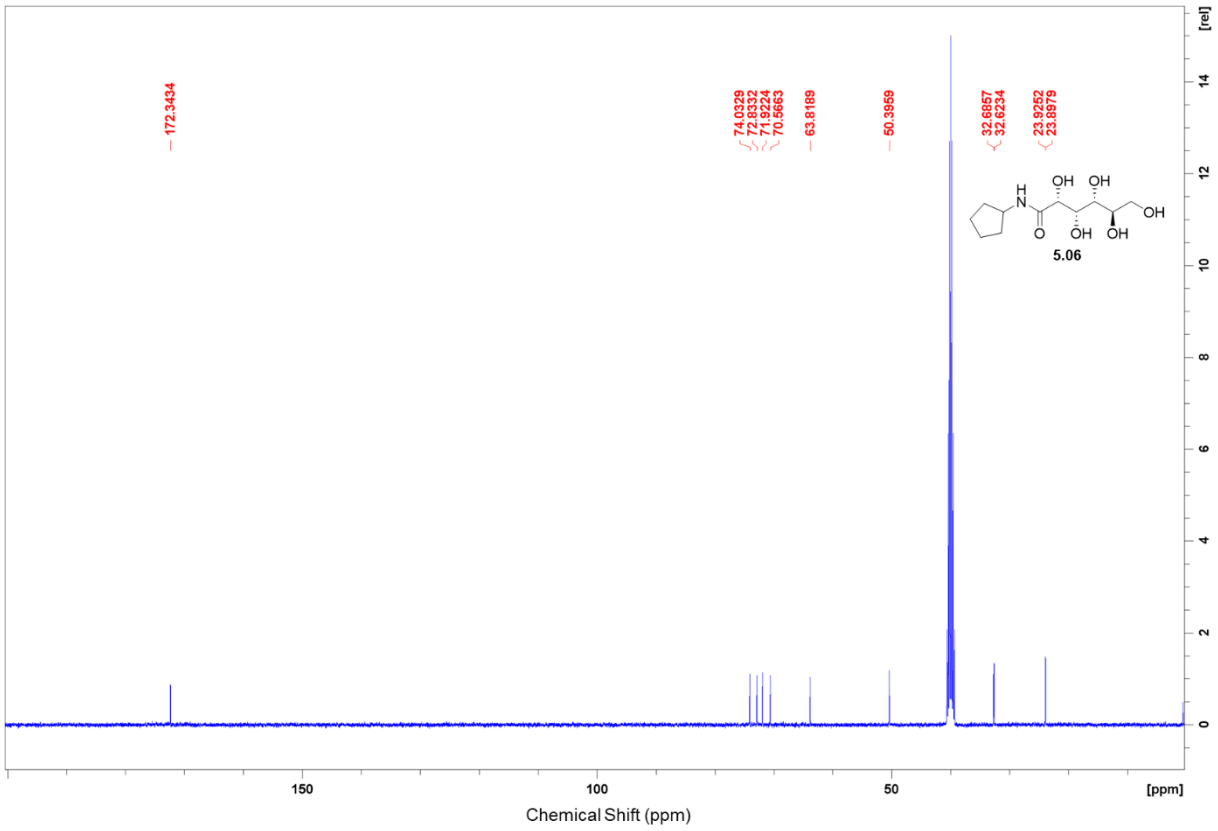
172.3434
74.0329
72.8332
71.9224
70.5663
63.8189
50.3959
32.6857
32.6234
23.9252
23.8979
OH
OH
OH
OH
OH
H
N
O
5.06
[rel]
[ppm]
Chemical Shift (ppm)

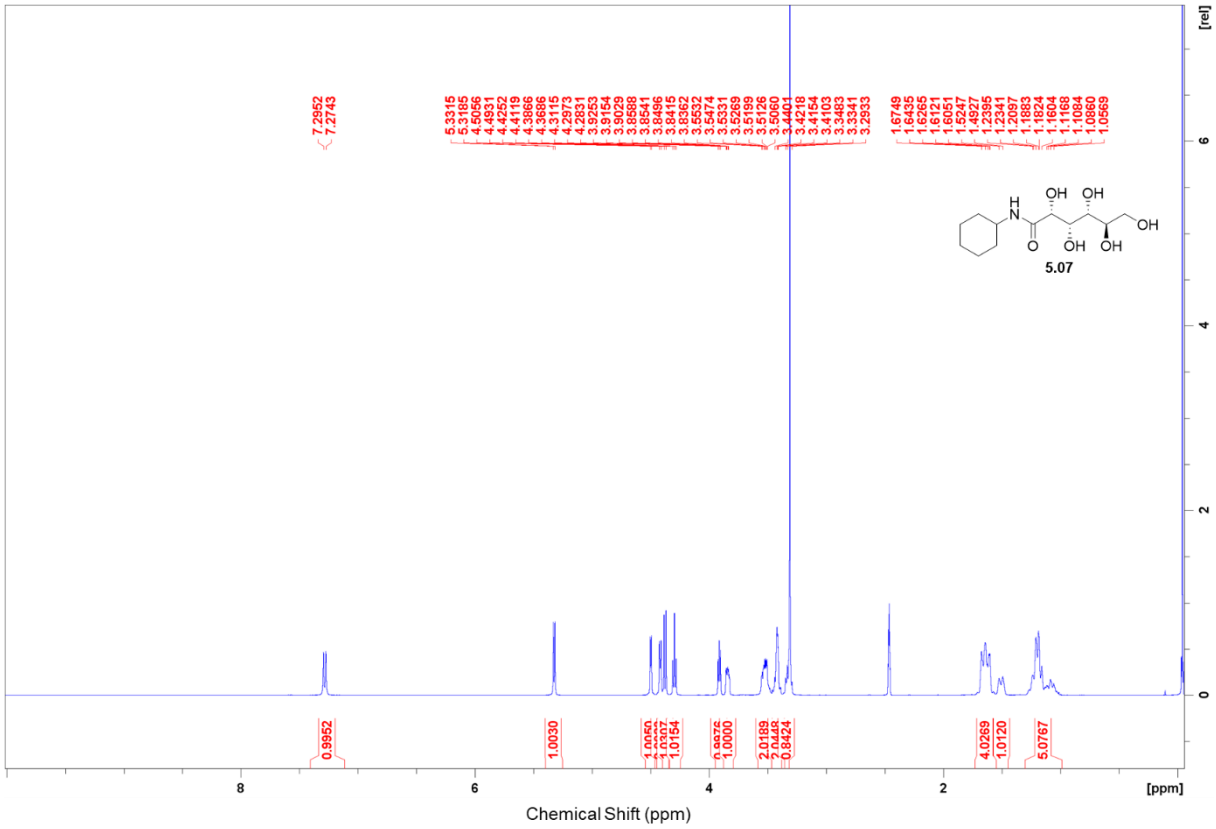
7.2952
7.2743
5.3315
5.3195
4.5056
4.4931
4.4252
4.4119
4.3866
4.3686
4.3115
4.2973
4.2831
3.9253
3.9154
3.9029
3.8888
3.8541
3.8496
3.8415
3.8362
3.5532
3.5474
3.5331
3.5269
3.5199
3.5126
3.5060
3.4401
3.4278
3.4154
3.4103
3.3483
3.3341
3.2933
1.6749
1.6435
1.6265
1.6121
1.6051
1.5247
1.4927
1.2395
1.2341
1.2097
1.1883
1.1624
1.1494
1.1168
1.1084
1.0860
1.0569
0.9952
1.0030
1.0050
1.0037
1.0154
0.8826
1.0000
2.0189
2.0448
0.8424
4.0269
1.0120
5.0767
OH
OH
OH
OH
OH
H
N
O
5.07
[rel]
[ppm]
Chemical Shift (ppm)

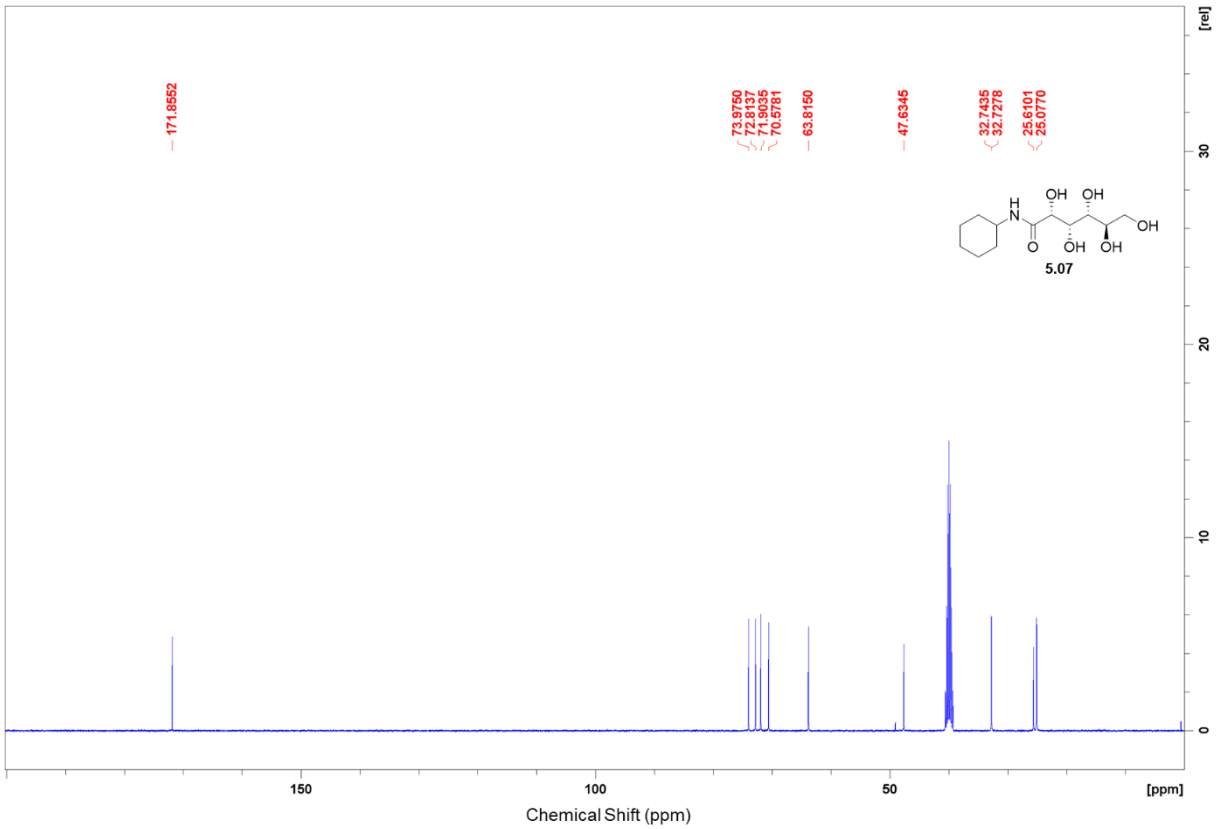
171.8552
73.9750
72.8137
71.9035
70.5781
63.8150
47.6345
32.7435
32.7278
25.6101
25.0770
OH
OH
OH
OH
OH
H
N
O
5.07
[rel]
[ppm]
Chemical Shift (ppm)

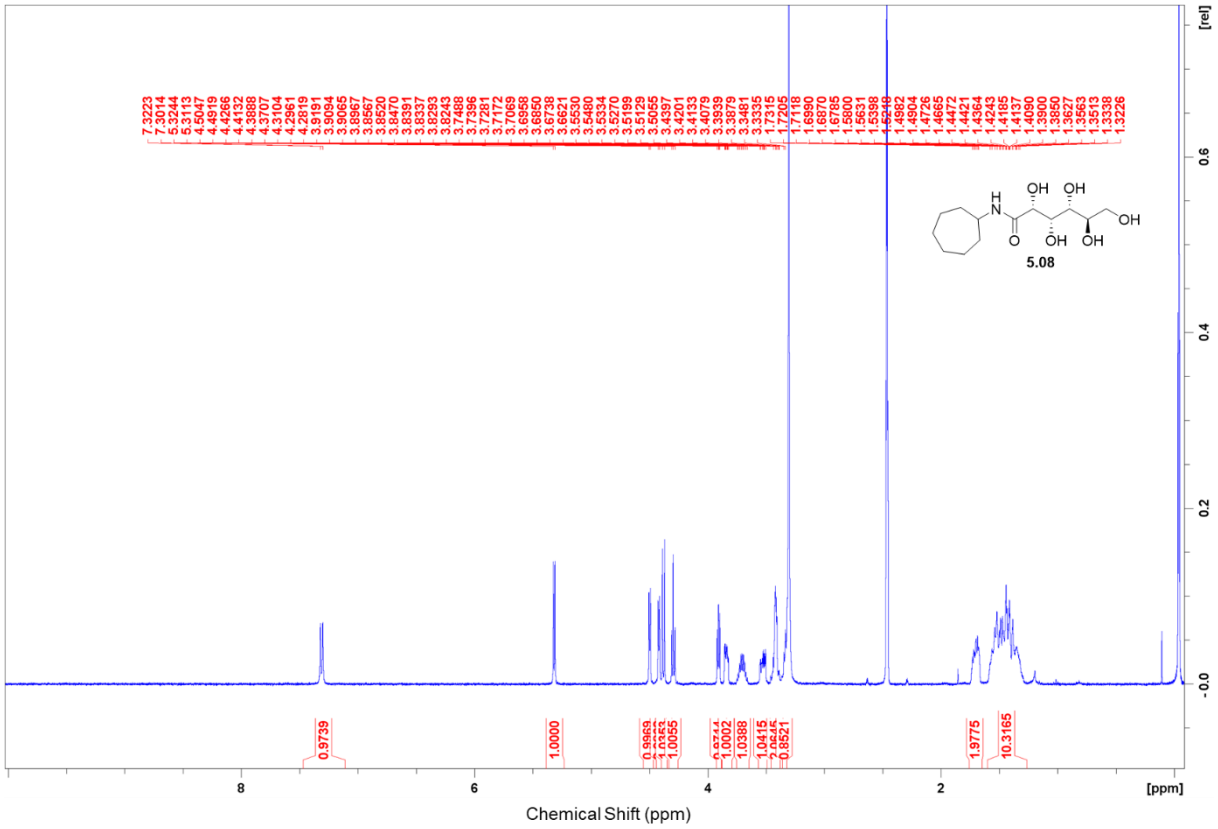
7.3223
7.3014
5.3244
5.3113
4.5047
4.4919
4.4796
4.4132
4.3888
4.3707
4.3104
4.2961
4.2819
3.9191
3.9094
3.9065
3.8967
3.8567
3.8520
3.8470
3.8391
3.8337
3.8293
3.8243
3.7488
3.7396
3.7281
3.7172
3.7069
3.6958
3.6850
3.6738
3.6621
3.5550
3.5480
3.5334
3.5270
3.5199
3.5129
3.5055
3.4397
3.4201
3.4133
3.4079
3.3939
3.3879
3.3491
3.3345
1.7315
1.7205
1.7118
1.6990
1.6870
1.6785
1.5800
1.5631
1.5398
1.5240
1.4962
1.4904
1.4726
1.4665
1.4472
1.4421
1.4364
1.4243
1.4185
1.4137
1.4090
1.3900
1.3850
1.3627
1.3563
1.3513
1.3338
1.3228
OH
OH
OH
OH
OH
N
H
O
5.08
0.9739
1.0000
1.0002
1.0388
1.0415
1.9775
10.3165
[rel]
[ppm]
Chemical Shift (ppm)

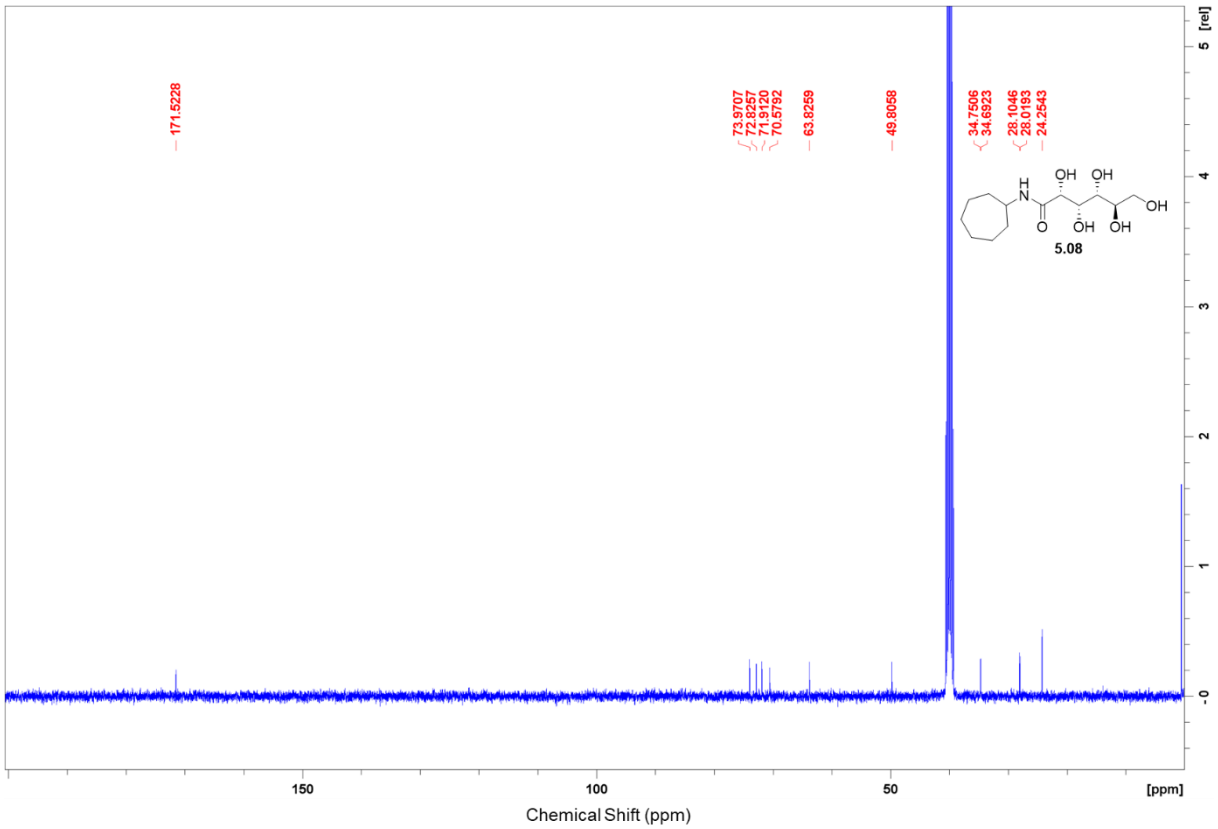
171.5228
73.9707
72.8257
71.9120
70.5792
63.8259
49.8058
34.7506
34.6923
28.1046
28.0193
24.2543
OH
OH
OH
OH
OH
N
H
O
5.08
[rel]
[ppm]
Chemical Shift (ppm)

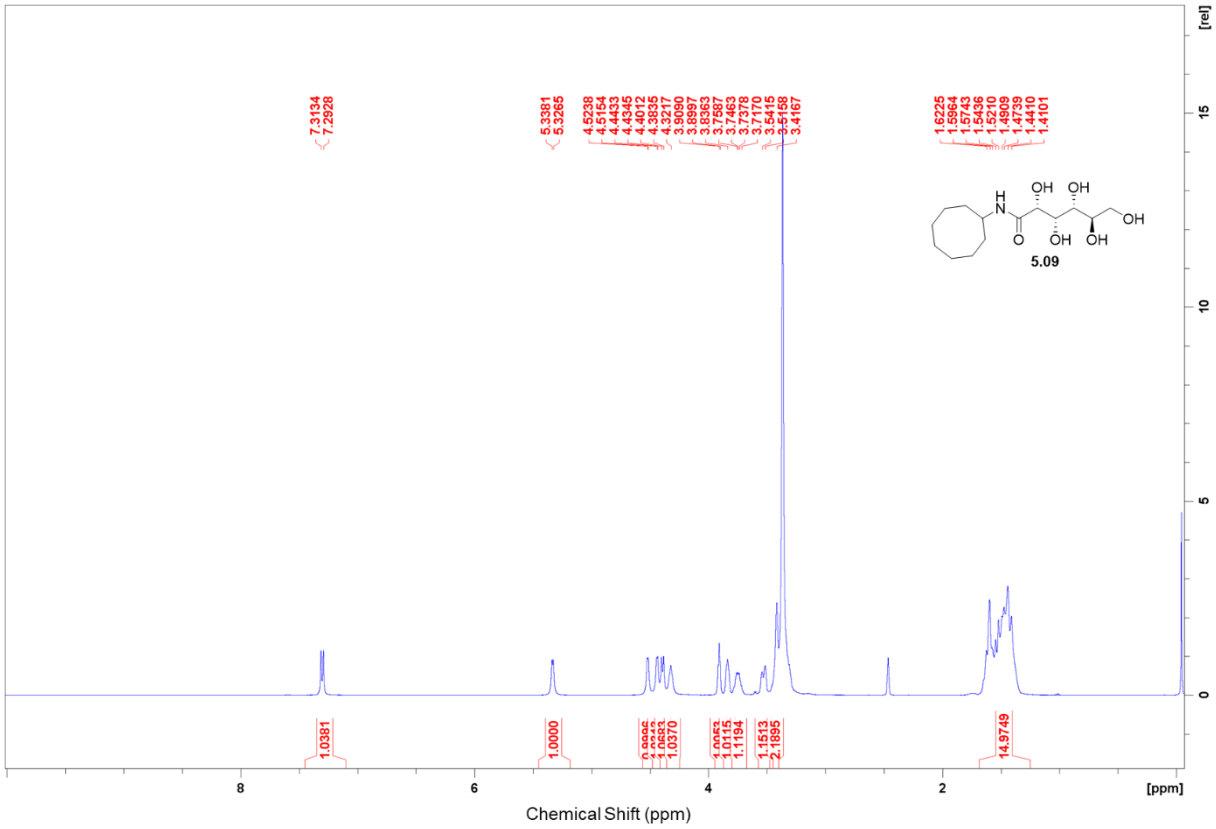
7.3134
7.2928
5.3381
5.3265
4.5238
4.5154
4.4433
4.4345
4.4012
4.3835
4.3217
3.9090
3.8997
3.8363
3.7587
3.7463
3.7178
3.7170
3.5415
3.5158
3.4167
1.6225
1.5964
1.5743
1.5436
1.5210
1.4909
1.4739
1.4410
1.4101
OH
OH
OH
OH
OH
H
N
O
5.09
1.0381
1.0000
1.0370
1.0115
1.1194
1.1513
2.1895
14.9749
[rel]
[ppm]
Chemical Shift (ppm)

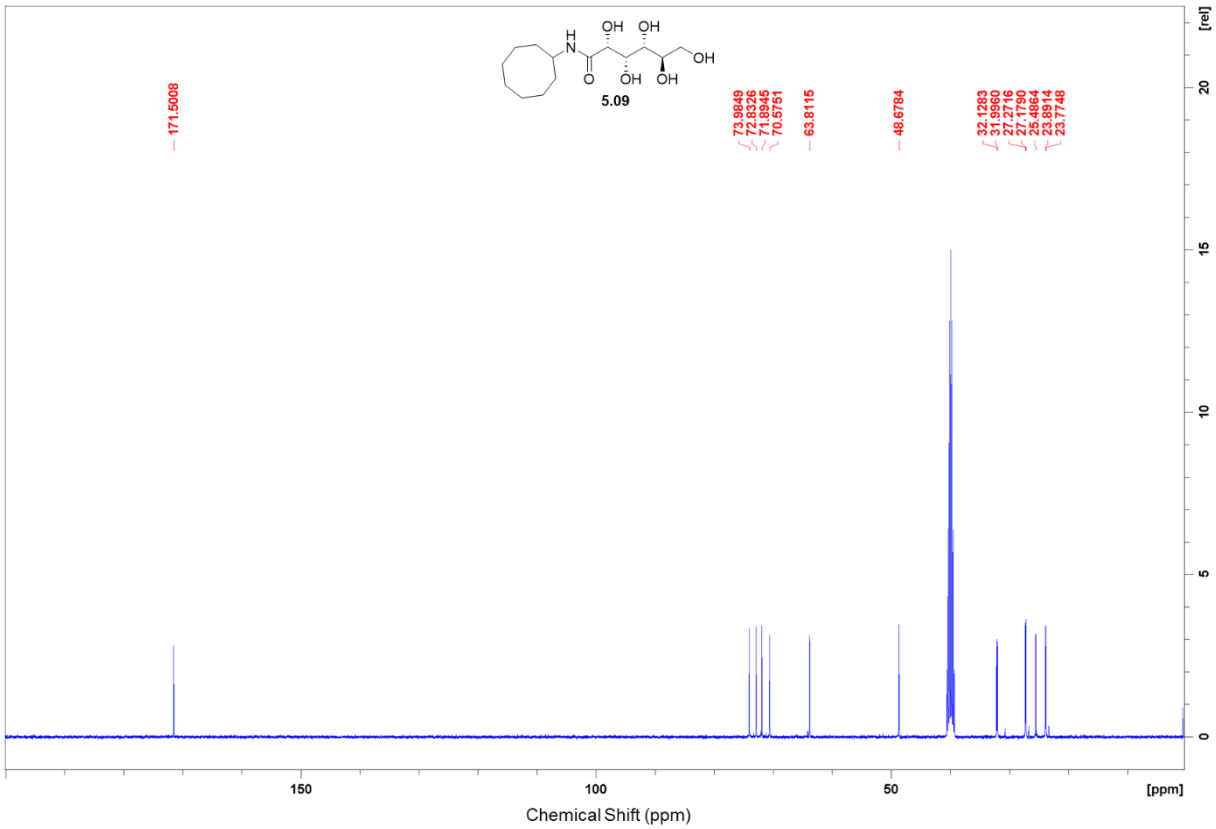
171.5008
73.9849
72.8326
71.8945
70.5751
63.8115
48.6784
32.1283
31.9960
27.2716
27.1790
25.4864
23.8914
23.7748
OH
OH
OH
OH
OH
H
N
O
5.09
[rel]
[ppm]
Chemical Shift (ppm)

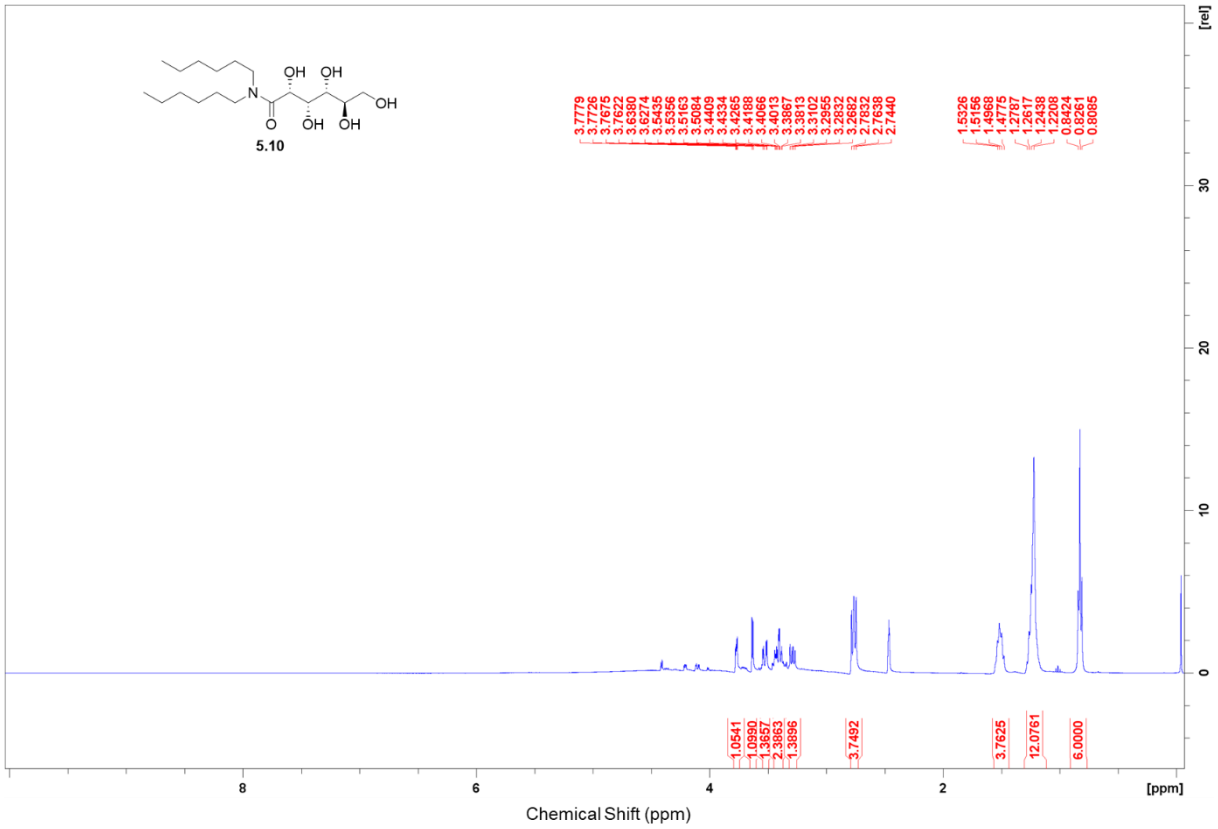
5.10
3.7779
3.7726
3.7675
3.7622
3.6590
3.6274
3.5435
3.5356
3.5163
3.5084
3.4409
3.4334
3.4265
3.4188
3.4066
3.4013
3.3867
3.3813
3.3702
3.2955
3.2832
3.2682
2.7832
2.7638
2.7440
1.5326
1.5156
1.4968
1.4775
1.2787
1.2617
1.2438
1.2208
0.8924
0.8781
0.0065
1.0541
1.0990
1.3657
2.3863
1.3896
3.7492
3.7625
12.0761
6.0000
[rel]
[ppm]
Chemical Shift (ppm)

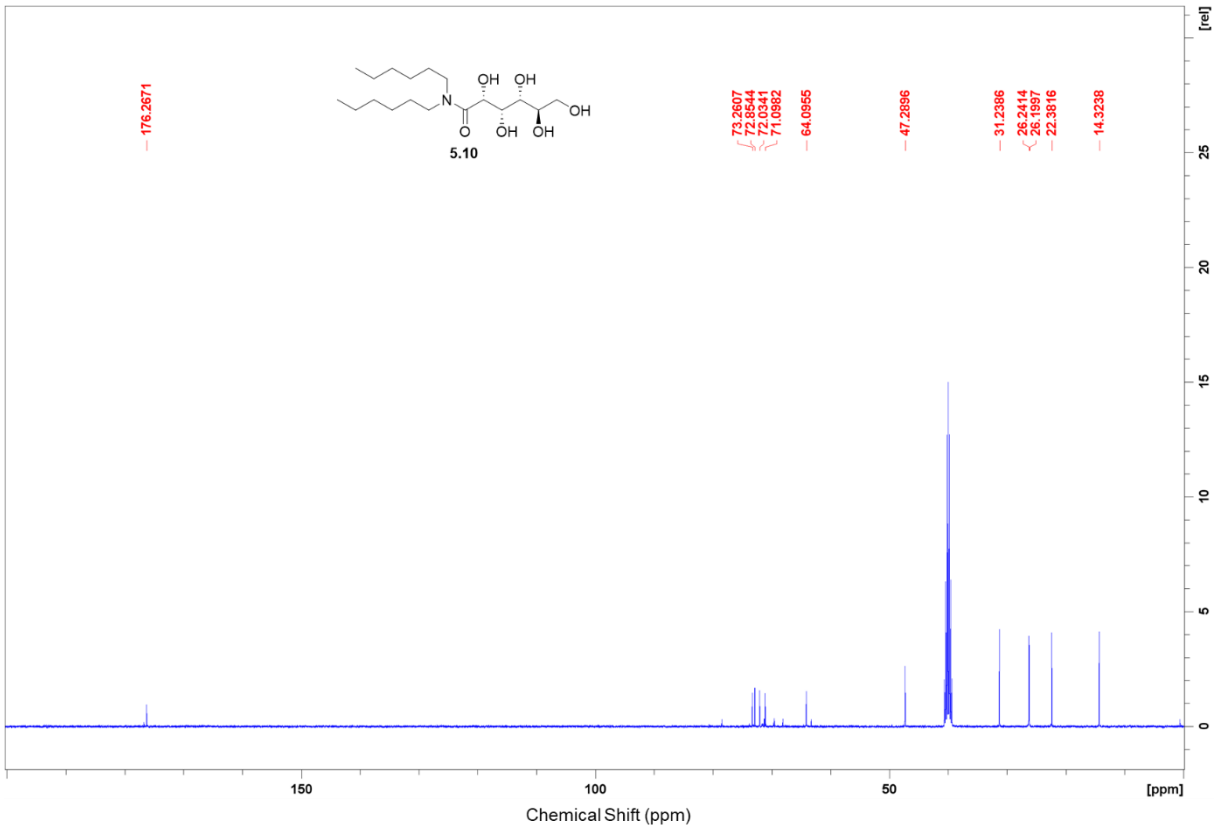
5.10
176.2671
73.2607
72.8544
72.0341
71.0882
64.0955
47.2896
31.2386
26.2414
26.1997
22.3816
14.3238
[rel]
[ppm]
Chemical Shift (ppm)

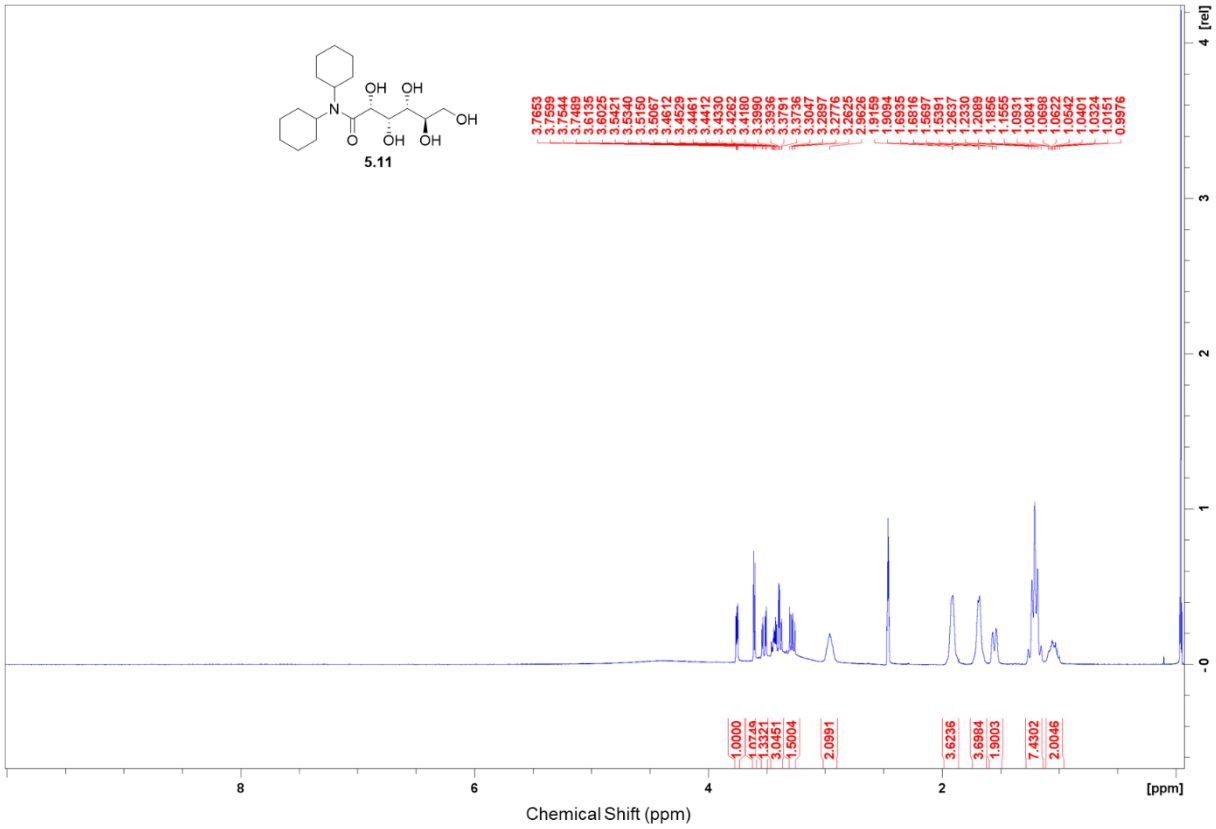
OH
OH
OH
N
O
OH
OH
5.11
3.7653
3.7599
3.7544
3.7489
3.6135
3.6025
3.5421
3.5340
3.5150
3.5067
3.4612
3.4529
3.4461
3.4412
3.4330
3.4262
3.4160
3.3990
3.3936
3.3791
3.3736
3.3047
3.2897
3.2776
3.2625
2.9626
1.9159
1.9094
1.6935
1.6816
1.6697
1.5391
1.2637
1.2330
1.2089
1.1856
1.1555
1.0931
1.0841
1.0698
1.0622
1.0542
1.0401
1.0324
1.0151
0.9976
1.0000
1.0748
1.3321
3.0451
1.5004
2.0991
3.6236
3.6984
1.9003
7.4302
2.0046
[rel]
[ppm]
Chemical Shift (ppm)

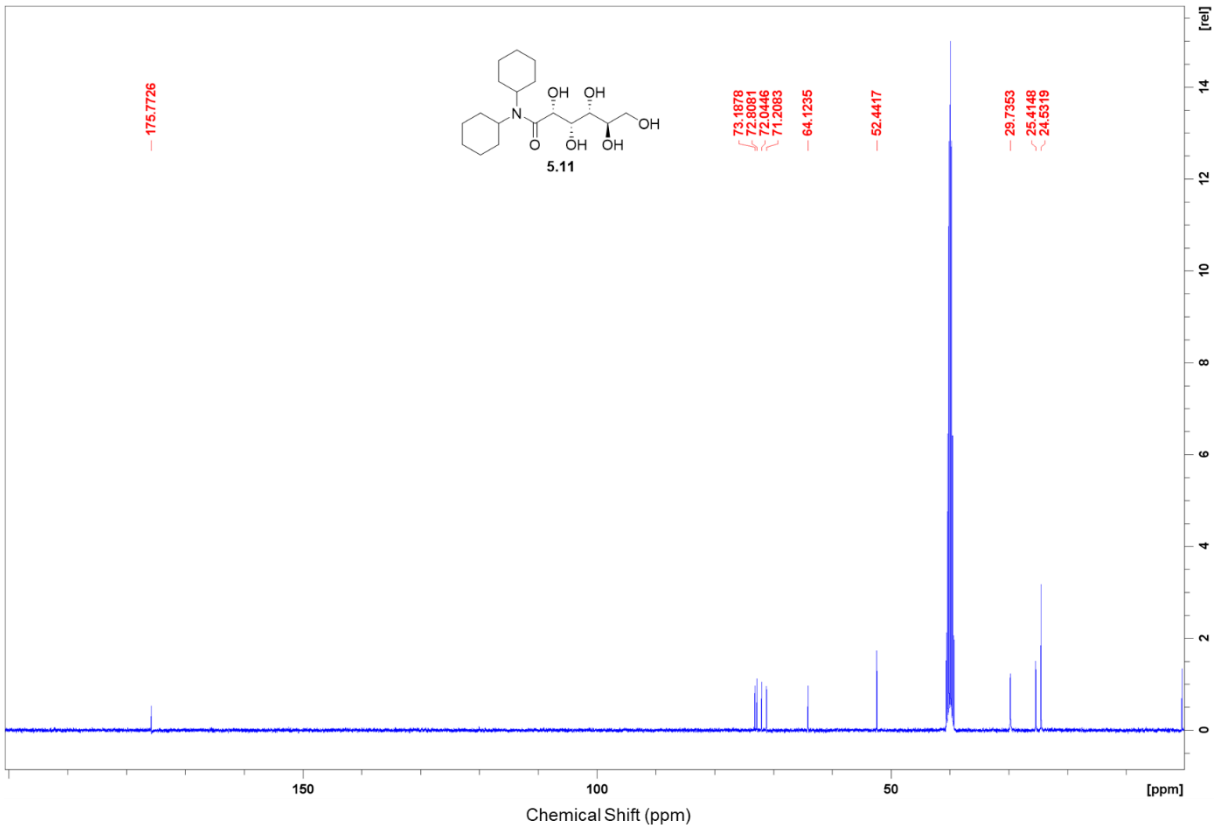
175.7726
OH
OH
OH
N
O
OH
OH
5.11
73.1878
72.8081
72.0446
71.2083
64.1235
52.4417
29.7353
25.4148
24.5319
[rel]
[ppm]
Chemical Shift (ppm)

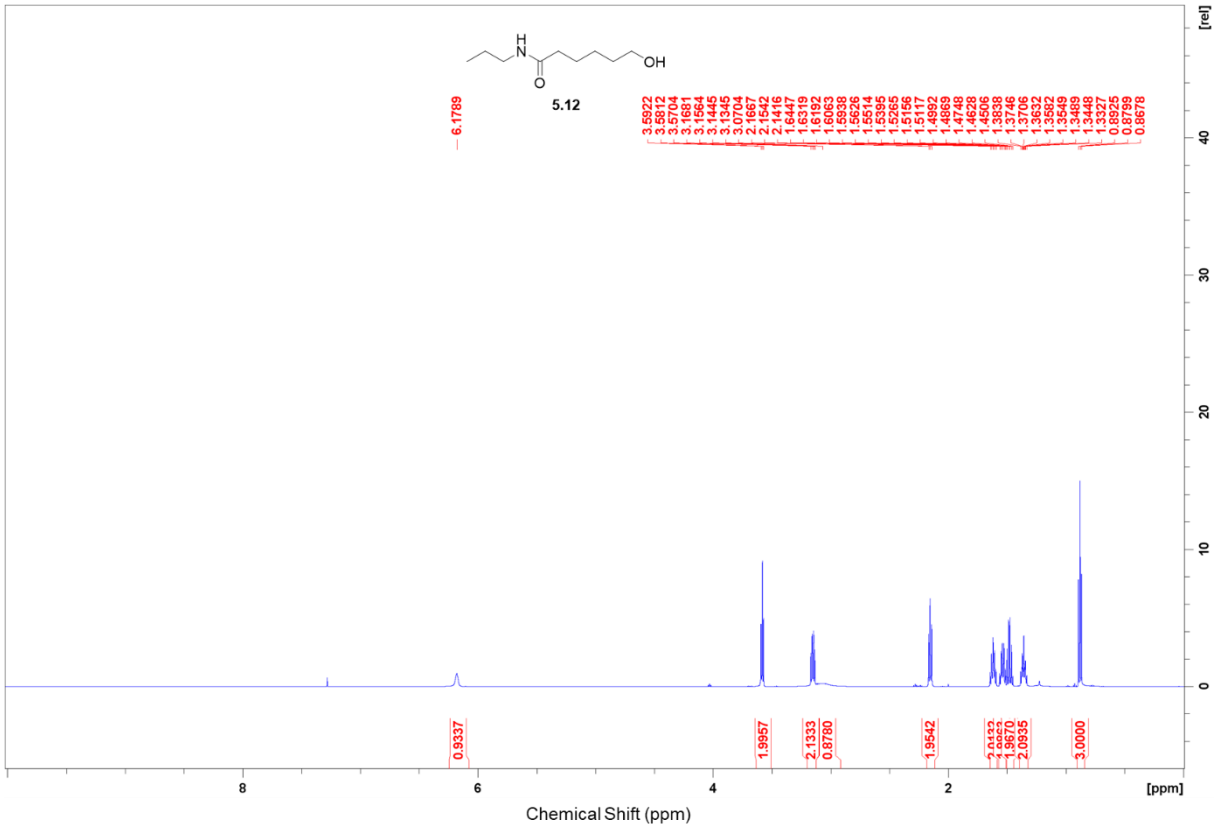
5.12
6.1789
3.5922
3.5712
3.5704
3.1681
3.1564
3.1445
3.1345
3.0704
2.1667
2.1542
2.1416
1.6447
1.6319
1.6192
1.6083
1.5993
1.5628
1.5514
1.5395
1.5265
1.5156
1.5117
1.4992
1.4869
1.4748
1.4628
1.4506
1.3838
1.3746
1.3706
1.3632
1.3582
1.3549
1.3489
1.3448
1.3327
0.8925
0.8799
0.8678
0.9337
1.9957
2.1333
0.8780
1.9542
3.0000
[rel]
[ppm]
Chemical Shift (ppm)

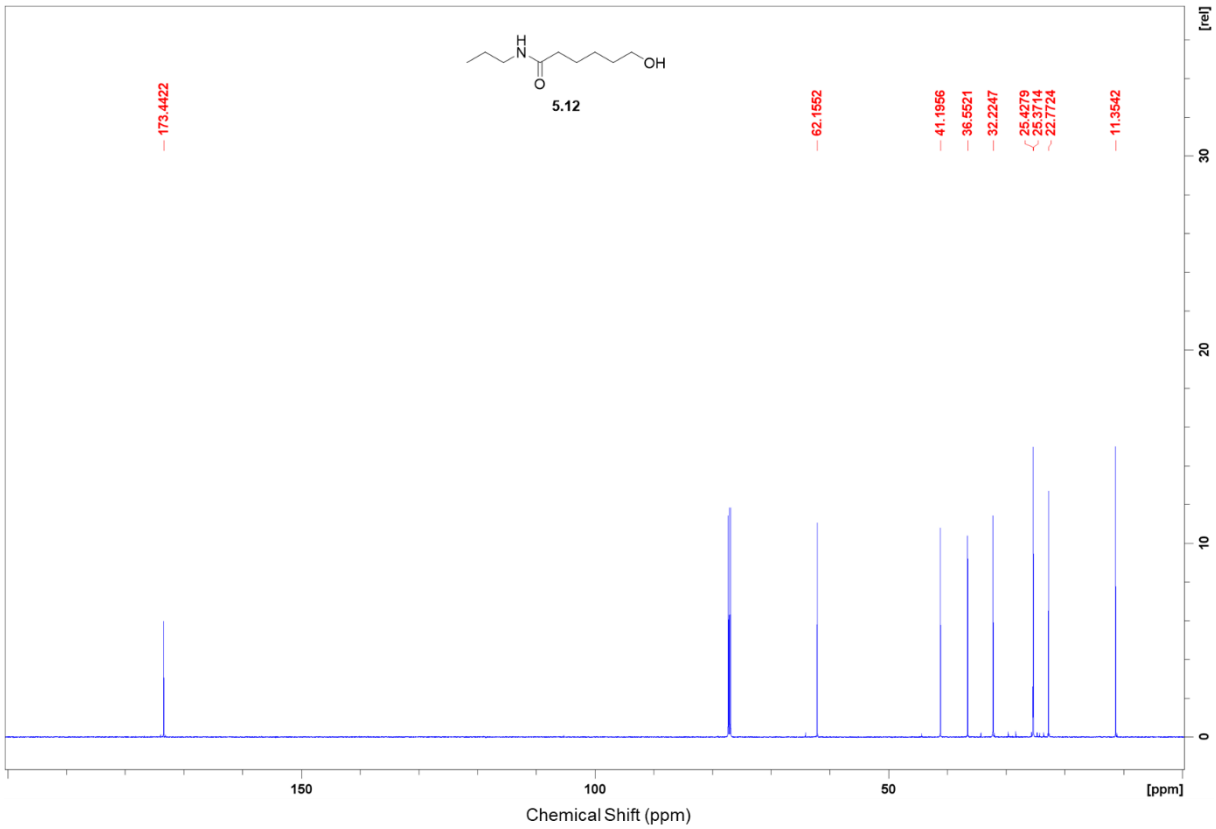
5.12
173.4422
62.1552
41.1956
36.5521
32.2247
25.4279
25.3714
22.7724
11.3542
[rel]
[ppm]
Chemical Shift (ppm)

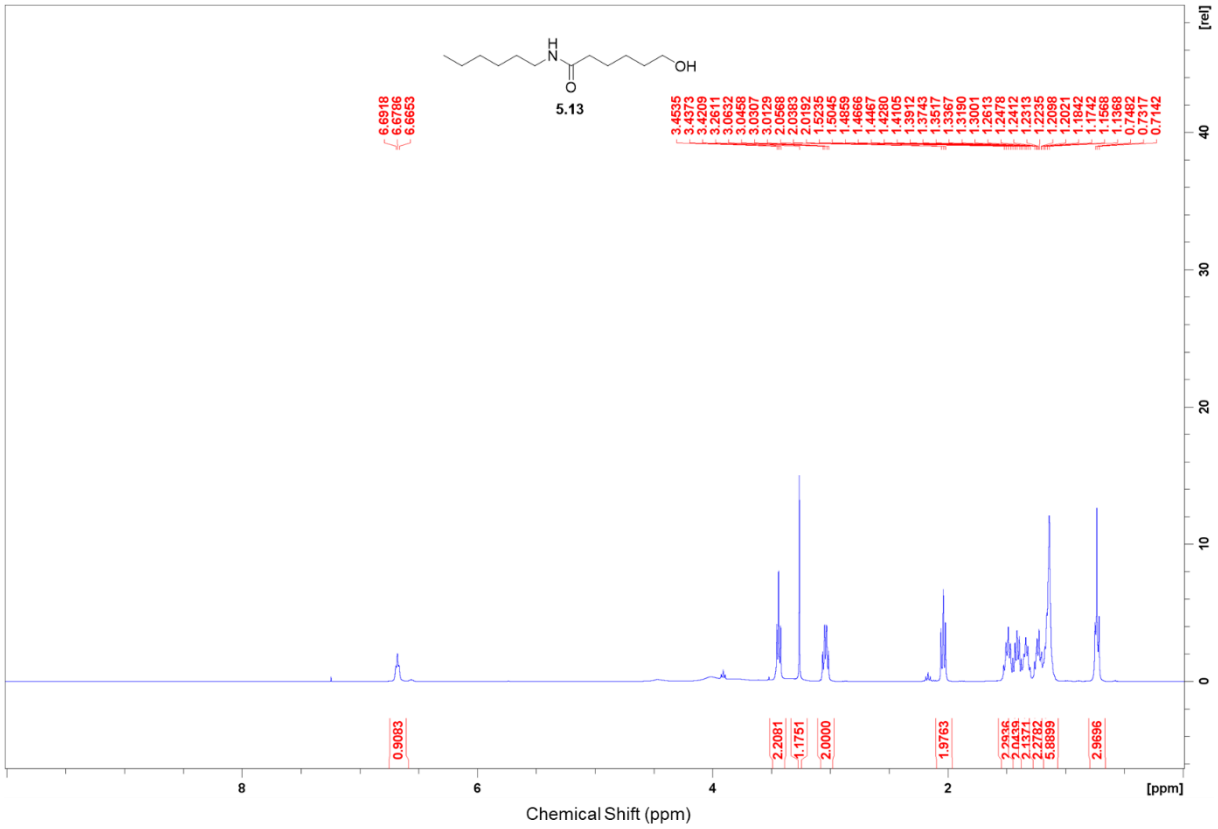
5.13
6.6918
6.6786
6.6653
3.4535
3.4373
3.4209
3.4041
3.0632
3.0458
3.0307
3.0129
2.0568
2.0383
2.0192
1.5235
1.5045
1.4859
1.4666
1.4467
1.4280
1.4105
1.3912
1.3743
1.3517
1.3367
1.3190
1.3001
1.2613
1.2478
1.2412
1.2313
1.2235
1.2098
1.2021
1.1842
1.1742
1.1568
1.1368
0.7482
0.7317
0.7142
0.9083
2.2081
1.1751
2.0000
1.9763
2.2936
2.0439
2.1371
2.7792
5.6899
2.9696
[rel]
[ppm]
Chemical Shift (ppm)

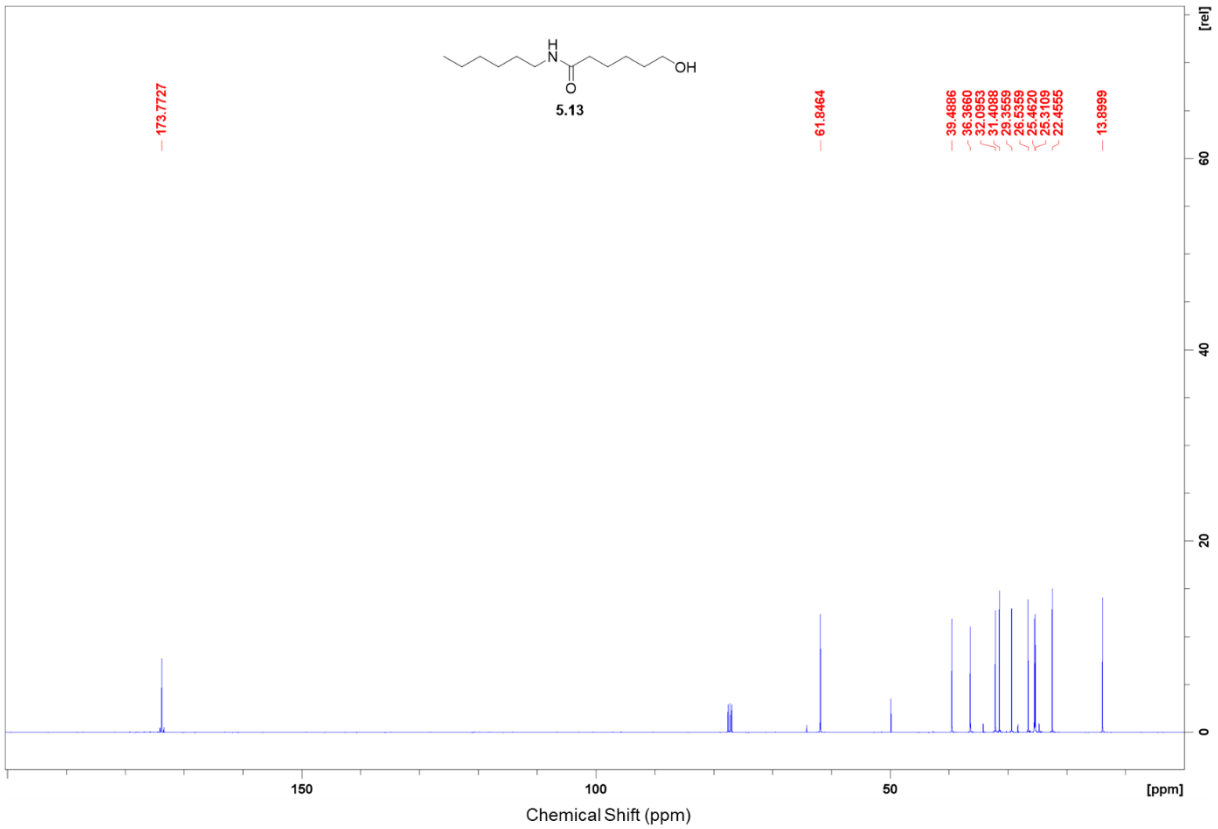
5.13
173.7727
61.8464
39.4886
36.3660
32.0953
31.4088
29.3559
26.5359
25.4620
25.3109
22.4555
13.8999
[rel]
[ppm]
Chemical Shift (ppm)

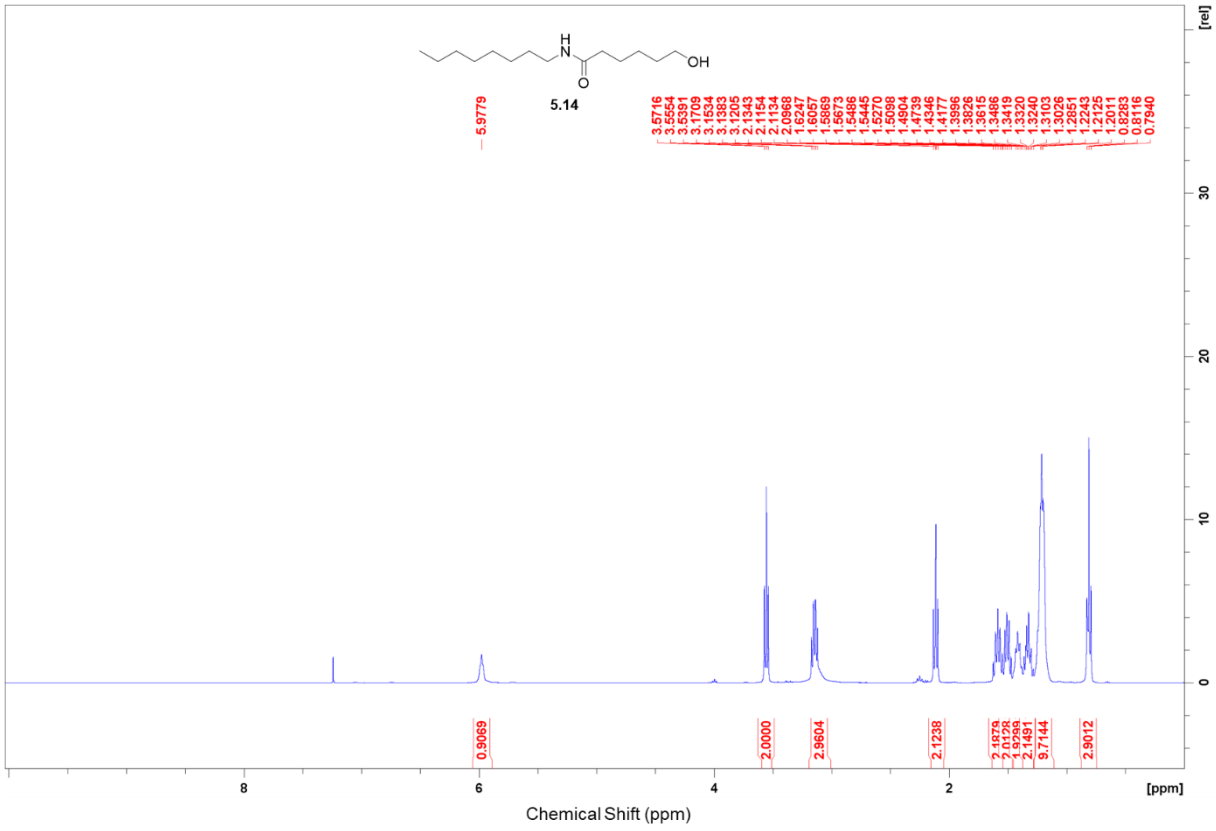
5.14
5.9779
3.5716
3.5554
3.5391
3.1709
3.1534
3.1383
3.1205
2.1343
2.1154
2.1134
2.0968
2.0047
1.6067
1.5869
1.5673
1.5486
1.5445
1.5270
1.5098
1.4904
1.4739
1.4346
1.4177
1.3996
1.3826
1.3615
1.3486
1.3419
1.3320
1.3240
1.3103
1.3026
1.2851
1.2243
1.2125
1.2011
0.8283
0.8116
0.7940
0.9069
2.0000
2.9604
2.1238
2.1978
2.0128
1.9299
2.1491
9.7144
2.9012
[rel]
[ppm]
Chemical Shift (ppm)

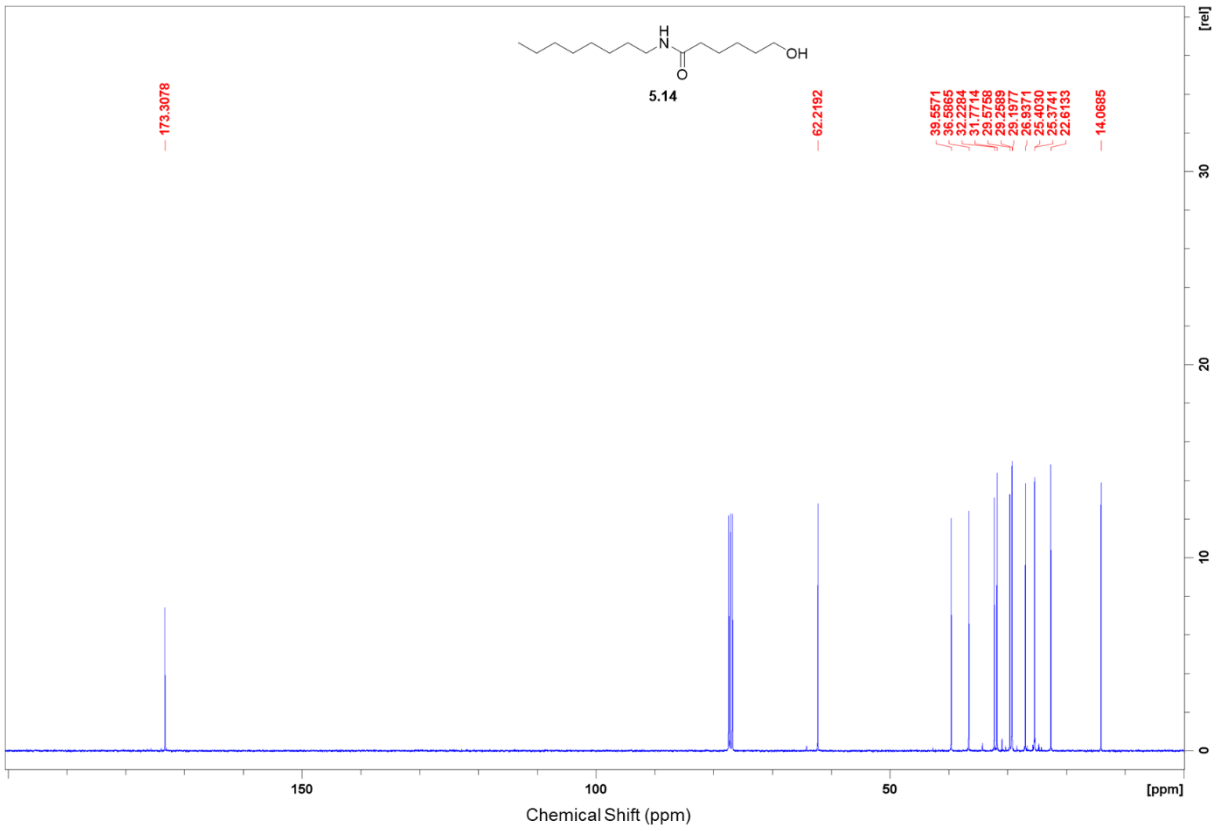
5.14
173.3078
62.2192
39.5571
36.5865
32.2284
31.7714
29.5758
29.2589
29.1977
26.9371
25.4030
25.3141
22.6133
14.0685
[rel]
[ppm]
Chemical Shift (ppm)

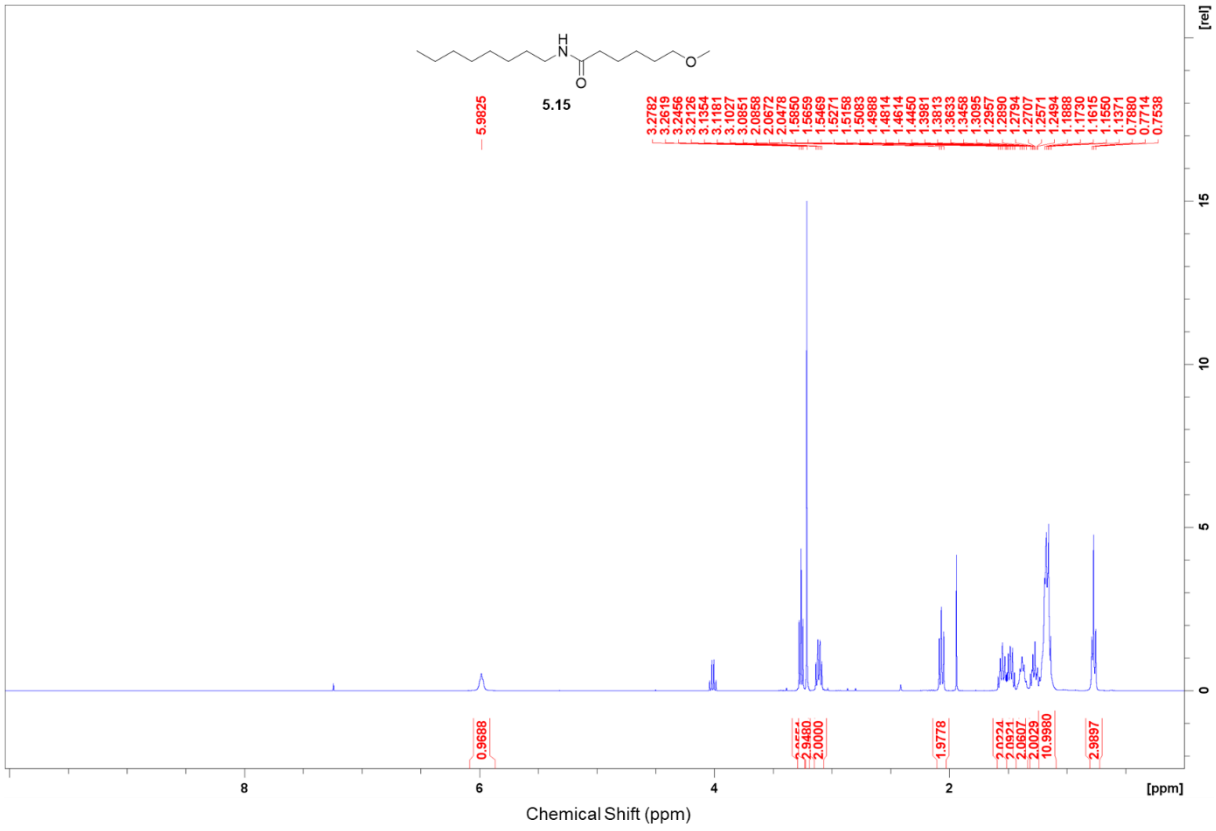
5.15
5.9825
3.2782
3.2619
3.2456
3.2126
3.1384
3.1161
3.0951
3.0027
2.0858
2.0672
2.0478
1.5850
1.5659
1.5469
1.5271
1.5158
1.5083
1.4988
1.4814
1.4654
1.4469
1.3981
1.3813
1.3633
1.3458
1.3095
1.2957
1.2890
1.2794
1.2707
1.2571
1.2494
1.1688
1.1570
1.1515
1.1371
0.7880
0.7714
0.7538
0.9688
2.9480
2.0000
1.9778
2.0224
2.0071
2.0607
2.0029
10.9980
2.9897
[rel]
[ppm]
Chemical Shift (ppm)

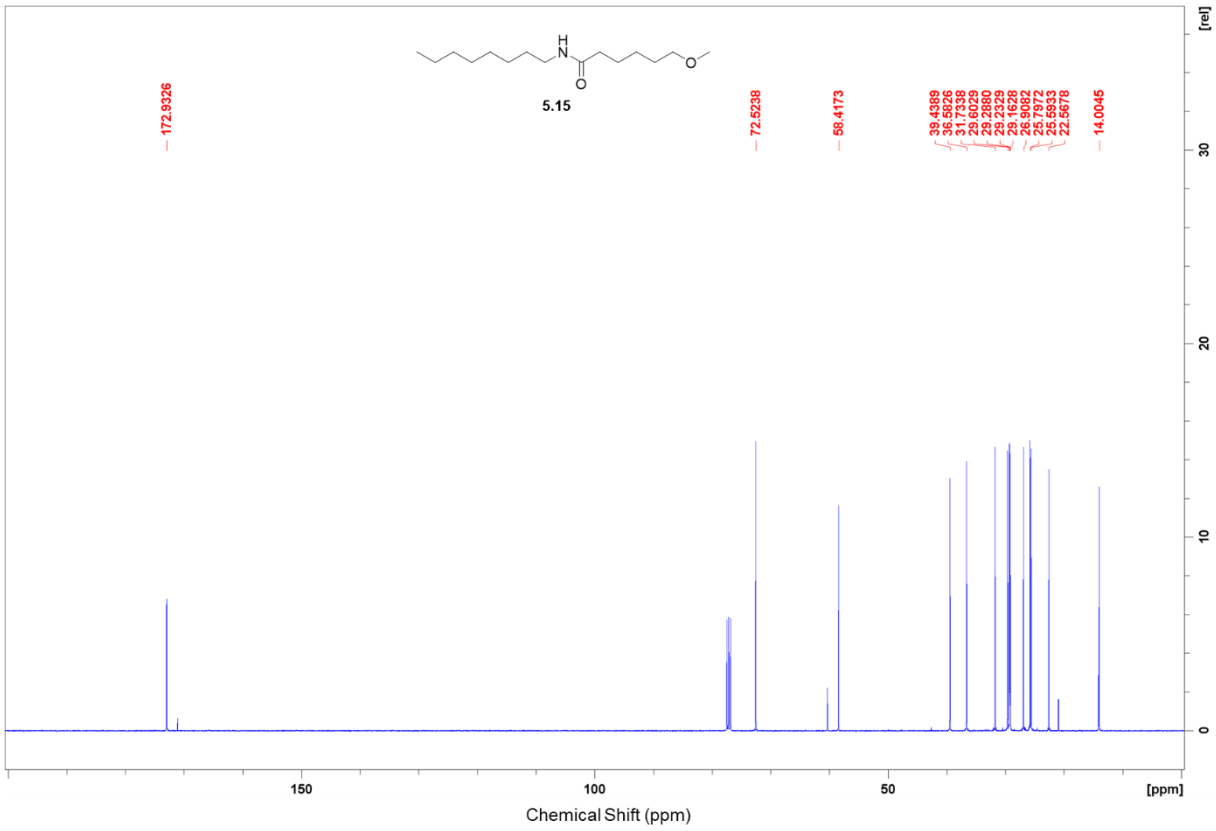
5.15
172.9326
72.5238
58.4173
39.4389
36.5826
31.7338
29.6029
29.2880
29.2329
29.1628
26.9982
25.7972
25.6833
22.5678
14.0045
[rel]
[ppm]
Chemical Shift (ppm)

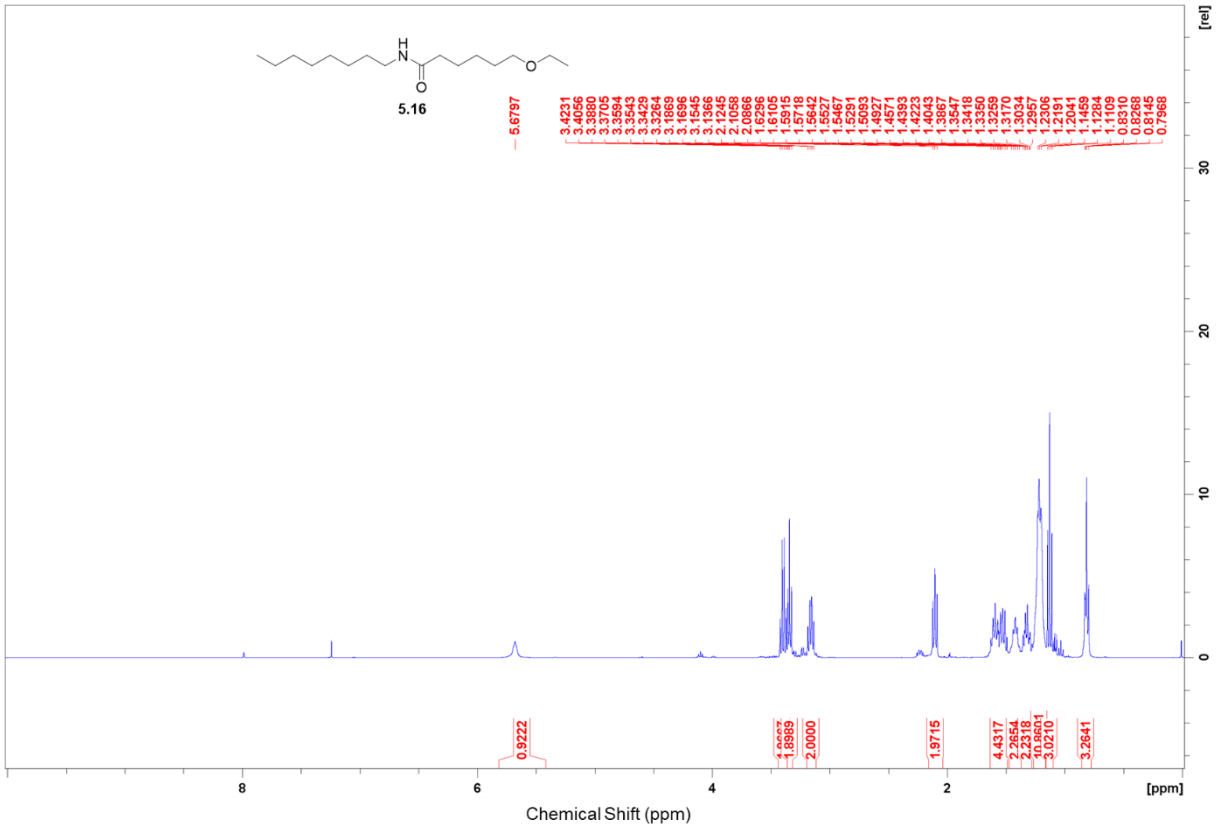
5.16
5.6797
3.4231
3.4056
3.3880
3.3705
3.3604
3.3543
3.3429
3.3264
3.1869
3.1696
3.1545
3.1366
2.1245
2.1058
2.0866
1.6296
1.6105
1.5915
1.5718
1.5642
1.5527
1.5467
1.5291
1.5093
1.4927
1.4571
1.4393
1.4223
1.4043
1.3867
1.3547
1.3418
1.3350
1.3259
1.3170
1.3034
1.2957
1.2306
1.2191
1.2041
1.1459
1.1284
1.1109
0.8510
0.8368
0.8145
0.7968
0.9222
1.8989
2.0000
1.9715
4.4317
2.2654
2.2318
3.0210
3.2641
[rel]
[ppm]
Chemical Shift (ppm)

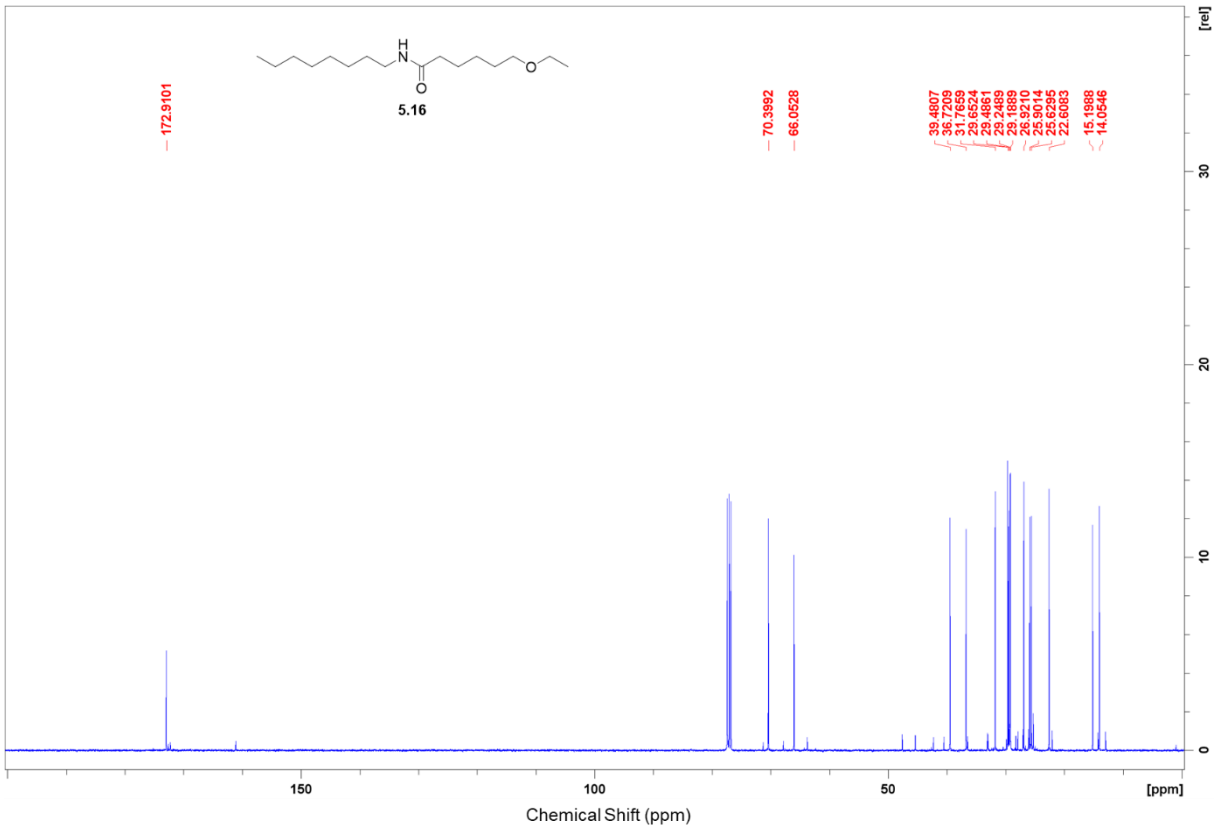
5.16
172.9101
70.3992
66.0528
39.4807
36.7209
31.7659
29.6524
29.4861
29.2489
29.1889
26.9210
25.8914
25.6295
22.6083
15.1988
14.0546
[rel]
[ppm]
Chemical Shift (ppm)

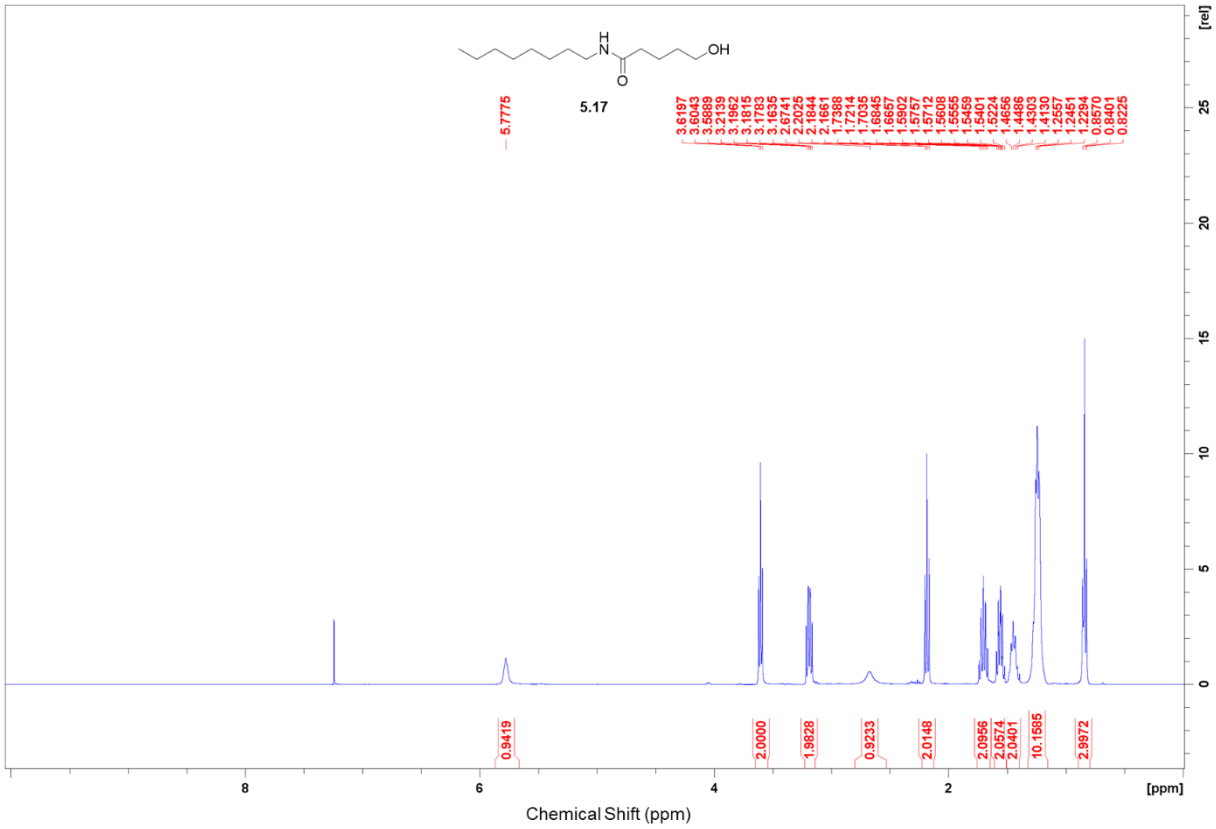
OH
5.17
5.7775
3.6197
3.6043
3.5689
3.2139
3.1962
3.1815
3.1783
3.1635
3.1541
2.2025
2.1844
2.1661
1.7388
1.7214
1.7035
1.6845
1.6657
1.5902
1.5757
1.5712
1.5608
1.5455
1.5469
1.5401
1.5224
1.4656
1.4486
1.4303
1.4130
1.2557
1.2451
1.2294
0.8570
0.8401
0.8225
0.9419
2.0000
1.9828
0.9233
2.0148
2.0956
2.0574
2.0401
10.1585
2.9972
[rel]
[ppm]
Chemical Shift (ppm)

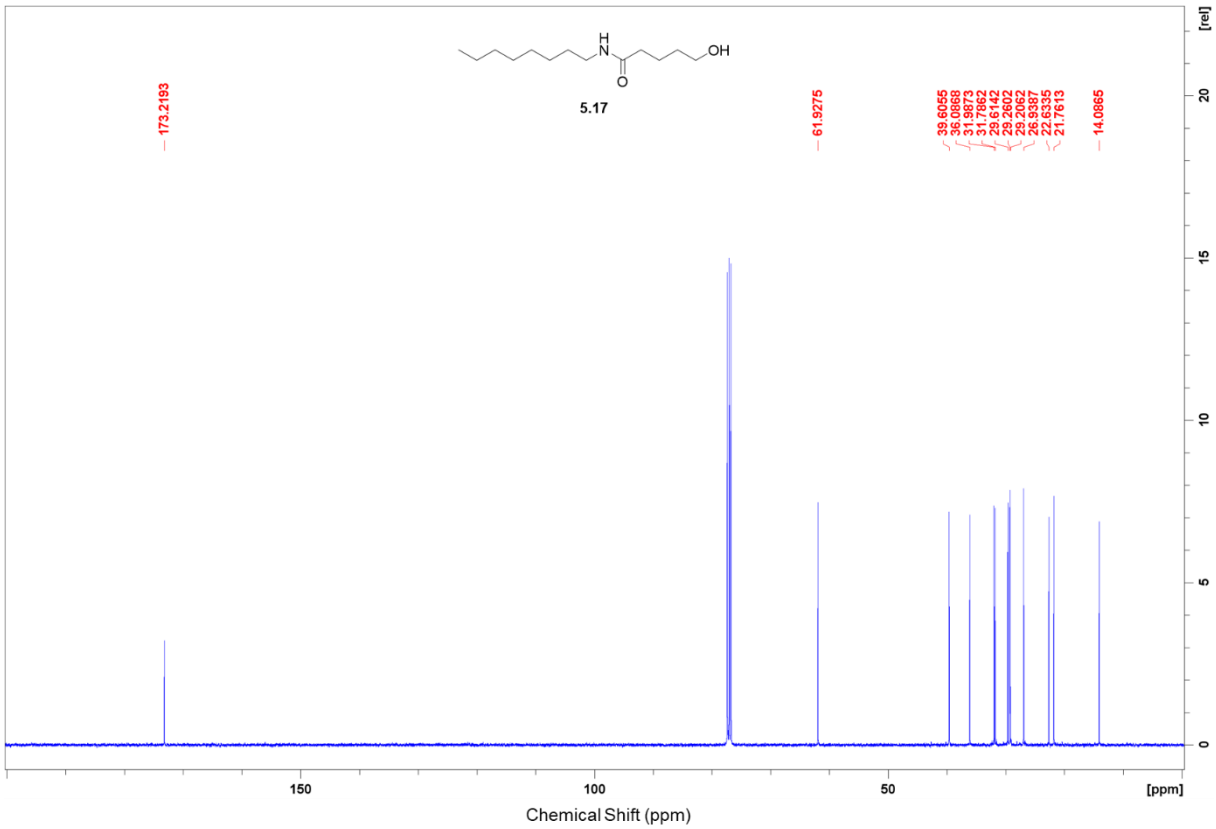
OH
5.17
173.2193
61.9275
39.6055
36.0868
31.9873
31.7662
29.6142
29.2602
29.2062
26.9387
22.6335
21.7613
14.0865
[rel]
[ppm]
Chemical Shift (ppm)

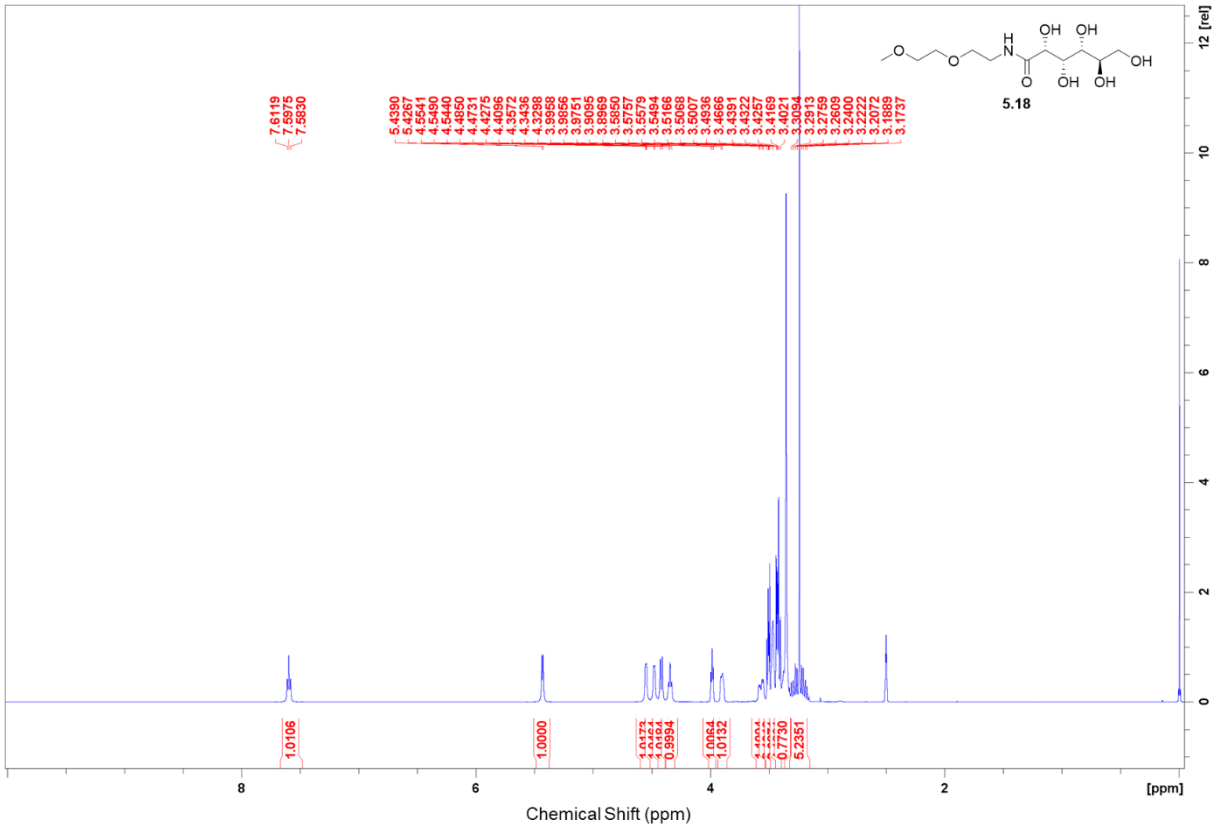
5.18
Chemical Shift (ppm)

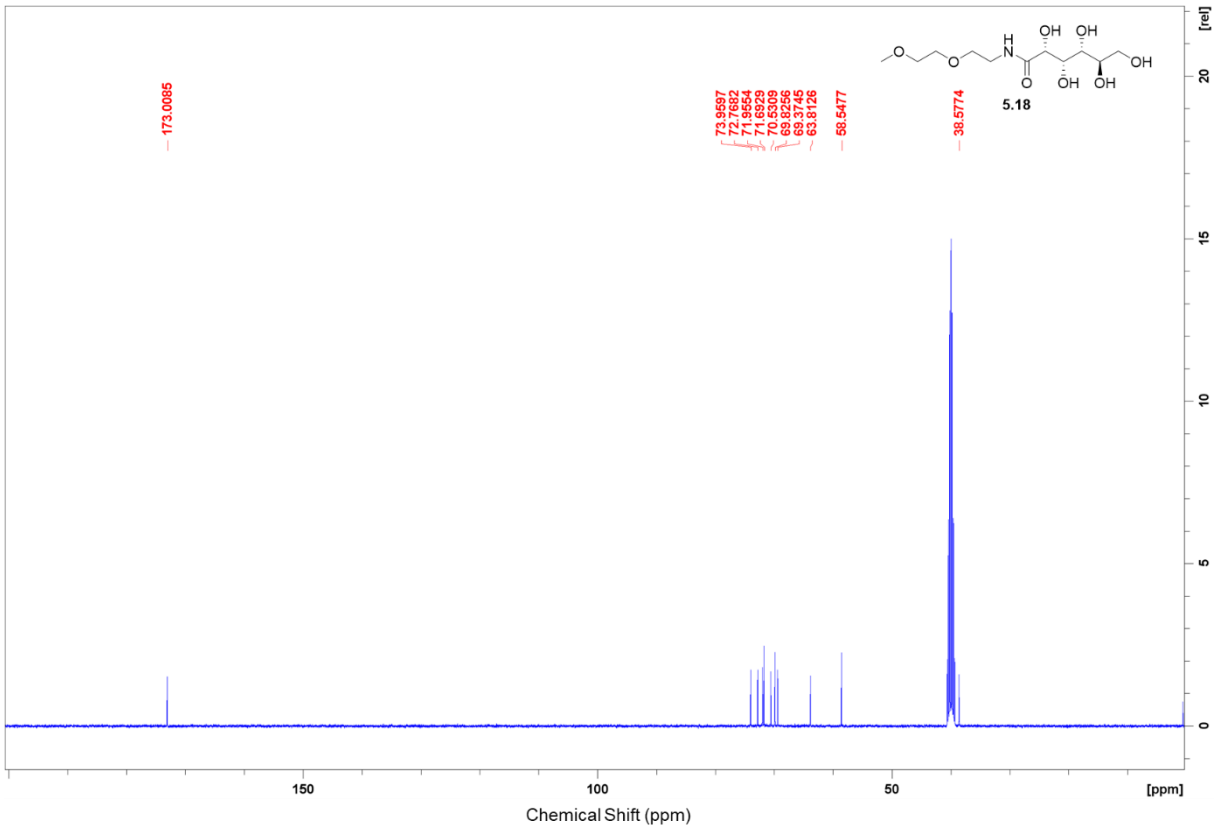
5.18
Chemical Shift (ppm)

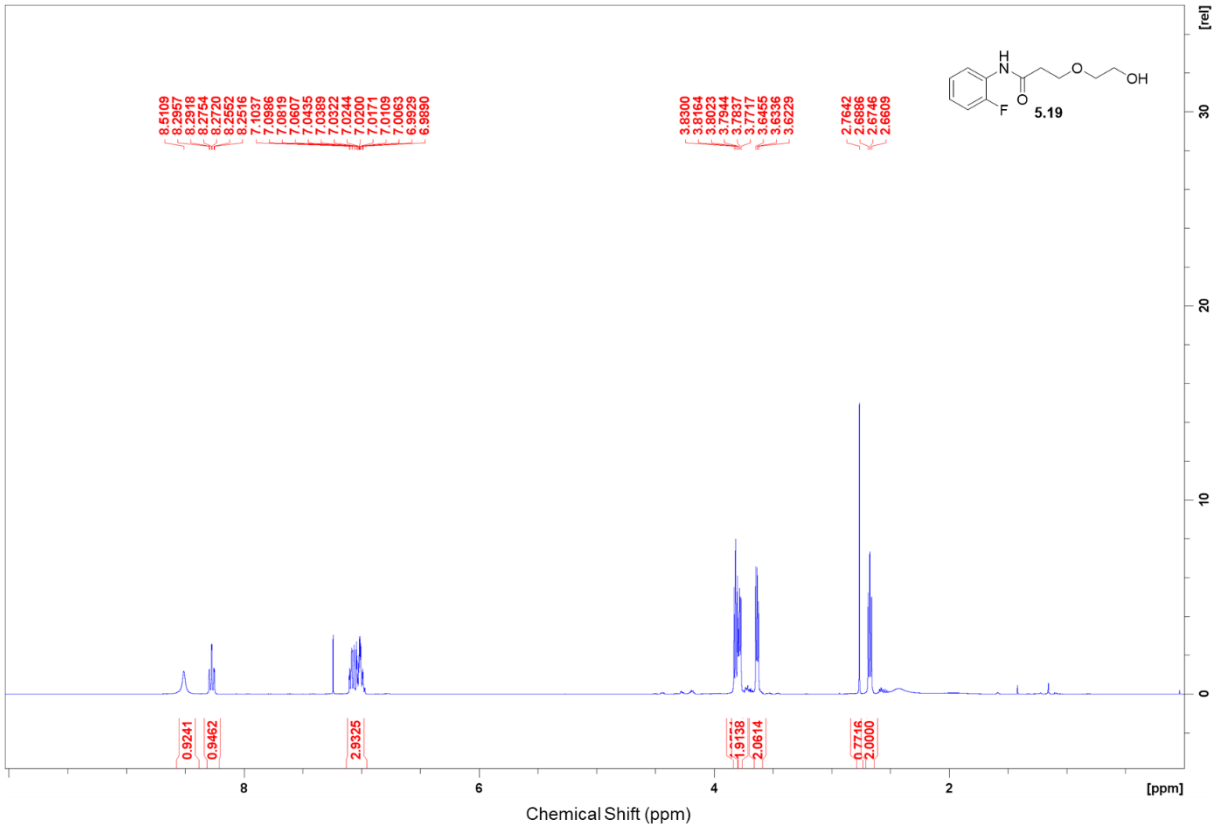
8.5109
8.2957
8.2918
8.2754
8.2720
8.2552
8.2516
7.1037
7.0986
7.0819
7.0607
7.0435
7.0389
7.0322
7.0244
7.0200
7.0171
7.0109
7.0063
6.9929
6.9890
3.8300
3.8164
3.8023
3.7944
3.7837
3.7717
3.6455
3.6336
3.6229
2.7642
2.6886
2.6746
2.6609
0.9241
0.9462
2.9325
1.9138
2.0614
0.7716
2.0000
5.19
[rel]
[ppm]
Chemical Shift (ppm)

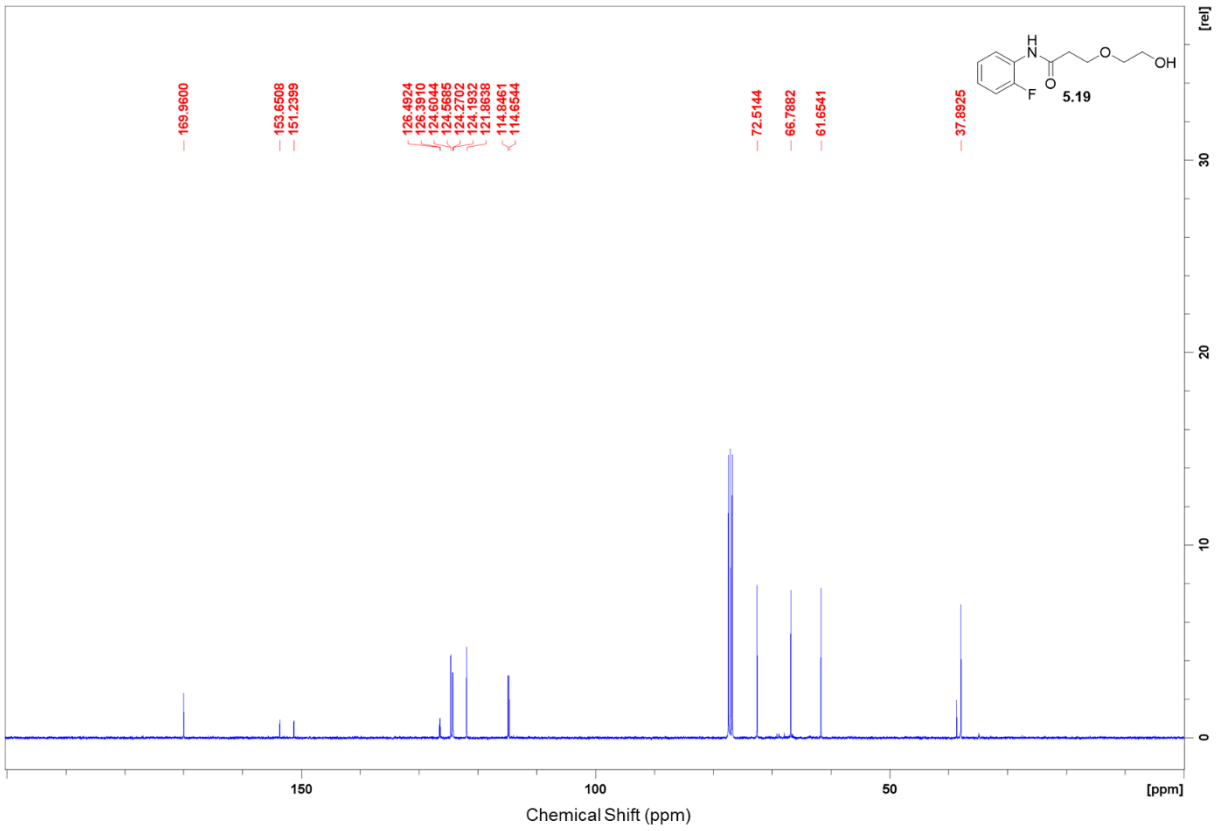
169.9600
153.6508
151.2399
126.4924
126.3910
124.6044
124.5685
124.2702
124.1932
121.8638
114.8461
114.6544
72.5144
66.7882
61.6541
37.8925
5.19
[rel]
[ppm]
Chemical Shift (ppm)

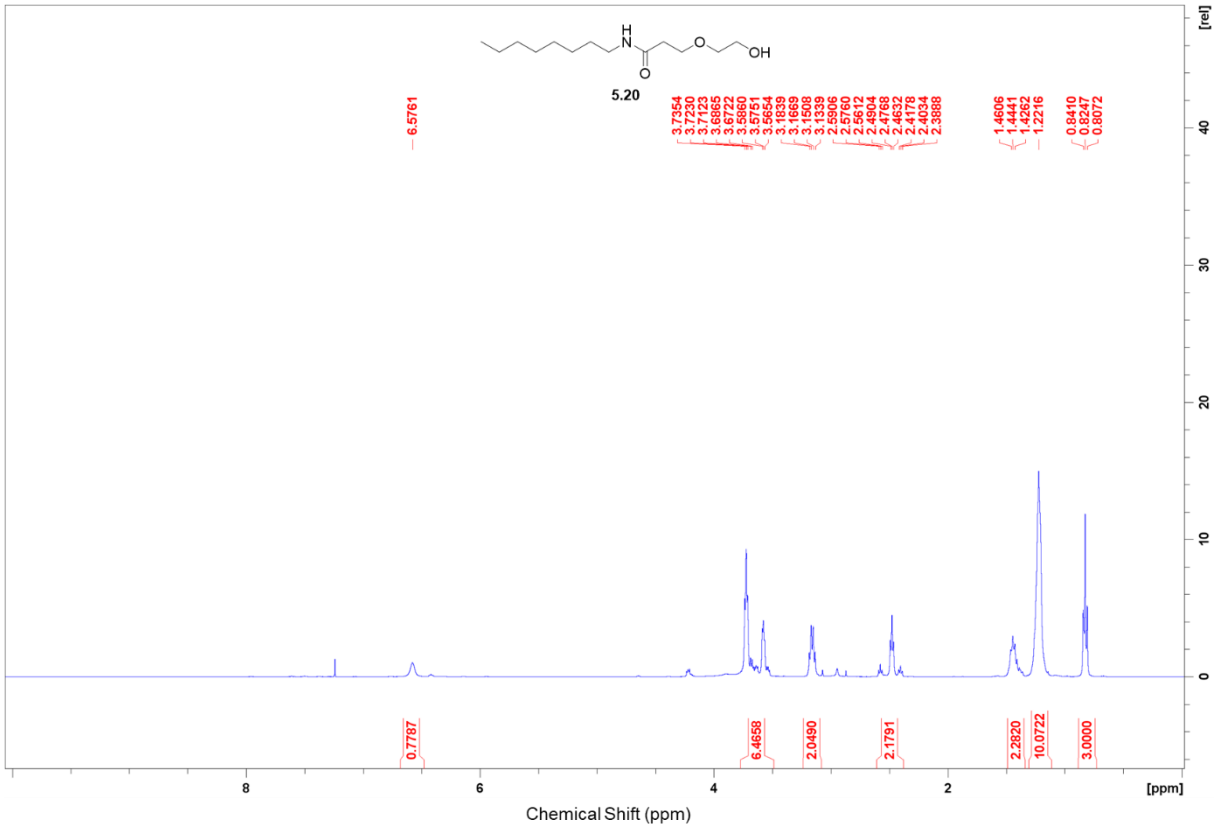
5.20
6.5761
3.7354
3.7230
3.7123
3.6925
3.6722
3.5660
3.5751
3.5654
3.1839
3.1669
3.1508
3.1339
2.5906
2.5760
2.5612
2.4904
2.4768
2.4652
2.4178
2.4034
2.3888
1.4606
1.4441
1.4262
1.2216
0.8410
0.8247
0.8072
0.7787
6.4656
2.0490
2.1791
2.2820
10.0722
3.0000
[rel]
[ppm]
Chemical Shift (ppm)

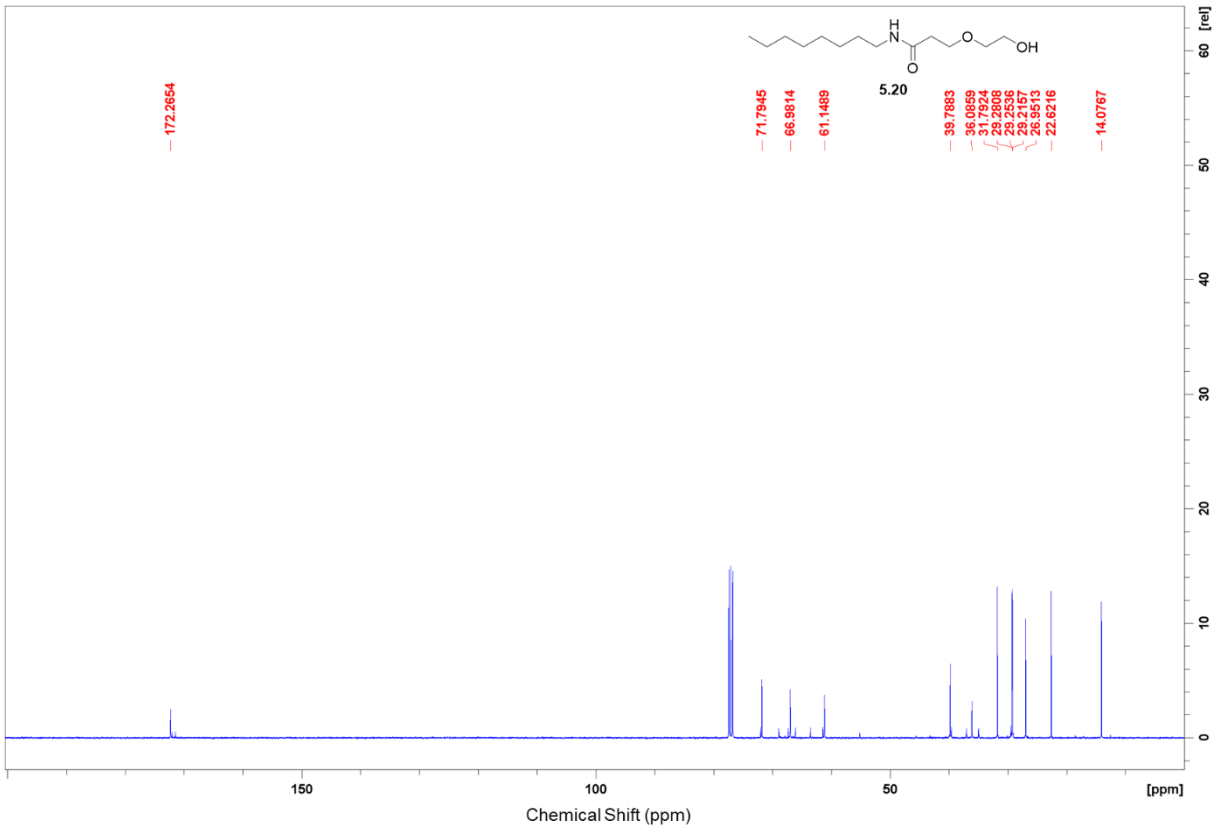
5.20
172.2654
71.7945
66.9814
61.1489
39.7883
36.0859
31.7924
29.2808
29.2567
29.2157
26.9513
22.6216
14.0767
[rel]
[ppm]
Chemical Shift (ppm)

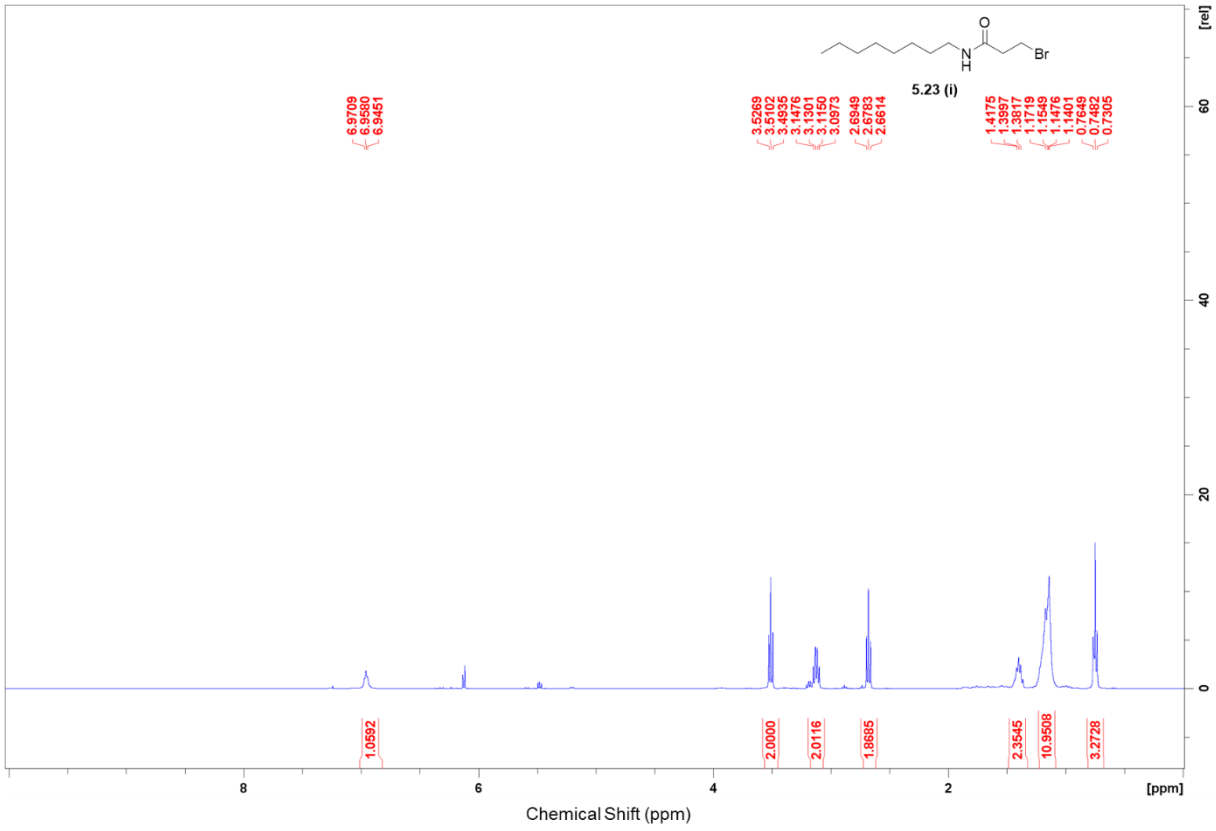
5.23 (i)
6.9709
6.9560
6.9451
3.5269
3.5102
3.4935
3.1476
3.1301
3.1150
3.0973
2.6949
2.6783
2.6614
1.4175
1.3997
1.3817
1.1719
1.1549
1.1476
1.1401
0.7649
0.7482
0.7305
1.0592
2.0000
2.0116
1.6685
2.3545
10.9508
3.2728
[rel]
[ppm]
Chemical Shift (ppm)

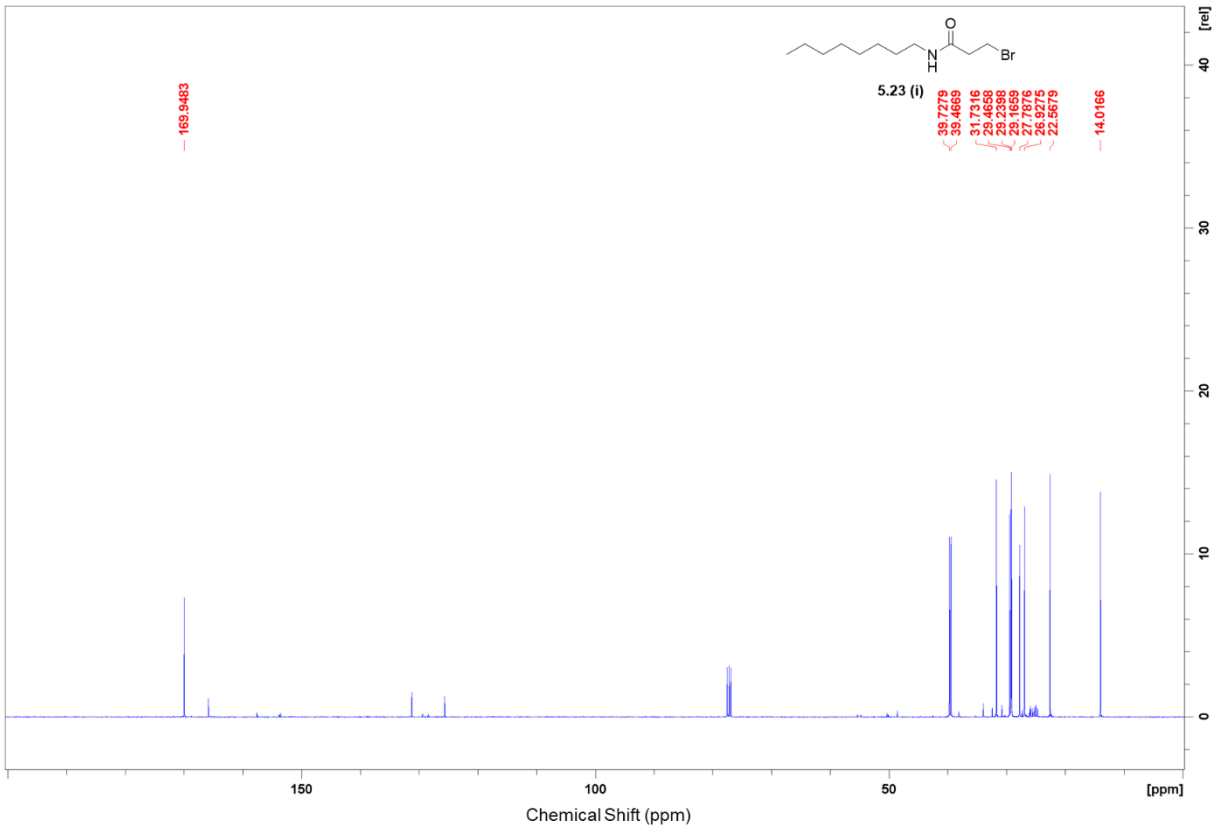
5.23 (i)
169.9483
39.7279
39.4669
31.7316
29.4658
29.2398
29.1659
27.7876
26.9275
22.5679
14.0166
[rel]
[ppm]
Chemical Shift (ppm)

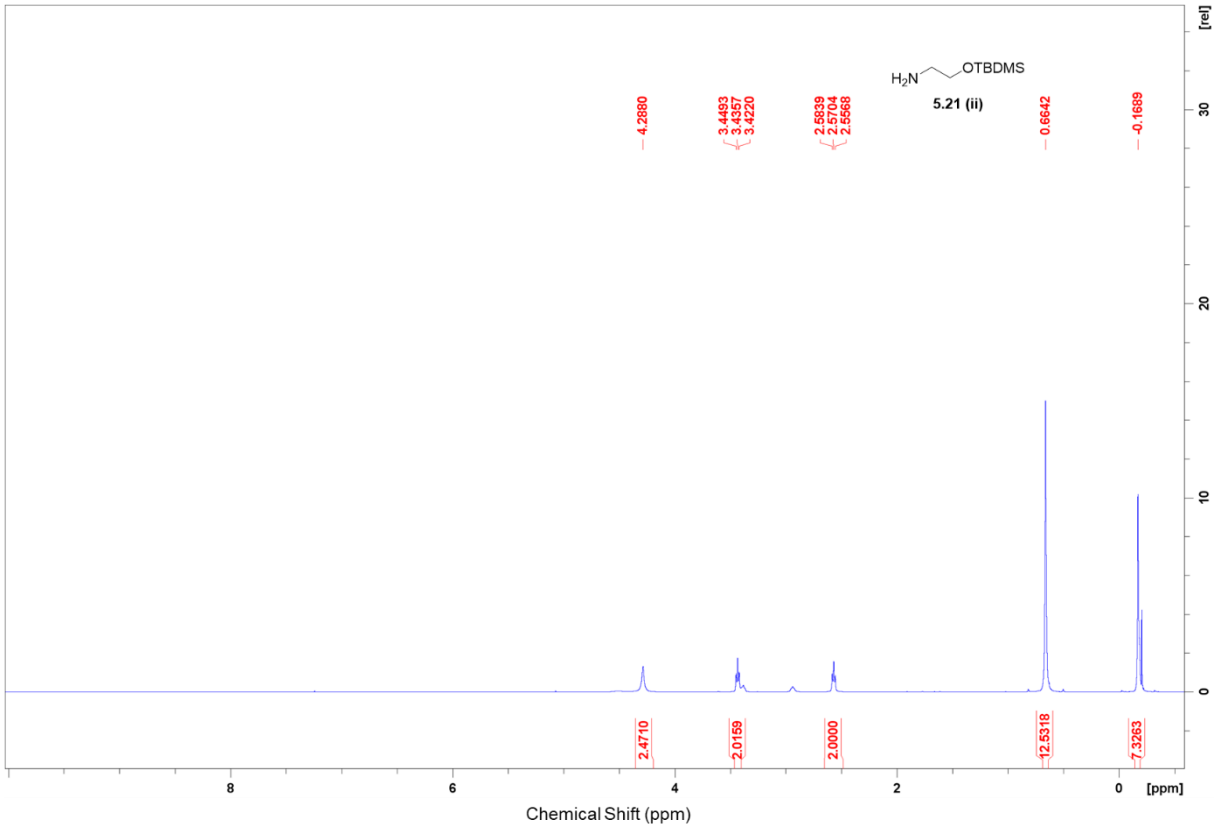
H2N
OTBDMS
5.21 (ii)
4.2880
3.4493
3.4357
3.4220
2.5839
2.5704
2.5568
0.6642
-0.1689
2.4710
2.0159
2.0000
12.5318
7.3263
[rel]
30
20
10
0
8
6
4
2
0
[ppm]
Chemical Shift (ppm)

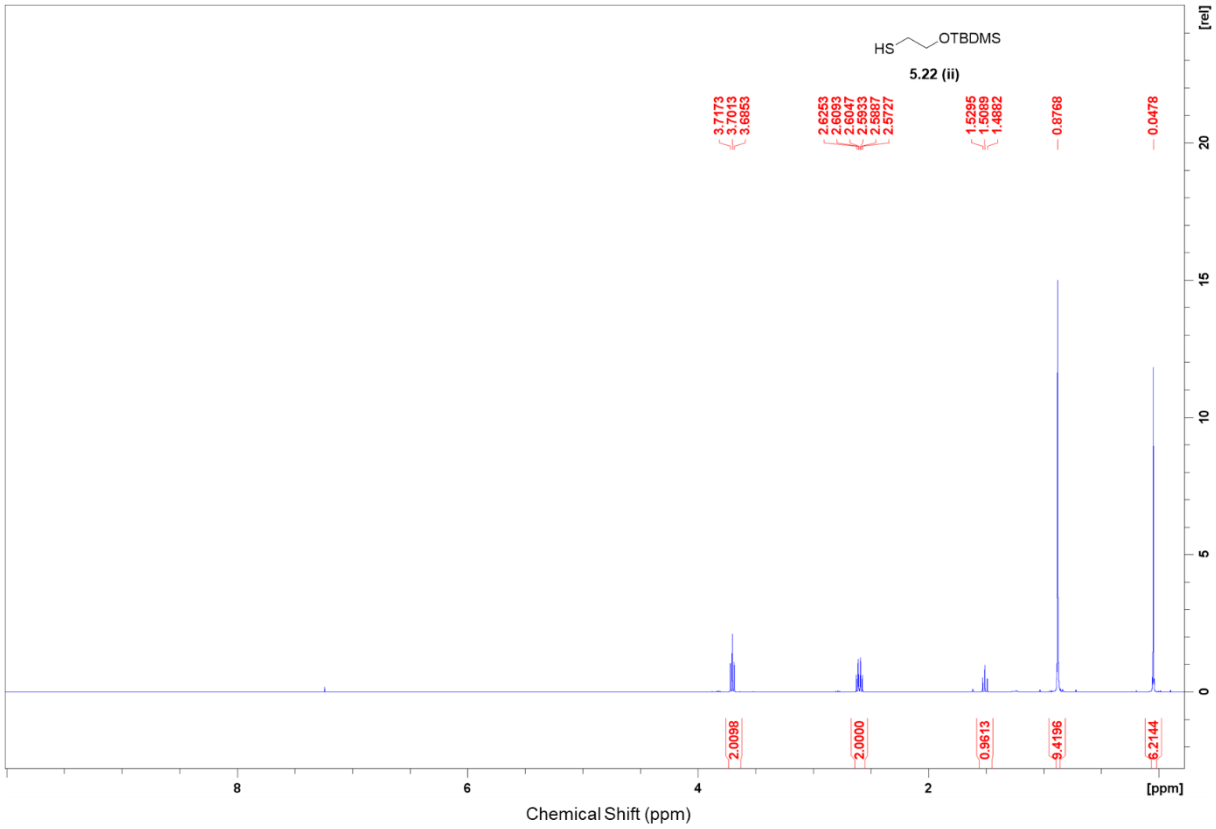
HS
OTBDMS
5.22 (ii)
3.7173
3.7013
3.6853
2.6253
2.6093
2.6047
2.5933
2.5887
2.5727
1.5295
1.5089
1.4882
0.8768
0.0478
2.0098
2.0000
0.9613
9.4196
6.2144
[rel]
[ppm]
Chemical Shift (ppm)

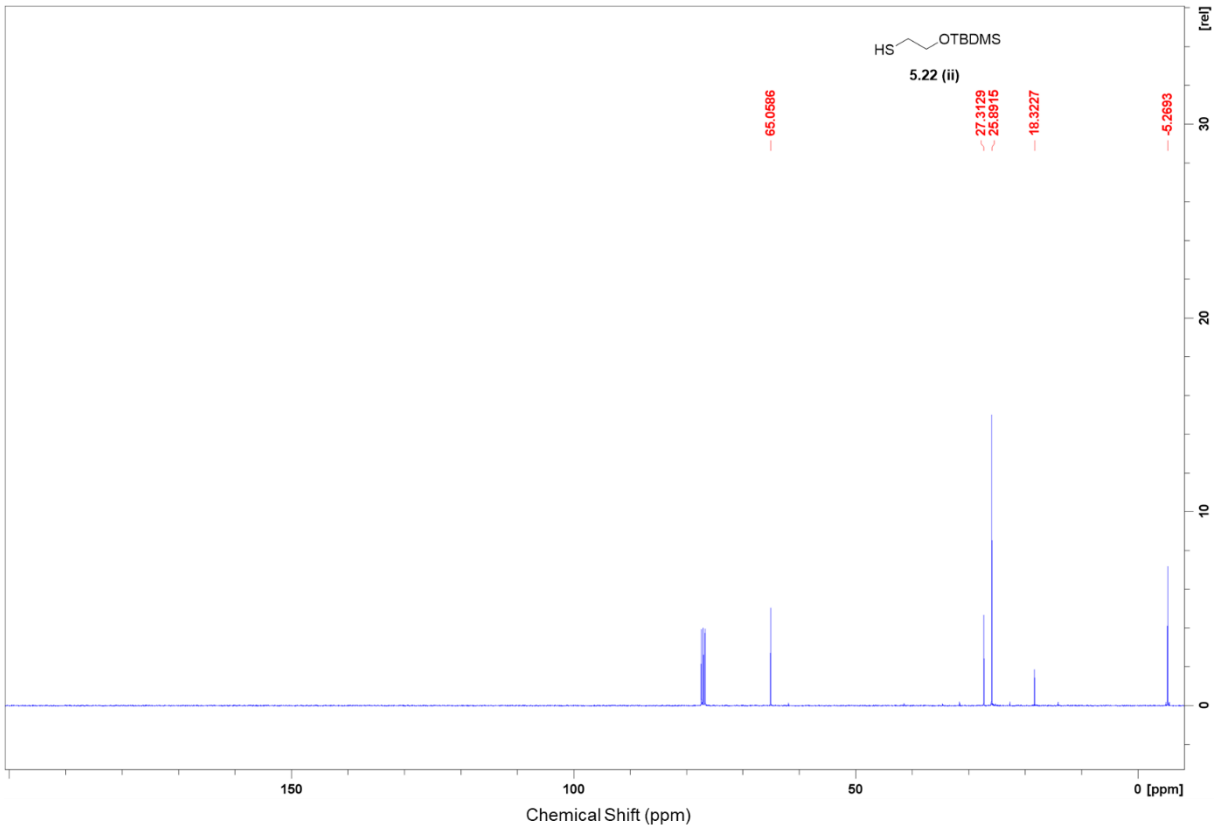
HS
OTBDMS
5.22 (ii)
65.0586
27.3129
25.8915
18.3227
-5.2693
[rel]
[ppm]
Chemical Shift (ppm)

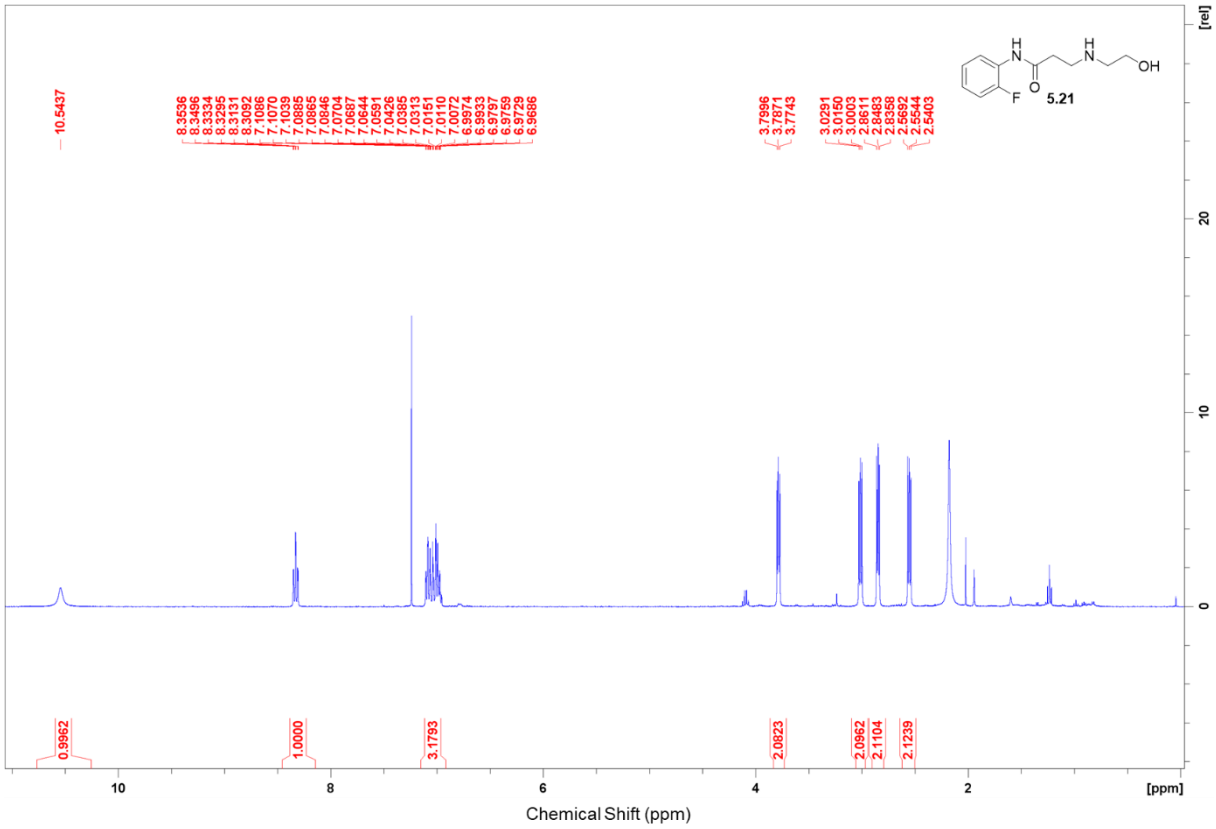
10.5437
8.3536
8.3496
8.3334
8.3295
8.3131
8.3092
7.1086
7.1070
7.1039
7.0885
7.0846
7.0704
7.0687
7.0644
7.0591
7.0426
7.0385
7.0313
7.0151
7.0110
7.0072
6.9974
6.9933
6.9797
6.9759
6.9729
6.9666
3.7996
3.7871
3.7743
3.0291
3.0150
3.0003
2.8611
2.8483
2.8358
2.5692
2.5544
2.5403
5.21
0.9962
1.0000
3.1793
2.0823
2.0962
2.1104
2.1239
[rel]
[ppm]
Chemical Shift (ppm)

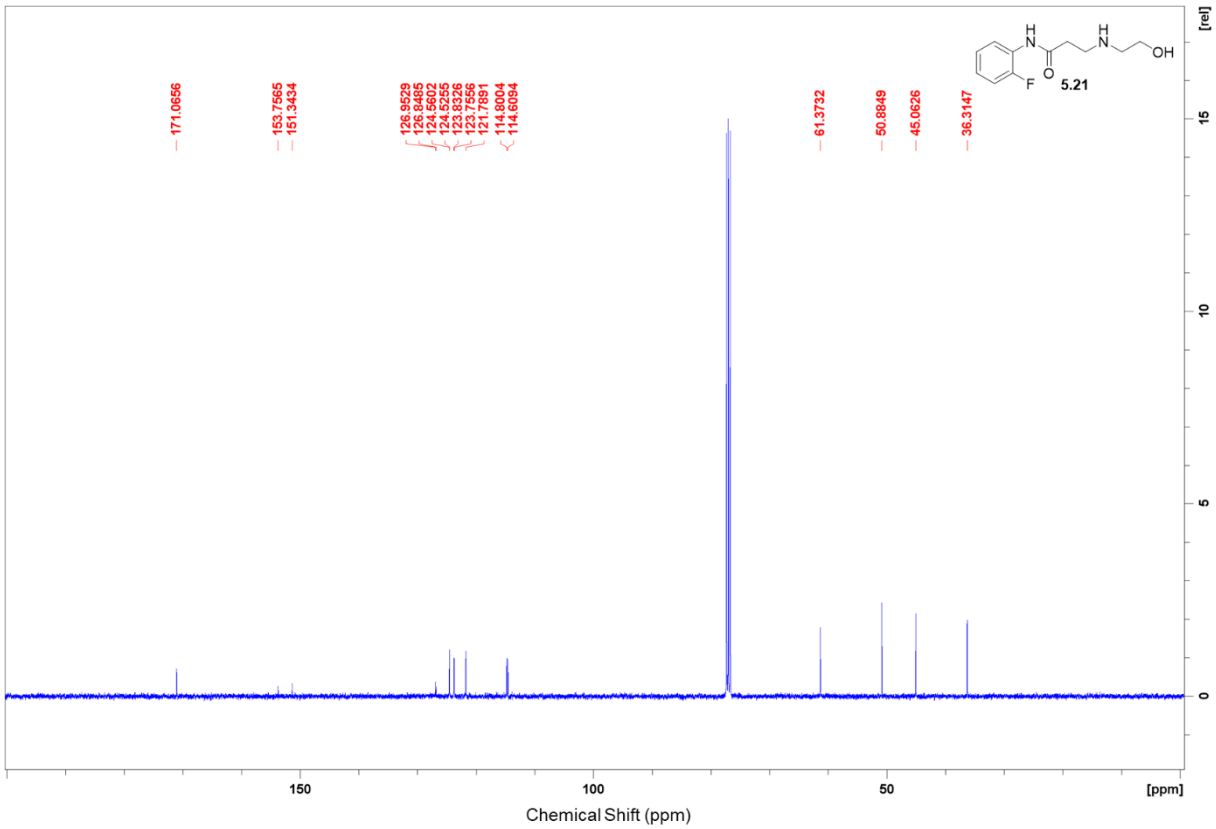
171.0656
153.7565
151.3434
126.9529
126.8485
124.5602
124.5255
123.8326
123.7556
121.7891
114.8004
114.6094
61.3732
50.8849
45.0626
36.3147
5.21
[rel]
[ppm]
Chemical Shift (ppm)

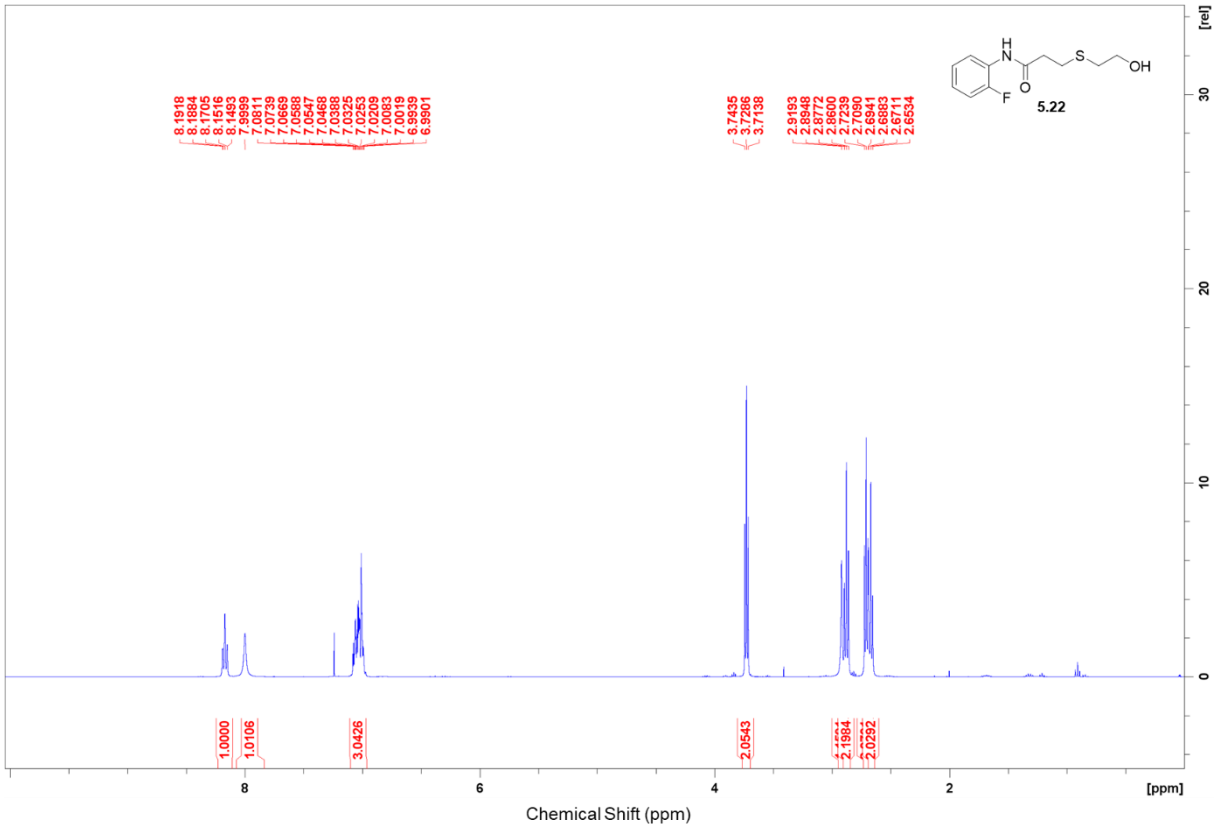
8.1918
8.1884
8.1705
8.1516
8.1493
7.3999
7.0811
7.0739
7.0689
7.0668
7.0547
7.0468
7.0388
7.0325
7.0253
7.0209
7.0083
7.0019
6.9939
6.9901
3.7435
3.7286
3.7138
2.9193
2.8948
2.8772
2.8600
2.7239
2.7090
2.6941
2.6863
2.6711
2.6534
5.22
1.0000
1.0106
3.0426
2.0543
2.1984
2.0292
[rel]
[ppm]
Chemical Shift (ppm)

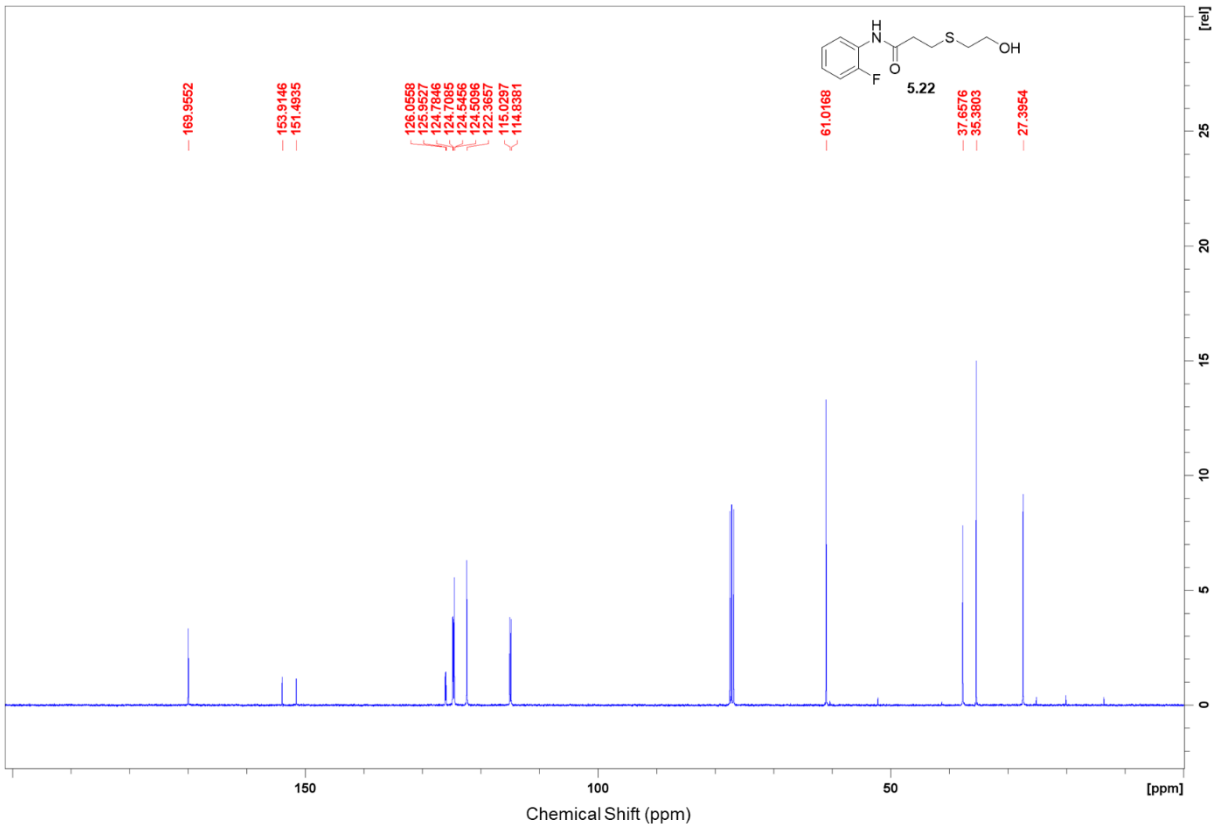
169.9552
153.9146
151.4935
126.0558
125.9527
124.7846
124.7085
124.5456
124.5096
122.3657
115.0297
114.8381
61.0168
37.6576
35.3803
27.3954
5.22
[rel]
[ppm]
Chemical Shift (ppm)

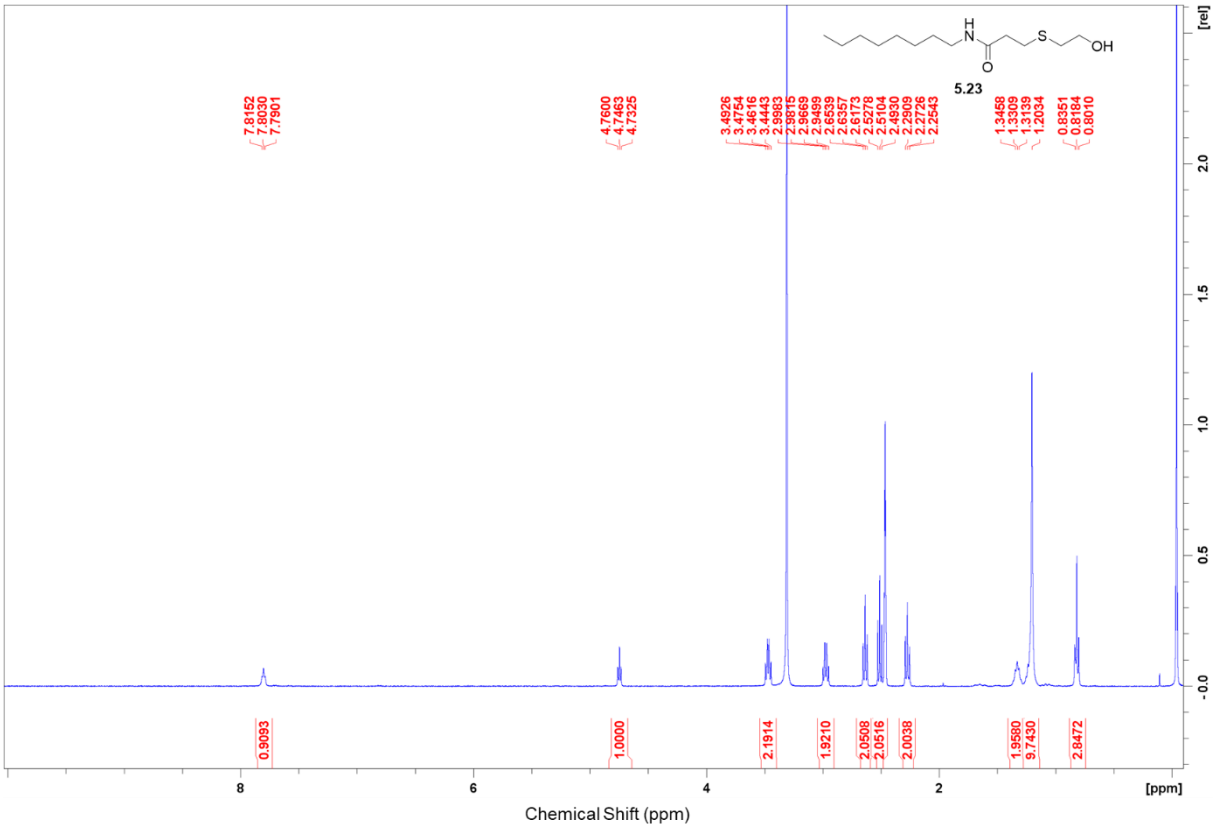
5.23
7.8152
7.8030
7.7901
4.7600
4.7463
4.7325
3.4926
3.4754
3.4616
3.4443
2.9669
2.9489
2.6539
2.6357
2.6173
2.5278
2.5104
2.4930
2.2909
2.2726
2.2543
1.3458
1.3309
1.3139
1.2034
0.8351
0.8184
0.8010
0.9093
1.0000
2.1914
1.9210
2.0508
2.0516
2.0038
1.9580
9.7430
2.8472
[rel]
[ppm]
Chemical Shift (ppm)

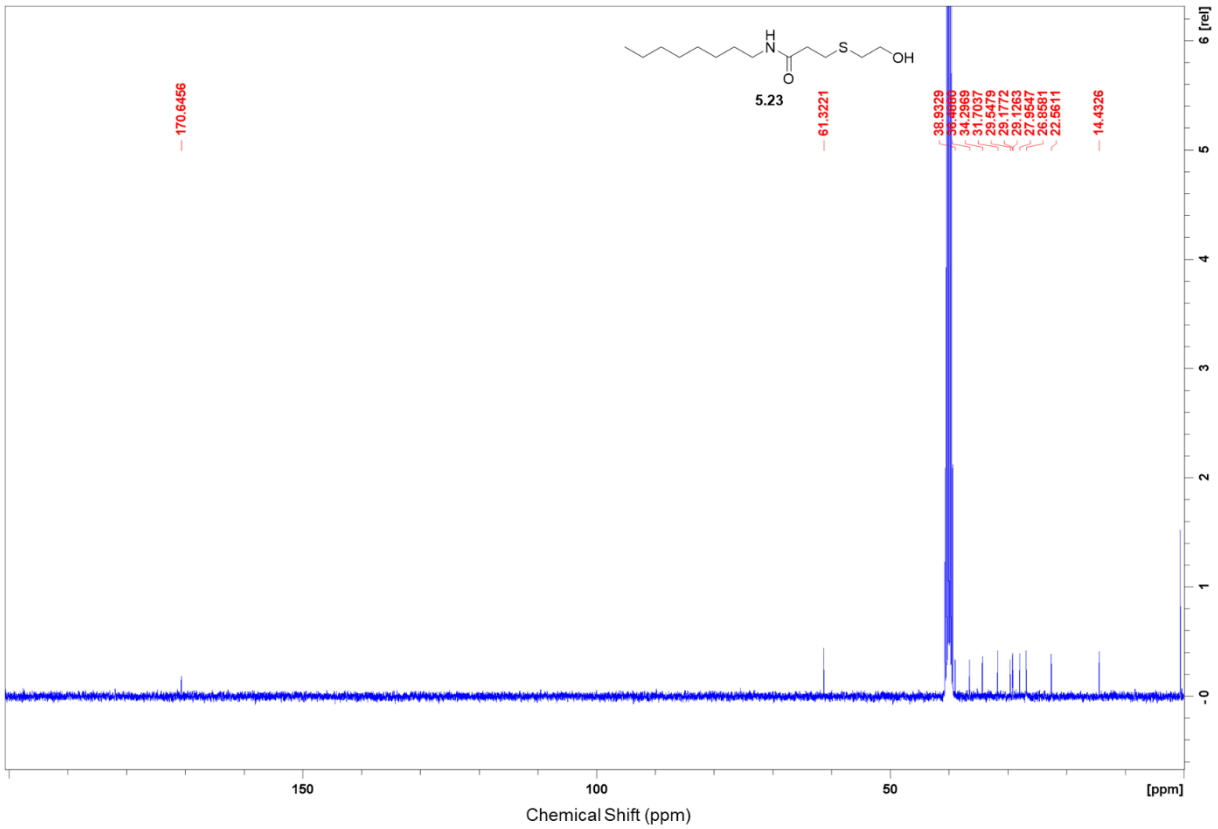
5.23
170.6456
61.3221
38.9329
34.2969
31.7037
29.5479
29.1772
29.1263
27.9547
26.8581
22.5611
14.4326
[rel]
[ppm]
Chemical Shift (ppm)

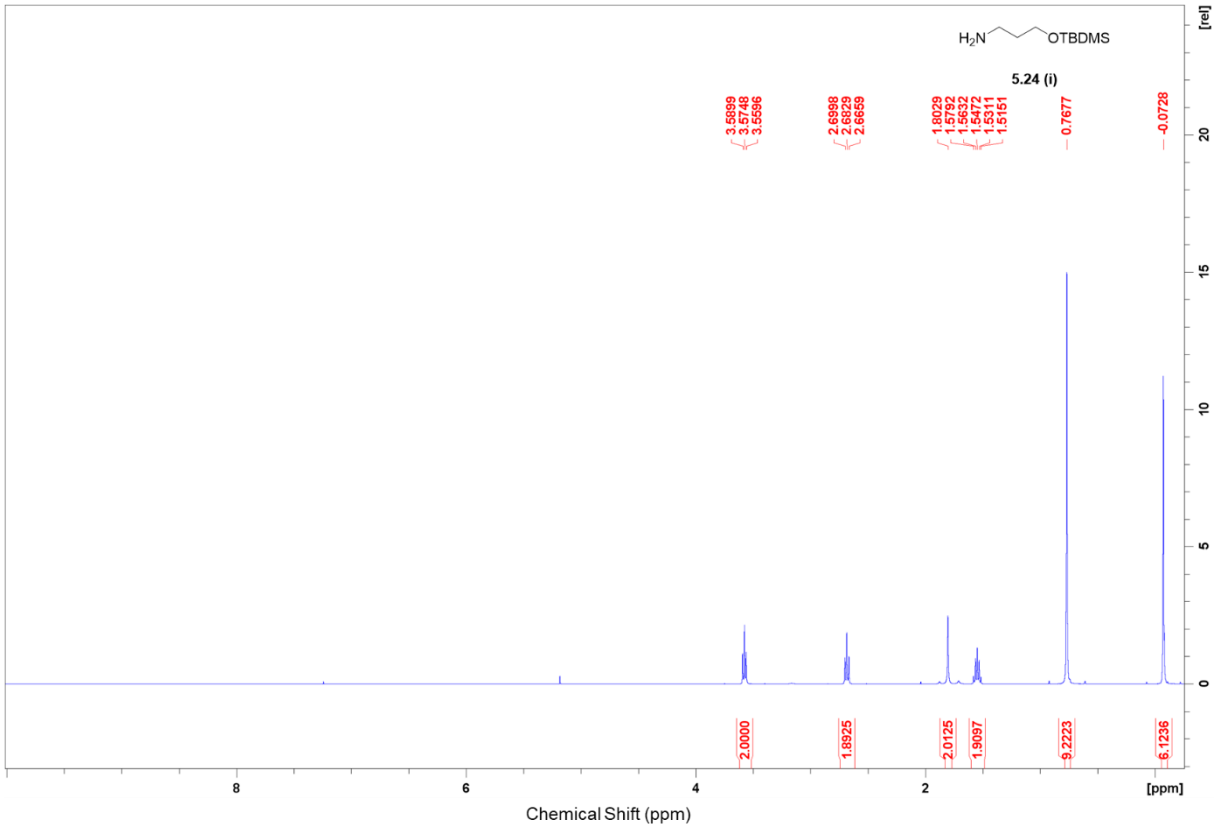
H2N
OTBDMS
5.24 (i)
3.5999
3.5748
3.5596
2.6998
2.6829
2.6669
1.8029
1.5792
1.5632
1.5472
1.5311
1.5151
0.7677
-0.0728
2.0000
1.8925
2.0125
1.9097
9.2223
6.1236
[rel]
[ppm]
Chemical Shift (ppm)

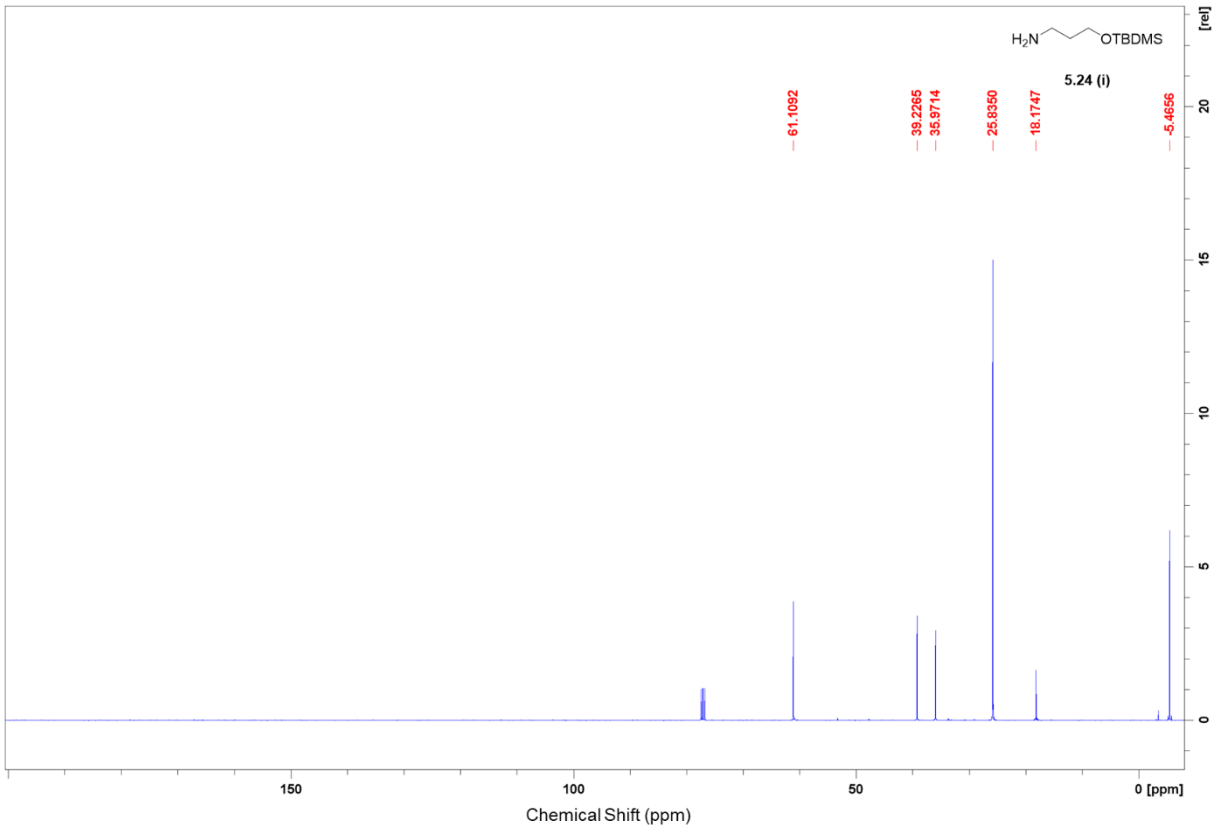
H2N
OTBDMS
5.24 (i)
61.1092
39.2265
35.9714
25.8350
18.1747
-5.4656
[rel]
[ppm]
Chemical Shift (ppm)

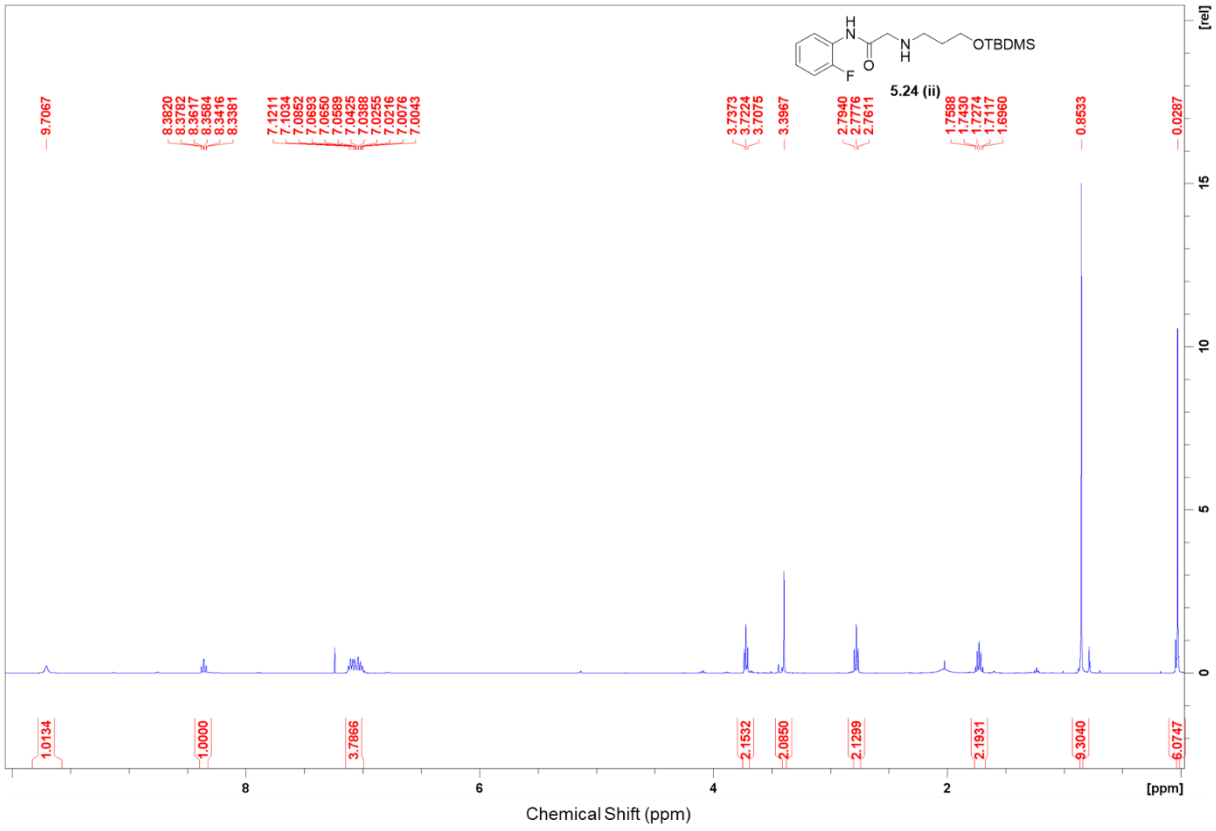
5.24 (ii)
OTBDMS
9.7067
8.3820
8.3782
8.3617
8.3584
8.3416
8.3381
7.1211
7.1034
7.0852
7.0693
7.0650
7.0599
7.0425
7.0388
7.0255
7.0216
7.0076
7.0043
3.7373
3.7224
3.7075
3.3967
2.7940
2.7776
2.7611
1.7588
1.7430
1.7274
1.7117
1.6960
0.8533
0.0287
1.0134
1.0000
3.7866
2.1532
2.0850
2.1299
2.1931
9.3040
6.0747
[rel]
[ppm]
Chemical Shift (ppm)

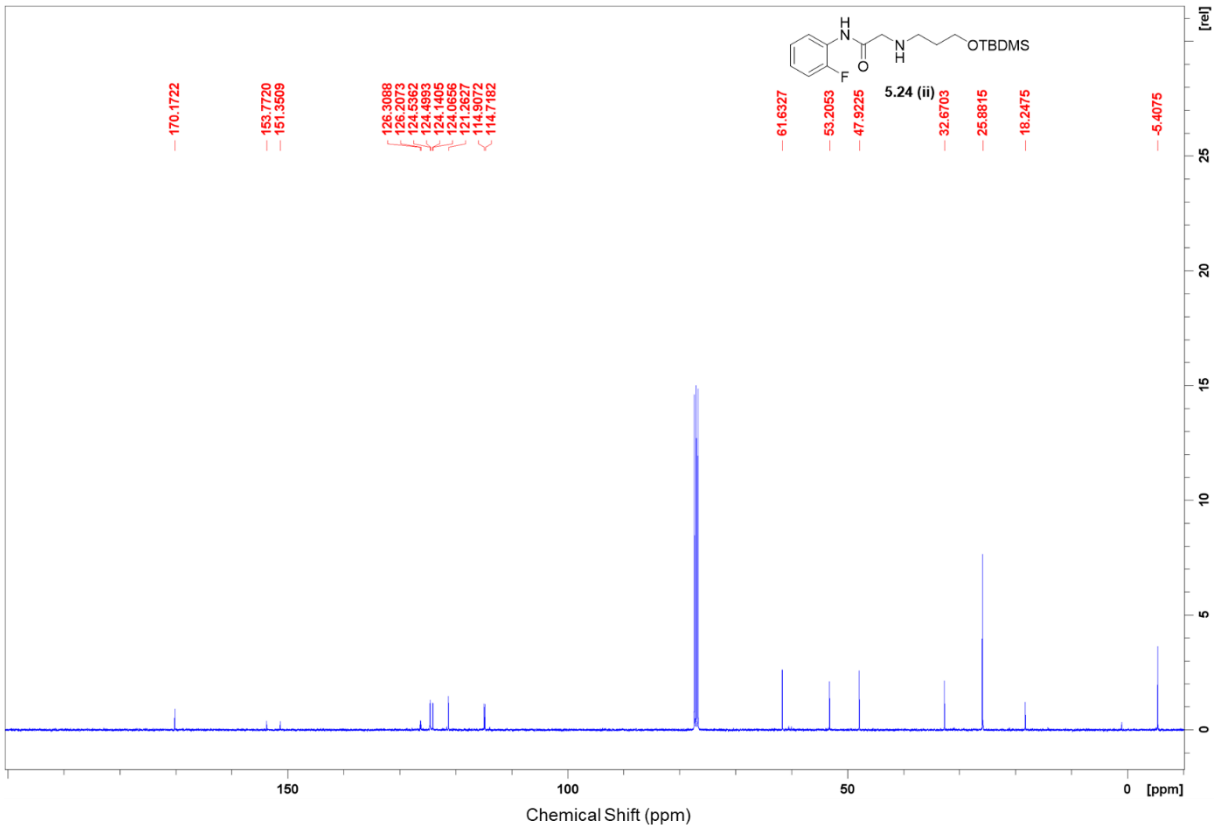
5.24 (ii)
OTBDMS
170.1722
153.7720
151.3509
126.3088
126.2073
124.5362
124.4983
124.1405
124.0656
121.2627
114.6972
114.7162
61.6327
53.2053
47.9225
32.6703
25.8815
18.2475
-5.4075
[rel]
[ppm]
Chemical Shift (ppm)

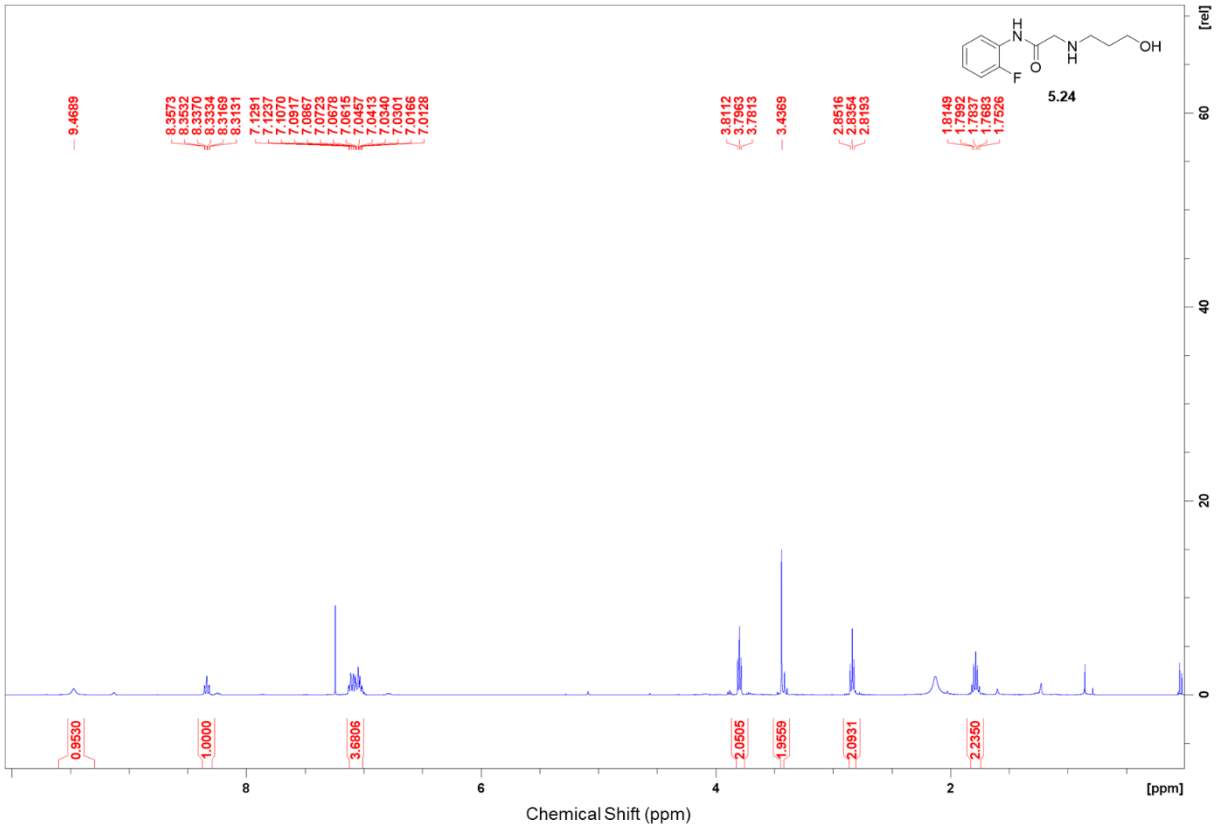
9.4689
8.3573
8.3552
8.3370
8.3334
8.3169
8.3131
7.1291
7.1237
7.1070
7.0917
7.0867
7.0723
7.0678
7.0615
7.0457
7.0413
7.0340
7.0301
7.0166
7.0128
3.8112
3.7963
3.7813
3.4369
2.8516
2.8354
2.8193
1.8149
1.7992
1.7837
1.7683
1.7526
0.9530
1.0000
3.6806
2.0505
1.9559
2.0931
2.2350
5.24
[rel]
[ppm]
Chemical Shift (ppm)

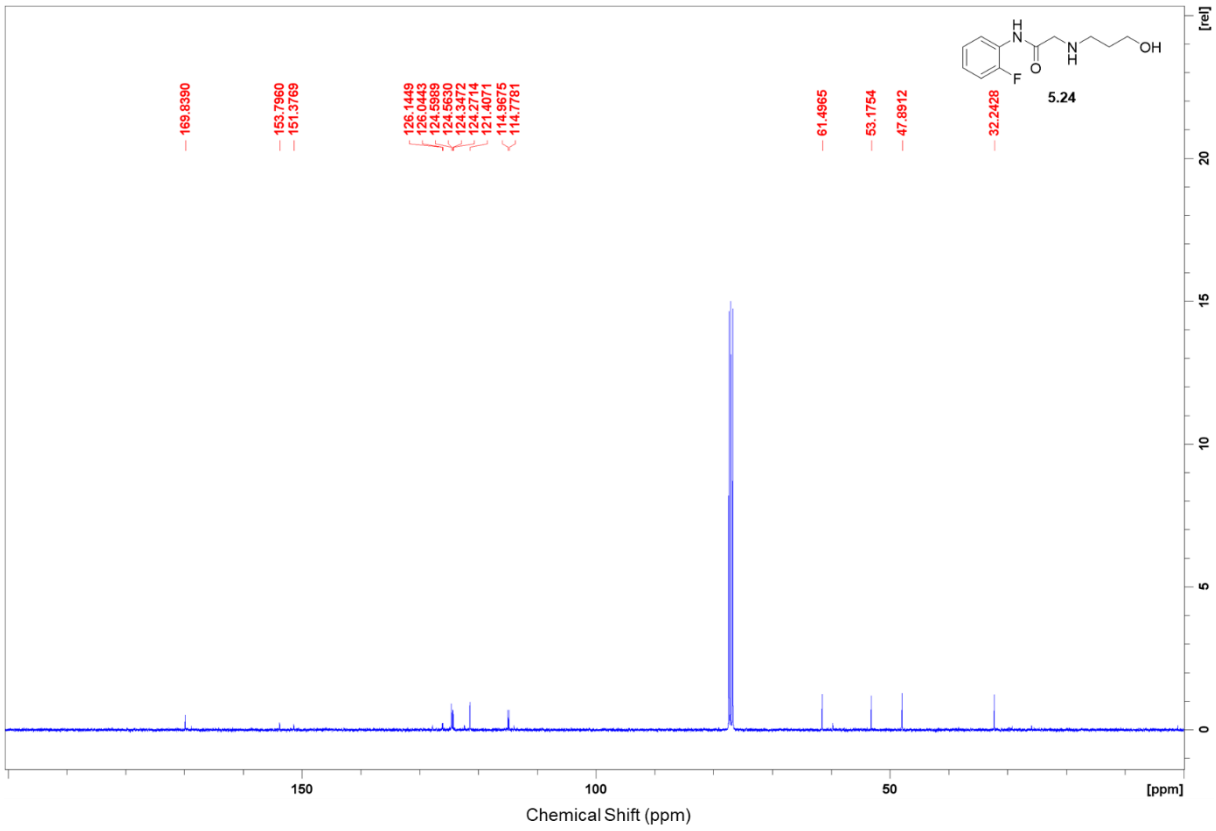
169.8390
153.7960
151.3769
126.1449
126.0443
124.5989
124.5630
124.3472
124.2714
121.4071
114.9675
114.7781
61.4965
53.1754
47.8912
32.2428
5.24
[rel]
[ppm]
Chemical Shift (ppm)

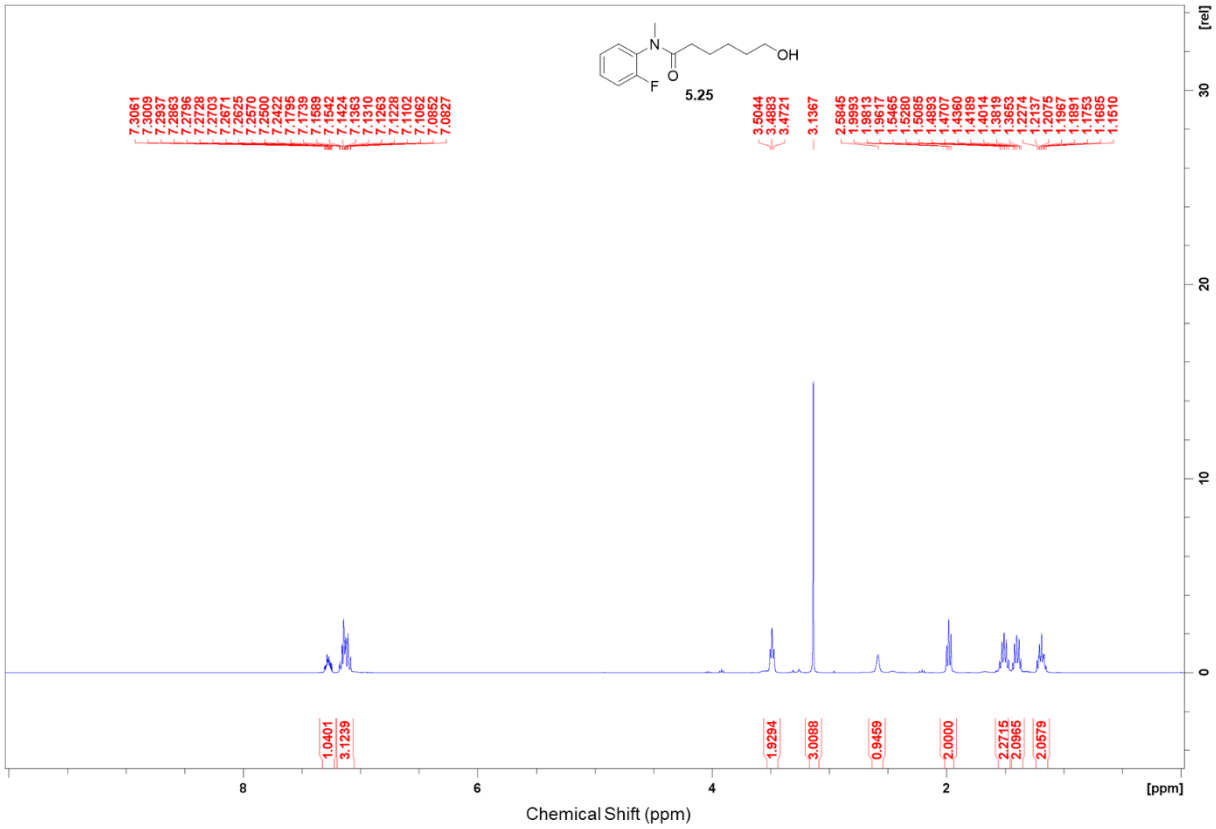
5.25
7.3061
7.3009
7.2937
7.2863
7.2796
7.2728
7.2703
7.2671
7.2625
7.2570
7.2500
7.2422
7.1795
7.1739
7.1589
7.1542
7.1424
7.1363
7.1310
7.1263
7.1228
7.1102
7.1062
7.0852
7.0827
3.5044
3.4883
3.4721
3.1367
2.5845
1.9993
1.9813
1.9617
1.5465
1.5280
1.5085
1.4893
1.4707
1.4360
1.4189
1.4014
1.3843
1.2274
1.2137
1.2075
1.1967
1.1891
1.1753
1.1685
1.1510
1.0401
3.1239
1.9294
3.0086
0.9459
2.0000
2.2715
2.0965
2.0579
[rel]
[ppm]
Chemical Shift (ppm)

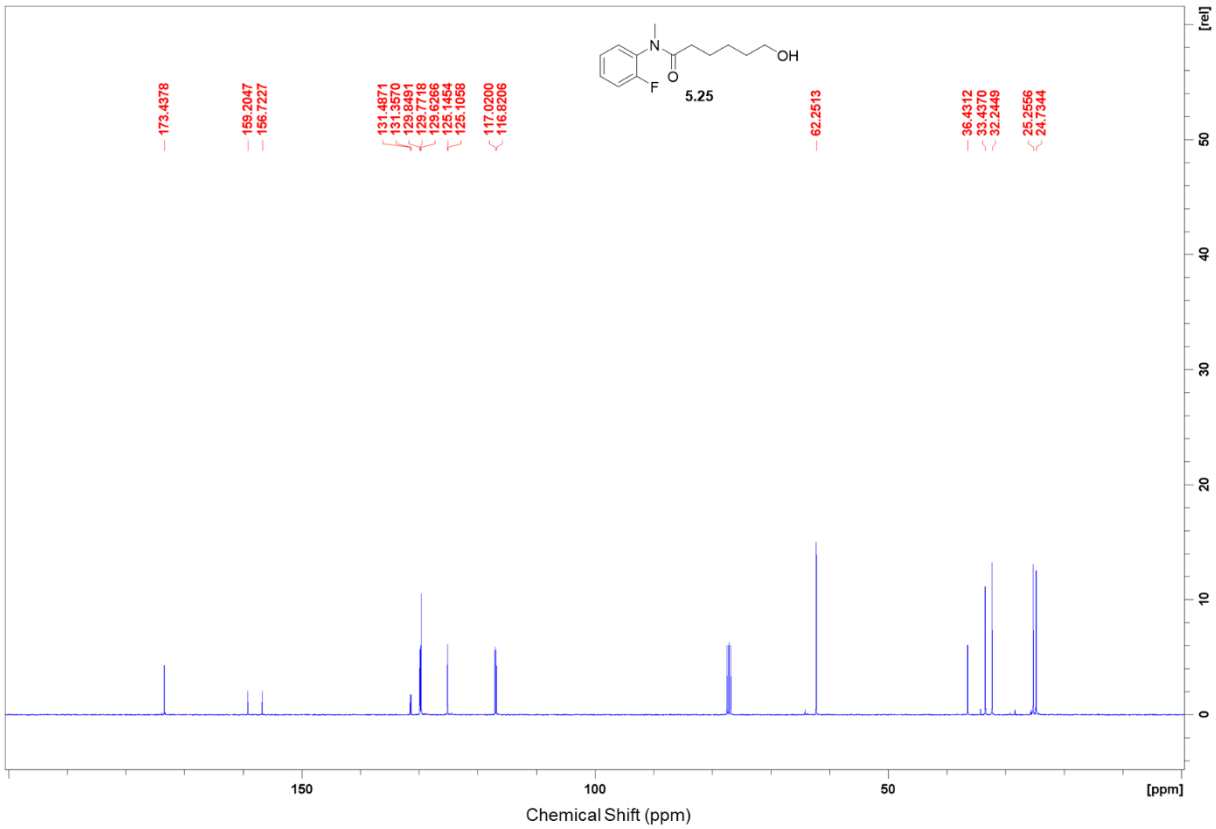
5.25
173.4378
159.2047
156.7227
131.4871
131.3570
129.9441
129.8778
129.6266
125.1454
125.1058
117.0200
116.8206
62.2513
36.4312
33.4370
32.2449
25.2556
24.7344
[rel]
[ppm]
Chemical Shift (ppm)

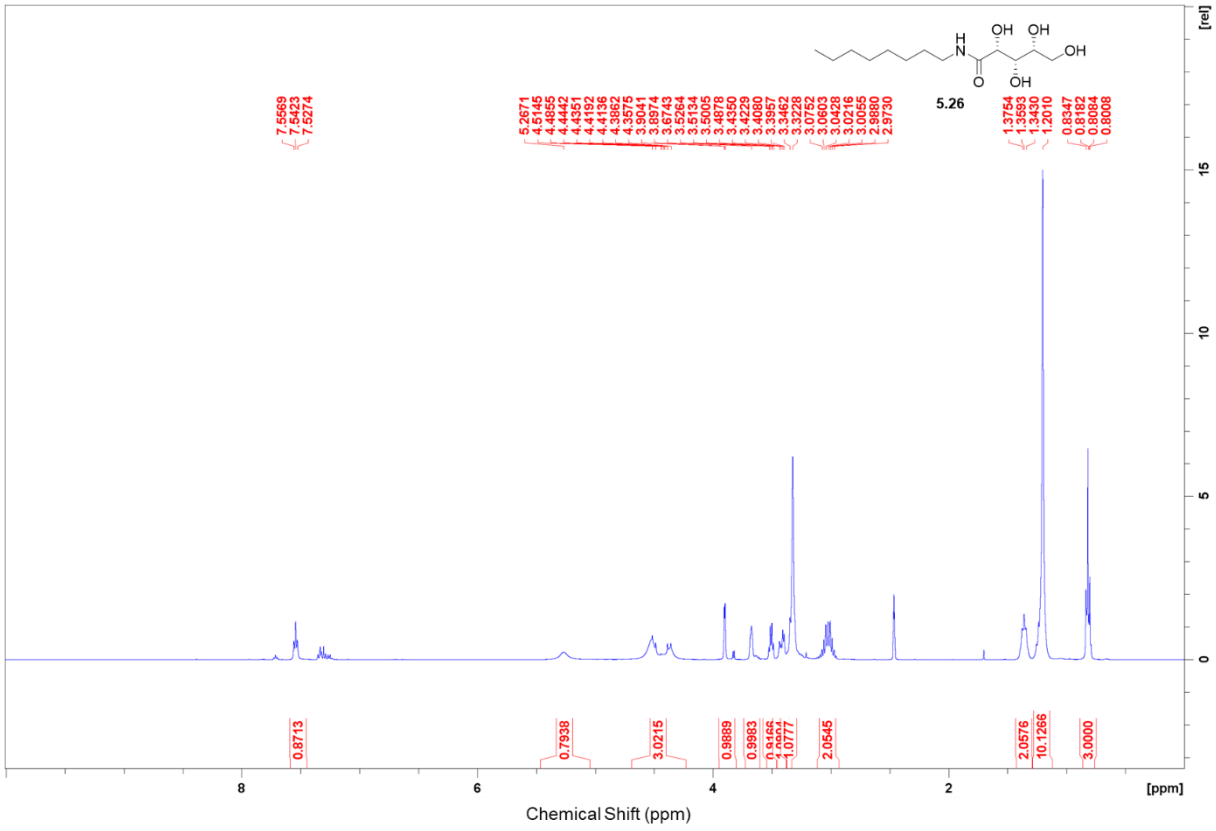
5.26
7.5669
7.5423
7.5274
5.2671
4.5145
4.4855
4.4442
4.4351
4.4193
4.4136
4.3862
4.3575
3.9041
3.8974
3.6743
3.5264
3.5134
3.5005
3.4878
3.4350
3.4229
3.4060
3.3957
3.3462
3.3228
3.0752
3.0603
3.0428
3.0216
3.0065
2.9880
2.9730
1.3754
1.3593
1.3430
1.2010
0.8347
0.8192
0.8084
0.8008
0.8713
0.7938
3.0215
0.9889
0.9983
2.0545
2.0576
10.1266
3.0000
[rel]
[ppm]
Chemical Shift (ppm)

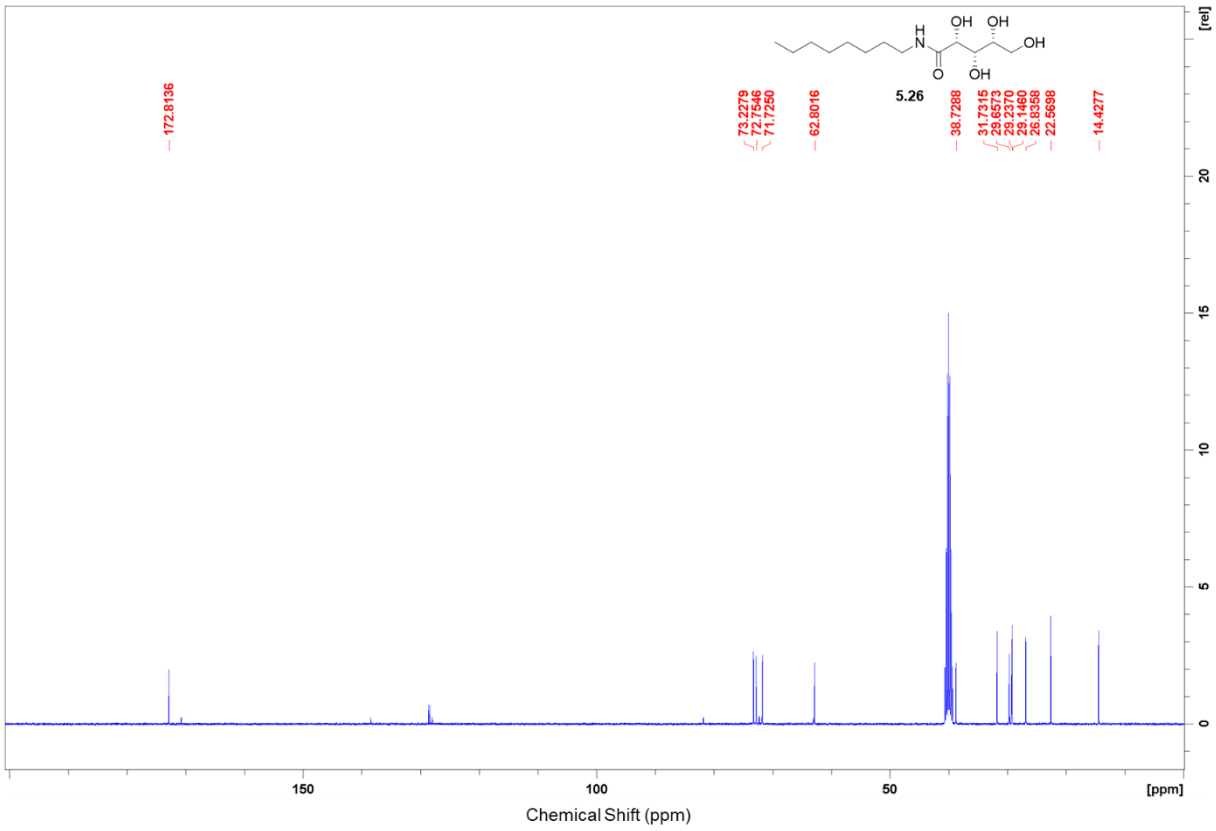
5.26
172.8136
73.2279
72.7546
71.7250
62.8016
38.7288
31.7315
29.6573
29.2770
29.1460
26.8358
22.5698
14.4277
[rel]
[ppm]
Chemical Shift (ppm)

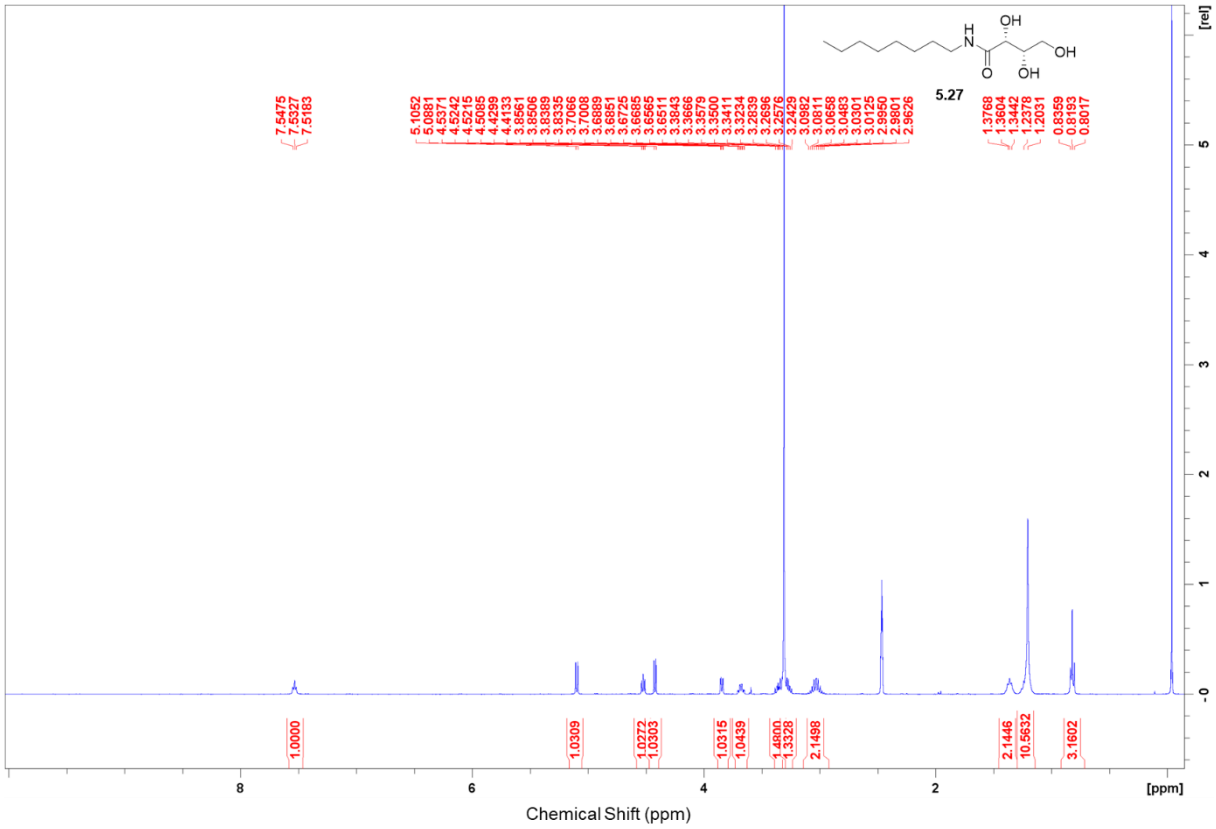
5.27
Chemical Shift (ppm)

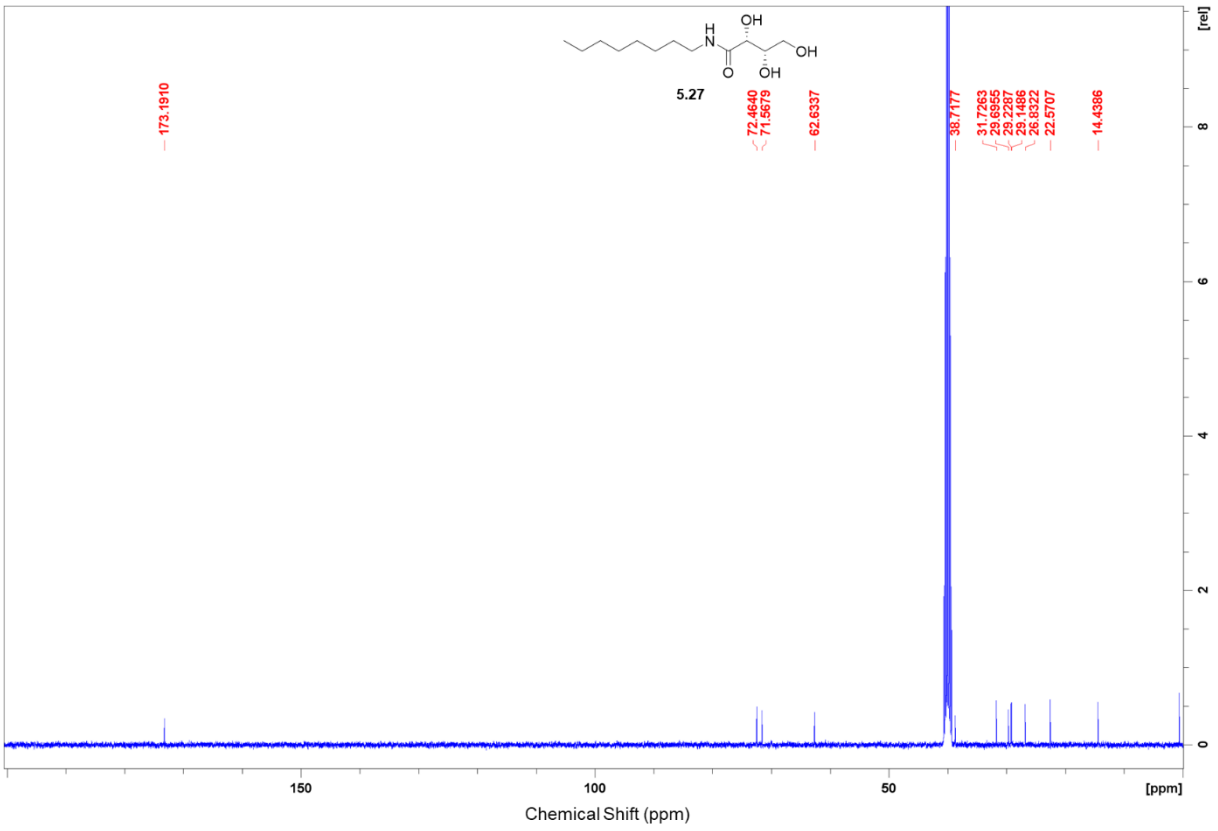
5.27
Chemical Shift (ppm)

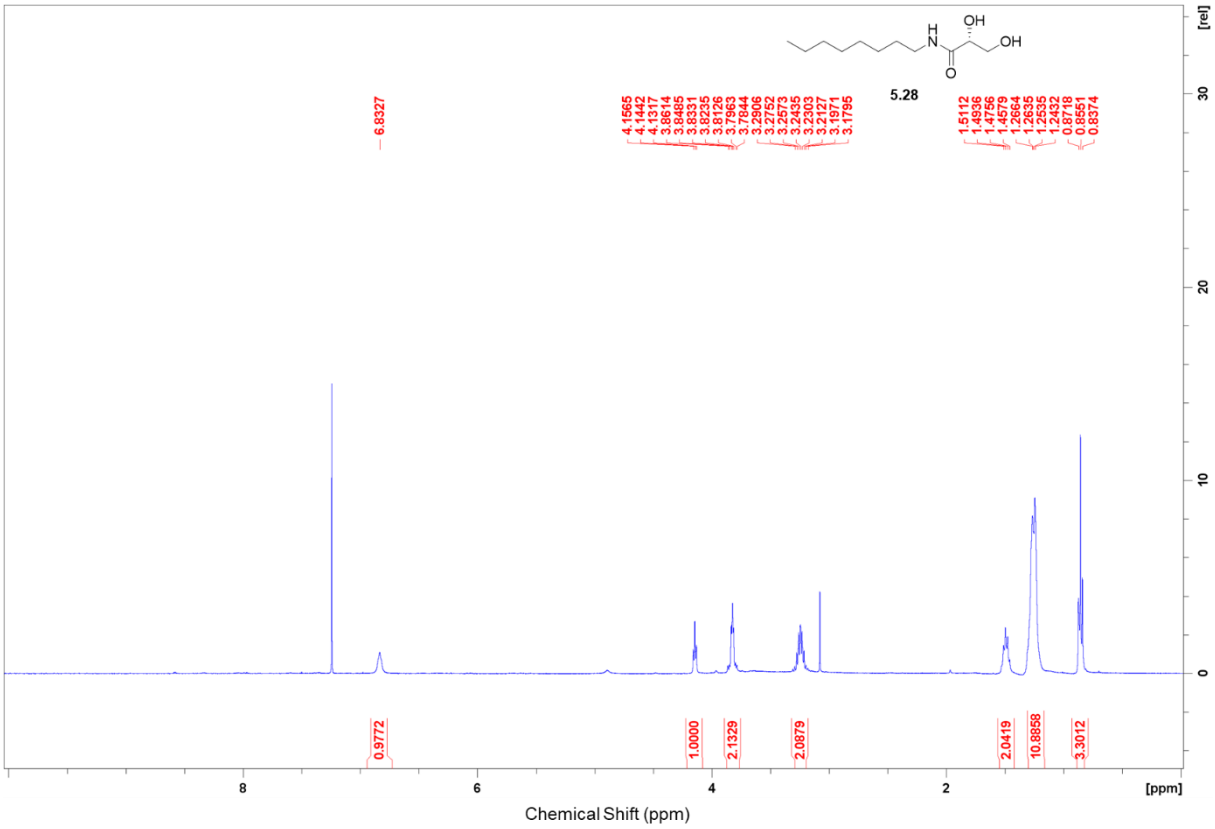
OH
OH
N
H
O
5.28
6.8327
4.1565
4.1442
4.1317
3.8614
3.8485
3.8351
3.8235
3.8126
3.7963
3.7844
3.2906
3.2752
3.2573
3.2435
3.2303
3.2127
3.1971
3.1795
1.5112
1.4936
1.4756
1.4579
1.2684
1.2535
1.2432
0.8718
0.8551
0.8374
0.9772
1.0000
2.1329
2.0879
2.0419
10.8858
3.3012
[rel]
30
20
10
0
8
6
4
2
[ppm]
Chemical Shift (ppm)

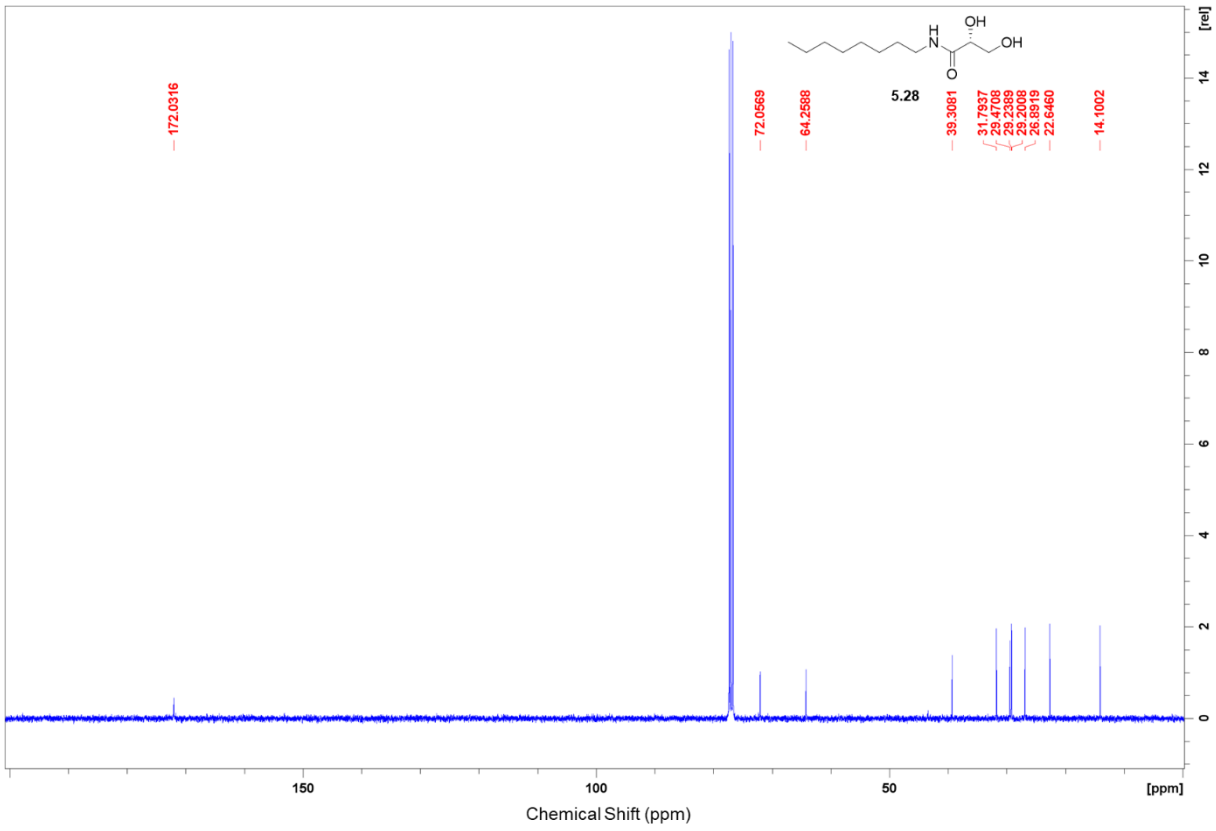
OH
OH
N
H
O
5.28
172.0316
72.0569
64.2588
39.3081
31.7937
29.4798
29.2369
29.2008
26.8919
22.6460
14.1002
[rel]
14
12
10
8
6
4
2
0
150
100
50
[ppm]
Chemical Shift (ppm)

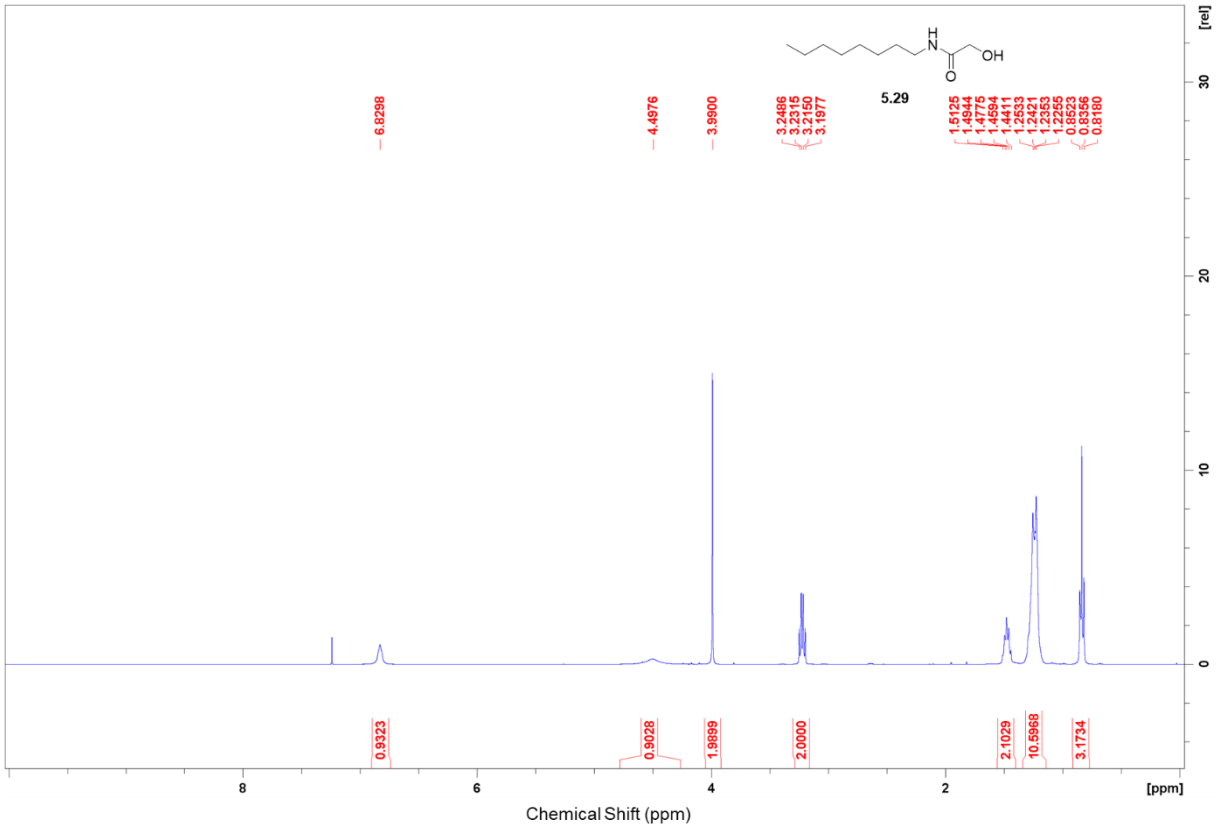
5.29
6.8298
4.4976
3.9900
3.2486
3.2315
3.2150
3.1977
1.5125
1.4944
1.4775
1.4584
1.4411
1.2533
1.2421
1.2353
1.2255
0.8523
0.8356
0.8180
0.9323
0.9028
1.9899
2.0000
2.1029
10.5968
3.1734
[rel]
[ppm]
Chemical Shift (ppm)

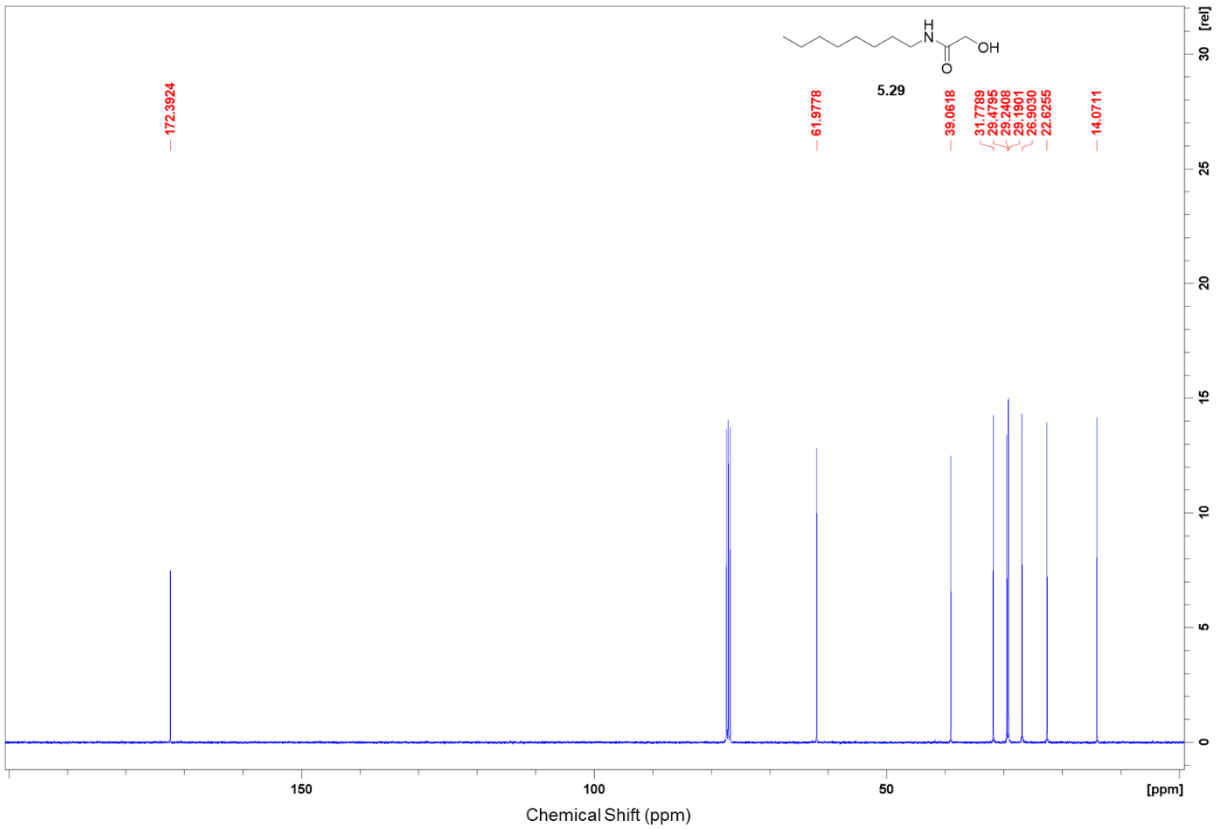
5.29
172.3924
61.9778
39.0618
31.7789
29.4795
29.2408
29.1901
26.9030
22.6255
14.0711
[rel]
[ppm]
Chemical Shift (ppm)

Appendix V. IRI data obtained on the modified splat cooling assay

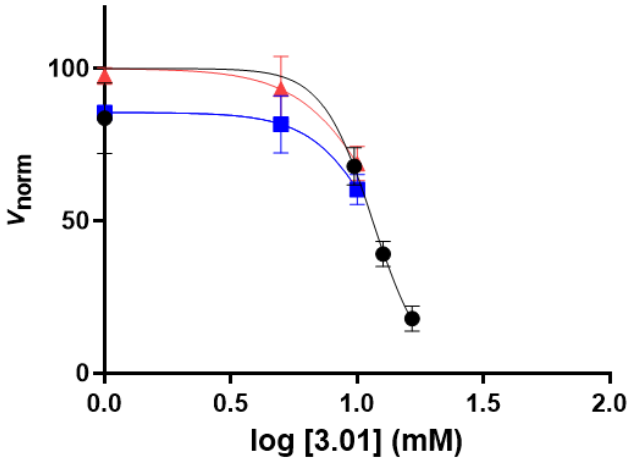

PBS Reference IC_{50} = 12 mM
AgI Norm PBS IC_{50} = 13 mM
AgI Norm AgI IC_{50} = 14 mM

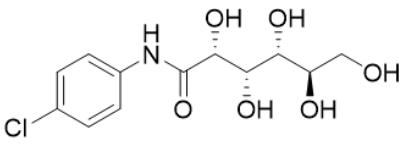

3.01

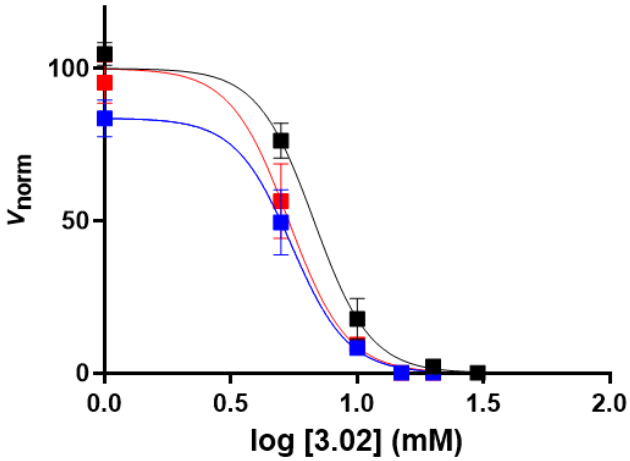

PBS Reference IC_{50} = 6.7 mM
AgI Norm PBS IC_{50} = 5.5 mM
AgI Norm AgI IC_{50} = 5.4 mM

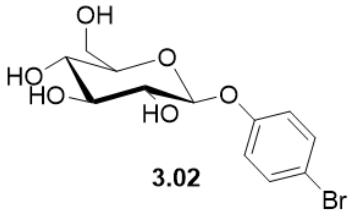

3.02

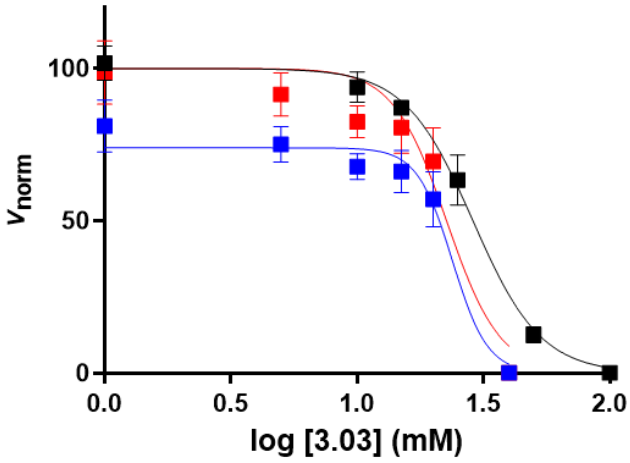

PBS Reference IC_{50} = 29 mM
AgI Norm PBS IC_{50} = 25 mM
AgI Norm AgI IC_{50} = 23 mM

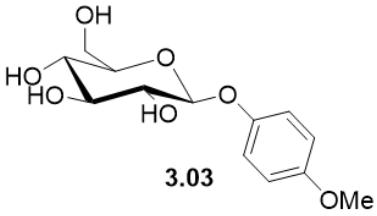

3.03

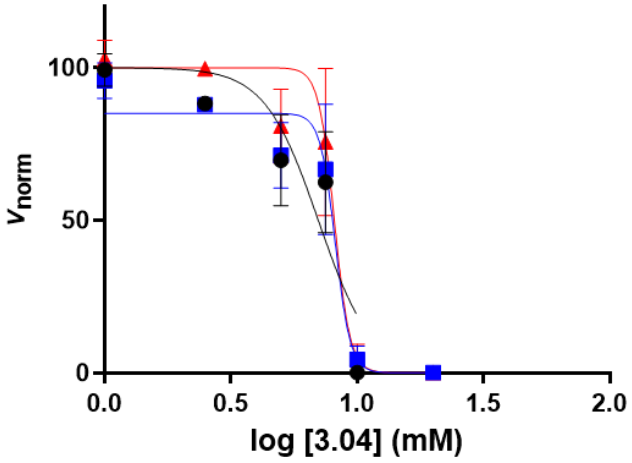

PBS Reference IC_{50} = 7.0 mM
AgI Norm PBS IC_{50} = 8.2 mM
AgI Norm AgI IC_{50} = 8.1 mM

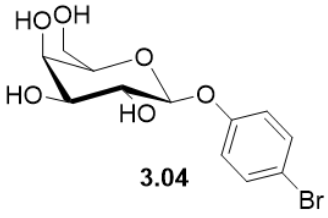

3.04

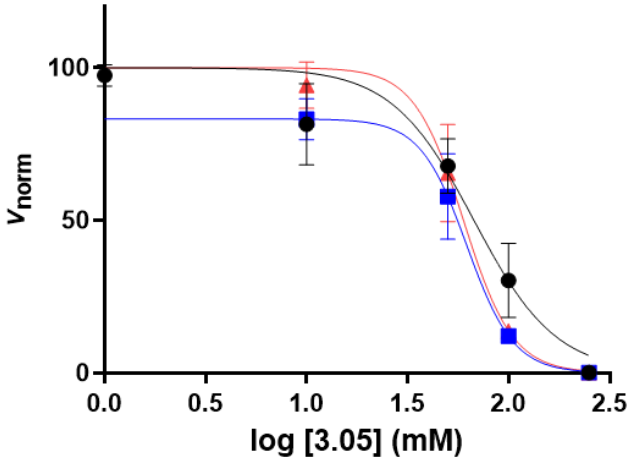

PBS Reference IC_{50} = 67 mM
AgI Norm PBS IC_{50} = 62 mM
AgI Norm AgI IC_{50} = 60 mM

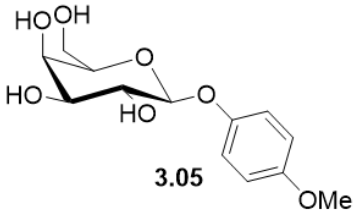

3.05

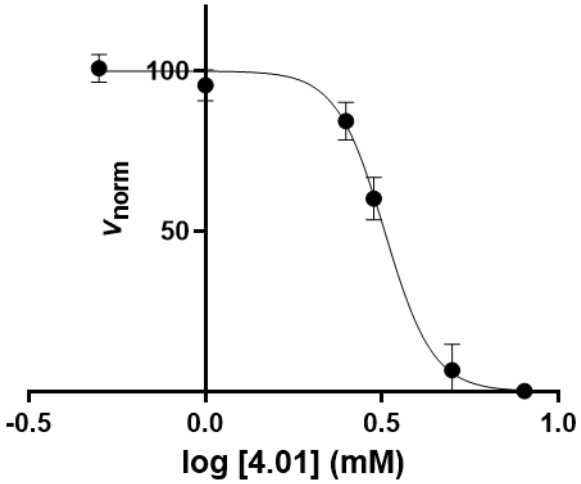

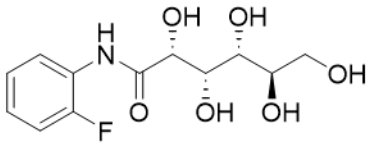

4.01

IC_{50} = 3.2 mM
$CI_{95\%}$ = [3.1 , 3.4]
Hillslope = -6.4
[Maximum] = 8 mM

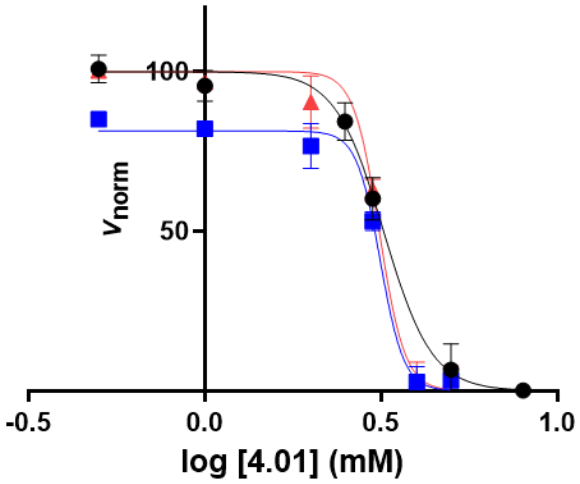

PBS Reference IC_{50} = 3.2 mM
AgI Norm PBS IC_{50} = 3.1 mM
AgI Norm AgI IC_{50} = 3.1 mM

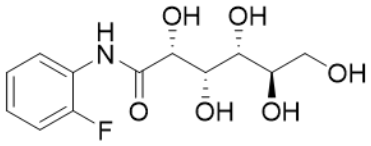

4.01

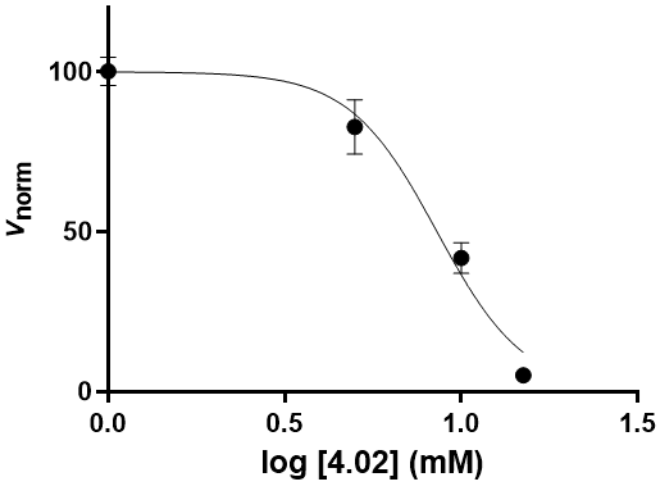

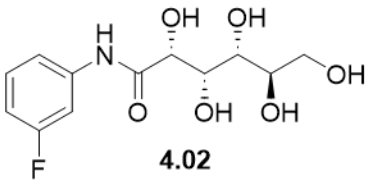

4.02

IC_{50} = 8.5 mM
$CI_{95\%}$ = [5.8 , 11]
Hillslope = -3.5
[Maximum] = 15 mM

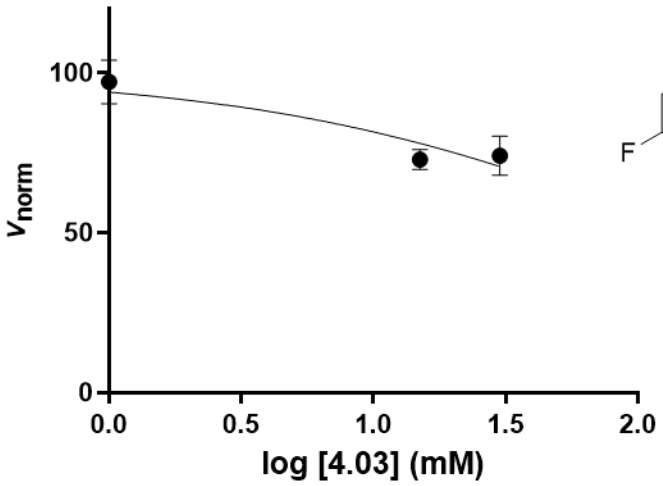

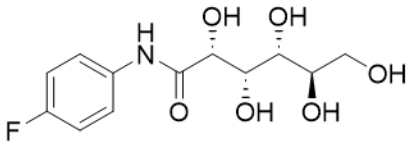

4.03

IC_{50} = N/A
$CI_{95\%}$ = N/A
Hillslope = N/A
[Maximum] = 30 mM

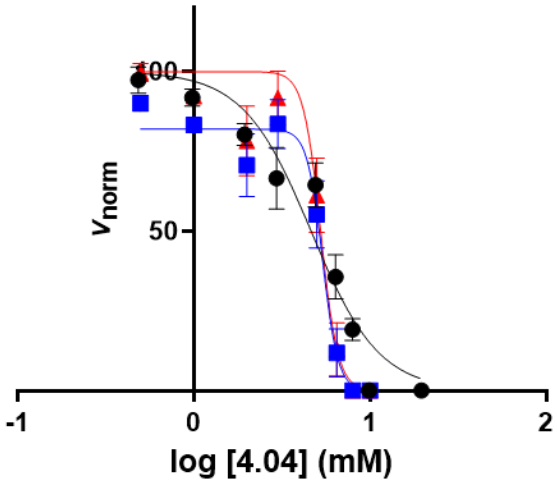

PBS Reference IC_{50} = 4.6 mM
AgI Norm PBS IC_{50} = 5.3 mM
AgI Norm AgI IC_{50} = 5.2 mM

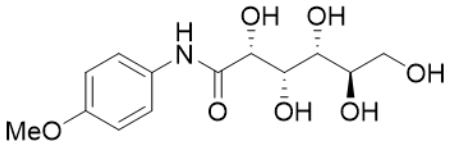

4.04

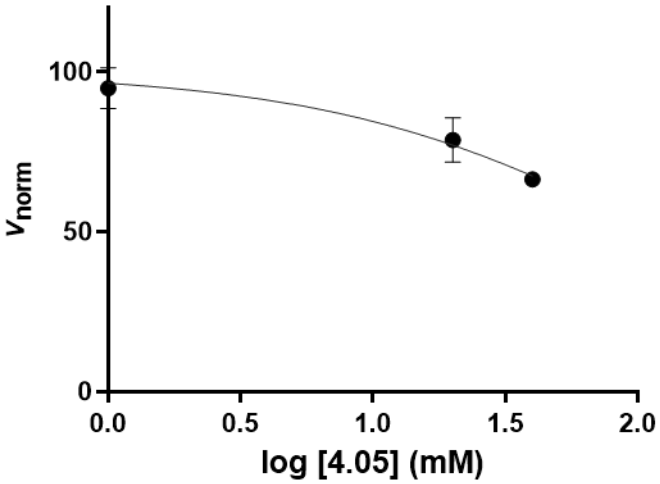

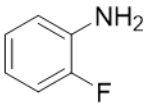

4.05

IC_{50} = N/A
$CI_{95\%}$ = N/A
Hillslope = N/A
[Maximum] = 40 mM

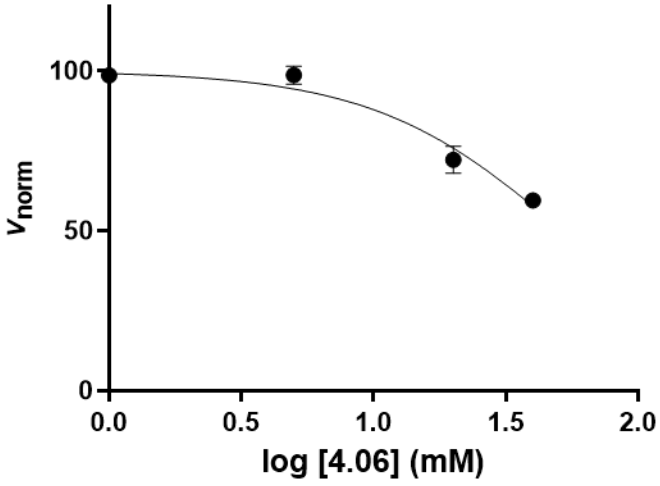

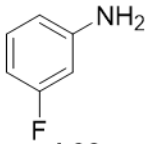

4.06

IC_{50} = N/A
$CI_{95\%}$ = N/A
Hillslope = N/A
[Maximum] = 40 mM

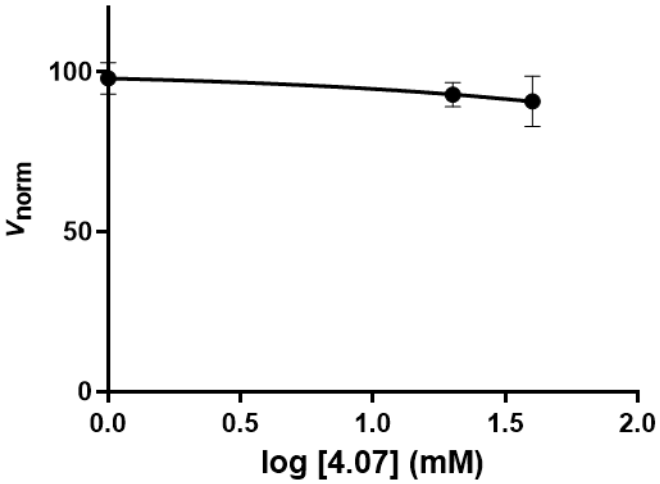

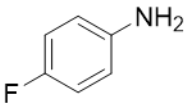

4.07

IC_{50} = N/A
$CI_{95\%}$ = N/A
Hillslope = N/A
[Maximum] = 40 mM

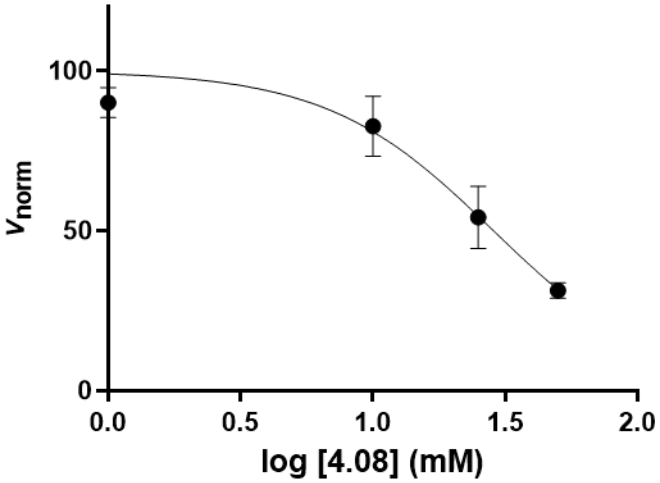

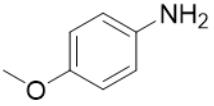

4.08

IC_{50} = 29 mM
$CI_{95\%}$ = [15 , 95]
Hillslope = -1.4
[Maximum] = 50 mM

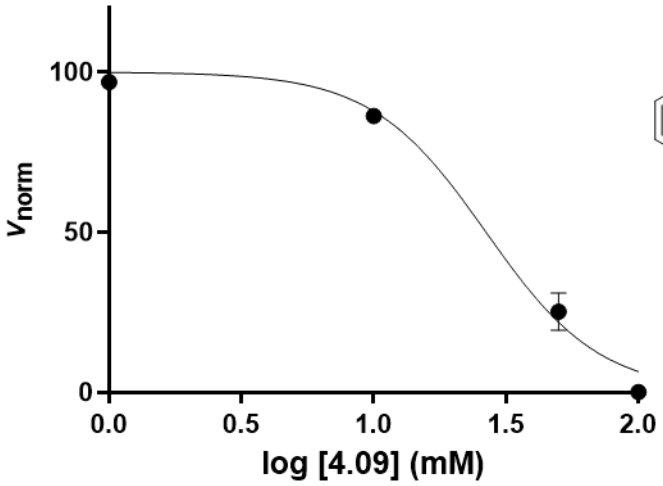

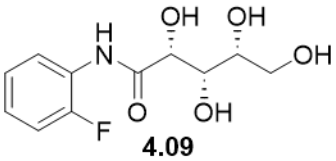

4.09

IC_{50} = 27 mM
$CI_{95\%}$ = [15 , inf]
Hillslope = -2.0
[Maximum] = 100 mM

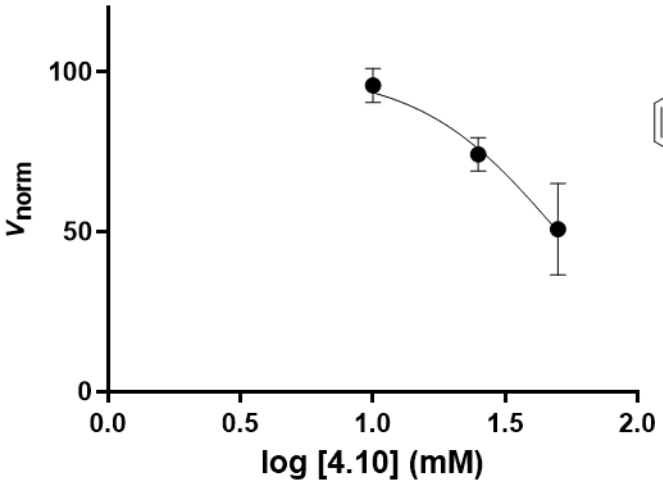

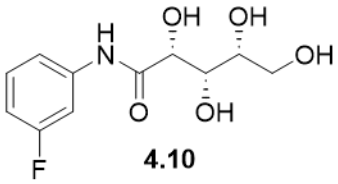

4.10

IC_{50} = 50 mM
$CI_{95\%}$ = [25 , inf]
Hillslope = -1.7
[Maximum] = 50 mM

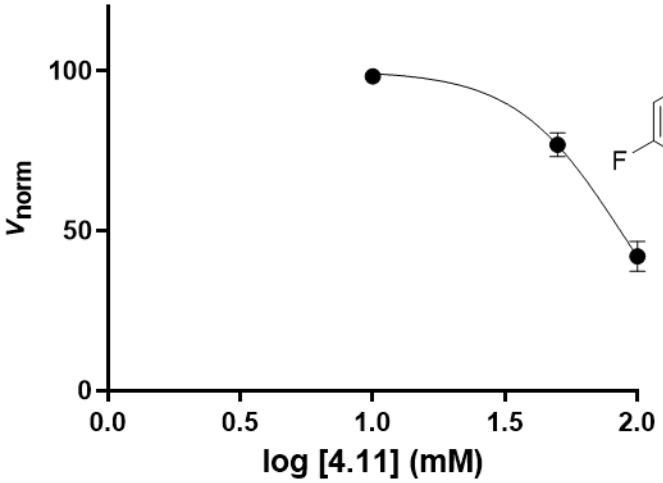

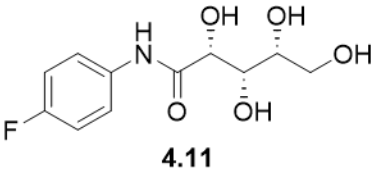

4.11

IC_{50} = 86 mM
$CI_{95\%}$ = [74 , 107]
Hillslope = -2.2
[Maximum] = 100 mM

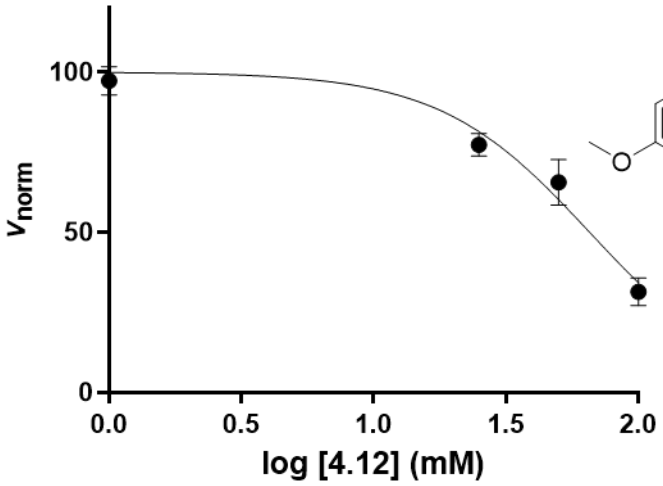

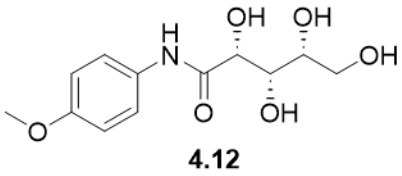

4.12

IC_{50} = 65 mM
$CI_{95\%}$ = [42 , 153]
Hillslope = -1.5
[Maximum] = 100 mM

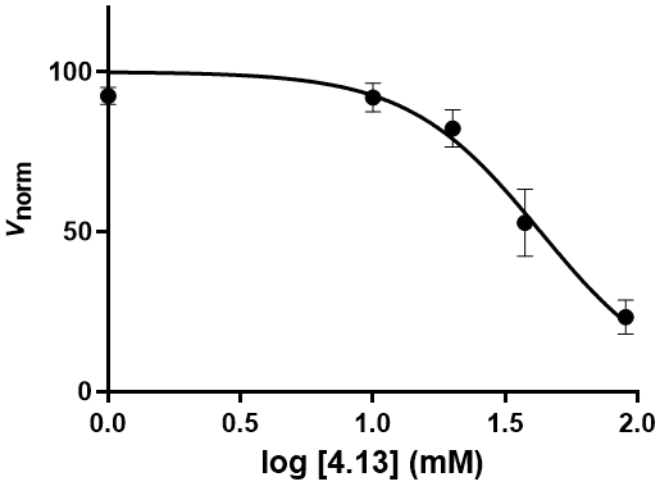

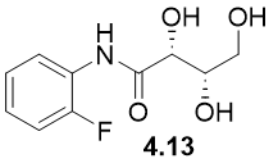

4.13

IC_{50} = 43 mM
$CI_{95\%}$ = [33 , 58]
Hillslope = -1.7
[Maximum] = 90 mM

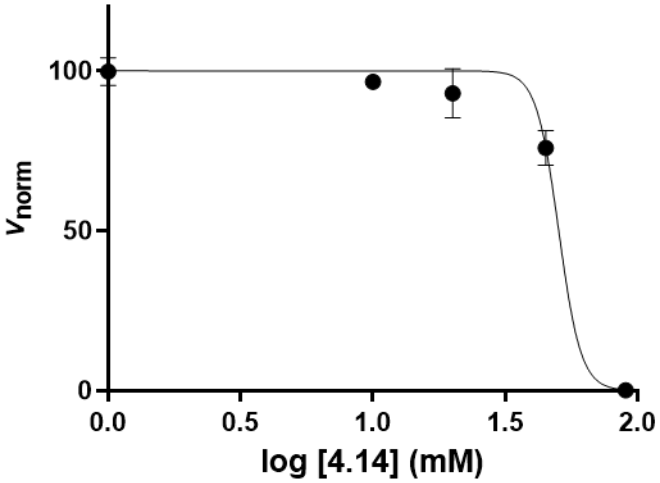

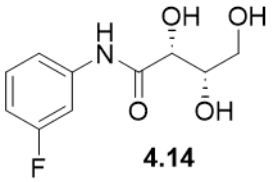

4.14

IC_{50} = 50 mM
$CI_{95\%}$ = [0 , 61]
Hillslope = -10
[Maximum] = 90 mM

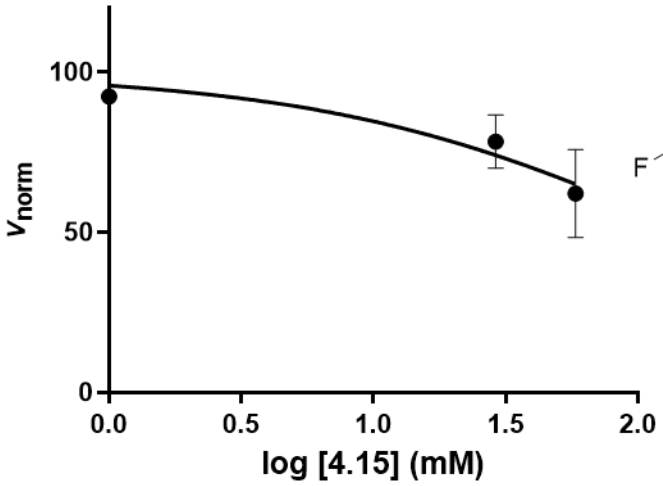

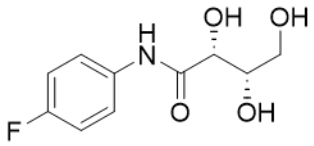

4.15

IC_{50} = N/A
$CI_{95\%}$ = N/A
Hillslope = N/A
[Maximum] = 58 mM

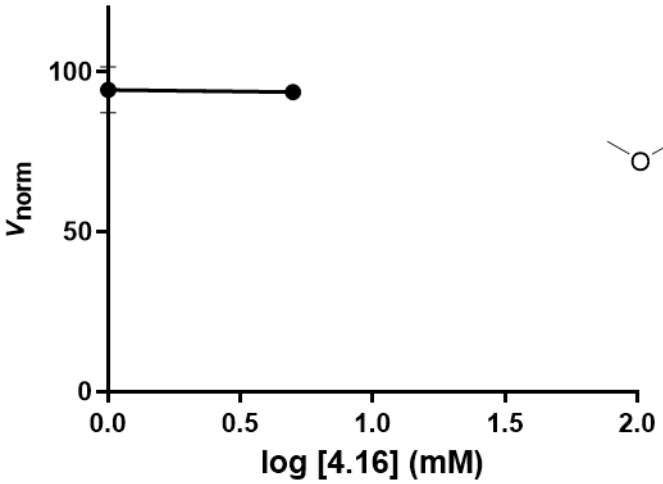

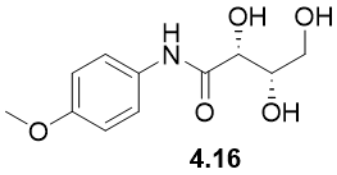

4.16

IC_{50} = N/A
$CI_{95\%}$ = N/A
Hillslope = N/A
[Maximum] = 5 mM

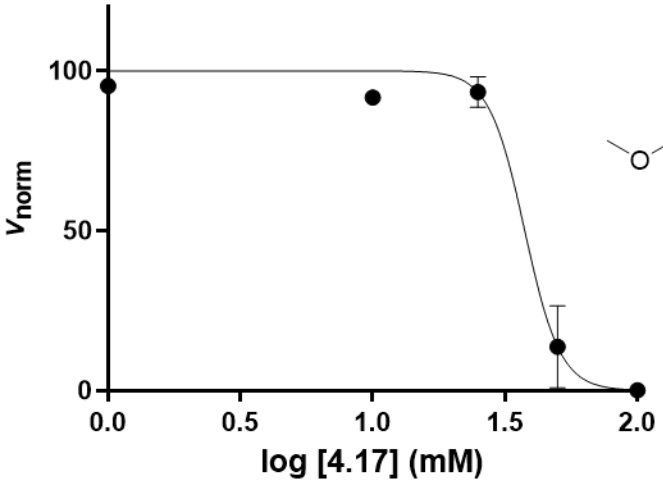

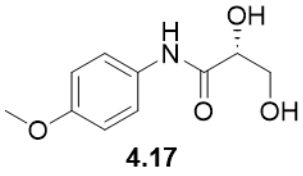

4.17

IC_{50} = 38 mM
$CI_{95\%}$ = N/A
Hillslope = -6.5
[Maximum] = 100 mM

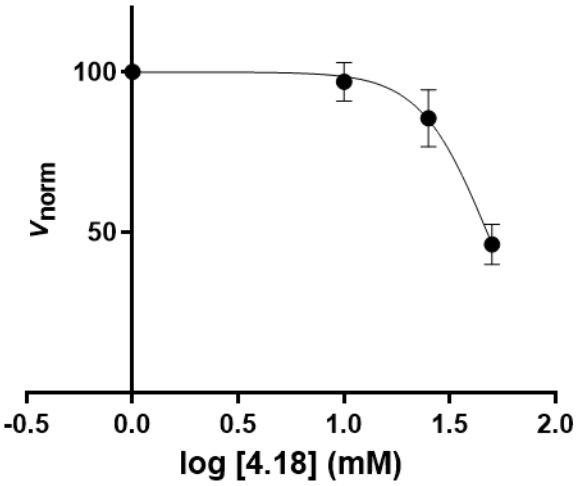

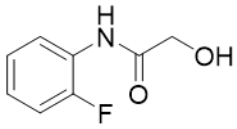

4.18

IC_{50} = 47 mM
$CI_{95\%}$ = [44 , 51]
Hillslope = -2.7
[Maximum] = 50 mM

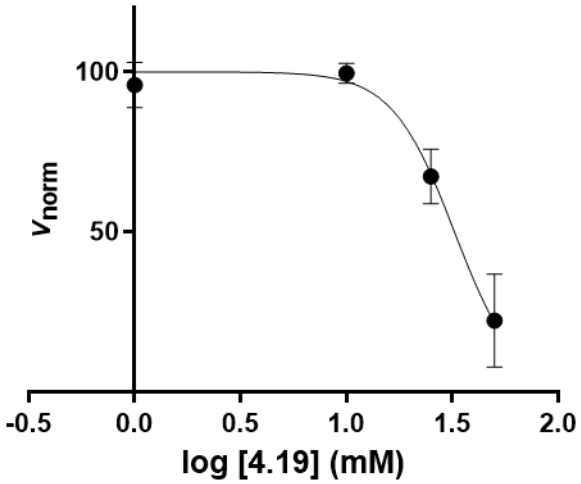

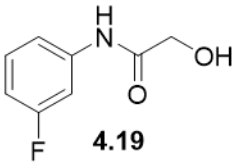

4.19

IC_{50} = 32 mM
$CI_{95\%}$ = [27 , 39]
Hillslope = -3.0
[Maximum] = 50 mM

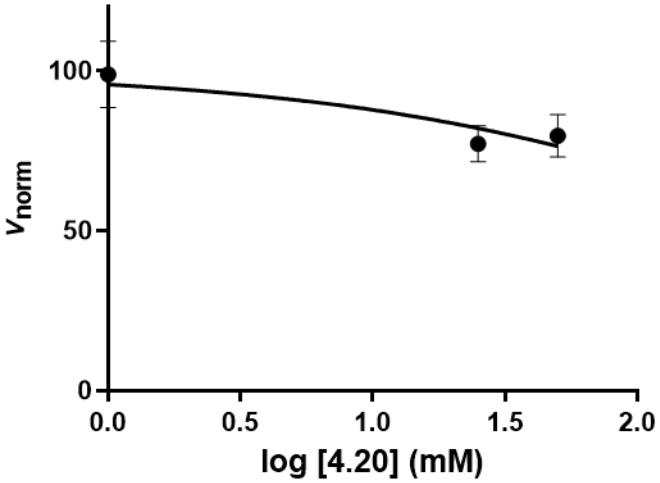

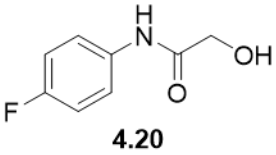

4.20

IC_{50} = N/A
$CI_{95\%}$ = N/A
Hillslope = N/A
[Maximum] = 50 mM

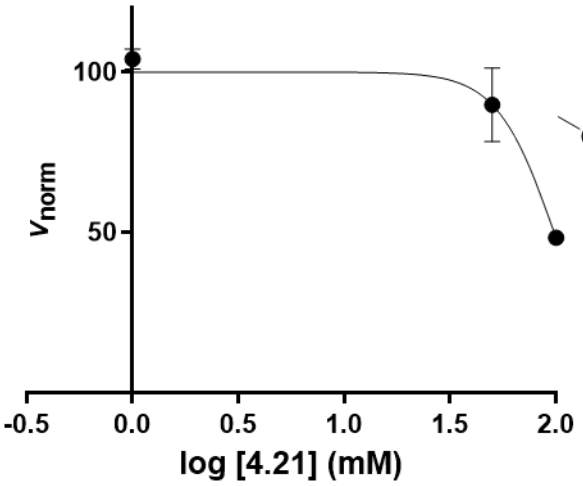

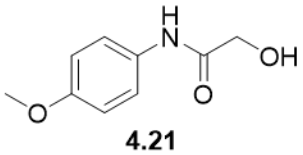

4.21

IC_{50} = 98 mM
$CI_{95\%}$ = [31 , inf.]
Hillslope = -3.2
[Maximum] = 100 mM

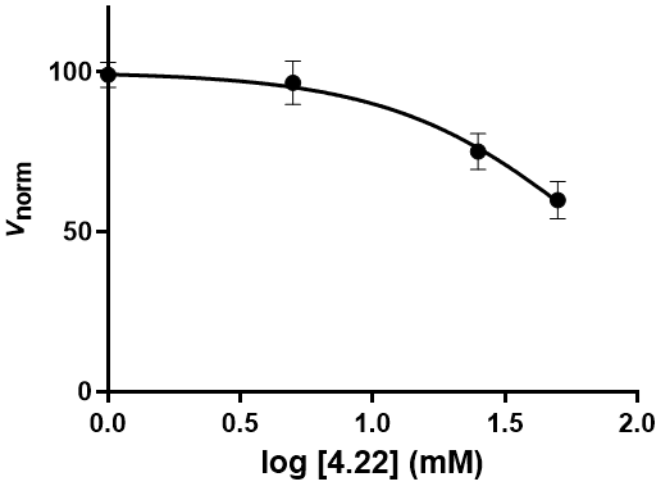

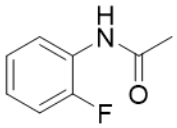

4.22

IC_{50} = N/A
$CI_{95\%}$ = N/A
Hillslope = N/A
[Maximum] = 50 mM

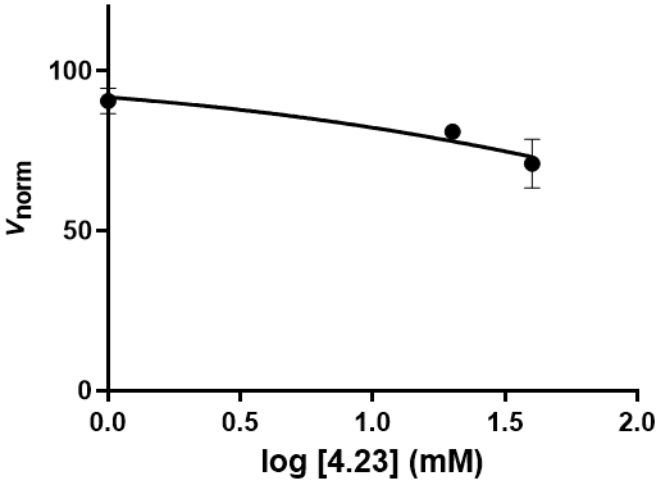

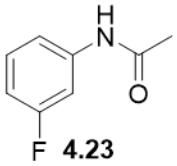

4.23

IC_{50} = N/A
$CI_{95\%}$ = N/A
Hillslope = N/A
[Maximum] = 40 mM

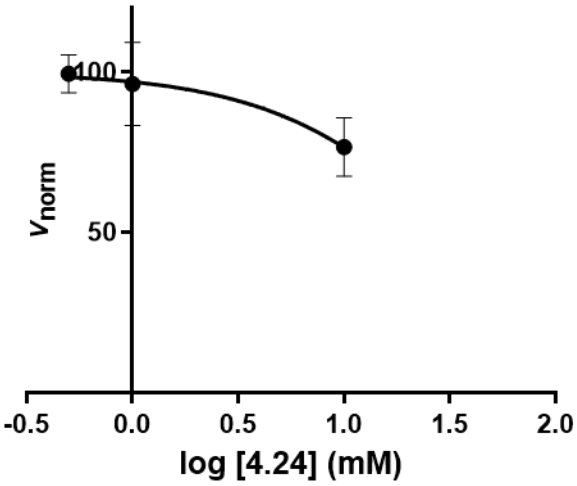

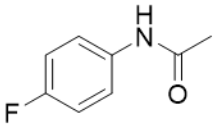

4.24

IC_{50} = N/A
$CI_{95\%}$ = N/A
Hillslope = N/A
[Maximum] = 10 mM

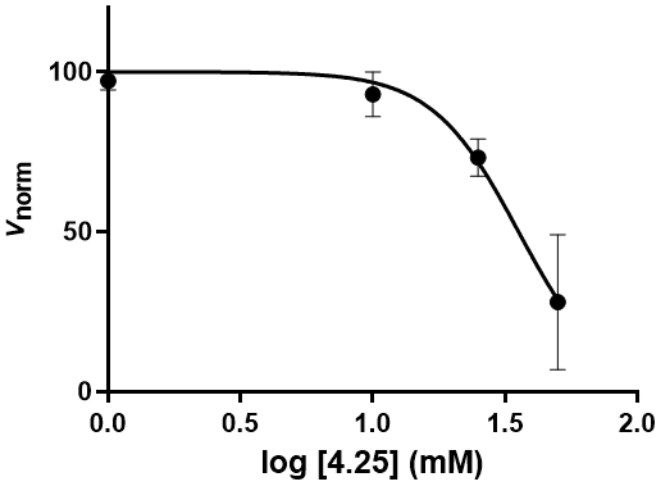

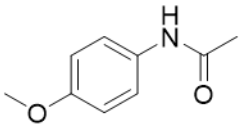

4.25

IC_{50} = 36 mM
$CI_{95\%}$ = [29 , 44]
Hillslope = -2.7
[Maximum] = 50 mM

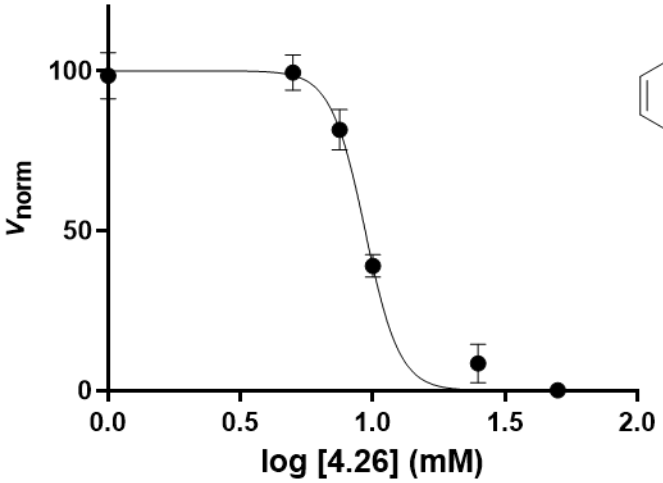

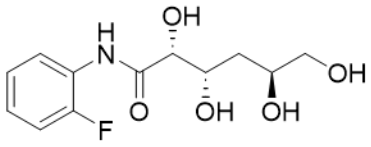

4.26

IC_{50} = 9.4 mM
$CI_{95\%}$ = [8.8 , 10]
Hillslope = -6.7
[Maximum] = 50 mM

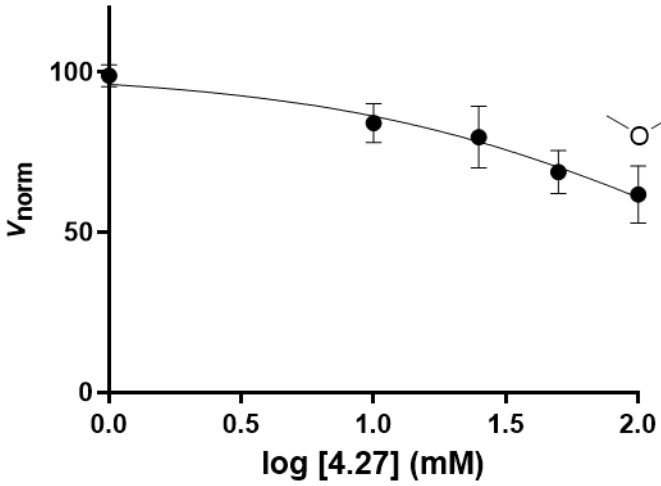

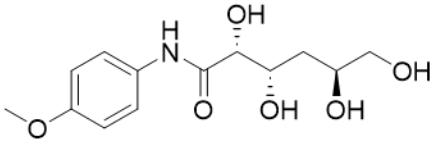

4.27

IC_{50} = N/A
$CI_{95\%}$ = N/A
Hillslope = N/A
[Maximum] = 100 mM

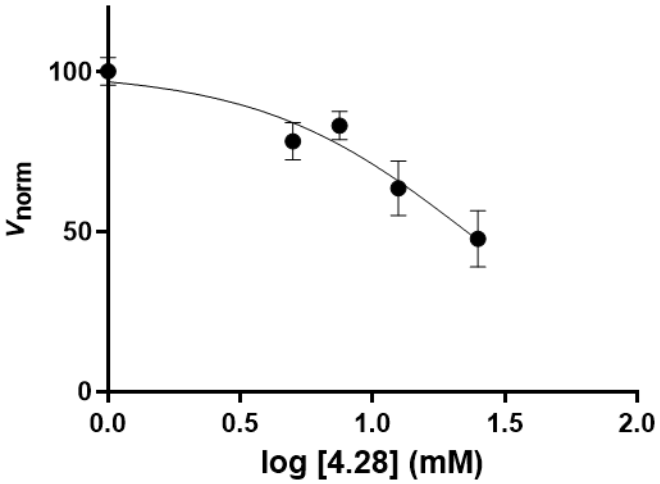

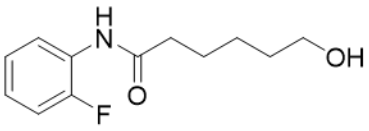

4.28

IC_{50} = 23 mM
$CI_{95\%}$ = [15 , 57]
Hillslope = -1.1
[Maximum] = 25 mM

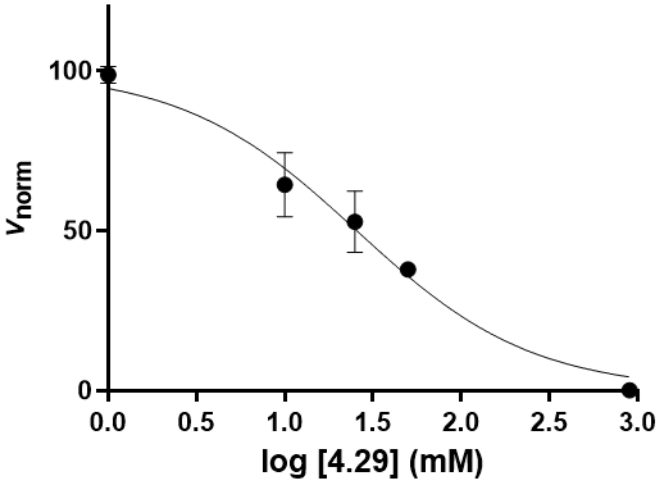

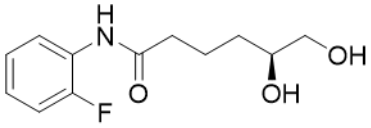

4.29

IC_{50} = 26 mM
$CI_{95\%}$ = [16 , 41]
Hillslope = -0.9
[Maximum] = 900 mM

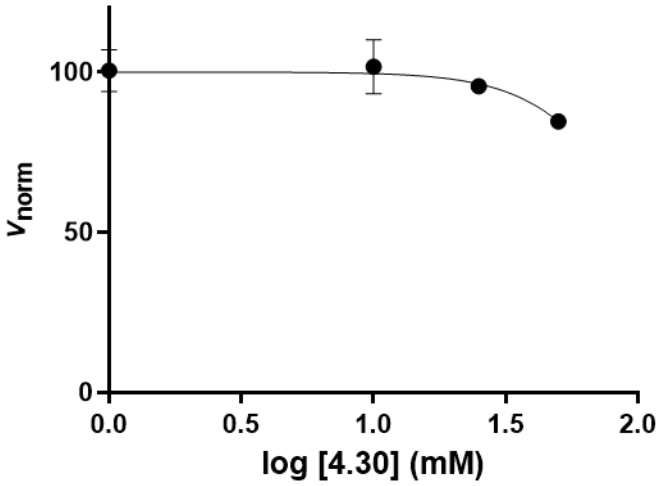

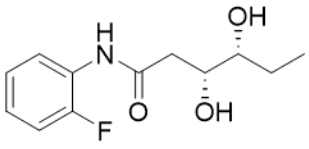

4.30

IC_{50} = N/A
$CI_{95\%}$ = N/A
Hillslope = N/A
[Maximum] = 50 mM

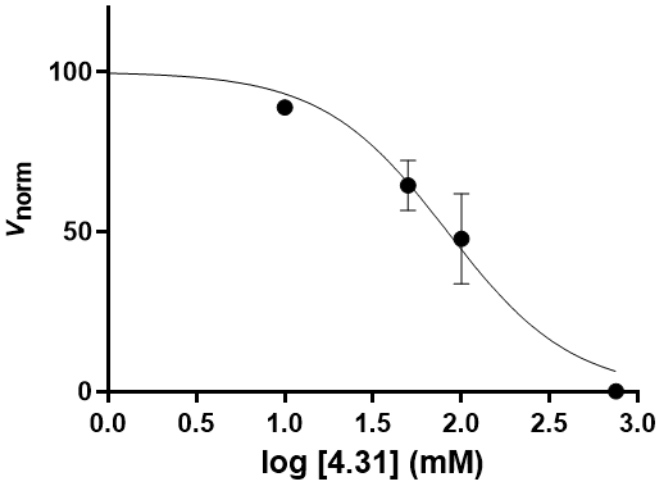

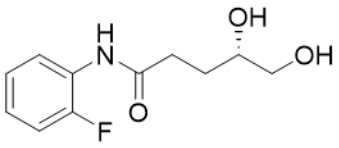

4.31

IC_{50} = 83 mM
$CI_{95\%}$ = [43 , 165]
Hillslope = -1.2
[Maximum] = 750 mM

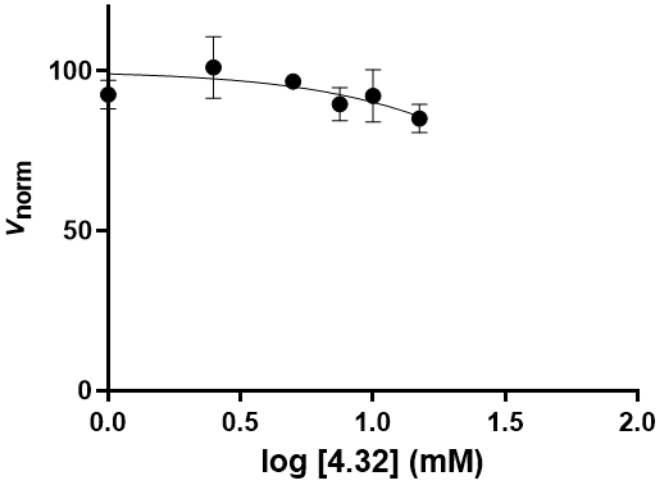

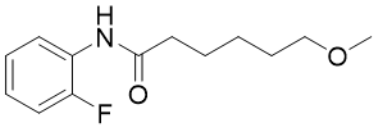

4.32

IC_{50} = N/A
$CI_{95\%}$ = N/A
Hillslope = N/A
[Maximum] = 15 mM

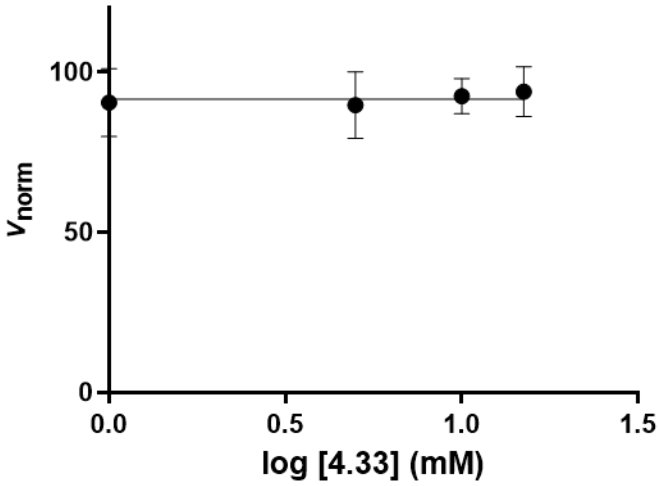

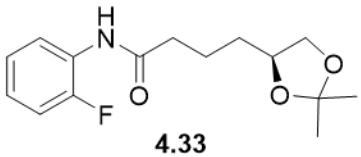

4.33

IC_{50} = N/A
$CI_{95\%}$ = N/A
Hillslope = N/A
[Maximum] = 15 mM

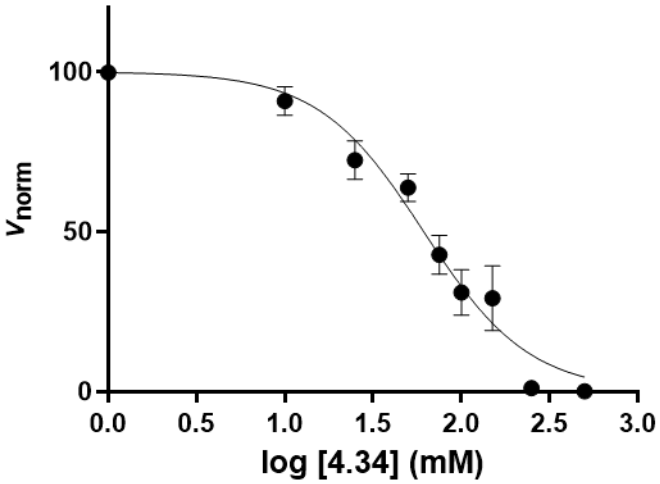

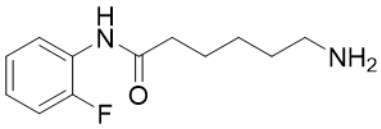

4.34

IC_{50} = 61 mM
$CI_{95\%}$ = [48 , 78]
Hillslope = -1.5
[Maximum] = 500 mM

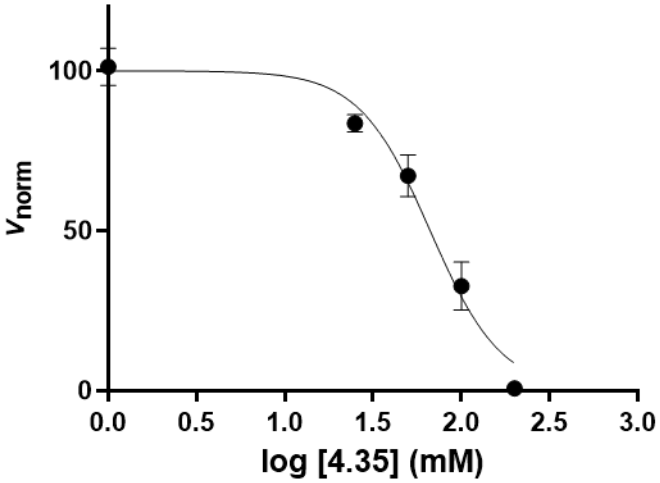

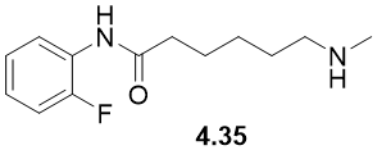

4.35

IC_{50} = 67 mM
$CI_{95\%}$ = [50 , 87]
Hillslope = -2.2
[Maximum] = 200 mM

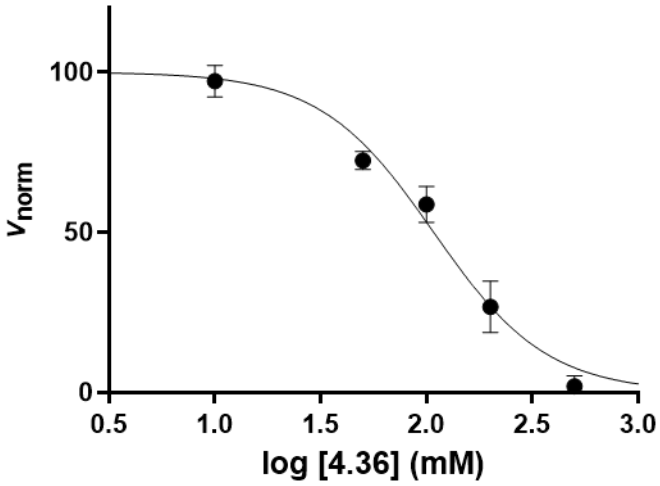

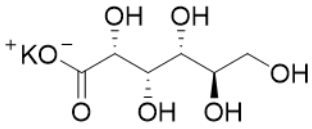

4.36

IC_{50} = 108 mM
$CI_{95\%}$ = [78 , 145]
Hillslope = -1.6
[Maximum] = 500 mM

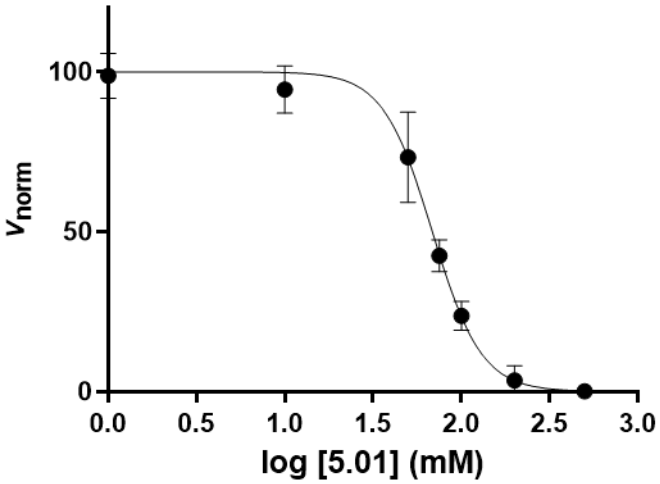

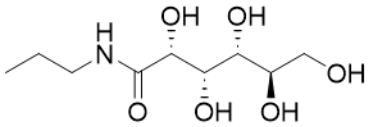

5.01

IC_{50} = 69 mM
$CI_{95\%}$ = [65 , 72]
Hillslope = -3.1
[Maximum] = 500 mM

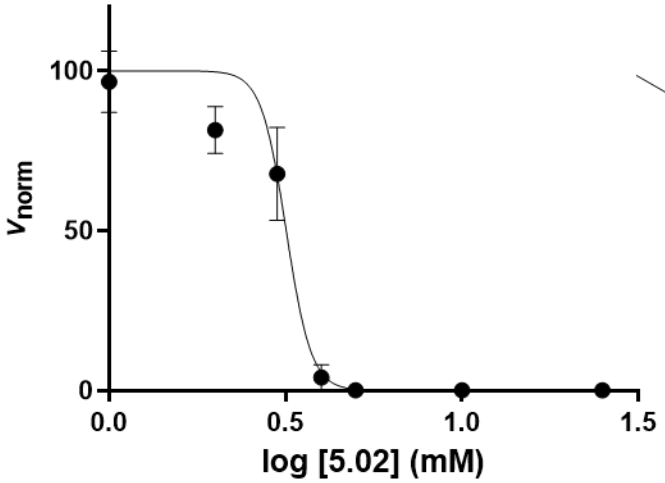

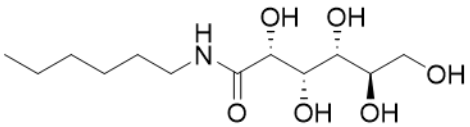

5.02

IC_{50} = 3.2 mM
$CI_{95\%}$ = [2.8 , 3.5]
Hillslope = -12
[Maximum] = 25 mM

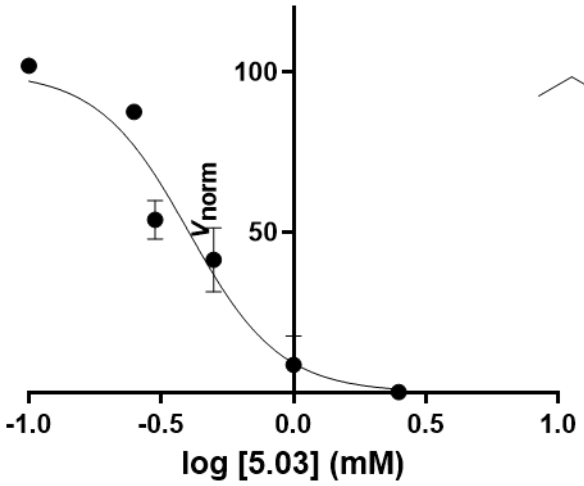

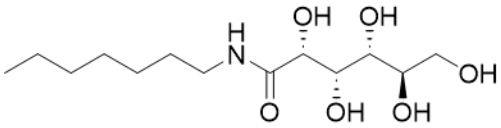

5.03

IC_{50} = 0.4 mM
$CI_{95\%}$ = [0.30 , 0.55]
Hillslope = -2.5
[Maximum] = 2.5 mM

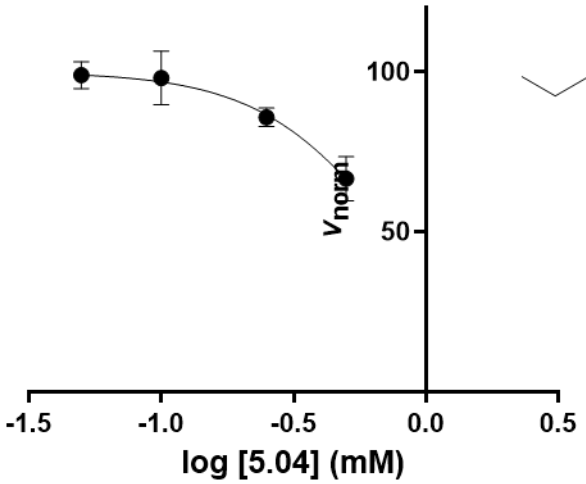

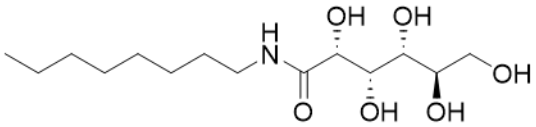

5.04

IC_{50} = N/A
$CI_{95\%}$ = N/A
Hillslope = N/A
[Maximum] = 0.5 mM

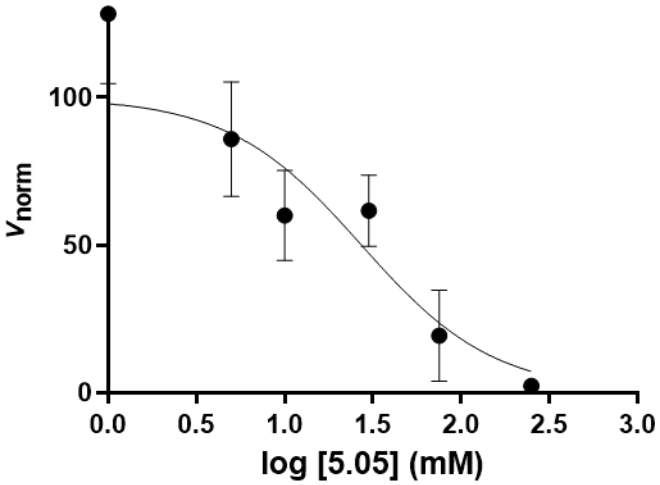

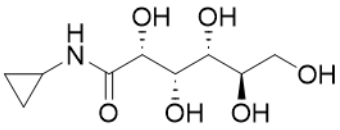

5.05

IC_{50} = 27 mM
$CI_{95\%}$ = [7.8 , 110]
Hillslope = -1.2
[Maximum] = 250 mM

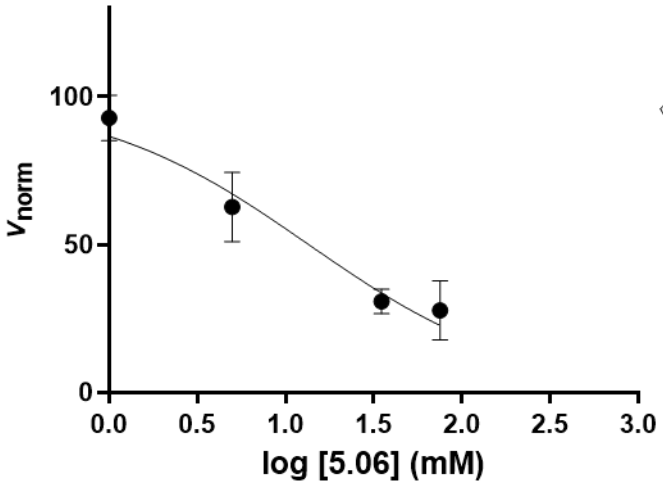

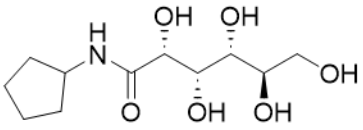

5.06

IC_{50} = 14 mM
$CI_{95\%}$ = [4.3 , 45]
Hillslope = -0.72
[Maximum] = 75 mM

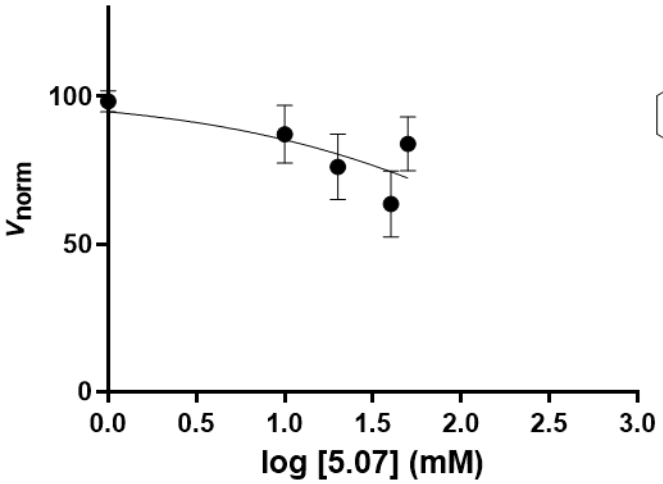

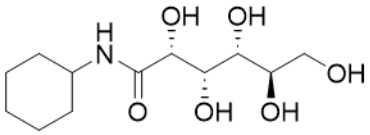

5.07

IC_{50} = N/A
$CI_{95\%}$ = N/A
Hillslope = N/A
[Maximum] = 50 mM

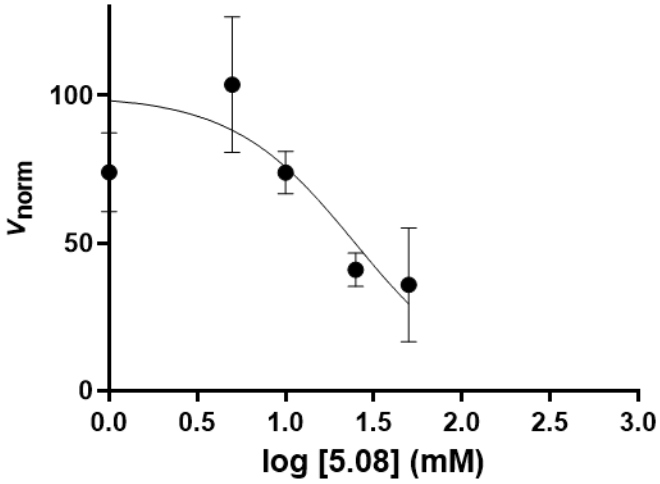

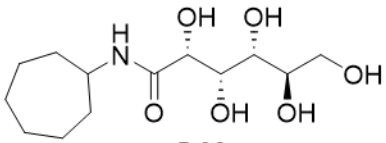

5.08

IC_{50} = 25 mM
$CI_{95\%}$ = [3.4 , inf.]
Hillslope = -1.3
[Maximum] = 50 mM

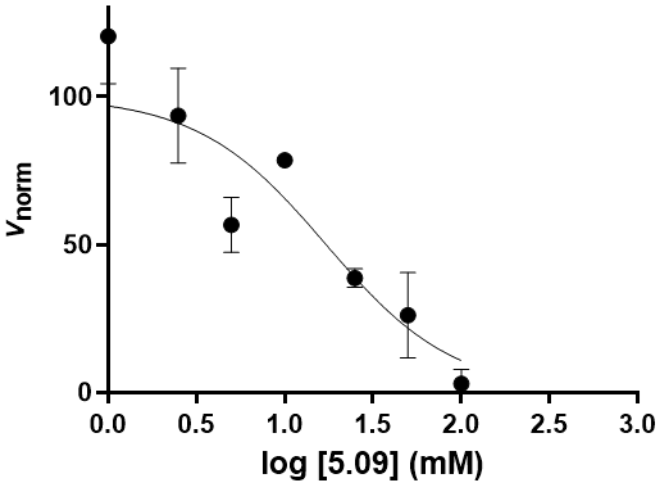

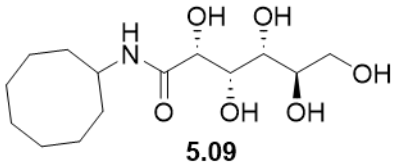

5.09

IC_{50} = 17 mM
$CI_{95\%}$ = [7.1 , 43]
Hillslope = -1.2
[Maximum] = 100 mM

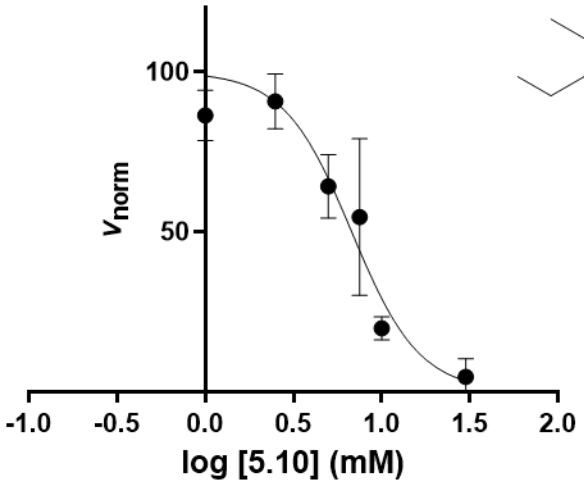

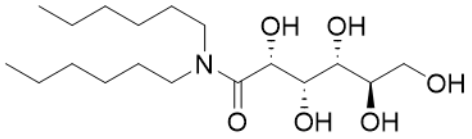

5.10

IC_{50} = 6.8 mM
$CI_{95\%}$ = [4.8 , 9.3]
Hillslope = -2.3
[Maximum] = 30 mM

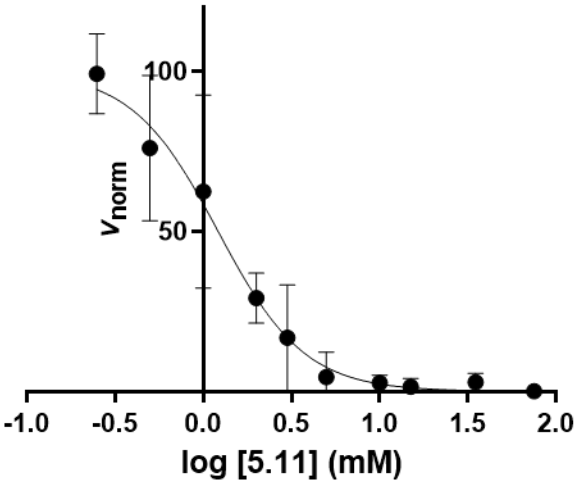

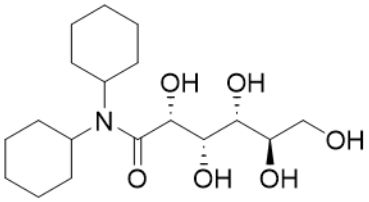

5.11

IC_{50} = 1.2 mM
$CI_{95\%}$ = [1.1 , 1.4]
Hillslope = -1.8
[Maximum] = 75 mM

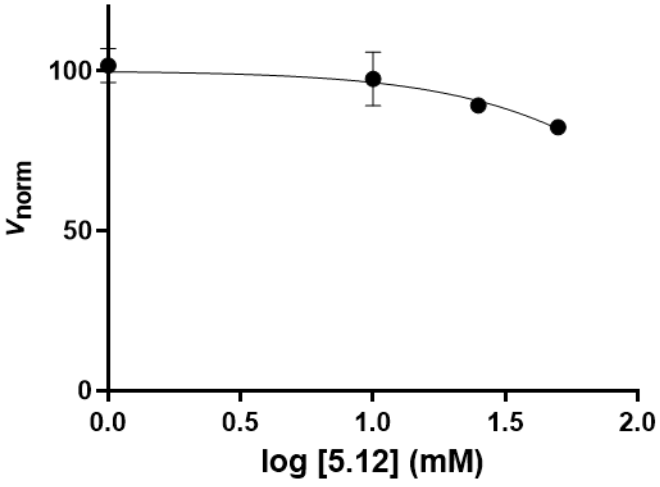

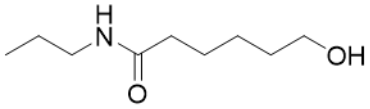

5.12

IC_{50} = N/A
$CI_{95\%}$ = N/A
Hillslope = N/A
[Maximum] = 50 mM

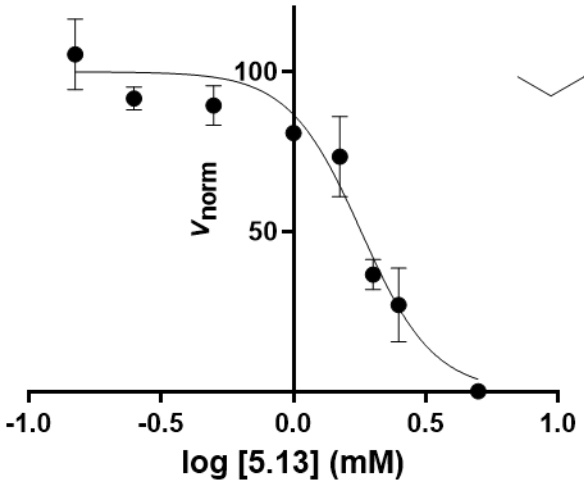

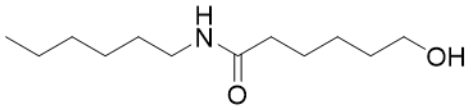

5.13

IC_{50} = 1.8 mM
$CI_{95\%}$ = [1.5 , 2.1]
Hillslope = -3.2
[Maximum] = 5 mM

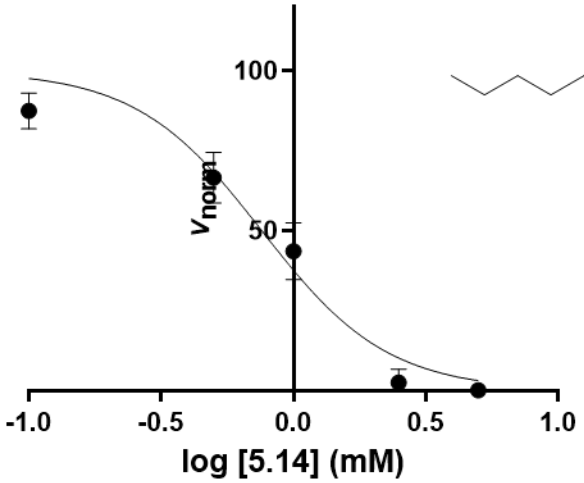

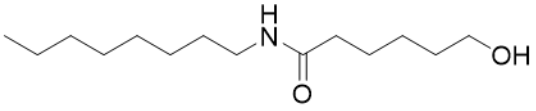

5.14

IC_{50} = 0.76 mM
$CI_{95\%}$ = [0.41 , 1.2]
Hillslope = -1.8
[Maximum] = 5 mM

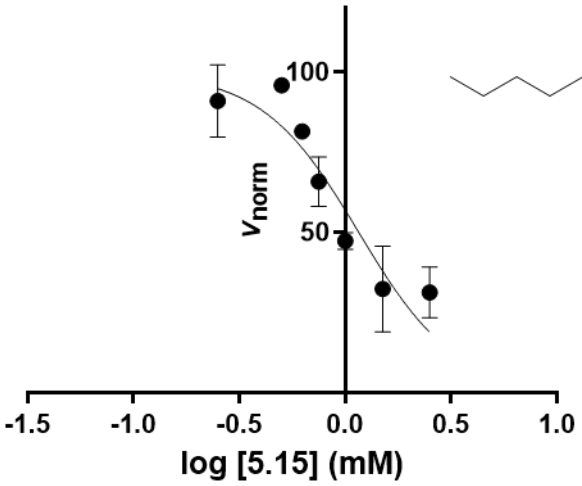

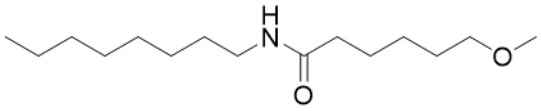

5.15

IC_{50} = 1.2 mM
$CI_{95\%}$ = [0.88 , 1.7]
Hillslope = -1.9
[Maximum] = 2.5 mM

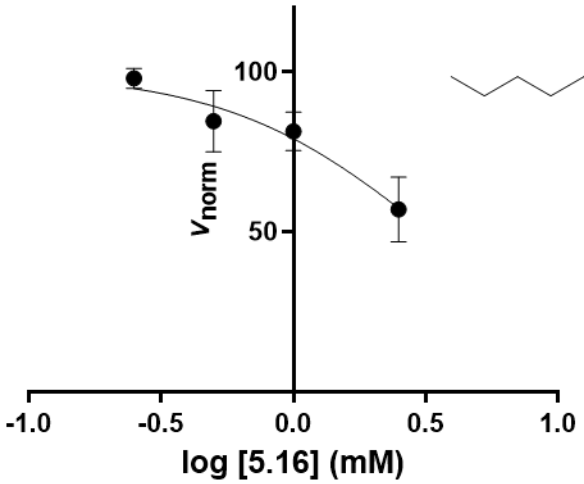

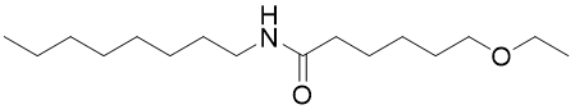

5.16

IC_{50} = 3.2 mM
$CI_{95\%}$ = [1.9 , 30]
Hillslope = -1.1
[Maximum] = 2.5 mM

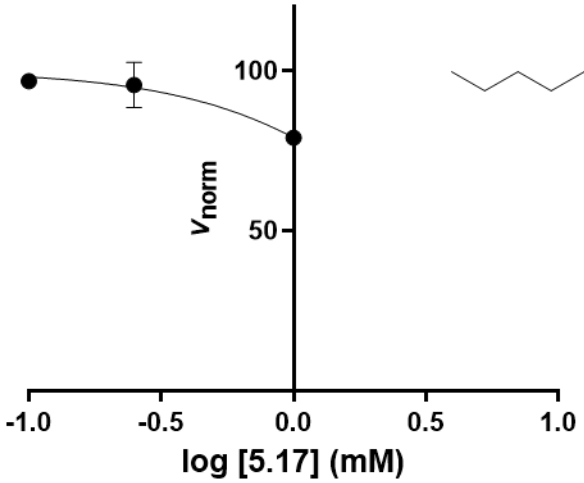

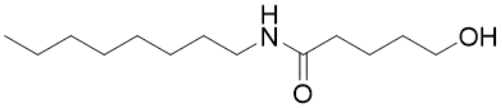

5.17

IC_{50} = N/A
$CI_{95\%}$ = N/A
Hillslope = N/A
[Maximum] = 1 mM

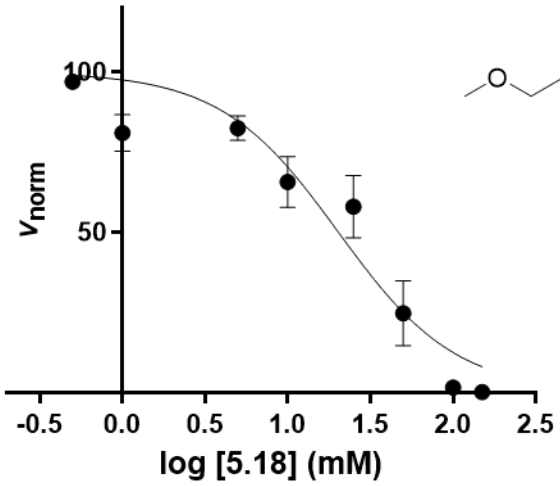

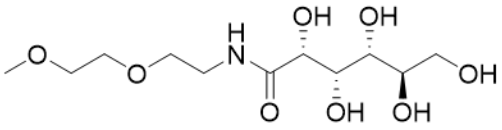

5.18

IC_{50} = 20 mM
$CI_{95\%}$ = [11 , 34]
Hillslope = -1.2
[Maximum] = 150 mM

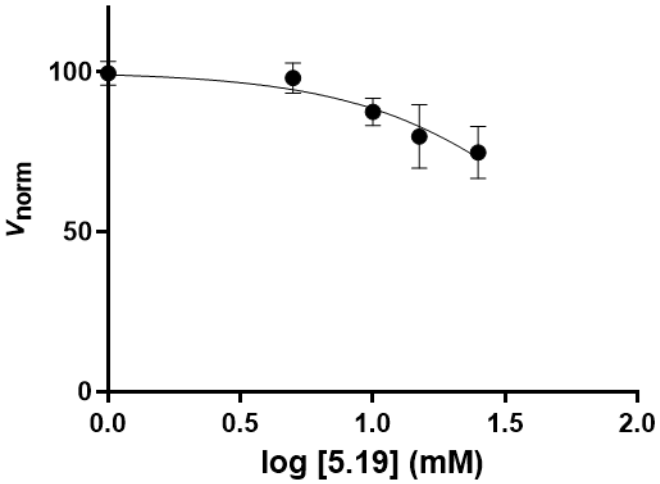

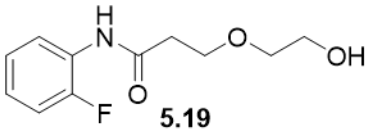

5.19

IC_{50} = N/A
$CI_{95\%}$ = N/A
Hillslope = N/A
[Maximum] = 25 mM

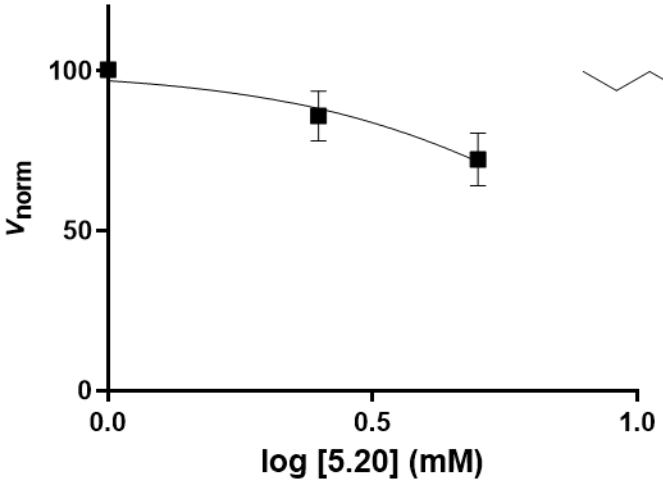

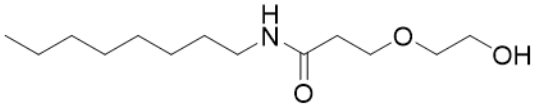

5.20

IC_{50} = N/A
$CI_{95\%}$ = N/A
Hillslope = N/A
[Maximum] = 5 mM

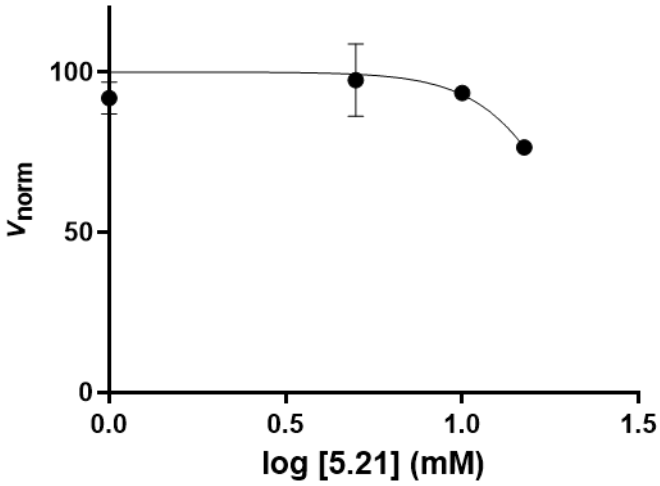

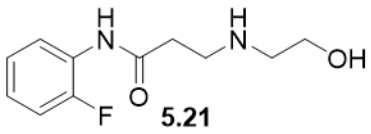

5.21

IC_{50} = N/A
$CI_{95\%}$ = N/A
Hillslope = N/A
[Maximum] = 15 mM

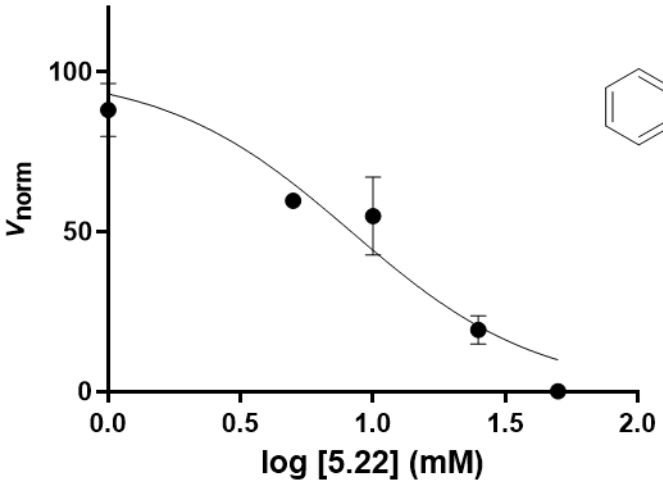

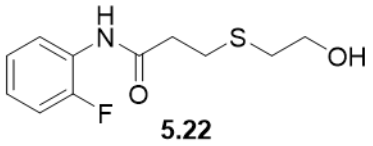

5.22

IC_{50} = 8.3 mM
$CI_{95\%}$ = [3.6 , 15]
Hillslope = -1.2
[Maximum] = 50 mM

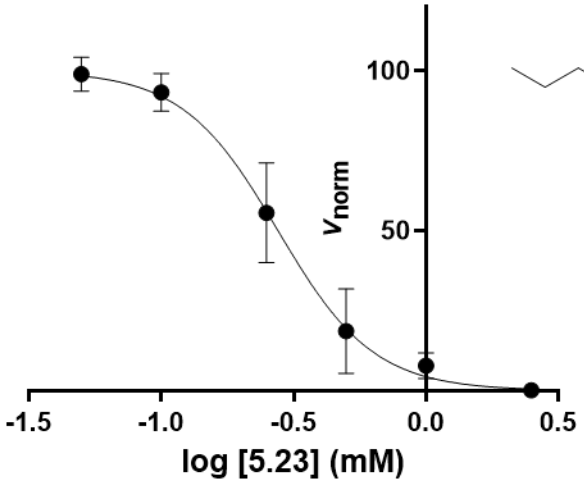

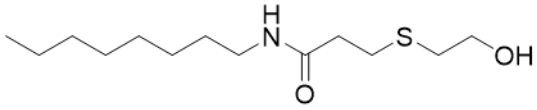

5.23

IC_{50} = 0.28 mM
$CI_{95\%}$ = [0.26 , 0.30]
Hillslope = -2.4
[Maximum] = 2.5 mM

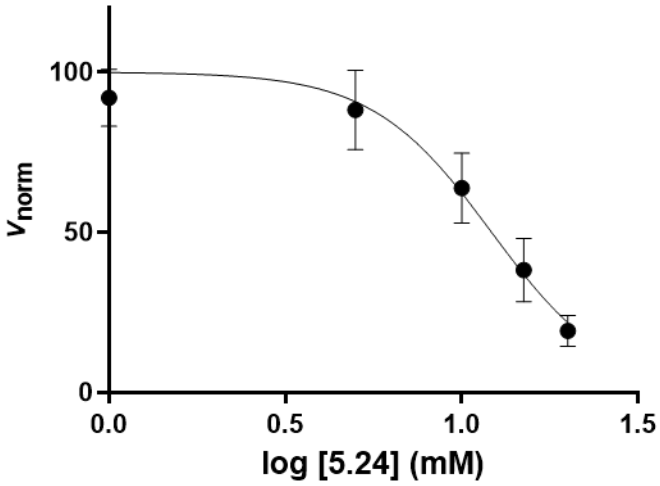

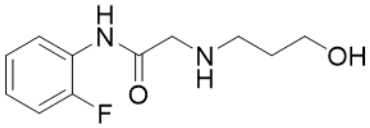

5.24

IC_{50} = 12 mM
$CI_{95\%}$ = [10 , 14]
Hillslope = -2.6
[Maximum] = 20 mM

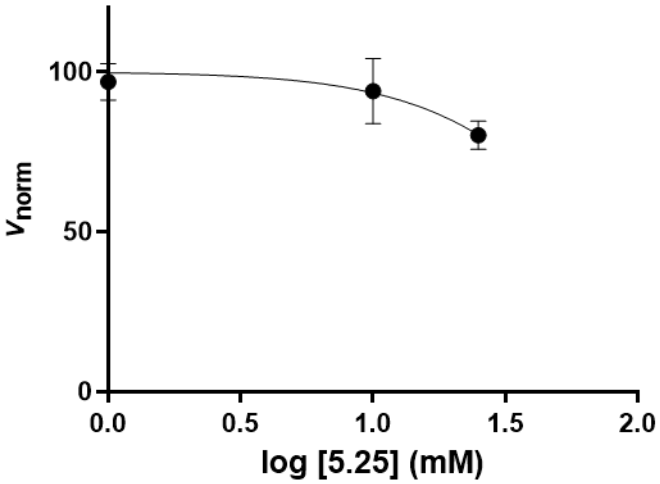

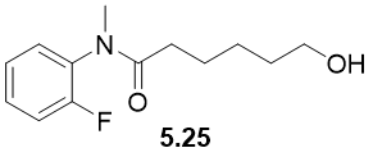

5.25

IC_{50} = N/A
$CI_{95\%}$ = N/A
Hillslope = N/A
[Maximum] = 25 mM

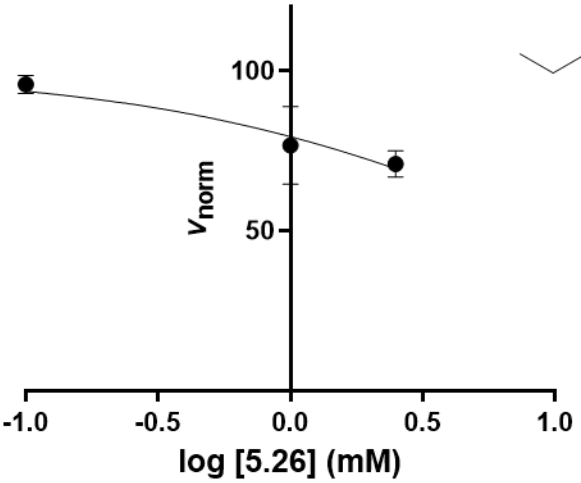

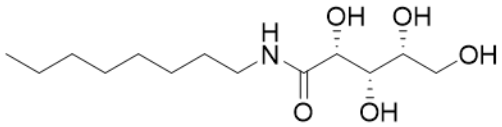

5.26

IC_{50} = N/A
$CI_{95\%}$ = N/A
Hillslope = N/A
[Maximum] = 2.5 mM

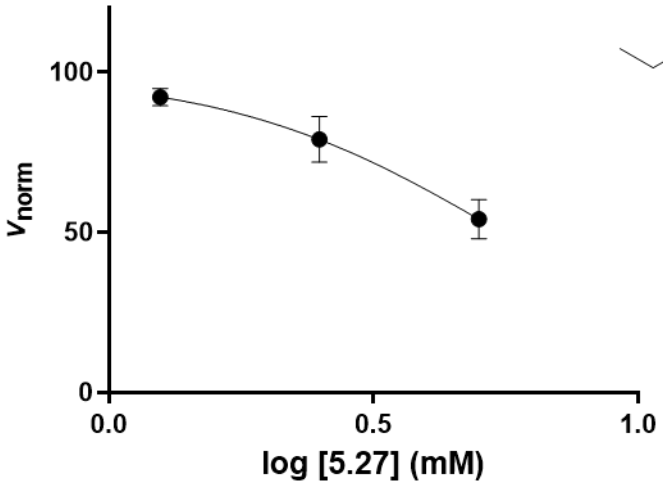

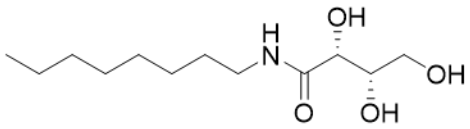

5.27

IC_{50} = N/A
$CI_{95\%}$ = N/A
Hillslope = N/A
[Maximum] = 5 mM

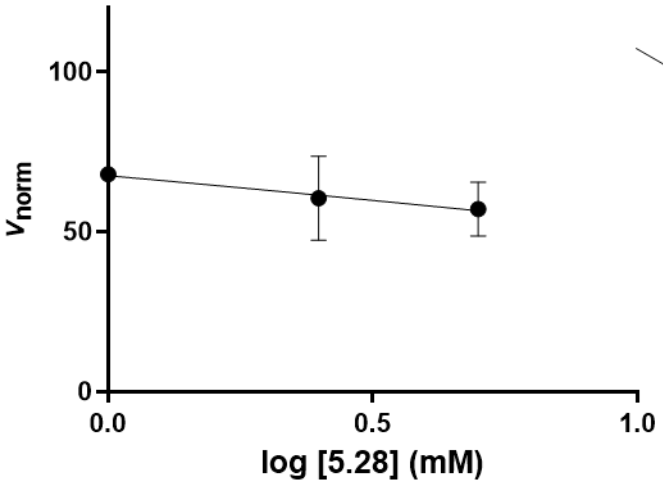

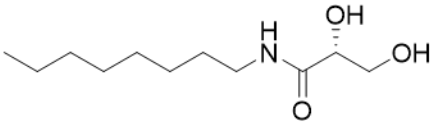

5.28

IC_{50} = N/A
$CI_{95\%}$ = N/A
Hillslope = N/A
[Maximum] = 5 mM

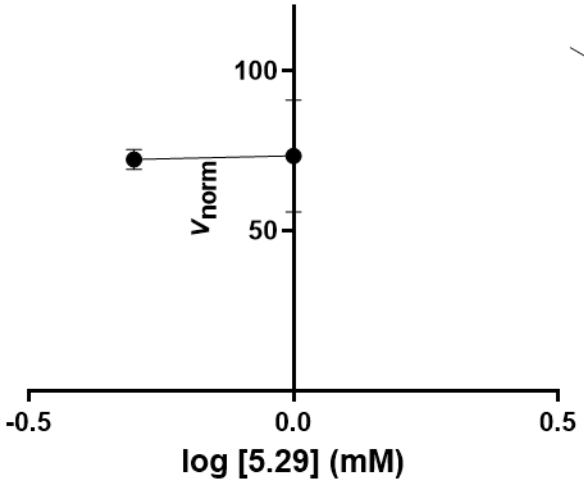

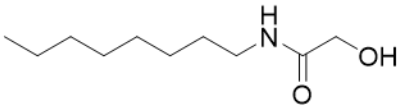

5.29

IC_{50} = N/A
$CI_{95\%}$ = N/A
Hillslope = N/A
[Maximum] = 1 mM

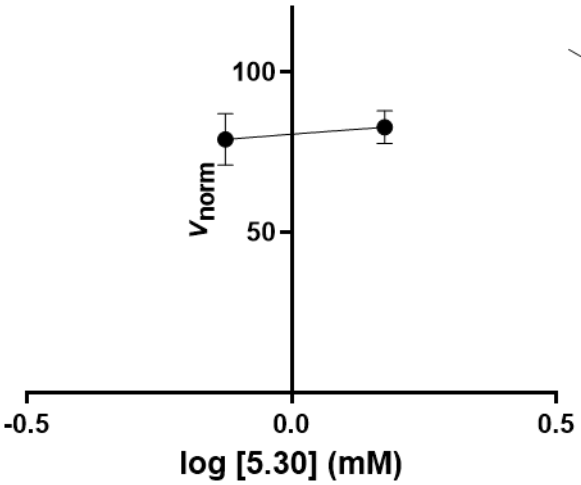

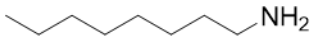

5.30

IC_{50} = N/A
$CI_{95\%}$ = N/A
Hillslope = N/A
[Maximum] = 1.5 mM